

METHODS AND APPLICATION IN DRUG METABOLISM AND TRANSPORT: 2021

EDITED BY: Ren-ai Xu, Jiao Zheng and Sabina Passamonti
PUBLISHED IN: Frontiers in Pharmacology





frontiers

Frontiers eBook Copyright Statement

The copyright in the text of individual articles in this eBook is the property of their respective authors or their respective institutions or funders. The copyright in graphics and images within each article may be subject to copyright of other parties. In both cases this is subject to a license granted to Frontiers.

The compilation of articles constituting this eBook is the property of Frontiers.

Each article within this eBook, and the eBook itself, are published under the most recent version of the Creative Commons CC-BY licence.

The version current at the date of publication of this eBook is CC-BY 4.0. If the CC-BY licence is updated, the licence granted by Frontiers is automatically updated to the new version.

When exercising any right under the CC-BY licence, Frontiers must be attributed as the original publisher of the article or eBook, as applicable.

Authors have the responsibility of ensuring that any graphics or other materials which are the property of others may be included in the CC-BY licence, but this should be checked before relying on the CC-BY licence to reproduce those materials. Any copyright notices relating to those materials must be complied with.

Copyright and source acknowledgement notices may not be removed and must be displayed in any copy, derivative work or partial copy which includes the elements in question.

All copyright, and all rights therein, are protected by national and international copyright laws. The above represents a summary only. For further information please read Frontiers' Conditions for Website Use and Copyright Statement, and the applicable CC-BY licence.

ISSN 1664-8714

ISBN 978-2-83250-796-4

DOI 10.3389/978-2-83250-796-4

About Frontiers

Frontiers is more than just an open-access publisher of scholarly articles: it is a pioneering approach to the world of academia, radically improving the way scholarly research is managed. The grand vision of Frontiers is a world where all people have an equal opportunity to seek, share and generate knowledge. Frontiers provides immediate and permanent online open access to all its publications, but this alone is not enough to realize our grand goals.

Frontiers Journal Series

The Frontiers Journal Series is a multi-tier and interdisciplinary set of open-access, online journals, promising a paradigm shift from the current review, selection and dissemination processes in academic publishing. All Frontiers journals are driven by researchers for researchers; therefore, they constitute a service to the scholarly community. At the same time, the Frontiers Journal Series operates on a revolutionary invention, the tiered publishing system, initially addressing specific communities of scholars, and gradually climbing up to broader public understanding, thus serving the interests of the lay society, too.

Dedication to Quality

Each Frontiers article is a landmark of the highest quality, thanks to genuinely collaborative interactions between authors and review editors, who include some of the world's best academicians. Research must be certified by peers before entering a stream of knowledge that may eventually reach the public - and shape society; therefore, Frontiers only applies the most rigorous and unbiased reviews. Frontiers revolutionizes research publishing by freely delivering the most outstanding research, evaluated with no bias from both the academic and social point of view. By applying the most advanced information technologies, Frontiers is catapulting scholarly publishing into a new generation.

What are Frontiers Research Topics?

Frontiers Research Topics are very popular trademarks of the Frontiers Journals Series: they are collections of at least ten articles, all centered on a particular subject. With their unique mix of varied contributions from Original Research to Review Articles, Frontiers Research Topics unify the most influential researchers, the latest key findings and historical advances in a hot research area! Find out more on how to host your own Frontiers Research Topic or contribute to one as an author by contacting the Frontiers Editorial Office: frontiersin.org/about/contact

METHODS AND APPLICATION IN DRUG METABOLISM AND TRANSPORT: 2021

Topic Editors:

Ren-ai Xu, First Affiliated Hospital of Wenzhou Medical University, China

Jiao Zheng, Shanghai Jiao Tong University, China

Sabina Passamonti, University of Trieste, Italy

Citation: Xu, R.-a., Zheng, J., Passamonti, S., eds. (2022). Methods and Application in Drug Metabolism and Transport: 2021.

Lausanne: Frontiers Media SA. doi: 10.3389/978-2-83250-796-4

Table of Contents

- 05** *Discovery of the Potential Novel Pharmacodynamic Substances From Zhi-Zi-Hou-Po Decoction Based on the Concept of Co-Decoction Reaction and Analysis Strategy*
Xin Feng, Yuelin Bi, Jiaqi Wang, Tianyi Li, Gengyuan Yu, Tonghua Zhang, Haoran Xu, Chenning Zhang and Yikun Sun
- 18** *A Retrospective Metabolomics Analysis of Gamma-Hydroxybutyrate in Humans: New Potential Markers and Changes in Metabolism Related to GHB Consumption*
Tingting Wang, Kirstine L. Nielsen, Kim Frisch, Johan K. Lassen, Camilla B. Nielsen, Charlotte U. Andersen, Palle Villesen, Mette F. Andreasen, Jørgen B. Hasselstrøm and Mogens Johannsen
- 34** *Comprehensive Metabolomics and Network Pharmacology to Explore the Mechanism of 5-Hydroxymethyl Furfural in the Treatment of Blood Deficiency Syndrome*
Wensen Zhang, Na Cui, Fazhi Su, Yangyang Wang, Bingyou Yang, Yanping Sun, Wei Guan, Haixue Kuang and QiuHong Wang
- 50** *Evaluation and Application of Population Pharmacokinetic Models for Identifying Delayed Methotrexate Elimination in Patients With Primary Central Nervous System Lymphoma*
Junjun Mao, Qing Li, Pei Li, Weiwei Qin, Bobin Chen and MingKang Zhong
- 62** *Elucidating a Complicated Enantioselective Metabolic Profile: A Study From Rats to Humans Using Optically Pure Doxazosin*
Dezhi Kong, Yuan Tian, Kunfeng Duan, Wenyan Guo, Qingning Zhang, Panpan Zhang, Zuxiao Yang, Xia Qin, Leiming Ren and Wei Zhang
- 81** *Application of Physiologically Based Pharmacokinetic Modeling in Preclinical Studies: A Feasible Strategy to Practice the Principles of 3Rs*
Yawen Yuan, Qingfeng He, Shunguo Zhang, Min Li, Zhijia Tang, Xiao Zhu, Zheng Jiao, Weimin Cai and Xiaoqiang Xiang
- 99** *Mechanism-Based Pharmacokinetic Model for the Deglycosylation Kinetics of 20(S)-Ginsenosides Rh2*
Hong-can Ren, Jian-guo Sun, Ji-ye A, Sheng-hua Gu, Jian Shi, Feng Shao, Hua Ai, Jing-wei Zhang, Ying Peng, Bei Yan, Qing Huang, Lin-sheng Liu, Yang Sai, Guang-ji Wang and Cheng-guang Yang
- 110** *Beneficial Effect of Edoxaban on Preventing Atrial Fibrillation and Coagulation by Reducing Inflammation via HBG1/HBD Biomarkers*
Chenguang Yang, Xiang Wang, Ying Guo, Xuyang Meng, Yi Li, Chenxi Xia, Lingbing Meng, Min Dong and Fang Wang
- 135** *Screening of Biomarkers and Toxicity Mechanisms of Rifampicin-Induced Liver Injury Based on Targeted Bile Acid Metabolomics*
Yang Deng, Xilin Luo, Xin Li, Yisha Xiao, Bing Xu and Huan Tong
- 149** *UPLC-MS/MS Technology for the Quantitative Methodology and Pharmacokinetic Analysis of Voxalisib in Rat Plasma*
Qingqing Li, Ya-nan Liu, Jing Wang, Yingying Hu, Jinyu Hu, Ren-ai Xu, Liu Shao and Lianguo Chen

- 156** *An Efficient UPLC-MS/MS Method Established to Detect Relugolix Concentration in Rat Plasma*
Liyang Xing, Ya-nan Liu, Hongye Yao, Tingting Wang, Fuchen Xie, Shunbin Luo, Pingping Luo and Shengling Tang
- 164** *Population Pharmacokinetics and Dosing Regimen of Lithium in Chinese Patients With Bipolar Disorder*
Zi-bin Jin, Zhuo Wu, Yi-fan Cui, Xue-peng Liu, Hong-bo Liang, Jia-yong You and Chen-yu Wang
- 172** *Instability Mechanism of Osimertinib in Plasma and a Solving Strategy in the Pharmacokinetics Study*
Zheng Yuan, Xin Yu, Siyang Wu, Xiaonan Wu, Qiutao Wang, Wenhao Cheng, Weiyu Hu, Chen Kang, Wei Yang, Yingfei Li and Xiao-Yang Zhou
- 183** *Simultaneous Absolute Protein Quantification of Seven Cytochrome P450 Isoforms in Rat Liver Microsomes by LC-MS/MS-based Isotope Internal Standard Method*
Fulin Jiang, Chang Zhang, Zihan Lu, Jingyu Liu, Peiqing Liu, Min Huang and Guoping Zhong



Discovery of the Potential Novel Pharmacodynamic Substances From Zhi-Zi-Hou-Po Decoction Based on the Concept of Co-Decoction Reaction and Analysis Strategy

Xin Feng¹, Yuelin Bi¹, Jiaqi Wang¹, Tianyi Li¹, Gengyuan Yu¹, Tonghua Zhang¹, Haoran Xu¹, Chenning Zhang^{1,2*} and Yikun Sun^{1*}

¹School of Chinese Materia Medica, Beijing University of Chinese Medicine, Beijing, China, ²Department of Pharmacy, Zigong First People's Hospital, Zigong, China

OPEN ACCESS

Edited by:

Sabina Passamonti,
University of Trieste, Italy

Reviewed by:

Xu Zhao,
Shenyang Pharmaceutical University,
China
Longshan Zhao,
Shenyang Pharmaceutical University,
China

*Correspondence:

Chenning Zhang
zhangcn1118@163.com
Yikun Sun
sunyk@bucm.edu.cn

Specialty section:

This article was submitted to
Drug Metabolism and Transport,
a section of the journal
Frontiers in Pharmacology

Received: 07 December 2021

Accepted: 24 December 2021

Published: 13 January 2022

Citation:

Feng X, Bi Y, Wang J, Li T, Yu G, Zhang T, Xu H, Zhang C and Sun Y (2022) Discovery of the Potential Novel Pharmacodynamic Substances From Zhi-Zi-Hou-Po Decoction Based on the Concept of Co-Decoction Reaction and Analysis Strategy. *Front. Pharmacol.* 12:830558. doi: 10.3389/fphar.2021.830558

Background: Zhi-Zi-Hou-Po Decoction (ZZHPD), a classic traditional Chinese medicine (TCM) formula, is clinically used to treat insomnia and depression. The analysis strategy based on the concept of co-decoction of TCM is helpful to analyse the effective substances of TCM formula in depth.

Aim of the study: This manuscript intends to take ZZHPD as a model sample to explore the phenomenon of co-decoction of complex formula in the combination of liquid chromatography-mass spectrometry (LC-MS) technology, data analysis, and molecular docking.

Materials and methods: In the current research, an innovative LC-MS method has been established to study the active ingredients in ZZHPD, and to identify the ingredients absorbed into the blood and brain tissues of mice. And molecular docking was used to study the binding pattern and affinities of known compounds of the brain tissue toward insomnia related proteins.

Results: Based on new processing methods and analysis strategies, 106 chemical components were identified in ZZHPD, including 28 blood components and 18 brain components. Then, by comparing the different compounds in the co-decoction and single decoction, it was surprisingly found that 125 new ingredients were produced during the co-decoction, 2 of which were absorbed into the blood and 1 of which was absorbed into brain tissue. Ultimately, molecular docking studies showed that 18 brain components of ZZHPD had favourable binding conformation and affinity with GABA, serotonin and melatonin receptors. The docking results of GABRA1 with naringenin and hesperidin, HCRTR1 with naringenin-7-O-glucoside, poncirenin and genipin 1-gentiobioside, and luteolin with SLC6A4, GLO1, MAOB

Abbreviations: ZZHPD, Zhi-Zi-Hou-Po Decoction; LC-MS, liquid chromatography-mass spectrometry; GF, Gardeniae Fructus; AFI, Aurantii Fructus Immaturus; MOC, Magnoliae Officinalis Cortex; TCM, traditional Chinese medicine; BBB, blood-brain barrier; BZRAs, Benzodiazepine receptor agonists; BZDs, benzodiazepines BZRDs, benzodiazepine related drugs; GABA, act on the gamma-aminobutyric acid.

and MTNR1A may clarify the mechanism of action of ZZHPD in treating insomnia and depression.

Conclusion: Our study may provide new ideas for further exploring the effective substances in ZZHPD.

Keywords: Zhi-Zi-Hou-Po decoction, co-decoction, UPLC-QE-Orbitrap-MS, new compound, molecular docking

INTRODUCTION

Fast-paced city life has aggravated the pressure on people's lives, causing people to fall into the dilemma of anxiety, insomnia and even depression, and prevalence of the symptoms has severely affected people's quality of life. Long-term insomnia can induce many complications, and can even cause sudden death (Liu X et al., 2021). Zhi-Zi-Hou-Po Decoction (ZZHPD) is composed of three Chinese medicinal herbs: *Gardeniae Fructus* (GF), *Aurantii Fructus Immaturus* (AFI) and *Magnoliae Officinalis Cortex* (MOC) (Table 1). ZZHPD is a classic herbal formula in traditional Chinese medicine (TCM), derived from “*Shang Han Lun*”, and has been used for the treatment of anxiety and insomnia for more than a thousand years (Xing et al., 2015). Scientists have revealed that the mechanism of ZZHPD in treating insomnia may be related to restoring the function of the hypothalamus-pituitary-adrenal axis, increasing the expression of hippocampal brain-derived neurotrophic factor and promoting the healing of the hippocampal nerve function (Zhu et al., 2020).

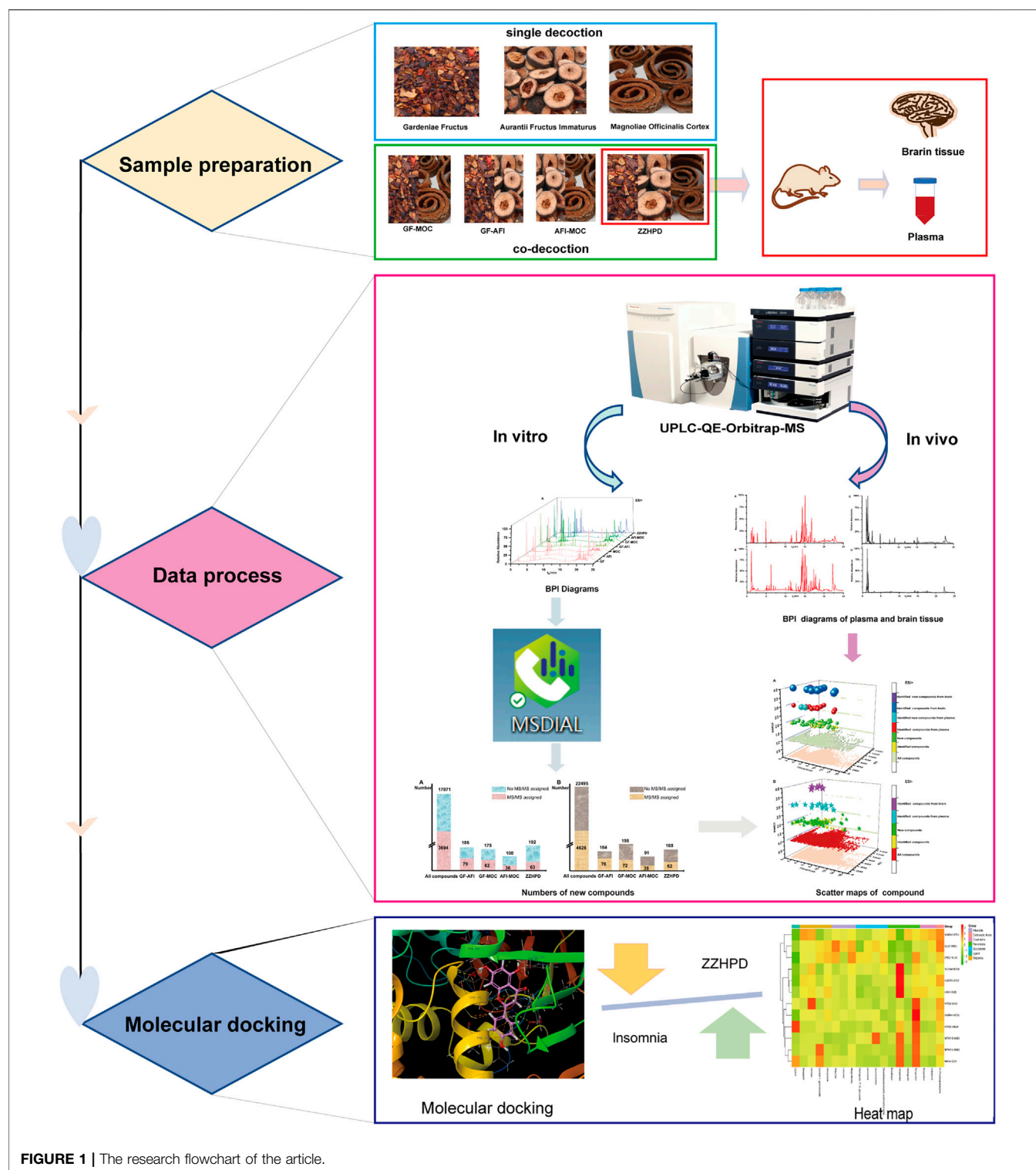
The controversy between the efficacy of TCM formula and single herb has always been the centre of discussion among scholars. Jin Xiaoling *et al.* found that the protective effect of each single herbs was weaker than that of the whole prescriptions when studying the protective effect of Sheng-Xian decoction on cardiomyocytes (Chen L et al., 2021). Compared with single herbs, Yi-Qi-Jie-Du-Hua-Yu formula plays a more important role in inhibiting the expression of Smad3 mRNA in glomerular mesangial cells and promoting the expression of Smad7 mRNA in mesangial cells (Wang et al., 2019). Similarly, Song Dongmei *et al.* confirmed that Tong-Xin-Luo formula has a better curative effect on vascular endothelial damage, collateral stasis and collateral dysfunction compared with single herbs (Song et al., 2013). The above studies have shown that the effect of TCM formula is better than that of single herbs. Single herbs are mostly used as prescriptions, and their role is to influence each other's efficacy on the basis of the efficacy of single herbs, rather than just generating a simple additive effect of the single herbs (Zhou et al., 2017). So, why does the prescription play a more important

role than the single herbs? Some scholars believe that the physical and chemical properties of single herbs are changed after compatibility, and that the efficacy will be enhanced to a certain extent (Zhang et al., 2020). Research has verified that the dissolution of the main ingredients in ZZHPD is affected by compatibility, and the anti-anxiety effect of ZZHPD is exerted based on the multi-component coordination (Chu et al., 2017). This effect is the biological performance of the TCM formula after intervention by active components under pathological conditions. According to the hypothesis of TCM, the multiple active phytochemical components in TCM formula can exert their medicinal effects through multiple molecules and multiple pathways, and may achieve better effects than a single herb. Therefore, it is of great significance to study the effective ingredients of TCM formula and explain the mechanism of compatibility (Wang et al., 2013). In the previous research, our research team found that when two kinds of TCM were decocted together, and apply the metabonomic data processing method to analysis the global compounds, and a variety of new formed unknown compounds were detected in co-decoction. Furthermore, a series of formulae of TCM were explored by our research team. Meanwhile, a novel concept of co-decoction reaction of TCM was put forward for the first time (Liu R et al., 2021; Wu et al., 2021; Zhang et al., 2021). In order to further explore the co-decoction phenomenon of the complex TCM formula consists of three or more kinds of herbal medicine, we carried out an exploratory study of Zhi-Zi-Hou-Po Decoction.

TCM has always been an indispensable source of medicine for treating various diseases. However, due to the inherent chemical diversity and complexity of TCM, its' safety and effectiveness in clinical application are limited. In the past 10 years, LC-MS has always been key tools for medicine research. The combination of LC and MS has made great contributions to the qualitative analysis of TCMs (Yu et al., 2021). The application of LC-MS in TCM mainly focuses on ingredients, metabolites and biologically active ingredients (Chen YH et al., 2021). This study has analysed the chemical components of a single decoction and co-decoction of ZZHPD based on UPLC-QE-Orbitrap-MS technology and MSDIAL software. We have also

TABLE 1 | Components of ZZHPD.

Plant names	Traditional Chinese medicine name	Abbreviations
<i>Gardenia jasminoides</i> J.Ellis	<i>Gardeniae Fructus</i>	GF
<i>Citrus aurantium</i> L.	<i>Aurantii Fructus Immaturus</i>	AFI
<i>Magnolia officinalis</i> Rehder and E.H.Wilson	<i>Magnoliae Officinalis Cortex</i>	MOC



explored whether there are new compounds in the process of co-decoction, which may provide a unique idea for others. The components of ZZHPD absorbed into the blood and brain tissue were also analysed, to study whether the new compounds entered the body of mice and played a role in treating insomnia and

depression. Finally, the binding ability of components absorbed into brain and insomnia-related targets was evaluated by molecular docking, revealing the mechanism of ZZHPD in treating insomnia and depression. The research flowchart is shown in **Figure 1**.

MATERIALS AND METHODS

Chemicals and Reagents

Gardeniae Fructus (GF), *Aurantii Fructus Immaturus* (AFI) and *Magnoliae Officinalis Cortex* (MOC) [Beijing Deshoutang Pharmaceutical Co., Ltd. (Beijing, China)], Acetonitrile, formic acid, methanol (LC-MS grade) (Thermo Fisher Scientific (China) Co. Ltd.), Watsons Distilled Water (Beijing, China).

Preparation of Zhi-Zi-Hou-Po Decoction Extraction

The preparation method of all sample according to the original composition and preparation method of ZZHPD recorded in “*Shang Han Lun*”, with a little modification. The prescription includes GF 9 g, AFI 10 g, and MOC 62.4 g. Seven sample were prepared as follow: the single herb decoctions included three groups (GF/AFI/MOC), and the co-decoction included three groups of two-herb co-decoction (GF-AFI/GF-MOC/AFI-MOC) and a three-herb co-decoction (ZZHPD). The extraction preparation process of the seven sample was operated in parallel in order to reduce the difference as much as possible. Herbs of the seven sample were separately immersed in water (1:10, w/v) for 30 min, and then decocted at $95 \pm 5^\circ\text{C}$ for 1 h. Subsequently, the extraction was filtered, and the residue was decocted twice more. The ratios of the total weight of the herbs to the volume of water for the second and third decoction were 1:8 and 1:5, respectively. The three filtrates were combined and diluted to 250 ml to obtain the samples. The samples were centrifuged for 15 min at 12,000 r/min, and 5 μl of supernatant was taken for mass spectrometry analysis. Moreover, the three-herb co-decoction was concentrated to 45 ml by rotary evaporator dried in vacuum conditions, and stored at low temperature (4°C) for animal experiment.

UPLC-QE-Orbitrap-MS

Chromatographic Separation Conditions: Waters HSS T3 UPLC C18 column (1.7 μm , 2.1×150 mm, Milford, MA, United States); Mobile phase: 0.1% formic acid aqueous solution (A) and acetonitrile (B); Elution gradient: 0–2 min: 5% B; 2–17 min: 5–98% B; 17–20 min: 98–98% B; 20–23 min: 98–5% B; 23–25 min: 5% B; Column temperature: 40°C ; Injection volume: 5 μl ; Flow rate: 0.3 ml/min.

Mass Separation Conditions: Electrospray ionization source (ESI); Positive ions mode (20 V, 40 V, 60 V) and negative ions mode (30 V, 50 V, 70 V); Spray voltage 3800 V (–), 3200 V (+); Sheath gas: 35 arb; Auxiliary gas: 15 arb; Scan mode: the full scan/data-dependent two-stage scan (full scan/ddMS2); Scanning mass range: m/z 100–1,300 Da; Capillary temperature: 350°C .

Animals

12 specific pathogen-free male ICR mice (4 weeks old, 25–30 g) were purchased from the Si pei fu (Beijing, China) Biotechnology Co., Ltd. (license number: SCXK (Jing) 2019-0010). Mice can freely obtain commercial standard chow diet and purified water, and are kept in an environmentally controlled room with a temperature of 25°C , a relative humidity of $60 \pm 5\%$, and a

12 h light/dark cycle. Allow them to acclimate to the environment 7 days before the experiment. Animal experiments were approved by the Animal Care and Use Committee of Beijing University of Chinese Medicine (BUCM-4-20211111004-4067), and in accordance with the “Guidelines for the Care and Use of Laboratory Animals” published by the National Institutes of Health (NIH Publication No. 85-23, revised in 1996). All the mice were randomly divided into two groups ($n = 6$): a control group and a ZZHPD group. Mice of ZZHPD group were given a ZZHPD condensed liquid (1.81 g/ml) at the dose of three times of clinical dosage for 5 days.

Preparation of Biological Sample

One hour after the last administration, blood samples were taken from the eyes of the mice, placed in an anticoagulation tube and stored in a refrigerator at 4°C . After blood collection, the mice were killed by cervical dislocation. The thoracic cavity was exposed, and the remaining blood in the mice was flushed with cardiac perfusion. Take out the brain tissue and homogenize with 1 ml of ultrapure water. Then the plasma and brain tissue were centrifuged at 4°C and 4,000 rpm for 15 min, and the supernatant was taken for subsequent operations. Three times the plasma volume of acetonitrile was added to the plasma supernatant to precipitate proteins. After acetonitrile was added, the mixture was vortexed for 3 min, and then the mixture was centrifuged at 8,000 rpm for 15 min at 4°C . The separated supernatant was dried with nitrogen, reconstituted with 100 μl of 50% methanol and vortexed for 3 min. The re-dissolved sample was centrifuged at 12,000 rpm for 15 min at 4°C , and the supernatant was taken as the final plasma sample. Perform the same operation on the brain tissue to obtain a brain tissue sample.

Molecular Docking

Molecular docking needs to prepare the 3D structure of the compound and protein for molecular docking. The 3D structure of the brain component is obtained from PubMed (<https://pubchem.ncbi.nlm.nih.gov/>), and the 3D structure of the protein is obtained from the PDB (Protein Data Bank) database. The Maestro 11.8 software includes roughly four parts, processing ligands, optimizing protein structure, constructing binding pockets, and performing molecular docking. Firstly, The LigPrep panel needs to be used to process small molecules to obtain suitable ligands. Then in order to make these structures suitable for molecular docking, we use the protein preparation tool ProteinPreparation Wizard to pre-process the protein. The protein preparation process mainly includes three main steps: processing, modification and refinement. Fill missing side chains and/or loops, optimize hydrogen bond networks, change the protonation state of residues and ligands, repair possible conflicts that may occur when hydrogen is added or fill missing side chains, and minimize capabilities. Furthermore, the mating pocket is defined according to the binding site of the original ligand in the protein, which means that the centre and size of the original ligand will be used as the centre and size of the interface pocket by the receptor grid generation. Finally, the prepared ligand is docked with the

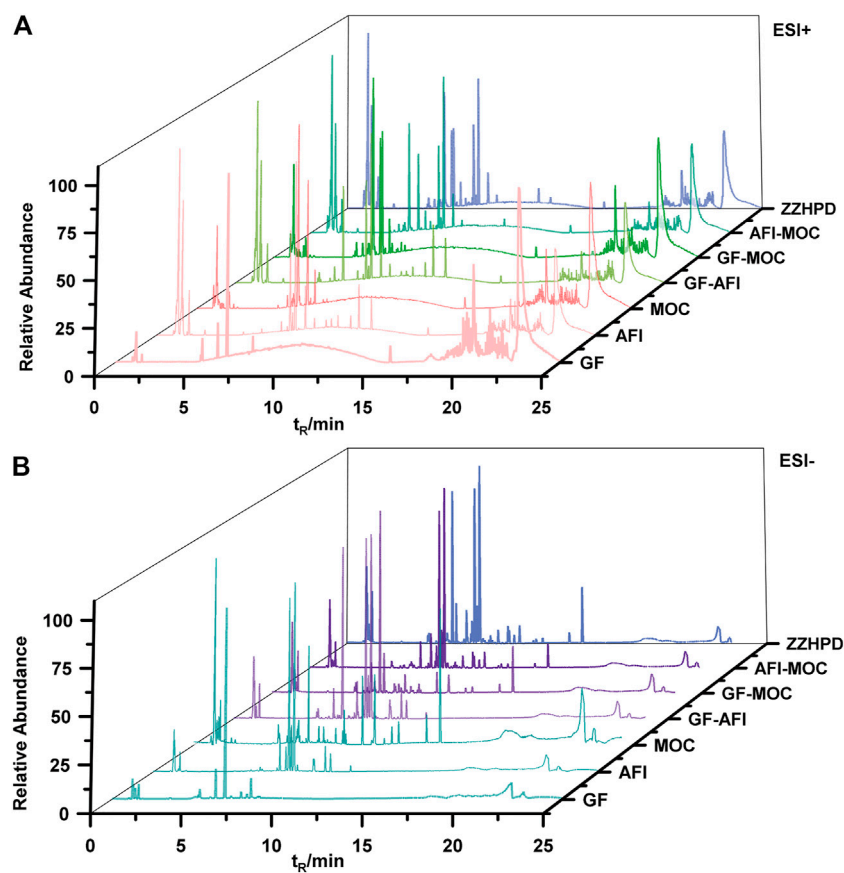


FIGURE 2 | Typical BPI of GF, AFI, MOC and co-decoction under the positive ion mode (A) and negative ion mode (B).

optimized protein in a standard precision mode, so that the result of the docking can refer to the result of the original ligand.

Data Processing and Analysis

The data collected by high-resolution mass spectrometry was processed using Compound Discoverer 3.1.1.12 software and MSDIAL software. Use Compound Discoverer software to perform peak alignment, peak detection, background subtraction and other operations to identify compounds. Due to the blindness of Compound Discoverer matching, it is necessary to combine M/Zcloud, Chempider, M/Zvalue with literatures to confirm related compounds and ensure the accuracy of results. Furthermore, excimer ion peaks and unique fragment ions in the spectrogram have been used to deduce related structure of compounds, which were not matched in the database and have high response peaks in the spectrogram. Next, use Analysis Base File Converter software to convert the mass spectrum into a format that MSDIAL can recognize, normalize the data, and compare different compounds in the co-decoction process. The Jvenn website (<http://jvenn.toulouse.inra.fr/app/example.html>) and origin 2021 software were used to analyse and visualize the processed data, and Maestro 11.8 software was used to accomplish molecular docking.

RESULTS

Compound Difference Between Single Decoction and Co-decoction

Although qualitative and quantitative analysis is usually performed on certain components by UPLC-QE-Orbitrap-MS, information about new compounds is rarely considered by most scholars from the perspective of single decoction and co-decoction. We used UPLC-QE-Orbitrap-MS to determine the active components in the single-decoctions and co-decoctions, and drew a base peak intensity chromatogram (BPI) of seven samples (Figure 2). Meanwhile, by comparing standard compound databases and the literature, 106 main compounds in ZZHPD were predicted or identified, including phenolic acids, flavonoids and alkaloids (Additional file 1: **Supplementary Table S1**).

In this research, the MSDIAL software was used to normalize all the mass spectra data collected in the single decoctions and co-decoctions samples, and compounds were labelled with retention-time and accurate mass. Subsequently, eliminate peaks without secondary fragments in the results, and construct an extracted ion chromatogram in order to further reduce false-positive results. After analysing and processing the mass spectrum data of the ZZHPD co-decoction, it was found

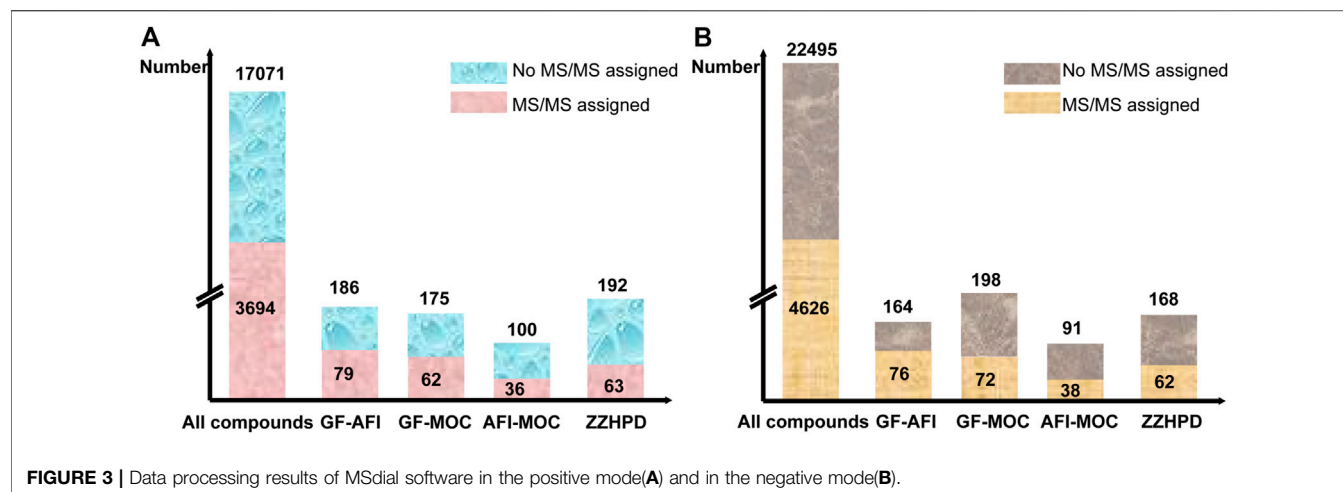


FIGURE 3 | Data processing results of MSdial software in the positive mode(A) and in the negative mode(B).

that a total of 17,071 peaks were detected in the positive ion mode, and a total of 22,495 peaks were detected in the negative ion mode. Then cross-analyse the data of seven samples in the positive ion mode, compare single decoction and co-decoction, and screen new compounds with a normalized value greater than 10^{-5} . The data in the negative ion mode were processed in the same way as in the positive ion mode process. We will be shocked by the findings that there are 653 compounds from the co-decoction including two-herb and three-herb in the positive mode, and these compounds do not exist in the single decoction. Only 240 compounds showed Ms/Ms assigned after normalization by MSDIAL, including 79 compounds from the co-decoction of GF-AFI, 62 compounds from GF-MOC, 36 compounds from AFI-MOC, and 63 compounds from ZZHPD, which indicates that new compounds appear through certain chemical reactions during co-decoction (Figure 3A.). Similarly, there were 621 compounds from the co-decoction including two-herb and three-herb in the negative mode, with only 248 compounds showing Ms/Ms assigned after normalization, including 76 compounds from GF-AFI, 72 compounds from GF-MOC, 38 compounds from AFI-MOC, and 62 compounds from ZZHPD (Figure 3B.).

125 new compounds have appeared in ZZHPD, and their mass spectra are shown in Additional file 2 **Supplementary Table S2**. The source of the new compounds produced by the three herbs co-decoction was then traced. Seven compounds are produced by the interaction of three herbs and the remaining 56 new compounds were derived from the two herbs co-decoctions (10 new compounds belonging to ZZHPD/GF-AFI, 13 new compounds belonging to ZZHPD/GF-MOC, 16 new compounds belonging to ZZHPD/AFI-MOC, eight new compounds belonging to ZZHPD/GF-AFI/GF-MOC, six new compounds belonging to ZZHPD/GF-AFI/AFI-MOC, 2 new compounds belonging to ZZHPD/GF-MOC/AFI-MOC, and 1 new compound belonging to ZZHPD/GF-AFI/GF-MOC/AFI-MOC) in the positive ion mode. It was found that nine new compounds were only derived from the three herb co-decoction, and the remaining 53 new compounds were derived from the two herb co-decoctions (8 new compounds belonging to

ZZHPD/GF-AFI, 15 new compounds belonging to ZZHPD/GF-MOC, seven new compounds belonging to ZZHPD/AFI-MOC, 12 new compounds belonging to ZZHPD/GF-AFI/GF-MOC, four new compounds belonging to ZZHPD/GF-AFI/AFI-MOC, five new compounds belonging to ZZHPD/GF-MOC/AFI-MOC, and 2 new compounds belonging to ZZHPD/GF-AFI/GF-MOC/AFI-MOC) in the negative ion mode. The results are shown in Figure 4. Unfortunately, Due to the incomplete structure identification information, there is insufficient evidence to accurately identify new compounds.

Analysis of the Components of ZZHPD Absorbed Into the Blood and Brain, Based on UPLC-QE-Orbitrap-MS

By comparing literatures, spectres, and results from the MSDIAL, we have initially identified the components of ZZHPD *in vitro*, and then verified whether the components *in vitro* were enriched in the blood and brain tissue, and played a pharmacological effect. The BPI diagram of drug-containing plasma and the brain extract samples under the negative ion mode and positive ion mode were shown in Figure 5.

In total, 30 compounds of ZZHPD were screened in plasma, including 28 known compounds and two new compounds under the positive and negative ion mode. And, 18 known compounds and one new compound were absorbed into brain tissue under the positive and negative ion mode. Origin software was used to draw the chromatographic scatter diagrams of all components of ZZHPD, identified components of ZZHPD, new components, blood components and brain components, as shown in Figure 6. More information was shown in additional files.

The components entering the blood and the brain tissue were far fewer than those outside the body. There are two reasons: the existence of the blood-brain barrier (BBB) and the influence of the intestinal flora. Specifically, the BBB, one of the internal barriers in the body regulating innate immunity, restrict drug delivery during the treatment of central nervous system diseases. TCM contains complex chemical components, and only a few chemical components of TCM, such as polar or lipid soluble small

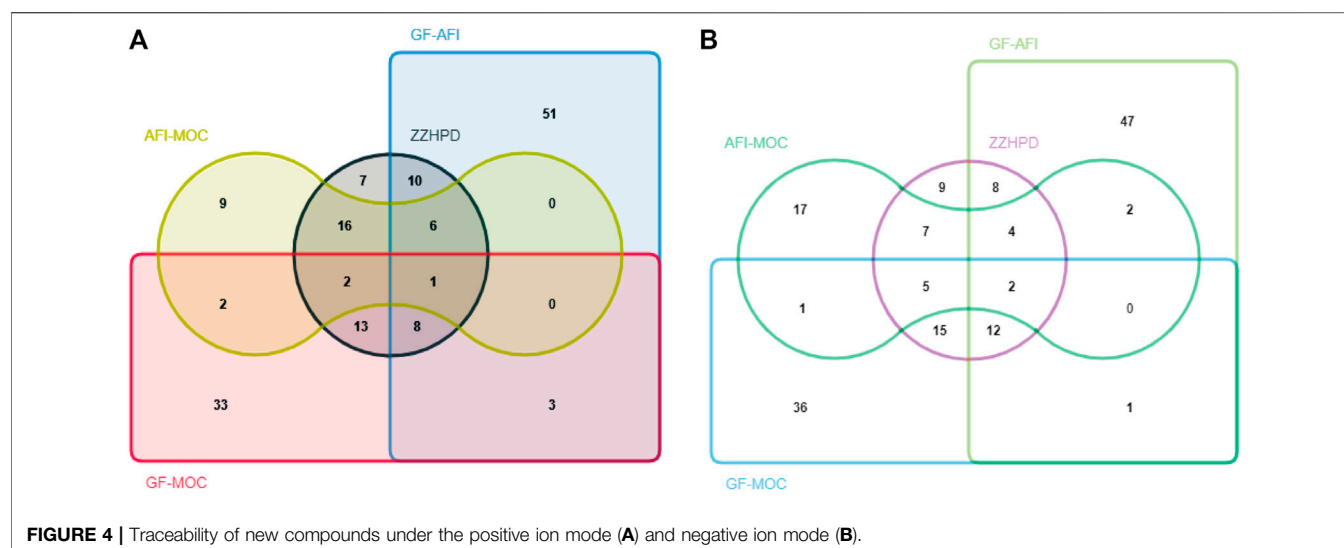


FIGURE 4 | Traceability of new compounds under the positive ion mode (A) and negative ion mode (B).

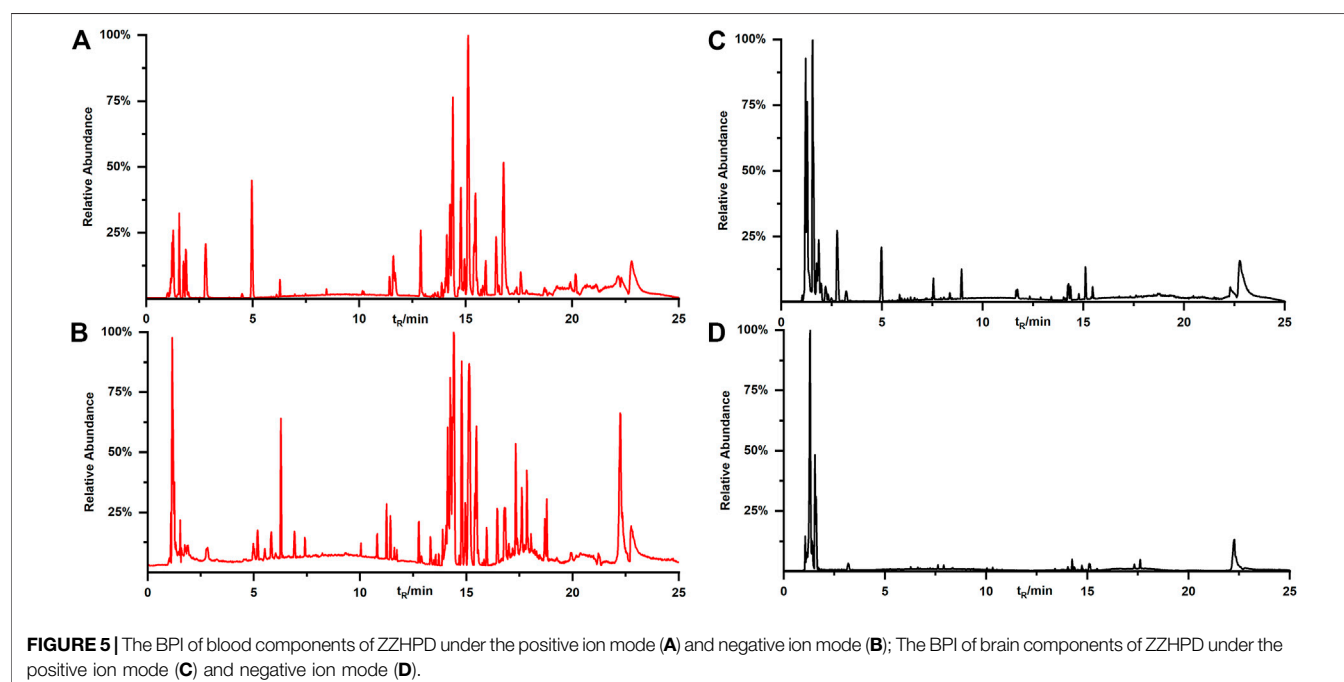


FIGURE 5 | The BPI of blood components of ZZHPD under the positive ion mode (A) and negative ion mode (B); The BPI of brain components of ZZHPD under the positive ion mode (C) and negative ion mode (D).

molecules, can exert therapeutic effects on central nervous system diseases through BBB (Jin et al., 2013). Furthermore oral administration of TCM is inevitably interacted with intestinal flora (Yi et al., 2021), and the interaction between the active ingredients of TCM and intestinal flora has become research hotspots in recent years. Some biologically active ingredients can't pass through the intestine, resulting in low bioavailability. The components of TCM are metabolized or biotransformed by the intestinal microbiota, thereby promoting the production and absorption of new active compounds. Meanwhile, the function of diseased organs/tissues is regulated by the ingredients of TCM by influencing the composition and structure of intestinal flora (Gong et al., 2020). Although there are few new compounds

found in brain and blood, they still have certain research value and significance.

Results of Molecular Docking Experiment

According to the key proteins of some cutting-edge drugs in fighting insomnia and depression, 12 proteins including GABA receptor, serotonin, histamine, dopamine and orexins were screened out. Among them, the Dong Ying-Jie team found that Modified Suan-Zao-Ren Decoction can effectively increase the content of 5-HT_{1A} protein in the hypothalamus of insomnia mice and down-regulate the expression of OX_{2R}, indicating that Modified Suan-Zao-Ren Decoction can effectively improve insomnia (Dong et al., 2021). Combined

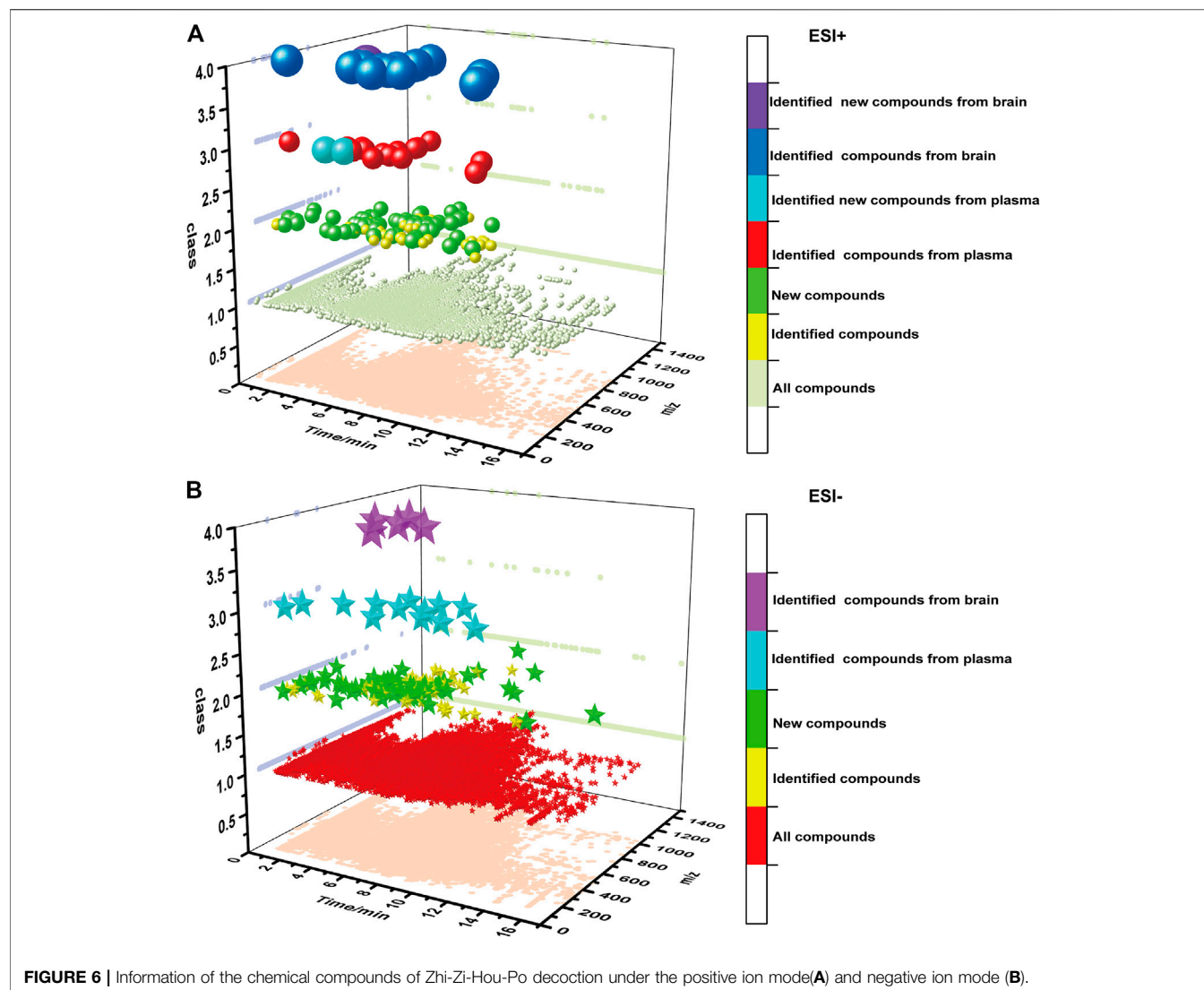


FIGURE 6 | Information of the chemical compounds of Zhi-Zi-Hou-Po decoction under the positive ion mode(A) and negative ion mode (B).

with the RCSB protein database (PDB), the proteins were finally obtained according to the source and resolution of proteins and the influence of the original ligand on the protein. After analysis and comparison, 12 proteins were obtained as targets related to insomnia and depression (Table 2.). All the components absorbed by the brain are used for docking with proteins. In order to verify the accuracy of the results, it is necessary to evaluate the original ligands in the protein crystal structure with active compounds and draw the results into a heat map (Figure 7.).

According to the results of molecular docking, there are seven proteins have higher binding affinity to the brain components than the original ligand, such as eriodictyol with HCRTR1, MTNR1A, GABRA1, HCRTR1, MAOA, GLO1 and HTR2A; naringenin-7-O-glucoside with HCRTR1, MTNR1A, MAOA, GLO1, HTR2A and HRH1; naringenin with MAOA, HCRTR1, MTNR1A, GABRA1, HCRTR1, GLO1 and HTR2A; as well as lotusine with MTNR1B, HCRTR1, MTNR1A, GABRA1, MAOA and HTR2A. The result shows that ZZHPD

may play an important role in treating insomnia. The docking results of components absorbed into brain and related receptors are shown in Figure 8.

DISCUSSION

With the improvement of modern science and technology, humans also need continuous progress. Particularly as pharmaceutical analysts, we should make full use of advanced equipment and different methods to settle various problems. People have been discovering new things and expanding their ideas since ancient times, and the emergence of something new often drives the development of things. In this study, whether the new compounds exist in the co-decoction of ZZHPD is analysed based on high-resolution mass spectrometry and MSDIAL software. The MSDIAL software was launched as a universal program for untargeted metabolomics, which has many features, including data-independent MS/MS and spectral deconvolution

TABLE 2 | Molecular docking results of 18 prototype components absorbed into the brain from Zhi-Zi-Hou-Po decoction.

Compound of brain	Classification	HCRT1 6TO7	GABRA1 6TPJ	MTNR1B 6ME9	MTNR1A 6ME2	GLO1 3W0U	DRD2 6LUQ	HTR2A 6A93	HTR2C 6BQH	SLC6A4 6DZW	GABRA1 6CDU	MAOA 2Z5X	HRH1 3RZE
Ligand	Ligand	-9.33	-8.96	-9.54	-8.62	-10.28	-9.63	-4.73	0.24	-8.76	-7.85	-1.92	-8.28
Bergaptol	Terpenes	-5.55	-5.43	-7.99	-7.43	-8.23	-5.87	-5.20	-4.47	-6.77	-5.38	-5.46	-6.28
Genipin	Terpenes	-5.77	-5.56	-7.78	-7.42	-8.19	-6.04	—	-4.44	-5.00	-5.32	-4.58	-6.04
Genipin 1-gentiobioside	Terpenes	-7.26	-8.13	-7.95	—	-7.76	-5.35	-5.91	-4.00	-7.99	-5.67	-1.49	-6.79
Geniposide	Terpenes	-5.88	-7.20	-10.19	-8.08	-7.38	-4.87	-4.91	-4.20	-5.99	-4.84	-5.26	-5.65
Deacetylasperulosidic acid methyl ester	Glycosides	-6.81	-6.70	-9.27	-8.99	-8.09	-5.03	-4.99	-4.02	-5.94	-6.89	-5.23	-7.27
Naringenin-7-O-glucoside	Glycosides	-8.05	-7.41	-7.31	-8.92	-11.00	-5.48	-5.53	-4.57	-6.53	-5.46	-5.89	-8.92
Poncirenin	Glycosides	-7.91	-7.46	-7.50	-8.79	-7.96	-5.52	-5.50	-5.09	-6.37	-5.42	-6.16	-7.94
Quercimeritrin	Glycosides	-6.78	-6.82	—	-8.14	-7.41	-6.10	-6.32	-4.02	-6.69	-5.27	-6.29	-8.07
Eriodictyol	Flavonoids	-6.60	-6.24	-8.16	-8.73	-11.64	-8.04	-6.14	-5.45	-6.97	-6.56	-6.32	-8.09
Hesperidin	Flavonoids	—	-8.94	—	—	-10.50	-6.97	-5.32	-2.69	—	-5.21	—	—
Naringenin	Flavonoids	-6.55	-6.07	-8.33	-9.21	-11.06	-7.77	-6.30	-4.38	-7.75	-6.31	-6.42	-7.43
Pentamethoxyflavone	Flavonoids	-5.81	-6.47	—	—	-8.69	-4.09	—	—	-5.21	—	—	-5.81
Scopoletin	Coumarins	-6.07	-6.14	-7.99	-7.55	-8.98	-6.54	-5.22	-5.16	-5.98	-5.67	-5.84	-5.86
Suberenol	Coumarins	-5.93	-5.80	-8.19	-7.77	-7.72	-6.14	-4.94	-4.79	-6.47	-5.56	-6.50	-6.60
N-Feruloylputrescine	Carboxylic Acids	-4.14	-5.12	-6.97	-4.90	-5.11	-4.97	-2.51	-3.01	-5.93	-3.97	-3.96	-6.26
Glaucine	Alkaloids	-6.62	-6.67	-9.65	-8.47	-5.05	-4.50	-5.08	-3.80	-7.27	-5.73	-4.69	-7.06
Lotusine	Alkaloids	-7.06	-6.91	-9.74	-9.36	-7.37	-6.87	-5.34	-4.88	-6.51	-5.41	-4.99	-7.58
Magnoflorine	Alkaloids	-6.19	-6.58	-8.54	-6.73	-6.42	-3.91	-4.79	-4.95	-5.89	-5.75	-4.60	-6.61

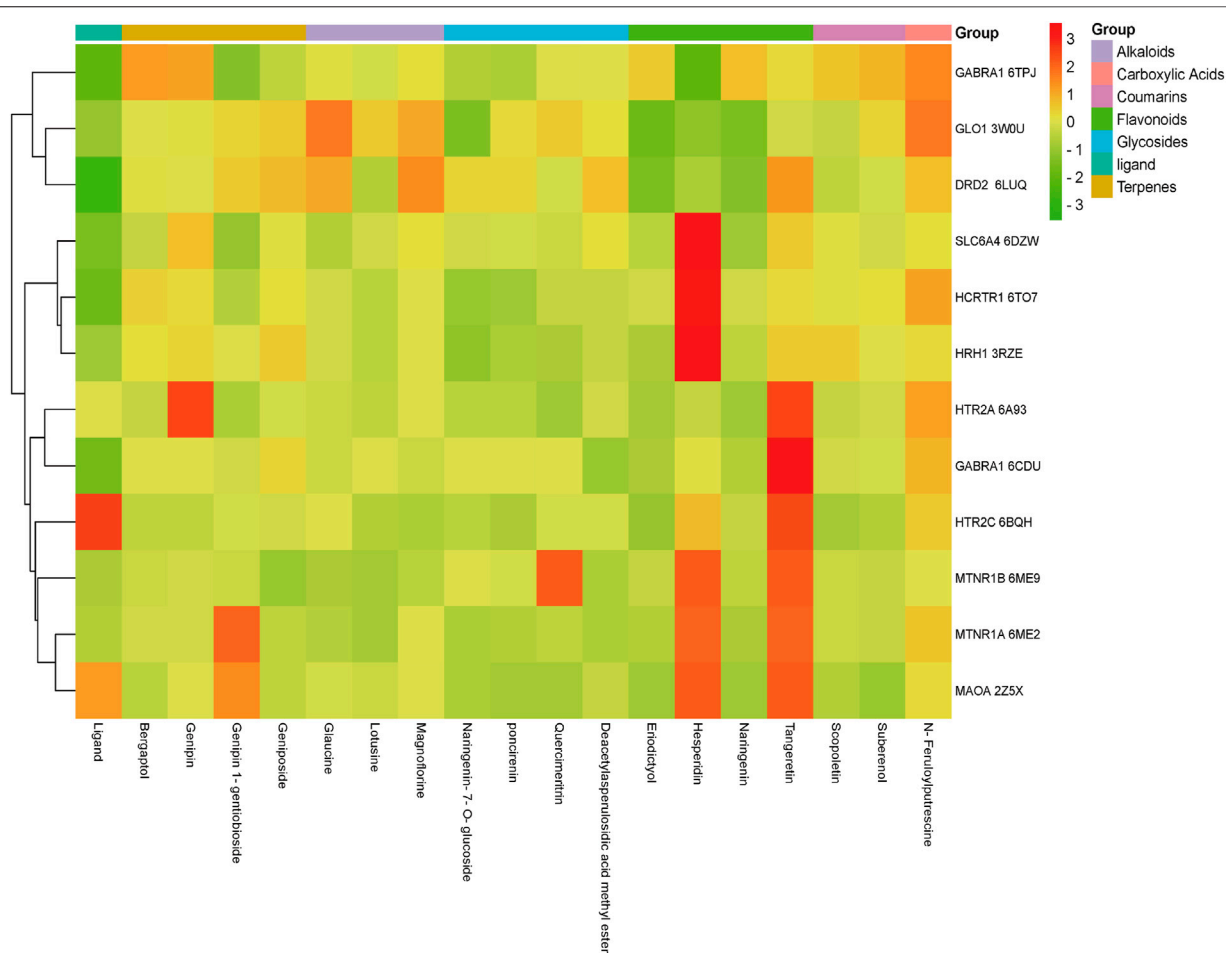


FIGURE 7 | The heat map of molecular docking results.

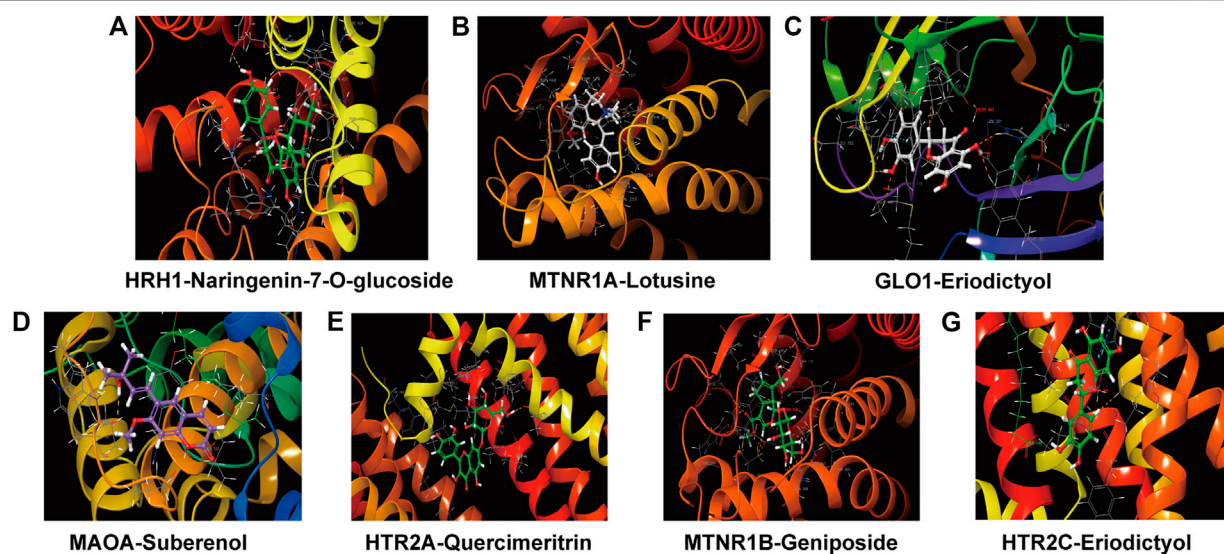


FIGURE 8 | Molecular docking of representative compounds and related receptors. The 3D diagram of the docking of HRH1 with Naringenin-7-O-glucoside (**A**), MTNR1A with Lotusine (**B**), GLO1 with Eriodictyol (**C**), MAOA with Suberenol (**D**), HTR2A with Quercimeritrin (**E**), MTNR1B with Geniposide (**F**), HTR2C with Eriodictyol (**G**).

for both GC/MS, conversion of raw data to analytical data and streamlined criteria for peak identification. The software-assisted data processing method had significantly improved the efficiency of MS data interpretation for complex TCM systems. Overall, 125 unique compounds were found in the co-decoction via spectral comparison. Mass spectrometry information (such as retention time, molecular weight and fragments) facilitated in the identification of the new compounds in plasma and brain tissue.

Insomnia and depression are a very common disease. The continuous medicinal needs of patients with insomnia have focused a lot of attention on the discovery of insomnia drugs (Feizi et al., 2019). Melatonin (melatonin receptor agonist), Benzodiazepine receptor agonists (BZRAs) and histamine antagonists, and orexin receptor antagonists are the most popular drugs in treating insomnia (Dujardin et al., 2020). BZRAs, including benzodiazepine related drugs (BZRDs) and benzodiazepines (BZDs), act on the gamma-aminobutyric acid (GABA) receptor and are the mainstay treatments for insomnia (Huang et al., 2021). Ramelteon, as a sleep-promoting agent, can reduce the arousal promotion signal from the suprachiasmatic nucleus (mainly through the melatonin MT1 receptor), and affect sleep time through the melatonin MT2 receptor. The ability of mirtazapine to antagonize 5HT_{2C}, 5-HTA and 5-HT₃ receptors causes the remaining serotonin concentration to interact with free 5-HT₁ receptors. The interaction with 5-HT₁ receptors (especially 5-HT_{1A} receptors) have antidepressant effects. It also exhibits moderate or weak antagonism to peripheral α 1-adrenergic receptors and muscarinic receptors (Jeong and Bahk, 2014). Reserpine, a vesicle reuptake inhibitor, can deplete neurotransmitters such as norepinephrine and serotonin, and cause physiological changes (Becker et al., 2021). Amitriptyline, as a tricyclic antidepressant, has been approved by the FDA in treating adults with depression (Di Pierro and Settembre, 2015; Anderson et al., 2017). Amitriptyline is also used off-label to treat anxiety, chronic pain syndrome and insomnia. Based on the important role of orexin in sleep/wake regulation, orexin receptor antagonists have become the focus of new therapies for the treatment of insomnia (Patel et al., 2015; Ito et al., 2021). Although the western medicine plays an important role in the treatment of insomnia, its side effects such as drug resistance and addiction cannot be ignored at present. (Wang et al., 2020).

TCM has a long history of treating insomnia and depression with fewer side effects. Many Chinese herbs and prescriptions have good effects on treating anxiety and insomnia (Zhao, 2019). The TCM prescription library for the treatment of insomnia had been built using an auxiliary platform of the inheritance of TCM. Scientists found that the most frequently used medicine was *Ziziphi Spinosae Semen* (*Ziziphus jujuba* var. *spinosa* (Bunge) Hu ex H.F.Chow), followed by *Poria* (*Poria cocos* (Schw.) Wolf), *Glycyrrhizae Radix Et Rhizoma* (*Glycyrrhiza uralensis* Fisch) and *Polygoni Multiflori Caulis* (*Polygonum multiflorum* Thunb.) (Ma et al., 2021). As a classic Chinese prescription, ZZHPD has been proven to have a good effect on depression-like symptoms with few side effects (Sun et al., 2021). However, due to the complex components and multi-target nature of ZZHPD, the mechanism in treating insomnia is still unclear. Studies have shown that the mechanism of ZZHPD in treating insomnia is

mainly related to GABA synthase and GABA metabolizing enzymes (Feizi et al., 2019). Naringenin can effectively improve the harm caused by an efavirenz-induced sleep-like disorder in the midbrain of white albino mice (Olufunke et al., 2020). An infusion of flowers of several species of the Citrus genera is used as a sedative to treat insomnia, and hesperidin may participate in the function of adenosine receptors and exert a sedative effect (Guzmán-Gutiérrez and Navarrete, 2009; Adhikari-Devkota et al., 2019). Geniposide ameliorates the depression-like behaviour induced by chronic unpredictable mild stress, through inhibition of ceramide-PP2A signalling via the PI3K/Akt/GSK3 β axis (Wang et al., 2021). Furthermore, LC-MS technology was used to identify components absorbed into the brain, and 18 compounds were found, which indicated that these prototype components play a key role in anti-insomnia activities. There are four terpenes, 4 glycosides, 4 flavonoids, 3 alkaloids, 2 coumarins and 1 organic acid, specifically including bergaptol, deacetylasperulosidic acid methyl ester, eriodictyol, genipin, genipin 1-gentiobioside, geniposide, glaucine, hesperidin, lotusine, magnoflorine, naringenin, naringenin-7-O-glucoside, n-Feruloylputrescine, poncirenin, quercimeritrin, scopoletin and suberenol. However, there are only four main ways for pharmaceutical ingredients to penetrate the BBB: 1) small water-soluble molecules directly diffuse through the intercellular space; 2) transmembrane diffusion of fat-soluble molecules; 3) pinocytosis mediated by specific receptors; 4) activation of specific carrier channels and enzyme systems (Jin et al., 2013). TCM contains complex components, and the main substances that can penetrate the BBB are currently polar or fat-soluble small molecules. It is worth noting that, as a macromolecular flavonoid compound, hesperidin can penetrate the BBB, but the penetration mechanism needs further research. Besides, the results of molecular docking indicated that GABRA1 has a strong binding power with naringenin and hesperidin, and HCRTR1 has strong binding power with naringenin-7-O-glucoside, poncirenin, and genipin 1-gentiobioside. The research provides a reference for research in treating insomnia and depression with ZZHPD *in vivo* and *in vitro*.

CONCLUSION

In this study, an LC-MS method was developed to detect the ZZHPD components, and 125 new compounds were investigated by analysing the MS information of the co-decoction of ZZHPD for the first time. Although there are few new compounds absorbed into the plasma and brain tissue, their effects could not be denied. Molecular docking also showed that Lotusine, Eriodictyol, Naringenin and Naringenin-7-O-glucoside are active ingredients acting on melatonin receptors, GABA receptors and serotonin-related pathways. The research takes the material changes of the ZZHPD complex reaction system as the breakthrough point to provide new ideas for the development of TCM, which is based on the theory of Chinese medicine co-decoction.

DATA AVAILABILITY STATEMENT

The original contributions presented in the study are included in the article/**Supplementary Material**, further inquiries can be directed to the corresponding authors.

ETHICS STATEMENT

The animal study was reviewed and approved by The animal study was reviewed and approved by Animal Experiment Ethics Committee of Beijing University of Chinese Medicine (BUCM-4-20211111004-4067).

AUTHOR CONTRIBUTIONS

YS and CZ conceived and designed the research methods. XF, YB, JW, and TL collected the data. XF and YB did the animal

experiment. GY, TZ, and HX helped with the animal experiment. XF analysed the data. XF wrote the original draft. YS and CZ reviewed and edited the manuscript. All authors have read and agreed to the published version of the manuscript. All authors read and approved the final manuscript.

FUNDING

The financial support was provided by the National Natural Science Foundation of China (NSFC) (Grant number 81373942).

SUPPLEMENTARY MATERIAL

The Supplementary Material for this article can be found online at: <https://www.frontiersin.org/articles/10.3389/fphar.2021.830558/full#supplementary-material>

REFERENCES

- Adhikari-Devkota, A., Elbashir, S. M. I., Watanabe, T., and Devkota, H. P. (2019). Chemical Constituents from the Flowers of Satsuma Mandarin and Their Free Radical Scavenging and α -glucosidase Inhibitory Activities. *Nat. Prod. Res.* 33, 1670–1673. doi:10.1080/14786419.2018.1425856
- Anderson, L. S., Bell, H. G., Gilbert, M., Davidson, J. E., Winter, C., Barratt, M. J., et al. (2017). Using Social Listening Data to Monitor Misuse and Nonmedical Use of Bupropion: A Content Analysis. *JMIR Public Health Surveill.* 3, e6. doi:10.2196/publichealth.6174
- Becker, M., Pinhasov, A., and Ornoy, A. (2021). Animal Models of Depression: What Can They Teach Us about the Human Disease? *Diagnostics (Basel)* 11, 123. doi:10.3390/diagnostics11010123
- Chen, L., Zhang, F., Huang, D., Liao, L., and Chen, W. (2021). Protective Effect of Shengxian Decoction and the Decoction of Single Herb Component against Myocardial Injury Induced by Hypoxia/reoxygenation. *J. Pharm. Pract.* 39, 240–244. doi:10.12206/j.issn.1006-0111.202006080
- Chen YH, Y. H., Bi, J. H., Xie, M., Zhang, H., Shi, Z. Q., Guo, H., et al. (2021). Classification-based Strategies to Simplify Complex Traditional Chinese Medicine (TCM) Researches through Liquid Chromatography-Mass Spectrometry in the Last Decade (2011-2020): Theory, Technical Route and Difficulty. *J. Chromatogr. A*. 1651, 462307. doi:10.1016/j.chroma.2021.462307
- Chu, Y., Jia, J., Tian, M., Liu, Y., Zheng, C., Song, X., et al. (2017). Research Progress on the Active Ingredients of Zhi-Zi-Hou-Po Decoction. *J. Tradit. Chin. Med.* 34, 127–129. doi:10.3969/j.issn.1002-2406.2017.06.036
- Di Pierro, F., and Settembre, R. (2015). Preliminary Results of a Randomized Controlled Trial Carried Out with a Fixed Combination of S-Adenosyl-L-Methionine and Betaine versus Amitriptyline in Patients with Mild Depression. *Int. J. Gen. Med.* 8, 73–78. doi:10.2147/IJGM.S79518
- Dong, Y. J., Jiang, N. H., Zhan, L. H., Teng, X., Fang, X., Lin, M. Q., et al. (2021). Soporific Effect of Modified Suanzaoren Decoction on Mice Models of Insomnia by Regulating Orexin-A and HPA axis Homeostasis. *Biomed. Pharmacother.* 143, 112141. doi:10.1016/j.biopha.2021.112141
- Dujardin, S., Pijpers, A., and Pevernagie, D. (2020). Prescription Drugs Used in Insomnia. *Sleep Med. Clin.* 15, 133–145. doi:10.1016/j.jsmc.2020.02.002
- Feizi, F., Namazi, N., Rahimi, R., and Ayati, M. H. (2019). Medicinal Plants for Management of Insomnia: A Systematic Review of Animal and Human Studies. *Galen Med. J.* 8, e1085. doi:10.31661/gmj.v8i0.1085
- Gong, X., Li, X., Bo, A., Shi, R. Y., Li, Q. Y., Lei, L. J., et al. (2020). The Interactions between Gut Microbiota and Bioactive Ingredients of Traditional Chinese Medicines: A Review. *Pharmacol. Res.* 157, 104824. doi:10.1016/j.phrs.2020.104824
- Guzmán-Gutiérrez, S., and Navarrete, A. (2009). Pharmacological Exploration of the Sedative Mechanism of Hesperidin Identified as the Active Principle of Citrus sinensis Flowers. *Planta Med.* 75, 295–301. doi:10.1055/s-0029-1185306
- Huang, K. H., Tai, C. J., Kuan, Y. H., Chang, Y. C., Tsai, T. H., and Lee, C. Y. (2021). Pneumonia Risk Associated with the Use of Individual Benzodiazepines and Benzodiazepine Related Drugs Among the Elderly with Parkinson's Disease. *Int. J. Environ. Res. Public Health* 18, 9410. doi:10.3390/ijerph18179410
- Ito, H., Ogawa, Y., Shimojo, N., and Kawano, S. (2021). Suvorexant Poisoning in a Patient with Cirrhosis and Renal Failure. *Cureus* 13, e14329. doi:10.7759/cureus.14329
- Jeong, J. H., and Bahk, W. M. (2014). Sleep-Related Eating Disorder Associated with Mirtazapine. *J. Clin. Psychopharmacol.* 34, 752–753. doi:10.1097/JCP.0000000000000216
- Jin, L., Wei, Y., and Gao, Y. (2013). Research Progress in Penetration Mechanism of Chemical Constituents in Chinese Materia Medica into Blood-Brain Barrier and Penetration Enhancing Methods. *Chin. Tradit. Herbal Drugs* 44, 2183–2188. doi:10.7501/j.issn.0253-2670.2013.15.027
- Liu R, R., Sun, Y., Wu, H., Ni, S., Wang, J., Li, T., et al. (2021). In-depth Investigation of the Effective Substances of Traditional Chinese Medicine Formula Based on the Novel Concept of Co-decoction Reaction-Using Zuojin Decoction as a Model Sample. *J. Chromatogr. B Analyt. Technol. Biomed. Life Sci.* 1179, 122869. doi:10.1016/j.jchromb.2021.122869
- Liu X, X., Yang, J., Zhang, L., Li, R., Li, B., Ge, X., et al. (2021). Efficacy and Safety of Tian Meng Oral Liquid for the Treatment of Insomnia. *Medicine (Baltimore)* 100, e26865. doi:10.1097/MD.00000000000026865
- Ma, K., Jiang, L., and Song, L. (2021). Analysis on Prescriptions for Treating Insomnia Based on Traditional Chinese Medicine Inheritance Auxiliary Platform. *J. Pract. Tradit. Chin. Intern. Med.* 35, 132–135+156. doi:10.13729/j.issn.1671-7813.Z20200800
- Olufunke, D., Edidiong, A., Oluwatomisin, F., and Alani, A. (2020). Therapeutic Activities of Naringenin on Efavirenz-Induced Sleep-like Disorder in the Midbrain of white Albino Mice. *Iran J. Basic Med. Sci.* 23, 1462–1470. doi:10.22038/ijbms.2020.47043.10852
- Patel, K. V., Aspesi, A. V., and Evoy, K. E. (2015). Suvorexant: a Dual Orexin Receptor Antagonist for the Treatment of Sleep Onset and Sleep Maintenance Insomnia. *Ann. Pharmacother.* 49, 477–483. doi:10.1177/1060028015570467
- Song, D. M., Wei, H., Li, E., and Li, W. (2013). Comparison Research on Meridians Effect of Single Herbs and Compound Tongxinluo Capsule. *Med. Recapitulate* 19, 2283–2285. doi:10.3969/j.issn.1006-2084.2013.12.067
- Sun, Y., Zhao, R., Liu, R., Li, T., Ni, S., Wu, H., et al. (2021). Integrated Screening of Effective Anti-insomnia Fractions of Zhi-Zi-Hou-Po Decoction via *Drosophila*

- melanogaster* and Network Pharmacology Analysis of the Underlying Pharmacodynamic Material and Mechanism. *ACS Omega* 6, 9176–9187. doi:10.1021/acsomega.1c00445
- Wang, L., Qiu, X. M., Hao, Q., and Li, D. J. (2013). Anti-inflammatory Effects of a Chinese Herbal Medicine in Atherosclerosis via Estrogen Receptor β Mediating Nitric Oxide Production and NF- κ B Suppression in Endothelial Cells. *Cell Death Dis.* 4, e551. doi:10.1038/cddis.2013.66
- Wang, S., Zhang, J., Yang, G., Ding, X., and Zheng, Y. (2019). Influence of Compound Prescription of Benefiting Qi, Detoxification and Removing Stasis and its Single Herbs on Smad3 and Smad7mRNA of Glomerular Mesangial Cells in Rats. *Liaoning J. Tradit. Chin. Med.* 46, 1755–1758. doi:10.13192/j.issn.1000-1719.2019.08.056
- Wang, Q., Ren, X., Zhang, X., Wang, G., Xu, H., Deng, N., et al. (2020). Therapeutic Effect of Berberine on Insomnia Rats by ErbB Signaling Pathway. *Med. Sci. Monit.* 26, e921831-1–e921831-11. doi:10.12659/MSM.921831
- Wang, M., Yang, L., Chen, Z., Dai, L., Xi, C., Wu, X., et al. (2021). Geniposide Ameliorates Chronic Unpredictable Mild Stress Induced Depression-like Behavior through Inhibition of Ceramide-PP2A Signaling via the PI3K/Akt/GSK3 β axis. *Psychopharmacology* 238, 2789–2800. doi:10.1007/s00213-021-05895-8
- Wu, H., Liu, R., Wang, J., Li, T., Sun, Y., Feng, X., et al. (2021). Liquid Chromatography-Mass Spectrometry In-depth Analysis and In Silico Verification of the Potential Active Ingredients of Baihe Dihuang Decoction In Vivo and In Vitro. *J. Sep. Sci.* 44, 3933–3958. doi:10.1002/jssc.202100434
- Xing, H., Zhang, K., Zhang, R., Zhang, Y., Gu, L., Shi, H., et al. (2015). Determination of Depression Biomarkers in Rat Plasma by Liquid Chromatography-Mass Spectrometry for the Study of the Antidepressant Effect of Zhi-Zi-Hou-Po Decoction on Rat Model of Chronic Unpredictable Mild Stress. *J. Chromatogr. B Analyt. Technol. Biomed. Life Sci.* 988, 135–142. doi:10.1016/j.jchromb.2015.02.037
- Yi, H., Duan, L., and Geng, Z. (2021). Research Progress on the Effective Material Basis of Chinese Herbal Compound Prescriptions. *Asia-Pacific Tradit. Med.* 17, 210–213. doi:10.11954/ytctyy.202108058
- Yu, Y., Yao, C., and Guo, D. A. (2021). Insight into Chemical Basis of Traditional Chinese Medicine Based on the State-Of-The-Art Techniques of Liquid Chromatography-Mass Spectrometry. *Acta Pharm. Sin B* 11, 1469–1492. doi:10.1016/j.apsb.2021.02.017
- Zhang, M., Sun, X., Song, H., Hu, Y., Liu, B., Wang, X., et al. (2020). Comparative Study In Situ on Rat Intestinal Absorption Mechanism of Paeoniflorin in Single Herb, Herbpair, and Complicated Chinese Herbal Formula. *Chin. Pharmacol. J.* 55, 715–721. doi:10.11669/cpj.2020.09.009
- Zhang, C., Liu, C., Wu, H., Wang, J., Sun, Y., Liu, R., et al. (2021). Global Analysis the Potential Medicinal Substances of Shuangxia Decoction and the Process In Vivo via Mass Spectrometry Technology. *Front. Pharmacol.* 12, 654807. doi:10.3389/fphar.2021.654807
- Zhao, R. (2019). Study on the Effect and Mechanism of Zhi-Zi-Hou-Po Decoction in Treating Insomnia. Available at: <https://kns.cnki.net/kcms/detail/detail.aspx?dbcode=CMFD&dbname=CMFD201902&filename=1019141279.nh&uniplatform=NZKPT&v=HPj4qSXmZx0beAS%25mmd2FggOsm8BM1TiNYWLcSEl87UNrRH7iWvRDO70k4a%25mmd2Fsy67KIgj%25mmd2F> (Accessed September 3, 2021).
- Zhou, M., Hong, Y., Lin, X., Shen, L., and Feng, Y. (2017). Recent Pharmaceutical Evidence on the Compatibility Rationality of Traditional Chinese Medicine. *J. Ethnopharmacol.* 206, 363–375. doi:10.1016/j.jep.2017.06.007
- Zhu, H., Guan, J., Shi, J., Pan, X., Chang, S., Zhang, T., et al. (2020). Simultaneous Determination of Eight Bioactive Constituents of Zhi-Zi-Hou-Po Decoction in Rat Plasma by Ultra High Performance Liquid Chromatography with Tandem Mass Spectrometry and its Application to a Pharmacokinetic Study. *J. Sep. Sci.* 43, 406–417. doi:10.1002/jssc.201900670

Conflict of Interest: The authors declare that the research was conducted in the absence of any commercial or financial relationships that could be construed as a potential conflict of interest.

Publisher's Note: All claims expressed in this article are solely those of the authors and do not necessarily represent those of their affiliated organizations, or those of the publisher, the editors, and the reviewers. Any product that may be evaluated in this article, or claim that may be made by its manufacturer, is not guaranteed or endorsed by the publisher.

Copyright © 2022 Feng, Bi, Wang, Li, Yu, Zhang, Xu, Zhang and Sun. This is an open-access article distributed under the terms of the Creative Commons Attribution License (CC BY). The use, distribution or reproduction in other forums is permitted, provided the original author(s) and the copyright owner(s) are credited and that the original publication in this journal is cited, in accordance with accepted academic practice. No use, distribution or reproduction is permitted which does not comply with these terms.



A Retrospective Metabolomics Analysis of Gamma-Hydroxybutyrate in Humans: New Potential Markers and Changes in Metabolism Related to GHB Consumption

Tingting Wang^{1*}, Kirstine L. Nielsen¹, Kim Frisch¹, Johan K. Lassen², Camilla B. Nielsen¹, Charlotte U. Andersen¹, Palle Villesen², Mette F. Andreassen¹, Jørgen B. Hasselstrøm¹ and Mogens Johannsen^{1*}

¹Department of Forensic Medicine, Section for Forensic Chemistry, Aarhus University, Aarhus, Denmark, ²Bioinformatics Research Centre, Aarhus University, Aarhus, Denmark

OPEN ACCESS

Edited by:

Ren-Ai Xu,

First Affiliated Hospital of Wenzhou
Medical University, China

Reviewed by:

Francesco Paolo Busardò,

Marche Polytechnic University, Italy

Fulvio Mattivi,

University of Trento, Italy

*Correspondence:

Tingting Wang

ting@forens.au.dk

Mogens Johannsen

mj@forens.au.dk

Specialty section:

This article was submitted to
Drug Metabolism and Transport,
a section of the journal
Frontiers in Pharmacology

Received: 19 November 2021

Accepted: 08 February 2022

Published: 03 March 2022

Citation:

Wang T, Nielsen KL, Frisch K, Lassen JK, Nielsen CB, Andersen CU, Villesen P, Andreassen MF, Hasselstrøm JB and Johannsen M (2022) A Retrospective Metabolomics Analysis of Gamma-Hydroxybutyrate in Humans: New Potential Markers and Changes in Metabolism Related to GHB Consumption. *Front. Pharmacol.* 13:816376. doi: 10.3389/fphar.2022.816376

GHB is an endogenous short-chain organic acid presumably also widely applied as a rape and knock out drug in cases of drug-facilitated crimes or sexual assaults (DFSA). Due to the endogenous nature of GHB and its fast metabolism *in vivo*, the detection window of exogenous GHB is however narrow, making it challenging to prove use of GHB in DFSA cases. Alternative markers of GHB intake have recently appeared though none has hitherto been validated for forensic use. UHPLC-HRMS based screening of blood samples for drugs of abuse is routinely performed in several forensic laboratories which leaves an enormous amount of unexploited data. Recently we devised a novel metabolomics approach to use archived data from such routine screenings for elucidating both direct metabolites from exogenous compounds, but potentially also regulation of endogenous metabolism and metabolites. In this paper we used UHPLC-HRMS data acquired over a 6-year period from whole blood analysis of 51 drivers driving under the influence of GHB as well as a matched control group. The data were analyzed using a metabolomics approach applying a range of advanced analytical methods such as OPLS-DA, LASSO, random forest, and Pearson correlation to examine the data in depth and demonstrate the feasibility and potential power of the approach. This was done by initially detecting a range of potential biomarkers of GHB consumption, some that previously have been found in controlled GHB studies, as well as several new potential markers not hitherto known. Furthermore, we investigate the impact of GHB intake on human metabolism. In aggregate, we demonstrate the feasibility to extract meaningful information from archived data here exemplified using GHB cases. Hereby we hope to pave the way for more general use of the principle to elucidate human metabolites of e.g. new legal or illegal drugs as well as for applications in more global and large scale metabolomics studies in the future.

Keywords: Gamma-hydroxybutyrate, retrospective study, metabolomics, biomarker discovery, whole blood samples, driving under the influence of drugs (DUID), drug metabolism, UPLC-QTOF analysis

INTRODUCTION

Gamma-hydroxybutyrate (GHB) is an endogenous short-chain organic acid derived from γ -aminobutyric acid (GABA) in the brain and periphery (Struys et al., 2006). GHB is approved as a prescription medication for the treatment of narcolepsy, and in the amelioration of drug and alcohol withdrawal in clinical practice (Carter et al., 2009). Also, GHB, or more recently its lactone prodrug γ -butyrolactone (GBL), is consumed recreationally as a drug of abuse, and is known as a rape drug and knock out drug in cases of drug-facilitated crimes or sexual assaults (DFSA) in forensic toxicology although the frequency apparently is low (Epperson and Ralston, 2016; Francesco et al., 2018). However, the low frequency of detection may be caused by the fast metabolism and thereby narrow detection window of typically up to 6 h in whole blood and 12 h in urine (Busardò and Jones, 2019). Many DFSA cases are likely reported late causing blood or urine samples to be drawn too late for detection of exogenous GHB intake (Kintz et al., 2001; Odujebi et al., 2007; Busardò and Jones, 2019). Therefore, the detection of GHB, discrimination between endogenous and exogenous GHB, and subsequently proving the ingestion of exogenous origin is challenging and likely underreported (Brenneisen et al., 2004; Abanades et al., 2007).

As alternative to direct detection of elevated levels of GHB, reliable and validated biomarkers that reflect prior ingestion of exogenous GHB intake can be useful though such are currently unknown. It is reported that GHB can be metabolized to succinic semialdehyde, followed by oxidation to succinate (Kaufman and Nelson, 1987). GHB can also be further catabolized to acetyl-CoA and glycolate by β -oxidation, and converted to 3-hydroxypropionyl-CoA by α -oxidation (Steuer et al., 2019). In addition, GHB-glucuronide and GHB-sulfate have been reported as Phase II metabolites of GHB (Petersen et al., 2013; Hanisch et al., 2016), but neither are apparently suitable to confirm GHB consumption (Mehling et al., 2017; Piper et al., 2017). Recently, Kraemer et al. (2022), also synthesized fatty acid esters of GHB that also were detected as potentially novel GHB metabolites in blood (Kraemer et al., 2022). GHB-carnitine and GHB-glutamate were tentatively identified for the first time as urinary metabolites of GHB in the study of Steuer et al. (2019), and the structures of GHB-carnitine was later confirmed by an authentic standard in their following study (Steuer et al., 2021). Furthermore, conjugates of GHB with glycine, taurine and pentose were found in urine, and GHB-pentose was reported to be promising for longer detection, while none of these GHB conjugates were found in blood samples (Steuer et al., 2021). 2,4-dihydroxybutyric, 3,4-dihydroxybutyric acid, and glycolic acid have also been reported to be potential GHB biomarkers by a control study with five participants (Jarsiah et al., 2021; Küting et al., 2021). Most of these studies for GHB biomarker discovery were based on a limited number of GHB-users, e.g., to our knowledge up to 20 participants and with a maximum dose of 50 mg/kg reported (Steuer et al., 2021). Furthermore, the time interval from ingestion of GHB to collection of samples is limited with

a maximum period of 30 h in a single arm study reporting succinate and glycolate as potential markers based on comparison with pre-intake levels (Palomino-Schätzlein et al., 2017). Novel reliable and importantly validated markers in whole blood is thus still needed for forensic toxicological analyses to confirm exogenous GHB intake.

Untargeted ultra-performance liquid-chromatography-high-resolution mass spectrometry (UHPLC-HRMS) based screening is increasingly used to analyze blood samples for drugs in forensic laboratories (Telving et al., 2016). This technique leaves much unexploited data and in particular if the same quality controlled method has been run over several years, a unique opportunity to mine the existing data for correlations between drug intake and formation of novel metabolites as well as impact on ordinary human metabolism. The feasibility of such a retrospective analysis in metabolomics was initially demonstrated in a seminal paper analyzing data from blood samples from humans exposed to 3,4-methylenedioxymethamphetamine (MDMA) over a 2-year period (Nielsen et al., 2016). The findings provided an initial proof-of-principle that meaningful results can be derived from retrospective data analysis of routine data from toxicological screenings. In contrast to MDMA, GHB is an endogenous compound, and the concept still needs further proof and verification for such more complicated cases. More recently, the principle was also applied by other groups to detect novel direct metabolites of valproate, as well as to examine whether data from post-mortem samples can be used to get insight into mechanism of death (Møllerup et al., 2019; Elmsjö et al., 2020). Still, the method is yet in its infancy and needs further development to, e.g., tackle archived data produced over a longer period, as the shift of retention time (RT) and intensity is much larger in retrospective analysis compared to single or consecutive runs as is custom in the field. Furthermore, a more thorough examination and validation of more advanced data analysis methods is wanted to prepare for future more large-scale studies. Finally, though important insight into direct metabolites of, e.g., MDMA and valproate was demonstrated in previous studies, a validation of the impact of the exogenous compound—here GHB—on endogenous metabolism would ultimately prove that the method merits further attention and use in the future.

Consequently, the aim of this study was to investigate a range of advanced analytical methods to discover those best suited for detecting novel and known biomarkers/direct adducts of GHB consumption in data from routine UHPLC-HRMS screenings. The results examined and potentially validated by comparison to data from controlled studies in the literature. Furthermore, to investigate the impact of GHB intake on human metabolism and also validate this to the literature. For the analysis we used HRMS data from 51 GHB positive and 51 negative driving under the influence of drugs (DUID) blood analysis acquired over a 6 year time period. Towards this aim, data normalization and a range of advanced analytical methods were applied to examine and develop our analytical approach in further depth and demonstrate the power using the GHB data and

simultaneously opening up for more large scale metabolomics studies using archived data in the future.

EXPERIMENTAL METHODS

Chemicals

Acetonitrile (LC-MS grade), methanol (LC-MS grade), formic acid and hydrochloric acid were purchased from Merck (Darmstadt, Germany). Purified water was prepared by a Milli-Q IQ 7000. All other chemical standards including GHB, amphetamine-*d*₅, cocaine-*d*₃, diazepam-*d*₅, and phenobarbital-*d*₅ were purchased from Sigma-Aldrich (Schnellendorf, Germany). 4-hydroxybutyryl-carnitine chloride was purchased from Toronto Research Chemicals (Toronto, Canada). GHB-glutamate was synthesized following the procedures in **Supplementary Material**.

Biological Material

Ante-mortem whole blood samples from drivers suspected of DUID were collected by the Danish police in tubes containing fluoride oxalate mixture and tubes containing a fluoride citrate mixture on different sites in western part of Denmark (4 police districts). The collected samples were subsequently sent to our department by normal mail. All samples were frozen and stored at -18°C immediately after arrival until analysis within a maximum of 7 days.

Sample Extraction

For the ultra-high-performance-liquid-chromatography quadrupole-time-of-flight mass spectrometry (UHPLC-QTOF) analysis, the extraction procedures followed the method in the study of Telving et al. (2016). An aliquot of the whole blood sample was precipitated with a mixture of methanol and acetonitrile and centrifuged. The supernatant was filtered through a 30 kDa filter and evaporated to dryness, reconstituted and transferred to a LC-vial. For quantitative analysis on ultra-high performance-liquid-chromatography triple-quadrupole (UHPLC-QQQ), the extraction procedures referred to the study of Sørensen and Hasselstrøm, (2012). In short an aliquot of the whole blood sample was precipitated with a mixture of methanol and acetonitrile and centrifuged. The supernatant was transferred to a cation exchange column and the eluate was transferred to a LC-vial.

Untargeted Screening Using UHPLC-QTOF

The qualitative analysis of the whole blood sample extracts was performed on an ACQUITY I-Class UHPLC system (Waters Corporation, Milford, MA, United States) coupled to a Bruker maXis Impact QTOF mass spectrometer (Bruker Daltonics, Bremen, Germany). The analysis was performed using an ACQUITY BEH C18 (100 mm \times 2.1 mm, 1.7 μm) column with mobile phases A consisting of 0.1% formic acid in water and B of acetonitrile, and the analytical method was carried out using the method by Telving et al., (2016).

An electrospray ionization source was operated in positive mode using *m/z* calibration range of 50–1000 Da at a rate of

10 Hz, and fragmentation analysis was carried out using broadband Collision Induced Dissociation (bbCID) with collision energy of 25 eV. The exactly same analytical method was applied over the 6 years, though the column, was changed regularly e.g. approximately every 6 months during the period. Auto-MS/MS with collisions carried out at energies from 10 to 35 eV was additionally used for some specific fragmentation of selected features after retrospective data analysis for further verification of structures.

Quantitative Analysis Using UHPLC-QQQ

Quantitative Analysis of GHB was routinely carried out using a validated method with UHPLC-QQQ. The method was described in a previous study (Sørensen and Hasselstrøm, 2012).

Data Collection and Preprocessing

Samples in this study were collected over 6 years from 2015 to 2020 both inclusive. Fifty-one samples with verified GHB concentrations above 10 mg/kg were matched against a control group of 51 samples with endogenous levels of GHB (<10 mg/kg), 10 mg/kg was selected as a threshold to be sure of GHB intake. Besides GHB, various other drugs were also detected providing both group similar “backgrounds” to level out potential confounding effects by other drugs (**Supplementary Table S1**). The detailed sample information including the GHB concentration and data collection years of both the control and the GHB positive group is shown in **Supplementary Table S2**.

Mass spectrometry data obtained from the UHPLC-QTOF were transformed to the *mzml* file format using Bruker Compass DataAnalysis (Bruker Daltonics, Bremen, Germany) after internal calibration. The *mzml* files were processed with XCMS in R (version 4.0). The XCMS parameters were optimized (**Supplementary Table S3**) and a tabulated data matrix list with aligned RT and *m/z* values was summarized in .csv format. The ions with null value in the data matrix file were imputed with one third of the lowest value of the given ion in all the samples in order to make log-transformation in the next step. Known adducts or isotopes of GHB, namely [(104.0467 + H+1)⁺, (104.0467 + Na)⁺, (104.0467 + Na+1)⁺, (104.0467-H₂O)⁺, (104.0467-H₂O+1)⁺] were also excluded in the statistics to get more reliable results for other GHB markers.

As alternative to ordinary quality controls samples in our retrospective analysis, we initially corrected the peak intensity using the internal standards (IS) with the NOMIS method (normalization using optimal selection of multiple internal standards). The data were log-transformed (log 10) to fit the assumptions of the NOMIS method and then normalized by four IS (“metabolomics” package), as illustrated in the study of Sysi-Aho et al. (2007). NOMIS uses variability information from multiple IS to find the optimal normalization factor for each feature. We validated our data quality and the accuracy of the “NOMIS” correction in retrospective analysis by comparing the GHB intensity (not corrected/corrected by NOMIS) in all samples obtained from UHPLC-QTOF to

GHB levels measured by UHPLC-QQQ using a linear regression analysis.

Statistics and Machine Learning T-Test, Fold Change, and PCA

The normalized data obtained by the NOMIS method were used for the following statistical analysis. Pairwise univariate T-tests were used to test the difference for each feature between groups (control/positive) using a critical value of 0.05 (Wang et al., 2021). To account for multiple testing, *p*-values were further adjusted using the false discovery rate (FDR). Also, the fold change (FC) was used to illustrate the ratio of the integrated peak areas between the control and the positive GHB group. Principle component analysis (PCA) by using “ggplot” R package was applied for multivariate analysis.

Pearson Correlation Analysis and Correlation Network

Pearson correlation analysis was used to quantitatively calculate the correlation between each feature's and GHB's intensity to find potential GHB metabolites. The correlation coefficients were calculated using the “rcorr” function in the “Hmisc” package in R. On the basis of Pearson correlation, we also constructed a correlation network (CN) using all selected GHB-related metabolites to explore the potential interaction between all these features and make a better understanding of the impact of GHB on metabolism. CN can be interpreted as a system biological data analysis method. Correlations between features were considered significant if FDR-corrected *q*-value < 0.1 and only significant features were displayed in the network. Each edge represents correlation between features, and each node represents one selected feature. Features were plotted with the R package “qgraph.” Only networks containing a minimum of three molecules were plotted.

Machine Learning Methods

The machine learning methods used for biomarker discovery in this study were selected based on previously reported methods (Nielsen et al., 2016; Liang et al., 2020; Liebal et al., 2020). Orthogonal partial least squares discriminant analysis (OPLS-DA) was applied for feature selection using SIMCA version 16 (Umetrics, Umeå, Sweden). Pareto scaling was applied to the data for the OPLS-DA model. The parameters Q2 and R2X (R2Y) were used to evaluate the performance of the OPLS-DA model. Q2 indicates the prediction quality of the model, whereas R2 explains how well the model fit the data. The accuracy of the OPLS-DA model was validated with 10-fold cross validation, and the dataset was further randomly divided into a training set and a test set containing 50% of the samples for each. Variable importance parameters (VIPs) from OPLS-DA indicate the importance of each feature that contributes to the separation of the two groups (VIP ≤ 0.5: unimportant; VIP > 1: significantly important according to usual interpretation of VIP) (Sinclair et al., 2021). Least absolute shrinkage and selection operator linear regression (LASSO) from the “glmnet” R package was used to predict metabolites associating to exogenous GHB intake. Random forest regression (RFR) and classification (RFC) from the “randomForest” R package were also applied to select the

potential metabolites that associated to GHB. RFR calculates the percentage increase of the mean squared error (%IncMSE), which is used to explain the importance of the features corresponding to GHB. %IncMSE indicates the increase in mean squared error (MSE) of predictions (estimated with out-of-bag-CV) as a result of variables being permuted (values randomly shuffled) (27). We also randomized all the samples and applied OPLS-DA model again as an example to see whether we could still identify any markers.

Metabolite Identification

We used the guidelines from the Metabolomics Standard Initiative to annotate features (Sumner et al., 2007). Selected features with high importance in correlation-based and statistic-based approach were searched from our in-house database with endogenous metabolites (ca. 400 metabolites) and/or online databases as METLIN (<https://metlin.scripps.edu>), the human metabolome database (<http://www.hmdb.ca>), lipid maps (<http://www.lipidmaps.org>), and KEGG (<http://www.genome.jp/kegg/>) using MetFrag (<http://msbi.ipb-halle.de/MetFrag>) *in silico* fragmentation for tentative identification. Structures of the selected features were confirmed by matching the *m/z*-values, fragment pattern, and RT to database or available authentic standards. Annotated metabolites were marked with identification levels. For features identified to level 1, we compared *m/z* of precursor, retention time and fragmentation spectra to an authentic standard. For level 2 identification, we compared the *m/z* of precursor, fragmentation spectra to public database.

RESULTS

XCMS & NOMIS Align and Normalize the Data Over 6 Years

The GHB concentration quantified by UHPLC-QQQ in the positive group is in the range from 10 mg/kg to 231 mg/kg whole blood, and the GHB level in 51 negative samples are all below 10 mg/kg. RT deviates with a maximum of 20 s before peak alignment, which indicates the variation between samples. Chromatograms of all studied samples before and after RT correction are shown in **Supplementary Figure S1**. The peak area variation of the four internal standards in all samples varies up to five times (**Supplementary Figure S2**). Regarding to the integration accuracy, we compared the integrated peak area of GHB by XCMS to the manually integrated peak area of GHB. As shown in **Supplementary Figures S3**, in general the peak integration accuracy is acceptable ($R^2 = 0.85$), and only six samples (11.8%) are a bit off from others with their xcms-integrated peak area around half of the true value.

The accuracy and performance of the “NOMIS” normalization method in retrospective analysis is evaluated by plotting the logarithmic peak area of GHB in all the positive samples integrated by XCMS using the routine screening data acquired on UHPLC-QTOF to the GHB concentration obtained by UHPLC-QQQ. As shown in

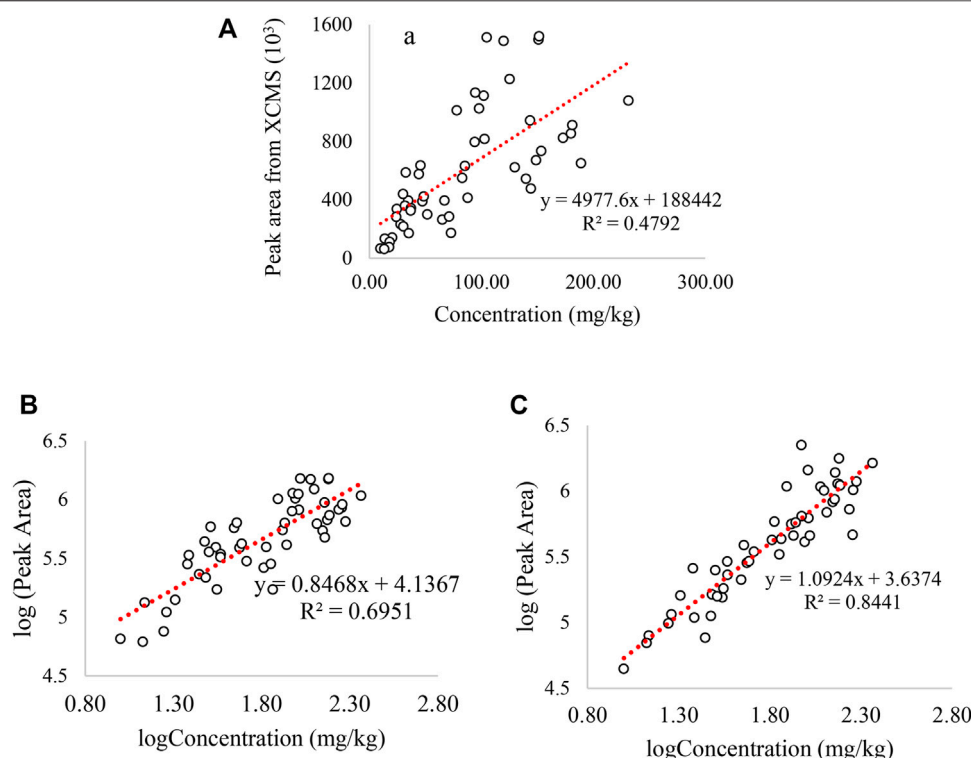


FIGURE 1 | Correlation between the GHB concentration and the GHB peak area integrated by XCMS: **(A)** correlation between GHB concentration and GHB peak area without log-transformation and data normalization, **(B)** correlation between GHB concentration and GHB peak area with log-transformation but without any data normalization, **(C)** correlation between GHB concentration and GHB peak area with log-transformation and NOMIS normalization. The peak area in y-axis is from screening method on UHPLC-QTOF, and concentration of x-axis is measured by UHPLC-QQQ. Only GHB positive samples were used in all the plots.

Figure 1, the R^2 is 0.48 before log-transformation and data normalization, and it is 0.69 after log-transformation but before normalization. The correlation further increases to 0.844 following NOMIS, which indicates a strong positive correlation across a long time period and which we evaluate as sufficient for the current purpose.

Statistical Analysis for Selection of Potential GHB-Markers

XCMS pre-processing extracted 3913 features. The FDR adjusted p -values (q -value) resulted in 554 features using a threshold of 0.05 and 110 features using a threshold of 0.01. For FC, 674 features were higher than 1.2, 147 were higher than 1.5, and 34 were higher than 2.0. Finally, 516 features had FC values lower than 0.8, and some of them could be potential down-regulated metabolites induced by GHB. M354T52, M507T82, M250T52 are top three features with highest FC, and their FC are 6.0, 4.0, and 3.8, respectively. The FC of all features can be found in **Supplementary Table S4**. The identified metabolite GHB-carnitine and the tentatively identified metabolite GABA-2-hydroxyglutarate also have relative high FC with values of 2.6 and 2.3 (The top 20 highest). A volcano plot is shown in **Figure 2**, and FC with

1.2 and q -value 0.05 were used as cutoff. PCA shows no clear clustering between the two groups, which indicates that GHB metabolites does not vary enough to affect the first two principal components of the PCA (**Supplementary Figure S4**).

Correlation and Machine Learning Models to Select Significant Features Correlated to GHB

Pearson correlation, OPLS-DA, RFR, RFC, and LASSO were applied to identify the potential metabolites correlated to GHB. In Pearson correlation, features with correlation coefficients (R) higher than 0.5 are defined as significant resulting in 11 positively correlated features ($R > 0.6$) and one negatively correlated feature (M165T51) to GHB ($R < -0.6$). These features with high correlation coefficients also show high VIP scores ($VIP > 2.5$) in OPLS-DA (**Figure 3A**) and are the most significant features in the S-plot (**Figure 3B**) and volcano plot (**Figure 2**).

OPLS-DA discriminates the two groups with $R^2Y = 0.86$, $R^2X = 0.42$, and $Q^2 = 0.36$. The returned root-mean-square error of estimation (RMSEE) is 0.19 using 10-fold cross-validation. The high R^2 and the low Q^2 indicates some overfitting, which is also seen by the low specificity in the

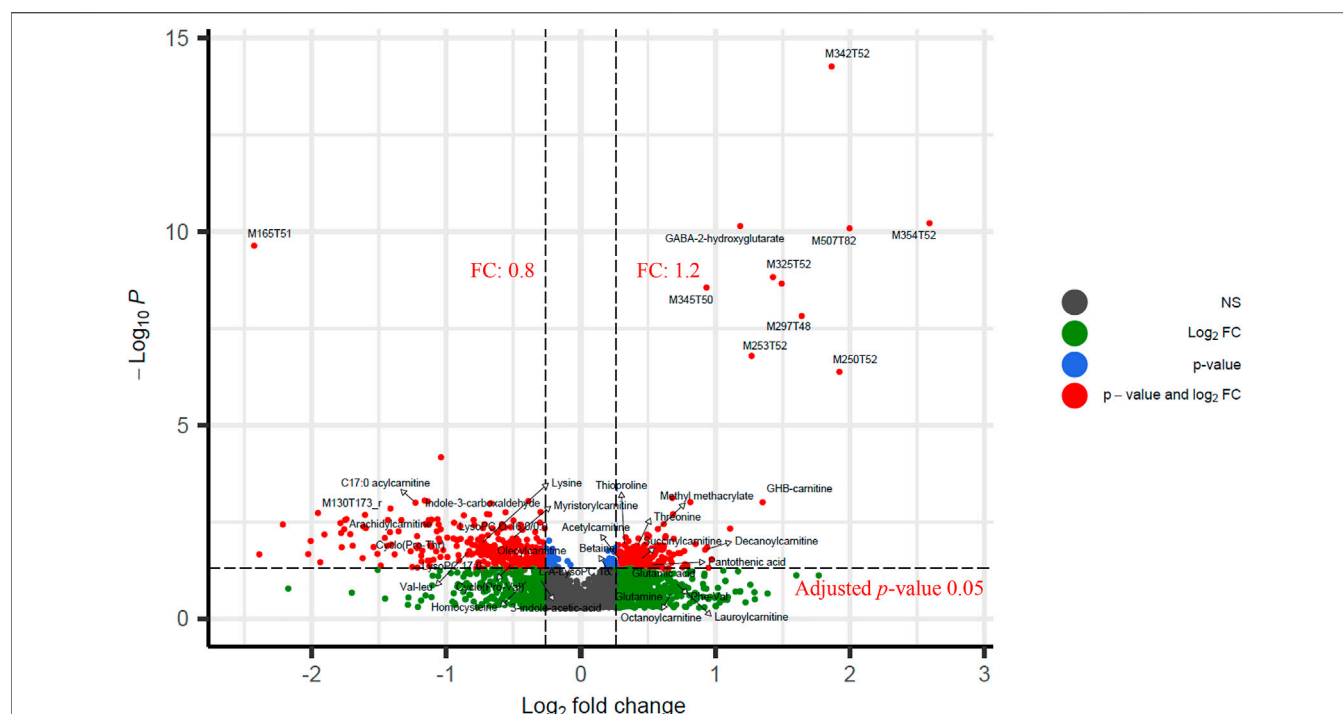


FIGURE 2 | Volcano plot of significant features between the GHB positive group and the control group. y-axis represents the log-transformed adjusted p -values calculated by t -test. x-axis is $\log_2(\text{FC})$. Cutoffs of 1.2 and 0.05 are used for fold change and adjusted p -values (q -value), respectively. FC of 674 features are higher than 1.2, and 516 features have FC lower than 0.8. Adjusted p -values of 554 features are higher than 0.05.

validation set. This could be explained by the endogenous nature of GHB. In OPLS-DA, the sensitivity (true positive) and specificity (true control) from test set validation are 92% and 76%. Among all the features, VIP values of 1350 features are higher than 1.0, and 353 features are higher than 1.5. The importance of features are shown in an S-plot (**Figure 3B**), where the x-axis indicates the magnitude of the variables and their importance, and the y-axis shows the reliability, the closer to ± 1 , the more reliable. The most discriminating features of GHB positive samples versus the control group are highlighted. M165T51, M507T82, M354T52, M342T52, M297T48 are the top five features with highest VIPs that discriminate the two groups. GHB-carnitine, GABA-2-hydroxyglutarate (tentatively identified) and some other endogenous metabolites or reported unknown features also show significant importance in S plot, which will be discussed further in the following sections. As a control of the approach, we finally randomized the united pool of samples and applied the OPLS-DA model again, the results are shown in **Supplementary Table S4**. As evident, we could not find any GHB markers among the top 50 features with highest VIP score using the randomized samples, e.g., GHB carnitine (M248T57) got a VIP score of only 0.41.

For the LASSO linear regression, the model is first validated by 10-fold cross-validation. The RMSE is 0.27 and the R^2 is 0.96, which is sufficient to make prediction. LASSO selects 14 features as important features, where four of them (M929T287, M495T277_2, M192T140, M410T173) are found to be

insignificant in Pearson correlation with correlation coefficients of 0.36, 0.35, and 0.23, and 0.17, respectively.

The RFR and RFC algorithm is another way to provide information on variable importance. The accuracy of RFC using 10-fold CV is 0.89 ($mtry = 58$). The RMSE of RFR is 0.62, and R^2 is 0.80 ($mtry = 88$). In the results, %IncMSE of 304 features are higher than 1.2, and 76 features are higher than 1.5. The top 11 features are consistent with the top significant features in the Pearson correlation with almost the same order. RFC calculates mean decrease accuracy (MDA) of each feature, which expresses how much accuracy the model losses by excluding each variable. In the results of RFC, MDA of 140 features are higher than 1.2, and 38 features are higher than 1.5. The prioritized features sorted by all the different data analysis methods and how they overlap are shown in **Supplementary Table S4**. **Table 1** shows all the information of selected metabolites that were prioritized and predicted by the different statistics and models. The ID, RT, annotations, T-test, FC, and importance of various models of these features are all shown here, and explanation of the content in this **Table 1** will be discussed in the following section.

Feature Selection for Further Analysis

Three feature selection strategies were used: a statistic-based approach, a correlation-based approach and a machine learning based approach. In the statistic-based approach, T-test and FC were used, and absolute fold-change (1.2) and q -value (0.1) were treated as statistical significance cutoffs. Both correlation and machine learning approaches were based on

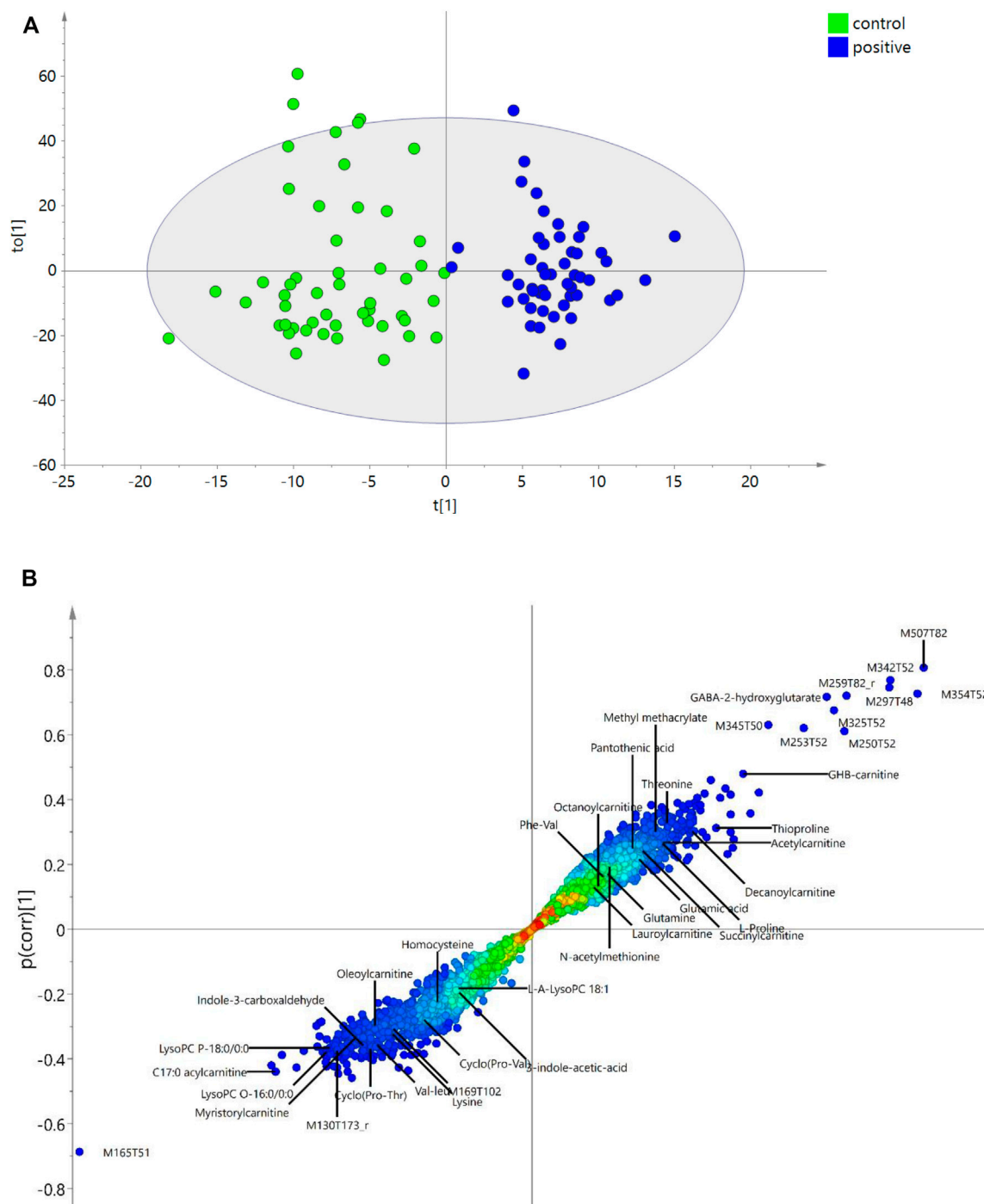


FIGURE 3 | OPLS-DA. (A) OPLS-DA plot showing the discrimination between control and the GHB positive group. **(B)** S-plot highlighting the most discriminating features of GHB intake in the positive samples compared to controls in the OPLS-DA model. The x-axis shows the magnitude of the variables and their importance, and the y-axis indicates the reliability; the closer to ± 1 , the more reliable. The annotation of each feature with ID refers to **Table 1**. The unknown features marked with “r” mean they were reported in the literature.

features with statistical significance. In the correlation-based approach, the top 50 features sorted by Pearson correlation were selected. The top 50 features with highest VIP values in OPLS-DA model were also selected. In addition, all features were

matched with our in-house database that includes endogenous metabolites and all the GHB-related metabolites reported in the literatures, and those metabolites showing significance in at least one method ($FC > 1.2/FC < 0.8$, $VIP > 1$ or $q\text{-value} < 0.1$) are also

TABLE 1 | Metabolites found to be associated with GHB intake that predicted by random forest, Pearson correlation, lasso, and OPLS VIP-Scores.

ID	Annotation	Formula	rt_min	Dir	Idl	FC	m/z	VIP	p-value	q-value	Lasso	% IncMSE	MDA	PC
M147T21	Glutamine Seo et al. (2018) ^a	C ₅ H ₁₀ N ₂ O ₃	0.35	↑	1	1.28	147.0764	1.05	0.072	0.126	0	-0.95	-1	0.18
M176T283	3-indole-acetic-acid	C ₁₀ H ₉ NO ₂	4.72	↓	1	0.81	176.0706	0.77	0.044	0.095	0	0.54	-1.42	-0.12
M385T74	5-adenosyl-homocysteine	C ₁₄ H ₂₀ N ₆ O ₅ S	1.23	↑	1	1.15	385.1288	1.29	0.196	0.214	0	-1	0	0.1
M204T23	Acetylcarnitine	C ₉ H ₁₇ NO ₄	0.38	↑	1	1.23	204.1238	1.48	0.006	0.031	0	1.39	0	0.26
M456T478	Arachidylcarnitine	C ₂₇ H ₅₃ NO ₄	7.97	↓	2	0.49	456.4044	2.18	<0.001	0.005	0	1	0.31	0.36
M118T24	Betaine	C ₅ H ₁₁ NO ₂	0.4	↑	1	1.18	118.0868	1.44	0.036	0.084	0	1.19	1	0.18
M428T460	C17:0 acylcarnitine	C ₂₅ H ₄₉ NO ₄	7.66	↓	2	0.43	428.3737	2.69	<0.001	0.001	0	-0.13	0	-0.38
M199T92	Cyclo (Pro-Thr)	C ₉ H ₁₄ N ₂ O ₃	1.53	↓	1	0.52	199.1076	1.63	<0.001	0.008	0	1	1	-0.3
M197T159	Cyclo (Pro-Val)	C ₉ H ₁₆ N ₂ O ₂	2.64	↓	1	0.7	197.1285	1.09	0.008	0.038	0	1.1	1	-0.23
M316T356	Decanoylcarnitine	C ₁₇ H ₃₃ NO ₄	5.93	↑	1	1.9	316.2493	1.68	0.002	0.017	0	-1	-0.21	0.26
M234T52	GABA-2-hydroxyglutarate	C ₉ H ₁₅ NO ₆	0.87	↑	2	2.27	234.0969	2.92	<0.001	<0.001	0.19	4.31	5.57	0.79
M248T57	GHB-carnitine Steuer et al. (2019) ^a	C ₁₁ H ₂₁ NO ₅	0.95	↑	1	2.55	248.149	2.11	<0.001	<0.001	0	2.09	2.37	0.43
M148T21	Glutamic acid Seo et al. (2018) ^a	C ₅ H ₉ NO ₄	0.35	↑	1	1.3	148.0604	1.29	0.032	0.079	0	-1	-1	0.26
M136T23_2	Homocysteine	C ₄ H ₉ NO ₂ S	0.38	↓	1	0.76	136.0425	1.05	0.051	0.103	0	0.97	-1	-0.2
M146T128	Indole-3-carboxaldehyde	C ₉ H ₇ NO	2.14	↓	2	0.55	146.0602	1.89	<0.001	0.002	0	-1	-0.37	-0.31
M206T246	3-Indole lactic acid	C ₁₁ H ₁₁ NO ₃	4.11	↓	1	0.85	206.081	0.66	0.042	0.091	0	0.67	1	-0.16
M522T480	L-A-LysoPC; 18:1	C ₂₆ H ₅₂ NO ₇ P	8	↓	1	0.77	522.3569	0.88	0.044	0.095	0	-1	0	-0.21
M344T387	Lauroylcarnitine	C ₁₉ H ₃₇ NO ₄	6.45	↑	1	1.68	344.2798	0.77	0.112	0.158	0	-1.08	-1	0.11
M116T22_2	Proline Seo et al. (2018)	C ₅ H ₉ NO ₂	0.37	↑	1	1.18	116.0711	1.42	0.015	0.051	0	0.83	0	0.26
M120T21	Threonine	C ₄ H ₉ NO ₃	0.35	↑	1	1.34	120.0656	1.37	0.001	0.014	0	1.46	0	0.32
M147T80	Lysine Seo et al. (2018)	C ₆ H ₁₄ N ₂ O ₂	1.33	↓	1	0.6	147.1127	1.62	<0.001	0.012	0	1.92	0	-0.27
M510T491	LysoPC 17:0	C ₂₅ H ₅₂ NO ₇ P	8.18	↓	1	0.57	510.3559	2.1	0.003	0.021	0	0	1	-0.27
M482T481	LysoPC O-16:0/0:0	C ₂₄ H ₅₂ NO ₆ P	8.02	↓	2	0.56	482.3605	2.24	<0.001	0.01	0	-1	-1	-0.32
M508T489	LysoPC P-18:0/0:0	C ₂₆ H ₅₄ NO ₆ P	8.15	↓	1	0.57	508.3765	2.23	<0.001	0.012	0	0.37	-1.73	-0.3
M101T88	Methyl methacrylate	C ₅ H ₈ O ₂	1.46	↑	2	1.49	101.0597	1.27	<0.001	0.005	0	0.9	-0.68	0.45
M298T130	Methylthioadenosine (MTA)	C ₁₁ H ₁₅ N ₅ O ₃ S	2.17	↑	1	1.89	298.0968	1.57	0.032	0.079	0	-0.34	0	0.19
M372T413	Myristoylcarnitine	C ₂₁ H ₄₁ NO ₄	6.88	↓	1	0.7	372.311	1.97	<0.001	0.008	0	-0.9	0	-0.31
M192T140	N-acetylmethionine Luca et al. (2014) ^a	C ₇ H ₁₃ NO ₃ S	2.34	↑	1	1.34	192.0689	0.87	0.018	0.058	0.04	1.38	1	0.22
M288T319	Octanoylcarnitine	C ₁₅ H ₂₉ NO ₄	5.32	↑	1	1.6	288.2173	0.95	0.186	0.208	0	-0.84	0	0.09
M426T443	Oleoacylcarnitine Luca et al. (2014)	C ₂₅ H ₄₇ NO ₄	7.38	↓	1	0.62	426.3583	1.74	0.002	0.018	0	-0.43	1	-0.26
M220T109	Pantothenic acid	C ₉ H ₁₇ NO ₅	1.82	↑	1	1.43	220.1182	1.01	0.01	0.041	0	1.05	-1	0.23
M265T151	Phe-Val	C ₁₄ H ₂₀ N ₂ O ₃	2.51	↑	1	1.63	265.1545	0.86	0.064	0.117	0	0.51	-0.64	0.17
M262T41	Succinylcarnitine Steuer et al. (2019) ^a	C ₁₀ H ₁₄ N ₄ O ₅	0.68	↑	2	1.36	262.1285	1.29	0.005	0.03	0	-1	0	0.22
M134T23	Thiopropine	C ₄ H ₇ NO ₂ S	0.38	↑	1	1.25	134.0271	2.04	<0.001	0.013	0	-1.38	1	0.33
M231T428	Val-leu	C ₁₁ H ₂₂ N ₂ O ₃	7.14	↓	2	0.56	231.1743	1.67	0.002	0.018	0	-1.54	0	-0.32
M153T52	Xanthine	C ₅ H ₄ N ₄ O ₂	0.86	↑	1	1.48	153.0407	1.37	0.046	0.097	0	0.98	-1	0.17
M218T81	Unknown		1.34	↓		0.46	218.059	2.76	0.0001	0.004	0	-0.77	0.74	0.37
M80T42	Unknown		0.71	↓		0.14	80.04935	2.63	<0.001	0.011	0	0	1	-0.26
M93T95	Unknown		1.58	↓		0.43	93.06945	2.73	<0.001	0.007	0	1.34	0.96	-0.33
M96T43	Unknown		0.71	↓		0.26	96.0443	2.55	<0.001	0.002	0	-1.02	0	0.32
M79T95	Unknown		1.58	↓		0.22	79.0541	2.5	0.0001	0.004	0	-1	1	0.29
M538T535	Unknown		8.92	↓		0.48	538.3872	2.47	<0.001	0.006	0	1.02	0.62	-0.34
M119T128	Unknown		2.13	↓		0.29	119.0683	2.44	0.0001	0.003	0	-1.08	1.41	0.29
M271T560	Unknown		9.33	↑		1.76	271.2744	2.27	<0.001	<0.001	0	-1.87	0	0.38
M262T52	Unknown		0.87	↑		2.16	262.0134	1.95	<0.001	0.005	0	4.28	2.32	0.54
M256T52	Unknown		0.87	↑		1.53	256.079	1.61	<0.001	0.004	0	1.5	2.84	0.47
M840T313	Unknown		5.22	↓		0.76	840.2059	1.42	<0.001	<0.001	0	1.16	-1.16	0.39
M733T286_3	Unknown		4.76	↑		1.26	733.2255	1.23	<0.001	0.008	0	1.21	0.92	0.4
M130T173	Unknown Steuer et al. (2019) ^a		2.89	↓		0.38	130.0498	2.15	<0.001	<0.001	0	-0.56	0	-0.34
M169T102	Unknown Steuer et al. (2019) ^a		1.71	↓		0.68	169.1331	1.47	0.01	0.042	0	0.03	0	-0.23
M367T466			7.76	↑		1.11	367.1415	1.05	0.069	0.122	0	0	0	0.15

(Continued on following page)

TABLE 1 | (Continued) Metabolites found to be associated with GHB intake that predicted by random forest, Pearson correlation, lasso, and OPLS VIP-Scores.

ID	Annotation	Formula	rt_min	Dir	Idl	FC	m/z	VIP	p-value	q-value	Lasso	% IncMSE	MDA	PC
M259T82	Unknown Steuer et al. (2019) ^a		1.37	↑		2.82	259.0786	3.1	<0.001	<0.001	0	3.91	6.85	0.73
M342T52	Unknown Steuer et al. (2019) ^a		0.87	↑		3.64	342.0608	3.54	<0.001	<0.001	0.17	5.81	7.29	0.83
M165T51	Unknown, adduct of GHB		0.84	↓		0.19	165.0868	4.48	<0.001	<0.001	-0.13	1.39	4.97	-0.63
M507T82	Unknown		1.36	↑		3.99	507.1547	3.87	<0.001	<0.001	0.33	4.47	6.3	0.8
M297T48	Unknown		0.81	↑		3.12	297.0812	3.54	<0.001	<0.001	0.7	2.76	5.1	0.71
M325T52	Unknown		0.86	↑		2.69	325.1072	2.99	<0.001	<0.001	0.02	5.8	5.12	0.8
M345T50	Unknown		0.84	↑		1.91	345.0675	2.36	<0.001	<0.001	0.02	3.37	4.43	0.65
M354T52	Unknown, adduct of GHB		0.87	↑		6.03	354.0608	3.81	<0.001	<0.001	0.94	6.18	7.11	0.85
M253T52	Unknown		0.87	↑		2.41	253.0213	2.71	<0.001	<0.001	0.13	4.41	3.77	0.75
M250T52	Unknown, adduct of GHB		0.87	↑		3.79	250.0135	3.11	<0.001	<0.001	0	4.33	5.01	0.7

^ameans the feature has been reported in the literature to be correlated to GHB.

%IncMSE, percentage increase of the mean squared error; MDA, mean decrease accuracy; Dir, direction of regulation by GHB; Idl, identification level. For features identified to level 1, we compared the m/z of precursor, retention time and fragmentation spectra using an authentic standard. For level 2 identification, we compared the m/z of precursor, fragmentation spectra to public database. PC, Pearson correlation coefficients.

listed in **Table 1**. In the end, all these features with high importance (statistically or the individual top 50 lists) in different strategies and the endogenous metabolites that match with our in-house database and shows significance were combined, resulting in 89 features (**Table 1**; **Supplementary Table S5**).

Metabolites Associated With GHB Levels

A range of features that correlated to GHB levels are identified or tentatively identified, as shown in **Table 1**, and their fragment patterns that obtained from DDA or DIA mode from UHPLC-QTOF are shown in **Supplementary Table S6**. In **Supplementary Table S6**, fragments without abundance mean that they were fragmented in b/cid mode since not all the precursors got fragmented, otherwise they were fragmented in auto-MS/MS mode. Among the identified features, GHB-carnitine is identified with an authentic standard, which has been reported in previous studies (Steuer et al., 2019; Steuer et al., 2021). GHB-carnitine is found to be a highly significant feature in both OPLS-DA (VIP: 2.11), Pearson correlation ($R = 0.43$), and FC (2.55). M428T460 is tentatively identified as a C17:0 acylcarnitine with VIP score of 2.69 and FC of 0.43, and M456T478 was tentatively identified as arachidylcarnitine. Nine carnitine conjugates are found to be correlated to GHB intake, the levels of myristoylcarnitine, oleoylcarnitine, C17:0 acylcarnitine, and arachidylcarnitine are negatively correlated to GHB according to their FC and Pearson correlation coefficients, while decanoyl carnitine, lauroylcarnitine, octanoylcarnitine, succinylcarnitine, and acetylcarnitine are upregulated by GHB.

Feature M234T52 has the 10th highest VIP among all detected features (2.92) and also high FC (2.27). This metabolite has the same mass as GHB-glutamate that was

reported in the study of Steuer et al. (2021), but has so far only been tentatively identified without an authentic standard as it is not commercially available. We therefore synthesized GHB-glutamate according to the structure they proposed in their paper and tested it against our samples (Steuer et al., 2019). However, the RT of the authentic GHB-glutamate did not fit with the RT of M234T52 detected in GHB samples with delta RT of 0.4 min, which means that M234T52 is not GHB-glutamate, but another compound with high correlation to GHB intake, possibly GABA-2-hydroxyglutarate as discussed below. The chromatogram of a GHB sample spiked with authentic GHB-glutamate is shown in **Supplementary Figure S5**. The two main fragments produced by M234T52 are m/z 84.05 and m/z 130.05, which are also found in GHB-glutamate but with different abundance (**Supplementary Figure S5**). Also, GHB-glutamate gives rise to two additional fragments, m/z 102.06 and m/z 69.03, which is not produced by M234T52. The detailed synthesis procedure and NMR spectra of GHB-glutamate are shown in **Supplementary Figures S6–S11**, and the proposed structure and possible pathway of GABA-2-hydroxyglutarate is shown in **Supplementary Figure S12**. Two unknown features M259T82 and M507T82 might belong to the same compound due to same RT and show particularly high significance in various statistics and models, but no matches are found in any database.

There are also several amino acids or conjugates of amino acids that are found to be correlated to GHB levels, namely glutamine, lysine, cyclo (Pro-Thr), cyclo (Pro-Val), Phe-Val, 5-adenosyl-homocysteine, homocysteine, threonine, glutamic acid, proline, and Val-Leu. The structures of these amino acids are all confirmed by authentic standards. Lysine, Val-Leu, cyclo (Pro-Thr), cyclo (Pro-Val), and homocysteine are all downregulated by

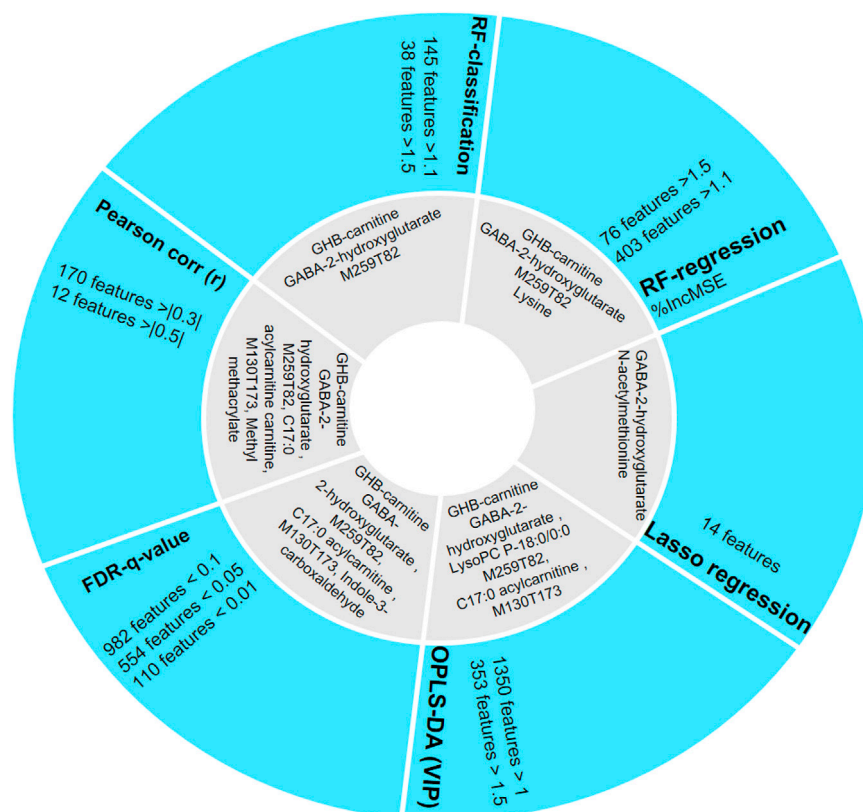


FIGURE 4 | Comparison of the different feature selection methods and identified compounds (as shown in grey area) among the top 50 most important features sorted by each method. FDR q -value, OPLS-DA, and Pearson correlation prioritize most metabolites in their top 50 features compared with control studies.

GHB, while the remaining metabolites are upregulated by GHB intake.

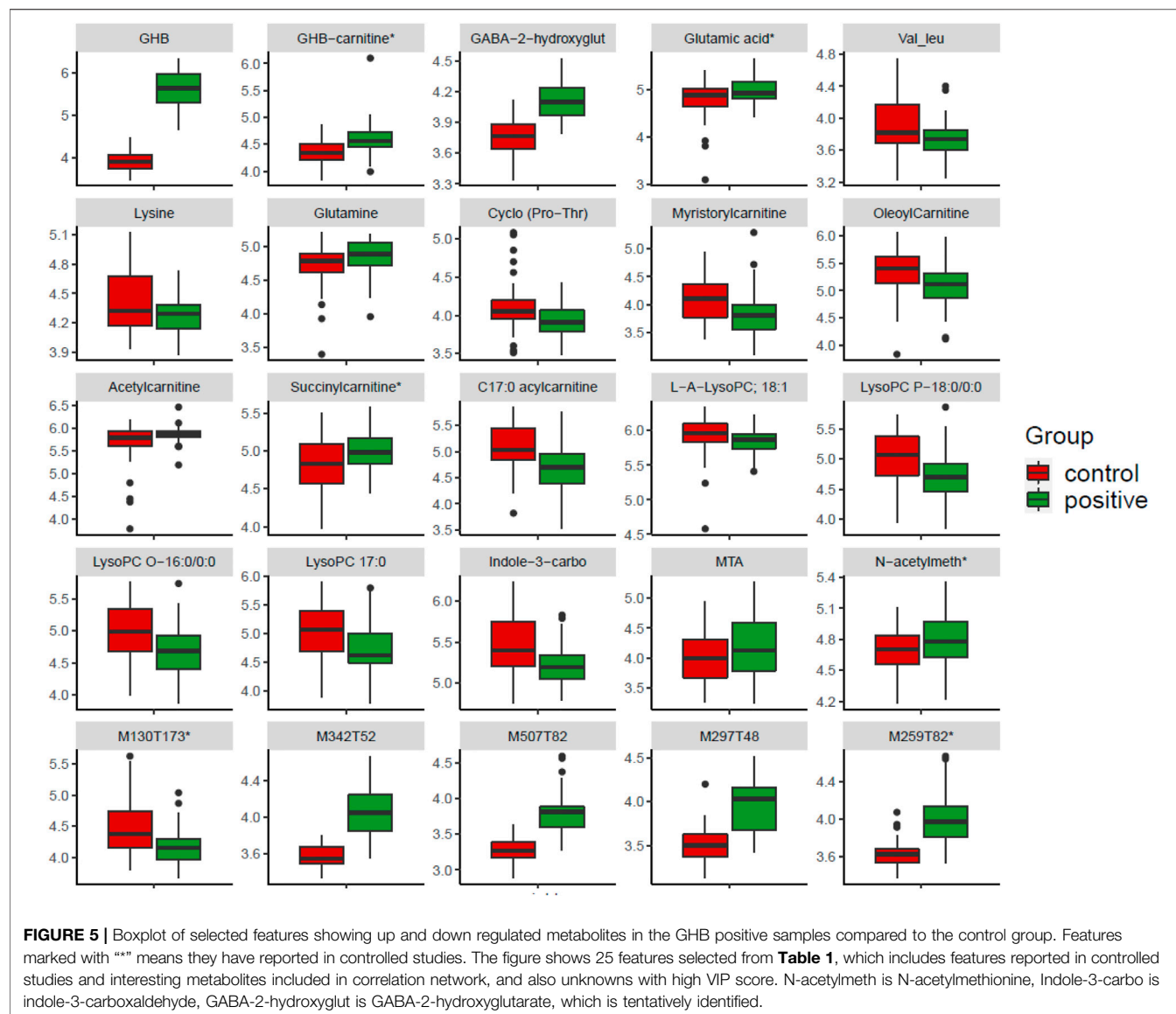
Validation of Different Feature Selection Methods by Comparison to Controlled GHB Studies

To further compare the performance of the different statistics and machine learning models, the identified GHB-related metabolites among the top 50 features sorted by each method are shown in **Figure 4**. Some of the identified metabolites have been reported previously in controlled GHB studies and can be used to validate our approach and the different analytical methods.

As GHB-carnitine, succinylcarnitine, and several reported unknowns are not found in LASSO, this method is considered less reliable for biomarker discovery in our case since it penalized these previously described GHB-related metabolites (Liebal et al., 2020). Relatively few GHB-related metabolites are also found in top 50 features sorted by RFR and RFC (**Figure 4**), with only two GHB-related features (GHB-carnitine and M259T82) consistent with the literature. Both RFR and RFC however prioritize M234T52 (possibly GABA-2-hydroxyglutarate). OPLS-DA is able to model the difference between the GHB positive and control group, and using this machine learning method four reported GHB-related metabolites could be found in top 50

features with high significance ($VIP > 1$). Pearson correlation provides valuable information to discover metabolites that are highly correlated to GHB intake, and is known as the best method of measuring the association between variables of interest. However, as our study is uncontrolled, Pearson correlation may not be the best method to interpret the results as the Pearson correlation coefficients we obtained from most relevant metabolites are not high enough to take as significant features according to a typical significance cutoff such as 0.5, but still provides additional information for the change of metabolism. FDR q -value gives valuable information for potential biomarkers and four of the top 50 prioritized features have previously been identified as GHB-related metabolites (Steuer et al., 2019). Random forest allows direct biological understanding of the decision and classification (Liebal et al., 2020). In aggregate, for our data, the outputs of RFR and RFC vary much compared to the OPLS-DA and FDR q -value, which provides less conservative results. Thus, we regard OPLS-DA as the machine learning method used for feature selection giving the most comprehensive information, while its combined use with other statistics such as T-test and Pearson correlation further strengthens the prioritization of relevant features/metabolites.

Based on our combined feature selection strategy, 89 features were selected for further correlation network analysis (see next

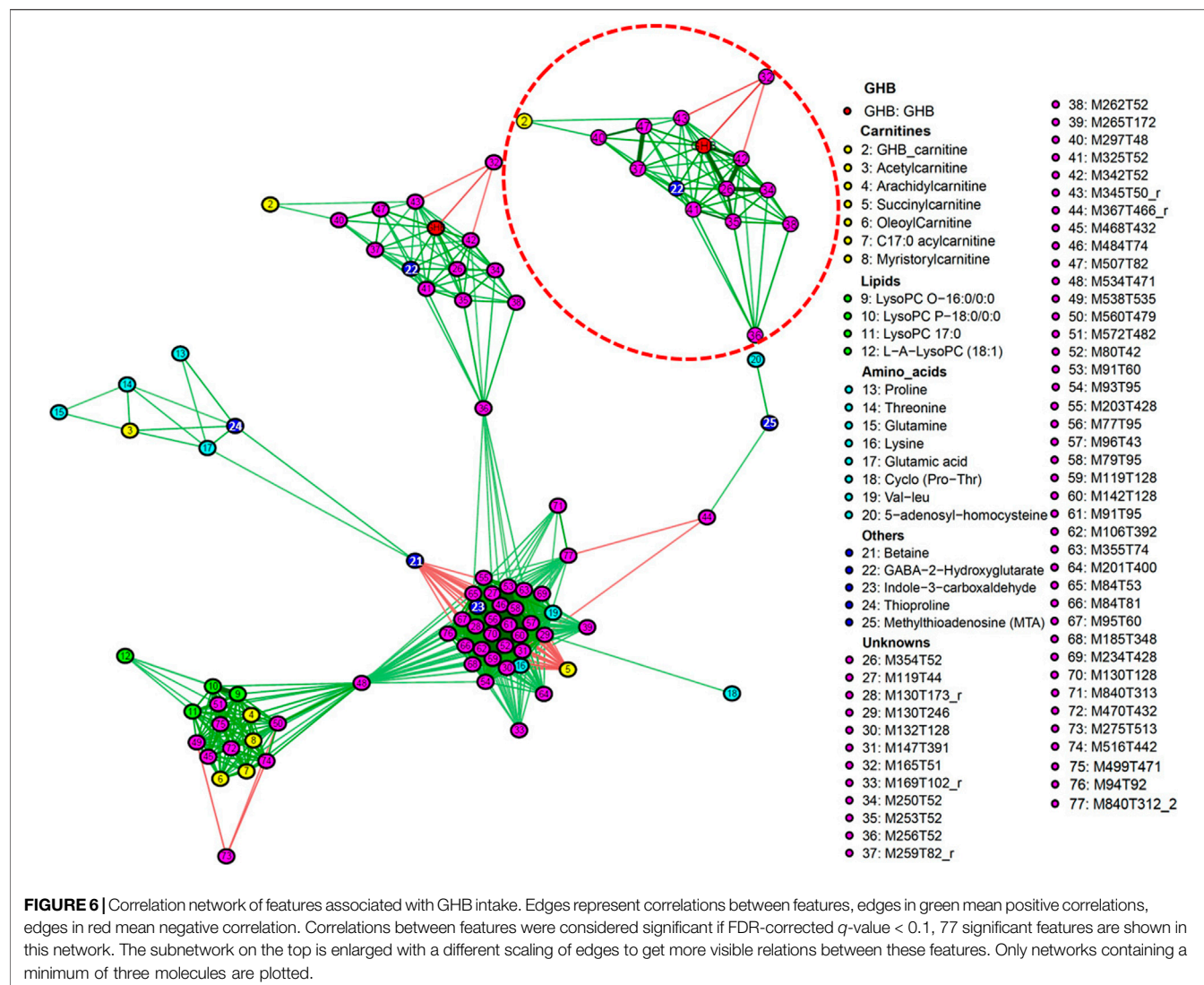


paragraph), and 77 of them show significant correlation with each other after FDR correction. **Table 1** only includes the features with the top 20 highest VIPs values and top 20 highest correlation coefficients, also together with all the identified metabolites that match with in-house database and shows significance in at least one method (FC, VIP, and q -value). The remaining unknowns are shown in **Supplementary Table S5**. Twenty-five features of the features included in **Table 1** are plotted in a box plot (**Figure 5**), to illustrate the difference of abundance between the control and positive group.

GHB Impacts on Human Metabolism as Reflected by a Correlation Network

The correlation network (CN) provides insights into the impact of GHB on metabolism and the interaction between the individual metabolites, this even though many features were not identified.

Based on our combined feature selection strategy, 89 features were initially selected for further analysis. Of these 77 features are included in **Figure 6**, as only networks containing a minimum of three molecules were plotted. The CN highlighted the role of important features, and there are three main subnetworks shown in the plot. The highlighted subnetwork on the top shows the main features that correlate to GHB directly, e.g., M354T52 (#26), M250T52 (#34), M342T52 (#42), M259T82 (#37), M507T82 (#47), M234T52 (#22, possibly GABA-2-hydroxyglutarate), M345T50 (#43), M297T348 (#40), are positively correlated to GHB, while M165T51 (#32) is negatively correlated to GHB, M342T52 (#42), and M345T50 (#43). To show the correlation of features to GHB more clearly, we also zoomed in on the subnetwork that includes GHB with a different scaling of edges. We speculate that the features #26, #34, #42 might be direct adducts of GHB as the wider edges show a stronger correlation. The intensity of feature #32 is not high enough to be fragmented in DDA mode, while it is still interesting to notice that



this feature is highly downregulated by GHB. GHB-carnitine (#2) is directly correlated to M297T48 (#40) and M345T50 (#43), and subsequently correlated to GHB. A strong correlation is found between feature #47 and #37, which indicates they may belong to the same compound as also noted previously. The subnetwork including GHB is connected to another subnetwork in the middle according to feature M256T52 (#36). Succinylcarnitine is negatively correlated to features including lysine, Indole-3-carboxaldehyde, and a number of unknowns (#27, 29, 46, 52, 57–60), and betaine is also negatively correlated to indole-3-carboxaldehyde, and a range of unknowns (#27, 31, 46, 52, 57–62). Top-left subnetwork contains acetylcarnitine, thioproline, and four amino acids (proline, glutamic acid, threonine, and glutamine), which are correlated to betaine and connected to the middle subnetwork. LysoPC O-16:0/0:0, LysoPC P-18:0/0:0, LysoPC (17:0), myristoylcarnitine, oleoylcarnitine, arachidylcarnitine, C17:0-acylcarnitine, and several unknowns are included in the subnetwork bottom-left side, which shows that carnitines and lipids are closely related. It is found that mainly carnitines and lipids are included in

this subnetwork, and they are connected to the middle subnetwork according to #48.

DISCUSSION

The main findings of the present study is the demonstration that it is indeed possible to use archived data normalized by NOMIS for identification of metabolites correlated to drug intake—here demonstrated with GHB using a combination of OPLS-DA, Pearson correlation and FDR q -value. In the data processing part, our results prove that the NOMIS normalization using multiple internal standards is a superior normalization method for retrospective analysis. The typical batch correction methods that are widely applied in metabolomics studies need a number of pooled quality control (QC) samples, while our data were efficiently normalized without using QC. Despite the large intensity variation in the raw data, the NOMIS can still take the analytical variation corresponding to sample preparation and ion

source variation into account, and makes it possible to get good correlation between actual concentration and corrected peak areas.

As use of archived data for metabolite correlation is still in its infancy, we performed a range of advanced both statistical and machine learning methods to evaluate which performs the best. In general, OPLS-DA, Pearson correlation, and FDR q -values give the most valuable information when evaluating based on the number of prioritized metabolites found, that also have been reported in previous controlled studies (Steuer et al., 2019). These feature selection methods have also been used in previous metabolomics studies (Nielsen et al., 2016; Elmsjö et al., 2020; Jung et al., 2021), where meaningful results also were reported using these methods. Mass spectrometry metabolome data analysis is complicated, since metabolites interact nonlinearly, and the data structures themselves are complex, especially when the study is retrospective and uncontrolled. Supervised machine learning has great potential in metabolomics research because of the ability to supply quantitative predictions (Jung et al., 2021). In this study, the machine learning model OPLS-DA gives better results than other machine learning models LASSO and random forest, while these models still provide compensatory information for feature selection that we could investigate in the future. Of important relevance is the combination of different feature selection methods to discover the potential biomarkers.

GHB-carnitine was first identified tentatively in urine samples in the study of Steuer et al. (2019), and further verified with standard in their latest study (Jung et al., 2021). Although GHB-carnitine was not detectable in serum in the study of Steuer et al. (2019), we routinely detected it using our analytical setup on the whole blood DUID cases. This is likely due to differences between our extraction or analytical methods or alternatively caused by the uncontrolled and potentially higher recreative consumption of GHB in the DUID cases. GHB-carnitine is the ester between GHB and carnitine. Carnitine is a small and highly polar zwitterionic compound that plays a critical role in energy metabolism and β -oxidation by facilitating transport of conjugated long chain fatty acids or more simple organic acids across the mitochondrial membrane (Bremer, 1983; Mo et al., 2014). Usually the synthesis of acylcarnitines proceed via an acyl SCoA intermediate, where the activated acyl group is then transferred to carnitine in a second step catalyzed by a carnitine acyltransferase. The current findings further suggest that whole blood GHB-carnitine could be a potential marker for exogenous GHB intake.

M259T82 shows particularly high significance in various statistics, and previously has been reported to be correlated to GHB intake even though it is still unknown without fragment pattern being provided (Steuer et al., 2019). The unknown features M507T82 also show very high significance being top 10 in all the models we applied, M259T82 and M507T82 might belong to the same compound due to the strong correlation in Pearson correlation (Figure 6) and also the same RT. A feature with similar mass to feature M234T52 has previously been identified tentatively as GHB-glutamate (Steuer et al., 2021). However, by comparison to a synthesized reference of GHB-glutamate we could not verify the identity in our case. Instead, we tentatively propose the feature as GABA-2-hydroxyglutarate (Supplementary Figure S12), which has the same mass as GHB-glutamate, but different

RT and fragmentation pattern. GABA-2-hydroxyglutarate is an ester of GABA and 2-hydroxyglutaric acid, the latter which has been shown to be a prominent metabolite of GHB in mammals (Struys et al., 2006), and it indicates GHB intake with very high correlation. M507T82 or M259T82, and the tentative metabolite GABA-2-hydroxyglutarate could all be used as potential biomarkers for GHB intake, and it is worthwhile to further identify these unknown features.

Various other carnitine metabolites are either found to be up or down regulated by GHB intake, e.g., oleoylcarnitine that has also been reported in a previous GHB study (Steuer et al., 2021). In relation to GHB-carnitine, succinylcarnitine is perhaps the most relevant one as a supportive biomarker to GHB-carnitine. Succinylcarnitine, was also observed to be upregulated in previous controlled studies as a result of GHB administration (Steuer et al., 2019; Jarsiah et al., 2020). Furthermore, succinate is known to be formed from GHB via oxidation to succinic semialdehyde and then to succinate, which then ultimately can enter into the citric acid cycle as an energy metabolite (Zhang et al., 2009). As succinate previously also have been reported to increase on GHB consumption, it seems likely that excess of succinate is diverted into succinyl SCoA and then finally succinylcarnitine following GHB intake. Increased levels of the two metabolites GHB and succinyl carnitine combined accordingly may more strongly support exogenous GHB intake. This together with the regulation of other strongly regulated metabolites we will need to verify in a controlled clinical study, in which the detection window of the relevant component can also be assessed.

In previous studies, several GHB-related acids have been reported in blood plasma and urine, such as glycolic acid, 3,4-DHB, 2,4-dihydroxybutyric acid, GA and some organic acids from the TCA cycle (Küting et al., 2021). None of these metabolites are found in our study as these acidic metabolites are mostly analyzed in negative mode, whereas only positive mode was used in this study. Therefore analysis in negative mode could be carried out in the future. In addition, three other unknowns, namely M127T391, M367T466, M169T102 that previously have been reported to be correlated to GHB intake (Steuer et al., 2019), are also detected in our work (Table 1). All these unknown features show significant effects in at least one of applied methods. These previously reported unknowns also validate our approach although they may not be direct GHB biomarkers.

To make a better understanding of the impact of GHB on human endogenous metabolism, a correlation network (CN) using all selected GHB-related metabolites was also constructed. The CN also reveals potential interaction or co-regulation between non-GHB features potentially revealing larger or more general metabolic impact on groups of related metabolites (Figure 4). From the Figure 4 it is evident that GHB impacts on the metabolism of many carnitines, lipids, amino acids, a range of unknowns as well as clustering of similar or biochemically related compounds further strengthens the evidence and insight. As previously mentioned, acylcarnitines mainly functions as entities for transporting organic acids into the mitochondria for oxidative metabolism (Skulachev, 1998; Alves et al., 2009). Increased levels of these compounds usually reflect increased levels of their immediate precursors, e.g., the increased level of acetyl carnitine reflects an

increase or surplus of acetylSCoA following GHB ingestion (Rubaltelli et al., 1987). Why we observe a build-up of acetylcarnitine following GHB ingestion is unknown, particularly as a range of long chain acylcarnitines as well as lysoPC are down-regulated indicating that lipid metabolism more generally is impeded. A high upregulation of lysoPCs and carnitines in the brain of mice following acute GHB ingestion is demonstrated in the Study of Luca et al. (2014), while they did not see the same regulation in the liver of the mice. Significant regulation of these metabolites are found in blood in our study, though the regulation is opposite to what is observed in the cortex of mice, but it may suggest a role for these metabolites following GHB intake that perhaps is not directly involved in energy metabolism (Luca et al., 2014). Based on the CN it however appears that acetylcarnitine is more strongly correlated to several amino acids, e.g., glutamate, glutamine, proline and threonine, and as these can serve as metabolic fuel generating acetylSCoA, the increased acetylcarnitine may simply reflect an increased energy dependence on catabolism of these amino acids perhaps as substitution for the retarded lipid metabolism. In the CN, we could also find that glutamate, proline, glutamine and acetylcarnitine are grouped together on the left, and as they are metabolites of each other and accordingly biochemically connected as reported (Tapiero et al., 2002; Susanna et al., 2010), it further validates the outcome of our method and analysis. It can be mentioned that GHB intake also in previous studies have been correlated to increased levels of some of these amino acids (Steuer et al., 2021), where, e.g., glutamic acid is identified with a relative high VIP score (1.29). Several studies have furthermore shown effects of GHB on glutamate release (Ferraro et al., 2001; Castelli et al., 2003), and these results also suggest that the effects of GHB on glutamate release might be mediated by GHB receptors and GABA_B receptors. Proline and lysine have also been reported to be up and down regulated respectively by GHB exposure in rat, which is consistent with our results, and it could also be an additional validation of our method (Seo et al., 2018). Finally, we also found some amino acids not previously reported to be regulated by GHB intake, such as homocysteine, threonine, Phe-Val and cyclo (Pro-Thr). These metabolites provides supplementary information for the GHB metabolism interpretation and used as second targets of methods to elucidate the metabolic impact.

In relation to use of the features as discriminative biomarkers for GHB consumption, it is at the present stage difficult to evaluate whether the obtained biomarkers of GHB intake will be sufficiently strong and also persists long enough *in vivo* to be useful. We however, note that several of the presumptive direct metabolites of GHB are 2–3 fold upregulated and furthermore are highly significant, so potentially they are. Even more if combined with further known metabolites from other recently published studies. Furthermore, based on our machine learning models we indeed can discriminate presumed GHB users from non-users with more than 80% accuracy, e.g., using the OPLS-DA model, we get more than 80% accuracy in average for classification of groups indicating that discrimination with some certainty already at the present stage is possible. In the future with controlled follow-up studies, we will most likely be able to get even more robust data and accordingly accurate discriminations.

An increasing number of laboratories use UHPLC-HRMS routinely for screening of biological samples for different metabolites or exogenous compounds leading to a huge amount of data of potential high value. As conducting clinical studies is expensive and ethical problems also arise particular when the studies involve new and untested drugs of abuse, a data set from a controlled cohort is not always easily available. Retrospective metabolomics studies, e.g., mining archived data from routine screenings gives a unique opportunity to access such data at almost no cost. This obviously is important within forensic science, where many new illegal drugs constantly are appearing, and little is known about their metabolites as well as their potential impact on human metabolism. Apart from solving this forensic toxicology issue, the use of archived data furthermore allows access to larger samples sizes than usual in controlled studies.

Our study demonstrates the power of this approach by initially detecting a range of potential biomarkers of GHB consumption as well as reveal how GHB intake further regulate endogenous metabolism. Many of the discoveries being validated by comparison to the literature. However, due to the uncontrolled population in this and future similar studies, there are obviously also several potential confounders such as the unknown interval from intake to blood sampling and dose, the varying metabolic rate between individuals, diet, the activity level, and the tolerance to continuous use of GHB (or another drug). Furthermore, the setup we use can also be improved, e.g., by inclusion of further QC samples to improve normalization as well as it is advisable also to perform routine analysis of the samples in the negative mode in future to include metabolite coverage. In the current study, we tried carefully to select a control group that matched the GHB positive group with regard to additional drug intake. This however cannot be perfect and should be kept in mind during data analysis. Despite various challenges corresponding to the cohort in this study, our findings and validation to the literature prove that it is still feasible to utilize UHPLC-HRMS screening data from long term forensic studies.

CONCLUSION

A general workflow is developed to carry out metabolomics studies on archived HRMS data from routine UHPLC-TOF screenings. The principle is demonstrated by using analytical data from a selection of GHB positive and matched control cases and validated by comparison of the results to those observed in controlled GHB studies. Generally, we rediscover a range of previously reported direct GHB metabolites, as well as we observe regulation of endogenous metabolites both some previously known, but also novel findings of potential biochemical relevance. We apply data acquired over a quite extensive time frame (6 years) indicating the robustness of the method. The study gives a further proof-of-principle on use of archived data when ordinary human data are unavailable, and paves the way for both a direct and simple elucidation of metabolites of new legal or illegal drugs as well as open up for large scale metabolomics studies for more general use of archived

data in the future. This can be from local databases as in this case or, e.g., more big-data approach to disease prevention and detection using more extensive data sets or blood samples. Obviously, a range of cofounders will always exist in such datasets due to the uncontrolled approach and this needs to be taken into consideration when evaluating the results. The use of archived data however has so many advantages including being significantly cheaper than performing clinical studies, that the approach merits further use and we strongly believe that it in the future will become routine in laboratories applying such screening procedures.

DATA AVAILABILITY STATEMENT

The original contributions presented in the study are included in the article/**Supplementary Material**, further inquiries can be directed to the corresponding authors.

ETHICS STATEMENT

The study was registered at the University and data was handled in accordance with the General Data Protection Regulation (GDPR) and the Danish Data Protection Act. The project did not include handling of biological material from human subjects

and was based on already registered data. According to the Danish Consolidation Act on Research Ethics Review of Health Research Projects, Consolidation Act number 1083 of 15 September 2017, section 14 (2) projects based on registers do not need approval from the Committees on Health Research Ethics.

AUTHOR CONTRIBUTIONS

TW: Methodology, formal analysis, investigation, visualization, data curation, validation, writing original draft. KN: Methodology, supervision, review and editing. KF: Chemical synthesis, writing, review and editing. JL: Review and editing. CN: Methodology, investigation. CA: Supervision, review and editing. PV: Methodology, supervision, review and editing. MA: Methodology, supervision, review and editing. JH: Study focus, investigation, supervision, review and editing. MJ: Conceptualization, supervision, writing—review and editing.

SUPPLEMENTARY MATERIAL

The Supplementary Material for this article can be found online at: <https://www.frontiersin.org/articles/10.3389/fphar.2022.816376/full#supplementary-material>

REFERENCES

- Abanades, S., Farré, M., Segura, M., Pichini, S., Pastor, A., Pacifici, R., et al. (2007). Disposition of Gamma-Hydroxybutyric Acid in Conventional and Nonconventional Biologic Fluids after Single Drug Administration: Issues in Methodology and Drug Monitoring. *Ther. Drug Monit.* 29, 64–70. doi:10.1097/FTD.0b013e3180307e5e
- Alves, E., Binienda, Z., Carvalho, F., Alves, C. J., Fernandes, E., de Lourdes Bastos, M., et al. (2009). Acetyl-L-carnitine Provides Effective *In Vivo* Neuroprotection over 3,4-Methylenedioxymethamphetamine-Induced Mitochondrial Neurotoxicity in the Adolescent Rat Brain. *Neuroscience* 158, 514–523. doi:10.1016/j.neuroscience.2008.10.041
- Bremer, J. (1983). Carnitine-Metabolism. *Physiol. Rev.* 63, 1421–1449. doi:10.1152/physrev.1983.63.4.1420
- Brenneisen, R., ElSohly, M. A., Murphy, T. P., Passarelli, J., Russmann, S., Salamone, S. J., et al. (2004). Pharmacokinetics and Excretion of Gamma-Hydroxybutyrate (GHB) in Healthy Subjects. *J. Anal. Toxicol.* 28, 625–630. doi:10.1093/jat/28.8.625
- Busardò, F. P., and Jones, A. W. (2019). Interpreting γ -hydroxybutyrate Concentrations for Clinical and Forensic Purposes. *Clin. Toxicol. (Phila)* 57, 149–163. doi:10.1080/15563650.2018.1519194
- Carter, L. P., Koek, W., and France, C. P. (2009). Behavioral Analyses of GHB: Receptor Mechanisms. *Pharmacol. Ther.* 121, 100–114. doi:10.1016/j.pharmthera.2008.10.003
- Castelli, M. P., Ferraro, L., Mocci, I., Carta, F., Carai, M. A., Antonelli, T., et al. (2003). Selective Gamma-Hydroxybutyric Acid Receptor Ligands Increase Extracellular Glutamate in the hippocampus, but Fail to Activate G Protein and to Produce the Sedative/hypnotic Effect of Gamma-Hydroxybutyric Acid. *J. Neurochem.* 87, 722–732. doi:10.1046/j.1471-4159.2003.02037.x
- Elmsjö, A., Vikingsson, S., Söderberg, C., Kugelberg, F. C., and Green, H. (2021). Post-mortem Metabolomics: A Novel Approach in Clinical Biomarker Discovery and a Potential Tool in Death Investigations. *Chem. Res. Toxicol.* 34, 1496–1502. doi:10.1021/acs.chemrestox.0c00448
- Epperson, D. L., and Ralston, C. A. (2016). Conceptual Model of Risk versus Threat and Risk Management versus Risk Reduction, 397, 415. doi:10.1007/978-1-4939-2416-5_17
- Ferraro, L., Tanganelli, S., O'Connor, W. T., Francesconi, W., Loche, A., Gessa, G. L., et al. (2001). Gamma-Hydroxybutyrate Modulation of Glutamate Levels in the hippocampus: an *In Vivo* and *In Vitro* Study. *J. Neurochem.* 78, 929–939. doi:10.1046/j.1471-4159.2001.00530.x
- Francesco, P. B. M. G., Tini, A., Minuttillo, A., Sirignano, A., and Marinelli, E. (2018). Replacing GHB with GBL in Recreational Settings A New Trend in Chemsex. *Curr. Drug Metab.* 19, 1080–1085.
- Hanisch, S., Stachel, N., and Skopp, G. (2016). A Potential New Metabolite of Gamma-Hydroxybutyrate: Sulfonated Gamma-Hydroxybutyric Acid. *Int. J. Leg. Med.* 130, 411–414. doi:10.1007/s00414-015-1235-x
- Jarsiah, P., Roehrich, J., Wyczynski, M., and Hess, C. (2020). Phase I Metabolites (Organic Acids) of Gamma-Hydroxybutyric Acid-Validated Quantification Using GC-MS and Description of Endogenous Concentration Ranges. *Drug Test. Anal.* 12, 1135–1143. doi:10.1002/dta.2820
- Jarsiah, P., Roehrich, J., Kueting, T., Martz, W., and Hess, C. (2021). GHB Related Acids Are Useful in Routine Casework of Suspected GHB Intoxication Cases. *Forensic Sci. Int.* 324, 110833. doi:10.1016/j.forsciint.2021.110833
- Jung, S., Kim, S., Seo, Y., and Lee, S. (2021). Metabolic Alterations Associated with γ -Hydroxybutyric Acid and the Potential of Metabolites as Biomarkers of its Exposure. *Metabolites* 11, 101. doi:10.3390/metabo11020101
- Kaufman, E. E., and Nelson, T. (1987). Evidence for the Participation of a Cytosolic NADP+-dependent Oxidoreductase in the Catabolism of Gamma-Hydroxybutyrate *In Vivo*. *J. Neurochem.* 48, 1935–1941. doi:10.1111/j.1471-4159.1987.tb05758.x
- Kintz, P., Goullé, J. P., Cirimele, V., and Ludes, B. (2001). Window of Detection of Gamma-Hydroxybutyrate in Blood and Saliva. *Clin. Chem.* 47, 2033–2034. doi:10.1093/clinchem/47.11.2033
- Kraemer, M., Broecker, S., Kueting, T., Madea, B., and Maas, A. (2022). Fatty Acid Esters as Novel Metabolites of γ -hydroxybutyric Acid: A Preliminary Investigation. *Drug Test. Anal.* 1–11. doi:10.1002/dta.3213
- Küting, T., Schneider, B., Heidbreder, A., Krämer, M., Jarsiah, P., Madea, B., et al. (2021). Detection of γ -hydroxybutyric Acid-related Acids in Blood Plasma and

- Urine: Extending the Detection Window of an Exogenous γ -hydroxybutyric Acid Intake? *Drug Test. Anal.* 13, 1635–1649. doi:10.1002/dta.3097
- Liang, L., Rasmussen, M. H., Piening, B., Shen, X., Chen, S., Röst, H., et al. (2020). Metabolic Dynamics and Prediction of Gestational Age and Time to Delivery in Pregnant Women. *Cell* 181, 1680–e15. doi:10.1016/j.cell.2020.05.002
- Liebal, U. W., Phan, A. N. T., Sudhakar, M., Raman, K., and Blank, L. M. (2020). Machine Learning Applications for Mass Spectrometry-Based Metabolomics. *Metabolites* 10, 1–23. doi:10.3390/metabo10060243
- Luca, G., Vienne, J., Vaucher, A., Jimenez, S., and Tafti, M. (2014). Central and Peripheral Metabolic Changes Induced by Gamma-Hydroxybutyrate. *Sleep* 38, 305–313. doi:10.5665/sleep.4420
- Mehling, L.-M., Piper, T., Spottke, A., Heidbreder, A., Young, P., Madea, B., et al. (2017). GHB-O- β -glucuronide in Blood and Urine Is Not a Suitable Tool for the Extension of the Detection Window after GHB Intake. *Forensic Toxicol.* 35, 263–274. doi:10.1007/s11419-016-0352-7
- Mo, J., Lim, L. Y., and Zhang, Z. R. (2014). L-carnitine Ester of Prednisolone: Pharmacokinetic and Pharmacodynamic Evaluation of a Type I Prodrug. *Int. J. Pharm.* 475, 123–129. doi:10.1016/j.ijpharm.2014.08.049
- Møllerup, C. B., Rasmussen, B. S., Johansen, S. S., Mardal, M., Linnet, K., and Dalsgaard, P. W. (2019). Retrospective Analysis for Valproate Screening Targets with Liquid Chromatography-High Resolution Mass Spectrometry with Positive Electrospray Ionization: An Omics-Based Approach. *Drug Test. Anal.* 11, 730–738. doi:10.1002/dta.2543
- Nielsen, K. L., Telving, R., Andreasen, M. F., Hasselstrøm, J. B., and Johannsen, M. (2016). A Metabolomics Study of Retrospective Forensic Data from Whole Blood Samples of Humans Exposed to 3,4-Methylenedioxymethamphetamine: A New Approach for Identifying Drug Metabolites and Changes in Metabolism Related to Drug Consumption. *J. Proteome Res.* 15, 619–627. doi:10.1021/acs.jproteome.5b01023
- Odujebi, O., Landman, A., and Hoffman, R. S. (2007). GHB Urine Concentrations after Single-Dose Administration in Humans. *J. Anal. Toxicol.* 31, 179–180. doi:10.1093/jat/31.3.179
- Palomino-Schätzlein, M., Wang, Y., Brailsford, A. D., Parella, T., Cowan, D. A., Legido-Quigley, C., et al. (2017). Direct Monitoring of Exogenous γ -Hydroxybutyric Acid in Body Fluids by NMR Spectroscopy. *Anal. Chem.* 89, 8343–8350. doi:10.1021/acs.analchem.7b01567
- Petersen, I. N., Tortzen, C., Kristensen, J. L., Pedersen, D. S., and Breindahl, T. (2013). Identification of a New Metabolite of GHB: Gamma-Hydroxybutyric Acid Glucuronide. *J. Anal. Toxicol.* 37, 291–297. doi:10.1093/jat/bkt027
- Piper, T., Mehling, L. M., Spottke, A., Heidbreder, A., Young, P., Madea, B., et al. (2017). Potential of GHB Phase-II-Metabolites to Complement Current Approaches in GHB post Administration Detection. *Forensic Sci. Int.* 279, 157–164. doi:10.1016/j.forsciint.2017.08.023
- Rubaltelli, F. F., Orzali, A., Rinaldo, P., Donzelli, F., and Carnielli, V. (1987). Carnitine and the Premature. *Biol. Neonate* 52 Suppl 1, 65–77. doi:10.1159/000242740
- Scafidi, S., Fiskum, G., Lindauer, S. L., Bamford, P., Shi, D., Hopkins, I., et al. (2010). Metabolism of Acetyl-L-Carnitine for Energy and Neurotransmitter Synthesis in the Immature Rat Brain. *J. Neurochem.* 114, 820–831. doi:10.1111/j.1471-4159.2010.06807.x
- Seo, C., Na, M., Jang, J., Park, M., Choi, B., Lee, S., et al. (2018). Monitoring of Altered Amino Acid Metabolic Pattern in Rat Urine Following Intraperitoneal Injection with γ -hydroxybutyric Acid. *Metabolomics* 14, 111–118. doi:10.1007/s11306-018-1409-x
- Sinclair, E., Trivedi, D. K., Sarkar, D., Walton-Doyle, C., Milne, J., Kunath, T., et al. (2021). Metabolomics of Sebum Reveals Lipid Dysregulation in Parkinson's Disease. *Nat. Commun.* 12, 1592–1599. doi:10.1038/s41467-021-21669-4
- Skulachev, V. P. (1998). Cytochrome C in the Apoptotic and Antioxidant Cascades. *FEBS Lett.* 423, 275–280. doi:10.1016/S0014-5793(98)00061-1
- Sørensen, L. K., and Hasselstrøm, J. B. (2012). A Hydrophilic Interaction Liquid Chromatography Electrospray Tandem Mass Spectrometry Method for the Simultaneous Determination of γ -hydroxybutyrate and its Precursors in Forensic Whole Blood. *Forensic Sci. Int.* 222, 352–359. doi:10.1016/j.forsciint.2012.07.017
- Steuer, A. E., Raeber, J., Steuer, C., Boxler, M. I., Dornbierer, D. A., Bosch, O. G., et al. (2019). Identification of New Urinary Gamma-Hydroxybutyric Acid Markers Applying Untargeted Metabolomics Analysis Following Placebo-Controlled Administration to Humans. *Drug Test. Anal.* 11, 813–823. doi:10.1002/dta.2558
- Steuer, A. E., Raeber, J., Simbuerger, F., Dornbierer, D. A., Bosch, O. G., Quednow, B. B., et al. (2021). Towards Extending the Detection Window of Gamma-Hydroxybutyric Acid-An Untargeted Metabolomics Study in Serum and Urine Following Controlled Administration in Healthy Men. *Metabolites* 11, 166. doi:10.3390/metabo11030166
- Struys, E. A., Verhoeven, N. M., Jansen, E. E., Ten Brink, H. J., Gupta, M., Burlingame, T. G., et al. (2006). Metabolism of Gamma-Hydroxybutyrate to D-2-Hydroxyglutarate in Mammals: Further Evidence for D-2-Hydroxyglutarate Transhydrogenase. *Metabolism* 55, 353–358. doi:10.1016/j.metabol.2005.09.009
- Sumner, L. W., Amberg, A., Barrett, D., Beale, M. H., Beger, R., Daykin, C. A., et al. (2007). Proposed Minimum Reporting Standards for Chemical Analysis Chemical Analysis Working Group (CAWG) Metabolomics Standards Initiative (MSI). *Metabolomics* 3, 211–221. doi:10.1007/s11306-007-0082-2
- Sysi-Aho, M., Katajamaa, M., Yetukuri, L., and Oresic, M. (2007). Normalization Method for Metabolomics Data Using Optimal Selection of Multiple Internal Standards. *BMC Bioinformatics* 8, 93–17. doi:10.1186/1471-2105-8-93
- Tapiero, H., Mathé, G., Couvreur, P., and Tew, K. D. (2002). II. Glutamine and Glutamate. *Biomed. Pharmacother.* 56, 446–457. doi:10.1016/s0753-3322(02)00285-8
- Telving, R., Hasselstrøm, J. B., and Andreasen, M. F. (2016). Targeted Toxicological Screening for Acidic, Neutral and Basic Substances in Postmortem and Antemortem Whole Blood Using Simple Protein Precipitation and UPLC-HR-TOF-MS. *Forensic Sci. Int.* 266, 453–461. doi:10.1016/j.forsciint.2016.07.004
- Wang, T., Duedahl-Olesen, L., and Lauritz Frandsen, H. (2021). Targeted and Non-targeted Unexpected Food Contaminants Analysis by LC/HRMS: Feasibility Study on rice. *Food Chem.* 338, 127957. doi:10.1016/j.foodchem.2020.127957
- Zhang, G. F., Kombu, R. S., Kasumov, T., Han, Y., Sadhukhan, S., Zhang, J., et al. (2009). Catabolism of 4-hydroxyacids and 4-hydroxynonenal via 4-Hydroxy-4-Phosphoacyl-CoAs. *J. Biol. Chem.* 284, 33521–33534. doi:10.1074/jbc.M109.055665

Conflict of Interest: The authors declare that the research was conducted in the absence of any commercial or financial relationships that could be construed as a potential conflict of interest.

Publisher's Note: All claims expressed in this article are solely those of the authors and do not necessarily represent those of their affiliated organizations, or those of the publisher, the editors and the reviewers. Any product that may be evaluated in this article, or claim that may be made by its manufacturer, is not guaranteed or endorsed by the publisher.

Copyright © 2022 Wang, Nielsen, Frisch, Lassen, Nielsen, Andersen, Villesen, Andreasen, Hasselstrøm and Johannsen. This is an open-access article distributed under the terms of the Creative Commons Attribution License (CC BY). The use, distribution or reproduction in other forums is permitted, provided the original author(s) and the copyright owner(s) are credited and that the original publication in this journal is cited, in accordance with accepted academic practice. No use, distribution or reproduction is permitted which does not comply with these terms.



Comprehensive Metabolomics and Network Pharmacology to Explore the Mechanism of 5-Hydroxymethyl Furfural in the Treatment of Blood Deficiency Syndrome

OPEN ACCESS

Edited by:

Ren-ai Xu,

First Affiliated Hospital of Wenzhou Medical University, China

Reviewed by:

Shun-bin Luo,

Lishui City People's Hospital, China

Fangbo Xia,

University of Macau, China

Meichen Liu,

Chengdu University of Traditional Chinese Medicine, China

*Correspondence:

Haixue Kuang

hxkuang@hljucm.net

QiuHong Wang

qhwwang668@sina.com

[†]These authors have contributed equally to this work

Specialty section:

This article was submitted to Drug Metabolism and Transport, a section of the journal *Frontiers in Pharmacology*

Received: 08 November 2021

Accepted: 27 December 2021

Published: 04 March 2022

Citation:

Zhang W, Cui N, Su F, Wang Y, Yang B, Sun Y, Guan W, Kuang H and Wang Q (2022) Comprehensive Metabolomics and Network Pharmacology to Explore the Mechanism of 5-Hydroxymethyl Furfural in the Treatment of Blood Deficiency Syndrome. *Front. Pharmacol.* 12:811331. doi: 10.3389/fphar.2021.811331

Wensen Zhang^{1†}, Na Cui^{1†}, Fazhi Su¹, Yangyang Wang¹, Bingyou Yang¹, Yanping Sun¹, Wei Guan¹, Haixue Kuang^{1*} and QiuHong Wang^{2*}

¹Key Laboratory of Basic and Application Research of Beiyao (Heilongjiang University of Chinese Medicine), Ministry of Education, Harbin, China, ²School of Traditional Chinese Medicine, Guangdong Pharmaceutical University, Guangdong, China

Radix Rehmanniae (RR, from Radix Rehmanniae (Gaertn.) DC.) is a natural medicine used in traditional Chinese medicine (TCM) since ancient times for the treatment of blood disorders. RR is steamed to get Rehmanniae Radix Praeparata (RP), which has a tonic effect on blood; the content of 5-hydroxymethylfurfural (5-HMF) increases more than four times after steaming. Studies have shown that 5-HMF has positive pharmacological effects on cardiovascular and hematological disorders. This study aimed to explore and verify the impact of 5-HMF on rats with chemotherapy-induced blood deficiency syndrome (BDS). Rats were given cyclophosphamide (CP) and acetophenhydrazine (APH) to induce BDS, the coefficients of some organs (liver, spleen, and kidney) were measured, and a routine blood test examined the coefficients of several peripheral blood cells. Metabolomics and network pharmacology were combined to find important biomarkers, targets, and pathways. Western blot was used to detect the expression of CYP17A1 and HSD3B1 proteins in the spleen. All these findings suggested that the 5-HMF significantly increased the number of peripheral blood cells and reversed splenomegaly in rats. In addition, 5-HMF upregulated CYP17A1 and HSD3B1 protein expression in splenic tissues. Also, 5-HMF ameliorated chemotherapy-induced BDS in rats, and its therapeutic mechanism might depend on steroid hormone biosynthesis and other pathways. It acts on blood deficiency via multiple targets and pathways, which is unique to Chinese medicine.

Keywords: 5-HMF, blood deficiency, network pharmacology, metabolomics, Radix Rehmanniae

Abbreviations: SD, Standard deviation; EDTA, Ethylenediaminetetraacetic acid; TCMSP, Traditional Chinese Medicine Systems Pharmacology Database and Analysis Platform; OMIM, Online Mendelian Inheritance in Man; KEGG, Kyoto Encyclopedia of Genes and Genomes; GO, Gene Ontology; VIP, Variable importance in the projection.

1 INTRODUCTION

According to the theory of traditional Chinese medicine (TCM), blood deficiency is a common disease and a pathological state of blood dysfunction and organ malnutrition (Li et al., 2015). Blood deficiency syndrome (BDS) is mainly related to excessive blood loss (Shi et al., 2014), deficient spleen and stomach function, insufficient hematogenesis, and blood stasis (Yong et al., 2012). The main diagnostic index is the decrease in blood cells or hemoglobin content, similar to anemia (Wang et al., 2013). Modern medicine holds that patients with BDS often have clinical manifestations such as impaired hematopoietic function, decreased visceral function, malnutrition, and bone marrow suppression (Zhang et al., 2014). BDS can cause spleen enlargement (Zhang et al., 2020). After chemotherapy, most patients have a hemoglobin synthesis disorder, which causes BDS and severely interferes with blood system circulation (Jiang et al., 2013). However, anemia is defined only as a decrease in the concentration of hemoglobin in the body, which is usually related to a reduction in red blood cells (Li et al., 2017). During cancer treatment, the standard treatment for BDS is iron and vitamin B12 supplementation to promote the synthesis of erythropoietin, which can accelerate the recovery of the hematopoietic system (Brown 2020). However, the application of these regimens is limited because of their unstable efficacy, high cost, and side effects (Milano and Schneider 2007).

A main component of TCM is 5-HMF, among which the most representative herb is *Rehmanniae Radix Praeparata* (RP) (Won et al., 2014). *Rehmanniae Radix* (RR) is steamed to obtain RP, which is a plant of the Scrophulariaceae family. RP has been used to treat BDS for thousands of years. It is a commonly used TCM in Asia (Li et al., 2021). The Compendium of Materia Medica records that RP is used as a blood tonic (Guo et al., 2016), which regulates and fortifies blood and treats BDS (Zee-Cheng 1992). The main components of RR are monosaccharides, oligosaccharides (Kitagawa et al., 1995), iridoids (Xia et al., 2020), and glycosides (Xu et al., 2012). The decomposition products of these compounds constitute RP, of which 5-HMF is the most prominent (Won et al., 2014). During the processing of RR, stachyose is reduced to hexose, and these components finally form 5-HMF, which increases the content of 5-HMF in RP after steaming by more than four times compared with RR (Zhu et al., 2007). Therefore, 5-HMF has become the main active component of RP and is used as a marker compound for quality control (Li et al., 2005; Korean Food and Drug Administration, 2008). This transformation of active ingredients in raw materials and processed products leads to differences in their efficacy. For example, RP is better at supplementing blood (Xia et al., 2020). According to current research results, 5-HMF has positive pharmacological effects on cardiovascular and blood diseases. For example, 5-HMF can increase hemoglobin's oxygen affinity to support cardiac function during severe hypoxia (Lucas et al., 2019). It also has sound biological effects, such as antioxidant activity (Li et al., 2011) and strengthening the resistance of sickle red blood cells to injury caused by hypoxia (Qiang et al., 2021). Therefore, we speculate that 5-HMF can be used as a potential therapeutic

drug for BDS. However, the treatment of BDS by 5-HMF has not been documented, and its therapeutic mechanism is unclear.

Network pharmacology and metabolomics are practical tools for elucidating the underlying mechanisms of TCM (Pan et al., 2020). First, a blood deficiency rat model induced by chemotherapy was used to evaluate the effect of 5-HMF on BDS. Second, a network pharmacology method was established to explore the mechanism of 5-HMF in treating BDS from the perspective of targets and pathways. At the same time, plasma metabolomics revealed the synergistic metabolic mechanism of metabolites and metabolic pathways. Finally, Western blot validated the metabolic pathway. This study was the first to use a combination of network pharmacology and plasma metabolomics to determine the mechanism of 5-HMF in the treatment of BDS. Hopefully, these results will provide a theoretical basis for elucidating the mechanism of 5-HMF in BDS treatment.

2 MATERIALS AND METHODS

2.1 Animals and Ethic Statement

We used 40 healthy male SD rats weighing 220–260 g, batch number SCXK (Liao) 2020–0001, from Liaoning Changsheng Biotechnology Co., Ltd. The animal experiment was approved by the Ethics Committee of Heilongjiang University of Traditional Chinese Medicine (approval number 2019121101). Animals were kept in a room at 25°C and 40–60% humidity. Rats were randomly divided into five groups with 8 rats in each group: control group, model group, 5-HMF-L group, 5-HMF-M group, and 5-HMF-H group.

2.2 Chemicals and Reagents

The 5-HMF was purchased from Aladdin (batch number H2020020, >95% (Gas chromatography), containing 3–5% water as a stabilizer). N-acetophenazine was purchased from Aladdin (batch number L1909182), and cyclophosphamide (CP) was purchased from MACKLIN (batch number C11147187).

2.3 Establishment of the Blood Deficiency Syndrome Model

The establishment of the BDS animal model was consistent with previous studies (Li et al., 2015). APH (20 mg/kg, 10 mg/kg) was injected subcutaneously on the first and fourth days. On the 4th day, 2 h after subcutaneous injection of APH, CP (20 mg/kg) was injected intraperitoneally. CP was injected for 4 consecutive days after that. On the 7th day, the indexes of red blood cells (RBC), white blood cells (WBC), hemoglobin (HGB), and hematocrit (HCT) in peripheral blood were measured. The control group was injected with the same volume of saline in the same way. From the first day, the treatment group was given 5-HMF (5.19 mg/kg, 2.595 mg/kg, 1.2975 mg/kg) by gavage (Duan 2021), respectively, and the control group and model group were given the same volume of saline by gavage for 15 days.

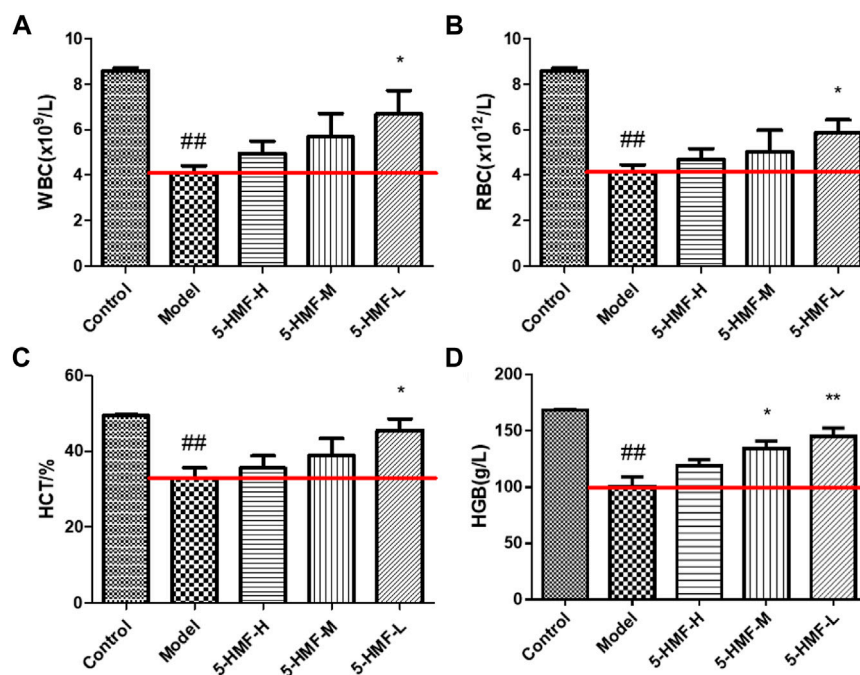


FIGURE 1 | The blood parameters of rats in the control and model groups treated with saline and different doses of 5-HMF. **(A)** The level of WBC. **(B)** The level of RBC. **(C)** The level of HGB. **(D)** The level of HCT. Each value represents the mean SD ($n = 8$); # $p < 0.05$ and ## $p < 0.01$, compared with the control group; * $p < 0.05$ and ** $p < 0.01$, compared with the model group.

2.4 Routine Blood Test

After the last administration, blood was taken from the abdominal aorta and collected in a sterile vacuum blood collection tube containing ethylenediaminetetraacetic acid (EDTA). The blood was analyzed by the HEMAVET 950 automatic hematology analyzer (Drew Scientific Group, Dallas, Texas, United States) to quantify RBC, WBC, HGB, and HCT.

2.5 Network Analysis

2.5.1 Target Prediction

The targets of 5-HMF were predicted in the following ways: Traditional Chinese Medicine Systems Pharmacology Database and Analysis Platform (TCMSP) (Ru et al., 2014), Swiss Target Prediction (Gfeller et al., 2014), Targetnet (Yao et al., 2016), PharmMapper (Wang et al., 2017). We used GeneCards (Stelzer et al., 2016), Online Mendelian Inheritance in Man (OMIM) (Amberger et al., 2015), Drugbank (Wishart et al., 2018) to identify targets related to BDS. In the OMIM database, we opened the Gene Map and entered “blood deficiency syndrome” to obtain 532 essential genes. We entered “blood deficiency syndrome” in the GeneCard database, selected genes with a relevance score >20 , and obtained a total of 1,542 critical genes. We entered “anemia” in the Drugbank database and got a total of 11 essential genes and then removed the duplicated genes.

2.5.2 Kyoto Encyclopedia of Genes and Genomes and Gene Ontology Enrichment Analysis

In analyzing the common targets of the 5-HMF action target and BDS-related targets, the server Metascape (Zhou et al., 2019) was

used for Kyoto Encyclopedia of Genes and Genomes (KEGG) and Gene Ontology (GO) enrichment analysis.

2.5.3 Network Construction

Two visualization networks were constructed: 1) Target point network, a network composed of 5-HMF, BDS, and common targets; 2) Targetpath network, in which the targets and their pathways were used to generate spatiotemporal networks. All networks were constructed by Cytoscape 3.8.0 (Liu et al., 2020).

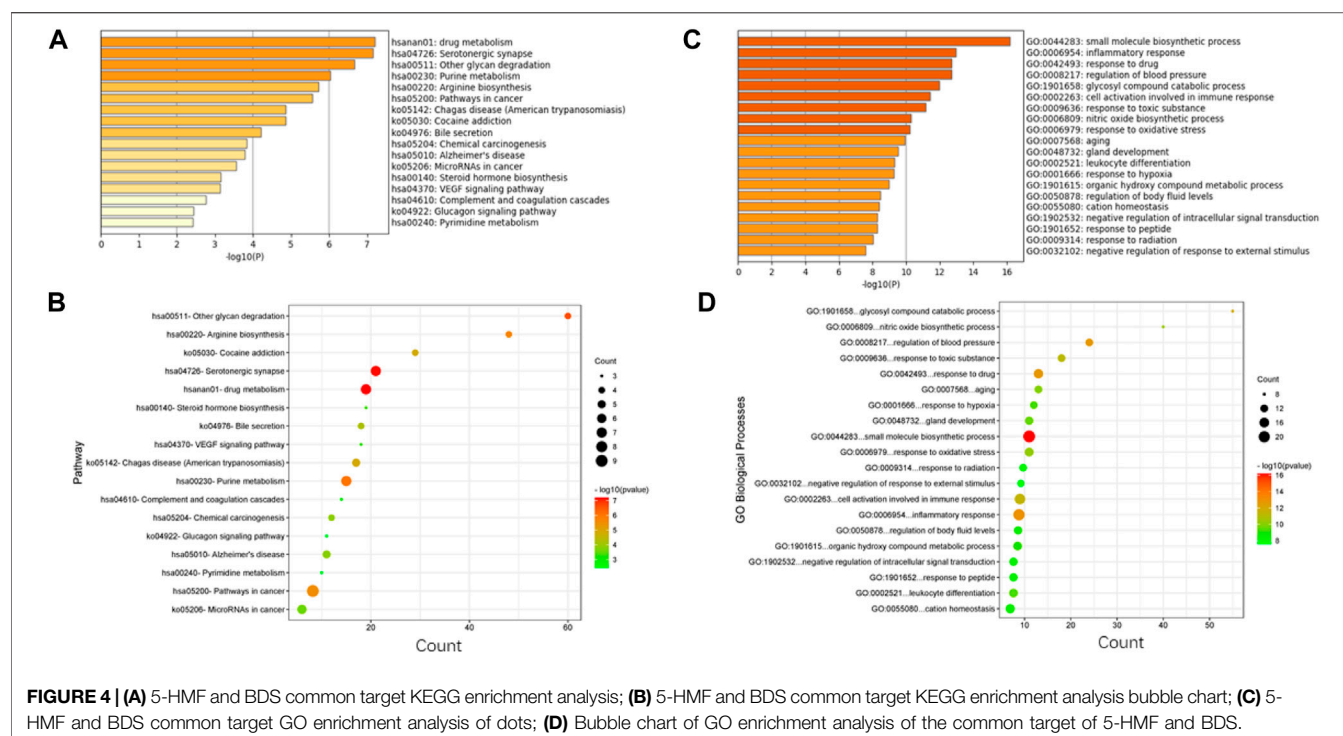
2.6 LC-MS Metabolomics Analysis

2.6.1 Sample Preparation

After the final administration, the blood of rats was collected from the abdominal aorta, left to stand for 30 min at 4°C, centrifuged at 3,500 rpm/min for 15 min. Then the plasma supernatant sample was mixed 1:3 with acetonitrile, vortexed for 30 s, and left to stand for 30 min at -20°C . The blood was centrifuged at 13,500 rpm/min for 15 min at 4°C, 300 μL of supernatant was evaporated, and 150 μL of 50% acetonitrile was added to redissolve the sample. After centrifugation, the sample was injected into the injection cup for testing (Gong et al., 2019).

2.6.2 UPLC-QTOF/MS Analysis

The G2-Si (Waters Q-TOF SYNAPT from Manchester Waters Company) has a continuous mode and is equipped with an electrospray ion source. The plasma samples were chromatographed on an Acquity UPLC HSS T3 column with a gradient elution program at the flow rate of 0.2 $\mu\text{L}/\text{min}$. The mobile phase was comprised of water and 0.1% formic acid (phase



obtained by OPLS-DA was used to evaluate the impact of each metabolite difference on the discrimination and interpretation ability of each sample. The greater the VIP value, the more significant the contribution of metabolites to sample differentiation. It is generally believed that there are significant differences between variables with $VIP > 1$. The potential biomarkers were the S-plot constructed by Ezinfo, and the V-plot was labeled.

2.7 Statistical Analysis

All data were expressed in terms of mean \pm standard deviation. The two-tailed unpaired *t*-test was performed using SPSS 21.0 software (from SPSS Corporation, United States). A value of $p < 0.05$ was considered to show a significant difference. A value of $p < 0.01$ was considered to indicate a highly significant difference. The histogram was drawn by GraphPad Prism 7 software (GraphPad Software, United States).

2.7.1 Pathway Analysis

The targets from network pharmacology and the metabolites from plasma metabolomics were jointly analyzed by MetaboAnalyst to select crucial metabolism pathways.

2.8 Western Blot Was Applied to Verify the Expression of Common Key Proteins in Metabolomics and Network Pharmacology

The bincinchoninic acid (BCA) method was used to determine the total protein of conventionally extracted splenocytes. The extract was separated by 10% SDS polyacrylamide gel electrophoresis and transferred to the PVDF membrane. It was blocked with 5% skim milk at room temperature for 1 h, and

antibodies of CYP17A1, HSD3B1 (all 1:1,000), and GAPDH (all 1:2,000) were added. These were incubated overnight at 4°C and rinsed with tris buffered saline with Tween 20 (TBST) three times for 10 min each. The membrane was immersed in the horseradish peroxidase-labeled secondary antibody (1:1,000), diluted in 2% skimmed milk, incubated at room temperature for 1 h, and rinsed with TBST 3 times, each for 10 min. Image Quant LAS 500 imaging equipment acquired the signal using the ECL chemiluminescence method.

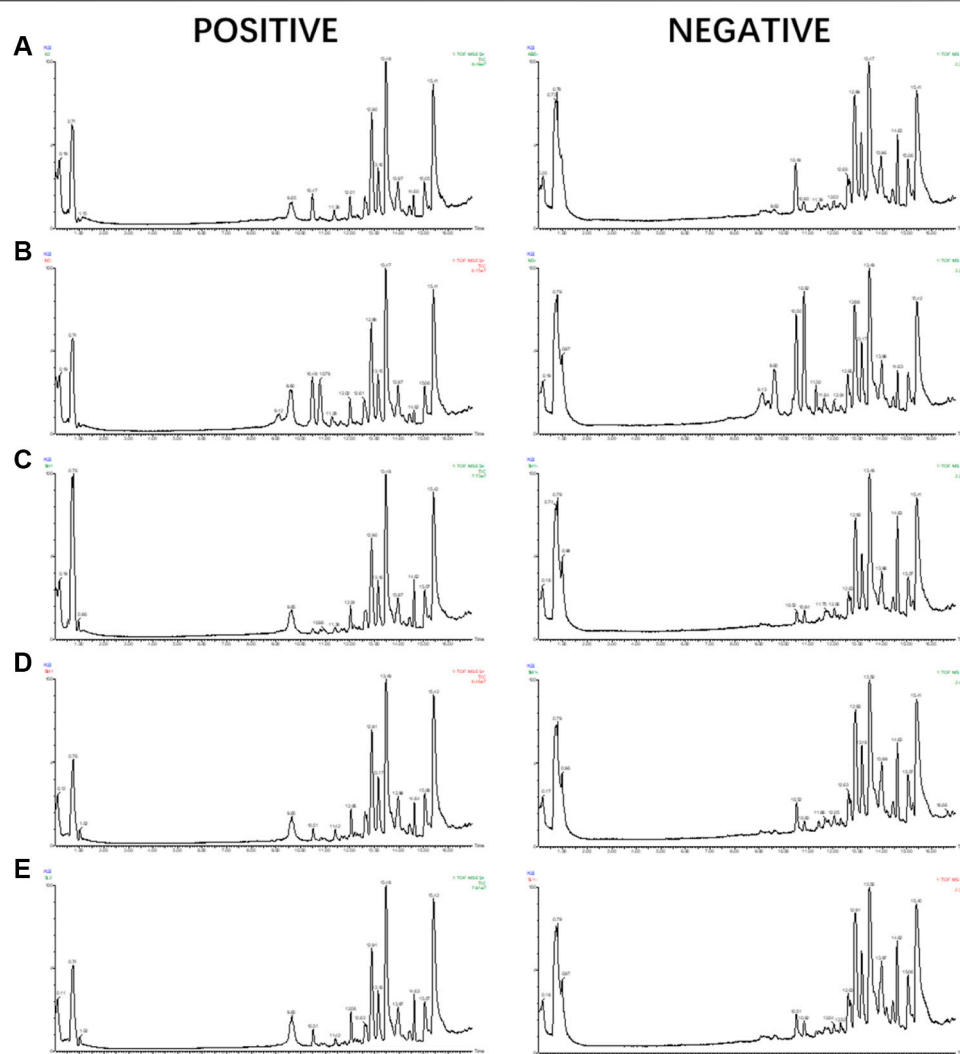
3 RESULTS

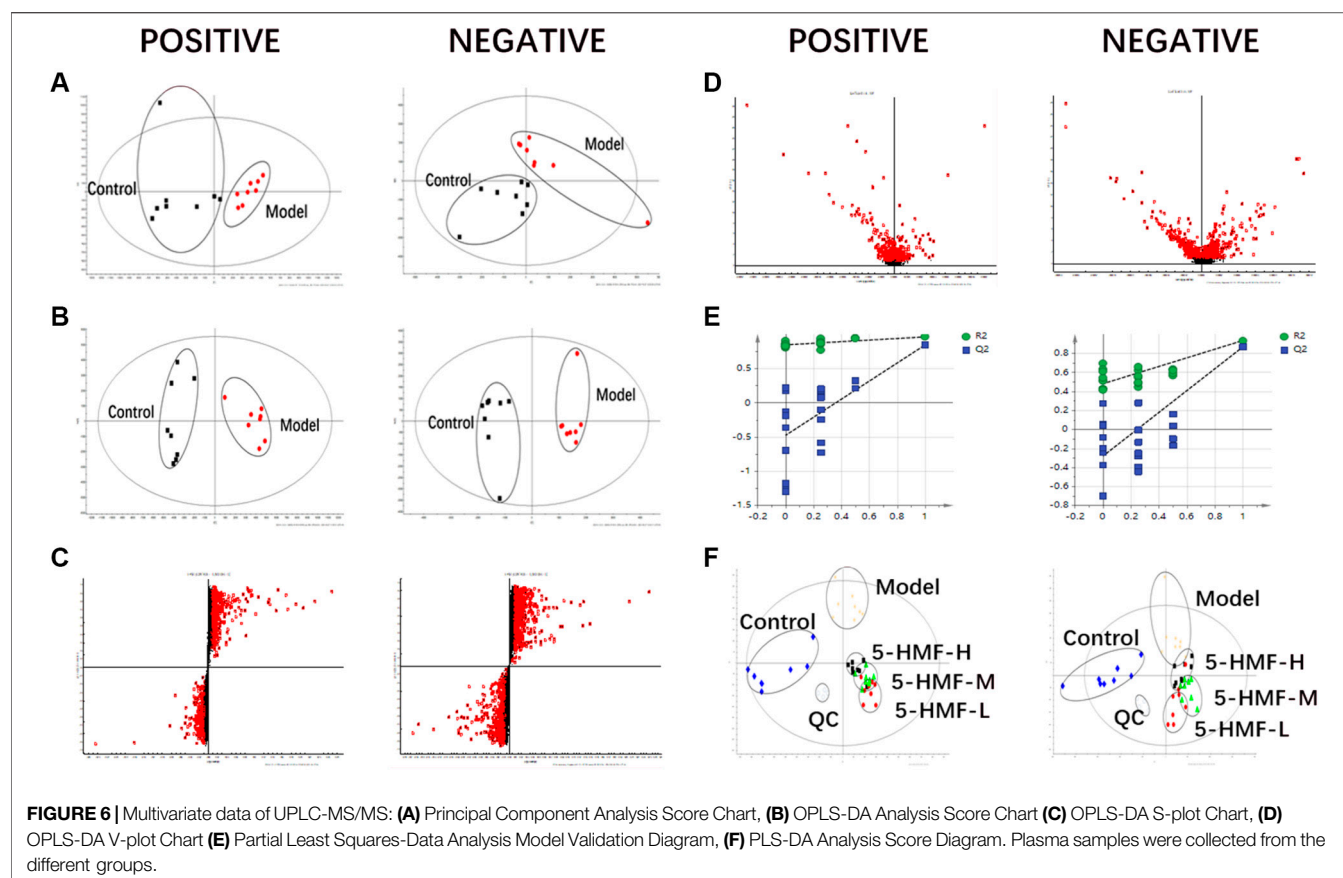
3.1 Behavioral Analysis of Rats

Changes in the general behavior of rats could reflect the occurrence of and recovery from BDS in rats. After BDS induction, rats in the model group developed fatigue and lethargy, accompanied by weight loss, thinning hair, pale ears and tails, and loss of appetite. These symptoms were consistent with the description of BDS in Chinese medicine. In contrast, the control and BDS-induced rats treated with 5-HMF were relatively robust, showing thick and shiny hair, pink and moist nose and lips, round and pink tails, and stable body weight along with increased appetite.

3.2 Routine Blood Testing

After 15 days of administration of normal saline and 5-HMF, the RBC, WBC, HGB, and HCT levels in the peripheral blood of the rats were measured (Figure 1). Compared with the control group, the RBC, WBC, HGB, and HCT levels in the model group were significantly reduced ($p < 0.01$), indicating that the blood





treatment of BDS has the characteristics of multiple pathways and multiple targets.

3.5 Results of Metabolomics Analysis

3.5.1 Multivariate Data Analysis

The samples were analyzed with the UPLC/Q-TOF metabolic spectrum. No abnormalities were found in the total ion chromatogram, and the retention time of chromatographic peaks and their ionic strength were observed (Figure 5). Masslynx and Progenesis Q1 software were used to analyze many raw files from G2-Si total quantification for data preprocessing, such as peak picking, denoising, and normalization, to generate a bioinformatics matrix. Then we exported the data set to Simca 14.1 software for chemometric analysis. The principal component analysis score chart showed that the model group was separated from the control group (Figure 6A). A significant separation between the model group and the control group was observed in the OPLS-DA chart (Figure 6B). The S-plot of OPLS-DA showed multiple metabolites (Figure 6C). The V-plot diagram of OPLS-DA showed a remarkable diversity of various metabolites (Figure 6D). The replacement test was used to verify the OPLS-DA mode (Figure 6E). Figure 6F shows that all experimental groups were separate in the liquid chromatography-mass spectrometry metabolic map. Among them, the metabolic profiles of the 5-HMF-H group, 5-HMF-

M group, and 5-HMF-L group were closer to the control group than the model group, suggesting that the model's metabolic disorder that was induced was reversed after drug treatment, and the 5-HMF-L group had a better separation effect. The four points in the QC group were clustered, which proved that the machine was stable.

3.5.2 Identification of Endogenous Metabolites

The difference metabolites between the control group and the model group were screened according to the VIP value ($VIP > 1.0$) and t -test ($p < 0.05$). As a result, a total of 65 different metabolites were screened (Table 1). Compared with the control group, 35 different metabolites (epitestosterone, etc.) were significantly increased, and 30 different metabolites (17 α -hydroxypregnenolone, etc.) significantly reduced. The 5-HMF-H group could regulate 48 metabolites (p-xanthine, etc.). The 5-HMF-M group could regulate 50 kinds of metabolites (5-KETE, etc.). The 5-HMF-L group could regulate 57 metabolites (5-KETE, etc.). The 5-HMF-L group had significantly more metabolic differences than the other two groups.

There were 9 metabolites involved in metabolism in the control group, model group, and 5-HMF-L group (Figure 7). To further clarify the distribution of 9 different metabolites in different groups, unsupervised clustering was performed by using a hierarchical clustering analysis heat map. As shown in Figure 8, there were significant differences between the model group and

TABLE 1 | Detection of BDS-related Metabolites in Plasma by LC-MS. Trend 1 is Control group compared with Model group; Trend 2 is Model group compared with 5-HML-L group.

NO.	Metabolites	TR (min)	m/z	Formula	VIP	p Value	Fold change	Trend 1	Trend 2	HMDB ID	Scan mode
1	PC(20:5 (5Z,8Z,11Z,14Z,17Z)/P-16:0)	20.98	764.5597	C ₄₄ H ₇₈ NO ₇ P	1.34	4.60E-02	1.14	↑	—	8,521	+
2	PC(18:2 (9Z,12Z)/P-16:0)	20.91	764.5466	C ₄₂ H ₈₀ NO ₇ P	1.51	3.11E-02	1.10	—	↑	8,159	+
3	Trihexosylceramide (d18:1/12:0)	20.71	985.6484	C ₄₈ H ₈₉ NO ₁₈	1.39	4.09E-02	1.21	—	↓	4,877	+
4	Trihexosylceramide (d18:1/16:0)	20.70	1,041.7068	C ₅₂ H ₉₇ NO ₁₈	4.17	6.76E-05	1.57	—	↓	4,879	+
5	LysoPC(22:2 (13Z,16Z))	20.68	593.4293	C ₃₀ H ₅₈ NO ₇ P	7.26	5.55E-08	1.47	—	↓	10400	+
6	DG (16:0/20:0/0:0)	20.67	647.5559	C ₃₉ H ₇₆ O ₅	1.90	1.26E-02	1.12	—	↓	7,107	+
7	DG (16:0/18:0/0:0)	20.65	596.9646	C ₃₇ H ₇₂ O ₅	2.02	9.58E-03	1.31	↑	↓	7,100	+
8	CE (18:3 (9Z,12Z,15Z))	20.64	669.5554	C ₄₅ H ₇₄ O ₂	7.65	2.23E-08	1.72	—	↓	10370	+
9	2,5-Furandicarboxylic acid	20.59	201.0376	C ₆ H ₄ O ₅	6.53	2.93E-07	1.30	—	↑	4,812	-
10	Phytofluene	20.39	542.9203	C ₄₀ H ₆₂	3.83	1.46E-04	3.22	↑	—	2871	+
11	Oleamide	20.27	282.2829	C ₁₈ H ₃₅ NO	2.39	4.10E-03	1.64	↑	—	2117	+
12	PC(20:0/18:4 (6Z,9Z,12Z,15Z))	20.18	810.1348	C ₄₆ H ₈₄ NO ₈ P	2.18	6.63E-03	1.60	↓	—	8,273	+
13	PC(20:4 (8Z,11Z,14Z,17Z)/18:0)	20.12	810.1348	C ₄₆ H ₈₄ NO ₈ P	3.93	1.16E-04	2.56	↓	—	8,464	+
14	PC(18:2 (9Z,12Z)/P-18:1 (11Z))	20.11	768.0981	C ₄₄ H ₈₂ NO ₇ P	1.80	1.58E-02	1.41	↓	—	8,161	+
15	PC(16:1 (9Z)/22:2 (13Z,16Z))	20.07	810.5913	C ₄₆ H ₈₆ NO ₈ P	2.95	1.12E-03	1.57	—	↓	8,020	-
16	PC(18:0/P-18:1 (11Z))	20.05	770.5976	C ₄₄ H ₈₆ NO ₇ P	2.91	1.22E-03	1.44	—	↑	8,062	-
17	PC(16:0/P-18:1 (11Z))	20.02	742.5653	C ₄₂ H ₈₂ NO ₇ P	2.05	8.90E-03	1.57	—	↓	7,996	-
18	LysoPC(22:1 (13Z))	19.95	577.7737	C ₃₀ H ₆₀ NO ₇ P	1.69	2.05E-02	1.14	↓	-	10399	+
19	PC(18:0/14:0)	19.94	734.5788	C ₄₀ H ₈₀ NO ₈ P	4.23	5.88E-05	1.48	—	↓	8,031	+
20	Arachidonic acid	19.94	304.4669	C ₂₀ H ₃₂ O ₂	2.93	1.18E-03	1.99	↑	—	1,043	-
21	PI(18:2 (9Z,12Z)/16:0)	19.94	852.5681	C ₄₃ H ₇₉ O ₁₃ P	2.95	1.11E-03	1.22	—	↓	9846	+
22	PC(20:1 (11Z)/P-16:0)	19.94	794.6085	C ₄₄ H ₈₆ NO ₇ P	8.07	8.47E-09	1.44	—	↑	8,324	+
23	PC(18:3 (9Z,12Z,15Z)/P-18:0)	19.94	768.5950	C ₄₄ H ₈₂ NO ₇ P	2.40	3.98E-03	1.40	—	↑	8,226	+
24	PC(20:4 (8Z,11Z,14Z,17Z)/16:0)	19.93	782.0817	C ₄₄ H ₈₀ NO ₈ P	9.10	7.91E-10	7.06	↑	—	8,462	+
25	PI(22:4 (7Z,10Z,13Z,16Z)/16:0)	19.93	887.5759	C ₄₇ H ₈₃ O ₁₃ P	3.77	1.70E-04	1.13	—	↓	9914	+
26	PC(20:2 (11Z,14Z)/14:0)	18.77	758.0603	C ₄₂ H ₈₀ NO ₈ P	1.85	1.40E-02	2.92	↑	—	8,328	+
27	PC(18:2 (9Z,12Z)/18:1 (9Z))	18.71	784.5924	C ₄₄ H ₈₂ NO ₈ P	2.63	2.34E-03	1.26	—	↓	8,137	+
28	PI(16:0/20:0)	18.71	911.5975	C ₄₈ H ₈₇ O ₁₃ P	4.67	2.16E-05	3.18	—	↑	9785	—
29	PC(18:4 (6Z,9Z,12Z,15Z)/18:1 (9Z))	18.71	780.0658	C ₄₄ H ₇₈ NO ₈ P	7.19	6.53E-08	6.71	↑	—	8,236	+
30	Trihexosylceramide (d18:1/24:0)	18.71	1,158.7722	C ₆₀ H ₁₁₃ NO ₁₈	4.80	1.58E-05	1.26	—	↓	4,886	+
31	DG (16:1 (9Z)/18:2 (9Z,12Z)/0:0)	18.70	591.5034	C ₃₇ H ₆₆ O ₅	15.11	7.77E-16	3.03	—	↓	7,132	+

(Continued on following page)

TABLE 1 | (Continued) Detection of BDS-related Metabolites in Plasma by LC-MS. Trend 1 is Control group compared with Model group; Trend 2 is Model group compared with 5-HML-L group.

NO.	Metabolites	TR (min)	m/z	Formula	VIP	p Value	Fold change	Trend 1	Trend 2	HMDB ID	Scan mode
32	DG (16:0/16:0/0:0)	18.69	568.9114	C ₃₅ H ₆₈ O ₅	1.60	2.50E-02	1.15	↑	↓	7,098	+
33	CE (22:5 (7Z,10Z,13Z,16Z,19Z))	18.69	721.5887	C ₄₉ H ₇₈ O ₂	12.48	3.31E-13	2.25	—	↓	10375	+
34	D-Erythrose 4-phosphate	18.69	245.0038	C ₄ H ₉ O ₇ P	5.49	3.20E-06	1.28	—	↑	1,321	-
35	LysoPC(22:6 (4Z,7Z,10Z,13Z,16Z,19Z))	18.67	567.6943	C ₃₀ H ₅₀ NO ₇ P	3.99	1.02E-04	4.47	↓	-	10404	+
36	Glucosylceramide (d18:1/12:0)	18.63	644.5063	C ₃₆ H ₆₉ NO ₈	5.40	3.99E-06	1.25	—	↓	4,969	+
37	S-Adenosylmethionine	17.87	399.4450	C ₁₅ H ₂₃ N ₆ O ₅ S+	1.99	1.03E-02	1.86	↑	—	1,185	—
38	SM(d18:0/14:1 (9Z) (OH))	17.84	689.5316	C ₃₇ H ₇₃ N ₂ O ₇ P	2.41	3.92E-03	1.39	—	↓	13462	+
39	PC(16:1 (9Z)/P-16:0)	17.83	733.5758	C ₄₀ H ₇₈ NO ₇ P	5.36	4.39E-06	1.45	-	↓	8,027	+
40	PC(20:3 (5Z,8Z,11Z)/P-18:1 (11Z))	17.82	816.6024	C ₄₆ H ₈₄ NO ₇ P	5.09	8.06E-06	1.43	—	↑	8,392	+
41	DG (18:1 (9Z)/18:2 (9Z,12Z)/0:0)	17.82	618.9701	C ₃₉ H ₇₀ O ₅	2.48	3.33E-03	1.26	↑	—	7,219	+
42	Secoisolariciresinol	17.81	407.1669	C ₂₀ H ₂₆ O ₆	3.11	7.70E-04	1.32	—	↓	13692	—
43	PC(22:2 (13Z,16Z)/14:0)	17.81	786.1134	C ₄₄ H ₈₄ NO ₈ P	2.20	6.34E-03	1.26	↓	—	8,590	+
44	17α-Hydroxypregnenolone	17.79	332.4770	C ₂₁ H ₃₂ O ₃	2.92	1.20E-03	1.61	↓	↑	363	+
45	PI(22:5 (7Z,10Z,13Z,16Z,19Z)/18:0)	17.68	913.1652	C ₄₉ H ₈₅ O ₁₃ P	2.91	1.23E-03	2.77	↑	—	9919	—
46	DG (18:1 (9Z)/20:0/0:0)	17.61	668.6202	C ₄₁ H ₇₈ O ₅	6.38	4.20E-07	2.13	—	↓	7,223	+
47	PC(18:0/20:3 (8Z,11Z,14Z))	17.59	812.6229	C ₄₆ H ₈₆ NO ₈ P	2.33	4.69E-03	1.41	—	↓	8,047	+
48	SM(d18:0/16:1 (9Z) (OH))	17.59	717.5618	C ₃₉ H ₇₇ N ₂ O ₇ P	1.98	1.05E-02	1.38	—	↓	13463	+
49	SM(d18:0/16:1 (9Z))	17.59	703.5811	C ₃₉ H ₇₉ N ₂ O ₆ P	1.40	3.97E-02	1.14	—	↓	13464	+
50	PC(20:3 (8Z,11Z,14Z)/14:0)	17.58	756.0444	C ₄₂ H ₇₈ NO ₈ P	1.51	3.10E-02	1.39	↑	—	8,394	+
51	LysoPC(22:0)	17.57	579.7895	C ₃₀ H ₆₂ NO ₇ P	2.26	5.51E-03	1.34	↓	—	10398	+
52	PI(16:0/18:0)	17.32	856.5954	C ₄₃ H ₈₃ O ₁₃ P	5.57	2.71E-06	1.54	—	↑	9781	+
53	PC(22:5 (7Z,10Z,13Z,16Z,19Z)/16:0)	17.31	808.1189	C ₄₆ H ₈₂ NO ₈ P	5.60	2.53E-06	3.07	↑	↓	8,692	+
54	Ceramide (d18:1/25:0)	17.29	664.1399	C ₄₃ H ₈₅ NO ₃	3.97	1.06E-04	11.72	↓	—	4,957	+
55	Glucosylceramide (d18:1/9Z-18:1)	17.19	726.0786	C ₄₂ H ₇₉ NO ₈	3.56	2.76E-04	1.47	↑	—	4,970	—
56	beta-Cryptoxanthin	16.94	552.8870	C ₄₀ H ₅₆ O	3.43	3.69E-04	1.90	↓	—	33844	+
57	9,10-Epoxyoctadecenoic acid	16.50	296.4449	C ₁₈ H ₃₂ O ₃	3.04	9.10E-04	1.27	↑	—	4,701	+
58	Adrenoyl ethanolamide	16.47	375.5878	C ₂₄ H ₄₁ NO ₂	2.10	7.90E-03	1.72	↑	—	13626	+
59	LysoPC(22:5 (4Z,7Z,10Z,13Z,16Z))	16.41	569.7101	C ₃₀ H ₅₂ NO ₇ P	3.22	6.07E-04	1.56	↓	—	10402	+
60	Chenodeoxycholic acid	15.90	393.3044	C ₂₄ H ₄₀ O ₄	2.20	6.35E-03	1.09	—	↑	518	+
61	Cer(d18:1/14:0)	15.43	508.4804	C ₃₂ H ₆₃ NO ₃	1.55	2.85E-02	1.48	—	↓	11773	—
62	LysoPC(20:3 (5Z,8Z,11Z))	15.42	546.3631	C ₂₈ H ₅₂ NO ₇ P	2.05	8.89E-03	1.11	—	↑	10393	+

(Continued on following page)

TABLE 1 | (Continued) Detection of BDS-related Metabolites in Plasma by LC-MS. Trend 1 is Control group compared with Model group; Trend 2 is Model group compared with 5-HML-L group.

NO.	Metabolites	TR (min)	m/z	Formula	VIP	p Value	Fold change	Trend 1	Trend 2	HMDB ID	Scan mode
63	PC(24:1 (15Z)/P-18:1 (11Z))	15.40	898.6832	C ₅₀ H ₉₆ NO ₇ P	1.52	2.99E-02	6.92	—	↓	8,819	—
64	PC(22:2 (13Z,16Z)/P-18:1 (11Z))	15.36	868.6364	C ₄₈ H ₉₀ NO ₇ P	1.59	2.58E-02	2.14	—	↓	8,621	—
65	Docosahexaenoic acid	14.85	328.4883	C ₂₂ H ₃₂ O ₂	3.07	8.49E-04	2.13	↑	—	2183	+
66	PC(14:0/18:3 (6Z,9Z,12Z))	14.63	745.5483	C ₄₀ H ₇₄ NO ₈ P	8.01	9.74E-09	2.41	—	↓	7,875	+
67	Retinal	14.62	284.4357	C ₂₀ H ₂₈ O	1.42	3.83E-02	1.72	↑	—	1,358	+
68	Dihydrofolic acid	14.51	443.4133	C ₁₉ H ₂₁ N ₇ O ₆	1.52	3.03E-02	2.22	↑	—	1,056	—
69	PC(20:5 (5Z,8Z,11Z,14Z,17Z)/P-18:1 (11Z))	14.46	834.5671	C ₄₆ H ₈₀ NO ₇ P	4.13	7.48E-05	3.39	—	↑	8,523	—
70	N1,N12-Diacetylspermine	14.28	286.4136	C ₁₄ H ₃₀ N ₄ O ₂	2.42	3.82E-03	3.41	↑	—	2172	—
71	LysoPC(22:4 (7Z,10Z,13Z,16Z))	14.25	571.7260	C ₃₀ H ₅₄ NO ₇ P	3.14	7.20E-04	1.41	↓	↑	10401	—
72	LysoPC(20:2 (11Z,14Z))	14.20	547.7046	C ₂₈ H ₅₄ NO ₇ P	2.72	1.89E-03	1.19	↓	—	10392	—
73	PC(20:4 (8Z,11Z,14Z,17Z)/P-18:1 (9Z))	14.06	792.1195	C ₄₆ H ₈₂ NO ₇ P	3.61	2.47E-04	2.05	↑	—	8,491	—
74	PC(22:6 (4Z,7Z,10Z,13Z,16Z,19Z)/P-18:0)	14.05	818.1568	C ₄₈ H ₈₄ NO ₇ P	4.43	3.73E-05	2.42	↑	—	8,752	—
75	PC(22:4 (7Z,10Z,13Z,16Z)/P-16:0)	13.98	794.1354	C ₄₆ H ₈₄ NO ₇ P	2.53	2.98E-03	3.69	↑	—	8,652	—
76	all-trans-Retinoic acid	13.73	300.4420	C ₂₀ H ₂₈ O ₂	2.86	1.37E-03	3.46	↑	—	1852	+
77	PC(18:4 (6Z,9Z,12Z,15Z)/P-18:1 (11Z))	13.62	808.5438	C ₄₄ H ₇₈ NO ₇ P	2.18	6.63E-03	2.28	—	↑	8,260	—
78	PS(18:0/18:1 (9Z))	13.60	788.5432	C ₄₂ H ₈₀ NO ₁₀ P	2.71	1.93E-03	1.32	—	↓	10163	—
79	Ceramide (d18:1/12:0)	13.53	480.4446	C ₃₀ H ₅₉ NO ₃	1.76	1.75E-02	1.24	—	↓	4,947	—
80	Ubiquinone-1	13.43	250.2903	C ₁₄ H ₁₈ O ₄	1.82	1.52E-02	1.41	↓	↑	2012	+
81	L-Cystathionine	13.16	222.2620	C ₇ H ₁₄ N ₂ O ₄ S	3.21	6.19E-04	1.30	↓	↑	99	+
82	L-Palmitoylcarnitine	12.95	400.6230	C ₂₃ H ₄₅ NO ₄	4.43	3.70E-05	1.76	↑	—	222	+
83	Ganglioside GM3 (d18:1/16:0)	12.93	1,151.6951	C ₅₇ H ₁₀₄ N ₂ O ₂₁	5.30	4.99E-06	1.24	—	↑	4,844	—
84	PS(18:0/22:6 (4Z,7Z,10Z,13Z,16Z,19Z))	12.69	836.0860	C ₄₆ H ₇₈ NO ₁₀ P	5.28	5.30E-06	6.79	↓	—	10167	—
85	LysoPC(18:2 (9Z,12Z))	12.67	519.6515	C ₂₆ H ₅₀ NO ₇ P	3.97	1.06E-04	1.26	↓	—	10386	—
86	5-KETE	12.41	318.4504	C ₂₀ H ₃₀ O ₃	5.22	6.06E-06	8.58	↓	—	10217	—
87	PS(18:0/20:4 (8Z,11Z,14Z,17Z))	12.40	812.0646	C ₄₄ H ₇₈ NO ₁₀ P	3.45	3.54E-04	9.39	↓	—	10165	—
88	PC(18:3 (6Z,9Z,12Z)/P-18:1 (11Z))	12.40	810.5626	C ₄₄ H ₈₀ NO ₇ P	3.30	4.96E-04	6.75	—	↑	8,194	—
89	13-cis-Retinoic acid	12.33	300.4351	C ₂₀ H ₂₈ O ₂	4.53	2.93E-05	7.08	↓	—	6219	+
90	LysoPC(16:1 (9Z)/0:0)	12.30	493.6142	C ₂₄ H ₄₈ NO ₇ P	1.93	1.17E-02	1.45	↑	—	10383	+
91	2-Methoxyestrone	12.06	300.3921	C ₁₉ H ₂₄ O ₃	5.28	5.29E-06	5.28	↓	—	10	—
92	LysoPC(14:0/0:0)	11.80	467.5769	C ₂₂ H ₄₆ NO ₇ P	1.56	2.73E-02	1.37	↑	—	10379	+
93	Testosterone glucuronide	11.74	464.5485	C ₂₅ H ₃₆ O ₈	3.81	1.56E-04	2.12	↑	—	3,193	-

(Continued on following page)

TABLE 1 | (Continued) Detection of BDS-related Metabolites in Plasma by LC-MS. Trend 1 is Control group compared with Model group; Trend 2 is Model group compared with 5-HMF-L group.

NO.	Metabolites	TR (min)	m/z	Formula	VIP	p Value	Fold change	Trend 1	Trend 2	HMDB ID	Scan mode
94	Sphinganine	11.67	301.5078	C ₁₈ H ₃₉ NO ₂	2.85	1.43E-03	1.58	↑	—	269	+
95	Sphingosine 1-phosphate	11.65	379.4718	C ₁₈ H ₃₈ NO ₅ P	4.85	1.42E-05	2.46	↑	—	277	+
96	15-Deoxy-d-12,14-PGJ2	11.51	316.4345	C ₂₀ H ₂₈ O ₃	5.39	4.09E-06	5.56	↓	↑	5079	—
97	Delta-12-Prostaglandin J2	11.34	334.4498	C ₂₀ H ₃₀ O ₄	2.79	1.64E-03	2.15	↓	—	4,238	—
98	Dehydroepiandrosterone	11.15	288.4244	C ₁₉ H ₂₈ O ₂	2.75	1.76E-03	2.16	↓	—	77	—
99	(9 <i>xi</i> ,10 <i>xi</i> ,12 <i>xi</i>)-9,10-Dihydroxy-12-octadecenoic acid	10.93	314.4660	C ₁₈ H ₃₄ O ₄	3.56	2.75E-04	22.15	↑	—	31679	—
100	LysoPC(20:5 (5Z,8Z,11Z,14Z,17Z))	10.64	541.6570	C ₂₈ H ₄₈ NO ₇ P	1.73	1.88E-02	1.65	↑	—	10397	+
101	15(S)-HPETE	10.49	336.4657	C ₂₀ H ₃₂ O ₄	3.91	1.22E-04	4.49	↓	—	4,244	—
102	Estrone	10.26	270.3661	C ₁₈ H ₂₂ O ₂	4.97	1.08E-05	4.93	↓	—	145	—
103	11,12,15-THETA	10.18	354.4810	C ₂₀ H ₃₄ O ₅	4.67	2.15E-05	3.48	↑	—	4,684	—
104	Palmitic acid	9.55	256.4241	C ₁₆ H ₃₂ O ₂	2.83	1.47E-03	1.29	↑	—	220	+
105	11b-Hydroxyprogesterone	9.46	330.4611	C ₂₀ H ₂₈ O ₄	4.70	2.00E-05	6.23	↓	—	4,031	—
106	Androstenedione	9.31	286.4085	C ₁₉ H ₂₆ O ₂	1.73	1.87E-02	5.19	↓	—	53	—
107	Allopregnanolone	9.16	363.2590	C ₂₁ H ₃₄ O ₂	1.42	3.77E-02	7.00	—	↓	1,449	—
108	Pyridoxamine 5'-phosphate	0.80	249.0656	C ₈ H ₁₃ N ₂ O ₅ P	1.87	1.33E-02	1.17	—	↑	1,555	+
109	Paraxanthine	0.78	180.1640	C ₇ H ₈ N ₄ O ₂	2.96	1.09E-03	1.53	↓	↑	1860	+
110	Indoleacetic acid	0.75	176.0683	C ₁₀ H ₉ NO ₂	2.14	7.17E-03	1.14	—	↑	197	+
111	Pyridoxamine	0.70	168.1931	C ₈ H ₁₂ N ₂ O ₂	2.17	6.73E-03	1.52	↓	—	1,431	—
112	15-KETE	0.17	341.2050	C ₂₀ H ₃₀ O ₃	2.81	1.55E-03	1.51	—	↑	10210	+
113	DG (18:2 (9Z,12Z)/20:1 (11Z)/0:0)	0.05	647.5553	C ₄₁ H ₇₄ O ₅	1.41	3.87E-02	1.54	—	↓	7,253	+

the control group. These metabolites could be significantly regulated, and metabolic disorders in rats after 5-HMF treatment were improved.

3.5.3 Analysis of Metabolic Pathways

The metabolites of the 5-HMF-L group were input into MetaboAnalyst to explore the metabolic pathways of 5-HMF in the treatment of BDS. The results showed that the 5-HMF-L group may play a role through metabolism of cysteine, methionine, glycerophospholipid, sphingolipid, caffeine, vitamin B6, glycerol, and tyrosine and steroid hormone biosynthesis (Figure 9).

3.5.4 Pathway Analysis of Targets and Metabolites

To explore the crucial metabolic pathways, joint pathway analysis by MetaboAnalyst was conducted with the 57 differential metabolites and 84 targets. The results showed that only

steroid hormone biosynthesis was simultaneously enriched with the targets from network pharmacology and the differential metabolites from metabolomics. According to the number of targets from the network pharmacology in the pathway, steroid hormones biosynthesis was selected as the most crucial metabolic pathway (Figure 10).

3.6 Effects of 5-Hydromethylfurfural on the Expression of Key Proteins in the Spleen of Blood Deficiency Rats

Compared with the control group, the expression of CYP17A1 and HSD3B1 protein in the spleen of the model group was decreased ($p < 0.05$). Compared with the model group, the 5-HMF-H group had increased expression of CYP17A1 protein ($p < 0.05$), and the 5-HMF-M and 5-HMF-L groups had significantly increased expression of CYP17A1 protein ($p <$

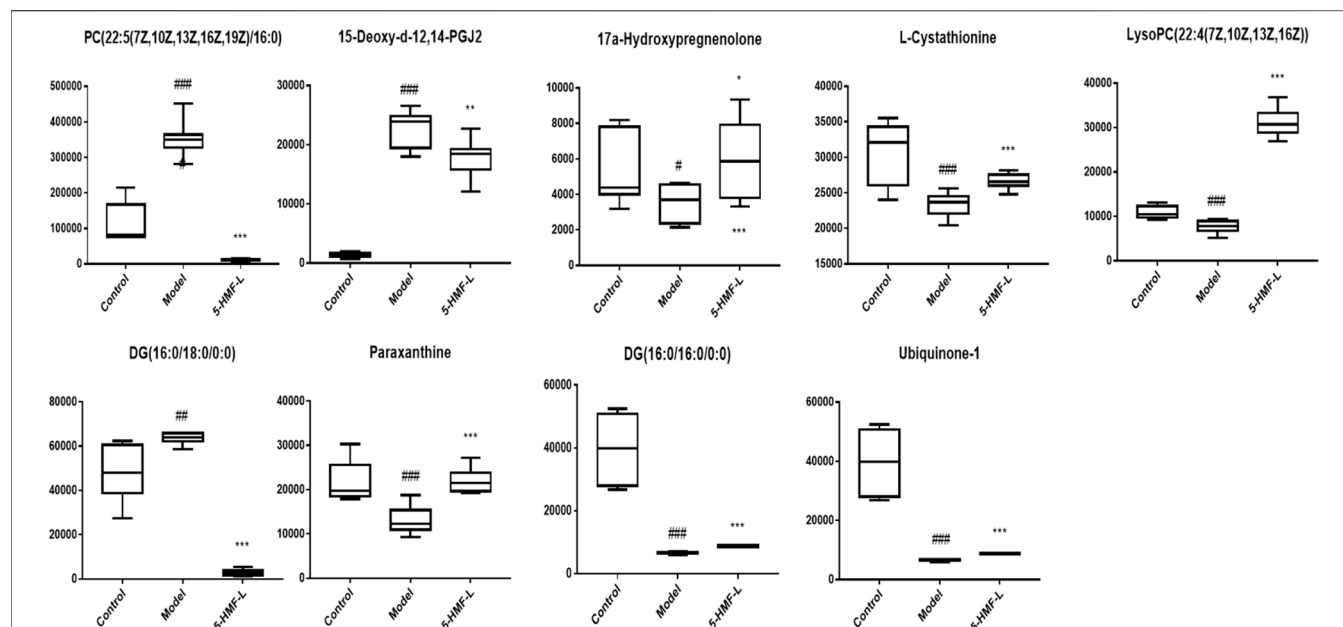


FIGURE 7 | Comparison of the relative content of different metabolites in plasma of the different administration groups. All data are expressed as mean \pm standard deviation ($n = 8$). # $p < 0.05$, ## $p < 0.01$, ### $p < 0.001$ compared with the control group; * $p < 0.05$, ** $p < 0.01$, *** $p < 0.001$ compared with the model group.

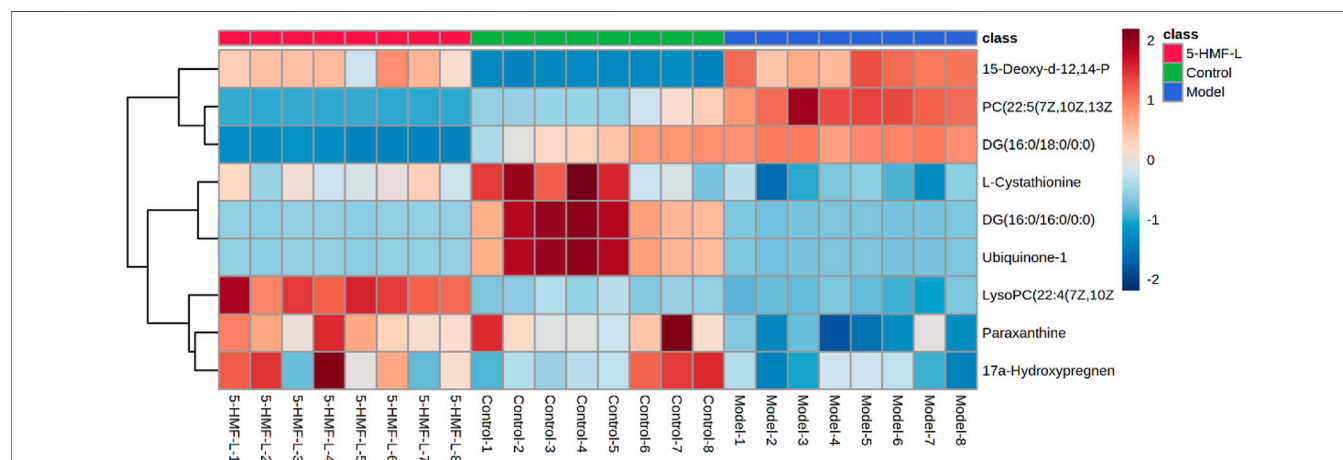


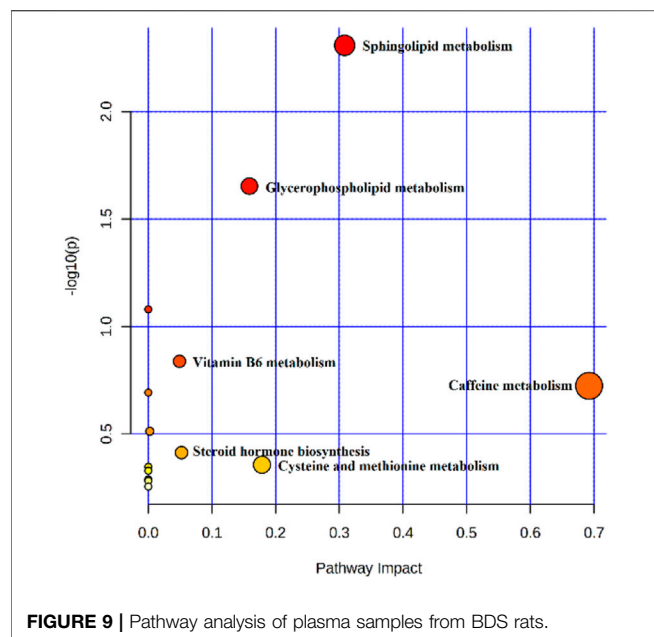
FIGURE 8 | Cluster analysis heatmap of different metabolites in BDS rat plasma. Brown and blue represent higher and lower than average levels of different metabolites, respectively. The rows represent different metabolites, and the columns represent rat plasma samples ($n = 8$).

0.01). Compared with the model group, the 5-HMF-L group had increased expression of HSD3B1 protein ($p < 0.05$) (Figure 11).

4 DISCUSSION

According to the theory of TCM, the pathogenesis of BDS might be qi-blood discord, the imbalance between yin and yang, blood stasis, and visceral dysfunction. Therefore, Chinese herbal medicines that could nourish yin and blood, fill the essence, and nourish the marrow were often used clinically to treat BDS and anemia (Bailly et al., 1978). Another medicine, RP, has been

used for more than 1,000 years to nourish yin and blood, but the possible mechanism of the effect of “tonifying blood” is still unclear. The appearance of rats in the model group changed significantly, including hair loss, slow movement, and weight loss. From the behavior of BDS rats, 5-HMF was effective in treating BDS. Peripheral RBC, WBC, HGB, and HCT were significantly reduced, a typical clinical manifestation of BDS and anemia (Safeukui et al., 2015). At the same time, the 5-HMF-H group did not have increases in WBC, RBC, and HGB, but the 5-HMF-M group and the 5-HMF-L group had more obvious therapeutic effects. Another indication of anemia is splenomegaly, which is one of the most common and earliest pathological manifestations



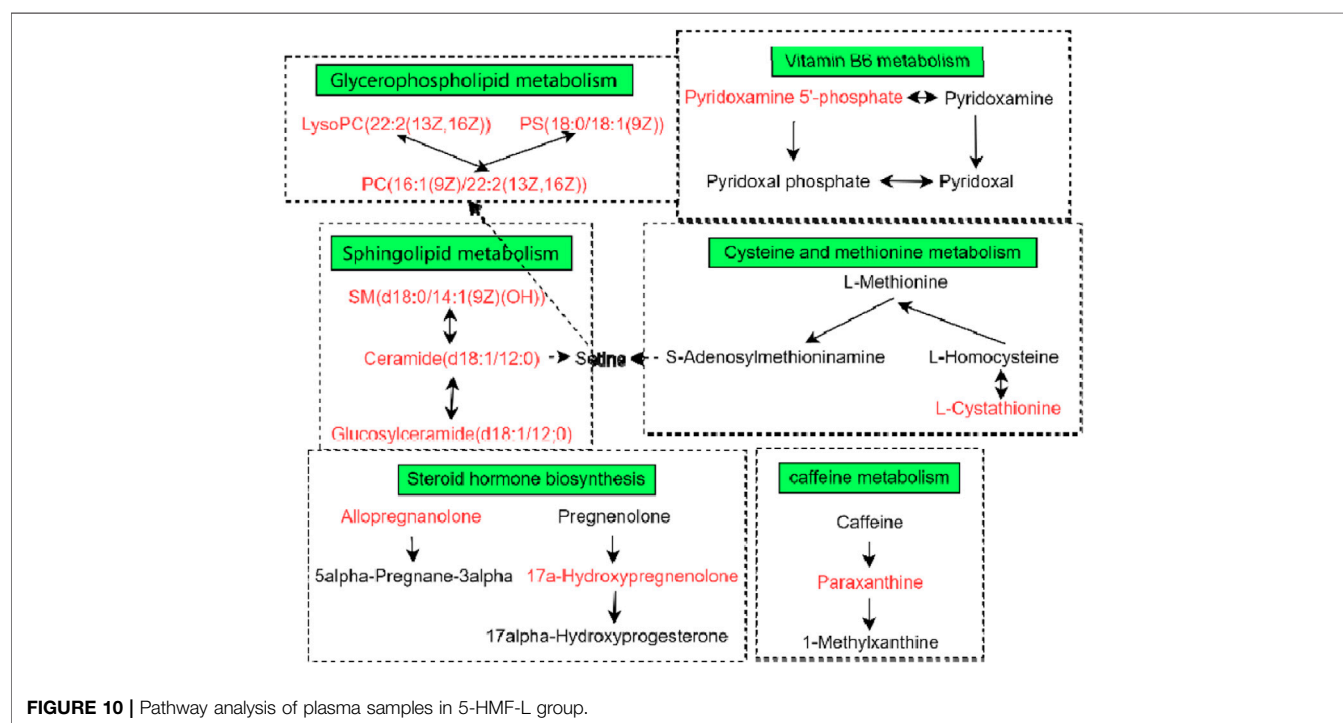
in different types of anemia (Altamura et al., 2019). It was generally believed that hematopoietic dysfunction was related to the discharge of bone marrow cells from bone marrow through blood, resulting in accumulation in the spleen (Koldkjaer et al., 2013). The collection of RBCs in the enlarged spleen could exacerbate anemia. Therefore, the reduction of RBCs in circulation and anemia are related to the degree of spleen enlargement (Gilep et al., 2011). According to **Figure 2**, the

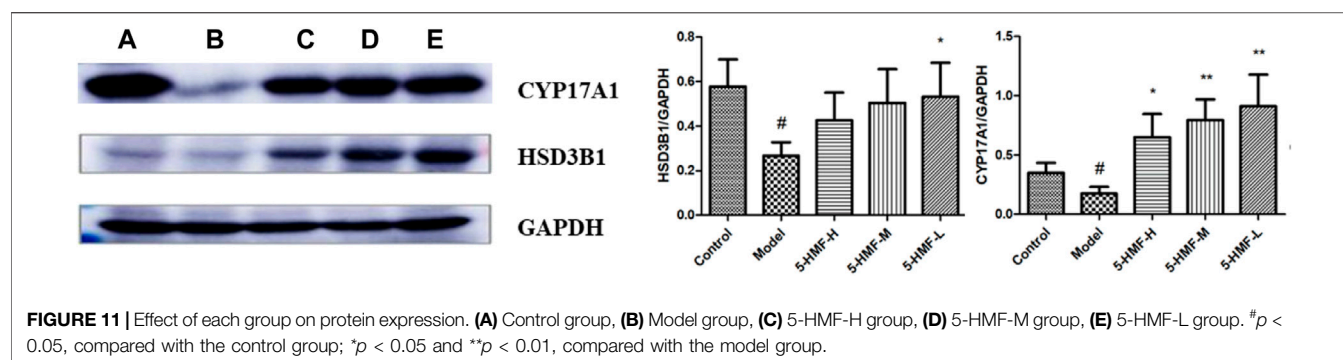
spleen mass in the model group was significantly greater than that in the control group. At the same time, compared with the model group, the spleen of the rats treated with 5-HMF was not enlarged. This showed that 5-HMF could reduce the side effects of chemotherapy on the spleen.

First, using the network pharmacology method, the therapeutic effect of 5-HMF on BDS was analyzed from the two perspectives of target and pathway. From the results of network pharmacology, the regulation of metabolic pathways might be one of the main mechanisms in 5-HMF treatment of BDS. Second, from the perspective of metabolomics, 5-HMF did have a curative effect on BDS, and the curative effect in the 5-HMF-L group was greater than that in the other two groups. Therefore, it showed the efficacy of 5-HMF in BDS treatment, and the most effective dose was in the 5-HMF-L group. Combined with network pharmacology and metabolomics analysis, the steroid hormone biosynthesis may be the key pathway of 5-HMF in the treatment of BDS.

Steroids are commonly used drugs to treat autoimmune hemolytic anemia, but long-term use of steroids can lead to drug resistance (Schiffer et al., 2019). Steroid hormones play a vital role in regulating water and salt balance, metabolism and stress response, and initiating and maintaining sexual differentiation and reproduction (Porcu et al., 2016). The production of new steroids produces steroid hormones in the adrenal cortex, gonads, and placenta. In addition, a series of neurosteroids are produced in the brain (Christakoudi et al., 2018; Sackett et al., 2018). They can promote the body's hematopoietic function, increase HGB, accelerate the circulation of oxygen and CO₂, and enhance physical strength (Wu et al., 2016).

The metabolic pathway of steroid hormone biosynthesis was entered into the KEGG database and compared with the





critical metabolic pathway genes predicted by network pharmacology. We found that CYP17A1 and HSD3B1 are essential proteins for steroid synthesis (Almassi et al., 2018). Western blot verified that in the 5-HMF-L group, the expression of CYP17A1 and HSD3B1 proteins was significantly up-regulated, which was consistent with the changing trends of metabolomics results, verifying the reliability of the metabolomics and network pharmacology prediction. Therefore, we have reason to believe that the steroid hormone biosynthesis pathway may be related to BDS and may be the potential mechanism of 5-HMF in the treatment of BDS. Our results suggest that 5-HMF provides a new therapeutic target by regulating related signaling pathways.

5 CONCLUSION

Our data showed that 5-HMF could ameliorate blood deficiency in rats induced by chemotherapy. Its mechanism might be regulating the expression of CYP17A1 and HSD3B1 in the steroid hormone biosynthesis pathway. These findings suggest that 5-HMF may be an effective alternative drug for BDS treatment.

DATA AVAILABILITY STATEMENT

The raw data supporting the conclusions of this article will be made available by the authors, without undue reservation.

REFERENCES

- Almassi, N., Reichard, C., Li, J., Russell, C., Perry, J., Ryan, C. J., et al. (2018). HSD3B1 and Response to a Nonsteroidal CYP17A1 Inhibitor in Castration-Resistant Prostate Cancer. *JAMA Oncol.* 4 (4), 554–557. doi:10.1001/jamaoncol.2017.3159
- Altamura, S., Vegi, N. M., Hoppe, P. S., Schroeder, T., Aichler, M., Walch, A., et al. (2019). Glutathione Peroxidase 4 and Vitamin E Control Reticulocyte Maturation, Stress Erythropoiesis and Iron Homeostasis. *Haematologica* 105 (4), 937–950. doi:10.3324/haematol.2018.212977
- Amberger, J. S., Bocchini, C. A., Schiettecatte, F., Scott, A. F., and Hamosh, A. (2015). OMIM.org: Online Mendelian Inheritance in Man (OMIM®), an Online Catalog of Human Genes and Genetic Disorders. *Nucleic Acids Res.* 43 (Database issue), D789–D798. doi:10.1093/nar/gku1205

ETHICS STATEMENT

The animal study was reviewed and approved by Ethics Committee of Heilongjiang University of Traditional Chinese Medicine.

AUTHOR CONTRIBUTIONS

WZ and NC have contributed equally to this work. HK and QW are responsible for this article.

FUNDING

Chief Scientist of Qi-Huang Project of National Traditional Chinese Medicine Inheritance and Innovation “One Hundred Million” Talent Project (2021). Qi-Huang Scholar of National Traditional Chinese Medicine Leading Talents Support Program (2018). Heilongjiang Touyan Innovation Team Program.

ACKNOWLEDGMENTS

The authors thank Charlesworth Author Services (www.dashboard.cwauthors.com.cn) for English language editing and review services.

- Bailly, Y., Sergeant, M., and Raynaud, G. (1978). Hepato- and Thyreotoxicity of Tifemoxone. *Arch. Toxicol. Suppl.* 1, 229–233. doi:10.1007/978-3-642-66896-8_42
- Brown, G. (2020). Towards a New Understanding of Decision-Making by Hematopoietic Stem Cells. *Int. J. Mol. Sci.* 21 (7), 2362. doi:10.3390/ijms21072362
- Christakoudi, S., Runglall, M., Mobillo, P., Rebollo-Mesa, I., Tsui, T. L., Nova-Lamperti, E., et al. (2018). Steroid Regulation: An Overlooked Aspect of Tolerance and Chronic Rejection in Kidney Transplantation. *Mol. Cell Endocrinol.* 473, 205–216. doi:10.1016/j.mce.2018.01.021
- Duan, S. (2021). Effects of Angelica on Na⁺-K⁺-ATPase and Ca²⁺-Mg²⁺-ATPase in Blood Deficiency Rats[J]. *Gansu Anim. Husbandry Vet. Med.* 51 (04), 50–53.
- Gfeller, D., Grosdidier, A., Wirth, M., Daina, A., Michielin, O., and Zoete, V. (2014). SwissTargetPrediction: a Web Server for Target Prediction of Bioactive Small Molecules. *Nucleic Acids Res.* 42 (Web Server issue), W32–W38. doi:10.1093/nar/gku293

- Gilep, A. A., Sushko, T. A., and Usanov, S. A. (2011). At the Crossroads of Steroid Hormone Biosynthesis: the Role, Substrate Specificity and Evolutionary Development of CYP17. *Biochim. Biophys. Acta* 1814 (1), 200–209. doi:10.1016/j.bbapap.2010.06.021
- Gong, W., Zhu, S., Chen, C., Yin, Q., Li, X., Du, G., et al. (2019). The Anti-depression Effect of Angelicae Sinensis Radix Is Related to the Pharmacological Activity of Modulating the Hematological Anomalies. *Front. Pharmacol.* 10, 192. doi:10.3389/fphar.2019.00192
- Guo, Z. J., Zhai, H. Q., Yuan, Y. P., Zhang, T., Li, R., Kong, L. T., et al. (2016). National Physician Master Jin Shiyuan's Dispensing Technology of Rehmanniae Radix Praeparata Based on Li Shizhen's Pharmaceutical Academic Thought. *Zhongguo Zhong Yao Za Zhi* 41 (9), 1759–1762. Chinese. doi:10.4268/cjcm20160930
- Jiang, C., Lin, S. Y., and Zhao, J. L. (2013). Zhongguo Zhong Xi Yi Jie He Za Zhi Zhongguo Zhongxiyi Jiehe Zazhi = Chinese Journal of Integrated Traditional and Western Medicine. *Chin. J. integrated traditional West. Med.* 33 (1), 44–46.
- Kitagawa, I., Fukuda, Y., Taniyama, T., and Yoshikawa, M. (1995). Chemical Studies on Crude Drug Processing. X. On the Constituents of Rehmanniae Radix (4) : Comparison of the Constituents of Various Rehmanniae Radixes Originating in China, Korea, and Japan. *Yakugaku Zasshi* 115 (12), 992–1003. doi:10.1248/yakushi1947.115.12_992
- Koldjaer, P., McDonald, M. D., Prior, I., and Berenbrink, M. (2013). Pronounced *In Vivo* Hemoglobin Polymerization in Red Blood Cells of Gulf Toadfish: a General Role for Hemoglobin Aggregation in Vertebrate Hemoparasite Defense? *Am. J. Physiol. Regul. Integr. Comp. Physiol.* 305 (10), R1190–R1199. doi:10.1152/ajpregu.00246.2013
- Li, J., Zhang, L. P., Liu, W., Zhang, Z. L., and Liu, L. J. (2005). Studies on the Changes of 5-hydroxymethyl Furfuraldehyde Content in Radix Rehmanniae Steamed for Different Time. *Zhongguo Zhong Yao Za Zhi* 30 (18), 1438–1440. Chinese. PMID: 16381466.
- Li, M., Jiang, H., Hao, Y., Du, K., Du, H., Ma, C., et al. (2021). A Systematic Review on Botany, Processing, Application, Phytochemistry and Pharmacological Action of Radix Rehmanniae. *J. ethnopharmacology* 2021, 114820. Advance online publication. doi:10.1016/j.jep.2021.114820
- Li, M. M., Wu, L. Y., Zhao, T., Xiong, L., Huang, X., Liu, Z. H., et al. (2011). The Protective Role of 5-HMF against Hypoxic Injury. *Cell Stress Chaperones* 16 (3), 267–273. doi:10.1007/s12192-010-0238-2
- Li, P. L., Sun, H. G., Hua, Y. L., Ji, P., Zhang, L., Li, J. X., et al. (2015). Metabolomics Study of Hematopoietic Function of Angelica Sinensis on Blood Deficiency Mice Model. *J. Ethnopharmacol* 166, 261–269. doi:10.1016/j.jep.2015.03.010
- Li, X., Dao, M., Lykotrafitis, G., and Karniadakis, G. E. (2017). Biomechanics and Biorheology of Red Blood Cells in Sickle Cell Anemia. *J. Biomech.* 50, 34–41. doi:10.1016/j.jbiomech.2016.11.022
- Liu, W., Fan, Y., Tian, C., Jin, Y., Du, S., Zeng, P., et al. (2020). Deciphering the Molecular Targets and Mechanisms of HGWD in the Treatment of Rheumatoid Arthritis via Network Pharmacology and Molecular Docking. *Evid. Based Complement. Alternat Med.* 2020, 7151634. doi:10.1155/2020/7151634
- Lucas, A., Ao-Ieong, E. S. Y., Williams, A. T., Jani, V. P., Muller, C. R., Yalcin, O., et al. (2019). Increased Hemoglobin Oxygen Affinity with 5-Hydroxymethylfurfural Supports Cardiac Function during Severe Hypoxia. *Front. Physiol.* 10, 1350. doi:10.3389/fphys.2019.01350
- Milano, M., and Schneider, M. (2007). EPO in Cancer Anemia: Benefits and Potential Risks. *Crit. Rev. Oncol. Hematol.* 62 (2), 119–125. doi:10.1016/j.critrevonc.2006.11.011
- Pan, L., Li, Z., Wang, Y., Zhang, B., Liu, G., and Liu, J. (2020). Network Pharmacology and Metabolomics Study on the Intervention of Traditional Chinese Medicine Huanglian Decoction in Rats with Type 2 Diabetes Mellitus. *J. Ethnopharmacol* 258, 112842. doi:10.1016/j.jep.2020.112842
- Porcu, P., Barron, A. M., Frye, C. A., Walf, A. A., Yang, S. Y., He, X. Y., et al. (2016). Neurosteroidogenesis Today: Novel Targets for Neuroactive Steroid Synthesis and Action and Their Relevance for Translational Research. *J. Neuroendocrinol* 28 (2), 12351. doi:10.1111/jne.12351
- Qiang, Y., Liu, J., Dao, M., and Du, E. (2021). *In Vitro* assay for Single-Cell Characterization of Impaired Deformability in Red Blood Cells under Recurrent Episodes of Hypoxia. *Lab. Chip* 21 (18), 3458–3470. doi:10.1039/d1lc00598g
- Ru, J., Li, P., Wang, J., Zhou, W., Li, B., Huang, C., et al. (2014). TCMSP: a Database of Systems Pharmacology for Drug Discovery from Herbal Medicines. *J. Cheminform* 6 (1), 13. doi:10.1186/1758-2946-6-13
- Sackett, K., Cohn, C. S., Fahey-Ahrndt, K., Smith, A. R., and Johnson, A. D. (2018). Successful Treatment of Pure Red Cell Aplasia Because of ABO Major Mismatched Stem Cell Transplant. *J. Clin. Apher.* 33 (1), 108–112. doi:10.1002/jca.21553
- Safeukui, I., Gomez, N. D., Adelani, A. A., Burte, F., Afolabi, N. K., Akondy, R., et al. (2015). Malaria Induces Anemia through CD8+ T Cell-dependent Parasite Clearance and Erythrocyte Removal in the Spleen. *mBio* 6 (1), e02493–14. doi:10.1128/mBio.02493-14
- Schiffer, L., Barnard, L., Baranowski, E. S., Gilligan, L. C., Taylor, A. E., Arlt, W., et al. (2019). Human Steroid Biosynthesis, Metabolism and Excretion Are Differentially Reflected by Serum and Urine Steroid Metabolomes: A Comprehensive Review. *J. Steroid Biochem. Mol. Biol.* 194, 105439. doi:10.1016/j.jsbmb.2019.105439
- Shi, X., Tang, Y., Zhu, H., Li, W., Li, Z., Li, W., et al. (2014). Comparative Tissue Distribution Profiles of Five Major Bio-Active Components in normal and Blood Deficiency Rats after Oral Administration of Danggui Buxue Decoction by UPLC-TQ/MS. *J. Pharm. Biomed. Anal.* 88, 207–215. doi:10.1016/j.jpba.2013.08.043
- Stelzer, G., Rosen, N., Plaschkes, I., Zimmerman, S., Twik, M., Fishilevich, S., et al. (2016). The GeneCards Suite: From Gene Data Mining to Disease Genome Sequence Analyses. *Curr. Protoc. Bioinformatics* 54, 1–33. doi:10.1002/cpb.5
- Wang, X., Shen, Y., Wang, S., Li, S., Zhang, W., Liu, X., et al. (2017). PharmMapper 2017 Update: a Web Server for Potential Drug Target Identification with a Comprehensive Target Pharmacophore Database. *Nucleic Acids Res.* 45, W356–W360. doi:10.1093/nar/gkx374
- Wang, Y., Li, C., Chuo, W., Liu, Z., Ouyang, Y., Li, D., et al. (2013). Integrated Proteomic and Metabolomic Analysis Reveals the NADH-Mediated TCA Cycle and Energy Metabolism Disorders Based on a New Model of Chronic Progressive Heart Failure. *Mol. Biosyst.* 9 (12), 3135–3145. doi:10.1039/c3mb70263d
- Wishart, D. S., Feunang, Y. D., Guo, A. C., Lo, E. J., Marcu, A., Grant, J. R., et al. (2018). DrugBank 5.0: a Major Update to the DrugBank Database for 2018. *Nucleic Acids Res.* 46 (D1), D1074–D1082. doi:10.1093/nar/gkx1037
- Won, T. H., Liao, L., Kang, S. S., and Shin, J. (2014). Simultaneous Analysis of Furfural Metabolites from Rehmanniae Radix Preparata by HPLC-DAD-ESI-MS. *Food Chem.* 142, 107–113. doi:10.1016/j.foodchem.2013.07.026
- Wu, Y. S., Chang, C. H., and Nan, F. H. (2016). Steroid Hormone "cortisone" and "20-hydroxycyclopentanone" Involved in the Non-specific Immune Responses of white Shrimp (*Litopenaeus Vannamei*). *Fish. Shellfish Immunol.* 56, 272–277. doi:10.1016/j.fsi.2016.07.005
- Xia, F., Liu, C., and Wan, J. B. (2020). Characterization of the Cold and Hot Natures of Raw and Processed Rehmanniae Radix by Integrated Metabolomics and Network Pharmacology. *Phytomedicine* 74, 153071. doi:10.1016/j.phymed.2019.153071
- Xu, J., Wu, J., Zhu, L. Y., Shen, H., Xu, J. D., Jensen, S. R., et al. (2012). Simultaneous Determination of Iridoid Glycosides, Phenethylalcohol Glycosides and Furfural Derivatives in Rehmanniae Radix by High Performance Liquid Chromatography Coupled with Triple-Quadrupole Mass Spectrometry. *Food Chem.* 135 (4), 2277–2286. doi:10.1016/j.foodchem.2012.07.006
- Yao, Z.-J., Dong, J., Che, Y.-J., Zhu, M.-F., Wen, M., Wang, N.-N., et al. (2016). TargetNet: a Web Service for Predicting Potential Drug-Target Interaction Profiling via Multi-Target SAR Models. *J. Computer-Aided Mol. Des.* 30, 413. doi:10.1007/s10822-016-9915-2
- Yong, W., Chun, L., Wenjing, C., Zhongyang, L., Yulin, O., Dong, L., et al. (2012). Integrated Proteomic and Metabolomic Analysis Reveals NADH-Mediated Tca Energy Metabolism Disorder in Chronic Progressive Heart Failure. *Heart* 98 (Suppl. 2), E115. doi:10.1136/heartjnl-2012-302920b.12
- Zee-Cheng, R. K. (1992). Shi-quan-da-bu-tang (Ten Significant Tonic Decoction), SQT. A Potent Chinese Biological Response Modifier in Cancer

- Immunotherapy, Potentiation and Detoxification of Anticancer Drugs. *Methods Find Exp. Clin. Pharmacol.* 14 (9), 725–736.
- Zhang, H., Wang, H. F., Liu, Y., Huang, L. J., Wang, Z. F., and Li, Y. (2014). The Haematopoietic Effect of *Panax Japonicus* on Blood Deficiency Model Mice. *J. Ethnopharmacol.* 154 (3), 818–824. doi:10.1016/j.jep.2014.05.008
- Zhang, Z., Zhang, Y., Gao, M., Cui, X., Yang, Y., van Duijn, B., et al. (2020). Steamed *Panax Notoginseng* Attenuates Anemia in Mice with Blood Deficiency Syndrome via Regulating Hematopoietic Factors and JAK-STAT Pathway. *Front. Pharmacol.* 10, 1578. doi:10.3389/fphar.2019.01578
- Zhou, Y., Zhou, B., Pache, L., Chang, M., Khodabakhshi, A. H., Tanaseichuk, O., et al. (2019). Metascape Provides a Biologist-Oriented Resource for the Analysis of Systems-Level Datasets. *Nat. Commun.* 10 (1), 1523. doi:10.1038/s41467-019-09234-6
- Zhu, M. F., Liu, X. Q., Ju-hee, O., Chang-soo, Y., and Je-Hyun, L. (2007). Zhongguo Zhong Yao Za Zhi = Zhongguo Zhongyao Zazhi = China Journal of Chinese Materia Medica. *China J. Chin. materia Med.* 32 (12), 1155–1157.

Conflict of Interest: The authors declare that the research was conducted in the absence of any commercial or financial relationships that could be construed as a potential conflict of interest.

Publisher's Note: All claims expressed in this article are solely those of the authors and do not necessarily represent those of their affiliated organizations, or those of the publisher, the editors and the reviewers. Any product that may be evaluated in this article, or claim that may be made by its manufacturer, is not guaranteed or endorsed by the publisher.

Copyright © 2022 Zhang, Cui, Su, Wang, Yang, Sun, Guan, Kuang and Wang. This is an open-access article distributed under the terms of the Creative Commons Attribution License (CC BY). The use, distribution or reproduction in other forums is permitted, provided the original author(s) and the copyright owner(s) are credited and that the original publication in this journal is cited, in accordance with accepted academic practice. No use, distribution or reproduction is permitted which does not comply with these terms.



Evaluation and Application of Population Pharmacokinetic Models for Identifying Delayed Methotrexate Elimination in Patients With Primary Central Nervous System Lymphoma

Junjun Mao¹, Qing Li^{2,3}, Pei Li², Weiwei Qin^{1*†}, Bobin Chen^{2,3*†} and Mingkang Zhong¹

¹Department of Pharmacy, Huashan Hospital, Fudan University, Shanghai, China, ²Department of Hematology, Huashan Hospital, Fudan University, Shanghai, China, ³Department of Hematology, Huashan Hospital North, Fudan University, Shanghai, China

OPEN ACCESS

Edited by:

Jiao Zheng,
Shanghai Jiaotong University, China

Reviewed by:

Zinnia P. Parra-Guillen,
University of Navarra, Spain
Chakradhara Rao Satyanarayana
Uppugunduri,
Université de Genève, Switzerland

*Correspondence:

Bobin Chen
bbchen@fudan.edu.cn
Weiwei Qin
wwqin@fudan.edu.cn

[†]These authors have contributed
equally to this work

Specialty section:

This article was submitted to
Drug Metabolism and Transport,
a section of the journal
Frontiers in Pharmacology

Received: 18 November 2021

Accepted: 14 February 2022

Published: 09 March 2022

Citation:

Mao J, Li Q, Li P, Qin W, Chen B and
Zhong M (2022) Evaluation and
Application of Population
Pharmacokinetic Models for Identifying
Delayed Methotrexate Elimination in
Patients With Primary Central Nervous
System Lymphoma.
Front. Pharmacol. 13:817673.
doi: 10.3389/fphar.2022.817673

Objective: Several population pharmacokinetic (popPK) models have been developed to determine the sources of methotrexate (MTX) PK variability. It remains unknown if these published models are precise enough for use or if a new model needs to be built. The aims of this study were to 1) assess the predictability of published models and 2) analyze the potential risk factors for delayed MTX elimination.

Methods: A total of 1458 MTX plasma concentrations, including 377 courses (1–17 per patient), were collected from 77 patients who were receiving high-dose MTX for the treatment of primary central nervous system lymphoma in Huashan Hospital. PopPK analysis was performed using the NONMEM[®] software package. Previously published popPK models were selected and rebuilt. A new popPK model was then constructed to screen potential covariates using a stepwise approach. The covariates were included based on the combination of theoretical mechanisms and data properties. Goodness-of-fit plots, bootstrap, and prediction- and simulation-based diagnostics were used to determine the stability and predictive performance of both the published and newly built models. Monte Carlo simulations were conducted to qualify the influence of risk factors on the incidence of delayed elimination.

Results: Among the eight evaluated published models, none presented acceptable values of bias or inaccuracy. A two-compartment model was employed in the newly built model to describe the PK of MTX. The estimated mean clearance (CL/F) was 4.91 L h⁻¹ (relative standard error: 3.7%). Creatinine clearance, albumin, and age were identified as covariates of MTX CL/F. The median and median absolute prediction errors of the final model were -10.2 and 36.4%, respectively. Results of goodness-of-fit plots, bootstrap, and prediction-corrected visual predictive checks indicated the high predictability of the final model.

Conclusions: Current published models are not sufficiently reliable for cross-center use. The elderly patients and those with renal dysfunction, hypoalbuminemia are at higher risk of delayed elimination.

Keywords: methotrexate, population pharmacokinetics, external evaluation, delayed elimination, Monte carlo simulations

1 INTRODUCTION

High-dose methotrexate (HD-MTX, $\geq 1 \text{ g m}^{-2}$) is the base therapy for the treatment of various lymphoid malignancies, such as acute lymphoblastic leukemia (Sakura et al., 2018) and non-Hodgkin's lymphoma (Reiter et al., 1999), especially for treating primary or secondary central nervous system lymphoma (Plotkin et al., 2004; Zhu et al., 2009). As an antifolate inhibitor of dihydrofolate reductase, MTX may cause the depletion of purines and thymidylate, which inhibits DNA synthesis, leading to cell death (Baram et al., 1987).

Following intravenous infusion, approximately 60% of MTX binds to plasma protein (Maia et al., 1996). As a small polar molecule, MTX elimination is highly correlated with renal function. Approximately only 10% of MTX is excreted as unchanged drug in the bile, whereas the majority is eliminated as unchanged drug through the kidneys within 24 h (Csordas et al., 2013).

Both the pharmacokinetic (PK) of MTX, which exhibit wide inter-individual variability (IIV), and its exposure are directly related to efficacy and toxicity (Evans et al., 1986; Evans et al., 1998). Patients experiencing delayed MTX elimination have been reported to be at an elevated risk of toxicity, such as nephrotoxicity, myelotoxicity, mucositis, neurological complications, and other adverse effects, which may lead to significant morbidity and delays in treatment (Howard et al., 2016). To prevent this systemic toxicity, supportive care, such as fluid hydration, urine alkalinization, and leucovorin rescue, is conducted as HD-MTX is administered (Widemann and Adamson, 2006). Post-dose therapeutic drug monitoring is routinely performed to maintain MTX plasma concentrations within the cytotoxic range for leukemic cells and, below those associated with toxicity (Wall et al., 2000; Paci et al., 2014).

Delayed MTX elimination is defined as plasma MTX concentrations above $50 \mu\text{mol L}^{-1}$ at 24 h, above $5 \mu\text{mol L}^{-1}$ at 48 h, or above $0.2 \mu\text{mol L}^{-1}$ at 72 h (Hospira, 2017). As MTX-induced nephrotoxicity correlates with clearance (CL), delayed elimination is closely related to acute kidney injury (Huang et al., 2020). Thus, if patients with delayed MTX CL can be identified, allowing for the implementation of a personalized dosage regimen before chemotherapy, concentration-related toxicity may be avoided (Ramsey et al., 2018). Although some oncology guidelines recommend MTX dosage based on the patient's body size (i.e., body surface area or actual body weight) (Gurney and Shaw, 2007; Griggs et al., 2012), this strategy is not always suitable for clinical practice, particularly for obese patients (Gallais et al., 2020; Pai et al., 2020). Therefore, determining the risk factors for delayed MTX elimination is essential.

Compared to conventional PK analysis, population pharmacokinetics (popPK) is a superior approach in facilitating the understanding and quantification of PK variability (Ette and Williams, 2004). PopPK models combined with maximum posterior Bayesian estimation can be used to guide dosing regimen individualization.

A few popPK models have been constructed to assess the sources of MTX PK variability. However, whether these popPK

models can be extrapolated to other clinical centers remains unknown. In addition, inconsistencies and differences in study design, research purpose, and population properties have been noted in some of the published popPK models with regard to model structure, parameter estimates, selected covariates, and their functional forms on PK parameters (Mao et al., 2018; Cheng et al., 2020). As the published models were developed based on specific populations, selecting an appropriate model to guide precision dosing in clinical practice is challenging.

Whether the published models are sufficiently precise for use in patients with primary central nervous system lymphoma, or whether a new popPK model based on our center is needed, remains unknown. Therefore, we summarized and assessed the predictability of published HD-MTX popPK models in adult patients with lymphoid malignancies. In addition, a new popPK model was constructed to investigate the effects of physiopathological parameters on the distribution and elimination of MTX. The predictability of this model was also compared with previously published models. Finally, the most suitable model was applied to identify the population with delayed elimination.

2 MATERIALS AND METHODS

2.1 Patient Data Collection

Data from 77 adults (49 men and 28 women) who were diagnosed with primary central nervous system lymphoma and received HD-MTX ($>1 \text{ g m}^{-2}$) for treatment between June 2011 and November 2016 were retrospectively collected.

To protect against MTX-induced renal dysfunction, hydration and alkalization (urine pH > 7) were achieved 12 h prior to initiating MTX therapy (Hospira, 2017). Serial plasma MTX levels were measured at 24, 48, and 72 h until the plasma concentration was $\leq 0.2 \mu\text{mol L}^{-1}$ (Dupuis et al., 2008). The leucovorin rescue was initiated and repeated every 6 h after 24 h from the MTX infusion until the MTX concentration was lower than $\leq 0.2 \mu\text{mol L}^{-1}$.

MTX concentrations in plasma were determined using a well-validated enzyme-multiplied immunoassay (EMIT) using the SYVA Viva-Emit 2000 Kit (Siemens Healthcare Diagnostics, Newark, DE, United States). The limit of detection was $0.3 \mu\text{mol L}^{-1}$, and the calibration concentrations ranged from $0.3 \mu\text{mol L}^{-1}$ – $2,600 \mu\text{mol L}^{-1}$.

Demographic covariates, including age, sex, weight, body surface area (BSA), and concomitant medication with benzimidazoles and corticoids, were included in the database. Clinical covariates, such as serum creatinine (SCr) levels, were recorded before each MTX infusion and in tandem with MTX plasma samples. According to the standard of 'drug interaction score' (Benz-de Bretagne et al., 2014), benzimidazoles and corticoids were assigned scores of 2 and 1, respectively.

The Ethics Committee of Huashan Hospital approved the study protocols. Written informed consent was obtained from all volunteers.

2.2 Population Pharmacokinetic Models

Our study consisted of the following steps:

- Step 1: PopPK models of HD-MTX in adult patients with lymphoid malignancies were selected and reviewed.
- Step 2: A new popPK model was constructed based on our dataset.
- Step 3: The predictability of published popPK models and that of the newly built model was evaluated.
- Step 4: The most suitable model was applied to identify the population with delayed elimination.

2.2.1 Review of Published popPK Studies on HD-MTX

A systematic review of popPK studies on HD-MTX published in English before 31 December 2020 was performed using PubMed, Web of Science, and Embase. According to the Preferred Reporting Items for Systematic Reviews and Meta-analyses statement, the relevant identification, screening, and assessment were conducted (Moher et al., 2015).

The inclusion criteria for published studies were as follows: 1) studied population: adult patients with lymphoid malignancies; 2) treatment: HD-MTX; 3) PK analysis using NONMEM® software package; and 4) language: English. Studies were excluded if they 1) lacked the required details for external evaluation and re-estimate or 2) overlapped with other data or cohorts. Reference lists of the identified reports were also screened.

The demographic characteristics and following popPK parameters were collected from each identified study: apparent clearance (CL/F), apparent volume of distribution (V/F), and corresponding between-subject variability and residual variability.

2.2.2 Development of a Model Based on Our Dataset

NONMEM® software package (version 7.4; ICON Development Solutions, Ellicott City, MD, United States) with Pirana® 2.9 as an interface for Perl Speaks NONMEM (PsN; version 4.9.0) was used for popPK analysis (Keizer et al., 2013). R software (version 3.5.0, <http://www.r-project.org/>) was used to construct the visualizations for output and model evaluations.

Based on a literature review and visual data inspection, the concentration-time profile of MTX was described by two-compartment models. Model variability and random effects were classified as one of three types of errors: between-subject variability (BSV), inter-occasion variability (IOV), and residual unexplained variability (RUV). BSV was assumed to be log-normally distributed and an estimate for all parameters. IOV was assumed to be the same for all occasions (Karlsson and Sheiner, 1993). RUV was described by testing proportional and combined proportional as well as additive structures. The first-order conditional estimation method including η - ϵ interaction (FOCE-I) was used for the model (Beal et al., 1989).

The evaluated covariates included demographic and pathophysiological data, as well as concomitant medications (Table 1). Age, body size, hematocrit (HCT), albumin (ALB), creatinine clearance (CrCL), and concomitant medications were evaluated as possible covariates of MTX PK. CrCL was estimated using the Cockcroft-Gault equation (Cockcroft and Gault, 1976).

TABLE 1 | Patient characteristics used to develop and evaluate population model.

Characteristics	Number or mean \pm SD	Median (range)
No. of patients (Male/Female) ^a	77 (49/28)	/
No. of Samples ^b	1,458	/
Age (years)	54.6 \pm 9.2	56 (28–76)
Height (cm)	169 \pm 7	170 (150–185)
Weight (kg)	67.8 \pm 10.7	69.0 (41.0–94.0)
Body surface area (m ²)	1.60 \pm 0.30	1.61 (0.85–2.32)
Methotrexate dose (g)	4.7 \pm 1.9	4.0 (2.0–15.8)
Methotrexate dose (g m ⁻²)	3.0 \pm 1.3	2.8 (1.1–10.2)
Dosing time (h)	3.9 \pm 3.7	3 (1–28.25)
Occasions (n)	4.9 \pm 3.6	4 (1–17)
Samples per individual (n)	19.0 \pm 13.7	16 (3–67)
Hematocrit (%)	36.0 \pm 4.5	36.1 (15.7–48.4)
Total Bilirubin (μ mol L ⁻¹)	9.8 \pm 3.9	9.5 (3.1–36.1)
Alanine aminotransferase (U L ⁻¹)	38.2 \pm 39.5	28.0 (4.0–420.0)
Aspartate transferase (U L ⁻¹)	24.7 \pm 22.0	20.0 (5.0–559.0)
Albumin (g L ⁻¹)	38.7 \pm 4.3	39.0 (24.0–50.0)
Total protein (g L ⁻¹)	64.2 \pm 6.3	64.0 (41.0–82.0)
Serum Creatinine (μ mol L ⁻¹)	70.5 \pm 28.7	66.0 (22.0–480.0)
Creatinine Clearance (ml min ⁻¹) ^c	104.2 \pm 34.2	98 (15.1–326.5)
Concomitant medications^b		
Omeprazole	214	/
Esomeprazole	19	/
Lanzoprazole	969	/
Pantoprazole	58	/
Dexamethasone	1,122	/

^aData are expressed as number of patients.

^bData are expressed as number of samples.

^cCalculate following the Cockcroft-Gault formula: $CrCL = [(140 - \text{Age (year)}) \times \text{WT (kg)}] / (0.818 \times \text{Scr } (\mu\text{mol L}^{-1})) \times (0.85 \text{ for female})$.

As the most frequently identified covariate, the effect of CrCL on MTX PK CL/F was tested first. The other covariates were screened according to a previous study and their clinical relevance (Mao et al., 2018). Each co-administered drug was assigned a “drug interaction score (DIS)” list (Supplementary Table S1), as presented previously (Benz-de Bretagne et al., 2014), and was considered individually by testing its effect on PK parameters as categorical variable.

The influence of continuous covariates was explored using the linear, exponential, and power function models, whereas that of categorical variables was described using a shift model. After considering the most frequently identified covariates in the model, the remaining covariates were screened using a stepwise approach primarily based on objective function value (OFV) (Beal et al., 1989), and parameter precision. Error estimates were also considered.

The likelihood ratio tests at a significance level of $p < 0.05$ ($\Delta\text{OFV} > 3.84$) and $p < 0.001$ ($\Delta\text{OFV} > 10.83$) were performed in forward inclusion and backward elimination procedures, respectively. Moreover, the clinical meaning of parameters with a significant reduction of model variability in covariate selection was also considered. In the modeling process, the condition numbers were calculated to avoid over-parameterization, accepting no more than 1,000 as the criterion (Owen and Fiedler-Kelly, 2014).

2.2.3 Implementation of Published Models

Published models were rebuilt and fixed parameters were reported in each study. Prediction- and simulation-based

diagnostics were then used to evaluate the predictive performance of the published models (Zhao et al., 2016; Mao et al., 2018). If specific continuous covariates were missing, the median of the dataset or the model population was imputed. The data were assumed to be in the negative category (e.g., not receiving concomitant omeprazole) if categorical covariates were not available.

2.3 Model Evaluation

The predictability of published popPK models and the newly built model was evaluated by prediction- and simulation-based diagnostics. To compare the accuracy and precision of model predictive performance, prediction-based prediction error (PE, Eq. 1), median prediction error (MDPE), and median absolute prediction error (MAPE) were calculated and estimated (Sheiner and Beal, 1981).

$$PE (\%) = \left(\frac{PRED - OBS}{OBS} \right) \times 100 \quad (1)$$

The percentages of PE within 20% (F_{20}) and 30% (F_{30}) were used as the combination index of both the accuracy and precision.

The goodness-of-fit plots were examined for model evaluation. The model stability and precision of parameter estimates were assessed using the bootstrap method (Ette et al., 2003). By random sampling with replacement in Perl modules, 2000 bootstrap datasets were generated (Ette, 1997). The final popPK model was compared with each of the bootstrap datasets to obtain 95% confidence intervals (CI) for all model parameters.

The predictability of the candidate model was evaluated using prediction-corrected visual predictive checks (pcVPCs) with 2000 simulations (Bergstrand et al., 2011). The 95% CI for the median, and the 5th and 95th percentiles of the simulations were calculated and compared with the observations, binning automatically.

2.4 Model Application

Using parameter estimates from the most suitable model, Monte Carlo simulations were performed. The objective of this study was to determine the influence of covariates on the incidence of delayed MTX elimination. The proportion of patients with MTX concentrations $\leq 0.2 \mu\text{mol L}^{-1}$ at 72 h was analyzed, as 3 g m^{-2} was administered for standard patients (with BSA 1.6 m^2) with different covariate levels (2.5th percentile, median, and 97.5th percentile). After simulating 1,000 hypothetical individuals, the time-concentration profiles were obtained in each scenario.

3 RESULTS

3.1 Patients and Data Collection

Patient demographic and physical characteristics are presented in Table 1. Data from 77 patients, covering 377 courses (1–17 per patient), and 1458 MTX plasma concentrations were available for analysis. The doses administered to patients ranged from 2 to 15.8 g. MTX dosage was transformed into molar equivalents by dividing them by the molecular weight (MTX: 222 g mol^{-1} , <http://chem.nlm.nih.gov/chemidplus/>). For 92.3% of the treatment cycles, patients had short infusions, ranging from 1 to 4 h,

whereas the remaining patients had long infusions, ranging up to 28.25 h.

In total, 567 concentrations were below the limit of quantification (LOQ), among which 236 were the second samples below the LOQ in the same treatment cycle. The M6 method was used to handle samples below the LOQ of $0.3 \mu\text{mol L}^{-1}$ as Gallais *et al.* done previously (Beal, 2001; Gallais et al., 2020). For concentrations under the lower LOQ (LLOQ), the first measurement in each continuous series was set to LLOQ/2, with the following measurements being treated as missing values. More complex approaches such as the M3/M4 method (likelihood estimation) did not improve model predictability, and thus were not evaluated further. The description of the sampling points and samples below the LOQ is provided in **Supplementary Table S2**.

3.2 Population Pharmacokinetic Models

3.2.1 Review of Published popPK Studies on HD-MTX

Eight eligible popPK studies (Faltaos et al., 2006; Min et al., 2009; Simon et al., 2013; Benz-de Bretagne et al., 2014; Nader et al., 2017; Mei et al., 2018; Gallais et al., 2020; Yang et al., 2020) were identified during the literature review for further analysis. The screening process is presented in Text S1. The details of each study are summarized in **Table 2**. Among them, seven were single-center studies, whereas one was conducted at two centers (Benz-de Bretagne et al., 2014). Additionally, four studies were primarily conducted in France (Faltaos et al., 2006; Simon et al., 2013; Benz-de Bretagne et al., 2014; Gallais et al., 2020), three in China (Min et al., 2009; Mei et al., 2018; Yang et al., 2020), and one in Qatar (Nader et al., 2017). Furthermore, seven studies in the analysis had a small sample size of less than 1,000 concentrations (Faltaos et al., 2006; Min et al., 2009; Simon et al., 2013; Benz-de Bretagne et al., 2014; Nader et al., 2017; Mei et al., 2018; Yang et al., 2020). Four bioassay methods, HPLC, EMIT, TDx, and HEI, were used in seven studies (**Table 2**). Bioassay information was not provided in one study (Nader et al., 2017).

The covariates of the published final CL/F models included age, SCr, CrCL, HCT, BSA, change in basal urinary coproporphyrin I/coproporphyrin I + III ratio value at the time of hospital discharge (MTX pre-administration [DP3]), co-administration with at least one drug of score 2 (SCO2), and ABCB2 genotype. SCr, CrCL, and age were the most frequently identified covariates in the final models and were reported in three, two, and two studies, respectively (**Supplementary Table S3** and **Supplementary Table S4**). Body size was screened in all studies, and three included it in the volume of distribution, whereas one included it in CL/F and Q/F. Moreover, ABCC2 polymorphisms were screened in two studies, and it was included in the final model in one study (Simon et al., 2013).

3.2.2 Population Pharmacokinetic Model Development

Data was described using a two-compartment PK structural model (ADVAN3, TRANS4 subroutine) with linear elimination. The exponential model provided the best result

TABLE 2 | Summary of published population pharmacokinetic studies of HD-MTX in adult patients with lymphoid malignancy.

Study (publication year)	Country (single/ multiple sites)	Number of samples/ Patients (M/F)	Dosage regimen		Sampling schedule	Bio- assay		PK parameters and formula	BSV% (IOV%)	Residual error	Evaluation
Faltaos et al. (2006)	France (Single)	496/51 (28/23)	1–8 g/m ² , 1–6 h, i.v.		C ₂₄ /C ₄₈ and other two samples ^a	EMIT	CL/F V _d /F Q/F V _p /F	7.1×(AGE/62) ^{−0.22} ×(SCR/67) ^{−0.43} 25.1 0.15 2.7	22.0 (16.5) 22.5 51.0 64.0	46.0% 0.015 μmol/L	GOF, Bootstrap, MPE,RMSE
Min et al. (2009)	China (Single)	400/82 (60/22)	1.5–9 g, 24 h, i.v.		Before and 6,12,18,24,30,36,44,50,56,68,74,80,92 h after infusion	TDx	CL/F V _d /F Q/F V _p /F	7.45×[1 + 0.224×(0.89-SCR/100)] 25.9×[1−0.00937×(66-WT)] 0.333 9.23	50.6 22.5 70.4 97.8	42.3% 0.039 μmol/L	GOF, MPE,RMSE, Cross-over validation
Simon et al. (2013)	France (Single)	496/50 (27/23)	1–8 g/m ² , 1–6 h, i.v.		At the end of infusion and 8–12,24,48, 72 h until <0.03 μmol/L	EMIT	CL/F V ₁ /F Q ₂ /F V ₂ /F Q ₃ /F V ₃ /F	3.99×(1.63, if ABCC2 CT or TT) + 1.91×(CrCL/89) 19.0×(1.63, if ABCC2 CT or TT) 0.1 1.58 0.021 1.99	28.7 ^d 36.7 ^d / / / /	44.4%	Bootstrap, VPC
Bretagne <i>et al.</i> (2014)	France (Multiple)	363/81 (46/35)	1–8 g/m ² , 3–24 h, i.v.		C ₂₄ /C ₄₈ /C ₇₂ , then q24 h until <0.2 μmol/L	EMIT (Paris) TDx (Tours)	CL/F V _d /F Q/F V _p /F	7.05×(CrCL/91.6) ^{0.27} ×(DP3/0.6) ^{0.16} −0.93×SCO2 23.5 0.13 3.01	23.0 34.0 / 32.1	41.7%	GOF, Bootstrap, NPDE
Nader et al. (2017)	Qatar (Single)	530/37 (31/6)	0.5–7 g/m ² , 4–6 h or 24 h, i.v.		q12 h or q24 h until <0.05 μmol/L	NA	CL/F V _d /F Q/F V _p /F	15.7×(HCT/32) ^{0.85} 79.2×(WT/69) ^{1.29} 0.97 51.4	34.9 (47.4) ^b (31.1) ^b / / 63.2	33.4%	GOF, VPC
Mei et al. (2018)	China (Single)	701/98 (53/45)	0.9–5.4 g/m ² 1.3–8.2 h, i.v.		C ₂₄ /C ₄₈ /C ₇₂ /C ₉₆	HPLC	CL/F V _d /F Q/F V _p /F	6.67×(SCR/68.1) ^{−0.48} ×(BSA/ 1.75) ^{1.17} 24.46×(AGE/57.16) ^{0.81} 0.047 1.32	40.0 42.7 25.1 63.0	3.02 μmol/L	GOF, Bootstrap, VPC
Yang et al. (2020)	China (Single)	852/91 (64/27)	1–3 g/m ² , i.v.		NA	HPLC	CL/F V _d /F Q/F V _p /F	6.03×(CrCL/115.1) ^{0.414} 20.7 0.074×(BSA/1.65) ^{1.43} 3.76	51.6 (15.4) 48.3 65.6 /	0.32 μmol/L	GOF, Bootstrap, VPC
Gallais et al. (2020)	France (Single)	1,179/328 (180/133) ^c	1–8 g/m ² , 0.5–36 h, i.v.		C ₃₆ /C ₄₈ , then q24 h until <0.2 μmol/L	HEI HPLC	CL/F V _d /F Q/F V _p /F	8.3×(AGE/50) ^{−0.317} 27.4 0.15 (fixed) 3.1×(WT/70) ^{0.453}	23.0 (22.0) / / 38.0	34.0%	GOF

ABCC2, -24 C > T SNP (rs717620) in 5'-UT of the ATP-binding cassette transporter; BSA, body surface area (m²); BSV, between subject variability; CL/F, apparent clearance (l h⁻¹); C_n, concentration at n hours post-dose; CrCL, creatinine clearance (ml min⁻¹); DP3, the change of basal value of urinary coproporphyrin I/coproporphyrin I + III ratio at the time of hospital discharge refer to the MTX pre-administration; EMIT, enzyme multiplied immunoassay technique; F, female; FPIA, fluorescence polarization immunoassay; GOF, goodness-of-fit plots; HCT, hematocrit (%); HD-MTX, high dose-methotrexate; HEI, homogeneous enzyme immunoassay; IOV, inter-occasion variability; LC/MS, liquid chromatography/mass; M, male; MPE, median prediction error; NPDE, normalized prediction distribution error; PCNSL, primary central nervous system lymphoma; Q/F, apparent inter-compartmental clearance (l h⁻¹); RMSE, root mean square error; SCO2, co-administered with at least one drug of score 2; SCR, serum creatinine (μmol L⁻¹); TDx, FPIA using TDx[®] analysers; V_d/F, apparent volume of distribution of central compartment (l); V_p/F, apparent volume of distribution peripheral compartment (l); VPC, visual predictive check; WT, bodyweight (kg).

^aTwo supplementary samples: at the end of infusion and between 8 and 12 h from the beginning of the infusion. Eventual follow up plasma level determination was done at 72 h, 96 h or more.

^bIOV of 47.4 and 31.1% on MTX CL, for the second and third dosing occasions.

^c15 patients not included owing to missing toxicity information.

^dCorrelation is CL ~ V_d, 0.78.

TABLE 3 | Parameter estimates for the base model, final model and bootstrap procedure.

Parameters	Base model		Final model			Bootstrap of final model	
	Estimate	RSE (%)	Estimate	RSE (%)	Shrinkage (%)	Median	95% CI
Objective function value	4306.6	/	3455.9	/	/	/	/
CL/F (L h ⁻¹)	4.8	4.3	4.91	3.7	/	4.97	4.37–5.44
V _c /F (L)	20.9	5.6	18.4	3.8	/	18.0	16.5–20.3
Q/F (L h ⁻¹)	0.09	14.0	0.063	9.8	/	0.073	0.022–0.10
V _p /F (L)	5.9	26.3	2.18	14.1	/	2.17	1.59–2.77
Covariate effect on CL/F							
CrCL	/	/	0.49	22.6	/	0.50	0.29–0.69
ALB	/	/	0.35	50.6	/	0.35	0.031–0.72
AGE	/	/	0.89	9.4	/	0.90	0.72–1.06
Between-subject variability							
CL/F (%)	39.2	24.9	20.9	25.5	25.5	20.3	1.5–29.5
V _c /F (%)	36.9	40.4	19.6	26.9	20.9	20.4	17.3–32.8
Q/F (%)	62.3	18.3	40.6	18.1	19.4	36.7	18.7–54.3
V _p /F (%)	44.2	14.4	30.4	17.5	47.7	29.2	13.8–40.7
Inter-occasion variability							
IOV on CL	/	/	24.7	20.4	43.8	24.2	5.6–35.4
Residual variability							
Proportional (%)	58.3	6.5	40.1	6.3	11.5	39.6	34.9–44.9

ALB, albumin; CI, percentile confidence intervals; CL/F, apparent clearance; CrCL, creatinine clearance; F, the bioavailability relative to 1; IOV, inter-occasion variability; Q/F, inter-compartmental clearance; RSE, relative standard error; V_c/F, apparent central volume of distribution; V_p/F, apparent peripheral volume of distribution; RSE, relative standard error.

for the residual variability from the results of the OFVs and the distribution of residuals in the diagnostic plots. The parameter estimates and associated precisions of the base model are presented in **Table 3**.

Mechanistic plausibility was mainly considered as a potential covariate incorporated into the base model. As MTX is primarily eliminated unchanged by renal excretion, the effect of CrCL on MTX PK CL/F was tested first. The OFV substantially declined when CrCL was included exponentially ($\Delta\text{OFV} -97.6$, $p < 0.001$), indicating a significant improvement in the model. A decrease (18.0%) in CL/F was observed as the CrCL decreased from 90 ml min⁻¹ to 60 ml min⁻¹.

The pathophysiological factors influencing MTX protein binding were then investigated empirically. ALB and HCT were included in the model to assess which was more suitable for describing the change in protein binding in the MTX PK process ($\Delta\text{OFV} -59.9$ vs. -14.8 , $p < 0.001$), and ALB was included in the final model. As 24.6% of patients were above 60 years old, age was also investigated by separating patients into two groups (i.e., older, or younger than 60 years). The CL/F of elderly patients (age >60) was 11.0% lower than that of the younger patients ($\Delta\text{OFV} -13.3$, $p < 0.001$).

Moreover, the influence of morphological characteristics, such as body weight, BSA, and body mass index (BMI), on PK disposition parameters was tested based on allometric scaling theory (West et al., 1997; Anderson and Holford, 2009). However, no significant differences were observed. The presence of DIS ≥ 2 was added to the CL/F to test the influence of drug-drug interaction factors on the MTX PK process. However, the drop in the OFV was 3.6 and no significant differences were observed. The step-by-step covariate screening procedure is shown in **Supplementary Table S5** and the correlation between BSVs is presented in **Supplementary Figure S1**.

TABLE 4 | Results of the prediction-based metrics.

Models	MDPE	MAPE	F ₂₀	F ₃₀
Published models				
Faltaos et al. (2006)	-35.4	47.7	18.5	27.4
Min et al. (2009)	-29.9	43.0	20.4	31.7
Simon et al. (2013)	-53.1	54.2	15.6	25.1
Bretagne et al. (2014)	-27.9	40.2	23.5	36.5
Nader et al. (2017)	-68.4	70.6	11.0	17.0
Mei et al. (2018)	-32.7	50.5	19.2	29.9
Yang et al. (2020)	-28.8	37.0	26.3	41.3
Gallais et al. (2020)	-45.7	47.6	16.0	28.3
Newly built model				
Final model	-10.2	36.4	29.7	42.3

F₂₀, the percentages of prediction errors within 20%; F₃₀, the percentages of prediction errors within 30%; MAPE, median absolute prediction error; MDPE, median prediction error.

The additional estimation of the IOV for CL, which was estimated to be 24.7%, significantly improved model predictions ($\Delta\text{OFV} -679.9$, $p < 0.001$), which suggests that elimination parameters vary across MTX courses.

The parameters of the final model are listed in **Table 3**. The final model with CL/F covariates was described as follows.

$$\text{CL/F} = 4.91 \times (\text{CrCL}/98)^{0.49} \times (\text{ALB}/40)^{0.35} \times (0.89, \text{ if age} > 60)$$

In the final model, all retained covariates caused a significant increase in OFV upon removal. The condition number of the final model was 83.6. Shrinkage analysis for CL showed a mean η -CL shrinkage of 25.5% and ϵ -shrinkage of 24.9%.

3.3 Model Evaluation

The predictive performance of published models was evaluated in the evaluation population dataset using the prediction- and

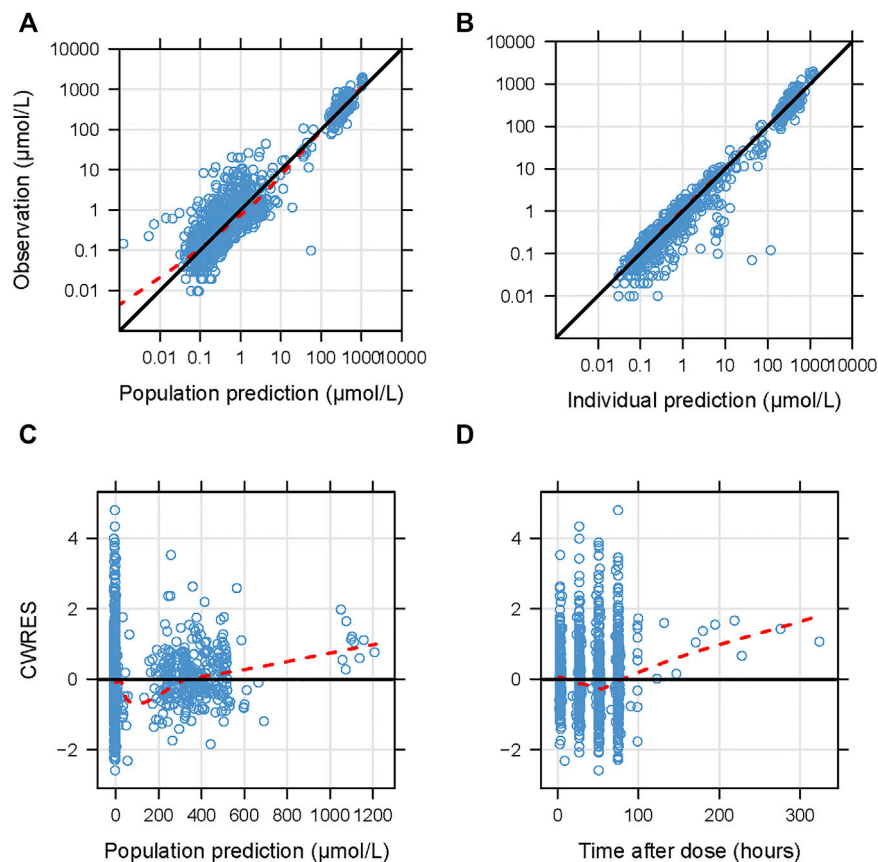


FIGURE 1 | Diagnostic goodness-of-fit plots for the final model. **(A)** Observations versus population predictions; **(B)** observations versus individual predictions; **(C)** conditional weighted residuals (CWRES) versus population predictions; **(D)** CWRES versus time after dose. **(A–D)** The locally weighted regression line (red dashed lines). **(A,B)** the line of unity (black solid lines), and **(C,D)** $y = 0$ (solid lines) are shown.

simulation-based diagnostics described above. **Supplementary Figure S2** shows the goodness-of-fit plots for all published models. The values of bias and inaccuracies of the published models are presented in **Table 4**. All models presented an underestimation of concentrations with large inaccuracies. The predictive performance of the predicted HD-MTX concentration-time profiles, as revealed by the pcVPC of the published models, was highly variable (**Supplementary Figure S3**). None of the models presented acceptable bias or inaccuracy values.

The goodness-of-fit plots for the newly built model are presented in **Figure 1** showing no structural bias. The pcVPCs of the final model are depicted in **Figure 2**. The data below the LOQ were included in the model evaluation to assess the capability of the final model to describe these points. The simulated data corresponded well with the observed data, except for data below the LOQ around 24 h and more than 100 h after the dose. However, as only 18 samples and 10 samples below the LOQ in these periods were included in our study, there were no significant model misspecifications. Model stability was also confirmed with consistent bootstrapped parameter estimates differing by no more than 15% from its corresponding estimate in the final model (**Table 3**). The MDPE and MAPE were -10.2% and 36.4%, respectively. The relatively low values of MDPE and

MAPE further confirmed the high prediction accuracy of the final model.

3.4 Model Application

The characteristics of the involved covariates in the simulation are listed in **Supplementary Table S6**. The results of the Monte Carlo simulation are presented in **Supplementary Table S7**. The predicted time course of MTX concentration in the scenarios with median covariate levels is presented in **Figure 3**. Based on the simulation, elderly patients with renal dysfunction and hypoalbuminemia have a higher incidence of delayed MTX elimination. The percentage decreased from 64.7% to 27.6% when the CrCL decreased from 98 ml min⁻¹ to 46.3 ml min⁻¹, and the percentage decreased from 64.7% to 54.8% when ALB decreased from 39 g L⁻¹ to 29 g L⁻¹.

4 DISCUSSION

To the best of our knowledge, this is the first comprehensive analysis of the predictability of published HD-MTX popPK models. Prediction-based metrics and simulation-based diagnostics were applied to assess the accuracy and precision

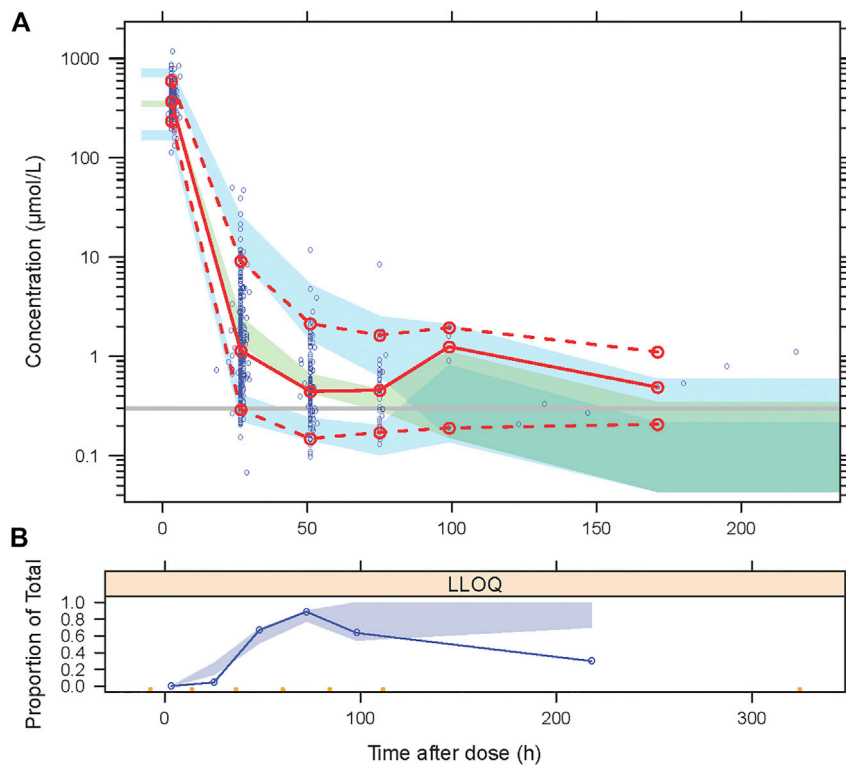


FIGURE 2 | Visual predictive checks (VPCs) for the final model, based on 2000 simulations. **(A)** The red solid line connects median observed values per bin, the red dashed lines connect the 5th and 95th percentiles of the observations. The blue areas represent the 95% confidence interval of the 5th and 95th percentiles. The green area indicates the confidence interval of the median. The Y-axis is shown in a logarithmic scale. **(B)** Open circles represent the observed fraction of censored data, and the shaded area represents the 95% confidence interval of the simulated fraction of censored data.

of the published models. According to our results, the published models were insufficient for cross-center use. Thus, constructing a new popPK model based on an independent dataset is a priority.

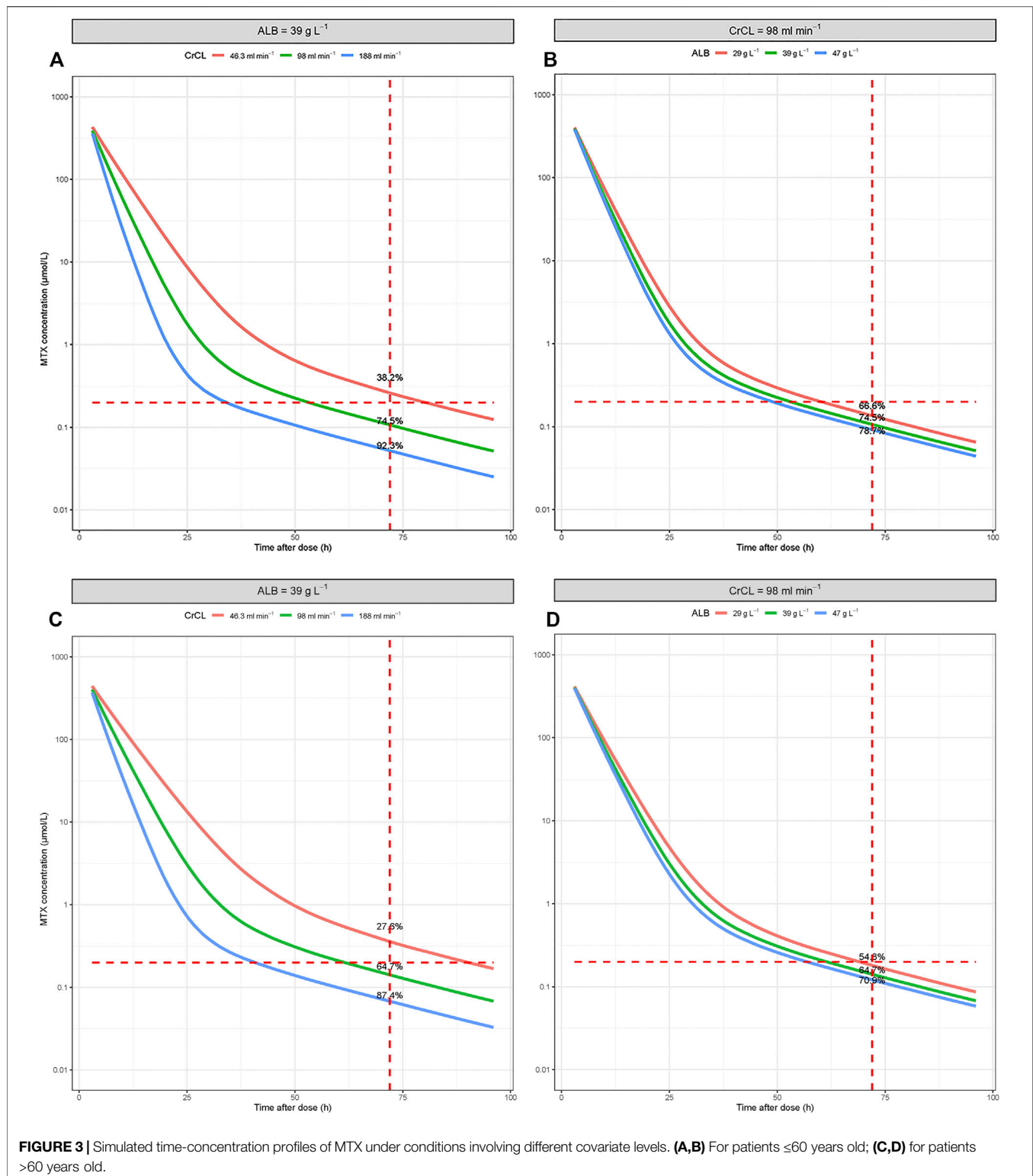
Whether the assumed description of the popPK model is in agreement with the population it is intended to treat, depends on two aspects: a well-developed model with reliable *a priori* PK parameter distribution (mixed and random) and center-related factors that may result in unexplained inter-study variability (Laporte-Simitsidis et al., 2000). The center-related factors, such as study design, ethnic differences, assay methods, and modeling strategies, may influence model predictability (Mao et al., 2018; Mao et al., 2020). In this study, the inclusion of older patients with primary central nervous system lymphoma, as well as inconsistencies in the assay methods, may be the primary causes of the poor cross-center predictability observed.

Although the published models were inadequate for cross-center use, the information included in these models can be utilized to guide the building of new models. In previous studies, we found that theory-based modeling is helpful to improve model predictability (Mao et al., 2020; Mao et al., 2021). Unlike empirical stepwise covariate selection, theory-based covariate selection allows the incorporation of relationships linking parameters and covariates based on a fundamental understanding of PK processes rather than only on the available data, and may improve model predictability (Danhof

et al., 2008). Therefore, we conducted modeling based on the combination of theoretical mechanisms and data properties in this study.

According to published studies, CrCL was the most frequently identified covariate. This was consistent with the PK characteristics of MTX. MTX and its major metabolite, 7-OH-MTX, are mainly eliminated by glomerular filtration and active secretion (Shitara et al., 2006). After analyzing HD-MTX serum samples and urine samples, it was revealed that MTX renal clearance is 83% of the total clearance and CrCL, as an index of glomerular filtration rate, has a great effect on renal clearance but not on non-renal clearance (Fukuhara et al., 2008). In the present study, as no urine samples were included, the influence of CrCL was added to the total clearance. As the CrCL doubling decreased from 120 ml min⁻¹ to 60 ml min⁻¹, the CL/F decreased by 28.8%, which is consistent with the results obtained using published models (17.1%–50%), and in patients with CrCL increase from 120 ml min⁻¹–180 ml min⁻¹, the CL/F increased by 22.0%, which is close to the results obtained using published models (11.6%–19.6%) (Simon et al., 2013; Benz-de Bretagne et al., 2014; Yang et al., 2020).

Alterations in HCT or hemoglobin may affect MTX binding and thus influence the PK process. Hypoalbuminemia is reportedly associated with a significantly increased time for MTX clearance (Reiss et al., 2016). Therefore, the reduction of ALB is a risk factor for delayed MTX elimination in HD-MTX



monotherapy (Kataoka et al., 2021). In the final model, a reduction in ALB from 50.0 g L⁻¹ to 24.0 g L⁻¹ may result in a 22.7% decrease in MTX CL/F. The change in MTX CL/F may have clinical effects on MTX exposure and treatment response.

Moreover, malignant cachexia or liver metastases induced by hypoalbuminemia may increase the half-life of MTX PK, which may be associated with unanticipated toxicity (Li and Gwilt, 2002).

The CL/F was decreased by 11.0% in elderly patients, which may also be a risk factor for delayed elimination. The incidence of delayed clearance of MTX is higher in older patients and during the first cycle of treatment (Bacci et al., 2003). After comparing the PK of total and free MTX in rheumatoid arthritis patients, it has been shown that elderly patients have a longer elimination half-life of free and total MTX (Bressolle et al., 1997). For elderly patients, altered metabolic functions are a result of the complex processes of aging-related physiological changes in the functional reserve of multiple systems and organs. Furthermore, renal excretion is reduced (up to 50%) in approximately two-thirds of elderly patients, which can potentially cause the delayed elimination of MTX (Klotz, 2009).

The estimated PK parameters in our final model were consistent with those in previous reports, except that the CL/F was lower than that in published studies. This phenomenon may be owing to the influence of drug-drug interactions. In our study, the proportion of samples with DIS ≥ 2 was more than 85.4%. Co-administration, such as that of non-steroidal anti-inflammatory drugs, β -lactams, and proton pump inhibitors, has been reported to be an important factor that influences MTX elimination (Iven and Brasch, 1990; Suzuki et al., 2009; Kawase et al., 2016), and may inhibit the excretion of MTX. A reduction in CL/F, by 0.929, as at least one score 2 drug was used (Benz-de Bretagne et al., 2014).

Previous studies have demonstrated that variability exists between MTX therapy cycles (Fukuhara et al., 2008; Min et al., 2009; Kim et al., 2012; Mei et al., 2018). In this study, we estimated course-to-course variability with the inclusion of IOV terms in the random effects model. IOV may arise from variable renal function owing to repeated chemotherapy, drug-drug interactions, or other environmental factors (Breedveld et al., 2004; El-Sheikh et al., 2007; Leveque et al., 2011).

No gene information was available for analysis in this study. The influence of polymorphisms in genes encoding transporters or enzymes during the MTX PK process was inconsistent between different studies, which may partly be accounted for by the different types of patients. The sample size did not have sufficient power to detect a significant association between the target single nucleotide polymorphisms (SNPs) and the MTX PK properties, and the different frequencies of SNPs owing to racial differences (Simon et al., 2013; Lui et al., 2018; Yang et al., 2020). We will consider this point in a future study.

In relative terms, body size and composition were less influential in the model of MTX CL (Pai et al., 2020). A statistically significant reduction in the IIV of CL in only 15% of anticancer drugs is associated with BSA. Moreover, the relative reduction in the variability of CL is between 15% and 35% (Baker et al., 2002). Among the eight published models, only one model included the influence of body size on CL. It is also worth mentioning that body size does not take into account abnormal body habitus such as cachexia or morbid obesity (Gurney and Shaw, 2007; Gallais et al., 2020). In our study, only two patients had a BMI ≥ 30 . Therefore, body size was not a risk factor identified in this study.

Certain limitations were noted in our study. First, this study relied on routine MTX monitoring data that was retrospectively collected and did not include information regarding aspects of supportive care, such as fluid hydration and urine pH, which may have impacted MTX CL and influenced model predictability.

Second, MTX concentrations were measured using multiple analytical methods between studies. No conversion of immunoassays may introduce uncertainty into the external evaluation results. Third, no information on MTX metabolites was available for this study. The inclusion of MTX metabolite information in the popPK model could provide more insights into MTX disposal. Therefore, this should be the focus of future studies.

Identifying ways to obviate MTX delays could facilitate toxicity prediction, rational dose adjustments, and theoretically improve treatment outcomes (Crews et al., 2004). According to our results, the currently published models are not sufficiently reliable for cross-center use; the newly built model provides better predictability. The elderly patients and those with renal dysfunction, hypoalbuminemia are at higher risk of delayed elimination.

DATA AVAILABILITY STATEMENT

The raw data supporting the conclusions of this article will be made available by the authors, without undue reservation.

ETHICS STATEMENT

The studies involving human participants were reviewed and approved by Clinical Research Ethics Committee of Huashan Hospital, Fudan University. The patients/participants provided their written informed consent to participate in this study.

AUTHOR CONTRIBUTIONS

JM, BC, and WQ participated in the study design; JM, QL, PL, WQ, BC, and MZ implemented and conducted the study; JM, QL, and WQ performed the study and analyzed the data. JM drafted the manuscript, which was revised and approved by all authors.

FUNDING

This work was supported in part by a grant from the Shanghai Shenkang Clinical Innovation Project (No. SHDC12020112) and Shanghai "Rising Stars of Medical Talent" Youth Development Program (No.2019-72) supported by Shanghai Municipal Health Commission.

ACKNOWLEDGMENTS

We would like to thank Editage (www.editage.cn/) for English language editing.

SUPPLEMENTARY MATERIAL

The Supplementary Material for this article can be found online at: <https://www.frontiersin.org/articles/10.3389/fphar.2022.817673/full#supplementary-material>

REFERENCES

- Bacci, G., Ferrari, S., Longhi, A., Forni, C., Loro, L., Beghelli, C., et al. (2003). Delayed Methotrexate Clearance in Osteosarcoma Patients Treated with Multiagent Regimens of Neoadjuvant Chemotherapy. *Oncol. Rep.* 10 (4), 851–857. doi:10.3892/or.10.4.851
- Baker, S. D., Verweij, J., Rowinsky, E. K., Donehower, R. C., Schellens, J. H., Grochow, L. B., et al. (2002). Role of Body Surface Area in Dosing of Investigational Anticancer Agents in Adults, 1991–2001. *J. Natl. Cancer Inst.* 94 (24), 1883–1888. doi:10.1093/jnci/94.24.1883
- Baram, J., Allegra, C. J., Fine, R. L., and Chabner, B. A. (1987). Effect of Methotrexate on Intracellular Folate Pools in Purified Myeloid Precursor Cells from normal Human Bone Marrow. *J. Clin. Invest.* 79 (3), 692–697. doi:10.1172/JCI112872
- Beal, S. L. (2001). Ways to Fit a PK Model with Some Data below the Quantification Limit. *J. Pharmacokinet. Pharmacodyn.* 28 (5), 481–504. doi:10.1023/a:1012299115260
- Beal, S. L., Sheiner, L. B., Boeckmann, A., and Bauer, R. J. (1989). *NONMEM User's Guides*. Ellicott City, MD, USA: Icon Development Solutions.
- Benz-de Bretagne, I., Zahr, N., Le Gouge, A., Hulot, J. S., Houllier, C., Hoang-Xuan, K., et al. (2014). Urinary Coproporphyrin I/(I + III) Ratio as a Surrogate for MRP2 or Other Transporter Activities Involved in Methotrexate Clearance. *Br. J. Clin. Pharmacol.* 78 (2), 329–342. doi:10.1111/bcp.12326
- Bergstrand, M., Hooker, A. C., Wallin, J. E., and Karlsson, M. O. (2011). Prediction-corrected Visual Predictive Checks for Diagnosing Nonlinear Mixed-Effects Models. *AAPS J.* 13 (2), 143–151. doi:10.1208/s12248-011-9255-z
- Breedveld, P., Zelcer, N., Pluim, D., Sönmezer, O., Tibben, M. M., Beijnen, J. H., et al. (2004). Mechanism of the Pharmacokinetic Interaction between Methotrexate and Benzimidazoles: Potential Role for Breast Cancer Resistance Protein in Clinical Drug-Drug Interactions. *Cancer Res.* 64 (16), 5804–5811. doi:10.1158/0008-5472.CAN-03-4062
- Bressolle, F., Bologna, C., Kinowski, J. M., Arcos, B., Sany, J., and Combe, B. (1997). Total and Free Methotrexate Pharmacokinetics in Elderly Patients with Rheumatoid Arthritis. A Comparison with Young Patients. *J. Rheumatol.* 24 (10), 1903–1909.
- Cheng, Y., Wang, C. Y., Li, Z. R., Pan, Y., Liu, M. B., and Jiao, Z. (2020). Can Population Pharmacokinetics of Antibiotics Be Extrapolated? Implications of External Evaluations. *Clin. Pharmacokinet.* 60, 53–68. doi:10.1007/s40262-020-00937-4
- Cockcroft, D. W., and Gault, M. H. (1976). Prediction of Creatinine Clearance from Serum Creatinine. *Nephron* 16 (1), 31–41. doi:10.1159/000180580
- Crews, K. R., Liu, T., Rodriguez-Galindo, C., Tan, M., Meyer, W. H., Panetta, J. C., et al. (2004). High-dose Methotrexate Pharmacokinetics and Outcome of Children and Young Adults with Osteosarcoma. *Cancer* 100 (8), 1724–1733. doi:10.1002/cncr.20152
- Csordas, K., Hegyi, M., Eipel, O. T., Muller, J., Erdelyi, D. J., and Kovacs, G. T. (2013). Comparison of Pharmacokinetics and Toxicity after High-Dose Methotrexate Treatments in Children with Acute Lymphoblastic Leukemia. *Anticancer Drugs* 24 (2), 189–197. doi:10.1097/CAD.0b013e32835b8662
- Danhof, M., de Lange, E. C., Della Pasqua, O. E., Ploeger, B. A., and Voskuyl, R. A. (2008). Mechanism-based Pharmacokinetic-Pharmacodynamic (PK-PD) Modeling in Translational Drug Research. *Trends Pharmacol. Sci.* 29 (4), 186–191. doi:10.1016/j.tips.2008.01.007
- Dupuis, C., Mercier, C., Yang, C., Monjanel-Mouterde, S., Ciccolini, J., Fanciullino, R., et al. (2008). High-dose Methotrexate in Adults with Osteosarcoma: a Population Pharmacokinetics Study and Validation of a New Limited Sampling Strategy. *Anticancer Drugs* 19 (3), 267–273. doi:10.1097/cad.0b013e3282f21376
- El-Sheikh, A. A., van den Heuvel, J. J., Koenderink, J. B., and Russel, F. G. (2007). Interaction of Nonsteroidal Anti-inflammatory Drugs with Multidrug Resistance Protein (MRP) 2/ABCC2- and MRP4/ABCC4-Mediated Methotrexate Transport. *J. Pharmacol. Exp. Ther.* 320 (1), 229–235. doi:10.1124/jpet.106.110379
- Ette, E. I. (1997). Stability and Performance of a Population Pharmacokinetic Model. *J. Clin. Pharmacol.* 37 (6), 486–495. doi:10.1002/j.1552-4604.1997.tb04326.x
- Ette, E. I., Williams, P. J., Kim, Y. H., Lane, J. R., Liu, M. J., and Capparelli, E. V. (2003). Model Appropriateness and Population Pharmacokinetic Modeling. *J. Clin. Pharmacol.* 43 (6), 610–623. doi:10.1177/0091270003253624
- Ette, E. I., and Williams, P. J. (2004). Population Pharmacokinetics I: Background, Concepts, and Models. *Ann. Pharmacother.* 38 (10), 1702–1706. doi:10.1345/aph.1D374
- Evans, W. E., Crom, W. R., Abromowitch, M., Dodge, R., Look, A. T., Bowman, W. P., et al. (1986). Clinical Pharmacodynamics of High-Dose Methotrexate in Acute Lymphocytic Leukemia. Identification of a Relation between Concentration and Effect. *N. Engl. J. Med.* 314 (8), 471–477. doi:10.1056/NEJM198602203140803
- Evans, W. E., Relling, M. V., Rodman, J. H., Crom, W. R., Boyett, J. M., and Pui, C. H. (1998). Conventional Compared with Individualized Chemotherapy for Childhood Acute Lymphoblastic Leukemia. *N. Engl. J. Med.* 338 (8), 499–505. doi:10.1056/NEJM199802193380803
- Faltaos, D. W., Hulot, J. S., Urien, S., Morel, V., Kaloshi, G., Fernandez, C., et al. (2006). Population Pharmacokinetic Study of Methotrexate in Patients with Lymphoid Malignancy. *Cancer Chemother. Pharmacol.* 58 (5), 626–633. doi:10.1007/s00280-006-0202-0
- Fukuhara, K., Ikawa, K., Morikawa, N., and Kumagai, K. (2008). Population Pharmacokinetics of High-Dose Methotrexate in Japanese Adult Patients with Malignancies: a Concurrent Analysis of the Serum and Urine Concentration Data. *J. Clin. Pharm. Ther.* 33 (6), 677–684. doi:10.1111/j.1365-2710.2008.00966.x
- Gallais, F., Oberic, L., Faguer, S., Tavitian, S., Lafont, T., Marsili, S., et al. (2020). Body Surface Area Dosing of High-Dose Methotrexate Should Be Reconsidered, Particularly in Overweight, Adult Patients. *Ther. Drug Monit.* 43, 408–415. doi:10.1097/FTD.0000000000000813
- Griggs, J. J., Mangu, P. B., Anderson, H., Balaban, E. P., Dignam, J. J., Hryniuk, W. M., et al. (2012). Appropriate Chemotherapy Dosing for Obese Adult Patients with Cancer: American Society of Clinical Oncology Clinical Practice Guideline. *J. Clin. Oncol.* 30 (13), 1553–1561. doi:10.1200/JCO.2011.39.9436
- Gurney, H., and Shaw, R. (2007). Obesity in Dose Calculation: a Mouse or an Elephant? *J. Clin. Oncol.* 25 (30), 4703–4704. doi:10.1200/JCO.2007.13.1078
- Hospira (2017). *Label for Methotrexate Injection*. Lake Forest, IL: Hospira. Available at: https://www.accessdata.fda.gov/drugsatfda_docs/label/2011/011719s117bl.pdf (Accessed Dec 29, 2019).
- Howard, S. C., McCormick, J., Pui, C. H., Buddington, R. K., and Harvey, R. D. (2016). Preventing and Managing Toxicities of High-Dose Methotrexate. *Oncologist* 21 (12), 1471–1482. doi:10.1634/theoncologist.2015-0164
- Huang, C., Xia, F., Xue, L., Liu, L., Bian, Y., Jin, Z., et al. (2020). Coadministration of Vindesine with High-Dose Methotrexate Therapy Increases Acute Kidney Injury via BCRP, MRP2, and OAT1/OAT3. *Cancer Chemother. Pharmacol.* 85 (2), 433–441. doi:10.1007/s00280-019-03972-6
- Iven, H., and Brasch, H. (1990). Cephalosporins Increase the Renal Clearance of Methotrexate and 7-hydroxymethotrexate in Rabbits. *Cancer Chemother. Pharmacol.* 26 (2), 139–143. doi:10.1007/BF02897260
- Karlsson, M. O., and Sheiner, L. B. (1993). The Importance of Modeling Interoccasion Variability in Population Pharmacokinetic Analyses. *J. Pharmacokinet. Biopharm.* 21 (6), 735–750. doi:10.1007/BF01113502
- Kataoka, T., Sakurashita, H., Kajikawa, K., Saeki, Y., Taogoshi, T., and Matsuo, H. (2021). Low Serum Albumin Level Is a Risk Factor for Delayed Methotrexate Elimination in High-Dose Methotrexate Treatment. *Ann. Pharmacother.* 55, 1195–1202. doi:10.1177/1060028021992767
- Kawase, A., Yamamoto, T., Egashira, S., and Iwaki, M. (2016). Stereoselective Inhibition of Methotrexate Excretion by Glucuronides of Nonsteroidal Anti-inflammatory Drugs via Multidrug Resistance Proteins 2 and 4. *J. Pharmacol. Exp. Ther.* 356 (2), 366–374. doi:10.1124/jpet.115.229104
- Keizer, R. J., Karlsson, M. O., and Hooker, A. (2013). Modeling and Simulation Workbench for NONMEM: Tutorial on Pirana, PsN, and Xpose. *CPT Pharmacometrics Syst. Pharmacol.* 2, e50. doi:10.1038/psp.2013.24
- Kim, I. W., Yun, H. Y., Choi, B., Han, N., Park, S. Y., Lee, E. S., et al. (2012). ABCB1 C3435T Genetic Polymorphism on Population Pharmacokinetics of Methotrexate after Hematopoietic Stem Cell Transplantation in Korean Patients: a Prospective Analysis. *Clin. Ther.* 34 (8), 1816–1826. doi:10.1016/j.clinthera.2012.06.022
- Klotz, U. (2009). Pharmacokinetics and Drug Metabolism in the Elderly. *Drug Metab. Rev.* 41 (2), 67–76. doi:10.1080/03602530902722679
- Laporte-Simitsidis, S., Girard, P., Mismetti, P., Chabaud, S., Decousus, H., and Boissel, J. P. (2000). Inter-study Variability in Population Pharmacokinetic Meta-Analysis: when and How to Estimate it? *J. Pharm.* 89 (2), 155–167. doi:10.1002/(SICI)1520-6017(200002)89:2<155::AID-JPS3>3.0.CO;2-2

- Levêque, D., Santucci, R., Gourieux, B., and Herbrecht, R. (2011). Pharmacokinetic Drug-Drug Interactions with Methotrexate in Oncology. *Expert Rev. Clin. Pharmacol.* 4 (6), 743–750. doi:10.1586/ecp.11.57
- Li, J., and Gwilt, P. (2002). The Effect of Malignant Effusions on Methotrexate Disposition. *Cancer Chemother. Pharmacol.* 50 (5), 373–382. doi:10.1007/s00280-002-0512-9
- Lui, G., Treluyer, J. M., Fresneau, B., Piperno-Neumann, S., Gaspar, N., Corradini, N., et al. (2018). A Pharmacokinetic and Pharmacogenetic Analysis of Osteosarcoma Patients Treated with High-Dose Methotrexate: Data from the OS2006/Sarcoma-09 Trial. *J. Clin. Pharmacol.* 58 (12), 1541–1549. doi:10.1002/jcph.1252
- Maia, M. B., Saivin, S., Chatelut, E., Malmay, M. F., and Houin, G. (1996). *In Vitro* and *In Vivo* Protein Binding of Methotrexate Assessed by Microdialysis. *Int. J. Clin. Pharmacol. Ther.* 34 (8), 335–341.
- Mao, J., Jiao, Z., Qiu, X., Zhang, M., and Zhong, M. (2020). Incorporating Nonlinear Kinetics to Improve Predictive Performance of Population Pharmacokinetic Models for Cyclosporin in Adult Renal Transplant Recipients: A Comparison of Modelling Strategies. *Eur. J. Pharm. Sci.* 153, 105471. doi:10.1016/j.ejps.2020.105471
- Mao, J., Qiu, X., Qin, W., Xu, L., Zhang, M., and Zhong, M. (2021). Factors Affecting Time-Varying Clearance of Cyclosporine in Adult Renal Transplant Recipients: A Population Pharmacokinetic Perspective. *Pharm. Res.* 38 (11), 1873–1887. doi:10.1007/s11095-021-03114-9
- Mao, J. J., Jiao, Z., Yun, H. Y., Zhao, C. Y., Chen, H. C., Qiu, X. Y., et al. (2018). External Evaluation of Population Pharmacokinetic Models for Cyclosporin in Adult Renal Transplant Recipients. *Br. J. Clin. Pharmacol.* 84 (1), 153–171. doi:10.1111/bcp.13431
- Mei, S., Li, X., Jiang, X., Yu, K., Lin, S., and Zhao, Z. (2018). Population Pharmacokinetics of High-Dose Methotrexate in Patients with Primary Central Nervous System Lymphoma. *J. Pharm. Sci.* 107 (5), 1454–1460. doi:10.1016/j.xphs.2018.01.004
- Min, Y., Qiang, F., Peng, L., and Zhu, Z. (2009). High Dose Methotrexate Population Pharmacokinetics and Bayesian Estimation in Patients with Lymphoid Malignancy. *Biopharm. Drug Dispos* 30 (8), 437–447. doi:10.1002/bdd.678
- Moher, D., Shamseer, L., Clarke, M., Ghersi, D., Liberati, A., Petticrew, M., et al. (2015). Preferred Reporting Items for Systematic Review and Meta-Analysis Protocols (PRISMA-P) 2015 Statement. *Syst. Rev.* 4, 1. doi:10.1186/2046-4053-4-1
- Nader, A., Zahran, N., Alshammaa, A., Altaheel, H., Kassem, N., and Wilby, K. J. (2017). Population Pharmacokinetics of Intravenous Methotrexate in Patients with Hematological Malignancies: Utilization of Routine Clinical Monitoring Parameters. *Eur. J. Drug Metab. Pharmacokinet.* 42 (2), 221–228. doi:10.1007/s13318-016-0338-1
- Owen, J. S., and Fiedler-Kelly, J. (2014). *Introduction to Population Pharmacokinetic/pharmacodynamic Analysis with Nonlinear Mixed Effects Models*. Hoboken, New Jersey, USA: John Wiley & Sons. doi:10.1002/9781118784860
- Paci, A., Veal, G., Bardin, C., Levêque, D., Widmer, N., Beijnen, J., et al. (2014). Review of Therapeutic Drug Monitoring of Anticancer Drugs Part 1--cytotoxics. *Eur. J. Cancer* 50 (12), 2010–2019. doi:10.1016/j.ejca.2014.04.014
- Pai, M. P., Debacker, K. C., Derstine, B., Sullivan, J., Su, G. L., and Wang, S. C. (2020). Comparison of Body Size, Morphomics, and Kidney Function as Covariates of High-Dose Methotrexate Clearance in Obese Adults with Primary Central Nervous System Lymphoma. *Pharmacotherapy* 40 (4), 308–319. doi:10.1002/phar.2379
- Plotkin, S. R., Betensky, R. A., Hochberg, F. H., Grossman, S. A., Lesser, G. J., Nabors, L. B., et al. (2004). Treatment of Relapsed central Nervous System Lymphoma with High-Dose Methotrexate. *Clin. Cancer Res.* 10 (17), 5643–5646. doi:10.1158/1078-0432.CCR-04-0159
- Ramsey, L. B., Balis, F. M., O'Brien, M. M., Schmiegelow, K., Pauley, J. L., Bleyer, A., et al. (2018). Consensus Guideline for Use of Glucarpidase in Patients with High-Dose Methotrexate Induced Acute Kidney Injury and Delayed Methotrexate Clearance. *Oncologist* 23 (1), 52–61. doi:10.1634/theoncologist.2017-0243
- Reiss, S. N., Buie, L. W., Adel, N., Goldman, D. A., Devlin, S. M., and Douer, D. (2016). Hypoalbuminemia Is Significantly Associated with Increased Clearance Time of High Dose Methotrexate in Patients Being Treated for Lymphoma or Leukemia. *Ann. Hematol.* 95 (12), 2009–2015. doi:10.1007/s00277-016-2795-7
- Reiter, A., Schrappe, M., Tiemann, M., Ludwig, W. D., Yakisan, E., Zimmermann, M., et al. (1999). Improved Treatment Results in Childhood B-Cell Neoplasms with Tailored Intensification of Therapy: A Report of the Berlin-Frankfurt-Münster Group Trial NHL-BFM 90. *Blood* 94 (10), 3294–3306.
- Sakura, T., Hayakawa, F., Sugiura, I., Murayama, T., Imai, K., Usui, N., et al. (2018). High-dose Methotrexate Therapy Significantly Improved Survival of Adult Acute Lymphoblastic Leukemia: a Phase III Study by JALSG. *Leukemia* 32 (3), 626–632. doi:10.1038/leu.2017.283
- Sheiner, L. B., and Beal, S. L. (1981). Some Suggestions for Measuring Predictive Performance. *J. Pharmacokinet. Biopharm.* 9 (4), 503–512. doi:10.1007/BF01060893
- Shitara, Y., Horie, T., and Sugiyama, Y. (2006). Transporters as a Determinant of Drug Clearance and Tissue Distribution. *Eur. J. Pharm. Sci.* 27 (5), 425–446. doi:10.1016/j.ejps.2005.12.003
- Simon, N., Marsot, A., Villard, E., Choquet, S., Khe, H. X., Zahr, N., et al. (2013). Impact of ABCC2 Polymorphisms on High-Dose Methotrexate Pharmacokinetics in Patients with Lymphoid Malignancy. *Pharmacogenomics J.* 13 (6), 507–513. doi:10.1038/tpj.2012.37
- Suzuki, K., Doki, K., Homma, M., Tamaki, H., Hori, S., Ohtani, H., et al. (2009). Co-administration of Proton Pump Inhibitors Delays Elimination of Plasma Methotrexate in High-Dose Methotrexate Therapy. *Br. J. Clin. Pharmacol.* 67 (1), 44–49. doi:10.1111/j.1365-2125.2008.03303.x
- Wall, A. M., Gajjar, A., Link, A., Mahmoud, H., Pui, C. H., and Relling, M. V. (2000). Individualized Methotrexate Dosing in Children with Relapsed Acute Lymphoblastic Leukemia. *Leukemia* 14 (2), 221–225. doi:10.1038/sj.leu.2401673
- West, G. B., Brown, J. H., and Enquist, B. J. (1997). A General Model for the Origin of Allometric Scaling Laws in Biology. *Science* 276 (5309), 122–126. doi:10.1126/science.276.5309.122
- Widemann, B. C., and Adamson, P. C. (2006). Understanding and Managing Methotrexate Nephrotoxicity. *Oncologist* 11 (6), 694–703. doi:10.1634/theoncologist.11-6-694
- Yang, L., Wu, H., de Winter, B. C. M., Sheng, C. C., Qiu, H. Q., Cheng, Y., et al. (2020). Pharmacokinetics and Pharmacogenetics of High-Dose Methotrexate in Chinese Adult Patients with Non-hodgkin Lymphoma: a Population Analysis. *Cancer Chemother. Pharmacol.* 85 (5), 881–897. doi:10.1007/s00280-020-04058-4
- Zhao, C. Y., Jiao, Z., Mao, J. J., and Qiu, X. Y. (2016). External Evaluation of Published Population Pharmacokinetic Models of Tacrolimus in Adult Renal Transplant Recipients. *Br. J. Clin. Pharmacol.* 81 (5), 891–907. doi:10.1111/bcp.12830
- Zhu, J. J., Gerstner, E. R., Engler, D. A., Mrugala, M. M., Nugent, W., Nierenberg, K., et al. (2009). High-dose Methotrexate for Elderly Patients with Primary CNS Lymphoma. *Neuro Oncol.* 11 (2), 211–215. doi:10.1215/15228517-2008-067

Conflict of Interest: The authors declare that the research was conducted in the absence of any commercial or financial relationships that could be construed as a potential conflict of interest.

The handling editor declared a past co-authorship with several of the authors (JM, MZ).

Publisher's Note: All claims expressed in this article are solely those of the authors and do not necessarily represent those of their affiliated organizations, or those of the publisher, the editors and the reviewers. Any product that may be evaluated in this article, or claim that may be made by its manufacturer, is not guaranteed or endorsed by the publisher.

Copyright © 2022 Mao, Li, Li, Qin, Chen and Zhong. This is an open-access article distributed under the terms of the Creative Commons Attribution License (CC BY). The use, distribution or reproduction in other forums is permitted, provided the original author(s) and the copyright owner(s) are credited and that the original publication in this journal is cited, in accordance with accepted academic practice. No use, distribution or reproduction is permitted which does not comply with these terms.



Elucidating a Complicated Enantioselective Metabolic Profile: A Study From Rats to Humans Using Optically Pure Doxazosin

Dezhi Kong^{1†}, Yuan Tian^{1,2†}, Kunfeng Duan², Wenyan Guo¹, Qingning Zhang¹, Panpan Zhang¹, Zuxiao Yang¹, Xia Qin¹, Leiming Ren¹ and Wei Zhang^{1*}

¹Department of Pharmacology of Chinese Materia Medica, School of Chinese Integrative Medicine, Hebei Medical University, Shijiazhuang, China, ²Department of Pharmacy, Third Hospital of Hebei Medical University, Shijiazhuang, China

OPEN ACCESS

Edited by:

Ren-Ai Xu,
First Affiliated Hospital of Wenzhou
Medical University, China

Reviewed by:

Nico P. E. Vermeulen,
VU Amsterdam, Netherlands
Shun-Bin Luo,
Lishui City People's Hospital, China

*Correspondence:

Wei Zhang
weizhang@hebmh.edu.cn

[†]These authors have contributed
equally to this work

Specialty section:

This article was submitted to
Drug Metabolism and Transport,
a section of the journal
Frontiers in Pharmacology

Received: 13 December 2021

Accepted: 26 January 2022

Published: 10 March 2022

Citation:

Kong D, Tian Y, Duan K, Guo W,
Zhang Q, Zhang P, Yang Z, Qin X,
Ren L and Zhang W (2022) Elucidating
a Complicated Enantioselective
Metabolic Profile: A Study From Rats to
Humans Using Optically
Pure Doxazosin.
Front. Pharmacol. 13:834897.
doi: 10.3389/fphar.2022.834897

Doxazosin (DOX) is prescribed as a racemic drug for the clinical treatment of benign prostatic hyperplasia and hypertension. Recent studies found that the two enantiomers of DOX exhibit differences in blood concentration and pharmacological effects. However, the stereoselective metabolic characteristics and mechanisms for DOX are not yet clear. Herein, we identified 34 metabolites of DOX in rats based on our comprehensive and effective strategy. The relationship among the metabolites and the most discriminative metabolites between (–)-DOX and (+)-DOX administration was analyzed according to the kinetic parameters using state-of-the-art multivariate statistical methods. To elucidate the enantioselective metabolic profile *in vivo* and *in vitro*, we carefully investigated the metabolic characteristics of metabolites after optically pure isomers administration in rat plasma, rat liver microsomes (RLMs) or human liver microsomes (HLMs), and recombinant human cytochrome P450 (CYP) enzymes. As a result, the differences of these metabolites were found based on their exposure and elimination rate, and the metabolic profile of (±)-DOX was more similar to that of (+)-DOX. Though the metabolites identified in RLMs and HLMs were the same, the metabolic profiles of the metabolites from (–)-DOX and (+)-DOX were greatly different. Furthermore, four human CYP enzymes could catalyze DOX to produce metabolites, but their preferences seemed different. For example, CYP3A4 highly specifically and selectively catalyzed the formation of the specific metabolite (M22) from (–)-DOX. In conclusion, we established a comprehensive metabolic system using pure optical isomers from *in vivo* to *in vitro*, and the complicated enantioselectivity of the metabolites of DOX was clearly shown. More importantly, the comprehensive metabolic system is also suitable to investigate other chiral drugs.

Keywords: pure optical isomers, enantioselectivity, doxazosin, liver microsomes, cytochrome P450 enzymes, comprehensive metabolic system

INTRODUCTION

Doxazosin (DOX), a long-acting and highly selective α_1 receptor blocker, is commonly used in treating benign prostatic hyperplasia (BEH) as the first-line therapy. It can relax the smooth muscle of the prostate and relieve the lower urinary tract symptoms related to BEH by targeting the α_1 -receptor in the prostate tissue, especially near the bladder neck (Cao et al., 2016; Fusco et al., 2016). DOX is also an additive drug for clinical antihypertensive treatment (Williams et al., 2015), especially suitable for elderly patients with BEH accompanied by hypertension. Recently, it has been described that DOX have anti-tumor effects by inhibiting cell proliferation, arresting cell cycle, and inducing apoptosis (Ramírez-Expósito and Martínez-Martos, 2019; Wade et al., 2019; Suzuki K. et al., 2020; Karaca et al., 2021). Nowadays, the prescribed drug of DOX is a racemic drug [(±)-DOX] composed of equal mixtures of (–)-DOX and (+)-DOX. However, differences in pharmacological effects between (–)-DOX and (+)-DOX have been reported; that is, the blocking effect of (–)-DOX on α_{1D} receptors in a rat vascular smooth muscle is weaker than that of (+)-DOX. They produce opposite inotropic effects in the rat atria, and the chiral carbon atom in the molecular structure of doxazosin does not affect its activity at the therapeutic target of α_{1A} receptors in the rabbit prostate (Zhao et al., 2012). Undoubtedly, the enantioselective pharmacodynamics is related to the difference of enantiomers in pharmacokinetics. Therefore, elucidating the pharmacokinetics of (–)-DOX, (+)-DOX, and (±)-DOX has become an important issue for DOX clinical application.

Actually, we have reported the differences in pharmacokinetics between (–)-DOX and (+)-DOX (Liu et al., 2010; Zhen et al., 2013; Li et al., 2015; Kapri et al., 2019). The plasma concentration ratio of (+)-DOX to (–)-DOX ($C_{(+)-DOX}/C_{(-)-DOX}$) is increased from 1.7 at 10 min to 17.1 at 360 min after a single injection of (±)-DOX into rat tail vein (Li et al., 2015). Moreover, the elimination of (+)-DOX was slower than that of (–)-DOX in rat liver microsomal system during incubation with (±)-DOX (Kong et al., 2015). The stereoselectivity of enzymes participating in drug metabolism is a well-known knowledge. For example, L-nebivolol was reported to be highly metabolized by CYP2D6, but CYP2C19 was the primary enzyme responsible for D-nebivolol (Lefebvre et al., 2007; Kelley et al., 2019). CYP2D6 preferentially metabolizes (–)-tramadol to (–)-O-desmethyltramadol rather than (+)-tramadol to (+)-O-desmethyltramadol (Suzuki S. et al., 2020). Though we found that CYP3A might be involved in the chiral metabolism of DOX in rats (Kong et al., 2015), a deeper understanding of the stereoselective metabolism is still poor due to the lack of knowledge regarding the metabolites of DOX and its metabolic pathways.

In recent years, liquid chromatography coupled with mass spectrometry (LC-MS) has emerged as one of the most powerful analytical tools for the screening and identifying drug metabolites with low-nanomolar sensitivity and high specificity (Pang et al., 2019; Higashi and Ogawa, 2020). Moreover, the Orbitrap mass detector with up to six orders of linear dynamic range in a high-resolution acquisition mode is beneficial to improving the simultaneous quantification of doxazosin and its metabolites. In our preliminary experiments, we found 98 potential

metabolites identified from the rat plasma after intravenous administration of (±)-DOX. Herein, we further plan to confirm the metabolites with chemical structures for DOX and elucidate the stereoselective metabolic characteristics and mechanisms by analyzing the kinetic properties of metabolites after optically pure isomers administration in rat plasma, rat liver microsomes (RLMs) or human liver microsomes (HLMs), and seven recombinant human cytochrome P450 (CYP) enzymes.

MATERIALS AND METHOD

Chemicals and Biological Reagents

(±)-Doxazosin mesylate [(±)-DOX], (+)-doxazosin mesylate [(+)-DOX], and (–)-doxazosin mesylate [(–)-DOX] standards (>99.9% purity) were provided by the New Drug Research and Development Center of the North China Pharmaceutical Group Corporation (Shijiazhuang, China). β -Nicotinamide adenine dinucleotide phosphate hydrate (NADP), glucose-6-phosphate dehydrogenase from Baker's yeast (*S. cerevisiae*), glucose-6-phosphate, prazosin (internal standard, IS), phenacetin, tolbutamide, and human CYP enzymes (CYP3A4, CYP2D6, CYP2C19, CYP2C8, CYP1A2, CYP2E1, and CYP2C9) were purchased from Sigma-Aldrich (St Louis, USA). Dextromethorphan hydrobromide, paclitaxel, and testosterone were provided by TCI Shanghai (Shanghai, China). Chlorzoxazone and omeprazole were purchased from J&K Chemical (Beijing, China). Heparin sodium injection was provided by the Jiangsu Wanbang Biochemical Pharmaceutical Group Co., Ltd. (Xuzhou, China). Human and rat liver microsomes were purchased from BD Gentest (Franklin, USA). Tris base and $MgCl_2$ were purchased from Tianjin Yongda Chemical Reagent Co., Ltd. (Tianjin, China). Ultrapure water was prepared by Thermo Scientific Nanopure Water Purifier (Waltham, USA). HPLC-grade methanol and acetonitrile were purchased from Thermo Fisher Scientific (Ottawa, ON, Canada). All the other chemicals were of analytical grade.

Animals

Specific pathogen-free healthy male SD rats (180–200 g) were purchased from the Vital River Laboratory Animal Company (Beijing, China; certificate no. SCXK 2016-0006). All rats were fed with standard guidelines and housed in well-ventilated cages at room temperature ($23 \pm 2^\circ C$) with a regular 12 h light-dark cycle. The rats were allowed free access to commercial aseptic food and pure water before the experiment. This study was approved by the Animal Ethics Committee of Hebei Medical University, complying with the National Research Council's Guide for the Care and Use of Laboratory Animals (Approval no. IACUC-Hebmu-2021017).

Quantitation of the Content of (+)-DOX, (–)-DOX, or (±)-DOX in Pure Form

To keep the same dosages for (+)-DOX, (–)-DOX, or (±)-DOX administration, (+)-DOX, (–)-DOX, or (±)-DOX were analyzed

on the achiral C18 column by an Agilent 1260 HPLC system coupled with fluorescence detector according to our previous report (Zhen et al., 2013). Isocratic elution was conducted using a mobile phase of phosphate buffer-acetonitrile (85: 15, v/v) at a flow rate of 0.8 ml/min. The fluorescence detection was set at $\lambda_{\text{Ex}} = 255$ nm and $\lambda_{\text{Em}} = 385$ nm. The ratio of the peak areas of (+)-DOX, (–)-DOX, and (±)-DOX is 1.02: 1.22: 1. Furthermore, the following administrations for (+)-DOX, (–)-DOX, and (±)-DOX were adjusted according to the ratio.

Administration and Sample Collection

The dosing and sampling procedures were similar to our former publication (Li et al., 2015). Briefly, 18 male rats were randomly divided into three groups ($n = 6$). The rats in each group received a single intravenous bolus injection of 6 mg/kg dose of (+)-DOX, (–)-DOX, or (±)-DOX without anesthesia, respectively. The blank blood samples were collected before administration, and blood samples were collected at 10, 30, 60, 90, 120, 240, 360, 480, and 600 min after drug administration. Samples were placed in heparinized centrifuge tubes and centrifuged at 2000 g for 10 min. The supernatants were collected and stored at -40°C until analysis.

Incubation of Doxazosin With Liver Microsomes/Cytochrome P450s

For the metabolic study *in vitro*, rat liver microsomes, human liver microsomes, and seven recombinant human CYP enzymes (CYP3A4, CYP2D6, CYP2C19, CYP2C8, CYP1A2, CYP2E1, and CYP2C9) were used as metabolized enzymes. The concentration of the microsomal protein or each recombinant CYP enzyme in the incubation system was applied according to earlier studies (Kong et al., 2015; Kim et al., 2016). Briefly, the incubation system (400 μL) contained a microsomal protein (0.5 g/L) or CYP enzyme (40 nmol/L) and Tris-HCl buffer (100 mmol/L, pH 7.4) with MgCl_2 (25 mmol/L). (–)-DOX, (+)-DOX, or (±)-DOX were the substrates with a concentration of 160 mg/ml. After 5 min of preincubation in the water bath at 37°C , reactions were initiated by adding 160 μL of NADPH-generating system (5.0 mM glucose-6-phosphate, 0.5 mM NADP^+ , 1 unit/ml glucose-6-phosphate dehydrogenase, and 5 mM MgCl_2). The reactions were terminated after incubation for 0, 5, 10, 20, 30, 45, 60, and 80 min by adding three times the volume of ice-cold methanol containing prazosin (IS). Incubation without the addition of NADPH or DOX was used as a negative or positive control, respectively. Control experiments using boiled microsomes were also carried out. In the control samples, Tris-HCl buffer was added instead of the protein, NADPH or drug solution to ensure that the incubation volumes and compositions remained the same. All tests were performed in triplicate. The samples were prepared with the same method as the following “Sample preparation” procedures.

Measurement of Recombinant Human CYP Enzymes Activity

The activity of each recombinant human CYP enzyme was evaluated by its CYP enzyme-specific substrate. The probe substrate for CYP3A4, CYP2D6, CYP2C19, CYP2C8, CYP1A2, CYP2E1, and

CYP2C9 is testosterone, dextromethorphan, omeprazole, paclitaxel, phenacetin, chlorzoxazone, and tolbutamide, respectively. The final concentration of each substrate in the incubation system was 5 $\mu\text{mol/L}$. Other incubation conditions were the same as mentioned above, and the incubation duration was 30 min. 6 β -Hydroxy testosterone metabolized by CYP3A4, dextromethorphan by CYP2D6, 5-hydroxy omeprazole by CYP2C19, 6 α -paclitaxel by CYP2C8, acetaminophen by CYP1A2, 6-hydroxy chlorzoxazone by CYP2E1, and 4'-hydroxytoluene butazone by CYP2C9 were determined using the UHPLC-HRMS system (Thermo Fisher Scientific, Waltham, MA, United States).

Sample Preparation

Before analysis, samples were thawed and equilibrated at room temperature. Then, 100 μL of each plasma sample was transferred into a new centrifuge tube and spiked with three times the volume of methanol containing prazosin (IS). Each sample was vortexed to mix for 3 min and prepared by centrifugation at 12,000 g for 5 min at 4°C . The supernatant was removed to a new centrifugation tube and evaporated to dryness with a gentle stream of nitrogen in a 40°C water bath. The dry residue was dissolved with 100 μL of an acetonitrile-water mixture (1:1, v/v), vortexed for 3 min, and then centrifuged at 12,000 g for another 5 min. A five-microliter supernatant was injected into the UHPLC-HRMS system for analysis.

UHPLC-HRMS Conditions

Thermo UltiMate 3000 UHPLC system coupled with Thermo Orbitrap Fusion high-resolution mass spectrometry (HRMS) detector with an H-ESI operating in a positive ion mode was used for all analyses. The chromatographic separations were performed on a Waters Xbridge C18 column (100 \times 3 mm, 3.5 μm , Milford, MA, United States). The column temperature was maintained at 35°C . The mobile phases consisted of 0.2% ammonia solution (A) and acetonitrile (B) at a total flow rate of 0.5 ml/min. The total analysis time was 25 min, and a linear gradient condition was used as follows: 0–5 min, 10% B; 5–8 min, 10%–30% B; 8–17 min, 30%–70% B; 17–20 min, 70%–95% B; and 20–25 min, 95% B. Mass spectrometry conditions are as follows: sheath gas 40 Arb, aux gas 12 Arb, sweep gas 1 Arb, ion transfer tube temperature 330°C , and vaporizer temperature 317°C . MS^1 and MS^2 data were collected by Xcalibur software (Thermo Fisher Scientific, Waltham, MA, United States), acquiring as many MS^2 data as possible within 0.6 s. A full scan was acquired in the range of 150–1,000 m/z at a resolution of 120,000 for the MS^1 method, and the automatic gain control (AGC) was set at 2.0×10^5 , RF-lens of 60%, and maximum injection time of 100 ms. The AGC was set at 5.0×10^4 , and maximum ion injection times were 45 ms for MS^2 scan. The activation type was high-energy collisional dissociation (HCD), and its energy was performed with 20%–40%. The dynamic exclusion duration time was set at 8 s.

Screening of the metabolites of DOX is shown by Gao et al. (2015), Vrobel et al. (2017), Bujak et al. (2020), and Izzo et al. (2020). In the analysis, data were processed with the Compound Discoverer (CD) 3.1 software and Mass Frontier 7.0 software (Thermo Fisher Scientific, Waltham, MA, United States). Raw files were imported into CD software to identify metabolites of DOX. The processing workflow “Find Expected metabolites with Fish Scoring and Background” was selected with the settings of mass

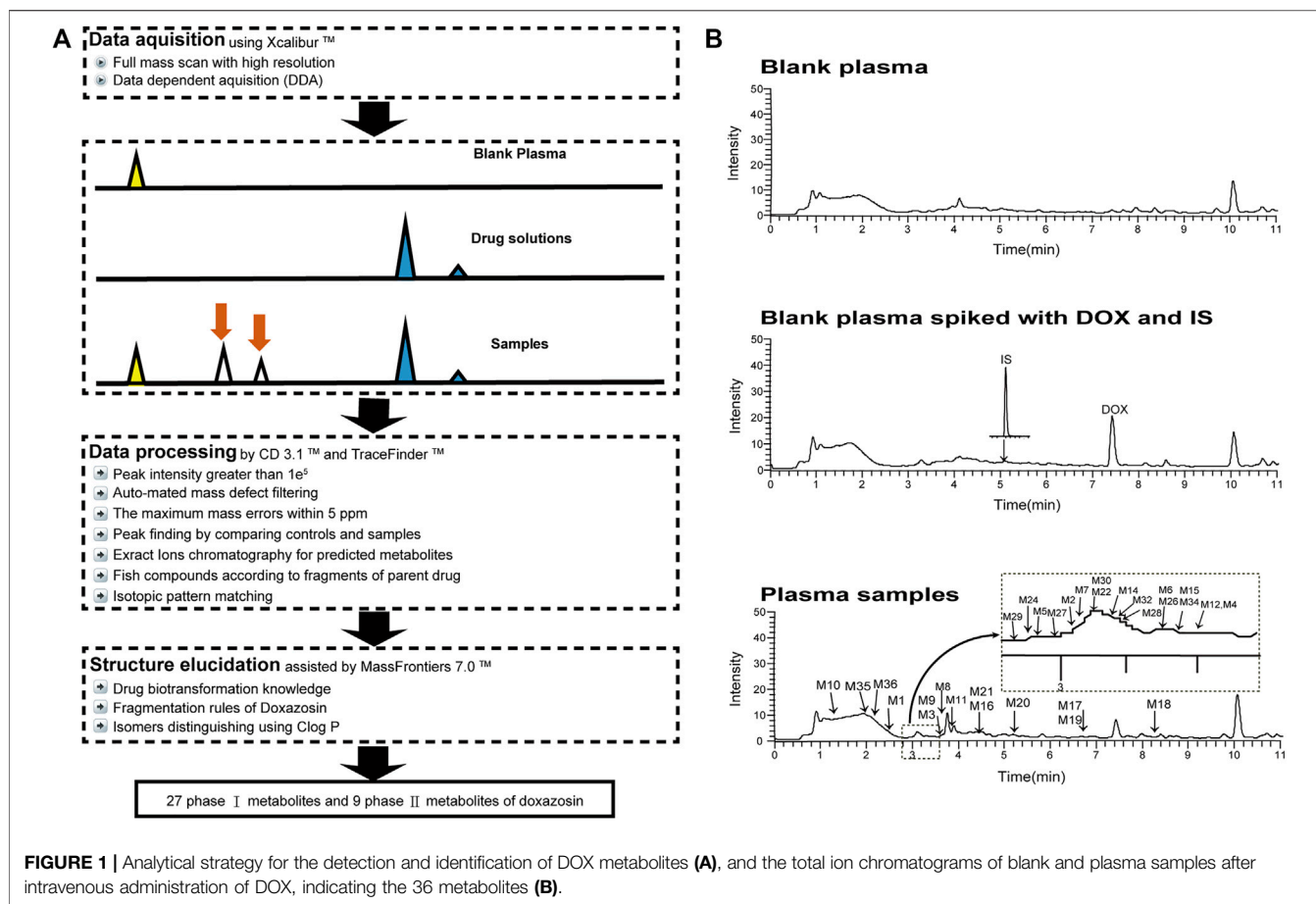


FIGURE 1 | Analytical strategy for the detection and identification of DOX metabolites (A), and the total ion chromatograms of blank and plasma samples after intravenous administration of DOX, indicating the 36 metabolites (B).

tolerance, 5 ppm; intensity tolerance, 30%; minimum peak intensity, 100,000; ions $(M + H)^+$, $(M + K)^+$, and $(M + Na)^+$; and RT tolerance, 0.3 min. The blank samples were used for the subtraction of the background compounds. The following filters were used: peak area >10,000; fish coverage >0; and no matches found in blank and solution samples. Considering the potential element compositions and the occurrence of possible reactions, the types and numbers of the predicted atoms were set as follows: C (0–35), H (0–50), O (0–25), S (0–2), N (0–7), and ring double bond (RDB) equivalent value (0–15). The maximum mass errors between the measured and the calculated values were fixed within 5 ppm. The detection of metabolites was accomplished *via* data processing with mass defect filtering (MDF) and control sample comparison. We also evaluated possible metabolites from isotopic ratios, peak shape, and fragments. The ClogP (Chemdraw Ultra 14.0, Cambridge Soft Corp., Cambridge, MA) was used to distinguish the structure of diastereoisomers containing two or more chiral centers because a diastereoisomer with a larger ClogP value had a longer retention time in reversed-phase liquid chromatography systems (Zhang et al., 2018). The possible structure of the metabolites was analyzed based on the MS^2 data. Then, Mass Frontier 7.0 software (Thermo Fisher Scientific, Waltham, MA, United States) was used for further structure verification, which predicted the structures of a fragment based on the HighChem Fragmentation Library™ (Thermo Fisher Scientific, Waltham, MA, United States). The

identified metabolites were added to our Local Compound Database for the following analysis to increase the chances of identifying the metabolites and reduce data processing time in a number of biological samples.

Calculating the Kinetic Parameters for Metabolites

Chromatographic peaks were integrated by the TraceFinder software (Thermo Fisher Scientific, Waltham, MA, United States). The concentrations of DOX in plasma or incubation systems were determined using a calibration curve generated with the known concentrations. A comparison of the same metabolite among different samples was achieved by calculating the peak area ratio of the metabolite versus the internal standard at the MS^1 level.

Pharmacokinetic parameters of (+)-DOX, (–)-DOX, and (±)-DOX and each metabolite were calculated based on concentration-time profiles of individual rat plasma samples using WinNonlin software (V.5.1, Pharsight, Mountain View, CA) by a noncompartmental analysis model. The maximum plasma concentration (C_{max}) and the time to reach C_{max} (t_{max}) were determined directly from the plot. The terminal phase rate constant (λ) was estimated as the absolute value of the slope of a linear regression during the apparent terminal phase of the natural logarithm transformed concentration-time profile. The area under the

TABLE 1 | Summary of 36 doxazosin metabolites with possible chemical structures.

Name	Formula	MS2: fragment ions	Δ Mass	RT (min)	#MI	m/z	Identification
DOX	C ₂₃ H ₂₅ N ₅ O ₅	344, 290, 247, 221	1.47	7.422	4	452,1935	
M1	C ₁₀ H ₁₂ N ₄ O ₂	221, 206, 177	6.49	2.615	2	221,1047	
M2	C ₁₃ H ₁₇ N ₅ O ₂	276, 247, 245, 221	1.79	3.03	3	276,1460	
M3	C ₁₄ H ₁₇ N ₅ O ₂	288, 245, 221, 170	7.12	3.089	2	288,1476	
M4	C ₁₄ H ₁₉ N ₅ O ₂	290, 247, 221	6.35	3.433	5	290,1630	
M5	C ₁₃ H ₁₇ N ₅ O ₃	292, 274, 247	6.98	2.919	4	292,1425	
M6	C ₁₄ H ₁₇ N ₅ O ₃	304, 276, 245, 221	1.39	3.328	2	304,1408	
M7	C ₁₄ H ₁₉ N ₅ O ₃	306, 288, 247, 221	1.70	3.056	2	306,1566	
M8	C ₁₅ H ₁₉ N ₅ O ₃	318, 290, 247	1.63	3.754	2	318,1566	
M9	C ₁₄ H ₁₇ N ₅ O ₄	319, 263, 245	1.48	3.682	2	320,1358	
M10	C ₁₄ H ₁₉ N ₅ O ₄	322, 247, 221	2.24	1.523	2	322,1517	
M11	C ₁₆ H ₂₁ N ₅ O ₃	331, 290, 247	6.91	3.925	2	332,1740	
M12	C ₁₆ H ₂₀ N ₆ O ₄	361, 290, 247	6.64	3.377	4	361,1643	

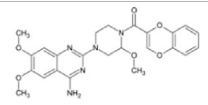
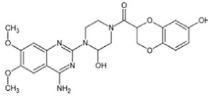
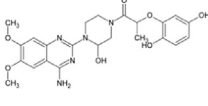
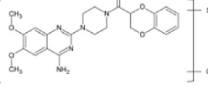
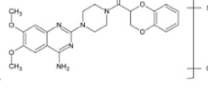
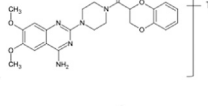
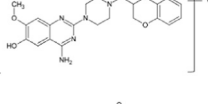
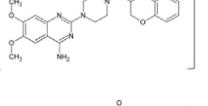
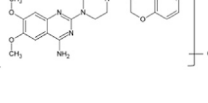
(Continued on following page)

TABLE 1 | (Continued) Summary of 36 doxazosin metabolites with possible chemical structures.

Name	Formula	MS2: fragment ions	Δ Mass	RT (min)	#MI	m/z	Identification
M13	C ₂₁ H ₂₃ N ₅ O ₅	426, 408, 221	5.92	5.528	2	426,1797	
M14		426, 408, 300, 221	3.13	3.167	3	426,1785	
M15	C ₂₂ H ₂₃ N ₅ O ₅	438, 330	1.86	3.331	2	438,1780	
M16		438, 342, 287	1.72	4.279	2	438,1780	
M17	C ₂₃ H ₂₃ N ₅ O ₅	450, 342, 287, 245	6.62	6.565	4	450,1802	
M18		450, 342, 287	4.79	8.322	3	450,1794	
M19	C ₂₃ H ₂₅ N ₅ O ₆	468, 450, 342, 247	6.55	6.594	3	468,1908	
M21		468, 450, 290, 221	4.59	4.305	2	468,1899	
M22		468, 289, 221	6.42	3.091	4	468,1908	
M20		468, 316, 290, 233	5.70	5.417	4	468,1904	
M23		468, 289, 221	6.22	2.861	2	468,1907	
M24	C ₂₃ H ₂₇ N ₅ O ₆	470, 360, 290, 233	7.57	2.877	3	470,2070	
M25		470, 452, 142	7.38	5.023	2	470,2069	

(Continued on following page)

TABLE 1 | (Continued) Summary of 36 doxazosin metabolites with possible chemical structures.

Name	Formula	MS2: fragment ions	Δ Mass	RT (min)	#MI	m/z	Identification
M26	C ₂₄ H ₂₅ N ₅ O ₆	480, 318, 290, 135	6.13	3.37	4	480,1907	
M27	C ₂₃ H ₂₅ N ₅ O ₇	484, 440, 290, 233	6.5	2.973	3	484,1858	
M28	C ₂₃ H ₂₇ N ₅ O ₇	486, 468, 289, 221	5.92	3.189	4	486,2012	
M29	C ₂₃ H ₂₅ N ₅ O ₉ S	548, 468, 344	6.60	2.908	3	548,1482	
M30	C ₂₃ H ₂₅ N ₅ O ₉ S	548, 468, 344	6.65	3.081	2	548,1482	
M31	C ₂₅ H ₃₂ N ₆ O ₉ S	592, 468, 221	6.22	3.073	4	593,2061	
M32	C ₂₈ H ₃₁ N ₅ O ₁₁	614, 438, 330	2.59	3.146	4	614,2109	
M33		614, 438	3.25	3.29	2	614,2109	
M34	C ₂₉ H ₃₃ N ₅ O ₁₁	628, 452	2.40	3.35	4	628,2264	
M35	C ₂₉ H ₃₃ N ₅ O ₁₂	644, 468, 344	6.54	2.459	3	644,2241	
M36		644, 468, 344	6.82	2.538	4	644,2242	

concentration-time curve (AUC) from time zero to the last quantifiable concentration (AUC_{0-t}) was calculated using the linear trapezoidal method.

The kinetic parameters AUC_{0-t} for each metabolite in incubation experiments were also calculated using the linear trapezoidal method by WinNonlin software.

Multivariate Statistical Analysis for the Metabolites Originating From (+)-DOX, (–)-DOX, and (±)-DOX

Multivariate data analysis was a powerful tool in the biological understanding and exploration of complex, multiparametric metabolic systems (Macherius et al., 2014; Commisso et al., 2017; Kim et al., 2018). Multivariate analyses were performed using the resulting matrix of $\lg(AUC)$ or $\lg(\lambda)$ of the observed

metabolites in each sample. In this study, hierarchical cluster analysis (HCA), principal component analysis (PCA), and Pearson correlation analysis were employed to analyze the matrix by the RStudio platform (Version 1.0.143) installed R (Version 3.5.1) with packages such as ggplot2, procomp, corrgram, and heatmap.

Other Statistical Analysis

All data were represented as mean \pm standard deviation (mean \pm SD). Logarithmic transformation was performed on AUC_{0-t} and C_{max} values before the statistical analysis. One-way ANOVA followed by Tukey's HSD test by GraphPad Prism 5.0 (GraphPad Software, Inc., San Diego, CA) was used to analyze the difference in AUC_{0-t} or C_{max} among (–)-DOX, (+)-DOX, and (±)-DOX and that among the same metabolites of (–)-DOX, (+)-DOX, and (±)-DOX. p -value < 0.05 was considered statistically significant.

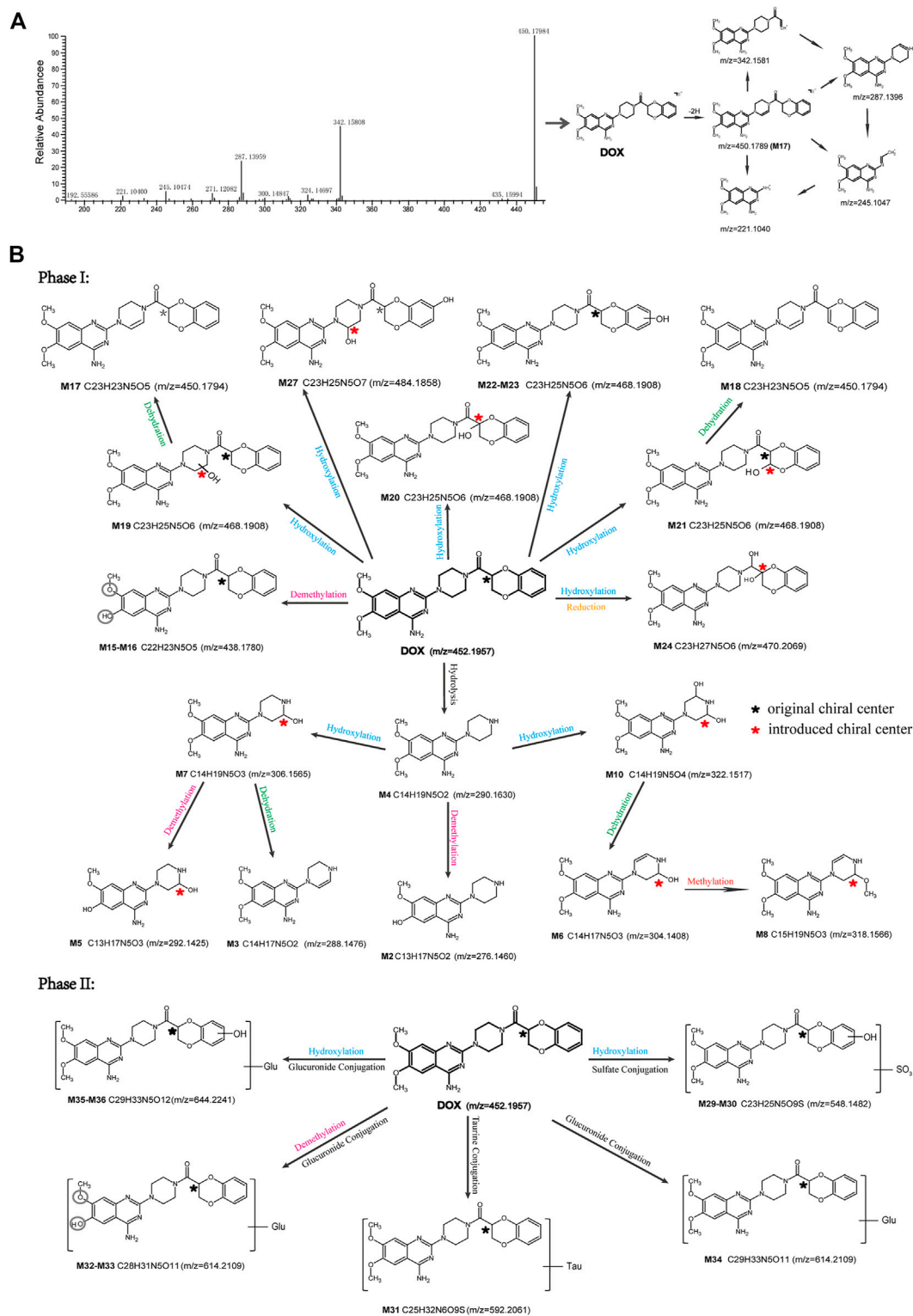


FIGURE 2 | Elucidation of the chemical structure and mass fragmentation pattern of the metabolite taking M17 as an example (A), and the proposed possible metabolic pathway for DOX (B).

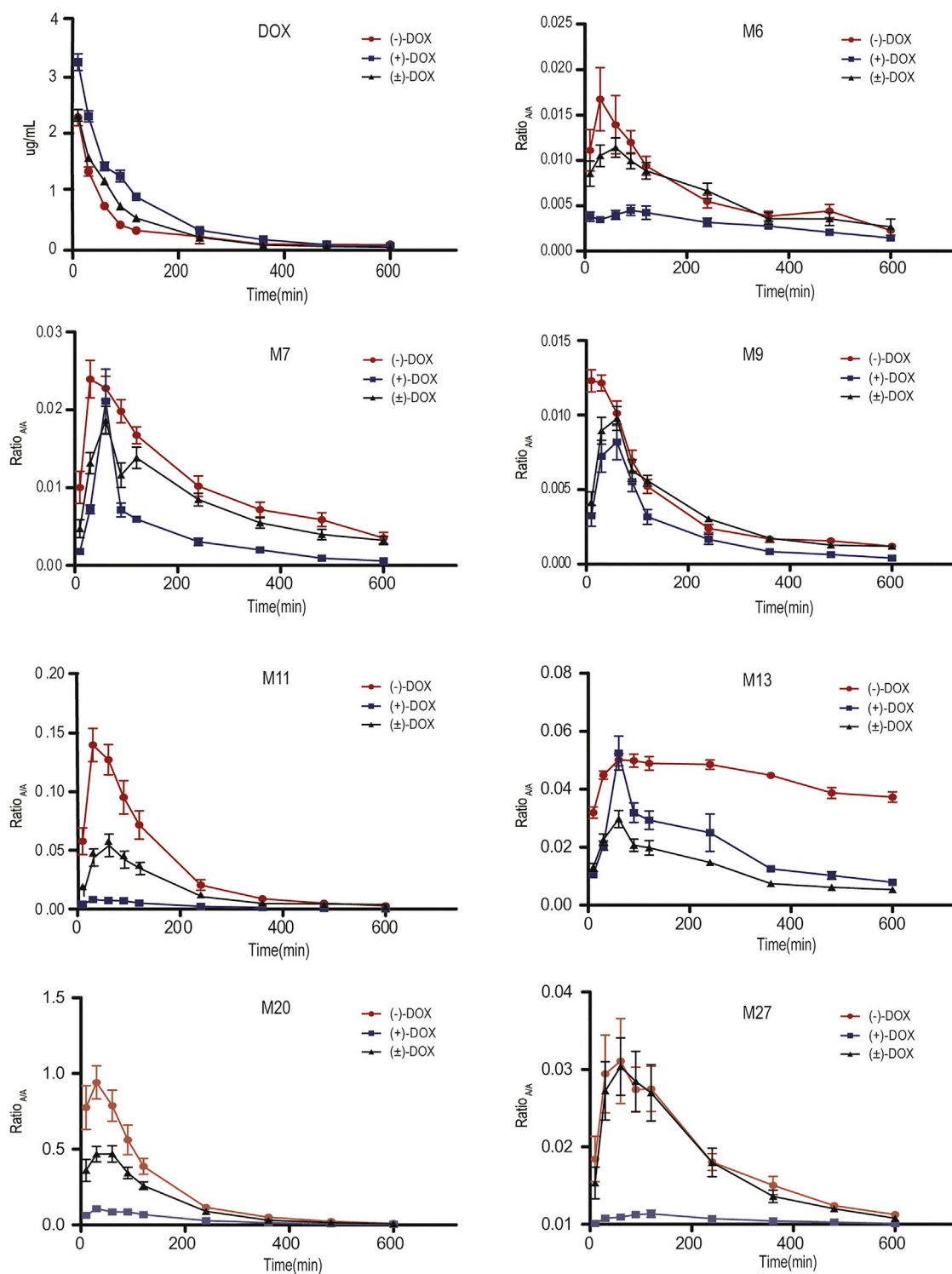
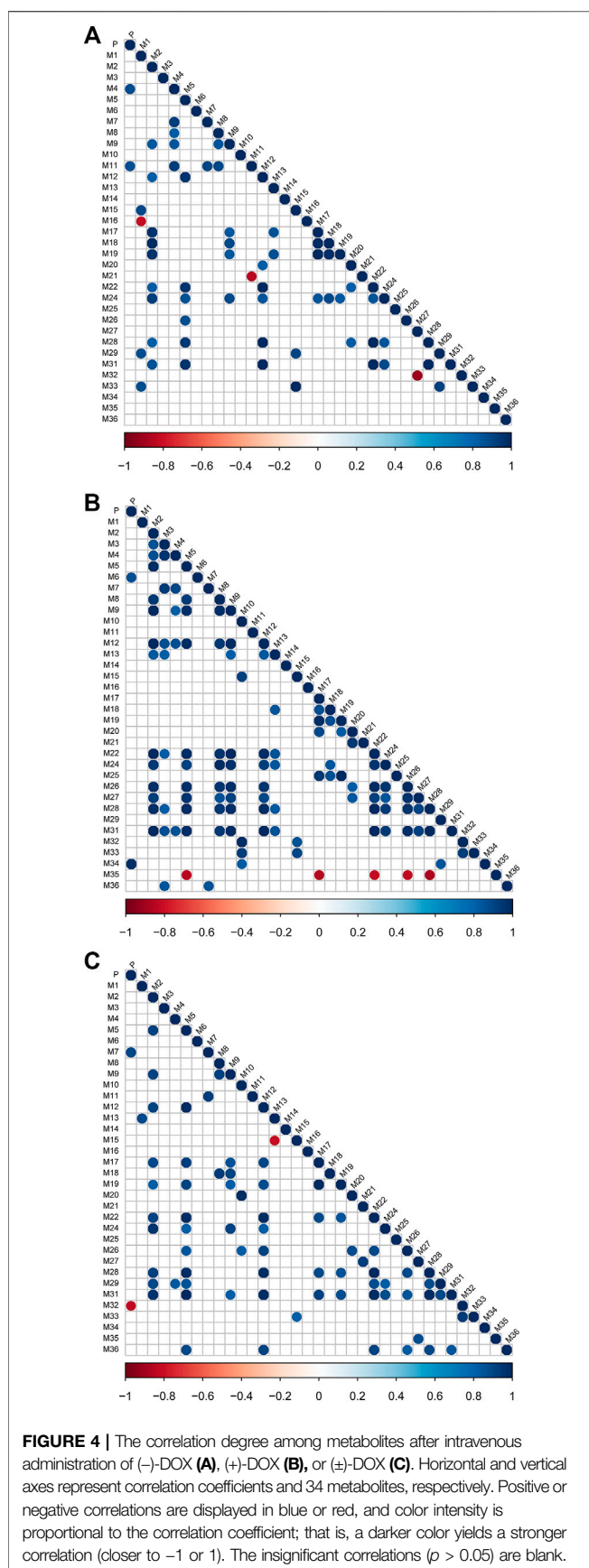


FIGURE 3 | Plasma concentration-time curves for DOX and its representative metabolites obtained from six rats after (-)-DOX, (+)-DOX, or (±)-DOX administration.

TABLE 2 | The pharmacokinetic parameters for doxazosin and its metabolites in six rats after (–)-DOX, (+)-DOX, or (±)-DOX administration (mean ± SD).

	AUC_{0-t}			λ			C_{max}		
	(–)-DOX	(+)-DOX	(±)-DOX	(–)-DOX	(+)-DOX	(±)-DOX	(–)-DOX	(+)-DOX	(±)-DOX
DOX	130.29 ± 35.42 ^{*,+}	295.81 ± 50.87 [#]	178.6 ± 11.97	0.015 ± 0.012	0.014 ± 0.004	0.013 ± 0.002	2.239 ± 0.357 [*]	3.228 ± 0.365 [#]	2.277 ± 0.252
M1	42.17 ± 8.81 [*]	18.29 ± 3.89 [#]	49.27 ± 11.05	—	0.002 ± 0.001	—	0.114 ± 0.037 [*]	0.039 ± 0.008 [#]	0.117 ± 0.026
M2	2.87 ± 0.43	2.73 ± 1.25	2.75 ± 0.56	0.002 ± 0.001 [*]	0.006 ± 0.002 [#]	0.003 ± 0.001	0.011 ± 0.004	0.026 ± 0.017	0.014 ± 0.003
M3	17.31 ± 3.23 ⁺	17.94 ± 5.25 [#]	25.17 ± 2.96	0.002 ± 0.001	0.004 ± 0.002	0.004 ± 0.001	0.081 ± 0.025 [*]	0.204 ± 0.095	0.117 ± 0.026
M4	493.78 ± 64.82 ^{*,+}	257.79 ± 57.59 [#]	359.55 ± 82.8	0.002 ± 0.001	0.003 ± 0.000	0.002 ± 0.001	2.195 ± 0.348	2.235 ± 1.071	1.369 ± 0.284
M5	17.03 ± 3.95	26.66 ± 11.73	21.17 ± 7.23	0.002 ± 0.001 ^{*,+}	0.005 ± 0.001	0.005 ± 0.002	0.067 ± 0.028 [*]	0.188 ± 0.081	0.134 ± 0.047
M6	3.85 ± 1.12 [*]	1.76 ± 0.24 [#]	3.51 ± 0.82	0.003 ± 0.001	0.004 ± 0.002	0.003 ± 0.001	0.017 ± 0.008 [*]	0.006 ± 0.001 [#]	0.012 ± 0.003
M7	6.29 ± 1.34 [*]	2.23 ± 0.67 [#]	4.69 ± 1.14	0.003 ± 0.001	0.006 ± 0.003	0.003 ± 0.001	0.025 ± 0.005	0.021 ± 0.01	0.019 ± 0.004
M8	2.38 ± 0.46 ^{*,+}	1.12 ± 0.28	1.04 ± 0.22	0.005 ± 0.002	0.007 ± 0.002	0.005 ± 0.003	0.015 ± 0.001 ^{*,+}	0.008 ± 0.003	0.005 ± 0.001
M9	2.14 ± 0.35 [*]	1.28 ± 0.4 [#]	1.99 ± 0.3	0.003 ± 0.001	0.004 ± 0.001	0.003 ± 0.001	0.013 ± 0.001 [*]	0.009 ± 0.003	0.01 ± 0.002
M10	1.4 ± 0.3 ^{*,+}	0.87 ± 0.12 [#]	0.64 ± 0.12	0.002 ± 0.001	0.002 ± 0.001	0.002 ± 0.001	0.008 ± 0.002 ^{*,+}	0.003 ± 0.001	0.003 ± 0.001
M11	20.68 ± 7.22 ^{*,+}	1.56 ± 0.49 [#]	9.95 ± 3.4	0.006 ± 0.002	0.008 ± 0.002	0.006 ± 0.001	0.14 ± 0.034 ^{*,+}	0.008 ± 0.002 [#]	0.058 ± 0.024
M12	6.25 ± 4.08 ^{*,+}	33.56 ± 15.99	22.22 ± 8.13	0.016 ± 0.022	0.006 ± 0.001	0.007 ± 0.001	0.048 ± 0.032 ^{*,+}	0.247 ± 0.111	0.161 ± 0.056
M13	26.33 ± 1.2 ^{*,+}	11.59 ± 3.02 [#]	7.47 ± 0.91	0.001 ± 0.000 ^{*,+}	0.003 ± 0.000	0.003 ± 0.001	0.054 ± 0.004 ⁺	0.052 ± 0.014 [#]	0.03 ± 0.007
M14	18.38 ± 2.7 ^{*,+}	11.48 ± 4.56	8.55 ± 1.57	0.001 ± 0.001	0.001 ± 0.000	0.002 ± 0.001	0.06 ± 0.012 ^{*,+}	0.026 ± 0.009	0.029 ± 0.01
M15	0.87 ± 0.39 ^{*,+}	2.87 ± 0.79	2.74 ± 0.59	0.004 ± 0.002 ⁺	0.006 ± 0.001	0.007 ± 0.002	0.008 ± 0.004 ^{*,+}	0.02 ± 0.005	0.02 ± 0.006
M16	1.00 ± 0.16	1.24 ± 0.32 [#]	0.81 ± 0.12	0.002 ± 0.001	0.003 ± 0.002	0.004 ± 0.004	0.004 ± 0.001	0.005 ± 0.001 [#]	0.003 ± 0.000
M17	70.22 ± 27.95 [*]	128.25 ± 25.44	83.42 ± 13.15	0.008 ± 0.003	0.008 ± 0.001	0.008 ± 0.002	0.65 ± 0.185	0.774 ± 0.186	0.614 ± 0.112
M18	15.59 ± 4.00 ^{*,+}	52.45 ± 14.19 [#]	33.67 ± 5	0.005 ± 0.002	0.005 ± 0.001	0.006 ± 0.001	0.108 ± 0.023 ^{*,+}	0.191 ± 0.041	0.148 ± 0.033
M19	18.75 ± 7.26 [*]	28.16 ± 6.38	19.62 ± 3.01	0.008 ± 0.002	0.008 ± 0.001	0.009 ± 0.002	0.177 ± 0.049	0.223 ± 0.078	0.147 ± 0.026
M20	128.12 ± 36.76 ^{*,+}	20.1 ± 2.45 [#]	77.52 ± 19.63	0.007 ± 0.001	0.006 ± 0.001	0.007 ± 0.001	0.945 ± 0.271 ^{*,+}	0.108 ± 0.023 [#]	0.497 ± 0.141
M21	5.17 ± 0.77 ^{*,+}	13.59 ± 1.92 [#]	7.49 ± 1.8	0.004 ± 0.001 [*]	0.007 ± 0.001	0.006 ± 0.001	0.048 ± 0.014 [*]	0.123 ± 0.037 [#]	0.054 ± 0.022
M22	82.59 ± 51.75 ^{*,+}	390.78 ± 173.79	371.55 ± 134.21	0.006 ± 0.003	0.005 ± 0.001	0.007 ± 0.001	0.585 ± 0.358 ^{*,+}	2.612 ± 1.213	2.502 ± 0.891
M24	5.88 ± 4.19 ^{*,+}	21.95 ± 16.81	25.69 ± 9.48	0.010 ± 0.011	0.004 ± 0.001	0.005 ± 0.002	0.035 ± 0.023 ^{*,+}	0.106 ± 0.072	0.15 ± 0.051
M25	10.87 ± 2.6	11.35 ± 2.9	12.07 ± 2.61	0.005 ± 0.001 ^{*,+}	0.003 ± 0.001	0.004 ± 0.001	0.052 ± 0.015	0.04 ± 0.009	0.045 ± 0.011
M26	2.83 ± 1.53 ^{*,+}	17.17 ± 8.39	10.92 ± 3.91	0.010 ± 0.006	0.004 ± 0.001	0.006 ± 0.002	0.032 ± 0.025 [*]	0.252 ± 0.126	0.075 ± 0.035
M27	5.01 ± 2.21 [*]	0.37 ± 0.28 [#]	4.62 ± 2.33	0.006 ± 0.001	0.005 ± 0.003	0.007 ± 0.001	0.022 ± 0.013 [*]	0.001 ± 0.001 [#]	0.021 ± 0.01
M28	6.44 ± 4.28 ^{*,+}	29.53 ± 12.76	31.85 ± 11.83	0.005 ± 0.002	0.005 ± 0.001	0.007 ± 0.001	0.045 ± 0.029 ^{*,+}	0.201 ± 0.097	0.216 ± 0.079
M29	4.79 ± 0.71 ^{*,+}	26.49 ± 5.58	27.13 ± 7.49	0.011 ± 0.003 ^{*,+}	0.007 ± 0.000	0.007 ± 0.002	0.063 ± 0.017 ^{*,+}	0.186 ± 0.028	0.197 ± 0.079
M31	3.66 ± 2.23 ^{*,+}	17.7 ± 7.36	25.58 ± 8.37	0.007 ± 0.002	0.005 ± 0.001	0.006 ± 0.001	0.024 ± 0.013 ^{*,+}	0.077 ± 0.03	0.162 ± 0.054
M32	4.3 ± 0.76 ^{*,+}	25.25 ± 8.32	26.78 ± 6.04	0.004 ± 0.002 [*]	0.001 ± 0.001	0.003 ± 0.001	0.003 ± 0.001 ^{*,+}	0.014 ± 0.003 [#]	0.032 ± 0.007
M33	0.41 ± 0.16 ^{*,+}	5.98 ± 1.64	8.66 ± 1.65	0.004 ± 0.001 [*]	0.001 ± 0.001 [#]	0.003 ± 0.001	0.026 ± 0.003 ^{*,+}	0.071 ± 0.012 [#]	0.127 ± 0.033
M34	4.59 ± 0.9 ^{*,+}	13.32 ± 4.18	14.08 ± 2.09	0.012 ± 0.002 ^{*,+}	0.004 ± 0.000 [#]	0.006 ± 0.001	0.034 ± 0.004 ⁺	0.038 ± 0.009 [#]	0.064 ± 0.007
M35	2.47 ± 1.58	3.33 ± 0.92 [#]	1.18 ± 0.31	0.010 ± 0.001 ^{*,+}	0.006 ± 0.002	0.005 ± 0.003	0.023 ± 0.012 ⁺	0.015 ± 0.006 [#]	0.008 ± 0.003
M36	6.51 ± 1.82 ^{*,+}	18.37 ± 4.74	20.79 ± 6.72	0.003 ± 0.002	0.004 ± 0.001	0.004 ± 0.002	0.053 ± 0.011 ⁺	0.077 ± 0.018	0.097 ± 0.036

"—" means it cannot be calculated. Logarithmic transform was performed on AUC_{0-t} and C_{max} values before statistical analysis. One-way ANOVA followed by Tukey's HSD test was used. *p < 0.05 versus (+)-DOX; #p < 0.05 versus (±)-DOX; ⁺p < 0.05 versus (–)-DOX.



RESULTS AND DISCUSSION

Identification and Structural Elucidation of Metabolites of Doxazosin

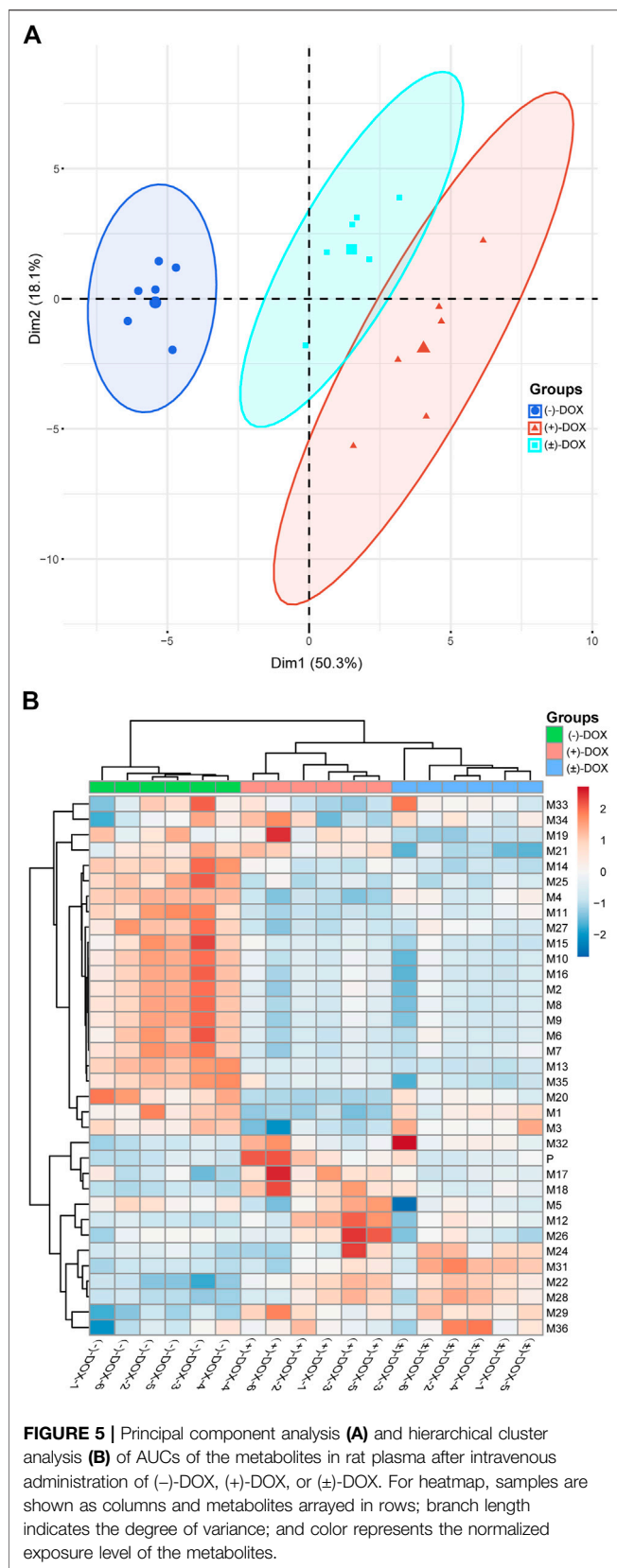
Up to now, no more than 10 known metabolites of DOX have been reported (Kaye et al., 1986). Therefore, a detailed study on the metabolites of DOX is necessary. For the identification of metabolites, (±)-DOX was administered to the rats through the caudal vein, and the blood was collected at different time points after administration and then analyzed by UHPLC-HRMS. To discover more metabolites of DOX, we used the method *in vivo* in the beginning rather than *in vitro* (such as microsomes or recombinant CYP enzymes) because there are many kinds of metabolic enzymes in the body, including carboxylases, dehydrogenases, lipooxygenases, oxidoreductases, kinases, lyases, and transferases (Alexander et al., 2011; Argikar et al., 2016).

In this study, we established a comprehensive and effective strategy (Figure 1A) to discover and identify the metabolites. Thirty-six metabolites were identified based on our strategy, and their possible chemical structures were inferred (Figure 1B and Table 1).

Firstly, the fragmentation patterns of DOX in ESI-HCD-MS were illustrated, which can provide useful information to deduce the structures of related metabolites. DOX showed a protonated ($M + H$)⁺ ion at m/z 452.1925 with a retention time of 7.4 min. It produced the base peak ion at m/z 344 [$M + H - C_6H_4O_2$]⁺ in the ESI-HCD-MS² spectrum. Because of the MS³ experiment, it is easy to know that the peak ion at m/z 290 was yielded from the ion at m/z 344 by losing C_3H_2O , and the other major characteristic ions at m/z 247 and 221 were yielded from the ion at m/z 290 by losing C_2H_5N and $C_3H_5N_2$ (Supplementary Figure S1). Taking metabolite M17 as an example, it was eluted at 2.92 min and 2 Da (2H) less than DOX but had a similar characteristic fragment of m/z 221. Besides, the ions at m/z 245, m/z 288, and m/z 342 were also found by successively losing 2 Da of m/z 247, m/z 290, and m/z 344. Therefore, we inferred that the elimination reaction occurred at the sites of the piperazine ring, and the structure of M17 can be inferred easily (Figure 2A).

M1 (m/z 290.1628, $C_{10}H_{12}N_4O_2$) and M4 (m/z 290.1628, $C_{10}H_{12}N_4O_2$) were detected at 2.62 and 3.43 min, respectively. Because m/z 221.1040 and 290.1628 were the typical fragment ions of DOX and the fragment ions of M4 were m/z 247.1197 and 221.1038, we inferred M1 to be formed by quinazoline amino group cleavage and M4 to be formed by cleavage of a piperazine ring and a carbonyl linkage (Table 1 and Supplementary Figure S2). M2 with a protonated [$M + H$]⁺ ion at m/z 276.146 was eluted at 3.03 min, and its fragments of m/z 247.1197 and m/z 221.1038 were found in the mass spectrum of MS² with no other characteristic ions observed. The molecular weight of M2 was 14 Da less than M4, showing a CH_2 group loss. Therefore, it can be inferred that M2 is an O-demethyl metabolite of M4 (Table 1 and Supplementary Figure S2).

M19, M20, M21, M22, and M23 showed the same theoretical [$M + H$]⁺ ion at m/z 468.1899, which was 16 Da higher than that of DOX. Furthermore, they were eluted at 2.86, 3.1, 4.30, 5.41, and 6.59 min, respectively. It has been reported that DOX has monohydroxy metabolites (Kaye et al., 1986). Five monohydroxy metabolites were detected in our study (Table 1 and Supplementary Figure S2).



Elucidations for other metabolites are shown in detail in Supplementary Files (Supplementary Appendix S1, Table 1, and Supplementary Figure S2). The metabolites of DOX were grouped into phase I metabolites and phase II metabolites. Phase I metabolites included M1~M11 and M13~M28, and phase II metabolites included M12 and M29~M36. According to the analysis of the structure of the metabolites, the possible metabolic pathways (Figure 2B) of DOX were proposed.

Plasma Concentration-Time Profiles of the Metabolites of (–)-DOX, (+)-DOX, and (±)-DOX

The analysis methodology for DOX quantitation in plasma using LC-MS has been reported by our lab (Du et al., 2016). Owing to a lack of standard substances of DOX metabolites, M1~M36 were semi-quantitatively analyzed by calculating peak area ratios of metabolites versus internal standard in extracted ion chromatograms. The method's stability was evaluated using DOX, and the intra-day and inter-day coefficients of variation for the assay were less than 3.4% for DOX. The two enantiomers were stable during the entire course of the study, including the sample preparation, centrifugation, and the LC-MS assay.

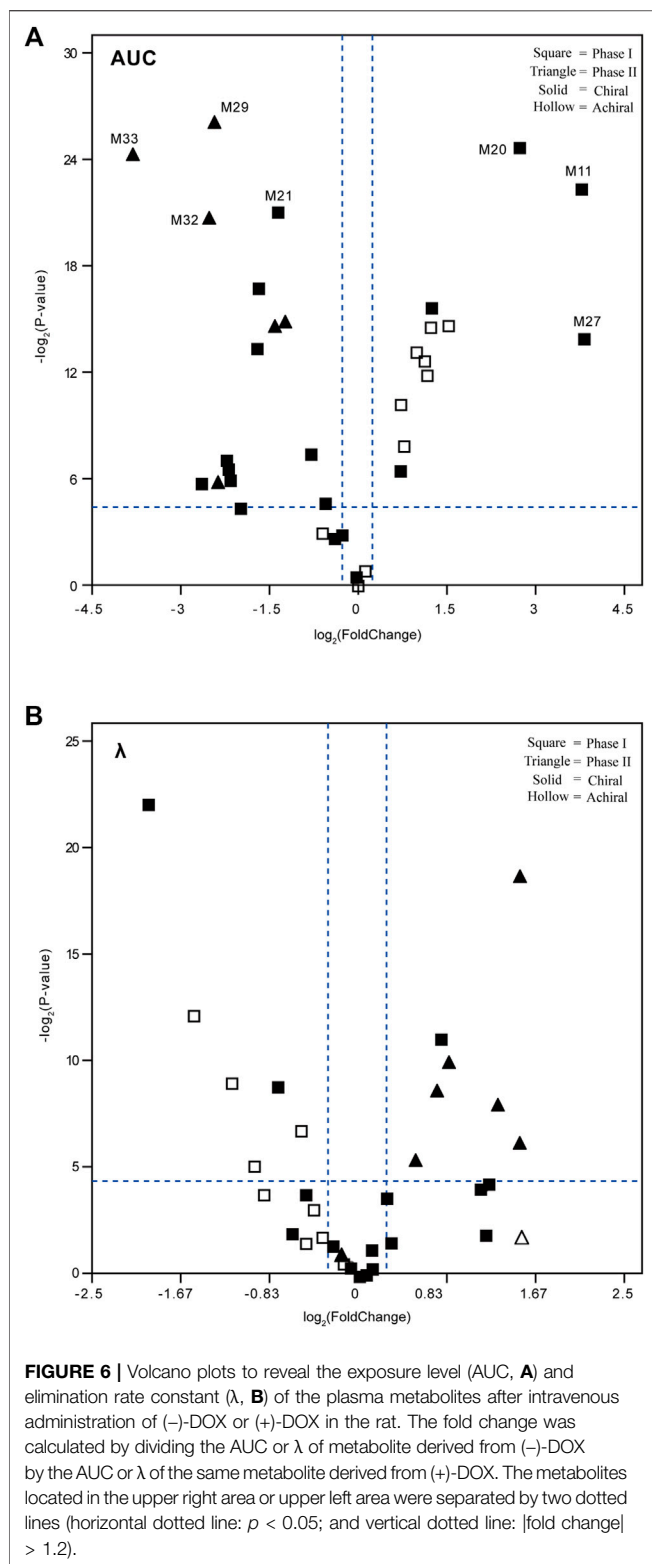
Figure 3 and Supplementary Figure S3 show the mean plasma concentration-time curves for DOX and its metabolites obtained from six rats after intravenous injection of (–)-DOX, (+)-DOX, or (±)-DOX, respectively. The major pharmacokinetic parameters, including AUC_{0-t} , C_{max} , and λ , are summarized in Table 2, and the pharmacokinetic behaviors of (–)-DOX, (+)-DOX, and (±)-DOX were consistent with our previous report (Li et al., 2015).

Thirty-six metabolites (M1~M36) mentioned above were all detected in rat plasma after intravenous administration of (–)-DOX, (+)-DOX, or (±)-DOX. Because the concentration-time curves for M23 and M30 did not show a tendency, making it difficult to calculate their AUC values, other 34 metabolites were used as the available metabolites in the following data analysis.

The plasma exposure level of drug metabolites depends on the rank order of their ratio of formation to elimination kinetics (Brill et al., 2012). In the three parent agents, the plasma exposure of (+)-DOX was significantly higher, and that of (–)-DOX was lower than that of (±)-DOX, respectively (Figure 3). However, plasma exposure trends for M6, M7, M9, M11, M13, M20, and M27 were obviously different from their parent drugs. For example, the plasma exposure of M11 originating from (+)-DOX was much lower, and that from (–)-DOX was higher than that from (±)-DOX, respectively (Figure 3). Because the plasma exposure for other metabolites was very complicated and difficult to explain, it is necessary to employ a new statistical and data presentation method to reveal the secrets behind the data.

The Complicated Relationship Among Metabolites

Based on the AUC_{0-t} values of each metabolite, we evaluated the strength of the relationship among metabolites by the Pearson correlation analysis test. Figure 4 represents the correlations for



all pairs of variables, indicating clear relationships among the metabolites of (-)-DOX, (+)-DOX, and (\pm)-DOX. Particularly, we found M2 positively associated with M9, M12, M22, M24, M28, and M31; M5 positively associated

with M12, M22, M24, M26, M28, and M31; and M12 positively associated with M22, M24, M28, and M31 in all metabolites obtained from (-)-DOX, (+)-DOX, and (\pm)-DOX. Positive associations between M8 and M9, M15 and M33, and M17 and M19 were also revealed. This abundant information showed the possible upstream or downstream relationships of the metabolites, which further confirmed the possibility of the above metabolic pathways of DOX (**Figure 2B**).

Revealing the Chiral Metabolism of DOX Using Multivariate Statistical Methods

PCA is an unsupervised technique where knowledge of prior groups is not required. Thus, it is useful to explore the potential grouping of samples in an experiment. To better understand the enantioselective metabolic profiles of DOX, we tried to interpret the complicated plasma exposure of 34 metabolites obtained from (-)-DOX, (+)-DOX, and (\pm)-DOX using PCA. As shown in **Supplementary Figure S4**, PC1 represents the most variant components (50.3%) among all the variant components, and PC2 occupies the other 18.1%. The PCA score plot (**Figure 5A**) for the two main principal components (PC1 and PC2) revealed a clear difference in the metabolism in rats among (-)-DOX, (+)-DOX, and (\pm)-DOX. The metabolites in the (-)-DOX group were significantly separated from those in the (+)-DOX and (\pm)-DOX groups in the PC1 direction (horizontal axis), but the metabolites in the (+)-DOX group and (\pm)-DOX group were overlapped partly. Therefore, the (-)-DOX metabolism in the rat was definitely different from (+)-DOX, and the (\pm)-DOX metabolism was more similar to (+)-DOX. As indicated in the 2D PCA loading plot (**Supplementary Figure S5**), M22, M28, and M31 had a powerful impact on PC1, and they were the main contributors to the significant separation of metabolism between (-)-DOX and (+)-DOX. Furthermore, M21, M15, and M32 were positively correlated with their parent drugs because these vectors were arranged very close to each other. However, M4, M7, and M20 were negatively correlated with their parent drug because of these vectors directing oppositely with parent drug (**Supplementary Figure S5**).

Based on the HCA analysis (**Figure 5B**), the samples in (-)-DOX, (+)-DOX, and (\pm)-DOX groups were clustered together, and the three groups were clearly separated. Moreover, the (+)-DOX and (\pm)-DOX groups had much more similarity, consistent with the PCA results. In the left dendrogram of **Figure 5B**, the horizontal direction represents the distance or dissimilarity between metabolites or clusters. It was easy to find that M27, M15, M10, M16, M2, M8, M9, M6, M7, M13, and M35 were arranged closely in one block part in the tree diagram, and these metabolites showed similar metabolic profiles in the (+)-DOX and (\pm)-DOX groups. Therefore, we could judge that the metabolism of DOX was obviously and complicatedly affected by stereospecificity.

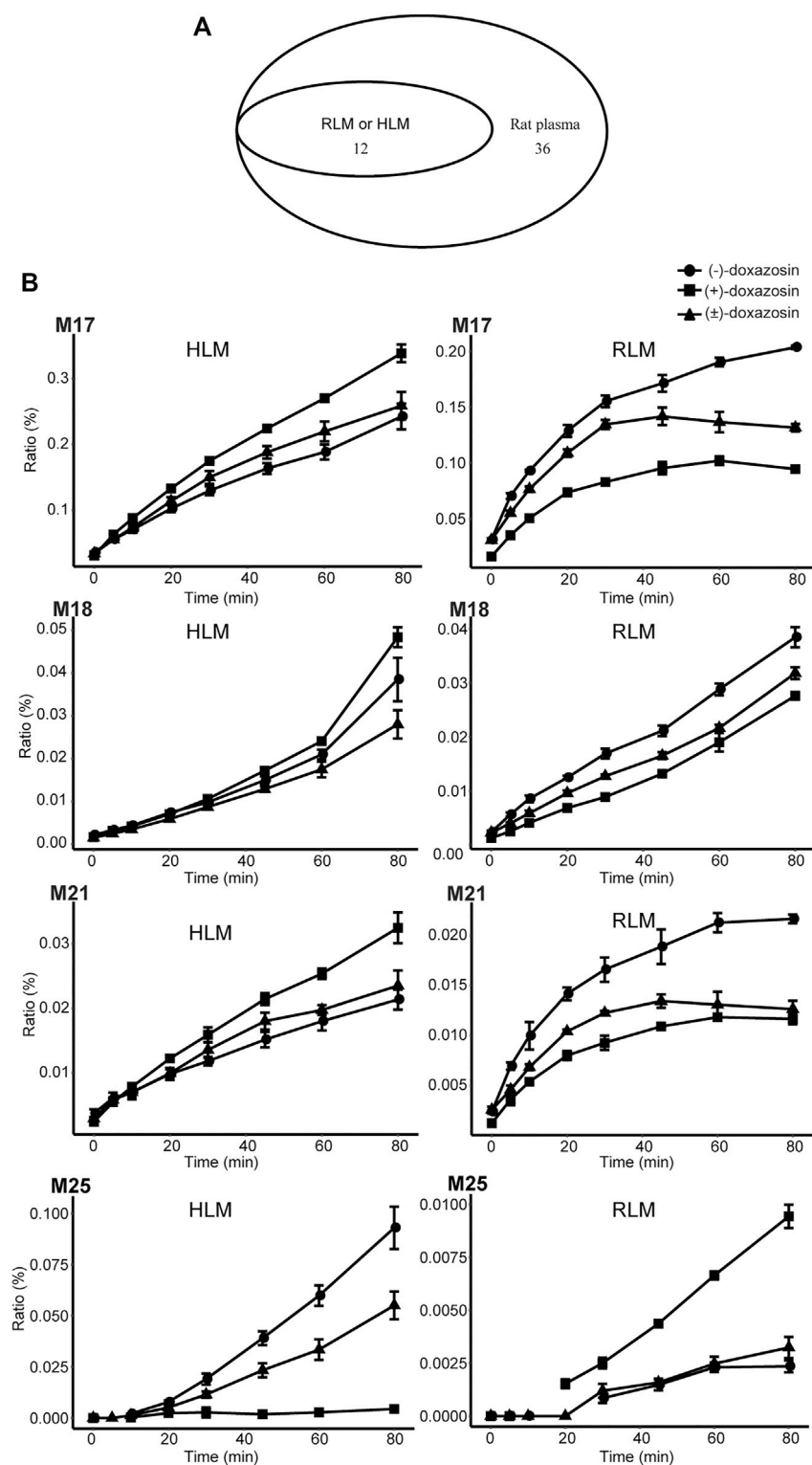


FIGURE 7 | Metabolism of doxazosin by rat and human liver microsomal enzymes. A Venn diagram **(A)** illustrated the comparison among the metabolites found in HLM, RLM, and rat plasma. The chiral metabolic characteristics were opposite for some metabolites (e.g., M17, M18, M21, and M25) between RLM and HLM incubation systems **(B)**. Also, see **Supplementary Figure S6**.

TABLE 3 | The formation of metabolites (AUC values) for DOX in HLMs and RLMs.

Metabolites	Human liver microsomes			Rat liver microsomes		
	(-)-DOX	(+)-DOX	(±)-DOX	(-)-DOX	(+)-DOX	(±)-DOX
M4	1.348 ± 0.055 ^{*,+}	26.004 ± 0.564 [#]	12.182 ± 0.204	7.349 ± 4.218 ^{*,+}	28.439 ± 1.006 [#]	15.66 ± 0.177
M14	0.375 ± 0.015	0.369 ± 0.009 [#]	0.393 ± 0.011	0.359 ± 0.012	0.341 ± 0.008	0.342 ± 0.013
M15	0.166 ± 0.013 ⁺	0.169 ± 0.014 [#]	0.142 ± 0.004	3.849 ± 0.064 ^{*,+}	8.97 ± 0.303 [#]	6.011 ± 0.081
M16	0.036 ± 0.009	NA	0.032 ± 0.005	0.507 ± 0.068 ^{*,+}	11.881 ± 1.387 [#]	0.851 ± 0.06
M17	11.697 ± 0.674 ^{*,+}	16.029 ± 0.227 [#]	13.162 ± 0.76	12.279 ± 0.299 ^{*,+}	6.516 ± 0.212 [#]	9.515 ± 0.342
M18	1.228 ± 0.09 ^{*,+}	1.418 ± 0.036 [#]	0.99 ± 0.068	1.639 ± 0.051 ^{*,+}	1.031 ± 0.032 [#]	1.268 ± 0.015
M20	143.531 ± 6.46 ^{*,+}	30.895 ± 0.628 [#]	68.479 ± 3.732	58.593 ± 2.14 ^{*,+}	37.531 ± 2.08 [#]	31.901 ± 0.802
M21	1.094 ± 0.05 ^{*,+}	1.503 ± 0.052 [#]	1.208 ± 0.072	1.337 ± 0.059 ^{*,+}	0.746 ± 0.023 [#]	0.896 ± 0.039
M22	24.859 ± 1.801 ^{*,+}	21.445 ± 0.83	19.094 ± 1.292	20.511 ± 0.57 ⁺	19.908 ± 0.793 [#]	15.675 ± 0.478
M24	0.225 ± 0.012 ⁺	0.305 ± 0.019 [#]	0.249 ± 0.019	0.052 ± 0.005 ⁺	NA	0.03 ± 0.009
M25	2.895 ± 0.25 ^{*,+}	0.183 ± 0.042 [#]	1.69 ± 0.224	0.1 ± 0.005 ^{*,+}	0.324 ± 0.012 [#]	0.115 ± 0.005
M27	3.586 ± 0.327 ⁺	2.833 ± 0.054	3.234 ± 0.312	2.372 ± 0.058 ^{*,+}	0.902 ± 0.131 [#]	1.916 ± 0.026

"NA" means it cannot be calculated. Logarithmic transform was performed before statistical analysis. One-way ANOVA followed by Tukey's HSD test was used. *p < 0.05 versus (+)-DOX;

⁺p < 0.05 versus (±)-DOX; [#]p < 0.05 versus (±)-DOX.

Chiral Characteristics of Metabolites Containing Chiral Center and Their Relationship With Phases I/II of Metabolism

A volcano plot was designed based on the exposure level (AUC) or elimination rate constant (λ) ratio value of each metabolite [metabolite [(-)-DOX]/metabolite [(+)-DOX]], in order to reveal metabolic characteristics of the metabolites containing chiral center or not. As shown in the left panel of **Figure 6A**, the AUC values of 14 metabolites with chiral center metabolized from (-)-DOX, including M21, M29, M32, and M33, were significantly smaller than those from (+)-DOX, and half of them metabolized from (-)-DOX had significantly larger λ values than those from (+)-DOX (**Figure 6B**, right panel).

In addition, AUC values of the other 12 metabolites from (-)-DOX, including M11, M20, and M27, were significantly higher than those from (+)-DOX (**Figure 6A**, right panel), and seven of them were achiral compounds. Moreover, the metabolites with statistical significance present in the right panel of **Figure 6A** and the left panel of **Figure 6B** were all phase I metabolites. We previously reported that the exposure of (-)-DOX was significantly less than that of (+)-DOX in rat plasma (Li et al., 2015; Liu et al., 2010), and no chiral conversion was observed between (-)-DOX and (+)-DOX at the chiral carbon center (Zhen et al., 2013). Therefore, we speculated that their metabolites with the chiral carbon could not undergo chiral conversion either. Taking these results together, the following explanations should be considered. Firstly, most of the metabolites were definitely produced by chirally metabolic processes in rats. Secondly, among the 34 metabolites from (-)-DOX, 12 metabolites were involved in phase I drug metabolism with much higher plasma concentrations than those derived from (+)-DOX, suggesting that the lower plasma concentration of (-)-DOX in rats was due to its more effective oxidative metabolism. Lastly, with respect to all the seven metabolites with significantly higher elimination rate (λ) involved in the (-)-DOX metabolism, six of them belonged to phase II drug metabolism (conjugation reactions), which could

be promoted to the faster conversion of (-)-DOX into the easily excreted metabolites.

Chiral Metabolism by Human or Rat Liver Microsomal Enzymes

The mammalian liver, the major site of drug metabolism, contains liver microsomes, especially CYPs, and they are involved mainly in phase I metabolic enzymes. In the present study, we investigated the chiral metabolism of DOX using rat and human liver microsomal enzymes *in vitro* and found 12 metabolites in either RLMs or HLMs (**Figure 7A**). However, 14 phase I metabolites found in the rat plasma, including M1, M2, M3, M5, M6, M7, M8, M9, M10, M11, M13, M19, M26, and M28, were not found in the liver microsomal system, indicating that other organs, tissues, and non-liver microsomal system of rats were certainly responsible for the 14 phase I metabolites of DOX. Moreover, an in-depth reanalysis of the metabolites of (-)-DOX and (+)-DOX in RLM showed that chiral metabolic characteristics, defined as the differences between the amount of the metabolite metabolized from (-)-isomer and the amount of the same metabolite metabolized from (+)-isomer, of most metabolites (M4, M14, M16, M17, M18, M21, M22, M24, and M25) in RLMs could not represent those in the rat plasma (**Table 2** and **Table 3**). Moreover, chiral metabolic characteristics of M15~M18, M21, M22, M24, and M25 in RLM were significantly different from those in HLMs (**Figure 7B** and **Supplementary Figure S6**), especially for metabolites M17, M18, M21, and M25. Their AUC values were completely opposite between RLMs and HLMs (**Figure 7B**).

It seems reasonable to replace HLMs with RLMs to investigate achiral drug metabolism, and both the microsomal systems could partly illustrate the biotransformation of achiral drug metabolism *in vivo*. For example, the same 12 metabolites of DOX existed in HLMs and RLMs, and they were also present in rat plasma. However, once our research involved the concept of chiral metabolism [(-)-DOX and (+)-DOX], the huge

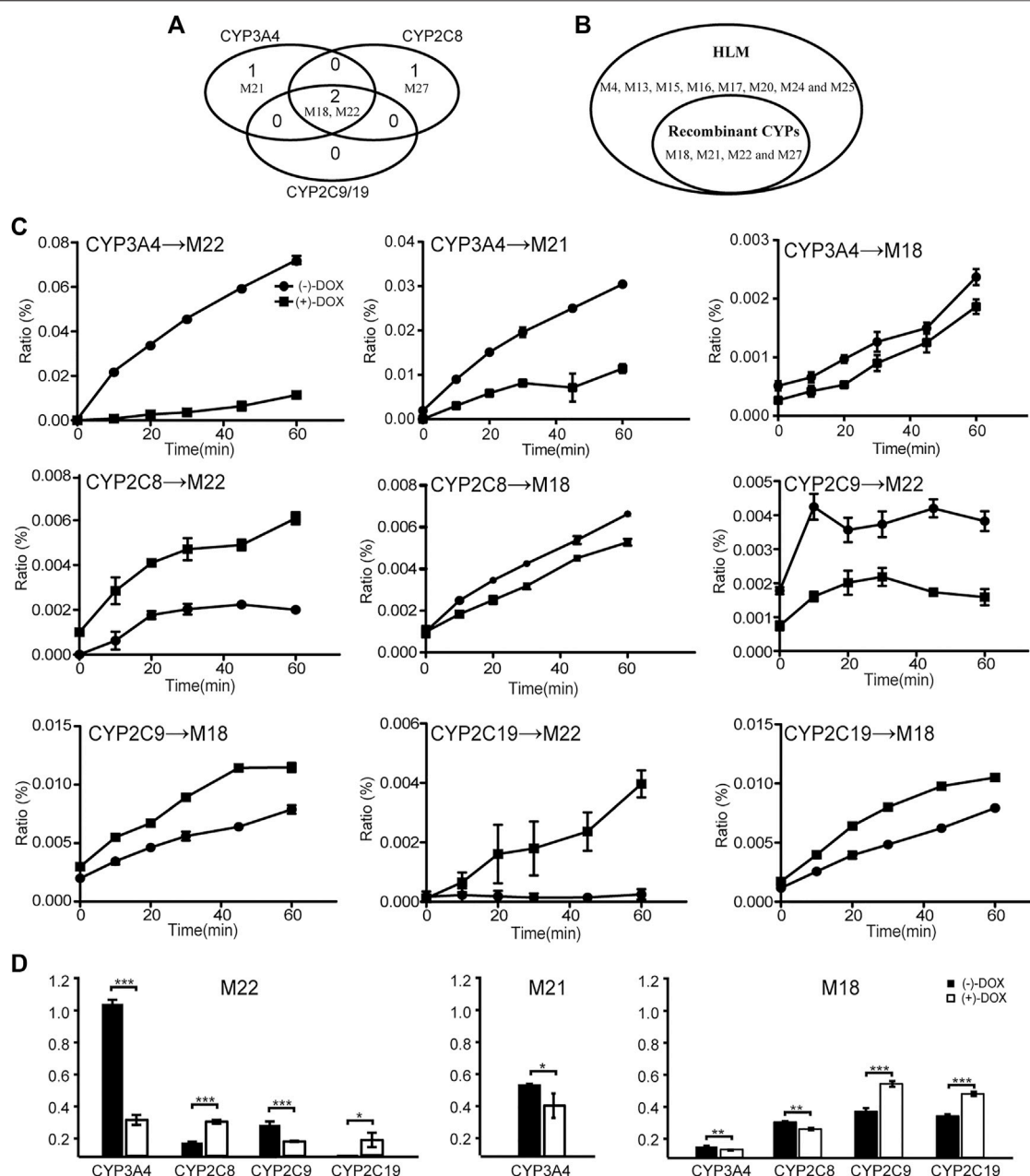


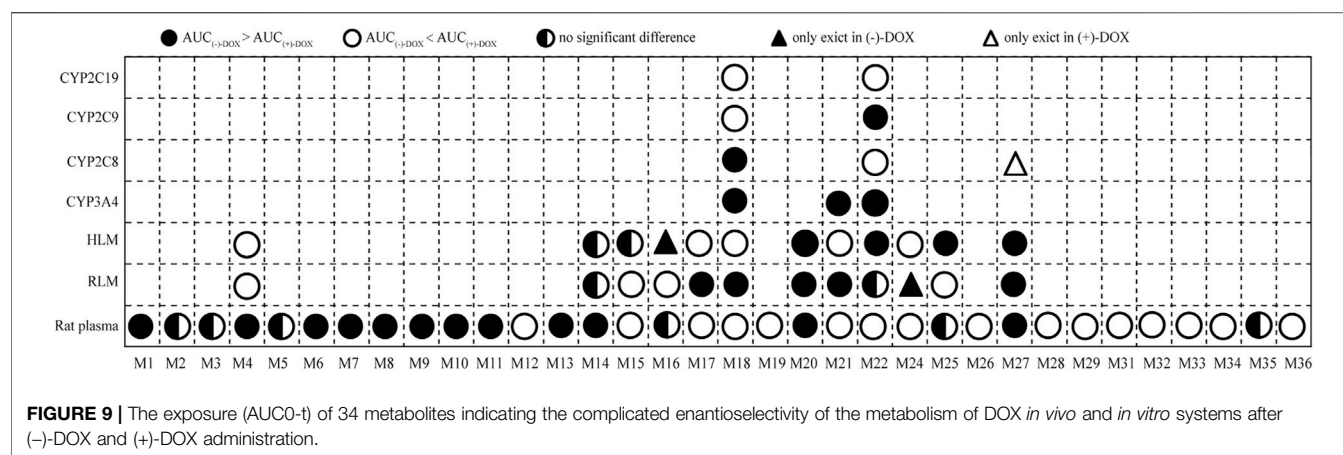
FIGURE 8 | The biotransformation of DOX by CYP enzymes. Four metabolites of DOX were found in CYP3A4, CYP2C8, and CYP2C19 incubation systems. **(A)** A Venn diagram. **(B)** The comparison of metabolites identified between HLM and human CYP enzymes. **(C)** Line charts of metabolites generated from (-)-DOX and (+)-DOX by different human CYP enzymes. **(D)** Summarized AUC values for each metabolite.

difference between HLMs and RLMs in drug metabolism was found. After the application of chiral drugs (-)-DOX and (+)-DOX in the HLMs and RLMs, only 4 of the 12 metabolites were in a similar metabolic pattern. Additionally, most metabolites (8/12) of (-)-DOX and (+)-DOX in the RLMs were considerably different in their metabolic patterns when compared with those in rat plasma, indicating that RLMs could not represent chiral phase I metabolism of DOX in rats.

Chiral Metabolism by Human CYP Enzymes

The activities of the seven important human CYP enzymes (CYP2E1, CYP2D6, CYP3A4, CYP2C19, CYP1A2, CYP2C8, and CYP2C9) were evaluated by their CYP enzyme-specific substrates (**Supplementary Table S1**), and their catalytic activities were retained and met the requirements in the following incubation experiments.

Even though 34 metabolites of DOX identified in rat plasma were not found in the CYP2E1, CYP2D6, or CYP1A2 incubation



system, two or three metabolites were identified in the CYP3A4, CYP2C19, CYP2C8, or CYP2C9 incubation system (**Figure 8A**), indicating a crucial role of the four CYPs in the oxidative metabolism of DOX. As shown in **Figure 8A**, it is easy to find that more than one enzyme participates in the same metabolic reactions, probably due to the poor substrate specificity of CYPs (Guengerich, 2018). Metabolites M4, M13, M15, M16, M17, M20, M24, and M25 found in HLM did not exist in the CYP systems (**Figure 8B**), suggesting other drug metabolic enzymes in charge of the generation of the eight metabolites in HLM.

As shown in **Figure 8C**, all the four CYP enzymes stereoselectively catalyzed the formation of corresponding metabolites from DOX (**Figure 8C**). Among them, CYP3A4 preferentially catalyzed the formation of M18, M21, and M22 from (-)-DOX, while CYP2C19 preferentially catalyzed the formation of M18 and M22 from (+)-DOX (**Figure 8C** and **Figure 8D**). In addition, when analyzing the production of metabolites from a relatively quantitative perspective, we found that CYP3A4 (the most abundant drug-metabolizing enzyme in the liver) contributed the most to the oxidative metabolism of DOX. Particularly, the M22 production from (-)-DOX was more than four times that from (+)-DOX. In humans and rats, following oral administration of (±)-DOX, the plasma concentration of the (-)-DOX is lower than that of the (+)-DOX (Liu et al., 2010; Li et al., 2015). When (±)-DOX is incubated with rat liver microsomes, (-)-DOX is depleted much faster than (+)-DOX because of a prominent and stereoselective inhibition of (-)-DOX over (+)-DOX at the CYP3A enzyme (Kong et al., 2015). In this study, we furtherly revealed that the action of CYP3A4 catalyzed the conversion of (-)-DOX to M18, M21, and M22 much stronger than that of (+)-DOX, especially for the conversion of (-)-DOX to M22. Therefore, the hydroxylation of (-)-DOX to M22 catalyzed by CYP3A4 was highly specific and selective.

Unlike 3A4 and 2C19, CYP2C8 preferentially catalyzed (+)-DOX to produce M22 and catalyzed (-)-DOX to produce M18 (**Figure 8D**). The chiral catalysis of CYP2C9 was just opposite to that of CYP2C8 (**Figure 8D**). We speculated that the formation of M22 was a hydroxylation reaction, and the formation of M18 was a dehydration reaction after the hydroxylation reaction. Particularly, we considered that it is difficult for the same

catalytic center of the same enzyme to have the opposite affinity for (-)-DOX and (+)-DOX. Therefore, we proposed that CYP2C8 or CYP2C9 should contain two active catalytic centers responsible for the formation of M18 and M22, respectively.

Moreover, in comparison with the results obtained from *in vitro* experiments, plasma concentrations of the sum of various (phases I and II) metabolites would reflect the stereoselectivity of DOX and DOX-enantiomers more correctly.

In summary, we identified 34 metabolites that showed trends over time in rat plasma. After optically pure (-)-DOX, (+)-DOX, and (±)-DOX administration, respectively, we used the multivariate statistical methods to discover the differences of these metabolites based on their exposure and elimination rate and found that the metabolic profile of (±)-DOX was more similar to that of (+)-DOX. The relationship among the metabolites and the most discriminative metabolites between (-)-DOX and (+)-DOX administration were also analyzed. The number of metabolites found in rat plasma was far more than that found in the RLM and HLM systems, indicating that the best way to comprehensively overview the metabolites is *in vivo* rather than *in vitro*. Though the metabolites identified in RLM and HLM were the same, the metabolic profiles of the metabolites from (-)-DOX and (+)-DOX were greatly different, which could be explained by the differences in amount and composition of the metabolic enzymes between RLM and HLM. Furthermore, four CYP enzymes could catalyze DOX to produce metabolites, but their preferences seemed to be different. For example, CYP3A4 highly specifically and selectively catalyzed the formation of M22 from (-)-DOX. The complicated enantioselectivity of the metabolism of DOX *in vivo* and *in vitro* systems, taking the exposure of the metabolites as an example, is summarized and shown in **Figure 9**.

As a limitation, the present study was not only to find new metabolites but also to see whether there was a chiral metabolic difference in the same metabolite derived from (-)-DOX, (+)-DOX, or (±)-DOX. Therefore, the AUC value of metabolites became the key factor in selecting available metabolites, which inevitably led to missing information on drug metabolites and metabolic pathways. A more detailed analysis of drug metabolites and metabolic pathways needs further investigation. Additionally, we performed a separation using an achiral C18 column in the present study. The enantiomers could not be separated but eluted together to form a single peak. Although optically

pure enantiomers were administrated, enantioselective analysis of DOX metabolism in the present study was limited to the chiral center of doxazosin. Enantioselectivity of the metabolites with a new chiral center was unknown, which needs to be studied further. Lastly, as two or three metabolites were identified when doxazosin was incubated with CYP3A4, CYP2C8, CYP2C9, or CYP2C19, it was difficult to simply study the Michaelis–Menten kinetics using recombinant human cytochrome P450 enzymes. We needed to carry out the specifically designed experiments in the near future.

CONCLUSION

We established a comprehensive metabolic system using pure optical isomers from *in vivo* to *in vitro*, and the complicated enantioselectivity of the metabolites of DOX was clearly shown either between rats and RLMs/HLMs, between RLMs and HLMs, or between CYP enzymes. Another interesting finding that should be mentioned is that CYP3A4 was a unique enzyme with very high selectivity and activity for (–)-DOX metabolism. More importantly, the comprehensive metabolic system is also suitable to investigate other chiral drugs.

DATA AVAILABILITY STATEMENT

The original contributions presented in the study are included in the article/**Supplementary Material**, further inquiries can be directed to the corresponding author.

REFERENCES

- Alexander, S., Mathie, A., and Peters, J. (2011). Enzymes. *Br. J. Pharmacol.* 164 (s1), S279–S324. doi:10.1111/j.1476-5381.2011.01649_9.x
- Argikar, U. A., Potter, P. M., Hutzler, J. M., and Marathe, P. H. (2016). Challenges and Opportunities with Non-CYP Enzymes Aldehyde Oxidase, Carboxylesterase, and UDP-Glucuronosyltransferase: Focus on Reaction Phenotyping and Prediction of Human Clearance. *AAPS J.* 18 (6), 1391–1405. doi:10.1208/s12248-016-9962-6
- Brill, M. J., Diepstraten, J., van Rongen, A., van Kralingen, S., van den Anker, J. N., and Knibbe, C. A. (2012). Impact of Obesity on Drug Metabolism and Elimination in Adults and Children. *Clin. Pharmacokinet.* 51 (5), 277–304. doi:10.2165/11599410-000000000-00000
- Bujak, I. T., Kralj, M. B., Kosyakov, D. S., Ul'Yanovskii, N. V., Lebedev, A. T., and Trebše, P. (2020). Photolytic and Photocatalytic Degradation of Doxazosin in Aqueous Solution. *Sci. Total Environ.* 740, 140131. doi:10.1016/j.scitotenv.2020.140131
- Cao, Y., Wang, Y., Guo, L., Yang, X., Chen, T., and Niu, H. (2016). A Randomized, Open-Label, Comparative Study of Efficacy and Safety of Tolerodine Combined with Tamsulosin or Doxazosin in Patients with Benign Prostatic Hyperplasia. *Med. Sci. Monit.* 22, 1895–1902. doi:10.12659/msm.896283
- Commisso, M., Anesi, A., Dal Santo, S., and Guzzo, F. (2017). Performance Comparison of Electrospray Ionization and Atmospheric Pressure Chemical Ionization in Untargeted and Targeted Liquid Chromatography/mass Spectrometry Based Metabolomics Analysis of Grapeberry Metabolites. *Rapid Commun. Mass Spectrom.* 31 (3), 292–300. doi:10.1002/rcm.7789
- Du, Q., Kong, D. Z., Zhang, P. P., and Ren, L. M. (2016). Quantification of (–) doxazosin at Very Low Concentration in Rat Plasma Samples by SPE-LC-MS/MS. *Yao Xue Xue Bao* 51 (7), 1125–1129. doi:10.16438/j.0513-4870.2016-0015
- Fusco, F., Palmieri, A., Ficarra, V., Giannarini, G., Novara, G., Longo, N., et al. (2016). α 1-Blockers Improve Benign Prostatic Obstruction in Men with Lower

ETHICS STATEMENT

The animal study was reviewed and approved by the Animal Ethics Committee of Hebei Medical University as complying with the National Research Council's Guide for the Care and Use of Laboratory Animals (Approval No. IACUC-Hebmu-2021017).

AUTHOR CONTRIBUTIONS

DK and YT carried out the experiments and performed data analysis. KD, WG, QZ, PZ, ZY, and XQ participated in part of the experiments. DK and LR wrote the manuscript. DK, LR, and WZ designed the research and revised the manuscript. All of the authors read and approved the final manuscript.

FUNDING

This research was supported by Hebei Natural Science Foundation (H2019206038, H2016206030, China) and NSFC foundation (81872848, China).

SUPPLEMENTARY MATERIAL

The Supplementary Material for this article can be found online at: <https://www.frontiersin.org/articles/10.3389/fphar.2022.834897/full#supplementary-material>

- Urinary Tract Symptoms: A Systematic Review and Meta-Analysis of Urodynamic Studies. *Eur. Urol.* 69 (6), 1091–1101. doi:10.1016/j.eururo.2015.12.034
- Gao, D., Chen, X., Yang, X., Wu, Q., Jin, F., Wen, H., et al. (2015). Stable Isotope Labeling Strategy for Curcumin Metabolite Study in Human Liver Microsomes by Liquid Chromatography-Tandem Mass Spectrometry. *J. Am. Soc. Mass Spectrom.* 26 (4), 686–694. doi:10.1007/s13361-014-1064-z
- Guengerich, F. P. (2018). Mechanisms of Cytochrome P450-Catalyzed Oxidations. *ACS Catal.* 8 (12), 10964–10976. doi:10.1021/acscatal.8b03401
- Higashi, T., and Ogawa, S. (2020). Derivatization-based Sample-Multiplexing for Enhancing Throughput in Liquid Chromatography/tandem Mass Spectrometry Quantification of Metabolites: an Overview. *J. Chromatogr. A.* 1634, 461679. doi:10.1016/j.chroma.2020.461679
- Izzo, L., Rodríguez-Carrasco, Y., Tolosa, J., Graziani, G., Gaspari, A., and Ritieni, A. (2020). Target Analysis and Retrospective Screening of Mycotoxins and Pharmacologically Active Substances in Milk Using an Ultra-high-performance Liquid Chromatography/high-Resolution Mass Spectrometry Approach. *J. Dairy Sci.* 103 (2), 1250–1260. doi:10.3168/jds.2019-17277
- Kapri, A., Gupta, N., and Raj, G. (2019). A Rapid and Sensitive Reversed Phase Liquid Chromatography-Tandem Mass Spectrometry Method for Quantification of Doxazosin Mesylate in Human Plasma Using Doxazosin Mesylate D8 as Internal Standard. *Anal. Chem. Lett.* 9 (3), 403–417. doi:10.1080/22297928.2019.1633953
- Karaca, B., Bakır, E., Yerer, M. B., Cumaoğlu, A., Hamurcu, Z., and Eken, A. (2021). Doxazosin and Erlotinib Have Anticancer Effects in the Endometrial Cancer Cell and Important Roles in ER α and Wnt/ β -catenin Signaling Pathways. *J. Biochem. Mol. Toxicol.* 35 (11), e22905. doi:10.1002/jbt.22905
- Kaye, B., Cussans, N. J., Faulkner, J. K., Stopher, D. A., and Reid, J. L. (1986). The Metabolism and Kinetics of Doxazosin in Man, Mouse, Rat and Dog. *Br. J. Clin. Pharmacol.* 21 (Suppl. 1), 19S–25S. doi:10.1111/j.1365-2125.1986.tb02849.x

- Kelley, E. F., Olson, T. P., Curry, T. B., Sprissler, R., and Snyder, E. M. (2019). The Effect of Genetically Guided Mathematical Prediction and the Blood Pressure Response to Pharmacotherapy in Hypertension Patients. *Clin. Med. Insights Cardiol.* 13, 1179546819845883. doi:10.1177/1179546819845883
- Kim, J. H., Jo, J. H., Seo, K. A., Hwang, H., Lee, H. S., and Lee, S. (2018). Non-targeted Metabolomics-Guided Sildenafil Metabolism Study in Human Liver Microsomes. *J. Chromatogr. B Analyt Technol. Biomed. Life Sci.* 1072, 86–93. doi:10.1016/j.jchromb.2017.11.009
- Kim, J. H., Kim, H. S., Kong, T. Y., Lee, J. Y., Kim, J. Y., In, M. K., et al. (2016). *In Vitro* metabolism of a Novel Synthetic Cannabinoid, EAM-2201, in Human Liver Microsomes and Human Recombinant Cytochrome P450s. *J. Pharm. Biomed. Anal.* 119, 50–58. doi:10.1016/j.jpba.2015.11.023
- Kong, D., Li, Q., Zhang, P., Zhang, W., Zhen, Y., and Ren, L. (2015). The Truth about the Lower Plasma Concentration of the (-)-isomer after Racemic Doxazosin Administration in Rats: Stereoselective Inhibition of the (-)-isomer by the (+)-isomer at CYP3A. *Eur. J. Pharm. Sci.* 77, 238–245. doi:10.1016/j.ejps.2015.06.022
- Lefebvre, J., Poirier, L., Poirier, P., Turgeon, J., and Lacourciere, Y. (2007). The Influence of CYP2D6 Phenotype on the Clinical Response of Nebivolol in Patients with Essential Hypertension. *Br. J. Clin. Pharmacol.* 63 (5), 575–582. doi:10.1111/j.1365-2125.2006.02796.x
- Li, Q., Kong, D., Du, Q., Zhao, J., Zhen, Y., Li, T., et al. (2015). Enantioselective Pharmacokinetics of Doxazosin and Pharmacokinetic Interaction between the Isomers in Rats. *Chirality* 27 (10), 738–744. doi:10.1002/chir.22483
- Liu, K., Zhong, D., and Chen, X. (2010). Enantioselective Determination of Doxazosin in Human Plasma by Liquid Chromatography-Tandem Mass Spectrometry Using Ovomucoid Chiral Stationary Phase. *J. Chromatogr. B Analyt Technol. Biomed. Life Sci.* 878 (26), 2415–2420. doi:10.1016/j.jchromb.2010.07.027
- Macherius, A., Seiwert, B., Schröder, P., Huber, C., Lorenz, W., and Reemtsma, T. (2014). Identification of Plant Metabolites of Environmental Contaminants by UPLC-QToF-MS: the *In Vitro* Metabolism of Triclosan in Horseradish. *J. Agric. Food Chem.* 62 (5), 1001–1009. doi:10.1021/jf404784q
- Pang, H., Jia, W., and Hu, Z. (2019). Emerging Applications of Metabolomics in Clinical Pharmacology. *Clin. Pharmacol. Ther.* 106 (3), 544–556. doi:10.1002/cpt.1538
- Ramírez-Expósito, M. J., and Martínez-Martos, J. M. (2019). Differential Effects of Doxazosin on Renin-Angiotensin-System-Regulating Aminopeptidase Activities in Neuroblastoma and Glioma Tumoral Cells. *CNS Neurol. Disord. Drug Targets.* 18 (1), 29–36. doi:10.2174/1871527317666181029111739
- Suzuki, K., Naito, T., Tanaka, H., Yamada, Y., Itoh, K., and Kawakami, J. (2020). A Reversed-phase Mode LC-MS/MS Method Using a Polysaccharide Chiral Selector for Simultaneous Quantitation of Each Enantiomer of Tramadol and its Metabolites in Human Plasma and Evaluation of CYP-Mediated Stereoselective Demethylation. *Ther. Drug Monit.* 42 (3), 503–511. doi:10.1097/FTD.0000000000000707
- Suzuki, S., Yamamoto, M., Sanomachi, T., Togashi, K., Sugai, A., Seino, S., et al. (2020). Doxazosin, a Classic Alpha 1-adrenoceptor Antagonist, Overcomes Osimertinib Resistance in Cancer Cells via the Upregulation of Autophagy as Drug Repurposing. *Biomedicines* 8 (8), 273. doi:10.3390/biomedicines8080273
- Vrobel, I., Friedecký, D., Faber, E., Najdekr, L., Mičová, K., Karlíková, R., et al. (2017). Novel sulphur-containing Imatinib Metabolites Found by Untargeted LC-HRMS Analysis. *Eur. J. Pharm. Sci.* 104, 335–343. doi:10.1016/j.ejps.2017.04.014
- Wade, C. A., Goodwin, J., Preston, D., and Kyrianiou, N. (2019). Impact of α -adrenoceptor Antagonists on Prostate Cancer Development, Progression and Prevention. *Am. J. Clin. Exp. Urol.* 7 (1), 46–60.
- Williams, B., Macdonald, T. M., Morant, S., Webb, D. J., Sever, P., McInnes, G., et al. (2015). Spironolactone versus Placebo, Bisoprolol, and Doxazosin to Determine the Optimal Treatment for Drug-Resistant Hypertension (PATHWAY-2): a Randomised, Double-Blind, Crossover Trial. *Lancet* 386 (10008), 2059–2068. doi:10.1016/S0140-6736(15)00257-3
- Zhang, X., Liang, C., Yin, J., Sun, Y., and Zhang, L. (2018). Identification of Metabolites of Liquiritin in Rats by UHPLC-Q-TOF-MS/MS: Metabolic Profiling and Pathway Comparison *In Vitro* and *In Vivo*. *RSC Adv.* 8 (21), 11813–11827. doi:10.1039/C7RA13760E
- Zhao, D., Duan, L. H., Wang, F. Y., Wang, M., Lu, H. G., Wu, Z. G., et al. (2012). Chiral Recognition of Doxazosin Enantiomers in 3 Targets for Therapy as Well as Adverse Drug Reactions in Animal Experiments. *Can. J. Physiol. Pharmacol.* 90 (12), 1623–1633. doi:10.1139/y2012-129
- Zhen, Y. Q., Kong, D. Z., Li, Q., Zhao, J., and Ren, L. M. (2013). Determination of Doxazosin Enantiomers in Rat Plasma and Investigation of Their Chiral Inversion. *Yao Xue Xue Bao* 48 (6), 901–905. doi:10.1016/j.jleo.2011.10.005

Conflict of Interest: The authors declare that the research was conducted in the absence of any commercial or financial relationships that could be construed as a potential conflict of interest.

Publisher's Note: All claims expressed in this article are solely those of the authors and do not necessarily represent those of their affiliated organizations or those of the publisher, the editors, and the reviewers. Any product that may be evaluated in this article, or claim that may be made by its manufacturer, is not guaranteed or endorsed by the publisher.

Copyright © 2022 Kong, Tian, Duan, Guo, Zhang, Zhang, Yang, Qin, Ren and Zhang. This is an open-access article distributed under the terms of the Creative Commons Attribution License (CC BY). The use, distribution or reproduction in other forums is permitted, provided the original author(s) and the copyright owner(s) are credited and that the original publication in this journal is cited, in accordance with accepted academic practice. No use, distribution or reproduction is permitted which does not comply with these terms.



Application of Physiologically Based Pharmacokinetic Modeling in Preclinical Studies: A Feasible Strategy to Practice the Principles of 3Rs

Yawen Yuan^{1,2†}, Qingfeng He^{1†}, Shunguo Zhang², Min Li¹, Zhijia Tang¹, Xiao Zhu¹, Zheng Jiao³, Weimin Cai^{1*} and Xiaoqiang Xiang^{1*}

¹Department of Clinical Pharmacy and Pharmacy Administration, School of Pharmacy, Fudan University, Shanghai, China,

²Department of Pharmacy, Shanghai Children's Medical Center, School of Medicine, Shanghai Jiao Tong University, Shanghai, China,

³Department of Pharmacy, Shanghai Chest Hospital, Shanghai Jiao Tong University, Shanghai, China

OPEN ACCESS

Edited by:

Shuiying Hu,
The Ohio State University,
United States

Reviewed by:

Yang Lu,
China Pharmaceutical University,
China
Yizhen Guo,
The Ohio State University,
United States

*Correspondence:

Weimin Cai
weimincai@fudan.edu.cn
Xiaoqiang Xiang
xiangxq@fudan.edu.cn

[†]These authors have contributed
equally to this work

Specialty section:

This article was submitted to
Drug Metabolism and Transport,
a section of the journal
Frontiers in Pharmacology

Received: 14 March 2022

Accepted: 14 April 2022

Published: 12 May 2022

Citation:

Yuan Y, He Q, Zhang S, Li M, Tang Z,
Zhu X, Jiao Z, Cai W and Xiang X
(2022) Application of Physiologically
Based Pharmacokinetic Modeling in
Preclinical Studies: A Feasible Strategy
to Practice the Principles of 3Rs.
Front. Pharmacol. 13:895556.
doi: 10.3389/fphar.2022.895556

Pharmacokinetic characterization plays a vital role in drug discovery and development. Although involving numerous laboratory animals with error-prone, labor-intensive, and time-consuming procedures, pharmacokinetic profiling is still irreplaceable in preclinical studies. With physiologically based pharmacokinetic (PBPK) modeling, the *in vivo* profiles of drug absorption, distribution, metabolism, and excretion can be predicted. To evaluate the application of such an approach in preclinical investigations, the plasma pharmacokinetic profiles of seven commonly used probe substrates of microsomal enzymes, including phenacetin, tolbutamide, omeprazole, metoprolol, chlorzoxazone, nifedipine, and baicalein, were predicted in rats using bottom-up PBPK models built with *in vitro* data alone. The prediction's reliability was assessed by comparison with *in vivo* pharmacokinetic data reported in the literature. The overall predicted accuracy of PBPK models was good with most fold errors within 2, and the coefficient of determination (R^2) between the predicted concentration data and the observed ones was more than 0.8. Moreover, most of the observation dots were within the prediction span of the sensitivity analysis. We conclude that PBPK modeling with acceptable accuracy may be incorporated into preclinical studies to refine *in vivo* investigations, and PBPK modeling is a feasible strategy to practice the principles of 3Rs.

Keywords: physiologically based pharmacokinetic modeling, 3Rs, preclinical studies, alternative for animal experiments, bottom-up model

1 INTRODUCTION

The pharmacokinetics study, including examining absorption, distribution, metabolism, and excretion (ADME) profiles of therapeutic agents, plays a vital role in drug discovery and development (Prentis et al., 1988). Because of poor extrapolation from *in vitro* to *in vivo* efficacy, pharmacokinetics profiling processes are routinely implemented in the pharmaceutical industry for early preclinical optimization (Lin and Lu, 1997). However, such processes commonly involve error-prone, labor-intensive, and time-consuming procedures. Not to mention ethics and the welfare of laboratory animals. It was estimated that more than 100 million laboratory animals were

sacrificed for biomedical research annually (Taylor and Alvarez, 2019). Therefore, William Russel and Rex Burch proposed the 3Rs principle (replacement, reduction, and refinement) in 1959 (Vitale et al., 2009; Wachsmuth et al., 2021), attempting to reduce animal use. The 2010 EU Directive states that animals have intrinsic values that need to be respected and that animal experiments should be carefully evaluated in biomedical research, with animal welfare considerations a top priority. Currently, the 3Rs have evolved into basic requirements for researchers to comply with based on animal welfare legislation. Several non-animal testings, including *in vitro* and *in silico* approaches describing the ADME properties, have also been developed to achieve high-throughput screening in drug development. However, unlike understanding the all-inclusive fate of compounds in the body through animal experiments, these conventional *in vitro* methods generally only cover a single-ADME process (Pelkonen and Turpeinen, 2007; Cascone et al., 2016). For example, the commonly used *in vitro* methods for studying drug absorption (Irvine et al., 1999; Verhoeckx et al., 2015; Dargó et al., 2019) or metabolism (Raunio et al., 2004; Hariparsad et al., 2006; Pelkonen and Turpeinen, 2007; van de Kerkhof et al., 2007), such as artificial biofilm models, cell models, and microsomal experiments. Similarly, *in silico* approaches, including the quantitative structure–activity relationship construction model (QSAR), were generally applied to predict the individual biological activity of candidate compounds such as apparent permeability (P_{app}), plasma protein binding rate, and apparent volume of distribution (V_{dss}) in the early drug discovery process (Ekins et al., 2000; Yamashita and Hashida, 2004; Lombardo et al., 2017). Despite the abundant data sources, a key challenge remains in correlating the *in vitro* results of ADME features to establish *in vivo* models to reflect the overall disposal.

PBPK modeling was raised back in 1937 and initially applied in predicting the distribution of environmental compounds in mammalian tissues (Lindstrom et al., 1974), and further gradually used for drug exposure prediction, dose extrapolation, and safety assessment (Andersen et al., 1987; Haddad et al., 2001; Meek et al., 2013; Li et al., 2021). PBPK modeling is a mathematical method following the material balance principle to predict the time course of xenobiotic levels in plasma and tissues based on the physiochemical and pharmacokinetic parameters of compounds (Nestorov, 2003). Tremendous progress has been made in PBPK modeling during the past decade. In addition to the rapidly gained industrial recognition (Rowland et al., 2011; Miller et al., 2019), PBPK analysis has also become a routine for the regulatory authorities, especially the United States Food and Drug Administration (FDA), upon new drug applications since 2016 (Zhang et al., 2020).

Currently, the PBPK model has been widely used in various stages of drug development (Chen et al., 2012; Huang et al., 2013), such as evaluating interspecies differences, drug–drug interactions (Jin et al., 2022), targeted tissue exposure, and disease effect (Rostami-Hodjegan and Tucker, 2007; Clewell and Clewell, 2008; Hans and Ursula, 2009; Rietjens et al., 2010; Mielke et al., 2011; Ball et al., 2014). In addition to the top–down modeling, many PBPK models have adopted *in vitro*

PK parameters for bottom–up modeling or experimental *in vivo* parameters for “middle-out” approaches as preliminary verification and model optimization (Rostami-Hodjegan and Tucker, 2007; Rietjens et al., 2010; Kostewicz et al., 2014; Templeton et al., 2018; Chang et al., 2019; Umehara et al., 2019). Moreover, given some mechanistic reasons (such as paracellular absorption, active absorption, and targeted transport), many bottom–up PBPK models still require animal data (Wagner, 1981; Clewell and Clewell, 2008). For example, the distribution parameters used in many PBPK models are tissue partition coefficients or steady state distribution parameters from *in vivo* experiments (Harrison and Gibaldi, 1977; Igari et al., 1983; S et al., 2007; T’jollyn et al., 2018). A few PBPK modelings are wholly constructed from *in vitro* parameters without *in vivo* parameters to be fitted and optimized, lacking universal application (Cheng and Ng, 2017). Therefore, constructing a universal PBPK model entirely only with *in vitro* data and the issue of estimating the predicted accuracy in the absence of *in vivo* PK data have caused widespread concern recently (Ellison, 2018; Paini et al., 2019).

To evaluate the feasibility of using PBPK modeling as an alternative for animal experiments, we developed bottom–up PBPK models solely with *in vitro* data using Simcyp® (Sheffield, United Kingdom) to predict the systemic disposition of seven commonly used liver microsomal enzyme probe substrates in rats. The reliability of each prediction was examined with sensitivity analysis. As a practice of 3Rs, this proof-of-concept study will shed light on the refinement of current drug development procedures and may reduce animal usage in drug development.

2 MATERIALS AND METHODS

2.1 Model Inputs Collection

Typical probe substrates of cytochrome P450 (CYP) 1A2, CYP2C9, CYP2C19, CYP2D6, CYP2E1, CYP3A4/5, and UDP-glucuronosyltransferase (UGT), namely, phenacetin, tolbutamide, omeprazole, metoprolol, chlorzoxazone, nifedipine, and baicalin were used as model drugs. The *in vitro* parameters were divided into three categories. Physical chemistry and blood binding-related parameters include molecular weight (MW), neutral species octanol: water partition coefficient ($\log P_{o:w}$), compound type (base/acid/mono/diprotic/ampholyte), negative decadic logarithm of the ionization constant of an acid (pK_a), blood to plasma partition ratio (B/P), and fraction unbound in plasma (f_u). Distribution is affected by the free fraction and the lipid solubility of the drug, which is related to the physiological characteristics mentioned, such as $\log P_{o:w}$, pK_a , and f_u . Parameters about absorption include apparent permeability coefficients (P_{app}), polar surface area (PSA), and hydrogen bond donors (HBD). *In vivo* elimination can be extrapolated via a well-stirred liver model together with the parallel tube model (Pang and Rowland, 1977) and the dispersion model (Iwatsubo et al., 1997) using *in vitro* metabolic data, including Michaelis–Menten constant for metabolism (K_m), maximum velocity for metabolism (V_{max}),

TABLE 1 | *In vitro* parameters used in each module of the PBPK model.

Application module	<i>In vitro</i> parameter	Unit	Acquisition method
Physical chemistry and blood binding	MW	g/mol	Calculation
	$\log P_{ow}$	—	<i>In vitro</i> measurement
	Compound type	Base/acid/mono/diprotic/ampholyte	Physicochemistry property
	pK_a	—	<i>In vitro</i> measurement ^a
	B/P	—	<i>In vitro</i> measurement
Absorption	f_u	—	<i>In vitro</i> measurement
	P_{app}	10^{-6} cm/s	<i>In vitro</i> experimentation ^b
	PSA	Å ²	Calculation or prediction
	HBD	—	Calculation or prediction
Elimination	CL _{int} (liver)	μl/min/mg protein	<i>In vitro</i> experimentation ^c
	CL _{int} (liver)	μl/min/10 ⁶ cells	<i>In vitro</i> experimentation ^d
	V_{max} , K_m , and $f_{u,inc}$ (liver)	pmol/min/mg protein, μM	<i>In vitro</i> experimentation ^c
	V_{max} , K_m , and $f_{u,inc}$ (liver)	pmol/min/10 ⁶ cells, μM	<i>In vitro</i> experimentation ^d
	CL _{int} (intestine)	μl/min/mg protein	<i>In vitro</i> experimentation ^e
	CL _{int} (intestine)	μl/min/g intestine	<i>In vitro</i> experimentation ^f
	V_{max} , K_m , and $f_{u,inc}$ (intestine)	pmol/min/mg protein, μM	<i>In vitro</i> experimentation ^e
	V_{max} , K_m , and $f_{u,inc}$ (intestine)	pmol/min/g intestine, μM	<i>In vitro</i> experimentation ^f

In vitro measurement of

^aIonization equilibrium constant.

^bInclude Caco-2 cell permeability experiment, MDCK II cell permeability experiment, and PAMPA (parallel artificial membrane permeability assay) experiment.

^cLiver microsome or liver S9 fraction (a post mitochondrial supernatant model containing both the microsomal enzymes and cytosolic fractions of the cell).

^dHepatocyte experimentation.

^eIntestinal microsome or intestinal S9 fraction.

^fIntestinal slice.

and intrinsic clearance (CL_{int}). Various *in vitro* data of model drugs collected from different literature and databases (DrugBank, PubChem, HSDB, TOXNET, etc.) were compiled in **Supplementary Table S1**, and the units of each parameter were uniformly converted.

2.2 Physiologically Based Pharmacokinetic Modeling

PBPK models were constructed with *in vitro* data alone using Simcyp® (Simcyp Rat Version 16, Certara, Sheffield, United Kingdom). The *in vitro* parameters used in the PBPK model are described in **Table 1**. The first-order one-compartment model was selected, and the gut was considered as a single compartment in this model. The permeability-limited basolateral membrane is assumed to mediate the absorption of drugs from enterocyte to the intestinal interstitial fluid, and effective permeability in rat (P_{eff}) was calculated based on its relationship with P_{eff} in human (Cao et al., 2006), which can be extrapolated from P_{app} , obtained from *in vitro* experiments (Sun et al., 2002; Tchapanian et al., 2008) or predicted using the PSA and HBD models (Winiwarter et al., 1998). Initially, our absorption model adopted the PSA and HBD models. A minimal PBPK model was selected to predict the volume of distribution at steady state (V_{ss}) with *in vitro* parameters of $\log P_{ow}$, compound type, and pK_a using mechanistic model 2 (Poulin and Theil, 2002; Berezhkovskiy, 2004; Rodgers et al., 2005; Rodgers and Rowland, 2007), which is a preset model in Simcyp. The tissue distribution was predicted using K_p scalar (tissue: plasma partition coefficient) based on a perfusion-limited model. The K_p scalar was selected as 1 by default in our model. The whole organ metabolic clearance pane was selected in the

elimination screen. The liver or intestinal clearance was extrapolated *via in vitro* metabolic data.

The drug plasma concentration–time profile and PK parameters {areas under the concentration–time curve to last time point [AUC_(0–t)], peak plasma concentration (C_{max}), and time to reach C_{max} (T_{max})} after orally administered single-dose of model drugs were predicted. Meanwhile, the PK process of some model drugs administrated with various doses was simulated.

2.2.1 Physiologically Based Pharmacokinetic Model for Phenacetin

The *in vitro* properties of phenacetin collected from various literatures and databases are listed in **Supplementary Table S1**. The reported f_u values ranged from 0.145 to 0.5. The metabolism of phenacetin by CYP1A2 is biphasic in microsome experiments (Kahn et al., 1987). Since the hepatic CL_{int} collected from reported microsome experiments varied widely (0.086–100 μl/min/mg protein), we selected the median value of f_u (0.3225) and hepatic CL_{int} (27 μl/min/10⁶ cells, 20.7–78 μl/min/10⁶ cells) from hepatocyte experiments as input values in our model. The *in vitro* data parameterized in phenacetin PBPK model are tabulated in **Table 2**. The simulated results of phenacetin after oral administration of 20, 10, and 5 mg/kg in rats were evaluated.

2.2.2 Physiologically Based Pharmacokinetic Model for Tolbutamide

Tolbutamide is mainly eliminated by CYP2C9 in human liver, and by CYP2C6 and CYP2C11 in rats to produce hydroxyl tolbutamide. f_u of tolbutamide varied from 0.0201 to 0.268 (listed in **Supplementary Table S1**), with the calculated

TABLE 2 | Input parameters in the PBPK models.

Parameter/Compound	Phenacetin	Tolbutamide	Omeprazole	Metoprolol	Chlorzoxazone	Nifedipine	Baicalein
MW (g/mol)	179.2	270.35	345.42	267.4	169.56	346.3	270.24
log P_{ow}	1.58	2.34	2.23	2.06	1.6	2.2	1.7
Compound type	Neutral	Monoprotic acid	Ampholyte	Monoprotic base	Monoprotic acid	Monoprotic base	Monoprotic acid
pK _{a1}	/	5.16	8.8	9.7	8.3	2.82	5.4
pK _{a2}	/	/	4.2	/	/	/	/
B/P	1	1.33	0.66	1	1.22	0.59	1.27
f_u	0.32	0.048	0.19	0.86	0.27	0.038	0.054
PSA (Å ²)	38.33	80.65	86.7	50.7	38.3	110	87
HBD	1	2	1	2	1	1	3
CL _{int} (LM) (μl/min/mg protein)	27 (μl/min/10 ⁶ cells)	4.7	158	32	14.9	139	436
CL _{int} (IM) (μl/min/mg protein)	/	/	/	10.5	/	6.4	298
V _{max} (IM) (pmol/min/mg)	0.25	/	780	/	/	/	/
K _m (IM) (μM)	56.7	/	6.97	/	/	/	/
$f_{u inc}$ (IM)	1	/	1	/	/	/	/

"/" means no input value exists.

median value to be 0.048. The CL_{int} ranged between 2.72 and 8.10 μl/min/mg protein from various literatures and the median of 4.7 μl/min/mg protein was applied in the PBPK model. The same process was performed for other parameters in **Table 2**. The PK parameters of tolbutamide at 50 mg/kg in rats were predicted.

2.2.3 Physiologically Based Pharmacokinetic Model for Omeprazole

As shown in **Supplementary Table S1**, various *in vitro* data were collected and the deviation of the reported *in vitro* parameters from different sources was slight. Omeprazole is rapidly absorbed in rats and the elimination is almost entirely through hepatic and intestinal metabolism *via* CYP2C19 (Regårdh et al., 1985; Paul, 1991). The penetration of omeprazole into the red cells is low with the value of B/P at 0.6–0.8 and the f_u is about 15% in rat plasma. Similarly, the median values of parameters were calculated for model construction (**Table 2**). Plasma concentration over time in rats following oral administration of omeprazole at 10, 20, and 40 mg/kg was predicted, respectively.

2.2.4 Physiologically Based Pharmacokinetic Model for Metoprolol

The elimination of metoprolol *in vivo* is mainly through liver CYP2D6 in human, leading to extensive first-pass effect and low bioavailability. In addition to CYP2D6, CYP3A also participates in the metoprolol metabolism in rats. As shown in **Supplementary Table S1**, f_u ranged from 0.8 to 0.925, the range of CL_{int} [liver microsomes (LM)] was 17.1–59.9 μl/min/mg protein and the range of CL_{int} [intestine microsomes (IM)] was 7.37–14.7 μl/min/mg protein. The median value of varied parameters was calculated as input parameters in **Table 2**. The disposition process of metoprolol in rats after oral administration of 2.5, 5, and 20 mg/kg was predicted.

2.2.5 Physiologically Based Pharmacokinetic Model for Chlorzoxazone

Chlorzoxazone is the probe substrate of CYP2E1. As shown in **Supplementary Table S1**, the value of f_u ranged from 0.046 to 0.373 and the CL_{int} was from 5.00 to 38.8 μl/min/mg protein. The

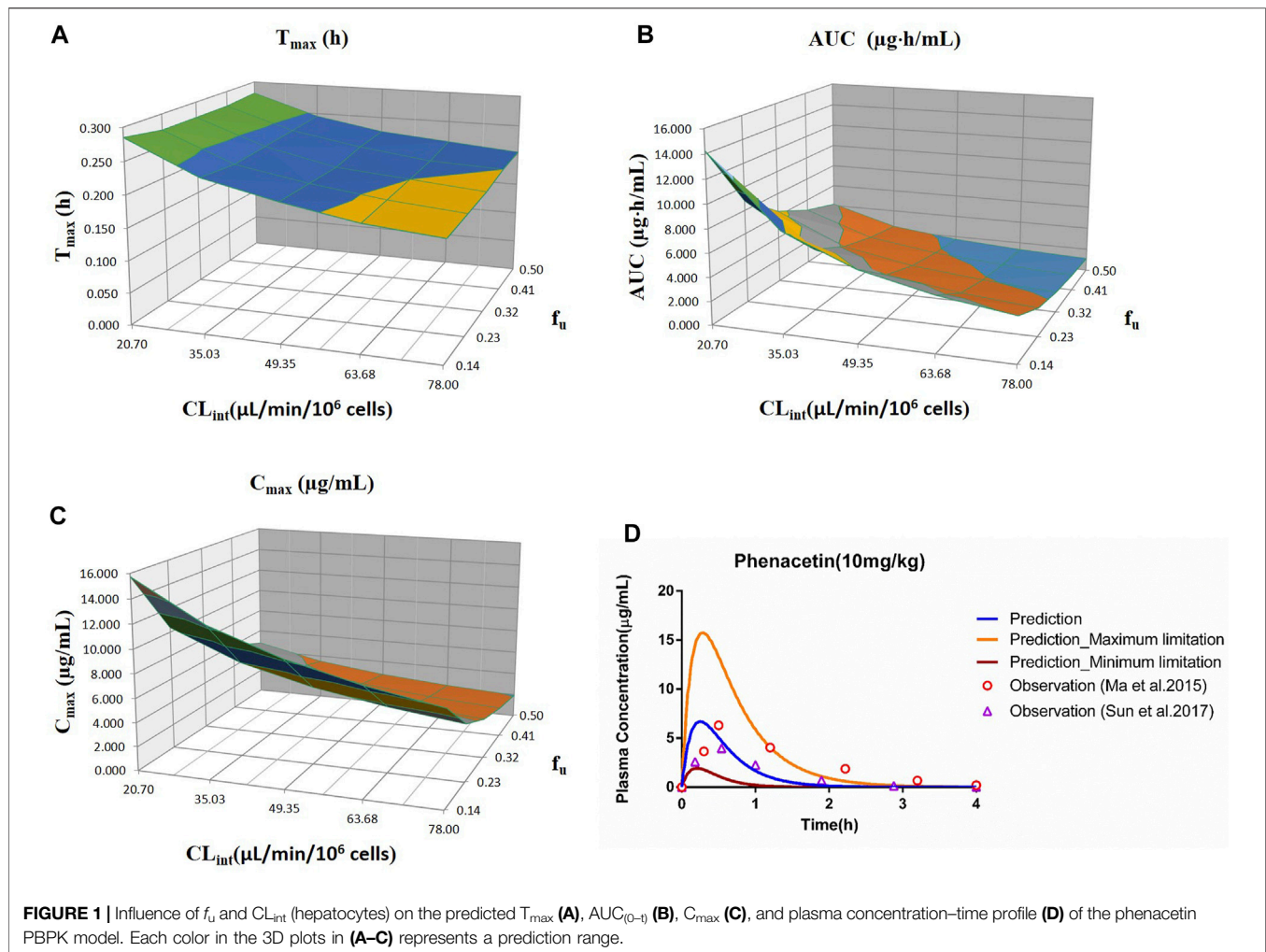
value of other parameters collected from different sources was relatively consistent. Similarly, the median value was taken as the input value in **Table 2**. Since a dose of 50 mg/kg was frequently used in the PK studies of chlorzoxazone in rats, the PK parameters of chlorzoxazone following oral administration of 50 mg/kg were predicted.

2.2.6 Physiologically Based Pharmacokinetic Model for Nifedipine

Nifedipine is mainly metabolized by CYP 3A1/2 in human and CYP 3A4/5 in rats. As shown in **Supplementary Table S1**, the value of f_u was 0.01–0.08, and the median value was calculated for input. The clearance of nifedipine was found related to concentration (Iwao et al., 2002). The CL_{int} in the liver was 159 μl/min/mg protein when the concentration was 1–5 μM, which was reduced to 119 μl/min/mg protein when the concentration ranged from 5 to 100 μM and eventually dropped to 10 μl/min/mg protein with concentration higher than 100 μM. The value of CL_{int} of small intestinal metabolism was estimated at 6.4 μl/min/mg protein when the concentration was lower than 5 μM and reduced to 2.8 μl/min/mg protein as the concentration was increased to 100 μM. Since the concentration in the liver was unlikely to be higher than 100 μM, the median of hepatic CL_{int} was calculated to be 139 μl/min/mg protein with the ignorance of the lowest value at 10 μl/min/mg protein. The median of CL_{int} of small intestinal metabolism was also calculated for the PBPK model (**Table 2**). The PK parameters of nifedipine in rats after oral administration of 3, 5, and 6 mg/kg were predicted.

2.2.7 Physiologically Based Pharmacokinetic Model for Baicalein

Baicalein, a bioactive flavonoid presented in the root of *Scutellaria baicalensis*, is isolated from traditional Chinese medicine “Huang Qin.” Baicalein was reported to be subjected to extensive first-pass metabolism due to the conjugated process by UGT in the liver and intestine. Few *in vitro* data were reported (listed in **Supplementary Table S1**), and the median value was calculated for model construction (shown in **Table 2**). The PK parameters of

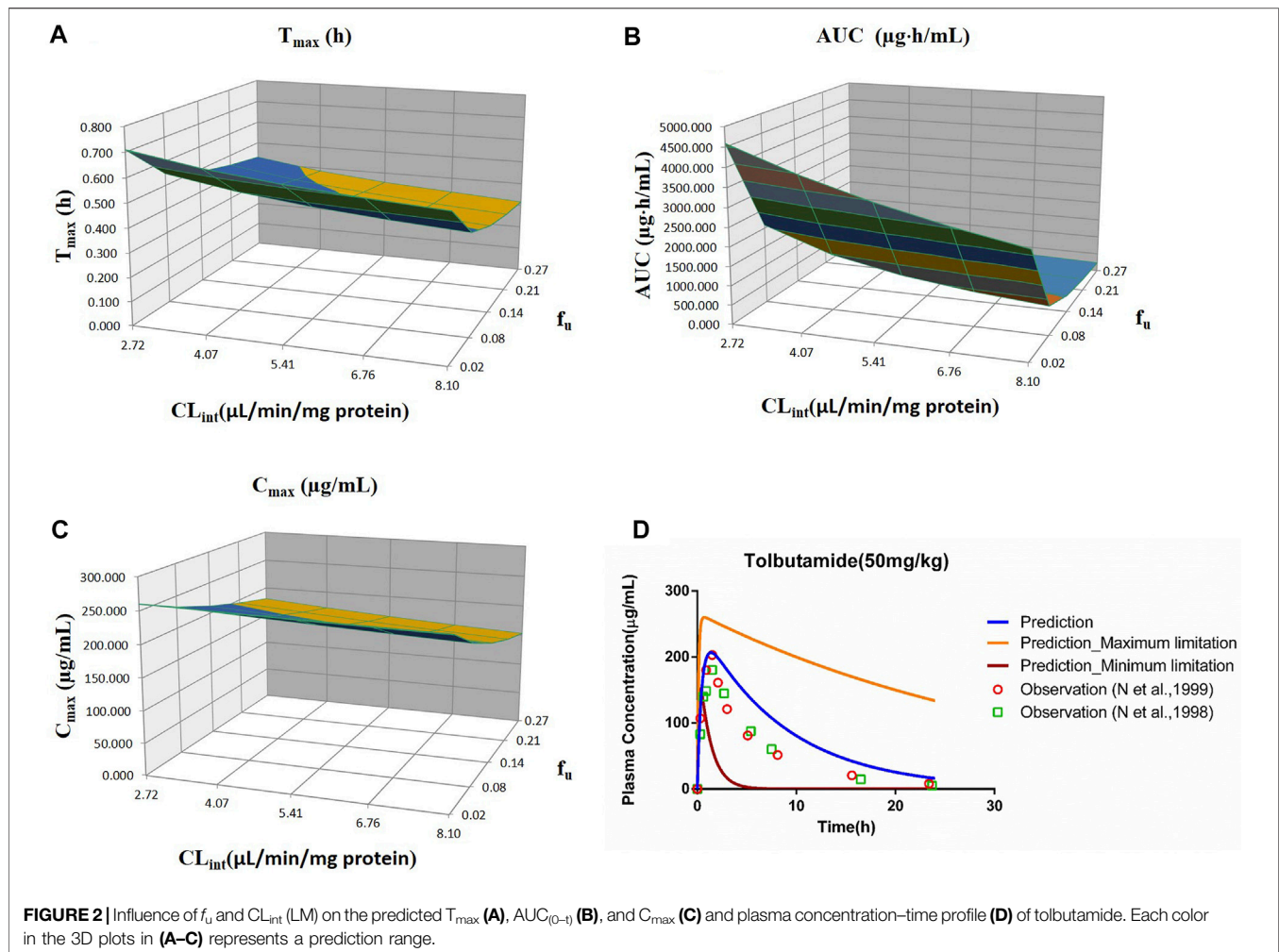


baicalein in rats after oral administration of 121 mg/kg were predicted.

2.3 Pharmacokinetic Data

PK parameters ($AUC_{(0-t)}$, C_{max} , and T_{max}) of model drugs in rats orally administrated with a different single-dose of the drugs were assembled from the literature. The $AUC_{(0-t)}$, C_{max} , and T_{max} units were unified as $\mu\text{g}\cdot\text{h}/\text{ml}$, $\mu\text{g}/\text{ml}$, and h, respectively. The observed drug plasma concentration–time data were extracted from concentration–time course curves using the GetData software (version 2.24, <http://getdata-graph-digitizer.com>). Multiple records of PK parameters of model drugs were summarized in **Supplementary Table S2**, showing significant variations on PK parameters, with those of reasonable trend from different doses selected to validate prediction accuracy. For example, it was found that the PK parameters of tolbutamide from the literature varied considerably. Interestingly, the values of C_{max} and $AUC_{(0-t)}$ at high doses were lower than low doses for some records (C_{max} : 91.1–151 $\mu\text{g}/\text{ml}$ at 20 mg/kg vs. 40.46 $\mu\text{g}/\text{ml}$ at 30 mg/kg, $AUC_{(0-t)}$: 761.7217–1,393 $\mu\text{g}\cdot\text{h}/\text{ml}$ at 20 mg/kg vs. 183.88 $\mu\text{g}\cdot\text{h}/\text{ml}$ at 20 mg/kg), and T_{max} also varied greatly (0.

89–7.1 h). The relatively consistent PK value at a 50 mg/kg dose was finally selected for the tolbutamide PBPK model accuracy evaluation. Meanwhile, it is difficult to detect baicalein's plasma concentration because of the complicated *in vivo* disposition, poor bioavailability, and extensive metabolism, leading to a considerable variation among the PK parameters. The ones after oral administration of 121 mg/kg were selected due to relatively consistent values (shown in **Supplementary Table S2**). Moreover, it was found to be partly due to the species, age, and gender differences of the rats and formulations. For example, it was reported that the $AUC_{(0-t)}$ and C_{max} of metoprolol were 5–7 times higher and 2 times higher in DA (Dark Agouti) rats and Sprague–Dawley rats, respectively, than those in Wistar rats after oral administration of 5 mg/kg (Belpaire et al., 1990; Komura and Iwaki, 2005; Wang et al., 2014; Ma et al., 2015; Sun et al., 2017). The $AUC_{(0-t)}$ of baicalein was 11.7 times higher after oral administration of baicalein–nicotinamide nano-cocrystals than coarse powder, 7.1 times higher than that of baicalein nanocrystals, and 1.8 times higher than that of baicalein–nicotinamide cocrystals (Pi et al., 2019). As a result, our PBPK model was constructed using male



Sprague–Dawley rats as the model animal with coarse powder form selected.

2.4 Sensitivity Analysis

As shown in **Supplementary Table S1**, physical chemistry properties such as $\log P_{ow}$, compound type, pK_a , and B/P and the predicted or calculated properties (MW, PSA, and HBD) were commonly consistent, while the f_u and CL_{int} (LM or hepatocytes) values obtained from the literature varied. To further explore the reliability of the PBPK model, the effect of f_u and CL_{int} (LM or hepatocytes) was investigated. The sensitivity analysis of f_u and CL_{int} (LM or hepatocytes) was determined *via* comparing the predicted results of PBPK models, which were constructed using the range values of f_u and CL_{int} (LM or hepatocytes) with all the other factors maintained constant. The uncertainty range of the PBPK model was defined as the predicted range of the PK parameters in the sensitivity analysis. The sensitivity results were plotted *via* Simcyp and showed in **Figures 1–7**. In order to make the 3D plots in A–C in **Figures 1–7** more clearly distinguished, the predicted values were divided into 5–8 range values at the same interval, and each range was displayed as a color. Since the colors are numerous and have no special meaning, they are not specifically listed in the figures.

2.5 Model Validation

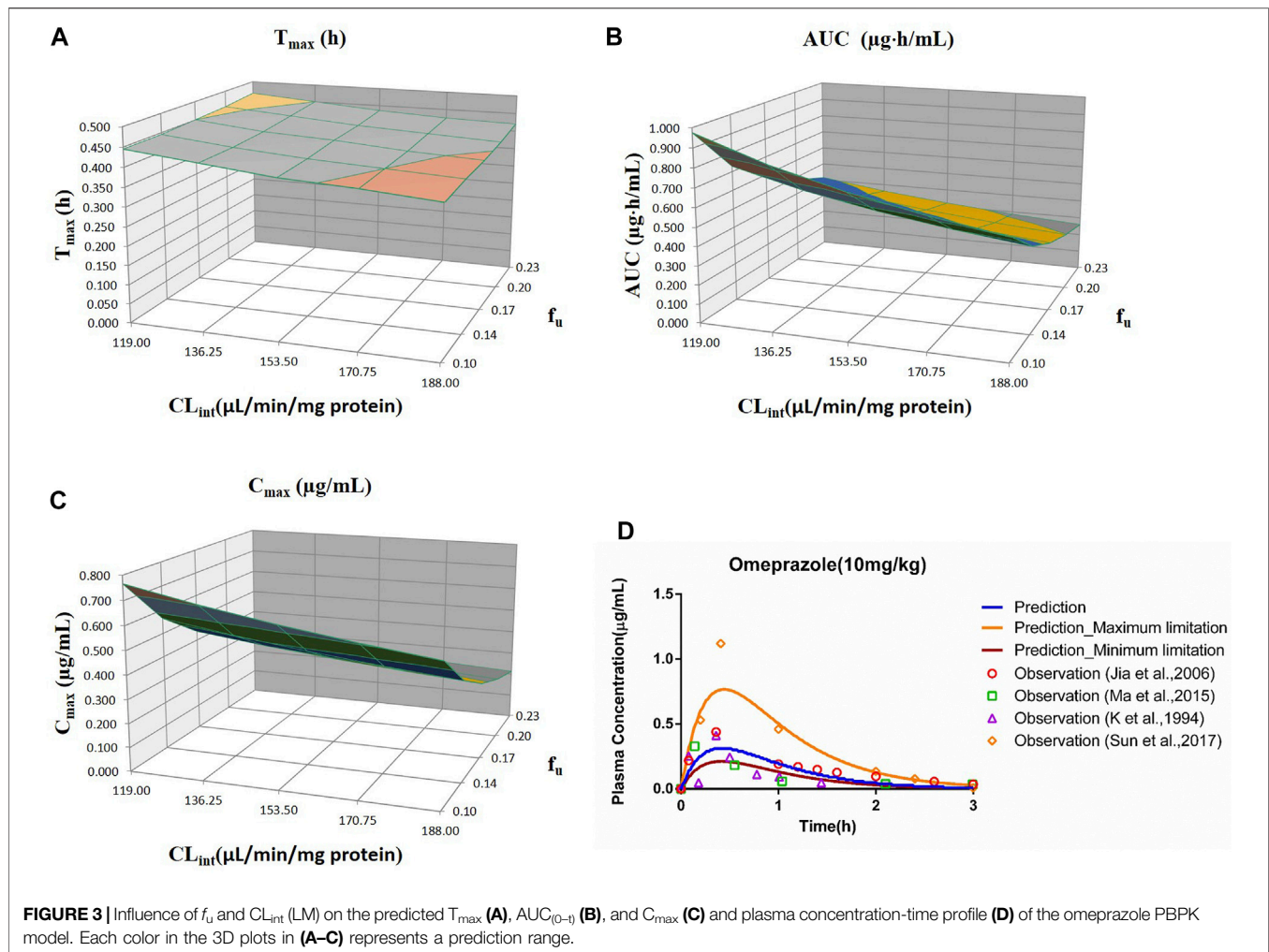
To verify the prediction accuracy of the PBPK model, we compared the predicted parameters with the experimental data, and fold error was introduced to measure the deviation. The fold error is the ratio between the predicted PK parameters and the corresponding observed values (shown in **Eqs. 1, 2**). The accuracy of the prediction results increases as the fold error decreases. The simulation is considered acceptable with a fold error of less than 2 (De Buck et al., 2007; Yamazaki et al., 2011).

$$\text{fold error} = \frac{\text{observed parameter}}{\text{predicted parameter}}; \text{ if observed value} > \text{predicted value} \quad (1)$$

$$\text{fold error} = \frac{\text{predicted parameter}}{\text{observed parameter}}; \text{ if predicted value} > \text{observed value.} \quad (2)$$

2.6 Model Performance

R^2 , mean absolute error (MAE), and root mean squared error (RMSE) were applied to evaluate the overall performance of the PBPK model. The equations are presented as follows (**Eqs. 3–5**). The lower the value of MAE and RMSE and the closer of R^2 to 1, the



better the performance of the PBPK model. The performance of the models was plotted using the GraphPad Prism software (version 6).

$$R^2 = 1 - \frac{\sum_i (x_i - y_i)^2}{\sum_i (x_i - \bar{x})^2}, \quad (3)$$

$$MAE = \frac{\sum_1^N |x_i - y_i|}{N}, \quad (4)$$

$$RMSE = \sqrt{\frac{\sum_1^N (x_i - y_i)^2}{N}}. \quad (5)$$

x_i and y_i are the observed and the predicted concentrations, respectively, \bar{x} is the average of the observed values, and N is the number of data points.

3 RESULTS

3.1 Physiologically Based Pharmacokinetic Model-Predicted Results

PBPK models for probe drugs (phenacetin, tolbutamide, omeprazole, metoprolol, chlorzoxazone, nifedipine, and baicalin)

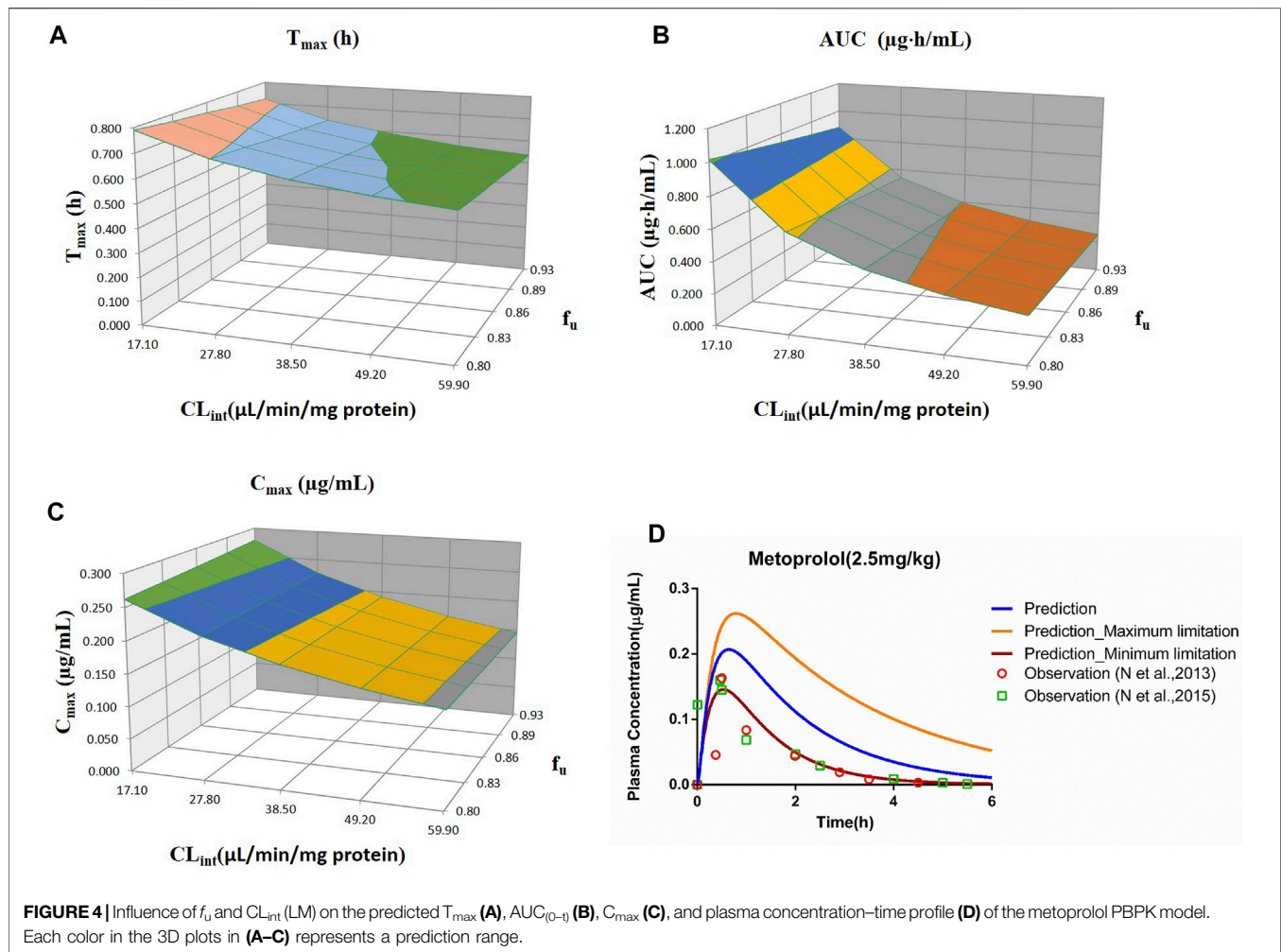
were constructed using *in vitro* parameters (MW, $\log P_{ow}$, compound type, pK_a , B/P, f_u , PSA, HBD, CL_{int} , V_{max} , K_m , and $f_{u,inc}$). The predicted results of each drug were presented later, and the PK curves are displayed in **Supplementary Figures S1–S7**.

3.1.1 Phenacetin

The predicted results of the phenacetin PBPK model are shown in **Table 3**. Although the predicted C_{max} was slightly higher than the observed one with the fold error of 1.93 at 5 mg/kg, the fold error values were all within the threshold of 2, indicating good simulation performance. Meanwhile, the predicted data were slightly higher than the observed ones at 5 mg/kg, while other observed points were around the predicted values at 10 and 20 mg/kg (**Supplementary Figure S1**). It could be concluded that the experimental CL_{int} value used in the model was underestimated at 5 mg/kg.

3.1.2 Tolbutamide

The prediction results are listed in **Table 4**. The fold error values were all less than 2 with the observed data around the predicted curve (**Supplementary Figure S2**), suggesting acceptable prediction accuracy.



3.1.3 Omeprazole

The predicted PK parameters of the omeprazole PBPK model were compared with the multiple records of experimental parameters (shown in Table 5). Although a few predicted values were slightly lower than the observed ones, most fold errors fell within 2, indicating good predicted accuracy. **Supplementary Figure S3** showed that most of the predicted points were around the observed concentration-time profile.

3.1.4 Metoprolol

The fold errors of the predicted parameters of the metoprolol PBPK model are evaluated in Table 6. The values of fold error in the 10 mg/kg group were less than 2, and the trend of the observed data coordinated the predicted profile (**Supplementary Figure S4**), indicating good simulation performance. Overall, all predicted concentration curves were slightly higher than the observation points, which is contributed by underestimating distribution and elimination.

3.1.5 Chlorzoxazone

The predicted results of the chlorzoxazone PBPK model are tabulated in Table 7. Most fold errors of predicted parameters

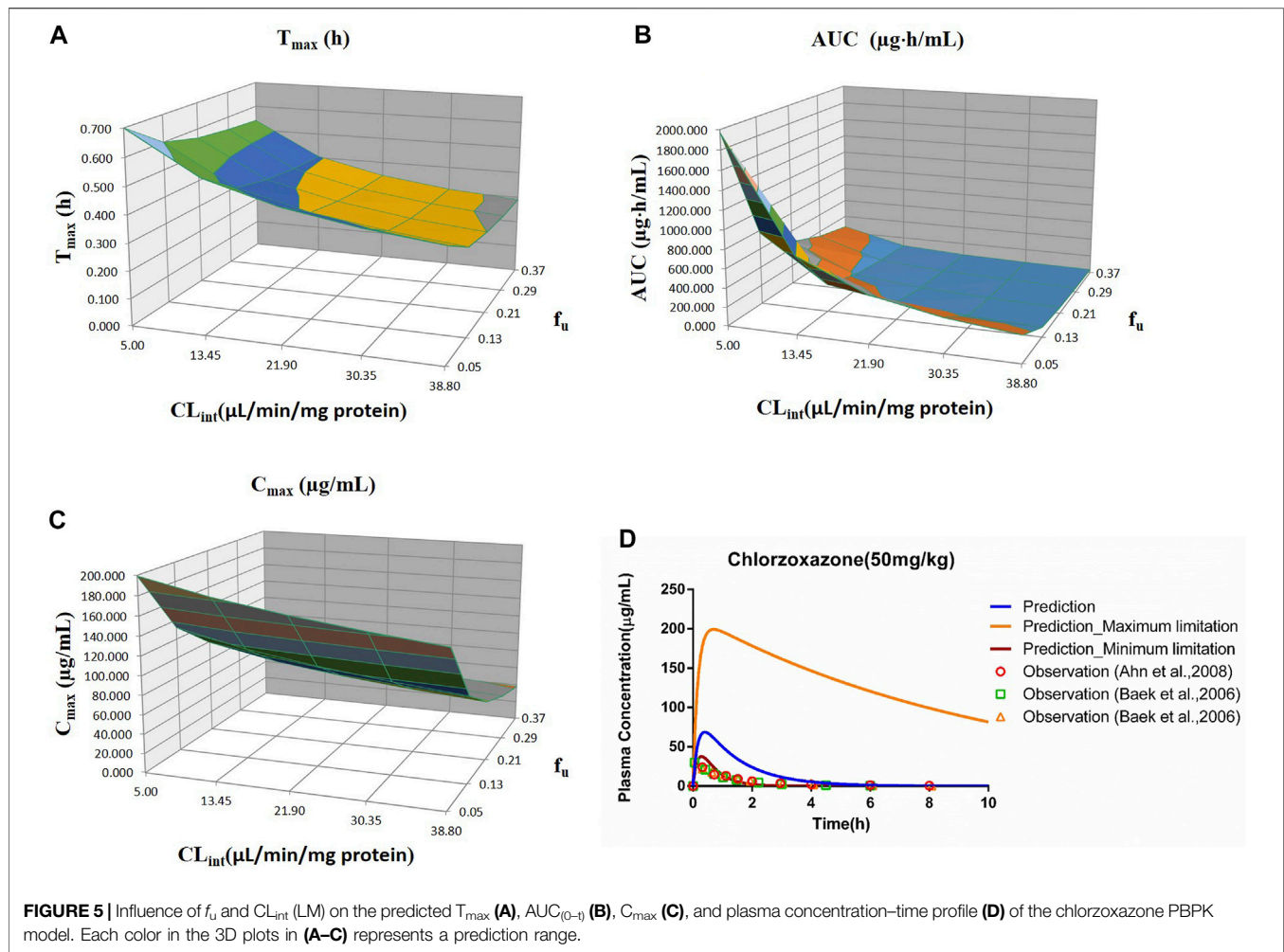
were larger than 2. The predicted curve was higher and deviated from the observed data (**Supplementary Figure S5**), which could be related to the underestimation of distribution and elimination. The influence of the two characteristics on the PBPK model will be further explored in the sensitivity analysis.

3.1.6 Nifedipine

The predicted results of the nifedipine PBPK model are shown in Table 8. The fold error of C_{max} and $AUC_{(0-t)}$ mainly were within 2, indicating acceptable prediction performance. Although the difference between predicted T_{max} and the observed values was more than 2 times (2.16 times), with a significant individual variation between the measured values of T_{max} (0.08–1.5 h), the fold errors of C_{max} and $AUC_{(0-t)}$ were within 2, indicating good prediction accuracy. As shown in **Supplementary Figure S6**, the predicted concentration curve was slightly shifted due to the difference in T_{max} at 5 mg/kg, while the observed dots were close to the predicted ones at 3 and 6 mg/kg.

3.1.7 Baicalein

The simulation results are shown in Table 9. The predicted curve is shown in **Supplementary Figure S7**. Although the predicted



C_{max} was slightly lower than the observed one, the fold errors were within 2. The observed PK data spread around the predicted profile, suggesting good prediction performance.

3.2 Sensitivity Analysis

The sensitivity analysis of f_u and CL_{int} (LM or hepatocytes) was evaluated with other factors maintained constant. The variation spans of f_u and CL_{int} (LM or hepatocytes) from various literatures are listed in Table 10. The uncertainty of the PBPK model-predicted results was estimated based on the range of f_u and CL_{int} (LM or hepatocytes) obtained from various literatures.

3.2.1 Phenacetin

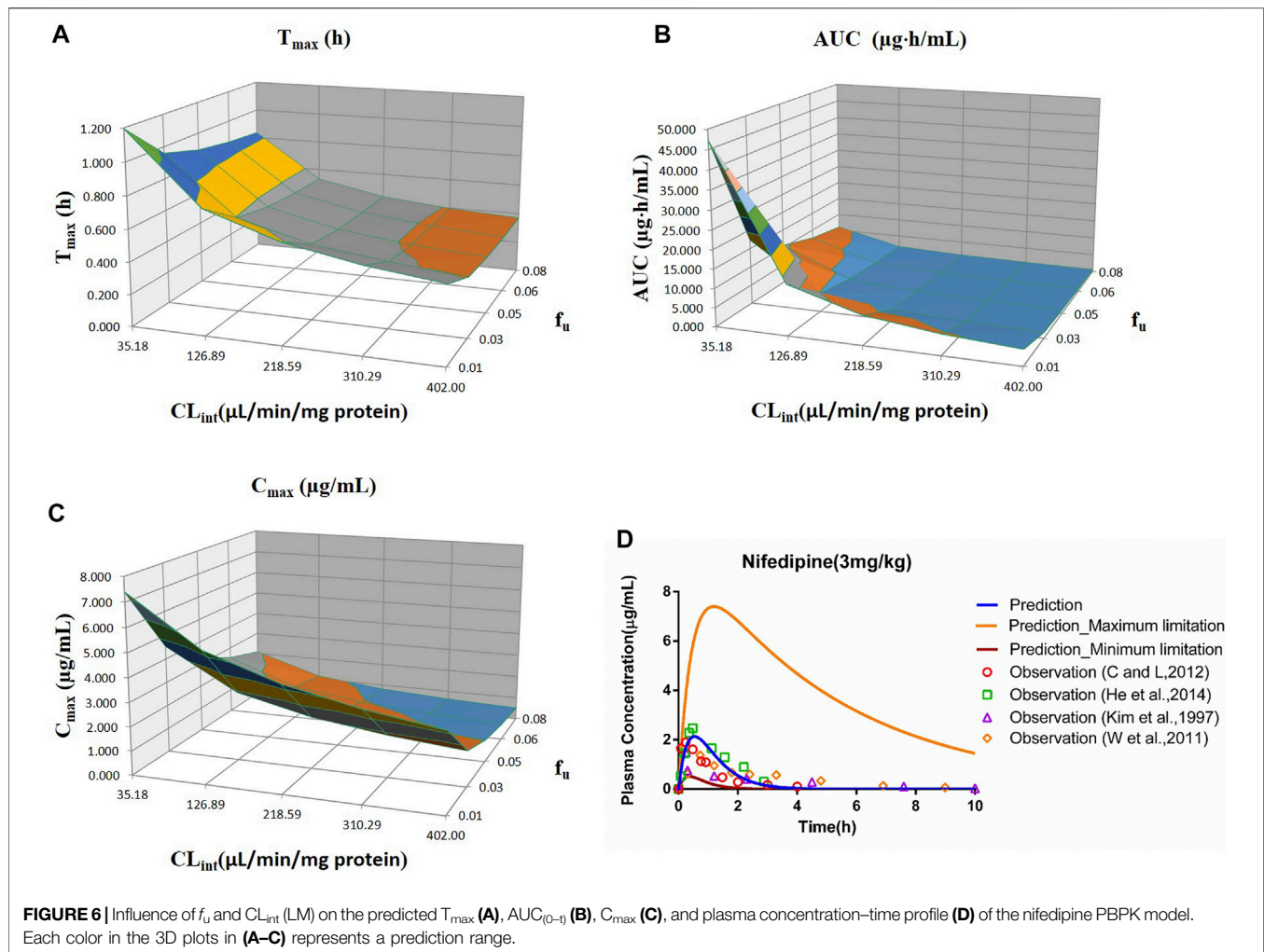
The sensitivity analysis of f_u (0.145–0.5) and CL_{int} (hepatocytes: 20.7–78 $\mu\text{L}/\text{min}/10^6$ cells) for the phenacetin PBPK model was performed at 10 mg/kg (shown in Figure 1). The predicted value of T_{max} , C_{max} , and $AUC_{(0-t)}$ ranged from 0.18 to 0.28 h, 1.93 to 15.74 $\mu\text{g}/\text{mL}$, and 1.10 to 14.25 $\mu\text{g}\cdot\text{h}/\text{mL}$, respectively. Most concentration points are within the uncertainty range.

3.2.2 Tolbutamide

The sensitivity analysis of f_u (0.0201–0.268) and CL_{int} (LM: 2.72–8.1 $\mu\text{L}/\text{min}/\text{mg}$ protein) was investigated for the tolbutamide PBPK model at 50 mg/ml (shown in Figure 2). As a result, the predicted T_{max} , C_{max} , and $AUC_{(0-t)}$ ranged from 0.32 to 0.71 h, 152.72 to 260.15 $\mu\text{g}/\text{mL}$, and 231.67 to 4,587.60 $\mu\text{g}\cdot\text{h}/\text{mL}$, respectively. The observed points were in the area between the median prediction curve and the lowest prediction curve (CL_{int} = 8.1 $\mu\text{L}/\text{min}/\text{mg}$ protein, f_u = 0.27).

3.2.3 Omeprazole

The range of f_u (0.105–0.232) and CL_{int} (LM: 119–188 $\mu\text{L}/\text{min}/\text{mg}$ protein) was applied for the sensitivity analysis of the omeprazole PBPK model at 10 mg/kg (shown in Figure 3). The results showed that the predicted T_{max} , C_{max} , and $AUC_{(0-t)}$ ranged from 0.38 to 0.46 h, 0.21 to 0.77 $\mu\text{g}/\text{mL}$, and 0.26 to 0.98 $\mu\text{g}\cdot\text{h}/\text{mL}$, respectively. As shown in Figure 3D, most observation dots were in the sensitivity prediction range.



3.2.4 Metoprolol

The sensitivity analysis of f_u (0.80–0.925) and CL_{int} (LM: 17.1–59.9 $\mu\text{L}/\text{min}/\text{mg}$ protein) was determined for the metoprolol PBPK model at 2.5 mg/kg in **Figure 4**. The predicted range of T_{max} , C_{max} , and $AUC_{(0-t)}$ were 0.54–0.79 h, 0.15–0.28 $\mu\text{g}/\text{mL}$, and 0.25–1.02 $\mu\text{g}\cdot\text{h}/\text{mL}$, respectively. It is illustrated in **Figure 4D** that the observation data were close to the lowest predicted curve.

3.2.5 Chlorzoxazone

Sensitivity analysis of the chlorzoxazone PBPK model was performed at 50 mg/kg with the f_u ranging from 0.046 to 0.373 and CL_{int} (LM) from 5 to 38.8 $\mu\text{L}/\text{min}/\text{mg}$ protein (shown in **Figure 5**). The results showed the predicted T_{max} , C_{max} , and $AUC_{(0-t)}$ ranged from 0.29 to 0.70 h, 37.69 to 199.27 $\mu\text{g}/\text{mL}$, and 34.69 to 1970.18 $\mu\text{g}\cdot\text{h}/\text{mL}$, respectively. The observation dots were around the lowest prediction curve (Prediction_Minimum limitation curve), as shown in **Figure 5D**.

3.2.6 Nifedipine

The sensitivity analysis of f_u (0.01–0.08) and CL_{int} (LM: 35.18–402 $\mu\text{L}/\text{min}/\text{mg}$ protein) was investigated for the nifedipine PBPK model at 3 mg/kg (shown in **Figure 6**). The predicted T_{max} , C_{max} , and $AUC_{(0-t)}$ ranged from 0.36 to 1.20 h, 0.51 to 7.40 $\mu\text{g}/\text{mL}$, and 0.52 to 47.27 $\mu\text{g}\cdot\text{h}/\text{mL}$, respectively. The observation points were centered on the median prediction curve, as shown in **Figure 6D**.

3.2.7 Baicalein

The sensitivity analysis of f_u and CL_{int} (LM) was performed with the range from 0.029 to 0.0791 and 338.9 to 574.11 $\mu\text{L}/\text{min}/\text{mg}$ protein for the baicalein PBPK model at 121 mg/kg (shown in **Figure 7**). The results showed the predicted T_{max} , C_{max} , and $AUC_{(0-t)}$ ranged from 0.19 to 0.36 h, 0.59 to 2.08 $\mu\text{g}/\text{mL}$, and 0.51 to 2.36 $\mu\text{g}\cdot\text{h}/\text{mL}$, respectively. As illustrated in **Figure 7D**, observation dots were within the sensitivity prediction range.

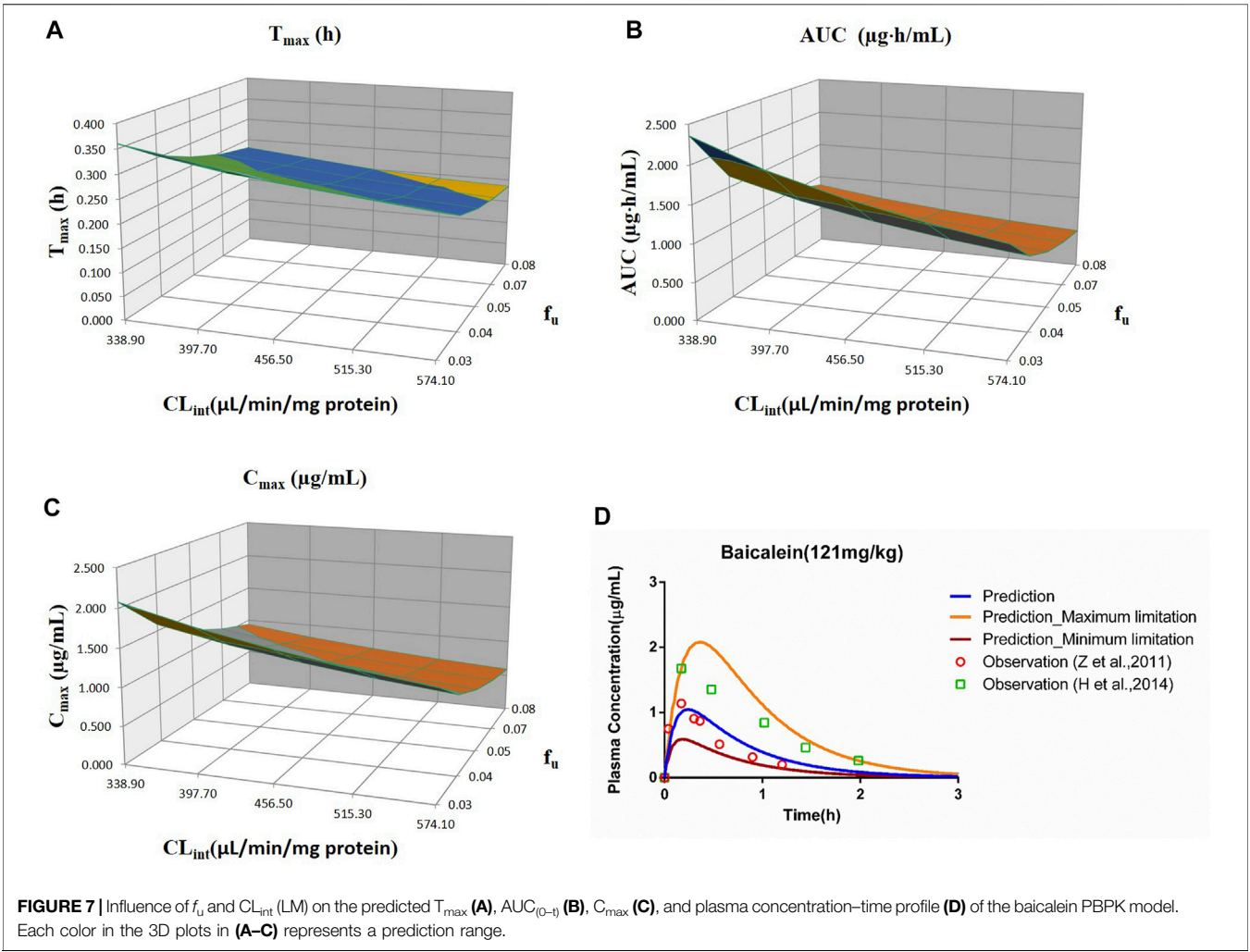


TABLE 3 | Comparison between the predicted and the observed PK parameters of the phenacetin PBPK model.

Dose		T_{max} (h)	C_{max} ($\mu\text{g}/\text{ml}$)	$AUC_{(0-t)}$ ($\mu\text{g}\cdot\text{h}/\text{ml}$)	Reference
5 mg/kg	Prediction	0.25	3.34	2.47	—
	Observation	0.33–0.50	1.73	1.52	Zhou et al. (2014)
	Fold error	1.31–2.00	1.93	1.62	—
10 mg/kg	Prediction	0.25	6.69	4.95	—
	Observation 1	0.50	6.28 ± 1.94	9.79 ± 3.58	Ma et al. (2015)
	Fold error	1.98	1.07	1.98	—
	Observation 2	—	3.94 ± 0.81	4.69 ± 0.86	Sun et al. (2017)
	Fold error	—	1.70	1.06	—
20 mg/kg	Prediction	0.25	13.37	9.90	—
	Observation	0.25	9.00	13.12	Welch et al. (1976)
	Fold error	1.01	1.49	1.33	—

3.3 Physiologically Based Pharmacokinetic Model Performance

The fold errors are summarized in **Figure 8**. Furthermore, to evaluate the overall performance of the PBPK model, we compared the prediction concentration data with the observed ones ($n = 390$, shown in **Figure 9**). Moreover, the prediction

performance of the PBPK model with absorption module using PSA and HBD was compared with that using P_{app} from *in vitro* experiments (Caco-2 experimentation). The input of P_{app} was also applied to the median data of the various values. As shown in **Table 11**, the model performance using PSA and HBD, with a lower value of MAE and RMSE and higher value of R^2 , was better

TABLE 4 | Comparison between the predicted PK parameters of the tolbutamide PBPK model and the observed PK parameters at 50 mg/kg.

50 mg/kg p.o.	T _{max} (h)	C _{max} (μg/ml)	AUC _(0-t) (μg•h/ml)	Reference
Prediction	1.38	206.74	1965.99	—
Observation 1	0.91 ± 0.37	232.00 ± 35.00	1,309.00 ± 40.00	Nishimura et al. (1999)
Fold error	1.51	1.12	1.50	—
Observation 2	1.42 ± 0.56	176.00 ± 37.20	1,228.00 ± 153.00	Nishimura et al. (1998)
Fold error	1.03	1.17	1.60	—

TABLE 5 | Comparison between the predicted PK parameters of the omeprazole PBPK model and the observed PK parameters.

	Dose	T _{max} (h)	C _{max} (μg/ml)	AUC _(0-t) (μg•h/ml)	Reference
10 mg/kg	Prediction	0.42	0.31	0.38	—
	Observation 1	0.36 ± 0.22	0.44 ± 0.12	0.59 ± 0.14	Jia et al. (2006)
	Fold error	1.16	1.40	1.55	—
	Observation 2	0.10 ± 0.10	0.33 ± 0.01	0.47 ± 0.13	Ma et al. (2015)
	Fold error	4.20	1.07	1.24	—
	Observation 3	0.21 ± 0.02	0.50 ± 0.12	0.29 ± 0.07	Kazuhide et al. (1994)
	Fold error	2.00	1.60	1.32	—
	Observation 4		1.13 ± 0.18	1.13 ± 0.16	Sun et al. (2017)
20 mg/kg	Fold error		3.60	2.97	—
	Prediction	0.40	0.81	0.96	—
	Observation 1	0.25 ± 0.02	1.43 ± 0.38	0.86 ± 0.15	Kazuhide et al. (1994)
	Fold error	1.58	1.77	1.11	—
	Observation 2	0.25 ± 0.00	1.01 ± 0.17	0.73 ± 0.06	Watanabe et al. (2002)
	Fold error	1.58	1.25	1.31	—
	Observation 3	0.50 ± 0.00	2.01 ± 0.14	1.50 ± 0.08	Singh and Asad (2010)
	Fold error	1.26	2.49	1.57	—
40 mg/kg	Prediction	0.37	2.88	3.26	—
	Observation 1	0.29 ± 0.22	2.11 ± 0.99	1.57 ± 0.54	Lee et al. (2009)
	Fold error	1.27	1.36	2.08	—
	Observation 2	0.17 ± 0.09	2.61 ± 0.55	2.10 ± 0.93	Young et al. (2007)
	Fold error	2.23	1.10	1.55	—
	Observation 3	0.68 ± 0.82	2.66 ± 2.00	3.08 ± 1.44	Lee et al. (2007b)
	Fold error	1.82	1.08	1.06	—
	Observation 4	0.35 ± 0.39	3.30 ± 1.65	2.27 ± 1.07	Lee et al. (2006)
	Fold error	1.06	1.15	1.44	—
	Observation 5	0.27 ± 0.02	2.44 ± 0.63	2.26 ± 0.52	Kazuhide et al. (1994)
	Fold error	1.38	1.18	1.44	—
	Observation 6	0.10 ± 0.06	4.89 ± 1.33	1.98 ± 0.60	Lee et al. (2007c)
	Fold error	3.58	1.70	1.64	—
	Observation 7	0.35 ± 0.32	2.43 ± 1.17	1.92 ± 0.88	Lee et al. (2007a)
	Fold error	1.05	1.18	1.70	—

than using P_{app} from Caco-2 experimentation. As displayed in **Figure 9B**, prediction 1 was closer to the correlation line with most dots within the $\pm 20\%$ of the observed concentration, indicating the overall good performance of PBPK model construction using the PSA and HBD methods.

4 DISCUSSION

While collecting *in vitro* parameters, we noticed the f_u and CL_{int} from different sources varied; therefore, the median values were applied to construct the model. A sensitivity analysis was performed to further explore the impact of these two parameters on the model prediction accuracy. The overall predicted accuracy of PBPK models using the median value was good with most fold errors within 2, and the R^2 between the predicted concentration data and the observed

data was more than 0.8 (**Figures 8, 9**). However, there was an exception that the chlorzoxazone PBPK model using median data was not satisfying with the prediction results, which is 2 times higher than the observed ones. It could be related to the underestimated distribution and clearance. In terms of the sensitivity analysis, the observed points were closest to the lowest prediction curve with the highest CL_{int} (38.8 $\mu\text{L}/\text{min}/\text{mg}$ protein) and f_u 0.373 (Moon et al., 2003; Baek et al., 2006). The lowest prediction parameters of T_{max} , C_{max} , and $AUC_{(0-t)}$ were 0.29 h, 37.69 $\mu\text{g}/\text{mL}$, and 34.69 $\mu\text{g}\cdot\text{h}/\text{mL}$, respectively. Moreover, most of the fold errors were within 2 (observation 1–3), indicating good prediction accuracy. Similarly, the prediction result of metoprolol using the median PBPK model was also slightly higher at 2.5 mg/kg, and the observed data was close to the lowest predicted curve. The prediction T_{max} , C_{max} , and $AUC_{(0-t)}$ of the metoprolol PBPK model using highest experimental CL_{int} (59.9 $\mu\text{L}/\text{min}/\text{mg}$) and f_u (0.93) at 2.5 mg/kg

TABLE 6 | Comparison between the predicted PK parameters of metoprolol PBPK models and the observed PK parameters at different doses.

Dose		T _{max} (h)	C _{max} (μg/ml)	AUC _(0-t) (μg•h/ml)	Reference
2.5 mg/kg	Prediction	0.65	0.21	0.51	—
	Observation 1	0.50 ± 0.00	0.16 ± 0.00	0.21 ± 0.02	Nandi et al. (2013)
	Fold error	1.30	1.27	2.39	—
	Observation 2	0.47 ± 0.07	0.16 ± 0.01	0.22 ± 0.02	Nandi et al. (2015)
5 mg/kg	Fold error	1.37	1.29	2.28	—
	Prediction	0.65	0.41	1.01	—
	Observation	0.50	0.40	0.45	Komura and Iwaki (2005)
	Fold error	1.30	1.04	2.25	—
10 mg/kg	Prediction	0.65	0.83	2.02	—
	Observation 1	0.60 ± 0.30	0.57 ± 0.25	1.66 ± 0.58	Ma et al. (2015)
	Fold error	1.08	1.45	1.22	—
	Observation 2	0.70 ± 0.50	0.81 ± 0.28	1.35 ± 0.59	Wang et al. (2014)
	Fold error	1.08	1.02	1.50	—
	Observation 3	—	0.53 ± 0.066	1.49 ± 0.39	Sun et al. (2017)
	Fold error	—	1.56	1.35	—

TABLE 7 | Comparison between the predicted PK parameters of the chlorzoxazone PBPK model and the observed PK parameters at 50 mg/kg.

50 mg/kg p.o.		T _{max} (h)	C _{max} (μg/ml)	AUC _(0-t) (μg•h/ml)	Reference
Prediction		0.40	68.66	124.78	—
Observation 1		0.25 (0.25–0.50)	23.10 ± 8.59	41.67 ± 8.48	Ahn et al. (2008)
Fold error		1.58	2.97	2.99	—
Observation 2		0.14 ± 0.08	31.80 ± 13.10	46.83 ± 16.00	Baek et al. (2006)
Fold error		2.85	2.16	2.66	—
Observation 3		0.10 ± 0.06	30.50 ± 8.17	39.83 ± 4.08	Baek et al. (2006)
Fold error		3.81	2.25	3.13	—

TABLE 8 | Comparison between the predicted PK parameters of nifedipine PBPK models and the observed PK parameters at different doses.

Dose		T _{max} (h)	C _{max} (μg/ml)	AUC _(0-t) (μg•h/ml)	Reference
3 mg/kg	Prediction	0.54	2.13	3.18	—
	Observation 1	0.25 (0.08–0.50)	2.00 ± 0.68	2.23 ± 0.42	Choi and Lee (2012)
	Fold error	2.16	1.07	1.42	—
	Observation 2	0.47 ± 0.03	2.46 ± 0.29	4.30 ± 0.45	He et al. (2014)
	Fold error	1.14	1.15	1.35	—
	Observation 3	0.25	1.48 ± 0.38	2.84 ± 0.19	Kim et al. (1997)
	Fold error	2.16	1.44	1.12	—
	Observation 4	0.58 ± 0.13	1.68 ± 0.58	3.38 ± 0.60	Wang et al. (2011)
5 mg/kg	Fold error	1.07	1.27	1.06	—
	Prediction	0.54	3.56	5.30	—
	Observation 1	0.38 ± 0.06	1.76 ± 0.20	2.72 ± 0.34	Mutsunobu et al. (2004)
	Fold error	1.42	2.02	1.95	—
	Observation 2	0.25 (0.12–0.50)	1.95 ± 0.26	2.73 ± 0.40	Ikehata et al. (2008)
	Fold error	2.16	1.82	1.94	—
	Observation 3	0.25 (0.12–1.50)	1.96 ± 0.23	3.75 ± 0.63	Ikehata et al. (2008)
	Fold error	2.16	1.81	1.41	—
6 mg/kg	Observation 4	0.25 (0.12–1.00)	2.56 ± 0.23	4.38 ± 0.29	Ikehata et al. (2008)
	Fold error	2.16	1.39	1.21	—
	Prediction	0.54	4.27	6.36	—
	Observation 1	0.38 (0.20–0.57)	5.23 (4.55–6.01)	5.75 (4.72–6.98)	Grundy et al. (1998)
	Fold error	1.41	1.23	1.11	—
	Observation 2	0.28 (0.16–0.40)	5.88 (3.33 ± 10.40)	5.90 (4.73–7.35)	Grundy et al. (1997)
	Fold error	1.94	1.38	1.08	—

were 0.53 h, 0.15 μg/ml, and 0.25 μg•h/ml, respectively and the fold errors were within 2 (Belpaire et al., 1989; Yoon et al., 2011). These results suggest that applying the PBPK model using *in vitro*

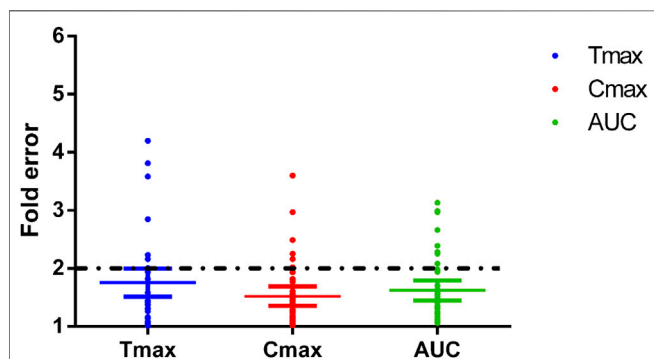
parameters in the early screening of candidate compounds is feasible and helpful, and the prediction accuracy of the model is related to the *in vitro* parameters, especially f_u and CL_{int} . It is worth

TABLE 9 | Comparison between the predicted PK parameters of the baicalein PBPK model and the observed PK parameters at 121 mg/kg.

121 mg/kg p.o.	T_{max} (h)	C_{max} ($\mu\text{g/ml}$)	$AUC_{(0-t)}$ ($\mu\text{g}\cdot\text{h/ml}$)	Reference
Prediction	0.24	1.05	0.98	—
Observation 1	0.17 ± 0.00	1.24 ± 0.78	0.79 ± 0.08	Zhang et al. (2011)
Fold error	1.44	1.19	1.25	—
Observation 2	0.17 ± 0.00	1.67 ± 0.85	0.79 ± 0.08	Huang et al. (2014)
Fold error	1.44	1.60	1.25	—

TABLE 10 | Variation span of the experimental *in vitro* parameters and prediction PK parameters in the sensitivity analysis.

	f_u	CL_{int} ($\mu\text{l/min/mg}$)	T_{max} (h)	C_{max} ($\mu\text{g/ml}$)	$AUC_{(0-t)}$ ($\mu\text{g}\cdot\text{h/ml}$)
Phenacetin	0.14–0.50	20.70–78.00	0.18–0.28	1.93–15.74	1.10–14.25
Fold range	3.45	3.77	1.56	8.16	12.95
Omeprazole	0.10–0.23	119.00–188.00	0.38–0.46	0.21–0.77	0.26–0.98
Fold range	2.21	1.58	1.21	3.67	3.77
Nifedipine	0.01–0.08	35.18–402	0.36–1.20	0.51–7.40	0.52–47.27
Fold range	8.00	11.43	3.33	14.51	90.90
Chlorzoxazone	0.05–0.373	5.00–38.80	0.29–0.70	37.69–199.27	34.69–1970.18
Fold range	8.11	7.76	2.41	5.29	56.79
Metoprolol	0.80–0.92	17.10–59.90	0.54–0.79	0.15–0.28	0.25–1.02
Fold range	1.16	3.50	1.46	1.87	4.08
Baicalein	0.03–0.08	338.90–574.11	0.19–0.36	0.59–2.08	0.51–2.36
Fold range	2.73	1.69	1.89	3.53	4.63
Tolbutamide	0.02–0.27	2.72–8.10	0.32–0.71	152.72–260.15	231.67–4587.60
Fold range	13.33	2.98	2.22	1.70	19.80

**FIGURE 8** | Fold errors of the PK parameters from the PBPK models of phenacetin, tolbutamide, omeprazole, metoprolol, chlorzoxazone, nifedipine, and baicalein. The three lines in each parameter represent mean with 95% confidence interval and the black dotted line across the fold error = 2 represent evaluation criteria.

noting that there is a potential correlation between f_u and CL_{int} under physiological conditions, which likewise may unnaturally increase the variability in predicted values. Furthermore, since the effect of f_u on CL_{int} might be poorly investigated and difficult to obtain from previous studies, the impact of such correlation on the variability of predicted values remains to be further explored.

In the sensitivity analysis, we summarized the variation span of the experimental *in vitro* parameters and prediction PK parameters in **Table 10**. Except for nifedipine (fold error of the observed T_{max} was 3.3), the variation of prediction T_{max} in the sensitivity analysis of other drugs was slight, meaning that the experimental difference of f_u

and CL_{int} had little impact on T_{max} compared with C_{max} and $AUC_{(0-t)}$. Compared with phenacetin, omeprazole, metoprolol, and baicalein, the experimental variation of f_u or CL_{int} of nifedipine, chlorzoxazone, and tolbutamide is relatively large (fold errors of f_u or CL_{int} > 8), which led to a large variation span in the sensitivity analysis with the fold errors of C_{max} or $AUC_{(0-t)}$ more than 10. Meanwhile, the variation of both f_u and CL_{int} was higher than 3, resulting in significant fold errors of C_{max} and $AUC_{(0-t)}$ (>8.0). Moreover, inflection points were noted in the change trend graph of f_u and CL_{int} of phenacetin, nifedipine, chlorzoxazone, and tolbutamide shown in the figure of sensitivity analysis, with the prediction value significantly fluctuating around. Therefore, sensitivity analysis is necessary for model construction. That is to say, when the *in vitro* parameters are close to the inflection point, extra attention should be paid to the PBPK model construction.

In addition to using the PSA and HBD methods to predict the absorption of model drugs in the PBPK model, we also explored the prediction accuracy of the PBPK model using P_{app} from *in vitro* experiments such as Caco-2 experimentation. Interestingly, the results showed that the overall prediction performance of PBPK models using the PSA and HBD methods was better. It could be related to defects in the *in vitro* absorption experiments, such as the inability to simulate the dynamic flow of fluids in the body, the lack of mucus layer, the more minor tight junctions, and the thicker unstirred water layer. These may cause the P_{app} to not to truly simulate the diffusion of drugs *in vivo* and thus cannot truly predict the drug absorption degree in the body.

It is worth mentioning that the PBPK model using *in vitro* parameters is beneficial to drug development, and the more accurate the value of *in vitro* parameters, the better fit the model.

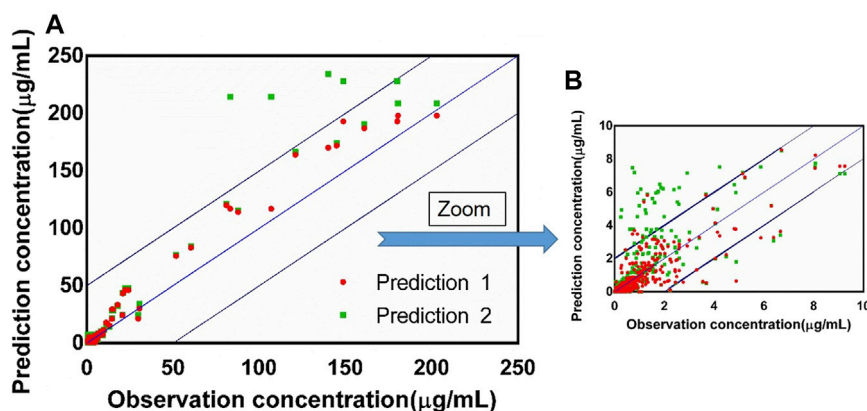


FIGURE 9 | (A) Observed concentration vs. predicted concentration ($n = 390$) based on the PBPK model with the absorption module using the PSA and HBD models (prediction 1) and the PBPK model using P_{app} from Caco-2 experimentation (prediction 2), blue box: $\pm 20\%$ of the observation concentration; **(B)** graph zoomed at 0–10 $\mu\text{g/mL}$.

TABLE 11 | Performance of the PBPK model with absorption module using PSA and HBD (prediction 1) and PBPK model using P_{app} from Caco-2 experimentation (prediction 2).

Performance	R^2	MAE	RMSE
Prediction 1	0.82	3.30	10.64
Prediction 2	0.58	4.99	16.01

However, the model compounds we applied were BCS (biopharmaceutics classification system) class II drugs, exhibited linear absorption and primarily cleared *via* metabolism. Therefore, our models were appropriate to the PK prediction of chemicals not affected by transporters such as P-gp (p-glycoprotein) efflux transporter. For other compounds with complex drug metabolism characteristics, using *in vitro* parameters alone to construct a PBPK model and the prediction accuracy still require further research and validation. Moreover, in recent years, with the development of computer technology and *in vitro* experiments, the contribution of PBPK models to advancing 3Rs in new drug development is undoubtedly a hot topic of discussion. Since rodents were widely used in preclinical pharmacological experiments, this study used rats as the model animal when constructing PBPK models based on *in vitro* parameters. It is expected that animal experiments can be reduced in the early stage of drug development with the validation of the feasibility and reliability of the models. However, due to the differences in physiological parameters of other species, the construction of their PBPK models needs further exploration and optimization, and due to the complexity of the human body, whether this method can be directly applied to predict the pharmacokinetic characteristics of candidate compounds in the humans and the reliability of the predicted results still need further exploration.

5 CONCLUSION

In our study, bottom-up PBPK models constructed with *in vitro* data were developed, and popular probe substrates were used as model drugs.

Most of the fold errors between the observed PK data with the predicted ones were within the threshold of 2, indicating good prediction accuracy. The influence of *in vitro* data was comprehensively analyzed, and results supported that the model accuracy is related to the precision of the *in vitro* data. Moreover, most of the observed PK data is within the uncertainty range, and R^2 is more than 0.8, indicating the applicability of the PBPK model in the absence of *in vivo* data in the early drug development. In conclusion, a strategy of the bottom-up PBPK model with the quantity of an uncertainty range is constructed, which helps reduce animal experiments and is a good practice of 3Rs in the early screening of candidate compounds.

DATA AVAILABILITY STATEMENT

The original contributions presented in the study are included in the article/**Supplementary Material**, further inquiries can be directed to the corresponding authors.

AUTHOR CONTRIBUTIONS

XX and WC are responsible for this manuscript.

FUNDING

This work was supported by the Shanghai Science and Technology Innovation Fund (18140900900). Certara UK (Simcyp Division) granted free access to the Simcyp® Simulators through an academic license.

SUPPLEMENTARY MATERIAL

The Supplementary Material for this article can be found online at: <https://www.frontiersin.org/articles/10.3389/fphar.2022.895556/full#supplementary-material>

REFERENCES

- Ahn, C. Y., Bae, S. K., Jung, Y. S., Lee, I., Kim, Y. C., Lee, M. G., et al. (2008). Pharmacokinetic Parameters of Chlorzoxazone and its Main Metabolite, 6-hydroxychlorzoxazone, after Intravenous and Oral Administration of Chlorzoxazone to Liver Cirrhotic Rats with Diabetes Mellitus. *Drug Metab. Dispos* 36 (7), 1233–1241. doi:10.1124/dmd.107.017442
- Andersen, M. E., Clewell, H. J., 3rd, Gargas, M. L., Smith, F. A., and Reitz, R. H. (1987). Physiologically Based Pharmacokinetics and the Risk Assessment Process for Methylene Chloride. *Toxicol. Appl. Pharmacol.* 87 (2), 185–205. doi:10.1016/0041-008x(87)90281-x
- Baek, H. W., Bae, S. K., Lee, M. G., and Sohn, Y. T. (2006). Pharmacokinetics of Chlorzoxazone in Rats with Diabetes: Induction of CYP2E1 on 6-hydroxychlorzoxazone Formation. *J. Pharm. Sci.* 95 (11), 2452–2462. doi:10.1002/jps.20698
- Ball, K., Bouzom, F., Scherrmann, J. M., Walther, B., and Declèves, X. (2014). Comparing Translational Population-PBPK Modelling of Brain Microdialysis with Bottom-Up Prediction of Brain-To-Plasma Distribution in Rat and Human. *Biopharm. Drug Dispos* 35 (8), 485–499. doi:10.1002/bdd.1908
- Belpaire, F. M., De Smet, F., Chindavijak, B., Fraeyman, N., and Bogaert, M. G. (1989). Effect of Turpentine-Induced Inflammation on the Disposition Kinetics of Propranolol, Metoprolol, and Antipyrine in the Rat. *Fundam. Clin. Pharmacol.* 3 (2), 79–88. doi:10.1111/j.1472-8206.1989.tb00667.x
- Belpaire, F. M., de Smet, F., Vynckier, L. J., Vermeulen, A. M., Rosseel, M. T., Bogaert, M. G., et al. (1990). Effect of Aging on the Pharmacokinetics of Atenolol, Metoprolol and Propranolol in the Rat. *J. Pharmacol. Exp. Ther.* 254 (1), 116–122.
- Berezhkovskiy, L. M. (2004). Volume of Distribution at Steady State for a Linear Pharmacokinetic System with Peripheral Elimination. *J. Pharm. Sci.* 93 (6), 1628–1640. doi:10.1002/jps.20073
- Cao, X., Gibbs, S. T., Fang, L., Miller, H. A., Landowski, C. P., Shin, H. C., et al. (2006). Why Is it Challenging to Predict Intestinal Drug Absorption and Oral Bioavailability in Human Using Rat Model. *Pharm. Res.* 23 (8), 1675–1686. doi:10.1007/s11095-006-9041-2
- Cascone, S., Lamberti, G., Marra, F., Titomanlio, G., d'Amore, M., and Barba, A. A. (2016). Gastrointestinal Behavior and ADME Phenomena: I. *In Vitro* Simulation. *J. Drug Deliv. Sci. Technol.* 35, 272–283. doi:10.1016/j.jddst.2016.08.002
- Chang, H. Y., Wu, S., Meno-Tetang, G., and Shah, D. K. (2019). A Translational Platform PBPK Model for Antibody Disposition in the Brain. *J. Pharmacokinet. Pharmacodyn* 46 (4), 319–338. doi:10.1007/s10928-019-09641-8
- Chen, Y., Jin, J. Y., Mukadam, S., Malhi, V., and Kenny, J. R. (2012). Application of IVIVE and PBPK Modeling in Prospective Prediction of Clinical Pharmacokinetics: Strategy and Approach during the Drug Discovery Phase with Four Case Studies. *Biopharm. Drug Dispos* 33 (2), 85–98. doi:10.1002/bdd.1769
- Cheng, W., and Ng, C. A. (2017). A Permeability-Limited Physiologically Based Pharmacokinetic (PBPK) Model for Perfluorooctanoic Acid (PFOA) in Male Rats. *Environ. Sci. Technol.* 51 (17), 9930–9939. doi:10.1021/acs.est.7b02602
- Choi, Y. H., and Lee, M. G. (2012). Pharmacokinetic and Pharmacodynamic Interaction between Nifedipine and Metformin in Rats: Competitive Inhibition for Metabolism of Nifedipine and Metformin by Each Other via CYP Isozymes. *Xenobiotica* 42 (5), 483–495. doi:10.3109/00498254.2011.633177
- Clewell, R. A., and Clewell, H. J. (2008). Development and Specification of Physiologically Based Pharmacokinetic Models for Use in Risk Assessment. *Regul. Toxicol. Pharmacol.* 50 (1), 129–143. doi:10.1016/j.yrtph.2007.10.012
- Dargó, G., Vincze, A., Müller, J., Kiss, H. J., Nagy, Z. Z., and Balogh, G. T. (2019). Corneal-PAMPA: A Novel, Non-cell-based Assay for Prediction of Corneal Drug Permeability. *Eur. J. Pharm. Sci.* 128, 232–239. doi:10.1016/j.ejps.2018.12.012
- De Buck, S. S., Sinha, V. K., Fenu, L. A., Nijssen, M. J., Mackie, C. E., and Gilissen, R. A. (2007). Prediction of Human Pharmacokinetics Using Physiologically Based Modeling: A Retrospective Analysis of 26 Clinically Tested Drugs. *Drug Metab. Dispos* 35 (10), 1766–1780. doi:10.1124/dmd.107.015644
- Ekins, S., Waller, C. L., Swaan, P. W., Cruciani, G., Wrighton, S. A., and Wikel, J. H. (2000). Progress in Predicting Human ADME Parameters In Silico. *J. Pharmacol. Toxicol. Methods* 44 (1), 251–272. doi:10.1016/s1056-8719(00)00109-x
- Ellison, C. A. (2018). Structural and Functional Pharmacokinetic Analogs for Physiologically Based Pharmacokinetic (PBPK) Model Evaluation. *Regul. Toxicol. Pharmacol.* 99, 61–77. doi:10.1016/j.yrtph.2018.09.008
- Grundy, J. S., Eliot, L. A., and Foster, R. T. (1997). Extrahepatic First-Pass Metabolism of Nifedipine in the Rat. *Biopharmaceutics & drug disposition* 18 (6), 509–522. doi:10.1002/(sici)1099-081x(199708)18:6<509::aid-bdd38>3.0.co;2-5
- Grundy, J. S., Eliot, L. A., Kulmatycki, K. M., and Foster, R. T. (1998). Grapefruit Juice and orange Juice Effects on the Bioavailability of Nifedipine in the Rat. *Biopharmaceutics & drug disposition* 19 (3), 175–183. doi:10.1002/(sici)1099-081x(199804)19:3<175::aid-bdd85>3.0.co;2-7
- Haddad, S., Béliveau, M., Tardif, R., and Krishnan, K. (2001). A PBPK Modeling-Based Approach to Account for Interactions in the Health Risk Assessment of Chemical Mixtures. *Toxicol. Sci.* 63 (1), 125–131. doi:10.1093/toxsci/63.1.125
- Hariparsad, N., Sane, R. S., Strom, S. C., and Desai, P. B. (2006). *In Vitro* methods in Human Drug Biotransformation Research: Implications for Cancer Chemotherapy. *Toxicol. Vitro* 20 (2), 135–153. doi:10.1016/j.tiv.2005.06.049
- Harrison, L. I., and Gibaldi, M. (1977). Physiologically Based Pharmacokinetic Model for Digoxin Disposition in Dogs and its Preliminary Application to Humans. *J. Pharm. Sci.* 66 (12), 1679–1683. doi:10.1002/jps.2600661206
- He, J. X., Ohno, K., Tang, J., Hattori, M., Tani, T., and Akao, T. (2014). Da-Chaihu-Tang Alters the Pharmacokinetics of Nifedipine in Rats and a Treatment Regimen to Avoid This. *J. Pharm. Pharmacol.* 66 (11), 1623–1630. doi:10.1111/jphp.12285
- Huang, S. M., Abernethy, D. R., Wang, Y., Zhao, P., and Zineh, I. (2013). The Utility of Modeling and Simulation in Drug Development and Regulatory Review. *J. Pharm. Sci.* 102 (9), 2912–2923. doi:10.1002/jps.23570
- Huang, Y., Zhang, B., Gao, Y., Zhang, J., and Shi, L. (2014). Baicalein-nicotinamide Cocrysal with Enhanced Solubility, Dissolution, and Oral Bioavailability. *J. Pharm. Sci.* 103 (8), 2330–2337. doi:10.1002/jps.24048
- Igari, Y., Sugiyama, Y., Sawada, Y., Iga, T., and Hanano, M. (1983). Prediction of Diazepam Disposition in the Rat and Man by a Physiologically Based Pharmacokinetic Model. *J. Pharmacokinet. biopharmaceutics* 11 (6), 577–593. doi:10.1007/BF01059058
- Ikehata, M., Ohnishi, N., Matsumoto, T., Kiyohara, Y., Maeda, A., Kawakita, T., et al. (2008). Effects of Sairei-To on the Pharmacokinetics of Nifedipine in Rats. *Phytother. Res.* 22 (1), 12–17. doi:10.1002/ptr.2234
- Irvine, J. D., Takahashi, L., Lockhart, K., Cheong, J., Tolan, J. W., Selick, H. E., et al. (1999). MDCK (Madin-Darby Canine Kidney) Cells: A Tool for Membrane Permeability Screening. *J. Pharm. Sci.* 88 (1), 28–33. doi:10.1021/js9803205
- Iwao, T., Inoue, K., Hayashi, Y., Yuasa, H., and Watanabe, J. (2002). Metabolic Extraction of Nifedipine during Absorption from the Rat Small Intestine. *Drug Metab. Pharmacokinet.* 17 (6), 546–553. doi:10.2133/dmpk.17.546
- Iwatsubo, T., Hirota, N., Ooie, T., Suzuki, H., Shimada, N., Chiba, K., et al. (1997). Prediction of *In Vivo* Drug Metabolism in the Human Liver from *In Vitro* Metabolism Data. *Pharmacol. Ther.* 73 (2), 147–171. doi:10.1016/s0163-7258(96)00184-2
- Jia, H., Li, W., and Zhao, K. (2006). Determination of Omeprazole in Rat Plasma by High-Performance Liquid Chromatography without Solvent Extraction. *J. Chromatogr. B Analyt. Technol. Biomed. Life Sci.* 837 (1–2), 112–115. doi:10.1016/j.jchromb.2006.04.007
- Jin, Z., He, Q., Zhu, X., Zhu, M., Wang, Y., Wu, X. A., et al. (2022). Application of Physiologically Based Pharmacokinetic Modelling for the Prediction of Drug-Drug Interactions Involving Anlotinib as a Perpetrator of Cytochrome P450 Enzymes. *Basic Clin. Pharmacol. Toxicol.* 130, 592. doi:10.1111/bcpt.13721
- Kahn, G. C., Rubenfield, M., Davies, D. S., and Boobis, A. R. (1987). Phenacetin O-Deethylase Activity of the Rat: Strain Differences and the Effects of Enzyme-Inducing Compounds. *Xenobiotica* 17 (2), 179–187. doi:10.3109/00498258709043927
- Kazuhide, W., Katsushi, F., Kohei, E., Ryozi, O., and Yutaka, G. (1994). First-Pass Metabolism of Omeprazole in Rats. *J. Pharm. Sci.* 83 (8), 1131. doi:10.1002/jps.2600830812
- Kim, Y. I., Fluckiger, L., Hoffman, M., Lartaud-Idjouadiene, I., Atkinson, J., and Maimont, P. (1997). The Antihypertensive Effect of Orally Administered Nifedipine-Loaded Nanoparticles in Spontaneously Hypertensive Rats. *Br. J. Pharmacol.* 120 (3), 399–404. doi:10.1038/sj.bjp.0700910

- Komura, H., and Iwaki, M. (2005). Pharmacokinetics and Metabolism of Metoprolol and Propranolol in the Female DA and Female Wistar Rat: the Female DA Rat Is Not Always an Animal Model for Poor Metabolizers of CYP2D6. *J. Pharm. Sci.* 94 (2), 397–408. doi:10.1002/jps.20255
- Kostewicz, E. S., Aarons, L., Bergstrand, M., Bolger, M. B., Galetin, A., Hatley, O., et al. (2014). PBPK Models for the Prediction of *In Vivo* Performance of Oral Dosage Forms. *Eur. J. Pharm. Sci.* 57, 300–321. doi:10.1016/j.ejps.2013.09.008
- Lee, D. Y., Kim, J. W., and Lee, M. G. (2007c). Pharmacokinetic Interaction between Oltipraz and Omeprazole in Rats: Competitive Inhibition of Metabolism of Oltipraz by Omeprazole via CYP1A1 and 3A2, and of Omeprazole by Oltipraz via CYP1A1/2, 2D1/2, and 3A1/2. *Eur. J. Pharm. Sci.* 32 (4–5), 328–339. doi:10.1016/j.ejps.2007.08.008
- Lee, D. Y., Jung, Y. S., Kim, Y. C., Kim, S. Y., and Lee, M. G. (2009). Faster Clearance of Omeprazole in Mutant Nagase Analbuminemic Rats: Possible Roles of Increased Protein Expression of Hepatic CYP1A2 and Lower Plasma Protein Binding. *Biopharm. Drug Dispos* 30 (3), 107–116. doi:10.1002/bdd.651
- Lee, D. Y., Lee, I., and Lee, M. G. (2007a). Effects of Cysteine on the Pharmacokinetic Parameters of Omeprazole in Rats with Protein-Calorie Malnutrition: Partial Restoration of Some Parameters to Control Levels by Oral Cysteine Supplementation. *J. Parenter. Enteral Nutr.* 31 (1), 37–46. doi:10.1177/014860710703100137
- Lee, D. Y., Lee, I., and Lee, M. G. (2007b). Pharmacokinetics of Omeprazole after Intravenous and Oral Administration to Rats with Liver Cirrhosis Induced by Dimethylnitrosamine. *Int. J. Pharm.* 330 (1–2), 37–44. doi:10.1016/j.ijpharm.2006.08.037
- Lee, D. Y., Shin, H. S., Lee, I., and Lee, M. G. (2006). Pharmacokinetics of Omeprazole in Rats with Water Deprivation for 72 hours. *Biopharm. Drug Dispos* 27 (8), 361–370. doi:10.1002/bdd.516
- Li, S., Yu, Y., Bian, X., Yao, L., Li, M., Lou, Y. R., et al. (2021). Prediction of Oral Hepatotoxic Dose of Natural Products Derived from Traditional Chinese Medicines Based on SVM Classifier and PBPK Modeling. *Arch. Toxicol.* 95 (5), 1683–1701. doi:10.1007/s00204-021-03023-1
- Lin, J. H., and Lu, A. Y. (1997). Role of Pharmacokinetics and Metabolism in Drug Discovery and Development. *Pharmacol. Rev.* 49 (4), 403–449.
- Lindstrom, F. T., Gillett, J. W., and Rodecap, S. E. (1974). Distribution of HEOD (Dieldrin) in Mammals. I. Preliminary Model. *Arch. Environ. Contam. Toxicol.* 2 (1), 9–42. doi:10.1007/bf01985798
- Lombardo, F., Desai, P. V., Arimoto, R., Desino, K. E., Fischer, H., Keefer, C. E., et al. (2017). In Silico Absorption, Distribution, Metabolism, Excretion, and Pharmacokinetics (ADME-PK): Utility and Best Practices. An Industry Perspective from the International Consortium for Innovation through Quality in Pharmaceutical Development. *J. Med. Chem.* 60 (22), 9097–9113. doi:10.1021/acs.jmedchem.7b00487
- Ma, J., Wang, S., Zhang, M., Zhang, Q., Zhou, Y., Lin, C., et al. (2015). Simultaneous Determination of Bupropion, Metoprolol, Midazolam, Phenacetin, Omeprazole and Tolbutamide in Rat Plasma by UPLC-MS/MS and its Application to Cytochrome P450 Activity Study in Rats. *Biomed. Chromatogr.* 29 (8), 1203–1212. doi:10.1002/bmc.3409
- Meek, M. E., Barton, H. A., Bessems, J. G., Lipscomb, J. C., and Krishnan, K. (2013). Case Study Illustrating the WHO IPCS Guidance on Characterization and Application of Physiologically Based Pharmacokinetic Models in Risk Assessment. *Regul. Toxicol. Pharmacol.* 66 (1), 116–129. doi:10.1016/j.yrtph.2013.03.005
- Mielke, H., and Gundert-Remy, U. (2009). Bisphenol A Levels in Blood Depend on Age and Exposure. *Toxicol. Lett.* 190 (1), 32–40. doi:10.1016/j.toxlet.2009.06.861
- Mielke, H., Partosch, F., and Gundert-Remy, U. (2011). The Contribution of Dermal Exposure to the Internal Exposure of Bisphenol A in Man. *Toxicol. Lett.* 204 (2–3), 190–198. doi:10.1016/j.toxlet.2011.04.032
- Miller, N. A., Reddy, M. B., Heikkinen, A. T., Lukacova, V., and Parrott, N. (2019). Physiologically Based Pharmacokinetic Modelling for First-In-Human Predictions: An Updated Model Building Strategy Illustrated with Challenging Industry Case Studies. *Clin. Pharmacokinet.* 58 (6), 727–746. doi:10.1007/s40262-019-00741-9
- Mutsunobu, Y., Noriaki, O., Noriko, S., Suguru, E., Koji, T., Teruyoshi, Y., et al. (2004). Studies on Interactions between Functional Foods or Dietary Supplements and Medicines. III. Effects of Ginkgo Biloba Leaf Extract on the Pharmacokinetics of Nifedipine in Rats. *Biol. Pharm. Bull.* 27 (12), 1315–1320. doi:10.1248/bpb.26.1315
- Nandi, U., Dan, S., and Pal, T. K. (2015). Development and Validation of a Liquid Chromatography–Mass Spectrometry Method for Simultaneous Determination of Metoprolol and Telmisartan in Rat Plasma and its Application to Pharmacokinetic Study. *J. Pharm. Invest.* 45 (3), 329–340. doi:10.1007/s40005-015-0180-5
- Nandi, U., Karmakar, S., Das, A. K., Ghosh, B., Padman, A., Chatterjee, N., et al. (2013). Pharmacokinetics, Pharmacodynamics and Toxicity of a Combination of Metoprolol Succinate and Telmisartan in Wistar Albino Rats: Safety Profiling. *Regul. Toxicol. Pharmacol.* 65 (1), 68–78. doi:10.1016/j.yrtph.2012.11.001
- Nestorov, I. (2003). Whole Body Pharmacokinetic Models. *Clin. Pharmacokinet.* 42 (10), 883–908. doi:10.2165/00003088-200342100-00002
- Nishimura, N., Naora, K., Hirano, H., and Iwamoto, K. (1999). A Chinese Traditional Medicine, Sho-Saiko-To (Xiao-chaihu-tang), Reduces the Bioavailability of Tolbutamide after Oral Administration in Rats. *Am. J. Chin. Med.* 27 (3–4), 355–363. doi:10.1142/S0192415X99000409
- Nishimura, N., Naora, K., Hirano, H., and Iwamoto, K. (1998). Effects of Sho-Saiko-To on the Pharmacokinetics and Pharmacodynamics of Tolbutamide in Rats. *J. Pharm. Pharmacol.* 50 (2), 231–236. doi:10.1111/j.2042-7158.1998.tb06181.x
- Paini, A., Leonard, J. A., Joossens, E., Bessems, J. G. M., Desalegn, A., Dorne, J. L., et al. (2019). Next Generation Physiologically Based Kinetic (NG-PBK) Models in Support of Regulatory Decision Making. *Comput. Toxicol.* 9, 61–72. doi:10.1016/j.comtox.2018.11.002
- Pang, K. S., and Rowland, M. (1977). Hepatic Clearance of Drugs. I. Theoretical Considerations of a "Well-Stirred" Model and a "parallel Tube" Model. Influence of Hepatic Blood Flow, Plasma and Blood Cell Binding, and the Hepatocellular Enzymatic Activity on Hepatic Drug Clearance. *J. Pharmacokinet. Biopharm.* 5 (6), 625–653. doi:10.1007/bf01059688
- Paul, N. M. (1991). Omeprazole. *N. Engl. J. Med.* 324, 965–975. doi:10.1056/NEJM199104043241406
- Pelkonen, O., and Turpeinen, M. (2007). In Vitro–In Vivo Extrapolation of Hepatic Clearance: Biological Tools, Scaling Factors, Model Assumptions and Correct Concentrations. *Xenobiotica* 37 (10–11), 1066–1089. doi:10.1080/00498250701620726
- Pi, J., Wang, S., Li, W., Kebebe, D., Zhang, Y., Zhang, B., et al. (2019). A Nano-Cocrystal Strategy to Improve the Dissolution Rate and Oral Bioavailability of Baicalein. *Asian J. Pharm. Sci.* 14 (2), 154–164. doi:10.1016/j.ajps.2018.04.009
- Poulin, P., and Theil, F. P. (2002). Prediction of Pharmacokinetics Prior to *In Vivo* Studies. I. Mechanism-Based Prediction of Volume of Distribution. *J. Pharm. Sci.* 91 (1), 129–156. doi:10.1002/jps.10005
- Prentiss, R. A., Lis, Y., and Walker, S. R. (1988). Pharmaceutical Innovation by the Seven UK-owned Pharmaceutical Companies (1964–1985). *Br. J. Clin. Pharmacol.* 25 (3), 387–396. doi:10.1111/j.1365-2125.1988.tb03318.x
- Raunio, H., Taavitsainen, P., Honkakoski, P., Juvonen, R., and Pelkonen, O. (2004). *In Vitro* methods in the Prediction of Kinetics of Drugs: Focus on Drug Metabolism. *Altern. Lab. Anim.* 32 (4), 425–430. doi:10.1177/026119290403200415
- Regårdh, C. G., Gabrielsson, M., Hoffman, K. J., Löfberg, I., and Skånberg, I. (1985). Pharmacokinetics and Metabolism of Omeprazole in Animals and Man - an Overview. *Scand. J. Gastroenterol.* 20 (Suppl. 108), 79–94. doi:10.3109/00365528509095821
- Rietjens, I. M. C. M., Punt, A., Schilter, B., Scholz, G., Delatour, T., and van Bladeren, P. J. (2010). In Silico methods for Physiologically Based Biokinetic Models Describing Bioactivation and Detoxification of Coumarin and Estragole: Implications for Risk Assessment. *Mol. Nutr. Food Res.* 54 (2), 195–207. doi:10.1002/mnfr.200900211
- Rodgers, T., Leahy, D., and Rowland, M. (2005). Tissue Distribution of Basic Drugs: Accounting for Enantiomeric, Compound and Regional Differences Amongst Beta-Blocking Drugs in Rat. *J. Pharm. Sci.* 94 (6), 1237–1248. doi:10.1002/jps.20323
- Rodgers, T., and Rowland, M. (2007). Mechanistic Approaches to Volume of Distribution Predictions: Understanding the Processes. *Pharm. Res.* 24 (5), 918–933. doi:10.1007/s11095-006-9210-3

- Rostami-Hodjegan, A., and Tucker, G. T. (2007). Simulation and Prediction of *In Vivo* Drug Metabolism in Human Populations from *In Vitro* Data. *Nat. Rev. Drug Discov.* 6 (2), 140–148. doi:10.1038/nrd2173
- Rowland, M., Peck, C., and Tucker, G. (2011). Physiologically-based Pharmacokinetics in Drug Development and Regulatory Science. *Annu. Rev. Pharmacol. Toxicol.* 51, 45–73. doi:10.1146/annurev-pharmtox-010510-100540
- Singh, D., and Asad, M. (2010). Effect of Soybean Administration on the Pharmacokinetics of Carbamazepine and Omeprazole in Rats. *Fundam. Clin. Pharmacol.* 24 (3), 351–355. doi:10.1111/j.1472-8206.2009.00762.x
- Sun, D., Lennernas, H., Welage, L. S., Barnett, J. L., Landowski, C. P., Foster, D., et al. (2002). Comparison of Human Duodenum and Caco-2 Gene Expression Profiles for 12,000 Gene Sequences Tags and Correlation with Permeability of 26 Drugs. *Pharm. Res.* 19 (10), 1400–1416. doi:10.1023/a:1020483911355
- Sun, W., Wang, Z., Chen, R., Huang, C., Sun, R., Hu, X., et al. (2017). Influences of Anlotinib on Cytochrome P450 Enzymes in Rats Using a Cocktail Method. *Biomed. Res. Int.* 2017, 3619723. doi:10.1155/2017/3619723
- Taylor, K., and Alvarez, L. R. (2019). An Estimate of the Number of Animals Used for Scientific Purposes Worldwide in 2015. *Altern. Lab. Anim.* 47 (5–6), 196–213. doi:10.1177/0261192919899853
- Tchaparian, E., Xu, G., Huang, T., and Jin, L. (2008). “Cell Based Experimental Models as Tools for the Prediction of Human Intestinal Absorption,” in Poster Presentation, 15th North American Regional International Society for the Study of Xenobiotics Meeting.
- Templeton, I. E., Jones, N. S., and Musib, L. (2018). Pediatric Dose Selection and Utility of PBPK in Determining Dose. *Aaps J* 20 (2), 31. doi:10.1208/s12248-018-0187-8
- T’jollyn, H., Vermeulen, A., and Van Bocxlaer, J. (2018). PBPK and its Virtual Populations: the Impact of Physiology on Pediatric Pharmacokinetic Predictions of Tramadol. *AAPS J.* 21 (1), 8. doi:10.1208/s12248-018-0277-7
- Umehara, K., Huth, F., Jin, Y., Schiller, H., Aslanis, V., Heimbach, T., et al. (2019). Drug-drug Interaction (DDI) Assessments of Ruxolitinib, a Dual Substrate of CYP3A4 and CYP2C9, Using a Verified Physiologically Based Pharmacokinetic (PBPK) Model to Support Regulatory Submissions. *Drug Metab. Pers Ther.* 34 (2). doi:10.1515/dmpt-2018-0042
- van de Kerkhof, E. G., de Graaf, I. A., and Groothuis, G. M. (2007). *In Vitro* methods to Study Intestinal Drug Metabolism. *Curr. Drug Metab.* 8 (7), 658–675. doi:10.2174/138920007782109742
- Verhoeckx, K., Cotter, P., López-Expósito, I., Kleiveland, C., Lea, T., Mackie, A., et al. (2015). *The Impact of Food Bioactives on Health: In Vitro and Ex Vivo Models*. Cham (CH): Springer. doi:10.1007/978-3-319-16104-4_10
- Vitale, A., Manciocco, A., and Alleva, E. (2009). The 3R Principle and the Use of Non-human Primates in the Study of Neurodegenerative Diseases: the Case of Parkinson’s Disease. *Neurosci. Biobehav. Rev.* 33 (1), 33–47. doi:10.1016/j.neubiorev.2008.08.006
- Wachsmuth, L., Mensen, A., Barca, C., Wiart, M., Tristão-Pereira, C., Busato, A., et al. (2021). Contribution of Preclinical MRI to Responsible Animal Research: Living up to the 3R Principle. *Magn. Reson. Mater. Phys. Biol. Med.* 34 (4), 469–474. doi:10.1007/s10334-021-00929-w
- Wagner, J. G. (1981). History of Pharmacokinetics. *Pharmacol. Ther.* 12 (3), 537–562. doi:10.1016/0163-7258(81)90097-8
- Wang, X., Chen, M., Chen, X., Ma, J., Wen, C., Pan, J., et al. (2014). The Effects of Acute Hydrogen Sulfide Poisoning on Cytochrome P450 Isoforms Activity in Rats. *Biomed. Res. Int.* 2014, 209393. doi:10.1155/2014/209393
- Wang, Y., Zou, M. J., Zhao, N., Ren, J. G., Zhou, H., and Cheng, G. (2011). Effect of Diallyl Trisulfide on the Pharmacokinetics of Nifedipine in Rats. *J. Food Sci.* 76 (1), T30–T34. doi:10.1111/j.1750-3841.2010.01960.x
- Watanabe, K., Matsuka, N., Okazaki, M., Hashimoto, Y., Araki, H., and Gomita, Y. (2002). The Effect of Immobilization Stress on the Pharmacokinetics of Omeprazole in Rats. *Acta Med. Okayama* 56 (1), 19–23. doi:10.14712/18059694.2019.52
- Welch, R. M., Hughes, C. R., and Deangelis, R. L. (1976). Effect of 3-methylcholanthrene Pretreatment on the Bioavailability of Phenacetin in the Rat. *Drug Metab. disposition: Biol. fate chemicals* 4 (4), 402–406.
- Winiwarter, S., Bonham, N. M., Ax, F., Hallberg, A., Lennernäs, H., and Karlén, A. (1998). Correlation of Human Jejunal Permeability (*In Vivo*) of Drugs with Experimentally and Theoretically Derived Parameters. A Multivariate Data Analysis Approach. *J. Med. Chem.* 41 (25), 4939–4949. doi:10.1021/jm9810102
- Yamashita, F., and Hashida, M. (2004). In Silico approaches for Predicting ADME Properties of Drugs. *Drug Metab. Pharmacokinet.* 19 (5), 327–338. doi:10.2133/dmpk.19.327
- Yamazaki, S., Skaptason, J., Romero, D., Vekich, S., Jones, H. M., Tan, W., et al. (2011). Prediction of Oral Pharmacokinetics of cMet Kinase Inhibitors in Humans: Physiologically Based Pharmacokinetic Model versus Traditional One-Compartment Model. *Drug Metab. Disposition* 39 (3), 383. doi:10.1124/dmd.110.035857
- Yoon, I. S., Choi, M. K., Kim, J. S., Shim, C. K., Chung, S. J., and Kim, D. D. (2011). Pharmacokinetics and First-Pass Elimination of Metoprolol in Rats: Contribution of Intestinal First-Pass Extraction to Low Bioavailability of Metoprolol. *Xenobiotica* 41 (3), 243–251. doi:10.3109/00498254.2010.538090
- Young, L. D., Lee, M. G., Sook, S. H., and Inchul, L. (2007). Changes in Omeprazole Pharmacokinetics in Rats with Diabetes Induced by Alloxan or Streptozotocin: Faster Clearance of Omeprazole Due to Induction of Hepatic CYP1A2 and 3A1. *J. Pharm. Pharm. Sci.* 10 (4), 420–433. doi:10.18433/j3wc7g
- Zhang, J., Lv, H., Jiang, K., and Gao, Y. (2011). Enhanced Bioavailability after Oral and Pulmonary Administration of Baicalein Nanocrystal. *Int. J. Pharm.* 420 (1), 180–188. doi:10.1016/j.ijpharm.2011.08.023
- Zhang, X., Yang, Y., Grimstein, M., Fan, J., Grillo, J. A., Huang, S. M., et al. (2020). Application of PBPK Modeling and Simulation for Regulatory Decision Making and its Impact on US Prescribing Information: An Update on the 2018–2019 Submissions to the US FDA’s Office of Clinical Pharmacology. *J. Clin. Pharmacol.* 60 (Suppl. 1), S160–S178. doi:10.1002/jcph.1767
- Zhou, Y., Wang, S., Ding, T., Chen, M., Wang, L., Wu, M., et al. (2014). Evaluation of the Effect of Apatinib (YN968D1) on Cytochrome P450 Enzymes with Cocktail Probe Drugs in Rats by UPLC-MS/MS. *J. Chromatogr. B Analyt. Technol. Biomed. Life Sci.* 973C, 68–75. doi:10.1016/j.jchromb.2014.10.013

Conflict of Interest: The authors declare that the research was conducted in the absence of any commercial or financial relationships that could be construed as a potential conflict of interest.

Publisher’s Note: All claims expressed in this article are solely those of the authors and do not necessarily represent those of their affiliated organizations, or those of the publisher, the editors, and the reviewers. Any product that may be evaluated in this article, or claim that may be made by its manufacturer, is not guaranteed or endorsed by the publisher.

Copyright © 2022 Yuan, He, Zhang, Li, Tang, Zhu, Jiao, Cai and Xiang. This is an open-access article distributed under the terms of the Creative Commons Attribution License (CC BY). The use, distribution or reproduction in other forums is permitted, provided the original author(s) and the copyright owner(s) are credited and that the original publication in this journal is cited, in accordance with accepted academic practice. No use, distribution or reproduction is permitted which does not comply with these terms.



Mechanism-Based Pharmacokinetic Model for the Deglycosylation Kinetics of 20(S)-Ginsenosides Rh2

Hong-can Ren^{1,2,3†}, Jian-guo Sun^{1†}, Ji-ye A^{1*}, Sheng-hua Gu^{1,4}, Jian Shi^{1,5}, Feng Shao¹, Hua Ai¹, Jing-wei Zhang¹, Ying Peng¹, Bei Yan¹, Qing Huang^{1,6}, Lin-sheng Liu^{1,7}, Yang Sai², Guang-ji Wang^{1*} and Cheng-guang Yang^{8*}

¹Key Lab of Drug Metabolism and Pharmacokinetics, State Key Laboratory of Natural Medicines, China Pharmaceutical University, Nanjing, China, ²DMPK and Clinical Pharmacology Group, Hutchison MediPharma Ltd., Shanghai, China, ³Department of Biology, GenFleet Therapeutics, Shanghai, China, ⁴School of Pharmacy, Shanghai University of Traditional Chinese Medicine, Shanghai, China, ⁵College of Pharmacy, University of Michigan, Ann Arbor, MI, United States, ⁶NMPA Key Laboratory for Impurity Profile of Chemical Drugs, Jiangsu Institute for Food and Drug Control, Nanjing, China, ⁷Department of Pharmacy, The First Affiliated Hospital of Soochow University, Suzhou, China, ⁸Department of General Surgery, Tongren Hospital, Shanghai Jiao Tong University School of Medicine, Shanghai, China

OPEN ACCESS

Edited by:

Ren-ai Xu,
First Affiliated Hospital of Wenzhou
Medical University, China

Reviewed by:

Wei-Hua Huang,
Central South University, China
Pengfei Li,
Capital Medical University, China

*Correspondence:

Ji-ye A
jiyea@cpu.edu.cn
Guang-ji Wang
guangjiwang@hotmail.com
Cheng-guang Yang
YCG1967@shtrhospital.com

[†]These authors have contributed
equally to this work

Specialty section:

This article was submitted to
Drug Metabolism and Transport,
a section of the journal
Frontiers in Pharmacology

Received: 29 October 2021

Accepted: 21 March 2022

Published: 25 May 2022

Citation:

Ren H-c, Sun J-g, A J-y, Gu S-h, Shi J,
Shao F, Ai H, Zhang J-w, Peng Y,
Yan B, Huang Q, Liu L-s, Sai Y,
Wang G-j and Yang C-g (2022)
Mechanism-Based Pharmacokinetic
Model for the Deglycosylation Kinetics
of 20(S)-Ginsenosides Rh2.
Front. Pharmacol. 13:804377.
doi: 10.3389/fphar.2022.804377

Aim: The 20(S)-ginsenoside Rh2 (Rh2) is being developed as a new antitumor drug. However, to date, little is known about the kinetics of its deglycosylation metabolite (protopanaxadiol) (PPD) following Rh2 administration. The aim of this work was to 1) simultaneously characterise the pharmacokinetics of Rh2 and PPD following intravenous and oral Rh2 administration, 2) develop and validate a mechanism-based pharmacokinetic model to describe the deglycosylation kinetics and 3) predict the percentage of Rh2 entering the systemic circulation in PPD form.

Methods: Plasma samples were collected from rats after the I.V. or P.O. administration of Rh2. The plasma Rh2 and PPD concentrations were determined using HPLC-MS. The transformation from Rh2 to PPD, its absorption, and elimination were integrated into the mechanism based pharmacokinetic model to describe the pharmacokinetics of Rh2 and PPD simultaneously at 10 mg/kg. The concentration data collected following a 20 mg/kg dose of Rh2 was used for model validation.

Results: Following Rh2 administration, PPD exhibited high exposure and atypical double peaks. The model described the abnormal kinetics well and was further validated using external data. A total of 11% of the administered Rh2 was predicted to be transformed into PPD and enter the systemic circulation after I.V. administration, and a total of 20% of Rh2 was predicted to be absorbed into the systemic circulation in PPD form after P.O. administration of Rh2.

Conclusion: The developed model provides a useful tool to quantitatively study the deglycosylation kinetics of Rh2 and thus, provides a valuable resource for future pharmacokinetic studies of glycosides with similar deglycosylation metabolism.

Keywords: traditional Chinese medicine, ginsenosides, pharmacokinetics, deglycosylation, modelling and simulation

1 INTRODUCTION

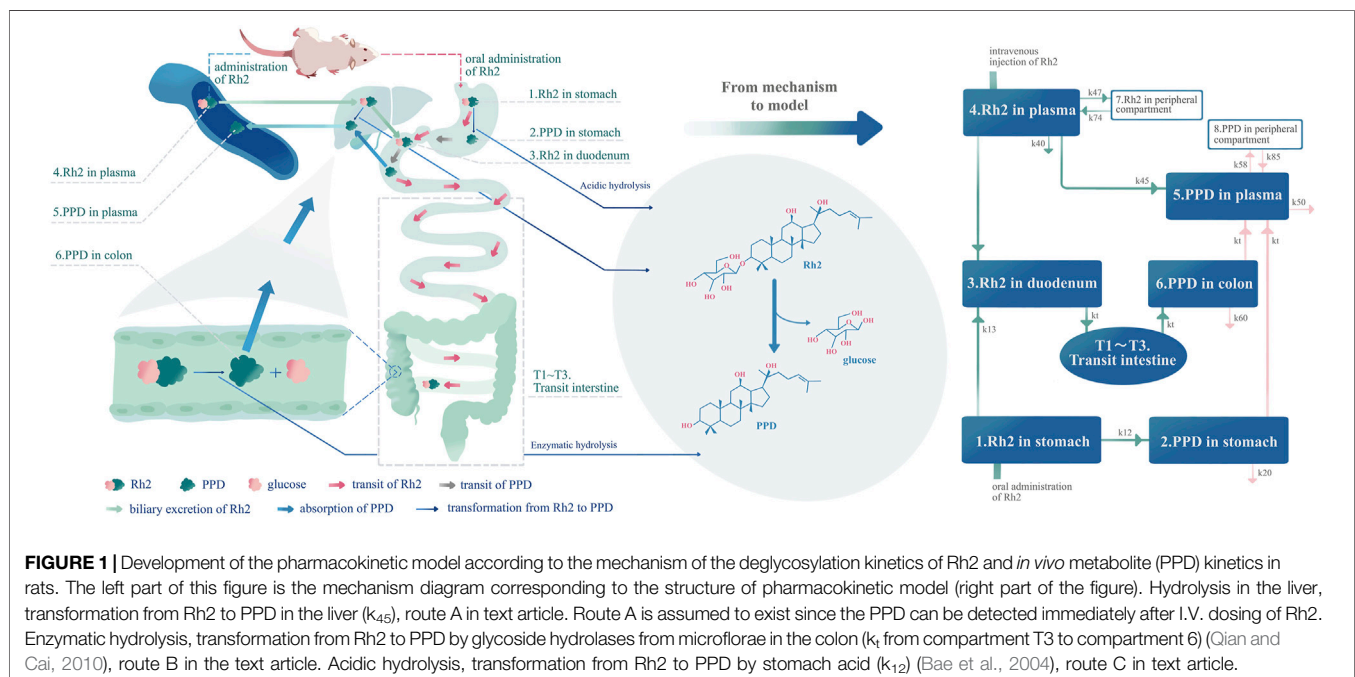
Ginseng is a traditional medicine that has been used for centuries. The global ginseng extracts market size was valued at USD 22.9 billion in 2019 and is expected to grow at a compound annual growth rate (CAGR) of 6.2% from 2020 to 2027 (Future Market Insights, 2020). Ginsenosides, a class of natural product steroid glycosides, have a wide effect on the cardiovascular system, central nervous system and immune system (Wang et al., 2014; Zhang et al., 2019a; Alolga et al., 2020; Zhu et al., 2020). Recent studies have found that 20(S)-ginsenosides Rh2 (Rh2), a substance isolated from red ginseng, may inhibit the growth of various cancer cells, reverse sleep deprivation-induced cognitive deficit, improve insulin sensitivity, and, enhance the antitumor immunological response in a melanoma mice model (Lee et al., 2007; Wang et al., 2017; Lu et al., 2018; Zhang et al., 2019b; Jeong et al., 2019; Qi et al., 2019).

However, the permeability of Rh2 in Caco-2 cells has been reported to be low, and it has also been reported to exhibit poor absolute bioavailability in rats (Qian et al., 2005; Gu et al., 2010). Here, Rh2's poor bioavailability and permeability do not appear to support its *in vivo* bioactivity. One of the hypotheses is that Rh2 is bio-transformed by gut microbiota, thereby producing new bioactive molecules with better absorption to exert the bioactivity (Gong et al., 2020). Rh2 is a protopanaxadiol (PPD)-type ginsenoside; this type has one glucose moiety at the C3 hydroxyl of PPD as shown in **Figure 1**. As the second genome of the body, the microbiome involves the metabolism of many drugs (Zimmermann et al., 2019; Brody, 2020; Savage, 2020). The glycosidase activities present in the human colonic microbiota act on many glycosides including Rh2 (Dabek et al., 2008; Gloster et al., 2008). For example, the bioavailability of ginsenoside Rb1 has been reported to be low (Akao et al., 1998).

Only the primary deglycosylation metabolite of ginsenoside Rb1 (compound K) could be detected in plasma, where its concentrations were found to be retained in the plasma for a long period of time following administration of ginsenoside Rb1 (Akao et al., 1998).

This hypothesis is further supported by the following evidence reported in the literature: 1) Rh2 can be deglycosylated into its metabolite, PPD, in the gastrointestinal tract (Bae et al., 2004), 2) the bioavailability of PPD is 36.8%, a bioavailability much greater than that seen in rats (Ren et al., 2008), and, 3) PPD is an active metabolite that demonstrates a potency in inducing apoptosis, altering membrane integrity, and inhibiting triple-negative breast cancer metastasis (Popovich and Kitts, 2002; Peng et al., 2019). However, to date, there is no direct evidence from any *in vivo* pharmacokinetic study to further validate this hypothesis and provide a comprehensive understanding of the kinetic profiles of Rh2 and its active metabolite.

The above studies provided the knowledge with regard to the pharmacokinetics of Rh2 and its active metabolite PPD, which could be integrated into a mechanism based pharmacokinetic model to study the deglycosylation kinetics of Rh2. As shown in **Figure 1**, the mechanism based pharmacokinetic model included all the possible deglycosylation kinetics of Rh2 in plasma (k_{45}), stomach (k_{12}), and colon (k_i). The classical two-compartment pharmacokinetic model was included in the mechanism based pharmacokinetic model to describe the distribution and elimination of Rh2 (compartment 4 and 7) and PPD (compartment 5 and 8). In doing so, it could facilitate the pharmacokinetic/pharmacodynamic (PK/PD) analysis of ginseng. On the other hand, Rh2 has been reported to be a potent non-competitive P-gp inhibitor (Gu et al., 2010). This has led to the concern that a potential herb-drug interaction may exist between ginseng and drugs that are P-gp substrates (Zhang et al.,



2010). The mechanistic pharmacokinetic model of Rh2 and PPD would be the starting point to quantitatively assess the potential existence of the herb-drug interaction.

The aim of this study was to gain a better understanding of the deglycosylation kinetics of 20(S)-Ginsenosides Rh2 by integrating experimental data with prior biological mechanism knowledge. To achieve the aim, the study comprised of the following three specific objectives: 1) to simultaneously characterise the pharmacokinetics of Rh2 and PPD following intravenous (I.V.) and oral (P.O.) Rh2 administration, 2) to develop a mechanism-based pharmacokinetic model based on the hypothesised deglycosylation kinetics and 3) predict the percentage of Rh2 elimination by gut bacteria using the developed model.

2 MATERIALS AND METHODS

The methods section is described in two parts. The first part provides the technical details of the animal experiment and sample analysis. The second part describes the details of the data analysis, which includes: 1) an exploratory data analysis, 2) the development of a mechanism-based model for the deglycosylation of glycosides *in vivo*, and 3) a quantitative assessment of the contribution of each elimination route.

2.1 Part I

2.1.1 Chemical and Reagents

20(S)-Ginsenosides Rh2 (Rh2), PPD and panoxadiol (purity over 99%) were purchased from the Department of Nature Medical Chemistry, School of Chemistry, Jilin University, Changchun, China. Deionized water was prepared using the Milli-Q system (Millipore, Bedford, MA, United States). Methanol of HPLC grade was purchased from Merck, Darmstadt Germany. Acetic ether and all other reagents (including solvents) were of analytical grade. Pure nitrogen gas was supplied by the Gas Supplier Center of Nanjing University, China.

2.1.2 Animal Experiments

Young adult Sprague–Dawley male rats with a body weight of 240–280 g were purchased from Sino-British Sippr/BK Lab Animal Ltd. (Shanghai, China). This research study and all animal handling procedures were approved by Research Animal Care and Laboratory Animal Resources of China Pharmaceutical University. The animal studies adhered to the European Community guidelines for laboratory animal care.

Prior to commencing the experiment, the rats were given 1 week to acclimatise to the animal facility. Rh2 was dissolved in saline with 50% hydroxypropyl- β -cyclodextrin for I.V. or P.O. administration—a volume of 5 ml/kg was given. Twelve rats were divided into four groups. Following an overnight fast (of at least 12 h), rats allocated to groups 1 and 2 ($n = 3$ per group) were administered an I.V. bolus of 10 mg/kg and 20 mg/kg of Rh2, respectively; whilst rats allocated to groups 3 and 4 received a 10 and 20 mg/kg oral dose of Rh2, respectively ($n = 3$ per group). The 20(S)-Ginsenosides Rh2 occurred as O-glycosides with glucose bound in nature, which could be hydrolysed by β -O-glycosidase

(Zheng et al., 2017). The activity of the glycosidase was not affected by sex difference significantly in mice as reported in a previous study (Doonan et al., 1978). Therefore, the authors assumed that the sex difference might have little effect on studying the transformation of PPD in this study. Herein, only males were included in this study. The relatively high dose levels were given to rats considering the poor bioavailability of Rh2. As the data were analysed by simultaneous global fitting of concentrations from the parent drug and metabolite at multiple time points, the effective sample size is far larger than experimental replication. In addition, no statistical comparison was performed on these data; rather, they were used for the development of a kinetic model of deglycosylation. Blood samples were collected by orbital sinus bleeding at 0 (prior to dosing), 0.25, 0.50, 1, 2, 4, 8, 12, 16, 20 (or 24) h post-drug administration. Water was freely accessible throughout the study, however access to food was restricted until 3 h post-drug administration. The collected samples were centrifuged at 4,000 rpm for 5 min. The separated plasma samples were then stored at -80°C .

2.1.3 Sample Preparation

Ten microliters of panoxadiol (2.0 $\mu\text{g/ml}$) were added to 0.1 ml of plasma creating an internal standard. This procedure was followed by a liquid–liquid extraction using 1.0 ml of acetic ether. The organic and aqueous phases of plasma were separated by centrifugation at 8,000 rpm for 5 min. The upper organic phase was transferred to another tube and evaporated using a Thermo Savant SPD 2010 Speed Vac System (Thermo Electron Corporation, United States) set at 40°C . The residue was reconstituted into 100 μl of the mobile phase using a vortex for 1 min. After centrifugation at 20,000 rpm for 10 min, 5 μl of the solution was injected into the column.

2.1.4 HPLC-MS Analysis for Determination of Plasma Concentrations

The method used to determine plasma concentration PPD has previously been published by Ren et al. (Ren et al., 2008). The HPLC method was revised for elution of the simultaneous determination of plasma Rh2 and PPD concentrations. Details of the method and validation are summarised in the Supporting Information.

2.2 Part II

2.2.1 Exploratory Data Analysis

A non-compartmental analysis (NCA) was performed to determine the following pharmacokinetic metrics for Rh2 and PPD: C_{max} , T_{max} , V_{ss} , and $T_{1/2}$. The NCA was performed using Phoenix 64 WinNonlin (Pharsight, a CertaraTM Company, Cary, NC, United States). For Rh2 the I.V. dosing option was selected, whilst the extravascular dosing option was selected for PPD.

2.2.2 Workflow of Model Development and Validation

A brief workflow describing model development and validation is presented as follows:

- (i) The known mechanism of deglycosylation kinetics (Figure 1) was summarised to explain the formation and

in vivo kinetics of the metabolite (PPD). A mechanism based pharmacokinetic model was then implemented (as shown in **Figure 1**).

- (ii) Based on the method of drug administration the proposed mechanistic model was further reduced into four sub-models (i.e., A, B, C, and D) for the estimation of model parameters. The observed data following I.V. or P.O. administration of Rh2 at 10 mg/kg was used for model fitting. Details of the sub-models are introduced in Appendix A. The model fitting results of the sub-models are provided in Supporting Information.
- (iii) The concentration versus time data of Rh2 and PPD at 20 mg/kg was used for external validation of the developed mechanistic model.

2.2.3 Overview of Mechanistic-Based Pharmacokinetic Model

As shown in **Figure 1**, the model accounts for the distribution (i.e., transit in the intestine) and elimination of Rh2, as well as the formation, absorption, distribution, and elimination of PPD. The proposed model can describe the concentration time profiles of both Rh2 and PPD simultaneously after I.V. and/or P.O. administration of Rh2 in rats. Following the I.V. administration of Rh2 it is eliminated by three routes: 1) direct transformation from Rh2 to PPD (k_{45}), 2) biliary excretion (k_{43}), and 3) other unknown routes (k_{40}) in the systemic circulation. Following the P.O. administration of Rh2 it is eliminated by two routes: 1) transformation of Rh2 to PPD in the stomach (k_{12}), 2) transfer from stomach to colon through the transit compartments T1-T3 and metabolism in colon. The transformation of Rh2 to PPD in the colon is known to be the primary route of formation for PPD. The absorption of PPD in the stomach (it may be transferred to the duodenum and then absorbed) and colon into the systemic circulation is described by k_p , whilst its elimination is described by the rate constant k_{50} . The peripheral compartments (compartment 7 and 8) are implemented to describe the distribution of Rh2 and PPD into the peripheral tissues, respectively. A detailed description of the model is provided in Appendix A.1. The model can be further reduced into sub-models to describe the concentration time profiles of Rh2 and PPD following I.V. and P.O. administration of Rh2 respectively (see in **Section 2.2.5**).

2.2.4 Software and Criteria for Model Development

The mechanism-based pharmacokinetic model was developed using the non-linear mixed effect modelling software Phoenix 64 NLME (version 8.2, Pharsight, a Certara™ Company, Cary, NC). Inter-individual variability was described using an exponential model. Residual error was described by a multiplicative error model. The initial estimates used in the model were obtained by manual adjustment of parameters and visual inspection. The FOCE ELS algorithm in Phoenix 64 NLME was used for parameter estimation. The code for the final model is provided in Supporting Information. The model was evaluated based on successful convergence, objective function value, parameter precision, visual inspection of goodness-of-fit plots and a visual predictive check (VPC) (Wang and Zhang, 2012).

2.2.5 Strategy of the Parameter Estimation

The final model was comprised of 11 compartments and 16 parameters. This led to challenges in model parameter estimation. Hence, to reduce computational workload, a model reduction strategy was applied using the following four steps:

Step 1: The full model was reduced to sub-model A, including compartments of “4. Rh2 in plasma” and “7. Rh2 in PC”. The parameters related to the elimination and distribution of Rh2 were then estimated using the raw data following I.V. administration of Rh2. Details for the sub-model A are provided in Appendix A.

Step 2: The full model was reduced to sub-model B including compartments of “5. Rh2 in plasma” and “8. Rh2 in PC”. Similar to sub-model A for the independent modelling of Rh2, the parameters related to the elimination and distribution of PPD were estimated using the raw data following I.V. administration of PPD for the independent modelling of PPD.

Step 3: Sub-model C was comprised of the following components: sub-model A, sub-model B, biliary excretion, transit of Rh2, transformation of Rh2 to PPD in the colon and absorption of PPD. The parameters were then estimated using the reported biliary excretion data of Rh2 and the concentration-time profile of PPD following a 10 mg/kg I.V. administered dose of Rh2 (Gu et al., 2009).

Step 4: Sub-model D was comprised of the following components: sub-model B, transit of Rh2 from the stomach to the intestine, transformation of Rh2 to PPD in the stomach, and elimination of PPD in the intestine compartments (linked by blue and purple arrows in **Figure 1**). The related parameters were estimated using plasma concentrations of PPD following a 10 mg/kg dose of Rh2 administered P.O.

Details for each of the sub-models is provided in Appendix A.

2.2.6 External Validation

The model was externally validated by performing a visual predictive check (VPC) (Wang and Zhang, 2012). The model parameters were fixed to simulate the concentration-time profiles for Rh2 and PPD following I.V. and P.O. administration when given at a 20 mg/kg dose. The 5th, 50th, and 95th percentiles were calculated from the empirical posterior distribution of 1000 replicates. If the majority of observed concentration data was within the 90% prediction interval the model was thought to be validated.

2.2.7 Evaluation of Elimination Contribution by Different Routes

The final model was used to quantitatively assess the contribution of each elimination route of Rh2. Following I.V. administration, Rh2 is eliminated via three different routes which are: 1) transformation from Rh2 to PPD in the plasma or liver (route A), 2) biliary excretion, transformation from Rh2 to PPD, and re-absorption into the systemic circulation (route B), and 3) other unknown metabolism routes. We assumed that route A exists without

robust evidence since the PPD could be detected immediately after IV dosing of Rh2. The extent of Rh2 transformation to PPD in plasma (route A) was quantified as the ratio of direct transformation rate constant from Rh2 to PPD to the total elimination rate constant of Rh2 (k_{45}/k_e). The excreted Rh2 by bile was partly transformed into PPD in the colon and further re-absorbed into the systemic circulation (route B). The extent of biliary excretion was quantified as the ratio of the biliary excretion rate constant to the total elimination rate constant of Rh2 (k_{43}/k_e). The extent of re-absorbed PPD was the product of the percentage of biliary excretion and the percentage of PPD absorbed from the colon to the systemic circulation ($k_{43}/k_e \cdot k_t/(k_t + k_{60})$). The extent of the other unknown elimination routes was quantified as the sum of unknown elimination of Rh2 in plasma and bile ($k_{40}/k_e + k_{43}/k_e \cdot k_{60}/(k_t + k_{60})$) or 100% minus the percentage of Rh2 entering the systemic circulation in PPD form ($100\% - k_{45}/k_e - k_{43}/k_3 \cdot k_t/(k_t + k_{60})$). After P.O. administration, Rh2 is transformed to PPD in the stomach and colon via metabolism. The total disposition rate constant of Rh2 in the stomach is the sum of the transit rate constant from the stomach to the intestine and the transformation rate constant from Rh2 to PPD in the stomach ($k_{12} + k_{13}$). The extent of Rh2 transiting from the stomach to the intestine was quantified as the ratio of transit rate constant from the stomach to the intestine and the total disposition of Rh2 in the stomach, expressed as $k_{13}/(k_{12} + k_{13})$. The extent of Rh2 metabolism in the stomach was expressed as $k_{12}/(k_{12} + k_{13})$. PPD present in the stomach can be transferred to the duodenum and absorbed into the systemic circulation, which has been simplified as absorption rate constant (k_t), or eliminated via unknown mechanisms (k_{20}). Hence, the total disposition rate constant of PPD in the stomach is the sum of both of the routes ($k_t + k_{20}$). The extent of PPD absorption in the stomach was quantified as the ratio of absorption rate constant of PPD to total disposition rate constant of PPD: $k_t/(k_t + k_{20})$. The extent of PPD elimination in the stomach was quantified as the ratio of elimination rate constant of PPD to total disposition rate constant of PPD in the stomach: $k_{20}/(k_t + k_{20})$. The percentage of Rh2 transformed to PPD in the colon and further absorbed into the systemic circulation (route B) was the product of the percentage of Rh2 transiting from the stomach to the intestine and the percentage of PPD absorbed from the colon to the systemic circulation ($k_{13}/(k_{12} + k_{13}) \cdot k_t/(k_t + k_{60})$). The percentage of Rh2 transformed to PPD in the stomach and absorbed into the systemic circulation (route C), was the product of the percentage of Rh2 transiting from the stomach to the intestine and the percentage of PPD absorption in the stomach: $k_{12}/(k_{12} + k_{13}) \cdot k_t/(k_t + k_{20})$. The extent of the other unknown elimination routes was quantified as the sum of unknown elimination of Rh2 in the stomach and colon ($k_{13}/(k_{12} + k_{13}) \cdot k_{60}/(k_t + k_{60}) + k_{12}/(k_{12} + k_{13}) \cdot k_{20}/(k_t + k_{20})$) or 100% minus the percentage of Rh2 entering the systemic circulation in PPD form ($100\% - k_{13}/(k_{12} + k_{13}) \cdot k_t/(k_t + k_{60}) - k_{12}/(k_{12} + k_{13}) \cdot k_t/(k_t + k_{20})$).

3 RESULTS

3.1 The Result of Exploratory Data Analysis

A summary of the non-compartmental analysis results is presented in **Table 1**. The pharmacokinetic profile of PPD

TABLE 1 | The pharmacokinetic parameters from non-compartment analysis.

Determination of	Parameters	10 mg/kg		20 mg/kg	
		Mean	CV (%)	Mean	CV (%)
I.V. administration of Rh2					
Rh2	V _{ss} (L/kg)	17.1	86.9	20.2	77.1
	AUC _{0-t} (h·nmol/L)	1457	42.2	3,850	77.5
	t _{1/2} (h)	2.23	10.6	2.36	29.0
PPD	C _{max} (nmol/L)	94.9	22.9	174	31.7
	T _{max} (h)	6.83	85.4	6.75	88.5
	AUC _{0-t} (h·nmol/L)	1039	37.7	2,827	40.5
P.O. administration of Rh2					
PPD	C _{max} (nmol/L)	255	17.1	442	49.5
	T _{max} (h)	8.00	0.00	10.7	21.7
	AUC _{0-t} (h·nmol/L)	2,377	15.3	4,611	44.8

following an I.V. or P.O. dose of Rh2 were characterised by an atypical double peak. Following an I.V. or P.O. dose of Rh2, PPD reached a maximum concentration by approximately 6 h post Rh2 administration. The T_{max} of PPD was longer than that after only oral dosing of PPD (2.5 h), indicating a long delay of transformation from Rh2 to PPD after dosing of Rh2. The PPD has high exposure after administration of Rh2: the exposure of PPD (AUC_{0-t} , 1039 h·nmol/L) is around 71% of the exposure of Rh2 (AUC_{0-t} , 1457 h·nmol/L) after I.V. administration of Rh2 at a dose level of 10 mg/kg. At an oral Rh2 dose of 10 mg/kg the concentration of Rh2 was lower than the lower limit of quantitation (LLOQ), though the AUC for PPD was 2,377 h·nmol/L. This was obviously higher than that after I.V. of Rh2 at the same dose in rats. The C_{max} and AUC_{0-t} of Rh2 and PPD were found to increase proportionally with the dose. The other PK parameters are shown in the Supporting Information.

3.2 Kinetic Modelling of Rh2 and PPD After I.V. Administration (Sub-model A and B)

Following an I.V. dose, the pharmacokinetic profiles of Rh2 and PPD were characterized by a rapid drop in plasma concentration followed by a relative slower decrease in the terminal phase. This conforms with the features of a classic two-compartment model. Sub-models A and B provided a reasonable description of the observed data (shown in **Figures 2A,B**). The parameters of sub-models A and B were precisely estimated (as shown in **Table 2**). The elimination rate constant of Rh2 (k_e) was estimated to be 4.67 h^{-1} , a value similar to the elimination rate constant of PPD (k_{50} , 4.88 h^{-1}). This indicates a similar *in vivo* elimination in rats. The distribution of Rh2 was notably different to PPD. This was evident by the large differences between the distribution related parameters of Rh2 (k_{47} , k_{74} , and $V_{Rh2, \text{ plasma}}$) and the corresponding parameters for PPD (k_{58} , k_{85} , and $V_{PPD, \text{ plasma}}$). These model parameters were fixed when estimating the parameters in sub-models C and D.

3.3 Kinetic Modelling of PPD After I.V. Administration of Rh2 (Sub-Model C)

Sub-model C provided a good description of the concentration-time course of PPD following an I.V. administration of Rh2

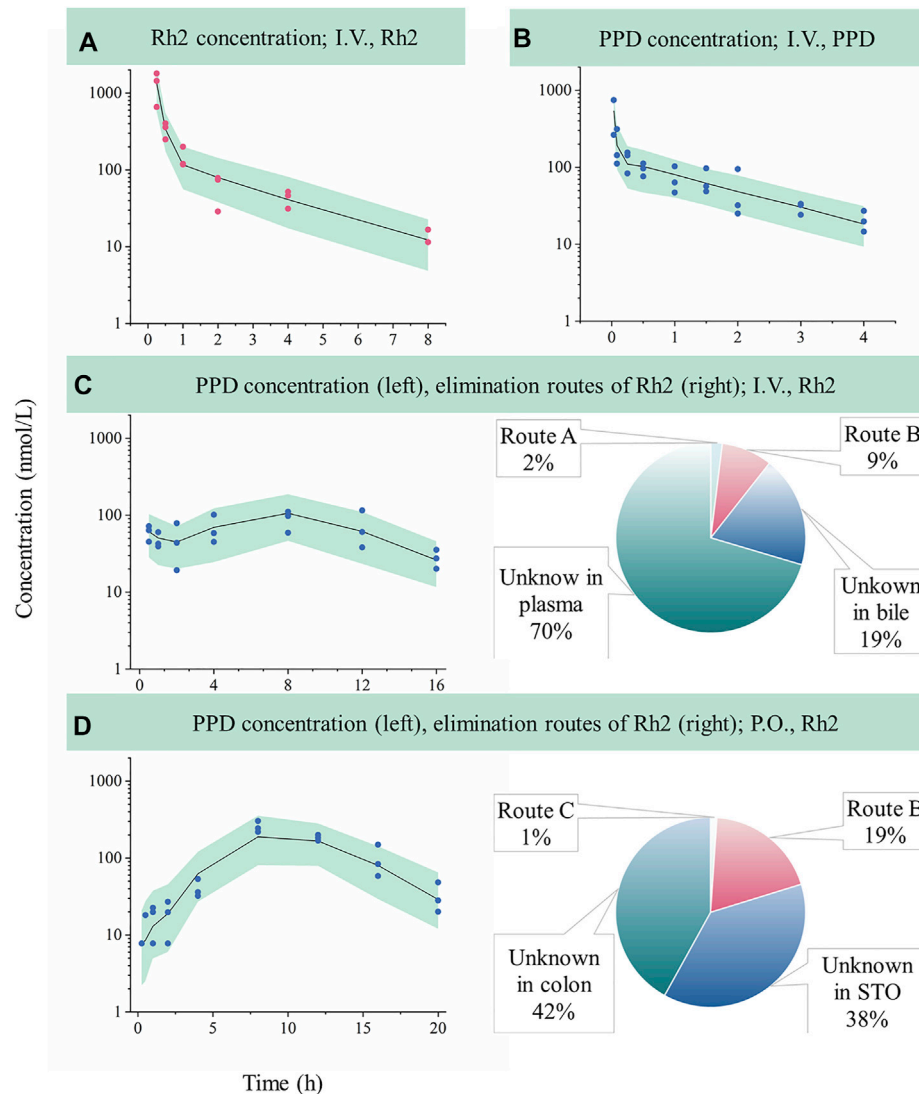


FIGURE 2 | Evaluation of model performance in rats and the calculated elimination routes of Rh2. Green areas represent the 90% confidence interval between the 5th and 95th of percentiles, solid lines are the median profile (50th point of percentile), red symbols represent raw observations of Rh2, and blue symbols represent raw observations of PPD. **(A)**, Rh2 pharmacokinetic profile after I.V. administration of Rh2 at 10 mg/kg; **(B)**, PPD pharmacokinetic profile after I.V. administration of PPD at 0.2 mg/kg; **(C)**, PPD pharmacokinetic profile after I.V. administration of Rh2 at 10 mg/kg; **(D)**, PPD pharmacokinetic profile after P.O. administration of Rh2 at 10 mg/kg. Route A is the percentage of the administered Rh2 transformed from Rh2 to PPD in the systemic circulation; Route B is the percentage of the administered Rh2 transformed to PPD in the colon and absorbed into the systemic circulation; Route C is the percentage of the administered Rh2 transformed to PPD in the stomach and absorbed into the systemic circulation. STO refers to stomach.

(shown in **Figure 2C**). This was shown by the majority of observations lying within the 90% confidence interval in **Figure 2C**. This finding was consistent with the visual inspection of the goodness-of-fit plots (shown in Figure S1 in Supporting Information). As shown in **Table 2**, the parameters in sub-model C were precisely estimated with CV values below 30%. The value for k_e (4.67 h^{-1}) was determined by summing k_{43} (1.29 h^{-1}), k_{40} (3.29 h^{-1}), and k_{45} (0.091 h^{-1}). Here, it was found that 2% of the administered Rh2 was eliminated via direct transformation from Rh2 to PPD in plasma. Around 28% of the administered Rh2 was eliminated via biliary excretion among which 9% of the administered Rh2 were transferred into the

colon, transformed into PPD, and then absorbed into the systemic circulation. The other 19% of the administered Rh2 in bile and 70% of the administered Rh2 in plasma were eliminated via unknown routes.

3.4 Kinetic Modelling of PPD After P.O. Administration of Rh2 (Sub-Model D)

Sub-model D provided a good description of the time course of PPD following P.O. administration of Rh2. This was shown by most of the observations lying within the 90% prediction interval shown in **Figure 2D**. This was consistent with the visual

TABLE 2 | Summary of estimated pharmacokinetic parameters.

Parameters		Definition	Estimate	CV%	95% CI	
					Lower	Upper
Rh2 independent parameters after I.V. administration of Rh2						
V _{Rh2, plasma} (L/kg)	Volume of central compartment distribution of Rh2	2.39	16.4	1.54	3.23	
K _e (1/h)	Elimination rate constant of Rh2 in central compartment	4.67	3.90	4.28	5.07	
K ₄₇ (1/h)	Transfer rate constant of Rh2 from central compartment to peripheral compartment	2.08	14.8	1.42	2.75	
K ₇₄ (1/h)	Transfer rate constant of Rh2 from peripheral compartment to central compartment	0.48	15.0	0.32	0.63	
PPD independent parameters after I.V. administration of PPD						
V _{PPD, plasma} (L/kg)	Volume of central compartment distribution of PPD	0.29	27.0	0.13	0.44	
K ₅₀ (1/h)	Elimination rate constant of PPD in central compartment	4.88	29.3	1.99	7.77	
K ₅₈ (1/h)	Transfer rate constant of PPD from central compartment to peripheral compartment	27.3	19.5	16.5	38.0	
K ₈₅ (1/h)	Transfer rate constant of PPD from peripheral compartment to central compartment	3.38	9.68	2.72	4.04	
PPD parameters after I.V. administration of Rh2						
K ₄₅ (1/h)	Transformation rate constant from Rh2 to PPD in systemic circulation	0.09	12.9	0.07	0.12	
K ₄₃ (1/h)	Excretion rate constant of Rh2 in bile	1.29	NA	NA	NA	
K ₄₀ (1/h)	Elimination rate constant of Rh2 by other routes in systemic circulation	3.29	NA	NA	NA	
K ₆₀ (1/h)	Elimination rate constant of PPD in colon	1.38	16.1	0.90	1.85	
K _t (1/h)	Transit rate constant of Rh2 in intestines	0.63	7.53	0.53	0.73	
PPD parameters after P.O. administration of Rh2						
K ₁₃ (1/h)	Transit rate constant of Rh2 from stomach to duodenum	0.22	9.66	0.17	0.26	
K ₁₂ (1/h)	Transformation rate constant from Rh2 to PPD in stomach	0.14	14.5	0.10	0.18	
K ₂₀ (1/h)	Elimination rate constant of PPD in stomach	22.2	20.6	12.6	31.8	

NA, not available. The estimates of k_{43} and k_{40} have been frozen. CI, confidence interval.

inspection of the goodness-of-fit plots (presented in Supporting Information). As shown in **Table 2**, the parameters in sub-model D were precisely estimated with RSE values below 30%. Around 61% of the administered Rh2 transited from the stomach into the colon among which 19% of the administered Rh2 was followed by deglycosylation, which might explain the high exposure of PPD following P.O. as opposed to I.V. administration when the same dose was given. Only 1% of the administered Rh2 was metabolised to PPD in the stomach and absorbed into the circulatory system as PPD. In total, 80% of administered Rh2 was eliminated by other unknown routes.

3.5 Model External Validation

The developed model based on data following a 10 mg/kg dose was used to predict the concentration versus time profiles for a 20 mg/kg dose. The predicted data were compared with the observed data for external validation via a VPC. As shown in **Figure 3**, most of the observed Rh2 or PPD concentrations was within the predicted 5th and 95th percentiles with the majority of observations being evenly distributed around the median. Hence, the results indicated that the developed model could describe the observed data when predicting a higher dose.

4 DISCUSSION

In recent years, the interaction between the bioactive ingredients of traditional Chinese medicine (TCM) and gut microbiota has attracted much attention (Laparra and Sanz, 2010; Dey, 2019; Feng et al., 2019; Yue et al., 2019; Gong et al., 2020; Jia et al., 2020). The bio-transformation by gut microbiota and their effect on the

pharmacokinetics and therapeutic role have been reported (Choi et al., 2018; Bridgeman et al., 2020; Savage, 2020). However, few reports used modelling and simulation to quantitatively study the bio-transformation from parent drug to metabolite. In this study, the parent drug and deglycosylation metabolite were detected simultaneously after dosing of Rh2 in rats and a model-based method was used for the study of bio-transformation with minimum data requirements. As a result, high concentrations of PPD were detected following the administration of Rh2. This highlights the importance of simultaneously investigating the pharmacokinetic profiles of Rh2 and PPD. Following I.V. or P.O. administration of Rh2, the pharmacokinetic profile of PPD showed atypical double peaks with a prolonged T_{max} . The mechanisms of PPD formation were summarized and the hypothesis of deglycosylation kinetics was proposed in **Figure 1** to qualitatively explain the formation and *in vivo* kinetics of the metabolite (PPD) based on the reported publications. The mechanism of deglycosylation kinetics involved the transformation from parent drug (Rh2) to metabolite (PPD) by acid in the stomach and by microflorae in the colon, as well as the transit of Rh2 and PPD in intestinal tracts, and biliary excretion of Rh2. Since the liver concentrations were not measured, we did not include a separate liver compartment in the final model; instead it was merged into the plasma compartment.

The mechanism-based pharmacokinetic model could provide a detailed assessment on the percentage of Rh2 elimination by different routes. Some elimination routes could be supported by the reported facts or data. After I.V. administration, the simulated biliary excretion is 28%, the same as the reported value (Gu et al., 2009). The excretion rate constant of Rh2 into faeces is zero,

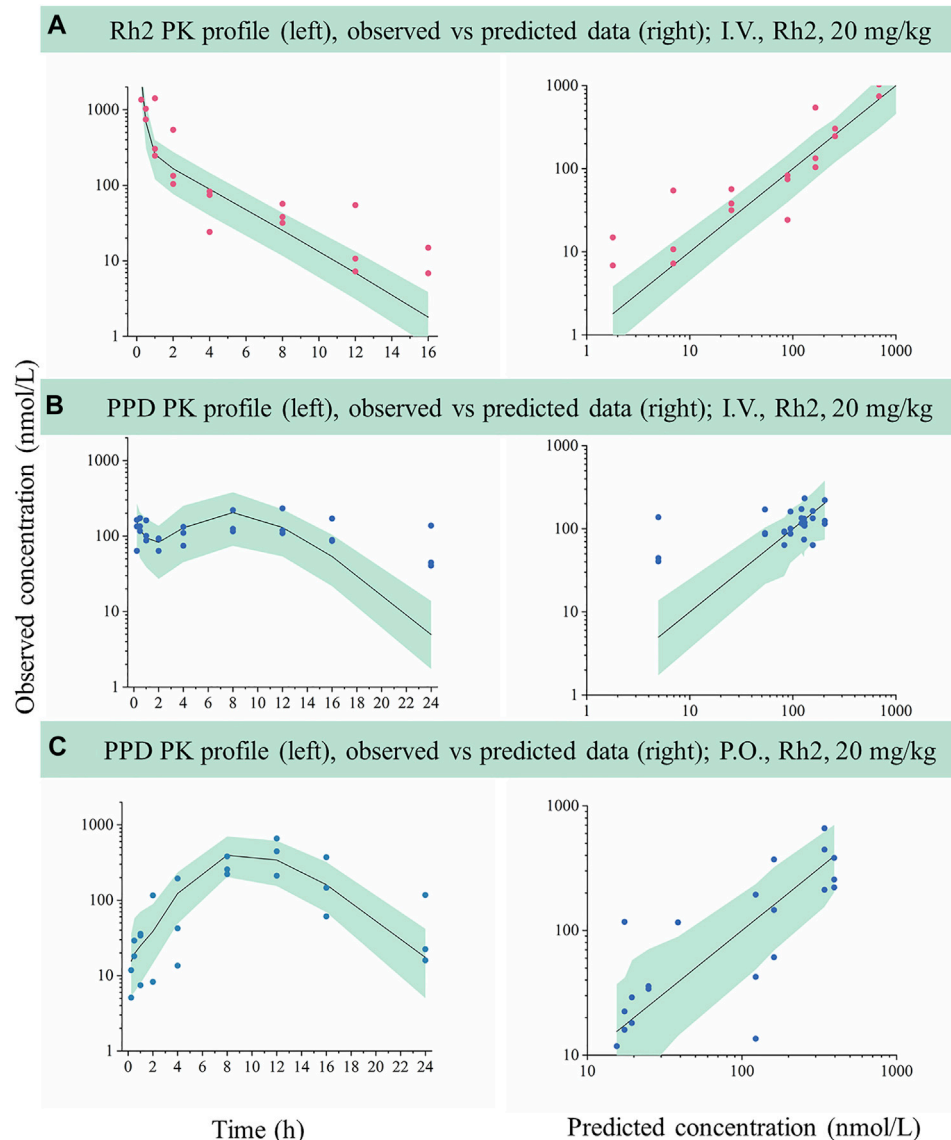


FIGURE 3 | External evaluation of the developed mechanistic pharmacokinetic model using the observed data from 20 mg/kg groups. Green areas represent the 90% model prediction interval between the 5th and 95th of percentiles, solid lines are the median model prediction (50th point of percentile), red symbols represent raw observations of Rh2, and blue symbols represent raw observations of PPD. **(A)**, Rh2 pharmacokinetic profile after I.V. administration of Rh2 at 20 mg/kg; **(B)**, PPD pharmacokinetic profile after I.V. administration of Rh2 at 20 mg/kg; **(C)**, PPD pharmacokinetic profile after P.O. administration of Rh2 at 20 mg/kg. The 90% model prediction intervals were predicted by the model developed by the data at 10 mg/kg. Most of the observed Rh2 or PPD concentrations lay within the predicted 5th and 95th percentiles with the majority of observations being evenly distributed around the median.

which is in accordance with the reported faeces excretion of Rh2 in rats (Gu et al., 2009). The other unknown metabolism route in plasma contributed to about 70% elimination of Rh2, which may be correlated with oxygenation (Qian et al., 2005). In addition, the predicted concentration time profiles of Rh2 and PPD could describe the observed data at 20 mg/kg (these data were not used in model building). These results supported the rationality of the hypothesis of deglycosylation kinetics.

The study predicted the percentage of Rh2 entering the systemic circulation in PPD form. In total, 11 and 20% of the administered Rh2 were predicted to be transformed into PPD and

enter the systemic circulation after I.V. administration and P.O. administration respectively. The predicted percentage was relatively reliable because it was determined by the exposure of PPD in plasma. The second peak of PPD was high and considered as the main transformation from Rh2 (route B). The first peak of PPD of I.V. administration was assumed to be caused by the transformation from Rh2 to PPD in the liver (route A). The first peak of PPD of P.O. administration might be caused by the transformation from Rh2 to PPD in the stomach (route C) (Bae et al., 2004), but route A and C only contributed to the formation of PPD slightly since the first peak was low.

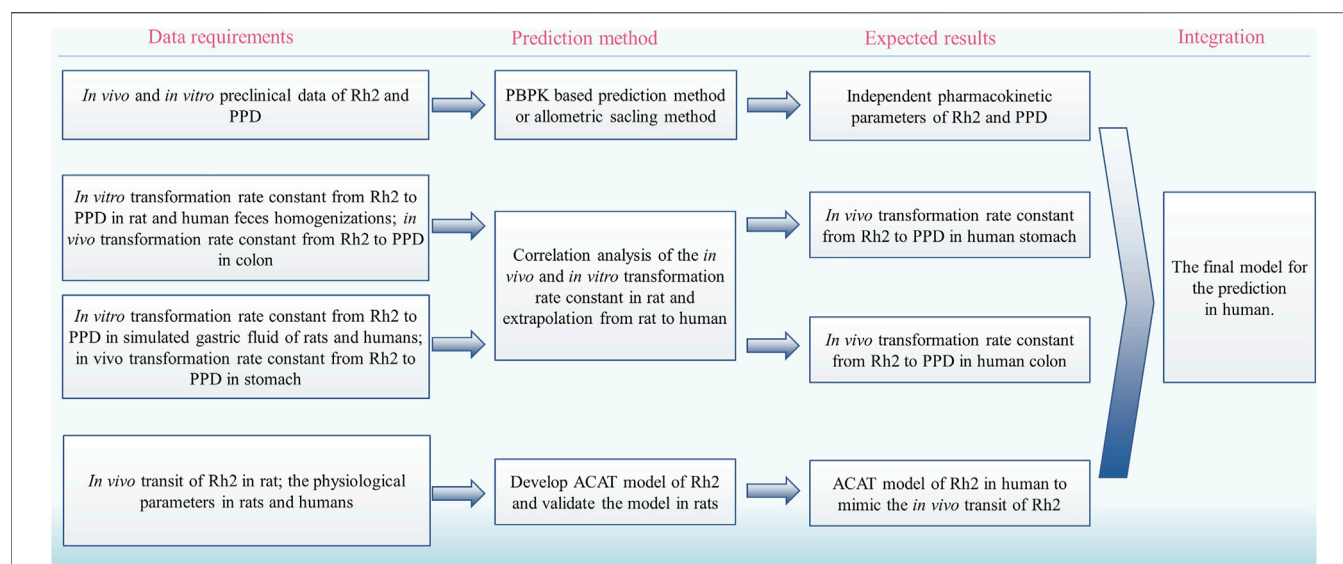


FIGURE 4 | The proposed strategy to translate the deglycosylation kinetics from rats to humans. PBPK, physiologically based pharmacokinetic; ACAT, advanced compartmental absorption and transit.

Most of the administered Rh2 were predicted to be eliminated by other unknown routes. The elimination of Rh2 by other unknown routes was evaluated in the stomach by matching the pharmacokinetic profile of PPD after oral administration of Rh2. We have considered three possible mechanisms to explain the elimination of Rh2 in the stomach by the following unknown routes: 1) Rh2 is absorbed into the liver and further metabolised there; 2) Rh2 is eliminated directly in the stomach; 3) Rh2 is transformed into PPD, and later eliminated in the stomach and intestine. Although all the assumptions could render similar performance and describe the observed data well, the third mechanism seems to be more biologically feasible. It should be noted that the details of other unknown routes should be used carefully since the assumption of an unknown route was not fully validated. But the predicted percentage of other unknown routes might be valuable for the next study of mass balance.

The developed models have potential to be applied for the pharmacokinetic study of other glycosides. Glycosides are popularly applied in food and medicine as important naturally occurring substances and include hormones, sweeteners, alkaloids, flavonoids, antibiotics, etc. (Khan et al., 2017; Momtazi-Borojeni et al., 2017; Osman et al., 2017; Botelho et al., 2019; Bundgaard Anker et al., 2019; Liu et al., 2019). Most glycosides have similar pharmacokinetics characteristics with Rh2. They can be hydrolysed into active aglycons in a biological body by the glycosidase in intestine microflorae (Tribolo et al., 2007; Winotapun et al., 2013; Mishra and Aeri, 2017). Herein, it is necessary to simultaneously investigate the kinetics of the glycoside and its aglycone for the pharmacokinetic study of glycoside. When the concentrations versus time data of glycoside and its aglycone are available, the developed models in this study may be a good starting point for pharmacokinetic modelling and simulation, which is the basis for further PK/PD modelling.

The deglycosylation metabolism of Rh2 could be observed in the rat and human intestinal bacteria indicating that the developed models had the possibility to translate preclinical findings into clinical practice (Bae et al., 2004; Qian and Cai, 2010). Considering the requirements on the quantitative translation, we proposed a strategy to translate the deglycosylation kinetics from rats to humans (Figure 4):

- (i) Use the reported method to predict the human pharmacokinetics of the parent drug after dosing of Rh2 and PPD, respectively, for the pharmacokinetic parameters of Rh2 and PPD, such as $V_{Rh2, plasma}$ and $V_{PPD, plasma}$ (Ren et al., 2019).
- (ii) Find the *in vitro* and *in vivo* correlation on the transformation rate constant from Rh2 to PPD in the colon and stomach in rats.
- (iii) Use the above relationship of *in vivo* and *in vitro* data to predict the human *in vivo* transformation rate constant from Rh2 to PPD based on the *in vitro* transformation rate constant from Rh2 to PPD in human faeces homogenates and simulated gastric fluid of humans, respectively.
- (iv) Develop the advanced compartmental absorption and transit (ACAT) model of Rh2 in rats and extrapolate the model from rats to humans (Gobeau et al., 2016).
- (v) Integrate the human pharmacokinetic parameters of Rh2 and PPD, transformation rate constants from Rh2 to PPD, and the intestinal transit of Rh2 to quantitatively predict the PK profiles of Rh2 and PPD in humans.

However, there are three key issues, which need more research: 1) the Rh2 may have better oral absorption in human than rats due to the longer intestine length and larger lumen area; 2) the extrapolation of excretion by faeces from rats to humans is challenging; 3) the proposed method of prediction needs to be validated by the actual data; but there are few publications involving

the Rh2 and PPD kinetics in humans. There are some challenges regarding the interspecies differences in deglycosylation activity of the colonic microbiota and large inter-individual differences in humans (Brody, 2020). However, the proposed strategy made the first step of this long journey to translate the deglycosylation kinetics from rats to humans and more studies are warranted.

5 CONCLUSION

This study has identified that PPD plays a critical role in the pharmacokinetics of Rh2. A mechanism-based pharmacokinetic model of Rh2 was developed to quantitatively describe the kinetics of Rh2 and PPD. The percentage of transformation from Rh2 to PPD could be predicted based on the model. The developed model has the potential to be used to describe the deglycosylation kinetics of other glycosides, the PK/PD analysis of ginseng, and the herb-drug interaction between ginseng and other P-gp substrates.

DATA AVAILABILITY STATEMENT

The original contributions presented in the study are included in the article/**Supplementary Material**, further inquiries can be directed to the corresponding authors.

ETHICS STATEMENT

The animal study was reviewed and approved by Research Animal Care and Laboratory Animal Resources of China Pharmaceutical University.

REFERENCES

- Akao, T., Kanaoka, M., and Kobashi, K. (1998). Appearance of Compound K, a Major Metabolite of Ginsenoside Rb1 by Intestinal Bacteria, in Rat Plasma after Oral Administration-Measurement of Compound K by Enzyme Immunoassay. *Biol. Pharm. Bull.* 21 (3), 245–249. doi:10.1248/bpb.21.245
- Aloga, R. N., Nuer-Allornuvor, G. F., Kuugbee, E. D., Yin, X., and Ma, G. (2020). Ginsenoside Rg1 and the Control of Inflammation Implications for the Therapy of Type 2 Diabetes: A Review of Scientific Findings and Call for Further Research. *Pharmacol. Res.* 152, 104630. doi:10.1016/j.phrs.2020.104630
- Bae, E. A., Han, M. J., Kim, E. J., and Kim, D. H. (2004). Transformation of Ginseng Saponins to Ginsenoside Rh2 by Acids and Human Intestinal Bacteria and Biological Activities of Their Transformants. *Arch. Pharm. Res.* 27 (1), 61–67. doi:10.1007/bf02980048
- Botelho, A. F. M., Pierezan, F., Soto-Blanco, B., and Melo, M. M. (2019). A Review of Cardiac Glycosides: Structure, Toxicokinetics, Clinical Signs, Diagnosis and Antineoplastic Potential. *Toxicol.* 158, 63–68. doi:10.1016/j.toxicol.2018.11.429
- Bridgeman, S. C., Northrop, W., Melton, P. E., Ellison, G. C., Newsholme, P., and Mamotte, C. D. S. (2020). Butyrate Generated by Gut Microbiota and its Therapeutic Role in Metabolic Syndrome. *Pharmacol. Res.* 160, 105174. doi:10.1016/j.phrs.2020.105174
- Brody, H. (2020). The Gut Microbiome. *Nature* 577 (7792), S5. doi:10.1038/d41586-020-00194-2
- Bundgaard Anker, C. C., Rafiq, S., and Jeppesen, P. B. (2019). Effect of Steviol Glycosides on Human Health with Emphasis on Type 2 Diabetic Biomarkers: A Systematic Review and Meta-Analysis of Randomized Controlled Trials. *Nutrients* 11 (9), 1965. doi:10.3390/nu11091965
- Choi, M. S., Yu, J. S., Yoo, H. H., and Kim, D. H. (2018). The Role of Gut Microbiota in the Pharmacokinetics of Antihypertensive Drugs. *Pharmacol. Res.* 130, 164–171. doi:10.1016/j.phrs.2018.01.019
- Dabek, M., McCrae, S. I., Stevens, V. J., Duncan, S. H., and Louis, P. (2008). Distribution of Beta-Glucosidase and Beta-Glucuronidase Activity and of Beta-Glucuronidase Gene Gus in Human Colonic Bacteria. *FEMS Microbiol. Ecol.* 66 (3), 487–495. doi:10.1111/j.1574-6941.2008.00520.x
- Dey, P. (2019). Gut Microbiota in Phytopharmacology: A Comprehensive Overview of Concepts, Reciprocal Interactions, Biotransformations and Mode of Actions. *Pharmacol. Res.* 147, 104367. doi:10.1016/j.phrs.2019.104367
- Doonan, S., Ho, T. K., Pearce, F. L., and Slaughter, C. A. (1978). Glycosidases in the Submaxillary Gland of the Mouse: Sexual Dimorphism and the Effects of Testosterone. *Int. J. Biochem.* 9 (4), 235–238. doi:10.1016/0020-711x(78)90004-6
- Feng, W., Ao, H., Peng, C., and Yan, D. (2019). Gut Microbiota, a New Frontier to Understand Traditional Chinese Medicines. *Pharmacol. Res.* 142, 176–191. doi:10.1016/j.phrs.2019.02.024
- Future Market Insights (2020). Global Ginseng Market: Forecast, Trend, Analysis & Competition Track - Global Review 2019 to 2027. Available at: <https://www.futuremarketinsights.com/reports/ginseng-market> (accessed Nov 24, 2020).
- Gloster, T. M., Turkenburg, J. P., Potts, J. R., Henrissat, B., and Davies, G. J. (2008). Divergence of Catalytic Mechanism within a Glycosidase Family Provides Insight into Evolution of Carbohydrate Metabolism by Human Gut flora. *Chem. Biol.* 15 (10), 1058–1067. doi:10.1016/j.chembiol.2008.09.005
- Gobeau, N., Stringer, R., De Buck, S., Tuntland, T., and Faller, B. (2016). Evaluation of the GastroPlus™ Advanced Compartmental and Transit (ACAT) Model in Early Discovery. *Pharm. Res.* 33 (9), 2126–2139. doi:10.1007/s11095-016-1951-z

AUTHOR CONTRIBUTIONS

Study design: H-cR, G-jW, J-yA and J-gS. Study conduct: H-cR, J-gS, S-hG, JS, FS, J-wZ, HA, BY, QH and L-sL. Data analysis and model development: H-cR, J-gS, and C-gY. Drafting manuscript: H-cR and J-gS. Revising manuscript: J-yA, C-gY, YS and G-jW. Approving final version of the manuscript: All authors.

FUNDING

The study was supported by “Double First-Class” University project (CPU2018GF01), Key project of National Natural Science Foundation of China (81530098), and the Key Medical Specialty of Shanghai (Grant No. ZK2019A15).

ACKNOWLEDGMENTS

The authors thank Yong-chao Fu at Tri-i Biotech (Shanghai) Inc. for technical support on the modelling and simulation. The authors would also like to thank Dr. Xiao Zhu (School of Pharmacy, Fudan University), Dr. Isabelle Hui San Kuan (Certara), and Carol Bennett (Lancaster University) for their proofreading of the manuscript.

SUPPLEMENTARY MATERIAL

The Supplementary Material for this article can be found online at: <https://www.frontiersin.org/articles/10.3389/fphar.2022.804377/full#supplementary-material>

- Gong, X., Li, X., Bo, A., Shi, R. Y., Li, Q. Y., Lei, L. J., et al. (2020). The Interactions between Gut Microbiota and Bioactive Ingredients of Traditional Chinese Medicines: A Review. *Pharmacol. Res.* 157, 104824. doi:10.1016/j.phrs.2020.104824
- Gu, Y., Wang, G. J., Sun, J. G., Jia, Y. W., Wang, W., Xu, M. J., et al. (2009). Pharmacokinetic Characterization of Ginsenoside Rh2, an Anticancer Nutrient from Ginseng, in Rats and Dogs. *Food Chem. Toxicol.* 47 (9), 2257–2268. doi:10.1016/j.fct.2009.06.013
- Gu, Y., Wang, G. J., Wu, X. L., Zheng, Y. T., Zhang, J. W., Ai, H., et al. (2010). Intestinal Absorption Mechanisms of Ginsenoside Rh2: Stereoselectivity and Involvement of ABC Transporters. *Xenobiotica* 40 (9), 602–612. doi:10.3109/00498254.2010.500744
- Jeong, D., Ham, J., Park, S., Kim, H. W., Kim, H., Ji, H. W., et al. (2019). Ginsenoside Rh2 Suppresses Breast Cancer Cell Proliferation by Epigenetically Regulating the Long Noncoding RNA C3orf67-AS1. *Am. J. Chin. Med.* 47 (7), 1643–1658. doi:10.1142/S0192415X19500848
- Jia, Q., Wang, L., Zhang, X., Ding, Y., Li, H., Yang, Y., et al. (2020). Prevention and Treatment of Chronic Heart Failure through Traditional Chinese Medicine: Role of the Gut Microbiota. *Pharmacol. Res.* 151, 104552. doi:10.1016/j.phrs.2019.104552
- Khan, H., Khan, Z., Amin, S., Mabkhot, Y. N., Mubarak, M. S., Hadda, T. B., et al. (2017). Plant Bioactive Molecules Bearing Glycosides as Lead Compounds for the Treatment of Fungal Infection: A Review. *Biomed. Pharmacother.* 93, 498–509. doi:10.1016/j.biopha.2017.06.077
- Laparra, J. M., and Sanz, Y. (2010). Interactions of Gut Microbiota with Functional Food Components and Nutraceuticals. *Pharmacol. Res.* 61 (3), 219–225. doi:10.1016/j.phrs.2009.11.001
- Lee, W. K., Kao, S. T., Liu, I. M., and Cheng, J. T. (2007). Ginsenoside Rh2 Is One of the Active Principles of Panax Ginseng Root to Improve Insulin Sensitivity in Fructose-Rich Chow-Fed Rats. *Horm. Metab. Res.* 39 (5), 347–354. doi:10.1055/s-2007-976537
- Liu, X., Gao, C., Liu, X., and Gao, T. (2019). Efficacy and Safety of Tripterygium Glycosides for Graves Ophthalmopathy: A Systematic Review and Meta-Analysis. *Medicine (Baltimore)* 98 (50), e18242. doi:10.1097/MD.00000000000018242
- Lu, C., Wang, Y., Lv, J., Jiang, N., Fan, B., Qu, L., et al. (2018). Ginsenoside Rh2 Reverses Sleep Deprivation-Induced Cognitive Deficit in Mice. *Behav. Brain Res.* 349, 109–115. doi:10.1016/j.bbr.2018.03.005
- Mishra, S., and Aeri, V. (2017). Biotransformation of Lignan Glycoside to its Aglycone by *Woodfordia fruticosa* Flowers: Quantification of Compounds Using a Validated HPTLC Method. *Pharm. Biol.* 55 (1), 360–366. doi:10.1080/13880209.2016.1238948
- Momtazi-Borojeni, A. A., Esmaili, S. A., Abdollahi, E., and Sahebkar, A. (2017). A Review on the Pharmacology and Toxicology of Steviol Glycosides Extracted from *Stevia rebaudiana*. *Curr. Pharm. Des.* 23 (11), 1616–1622. doi:10.2174/1381612822666161021142835
- Osman, M. H., Farrag, E., Selim, M., Osman, M. S., Hasanine, A., and Selim, A. (2017). Cardiac Glycosides Use and the Risk and Mortality of Cancer; Systematic Review and Meta-Analysis of Observational Studies. *PLoS One* 12 (6), e0178611. doi:10.1371/journal.pone.0178611
- Peng, B., He, R., Xu, Q., Yang, Y., Hu, Q., Hou, H., et al. (2019). Ginsenoside 20(S)-Protopanaxadiol Inhibits Triple-Negative Breast Cancer Metastasis *In Vivo* by Targeting EGFR-Mediated MAPK Pathway. *Pharmacol. Res.* 142, 1–13. doi:10.1016/j.phrs.2019.02.003
- Popovich, D. G., and Kitts, D. D. (2002). Structure-Function Relationship Exists for Ginsenosides in Reducing Cell Proliferation and Inducing Apoptosis in the Human Leukemia (THP-1) Cell Line. *Arch. Biochem. Biophys.* 406 (1), 1–8. doi:10.1016/s0003-9861(02)00398-3
- Qi, Z., Li, W., Tan, J., Wang, C., Lin, H., Zhou, B., et al. (2019). Effect of Ginsenoside Rh2 on Renal Apoptosis in Cisplatin-Induced Nephrotoxicity *In Vivo*. *Phytomedicine* 61, 152862. doi:10.1016/j.phymed.2019.152862
- Qian, T., and Cai, Z. (2010). Biotransformation of Ginsenosides Rb1, Rg3 and Rh2 in Rat Gastrointestinal Tracts. *Chin. Med.* 5, 19. doi:10.1186/1749-8546-5-19
- Qian, T., Cai, Z., Wong, R. N., and Jiang, Z. H. (2005). Liquid Chromatography/Mass Spectrometric Analysis of Rat Samples for *In Vivo* Metabolism and Pharmacokinetic Studies of Ginsenoside Rh2. *Rapid Commun. Mass. Spectrom.* 19 (23), 3549–3554. doi:10.1002/rcm.2232
- Ren, H. C., Sai, Y., and Chen, T. (2019). Evaluation of Generic Methods to Predict Human Pharmacokinetics Using Physiologically Based Pharmacokinetic Model for Early Drug Discovery of Tyrosine Kinase Inhibitors. *Eur. J. Drug Metab. Pharmacokinet.* 44 (1), 121–132. doi:10.1007/s13318-018-0496-4
- Ren, H. C., Sun, J. G., Wang, G. J., A, J.-Y., Xie, H.-T., Zha, W. B., et al. (2008). Sensitive Determination of 20(S)-Protopanaxadiol in Rat Plasma Using HPLC-APCI-MS: Application of Pharmacokinetic Study in Rats. *J. Pharm. Biomed. Anal.* 48 (5), 1476–1480. doi:10.1016/j.jpba.2008.09.045
- Savage, N. (2020). The Complex Relationship between Drugs and the Microbiome. *Nature* 577 (7792), S10–S11. doi:10.1038/d41586-020-00196-0
- Tribolo, S., Berrin, J. G., Kroon, P. A., Czjzek, M., and Juge, N. (2007). The crystal Structure of Human Cytosolic Beta-Glucosidase Unravels the Substrate Aglycone Specificity of a Family 1 Glycoside Hydrolase. *J. Mol. Biol.* 370 (5), 964–975. doi:10.1016/j.jmb.2007.05.034
- Wang, D. D., and Zhang, S. (2012). Standardized Visual Predictive Check Versus Visual Predictive Check for Model Evaluation. *J. Clin. Pharmacol.* 52 (1), 39–54. doi:10.1177/0091270010390040
- Wang, M., Yan, S. J., Zhang, H. T., Li, N., Liu, T., Zhang, Y. L., et al. (2017). Ginsenoside Rh2 Enhances the Antitumor Immunological Response of a Melanoma Mice Model. *Oncol. Lett.* 13 (2), 681–685. doi:10.3892/ol.2016.5490
- Wang, Y., Dong, J., Liu, P., Lau, C. W., Gao, Z., Zhou, D., et al. (2014). Ginsenoside Rb3 Attenuates Oxidative Stress and Preserves Endothelial Function in Renal Arteries from Hypertensive Rats. *Br. J. Pharmacol.* 171 (13), 3171–3181. doi:10.1111/bph.12660
- Winotapun, W., Opanasopit, P., Ngawhirunpat, T., and Rojanarata, T. (2013). One-Enzyme Catalyzed Simultaneous Plant Cell Disruption and Conversion of Released Glycoside to Aglycone Combined with *In Situ* Product Separation as green One-Pot Production of Genipin from Gardenia Fruit. *Enzyme Microb. Technol.* 53 (2), 92–96. doi:10.1016/j.enzmictec.2013.05.001
- Yue, S. J., Wang, W. X., Yu, J. G., Chen, Y. Y., Shi, X. Q., Yan, D., et al. (2019). Gut Microbiota Modulation with Traditional Chinese Medicine: A System Biology-Driven Approach. *Pharmacol. Res.* 148, 104453. doi:10.1016/j.phrs.2019.104453
- Zhang, J., Li, W., Yuan, Q., Zhou, J., Zhang, J., Cao, Y., et al. (2019). Transcriptome Analyses of the Anti-Proliferative Effects of 20(S)-Ginsenoside Rh2 on HepG2 Cells. *Front. Pharmacol.* 10, 1331. doi:10.3389/fphar.2019.01331
- Zhang, J., Liu, M., Huang, M., Chen, M., Zhang, D., Luo, L., et al. (2019). Ginsenoside F1 Promotes Angiogenesis by Activating the IGF-1/IGF1R Pathway. *Pharmacol. Res.* 144, 292–305. doi:10.1016/j.phrs.2019.04.021
- Zhang, J., Zhou, F., Wu, X., Gu, Y., Ai, H., Zheng, Y., et al. (2010). 20(S)-Ginsenoside Rh2 Noncompetitively Inhibits P-Glycoprotein *In Vitro* and *In Vivo*: A Case for Herb-Drug Interactions. *Drug Metab. Dispos.* 38 (12), 2179–2187. doi:10.1124/dmd.110.034793
- Zheng, M. M., Xu, F. X., Li, Y. J., Xi, X. Z., Cui, X. W., Han, C. C., et al. (2017). Study on Transformation of Ginsenosides in Different Methods. *Biomed. Res. Int.* 2017, 8601027. doi:10.1155/2017/8601027
- Zhu, Y., Zhu, C., Yang, H., Deng, J., and Fan, D. (2020). Protective Effect of Ginsenoside Rg5 against Kidney Injury via Inhibition of NLRP3 Inflammasome Activation and the MAPK Signaling Pathway in High-Fat Diet/Streptozotocin-Induced Diabetic Mice. *Pharmacol. Res.* 155, 104746. doi:10.1016/j.phrs.2020.104746
- Zimmermann, M., Zimmermann-Kogadeeva, M., Wegmann, R., and Goodman, A. L. (2019). Mapping Human Microbiome Drug Metabolism by Gut Bacteria and Their Genes. *Nature* 570 (7762), 462–467. doi:10.1038/s41586-019-1291-3

Conflict of Interest: YS and SG was employed by Hutchison MediPharma Ltd.

The remaining authors declare that the research was conducted in the absence of any commercial or financial relationships that could be construed as a potential conflict of interest.

Publisher's Note: All claims expressed in this article are solely those of the authors and do not necessarily represent those of their affiliated organizations, or those of the publisher, the editors, and the reviewers. Any product that may be evaluated in this article, or claim that may be made by its manufacturer, is not guaranteed or endorsed by the publisher.

Copyright © 2022 Ren, Sun, A, Gu, Shi, Shao, Ai, Zhang, Peng, Yan, Huang, Liu, Sai, Wang and Yang. This is an open-access article distributed under the terms of the Creative Commons Attribution License (CC BY). The use, distribution or reproduction in other forums is permitted, provided the original author(s) and the copyright owner(s) are credited and that the original publication in this journal is cited, in accordance with accepted academic practice. No use, distribution or reproduction is permitted which does not comply with these terms.



Beneficial Effect of Edoxaban on Preventing Atrial Fibrillation and Coagulation by Reducing Inflammation *via* HBG1/HBD Biomarkers

Chenguang Yang^{1†}, Xiang Wang^{1,2†}, Ying Guo¹, Xuyang Meng¹, Yi Li¹, Chenxi Xia¹, Lingbing Meng^{1,2}, Min Dong^{1*} and Fang Wang^{1,2*}

¹Department of Cardiology, Beijing Hospital, National Center of Gerontology, Institute of Geriatric Medicine, Chinese Academy of Medical Sciences, Beijing, China, ²Graduate School of Peking Union Medical College, Chinese Academy of Medical Science, Beijing, China

OPEN ACCESS

Edited by:

Ren-ai Xu,
First Affiliated Hospital of Wenzhou
Medical University, China

Reviewed by:

Lu Hua,
Chinese Academy of Medical
Sciences and Peking Union Medical
College, China
Zhigang Guo,
Tianjin Chest Hospital, China

*Correspondence:

Fang Wang
bjh_wangfang@163.com
Min Dong
13701054558@163.com

[†]These authors have contributed
equally to this work.

Specialty section:

This article was submitted to
Drug Metabolism and Transport,
a section of the journal
Frontiers in Pharmacology.

Received: 25 March 2022

Accepted: 20 April 2022

Published: 03 June 2022

Citation:

Yang C, Wang X, Guo Y, Meng X, Li Y,
Xia C, Meng L, Dong M and Wang F
(2022) Beneficial Effect of Edoxaban on
Preventing Atrial Fibrillation and
Coagulation by Reducing Inflammation
via HBG1/HBD Biomarkers.
Front. Pharmacol. 13:904317.
doi: 10.3389/fphar.2022.904317

Background: Atrial fibrillation (AF) is the most common cardiac arrhythmia. The effectiveness and mechanism of edoxaban in preventing stroke after atrial fibrillation remain unclear.

Methods: The expressions of HBG1 and HBD in red blood cells were tested in AF. Sixty C57B/6J mice were randomly divided into the following groups: the control (CON) group, atrial fibrillation (AF) group, AF + edoxaban group, and AF + rivaroxaban group. H&E staining assay and reticular fiber staining were performed. Myocardial fibrosis was evaluated by the Masson staining assay, Sirius red staining assay, and immunohistochemical assay for the expressions of α -SMA and COL1A1. ELISA and RT-PCR assay were performed for the detection of inflammatory parameters (TNF- α , IL-1 β , IL-6, and IL-10). Blood lipids were detected by using the Beckman automatic biochemical analyzer. Furthermore, four items of coagulation were detected, and molecular docking among HBG1, HBD, and MASP1 (Xa) was performed by PyMOL 2.1 software. The BP neural network model, cubic spline interpolation, and support vector machine model were constructed to predict prothrombin time based on HBG1 and HBD expressions. COIP assay was performed to construct the interaction between HBG1 and HBD. The functional enrichment analysis was performed by DAVID and Metascape tools.

Results: The expressions of HBG1 and HBD in red blood cells of the patients with atrial fibrillation were decreased. The results showed a lower level of hemoglobin in red blood cells with HBG1-siRNA and HBD-siRNA. Compared with the AF group, the collagen fiber percentage in the AF + edoxaban group was decreased ($p < 0.05$). After using edoxaban, the expressions of TNF- α , IL-1 β , IL-6, and IL-10 were significantly decreased ($p < 0.05$). The LDL-C, TC, and TG levels were downregulated in the AF + edoxaban group. The PT and APTT levels in the AF + edoxaban group were more increasing than in the AF mice ($p < 0.05$). Compared with the AF group, the expressions of HBG1 and HBD were downregulated in the AF + edoxaban group ($p < 0.05$). HBG1 protein matched well

with HBD and MASP1(Xa) protein surfaces. There exists a significant interaction between HBG1, HBD, and PT *via* the BP neural network and support vector machine. Enrichment analysis showed that HBG1 and HBD were mainly enriched in blood coagulation.

Conclusion: Edoxaban could prevent atrial fibrillation and coagulation by reducing inflammation, lipids, and fibrosis *via* HBG1/HBD biomarkers effectively, and the effect was superior to that of rivaroxaban.

Keywords: atrial fibrillation, HBG1, HBD, edoxaban, inflammation, rivaroxaban

INTRODUCTION

Atrial fibrillation (AF) is the most common cardiac arrhythmia (Miyasaka et al., 2006), affecting 33 million people worldwide annually (Chugh et al., 2013). AF is associated with a threefold-to-fivefold increased risk of stroke (Wolf et al., 1998), and AF-related strokes are typically severe, causing significant long-term physical disability, cognitive dysfunction, and high mortality and healthcare costs, compared to other stroke subtypes (Bruins et al., 1997; Kirchhof et al., 2016, 2016). Since first reported by Bruins et al. (Bruins et al., 1997), there has been increasing evidence that the inflammatory status is closely related to the development of atrial fibrillation ((Katrakis 2006; Zhang et al., 2017; Zhou and Dudley 2020). Inflammatory responses, as evidenced by increased circulating levels of inflammatory mediators such as C-reactive protein (CRP), contribute to the persistence of AF (Bruins et al., 1997). Inflammatory mediators including ILs are thought to promote arrhythmogenesis as a result of structural and contractile remodeling of the atria and endocardium (Issac et al., 2007). The number of T lymphocytes and monocytes/macrophages in atrial myocardium was increased in AF patients (Smorodinova et al., 2017). With regard to thrombosis, elevated plasma CRP and interleukin (IL)-6 levels were independently associated with stroke risk (Lip et al., 2007; Roldán et al., 2012; Hu et al., 2015). Taken together, these studies suggest that patients with atrial fibrillation may benefit from the use of anticoagulants with anti-inflammatory properties or other aspects.

Edoxaban is a once-daily oral inhibitor of factor Xa, currently indicated for the prevention of stroke or systemic embolism in patients with nonvalvular AF (Giugliano et al., 2013). The protective effect might be explained by reduced factor Xa-mediated thrombin activation because thrombin triggers thrombus formation *via* activation of fibrinogen and platelets and induces inflammatory processes *via* protease-activated receptor (PAR) 1, 3, and 4 signaling (Popović et al., 2012).

HBG1 and HBD are important genetic components of hemoglobin β -globin (Patrinos et al., 2005). HBD has been found to be closely associated with inflammation (James et al., 2018), and upregulation of HBD has been observed during infection and inflammation (Özdemir et al., 2020). In agreement with previous studies, the GO annotations related to HBD are oxygen transport, iron ion binding, blood coagulation, and combination with oxygen (Chen et al., 2020). In previous studies, we found that HBG1/HBD may induce the occurrence and development of AF through inflammation and hemoglobin levels (Wang et al., 2022). We need further studies to

evaluate the clinical implications of our results and whether patients with atrial fibrillation will benefit from the anti-inflammatory effects of edoxaban.

Therefore, in this study, AF model mice were used to explore the inhibitory effect of edoxaban on HBG1/HBD, which on the one hand reduced the degree of effect of AF on the myocardium and on the other hand plays a role in the inhibition of inflammation, lipids, and fibrosis. Meanwhile, we further compared the protective effects of edoxaban and rivaroxaban by inhibiting inflammation, lipids, and fibrosis.

METHODS

Isolation of Red Blood Cells

The peripheral blood was taken from patients with and without AF using an anticoagulant tube. The sedimentation rate of normal peripheral blood erythrocytes and leukocytes is different, so it can be separated from normal peripheral blood erythrocytes. Anticoagulant venous blood was added to 3% gelatin brine or 6% dextran solution and then mixed. The tube is made to stand upright in a temperature box at room temperature or 37°C for 30–60 min. Gelatin and the red blood cell bonding effect make red blood cells sink quickly and white blood cells stay in the gelatin solution. A capillary pipette was used to absorb the upper layer of the fluid rich in white blood cells, which is then transferred to another tube. Ca^{2+} , Mg^{2+} and Hank's balanced salt solution were added to reach 3 cm from the mouth of the test tube and mixed well. The mixture was centrifuged at 2000 r/min for 10 min, and the supernatant was discarded and washed twice in the same way. The precipitated cells were suspended with Hank's solution of 10–20% inactivated fetal calf serum and prepared with a suspension of desired cell concentration, usually 2×10^6 /min.

Immunofluorescence Assay of the Cell Smear

The cell suspension was centrifuged at 2800 rpm and 4°C for 5 min, the supernatant was discarded, and 2 ml of 4% paraformaldehyde was added to fix the cell suspension, according to the number of cells deposited at the bottom. The fixed cell suspension was centrifuged at 2,800 rpm/min and at 25°C for 5 min, the supernatant was discarded, and PBS was added according to the amount of sediment deposited at the bottom. The cell suspension was spread over the circle with a

pipette placed to dry naturally. A measure of 50–100 μ l of fixing solution was added inside the circle, and the serum was blocked. HBG1 protein was detected using a HBG1 polyclonal antibody (dilution rate = 1:1,000, 16824-1-AP; ProteinTech, Rosemont, United States). HBD proteins were detected using an HBD polyclonal antibody (dilution rate = 1:1,000, 25728-1-AP; ProteinTech, Rosemont, United States). The primary antibody was added overnight at 4°C. Cell climbing slides were covered with the secondary antibody for 50 min. The liquid was discarded slightly. Fluorescent microscopy was employed to observe the image. Positive cells are observed in red.

Synthesis of HBG1-siRNA and HBD-siRNA and the Detection of Hemoglobin

The cells in the logarithmic growth phase were placed on 6-well plates with 5×10^5 cells/well and transfected overnight. HBG1-siRNA and HBD-siRNA were constructed and obtained from the Beijing Qingke Biotechnology Co., Ltd. (Beijing, China). HBG1-siRNA and HBD-siRNA were transfected into peripheral blood erythrocytes by using the LipofectamineTM 3000 transfection reagent (Invitrogen, L300008). Before adding the transfection mixture, the liquid was drawn out from the 6-well plate and re-added to 2 ml fresh medium. A measure of 250 F06D1 of transfection mixture was added to the corresponding well, drop by drop, then shaken gently and mixed well. After 6-well plates were placed in a CO₂ incubator for culturing, the cells were collected to extract RNA, and the expression levels of HBG1 and HBD were detected by qPCR. An automatic blood cell analyzer (Mindray, V500085) was used to detect the hemoglobin content.

Construction of the Atrial Fibrillation Mouse Model

Sixty C57B/6J mice were randomly divided into the following groups: the control (CON) group, atrial fibrillation (AF) group, AF + edoxaban group, and AF + rivaroxaban group, with 15 mice in each group. The mice in the atrial fibrillation model group were intraperitoneally injected with 2.5 mg/kg/d isoproterenol (Southwest Taiji, 2 ml: 1mg, Southwest Pharmaceutical Co., Ltd.), and the mice in the blank control group were intraperitoneally injected with the same amount of normal saline. In order to increase the success rate of construction of the AF model, the high-fat diet was used. The ECG of mice was collected by using an electrocardiogram machine (VECG-230B, three sharp beasts) after 4 weeks of continuous injection. The control group had a standard II lead electrocardiogram, and the mice in the modeling group had standard II lead atrial fibrillation, suggesting that the atrial fibrillation model was successfully established. The AF + edoxaban and the AF + rivaroxaban group were given edoxaban 0.03 mg/d and rivaroxaban 0.01 mg/d on the next day after the successful modeling, respectively. The drugs were dissolved in the daily drinking water of mice and fed for 14 days. The blank control group and the atrial fibrillation model group were given the same amount of drinking water. After 14 days, the mice were killed, and their blood and heart tissue were collected.

H&E Staining Assay

The heart tissue was paraffin-embedded and sectioned. The paraffin sections were dewaxed using water. The sections were stained with Harris's hematoxylin for 3–8 min, washed with tap water, and differentiated with 1% of ethyl hydrochloric acid within seconds. Again, the sections were washed with tap water, which then returned to blue with 0.6% ammonia, followed by washing with tap water. The sections were stained with eosin solution (1–3 min). The slices were dehydrated, dried, and then sealed with neutral gum. Microscopic examination, image collection, and analysis were performed.

Masson's Staining Assay

The heart tissue was paraffin-embedded and sectioned. The paraffin sections were dewaxed with water. The slices were soaked in Masson's A solution overnight and washed under running water. The solution was sectioned into Masson B solution and Masson C solution in an equal ratio mixture of dye for 1 min, washed with tap water, and differentiated with 1% hydrochloric acid alcohol, followed by washing with tap water. The slices were soaked in Masson's D solution for 6 min and rinsed with tap water, followed by soaking in Masson's E solution for 1 min. The slices were stained directly with Masson F solution for 2–30 s. Sections were rinsed and differentiated with 1% glacial acetic acid and dehydrated with two cylinders of anhydrous ethanol. Using the transparent sealing sheet, the slices were put into the third cylinder of anhydrous ethanol for 5 min and xylene for 5 min for sealing with transparent neutral gum. Microscopic examination, image collection, and analysis were performed.

Sirius Red Staining Assay

The slice was dewaxed. The section was stained with Sirius red solution (8 min) and then dehydrated quickly with two or three cups of anhydrous ethanol. The microscope was used to observe the image and analysis. Under an optical microscope, it was observed that collagen fibers are red with a yellow background.

Reticular Fiber Staining

Reticular fiber incubation solution is prepared with 2 ml of 10% silver nitrate; the concentrated ammonia was added drop by drop by shaking the container while adding, and then, the concentrated aqueous ammonia drop was added after precipitation occurs, until the precipitation is just dissolved. Then, 2 ml of 3% NaOH was added until the precipitate forms again, and the concentrated aqueous ammonia was added drop by drop, until the precipitation is just dissolved; ultra-pure water was added to the mixture to make up to 40 ml (Miyasaka et al., 2006). For paraffin section deparaffinization and rehydration, the slides were washed with xylene I for 20 min, xylene II for 20 min, absolute ethanol I for 5 min, absolute ethanol II for 5 min, and 75% alcohol for 5 min, followed by tap water washing (Chugh et al., 2013). For tissue acidification, a circle was drawn to enclose the tissue, and then acidification solution (0.5% potassium permanganate and 0.5% sulfuric acid mixed in 1:1 ratio) was added drop by drop to oxidize the tissue for 5 min. The slides were then washed for 10 s by transferring it into two cylinders of ultra-pure water, and the

TABLE 1 | Primers of the genes.

Gene name	Primer (5'-3')
HBG1-S	ATGGGTTCATTTACAGAGGAGG
HBG1-A	ATGGGTAGACAACCAGGAGCC
HBD-S	TGCCTTTAGTGATGGCCTGG
HBD-A	AACAGTCCAGGATCTCAATGGT
α -SMA-S	GTCTCAGTCAGCCTAAGGAAGCC
α -SMA-A	GAGAAATGTTGGGCAAAGGGA
COL1A1-S	CAGCAGTAGCCAGAACACAGT
COL1A1-A	GGCATTTCATAAGCCTCATTGTC
TNF- α -S	TGGAGGGCTAGGATTGG
TNF- α -A	TGGTAGGAGACGGCGATGC
IL-1 β -S	AAACAAGAAGGCTGGAA
IL-1 β -A	GGTGGCTAAGAACACTGGA
IL-6-S	CCAAGTTGTGCGACTCAC
IL-6-A	CTGCACTCTTGCCCTTGT
IL-10-S	GCTCCGCAGAAAGAAAGAC
IL-10-A	TCAAAGCGAAGGAAACAA

slides were dried to remove excess water (Wolf et al., 1998). For tissue bleaching, a drop of 2% oxalic acid was added to the tissues for 2 min, the slides were washed in ultra-pure water for 3 times, 5 s each, and the slides were dried to remove excess water (Kirchhof et al., 2016). For mordant staining, a drop of the Gordon and Sweet's staining solution F was added to the tissue for 15 min (light-proof), the slides were washed in ultra-pure water for 3 times, 5 s each, and the slides were dried to remove excess water (Bruins et al., 1997). For Gordon and Sweet's incubation solution staining, a drop of the Gordon and Sweet's incubation solution was added to the tissues for 5 min (light-proof), the slides were washed in ultra-pure water for 3 times, 5 s each, and the slides were dried to remove excess water (Zhang et al., 2017). For reduction, a drop of 10% neutral formaldehyde solution was added to the tissue for 3 min, the slides were washed in ultra-pure water for 3 times, 5 s each, and the slides were dried to remove excess water (Katritsis 2006). For dehydration and sealing with neutral balsam, the slides were washed in absolute ethanol I for 5 min, absolute ethanol II for 5 min, absolute ethanol III for 5 min, dimethyl I for 5 min, and xylene II for 5 min. (Zhou and Dudley 2020). Then, microscopic examination, image collection, and analysis were performed. The reticular fibers are black in color, and the background is brownish yellow.

Immunohistochemical Assay

The paraffin section was deparaffinized and rehydrated. Antigen retrieval was performed by citric acid (pH 6.0) antigen retrieval buffer. For the assay, 3% hydrogen peroxide was used to block the endogenous peroxidase activity (25 min). Then, 3% BSA was added for serum sealing (30 min). α -SMA protein was detected using a α -SMA polyclonal antibody (dilution rate = 1:2,000, 14395-1-AP; ProteinTech, Rosemont, United States). COL1A1 proteins were detected using a COL1A1 polyclonal antibody (dilution rate = 1:3,000, 67288-1-Ig; ProteinTech, Rosemont, United States). The primary antibody was added overnight at 4°C. Tissues are covered with the secondary antibody (50 min). The DAB chromogenic reaction was performed. The positive target is brownish yellow. The sections are counterstained with

hematoxylin stain solution for about 3 min. A microscope (Nikon, E100) was used to observe the image.

Detection of the mRNA Expression via RT-qPCR

RNA was extracted using the TRIzol reagent, as per the manufacturer's instructions. RNA concentration and purity were detected by using a NanoDrop 2000 spectrophotometer. After the instrument is reset blank, 2.5 μ L of RNA solution was taken to be measured on the testing base, and the sample arm was lowered to take the readings. The absorbance was tested using a piece of computer software. Reverse transcription was performed by using the Sensiscript RT Kit (G3330, Servicebio), and the reagent was mixed gently and centrifuged. The primers are shown in Table 1. The reverse transcription program conditions are as follows: 25°C for 5 min; 42°C for 30 min; and 85°C for 5 s. A 0.1-ml PCR plate was taken to prepare the reaction system as follows: 2 \times SYBR Green qPCR Master Mix (None ROX), 7.5 μ L; F/R primers, 1.5 μ L; cDNA, 2.0 μ L; and nuclease-free water, 4.0 μ L. Then, PCR amplification was performed. In the first step, predegeneration was performed for 30 s under the temperature of 95°C. The second step included 40 cycles, and each cycle consists of degeneration for 15 s under the temperature of 95°C and annealing/extension for 30 s under the temperature of 60°C. In the third step, the melting curve method was performed. Also, in this step, the temperature was changed from 65 to 95°C, and the fluorescence signal was collected at a 0.5 temperature rise. The relative quantitative expression data of genes were analyzed by the $2^{-\Delta\Delta C_t}$ method.

ELISA for the Detection of Inflammatory Parameters

The inflammatory biomarkers TNF- α , IL-1 β , IL-6, and IL-10 were detected using the Mouse TNF- α Simple Step ELISA[®] Kit (ab208348, Abcam, United States), Mouse IL-1 β Simple Step ELISA[®] Kit (ab197742, Abcam, United States), Mouse IL-6 Simple Step ELISA[®] Kit (ab222503, Abcam, United States), and Mouse IL-10 Simple Step ELISA[®] Kit (ab100697, Abcam, United States), respectively, as per the manufacturer's instructions. The following steps were carried out to detect the inflammatory biomarkers using ELISA.

The buffer was encapsulated with carbonate; the antibody was diluted to a protein content of 1–10 μ g/ml. A measure of 100 μ L was added to each well of the polystyrene plate overnight at 4°C. Then, 200 F06D1 sealing solution was added to each well and incubated at 37°C for 1–2 h. The sealing plate film was removed carefully, placed into the washing machine, and washed for 3–5 times. Thereafter, 100 μ L of the appropriately diluted sample was added to the coated reaction well. After sealing with a sealing plate membrane, it was incubated at 37°C for 1–2 h. Then, 100 μ L of diluted biotinylated antibody working solution was added to each well. After sealing with a sealing plate membrane, it was incubated at 37°C for 1 h. It was followed by addition of 100 μ L of the diluted enzyme conjugate to each well. After sealing the plate with sealing plate membrane, the plate was incubated at 37°C

away from light for 30 min. Then, 100 μ L TMB substrate solution was added to each well. At 37°C, the reaction was protected from light for 10–30 min until a distinct color gradient in the multiple dilution standard hole was found. Furthermore, 100 μ L of 2M sulfuric acid was added to each reaction well, and the color changes from blue to yellow within 10 min on the microplate reader at 450 nm. The OD value of each hole was measured after adjusting the blank control hole. According to the standard concentration and OD value of the standard curve, the sample concentration was calculated.

Determination of Blood Lipid

Whole blood samples were placed at room temperature for 2 h and separated at 2–8°C at 3000 rpm for 15 min. The supernatant was taken for packaging, and the specimen was stored at –80°C. The thawed samples were centrifuged again and then tested for blood lipids. Total cholesterol (TG), triglyceride (TG), low-density lipoprotein cholesterol (LDL-C), and high-density lipoprotein cholesterol (HDL-C) were determined by the Beckman automatic biochemical analyzer.

Detection of Four Items of Coagulation

The mouse blood was slowly injected into a plastic tube containing 0.5 ml of 109 mmol/L sodium citrate solution and thoroughly mixed. The platelets were removed, and the plasma was separated by centrifugation at 3,000 rpm for 15 min. An automatic coagulation analyzer is used (Redu Life Science Co., Ltd., RAC-030) for the determination of four coagulation items: prothrombin time (PT), activated partial prothrombin time (APTT), thrombin time (TT), and fibrinogen content (FIB). The kits used in this experiment are as follows: prothrombin time (PT) kit (Batch No: 105090), Laibo Institute of Biological Experimental Materials; activated partial thrombin time (APTT) kit (Batch No. 111021), Laibo Institute of Biological Experimental Materials; thrombin time (TT) kit (Batch No.: 111027), Laibo Institute of Biological Experimental Materials; and fibrinogen (FIB) kit (Batch No.: 1110131), Beijing Laibo Institute of Biological Experimental Materials.

Molecular Docking Among HBG1, HBD, and MASP1 (Xa)

HBG1 (PDB ID:1I3D), HBD (PDB ID : 1SHR), and MASP1 (PDB ID : 4KKD) target protein structures were obtained from the RCSB database (<https://www.rcsb.org/>). All protein structures were processed in the molecular operating environment (MOE 2019.1). The position selected was Amber10, including the removal of water and ions, protonation, addition of missing atoms and completion of missing groups, and protein–energy minimization. Using HDock, the protein is set to rigid. The docking contact site is set to the full surface, and the conformation generated after docking is set to 100. The most negative conformation was selected by the scoring function and visualized by the PyMOL 2.1 software.

Construction of the BP Neural Network Model and Cubic Spline Interpolation to Predict Prothrombin Time Based on HBG1 and HBD Expressions

Through the training of sample data, the BP neural network constantly revises the network weights and thresholds to make the error function descend along the negative gradient direction and approach the desired output. The model takes HBG1 and HBD expressions of each group of data as input and prothrombin time as output, so the number of nodes in the input layer is 2 and the number of nodes in the output layer is 1. A neural network with a hidden layer can approach a nonlinear function with arbitrary precision as long as there are enough hidden nodes. Therefore, a three-layer multi-input single-output BP network with a hidden layer is used to build a prediction model. In addition, the S-type tangent function *tansig* was selected as the excitation function of hidden layer neurons in this study. Since the output of the network is within the range of [–1, 1], the prediction model selects the S-type logarithmic function *tansig* as the excitation function of the neurons at the output layer. The neural network toolbox in MATLAB (MathWorks, 2017a) was used for network training. HBG1, HBD, and prothrombin time were quantified by cubic spline interpolation.

Construction of the Support Vector Machine Model Based on HBG1, HBD, and PT

The support vector machine (SVM) can improve the generalization ability of the learning machine as much as possible. Even if the discriminant function is obtained from the limited data set, it can still get a small error for an independent test set. In addition, the support vector machine is a quadratic optimization problem, which can ensure that the extremum solution is the global optimal solution. SVM uses the hinge loss function to calculate empirical risk and adds a regularization term to the solving system to optimize structural risk. It is a classifier with sparsity and robustness. SVM, one of the common kernel learning methods, can be used for nonlinear classification by the kernel method. This study intends to use the support vector machine algorithm to build the correlation model between HBG1, HBD and PT.

COIP Assay

Peripheral blood erythrocytes were isolated from mice for cell culture. An appropriate amount of the pre-cooled IP cell lysate was added to the cell culture dish, and the cells were lysed at 4°C for 10 min. During this period, the cells were repeatedly blown with a pipette, and then, the cell suspension was transferred to a 1.5-ml centrifuge tube for ice lysing for 20 min. After centrifugation at 12,000 r/min at 4°C for 10 min, the supernatant was transferred into a new 1.5-ml centrifuge tube, and the protein concentration was determined by the BCA method. A small amount of supernatant was taken for input experiment after denaturation, that is, WB detection of

target protein. Then, 1.0 μg IgG and 20 μL protein A/G beads were added to the negative control (IgG) group protein supernatant. The experimental group was directly added with 20 μL protein A/G beads, and the mixture was shaken at 4°C and incubated for 1 h. Centrifugation was performed at 4°C for 5 min, and the supernatant was taken. 1–10 μL (0.2–2 μg) of antibody was added to the mixture and incubated overnight at 4°C. Thereafter, 80 μL protein A/G-beads were added, which were gently folded with fingers and incubated at 4°C for 2 h. Centrifugation was performed at 4°C for 5 min, the supernatant was carefully discarded, and the immunoprecipitation complex was collected. After the last washing, the supernatant was removed as much as possible; then, 80 μL of 1 \times reduced sample loading buffer was added and boiled for 10 min. The supernatant was centrifuged at 4°C for 5 min, and the 10 μL supernatant sample was taken for Western blotting detection.

Exploration of the Protein–Protein Interaction Network and Core Modules of HBG1- and HBD-Related Genes

HBG1- and HBD-related gene columns are searched in the Comparative Toxicogenomics Database (CTD). STRING software (version 10.5) was used to study the network of interactions between proteins, helping to mine core regulatory genes. There are many databases of protein interactions, and STRING is the largest of them. A single input of HBG1 and multiple proteins related to HBD will provide the interaction network between the input proteins, which is more suitable for mining the interaction between the input proteins. Each node represents a protein. The lines between the nodes represent the interaction between two proteins.

Specific parameters in the protein–protein interaction (PPI) network analysis were followed.

Network type: full STRING network (the edges indicate both functional and physical protein associations).

Meaning of network edges: evidence (line color indicates the type of interaction evidence).

Active interaction sources: textmining; experiments; databases; co-expression; neighborhood; gene fusion; co-occurrence.

Minimum required interaction score: 0.150.

Max number of interactors to show: none.

Network display mode: interactive svg (network is a scalable vector graphic [SVG]; interactive).

Cytoscape software (V3.8.0) was used to visualize the network. Cytoscape is an open source web software that helps users build networks by integrating, analyzing, and visualizing data. The software comes with an editor module that allows users to set up networks directly within the software. MCODE plug-in and cytoHubba were used to find active core modules in the PPI network. According to the gene expression data, the network was screened to find the interaction connectome, that is, the interaction subnetwork, whose genes showed particularly high differential expression level.

Functional Enrichment Analysis of HBG1- and HBD-Related Genes

GO (gene ontology, <http://geneontology.org/>, GO release date: 2019–01–01 and “doi:10.5281/zenodo.2529950”) annotates gene products in terms of function, participating biological pathway, and localization in cells. KEGG (Kyoto Encyclopedia of Genes and Genomes, <https://www.genome.jp/kegg/pathway.html>, version: 24 March 2022) is a comprehensive database integrating genomic, chemical, and systematic functional information. The Database for Annotation, Visualization, and Integrated Discovery (DAVID, version 6.8) is a biological information database that integrates biological data and analytical tools, and provides systematic and comprehensive biofunctional annotation information for large-scale gene or protein lists. At present, the DAVID database is mainly used for functional and pathway enrichment analysis of differential genes. Metascape (version 3.5) integrates more than forty bioinformatics databases. It includes enrichment analysis of biological pathways, structural analysis of protein interaction networks, and abundant gene annotation capabilities, and presents the results in a high-quality graphic language that biologists can easily understand. In this study, DAVID and Metascape software were used to analyze the functional enrichment of HBG1- and HBD-related genes.

Screening of the Small Molecule Compounds of HBG1- and HBD-Related Genes Based on the Comparative Toxicogenomics Database

Small molecule compounds of HBG1- and HBD-related genes were screened using the Comparative Toxicogenomics Database (CTD).

Statistical Analysis

SPSS software, version 23.0 (IBM Corp., Armonk, NY, United States), was used for data statistics. Data are expressed as mean \pm standard deviation. One-way ANOVA was used for the comparison between the four groups, and LSD and Dunnett's test were used for pairwise comparison. Student's *t* test was used for the comparison between the two groups. $p < 0.05$ (two-tailed) was considered statistically significant.

RESULTS

Expressions of HBG1 and HBD in the Red Blood Cells of the Patients With Atrial Fibrillation

Through the immunofluorescence assay, compared with the red blood cells of the control individuals, the expression of HBG1 was higher in the red blood cells of the patients with atrial fibrillation (Wang et al., 2022) ($p < 0.05$, **Figure 1A**). In addition, the expression of HBD was also higher in the red blood cells of the patients with atrial fibrillation than in those of the control individuals ($p < 0.05$; **Figure 1B**).

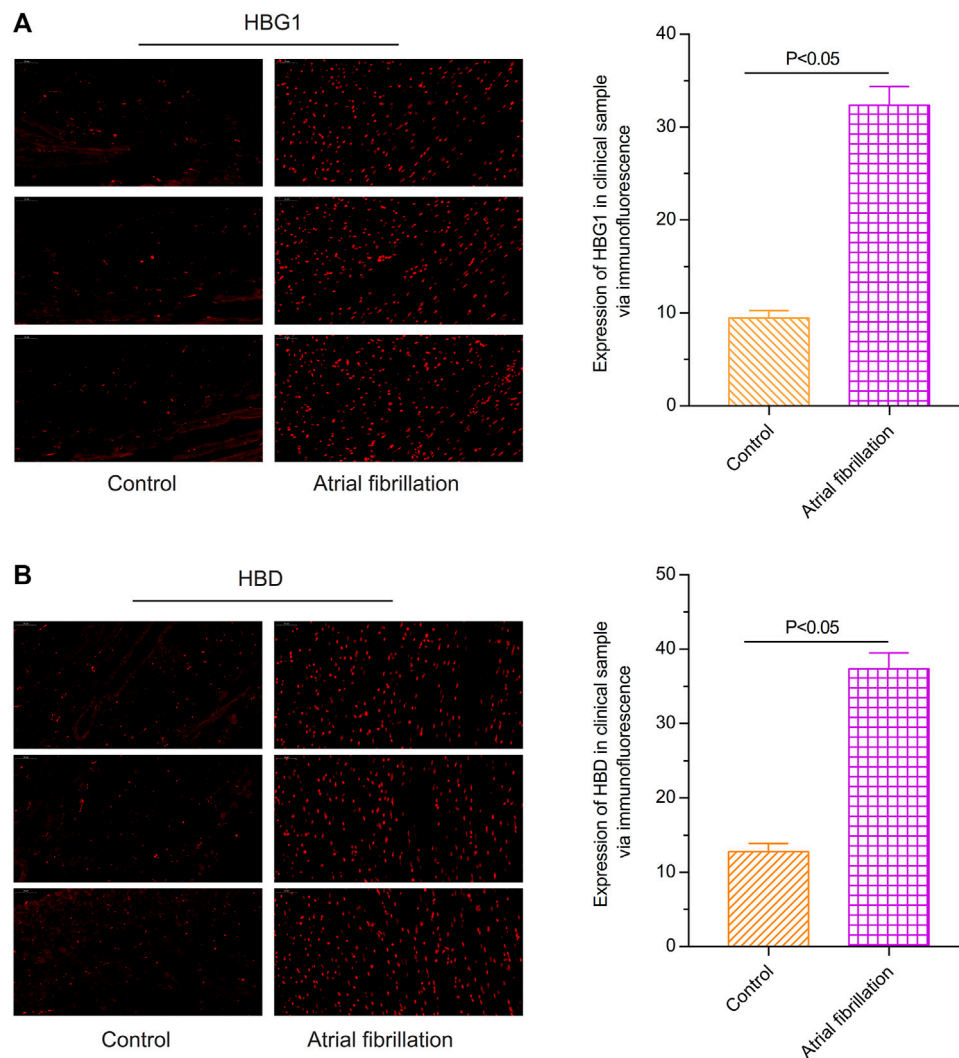


FIGURE 1 | Expressions of HBG1 and HBD in the red blood cells of the patients with atrial fibrillation via the immunofluorescence assay. Compared with the red blood cells of the control individuals, the expressions of **(A)** HBG1 and **(B)** HBD were higher in the red blood cells of the patients with atrial fibrillation.

Lower Level of Hemoglobin in the Red Blood Cells With HBG1-siRNA and HBG1-siRNA

Compared with the control and MOCK groups, the expressions of HBG1 and HBD were significantly downregulated in the red blood cells with HBG1-siRNA and HBG1-siRNA ($p < 0.05$). Furthermore, at every point in time, the level of hemoglobin was lower in the red blood cells with HBG1-siRNA and HBG1-siRNA significantly (Lim et al., 2020) ($p < 0.05$). With the passage of time (12, 24, and 48 h), the hemoglobin levels are getting lower and lower ($p < 0.05$; **Figure 2**).

Better Effect of Edoxaban on the Pathogeny Structure of Cardiac Muscle Tissue

Compared with the control group, the structure of cardiac muscle tissue in the atrial fibrillation mice was destroyed more seriously ($p < 0.05$). However, the structure of cardiac muscle tissue in the

AF + edoxaban group was better than in the AF group and the AF + rivaroxaban group ($p < 0.05$; **Figure 3A**).

Different Degrees of Myocardial Fibrosis in the Four Groups

Through the Masson assay, the collagen fiber percentage in the AF group was significantly higher than in the CON group ($p < 0.05$), which manifested that myocardial fibrosis would be an occurrence in the AF cases (Gyöngyösi et al., 2017). Furthermore, compared with the AF group, the collagen fiber percentage in the AF + edoxaban group was decreased significantly ($p < 0.05$), which demonstrated that edoxaban is beneficial to the myocardium and reduced the situation of myocardial fibrosis (**Figure 3B**).

Furthermore, through the Sirius red staining, the aforementioned result by the Masson assay was demonstrated

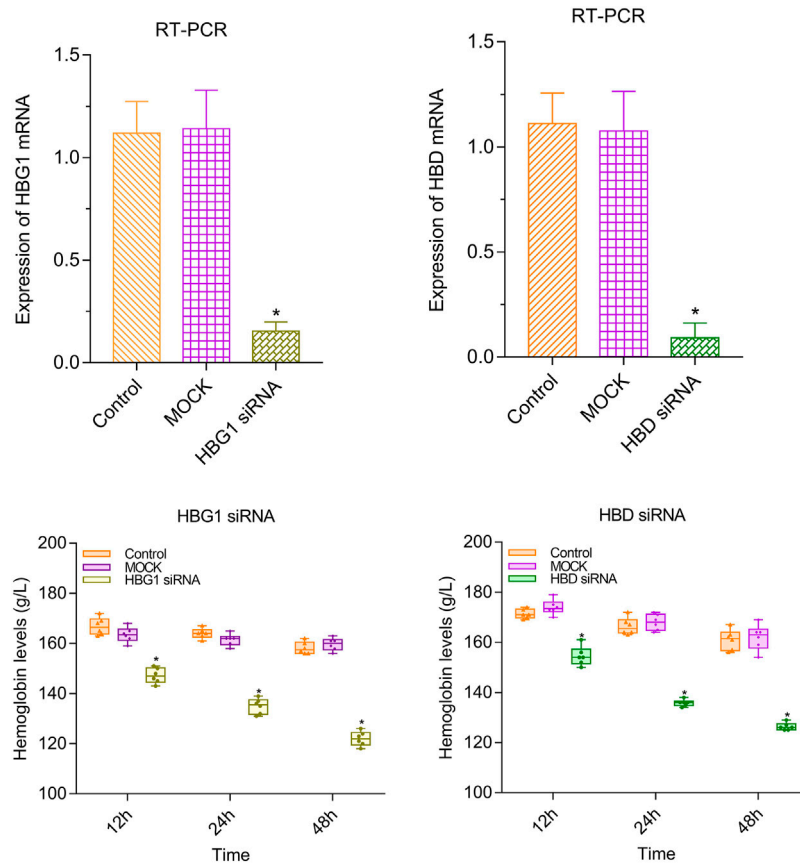


FIGURE 2 | Lower level of hemoglobin in the red blood cells with HBG1-siRNA and HBD-siRNA than the CON red blood cells.

again. The collagen fibers are red in color. The collagen fiber percentage in the AF group was significantly higher than in the CON group ($p < 0.05$). Also, compared with the AF group, the collagen fiber percentage in the AF + edoxaban group was decreased significantly ($p < 0.05$; **Figure 3C**).

Lower Degree of Destruction of Reticular Fibers in the Atrial Fibrillation + Edoxaban Group

Through the reticular fiber staining, compared with the CON group, the degree of destruction of reticular fibers was significantly increased in the AF group ($p < 0.05$). However, the degree of destruction of reticular fibers in the AF + edoxaban group or the AF + rivaroxaban group was lower than that in the AF group. In addition, the degree of destruction of reticular fibers was higher in the AF + rivaroxaban group than in the AF + edoxaban group ($p < 0.05$). (**Figure 4A**).

Expressions of α -SMA and COL1A1 in the Atrial Fibrillation Mice

By the immunohistochemistry assay, the expressions of α -SMA and COL1A1 in the cardiac muscle tissue in the AF group were

upregulated compared with the CON group ($p < 0.05$). After using edoxaban or rivaroxaban, the expressions of α -SMA and COL1A1 were significantly decreased ($p < 0.05$). Furthermore, compared with the AF + rivaroxaban group, the expressions of α -SMA and COL1A1 in the AF + edoxaban group were downregulated ($p < 0.05$) (**Figure 4B,C**).

In addition, the aforementioned results were demonstrated via the RT-PCR. At the mRNA level, the expressions of α -SMA and COL1A1 in the cardiac muscle tissue in the AF group were upregulated compared with the CON group ($p < 0.05$). Compared with the AF group, the expressions of α -SMA and COL1A1 in the cardiac muscle tissue were downregulated in the AF + edoxaban group and the AF + rivaroxaban group ($p < 0.05$). Furthermore, there exists a significant interaction between the α -SMA and COL1A1, which were all the parameters reflecting the degree of fibrosis. (**Figure 5A**).

Edoxaban Reduced the Level of Inflammation in the Heart of the Atrial Fibrillation Mouse Model

The inflammatory biomarkers (TNF- α , IL-1 β , IL-6, and IL-10) in the heart were detected via the RT-PCR assay. Compared with the CON group, the expressions of inflammatory biomarkers (TNF- α , IL-1 β ,

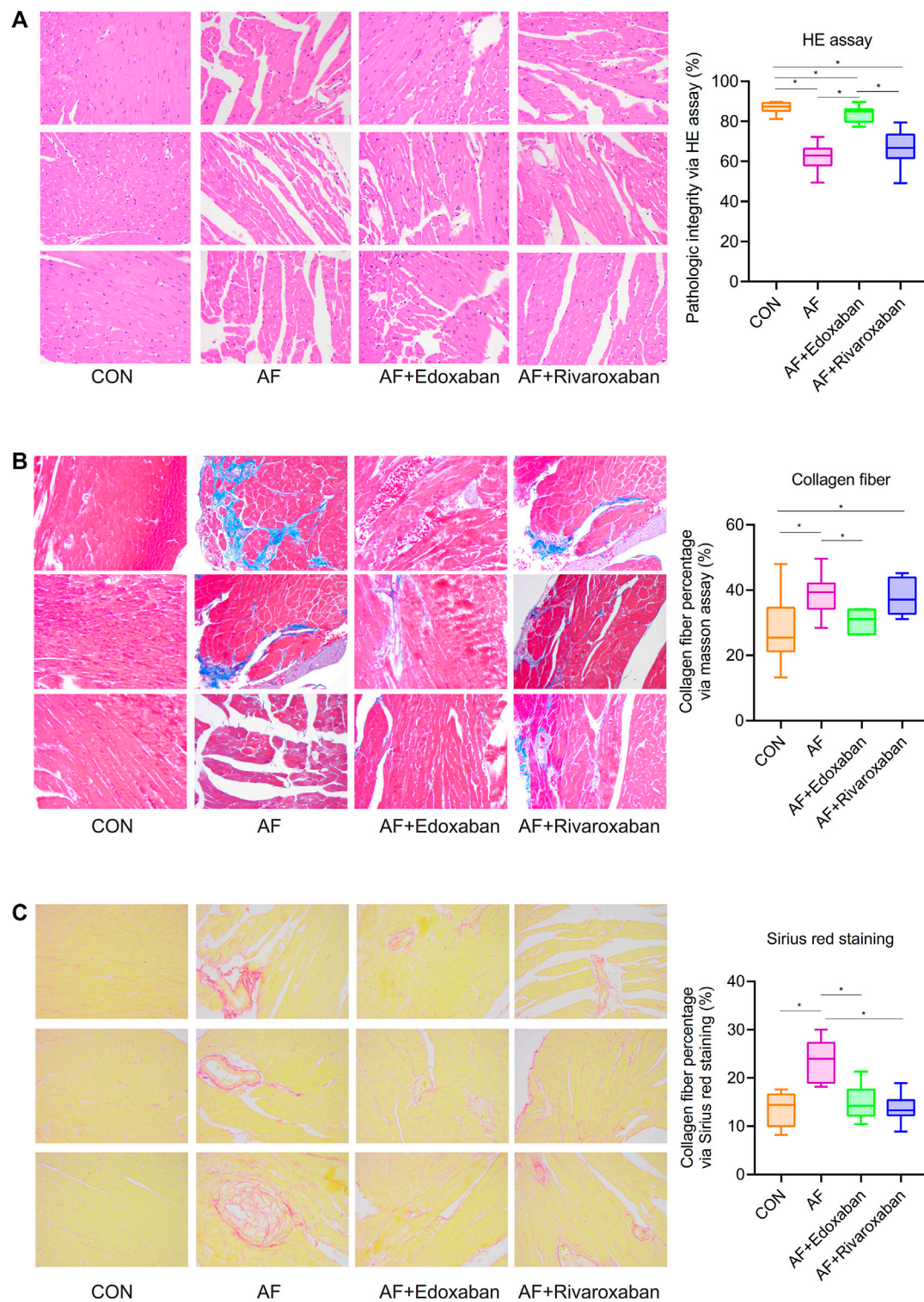


FIGURE 3 | Better effect of edoxaban on the pathology structure of cardiac muscle tissue and the different degrees of myocardial fibrosis in the four groups. **(A)** Structure of cardiac muscle tissue in the AF + edoxaban group was better than in the AF group and the AF + rivaroxaban group. **(B)** Through the Masson assay, compared with the AF group, the collagen fiber percentage in the AF + edoxaban group was decreased significantly. **(C)** Through Sirius red staining, compared with the AF group, the collagen fiber percentage in the AF + edoxaban group was decreased significantly.

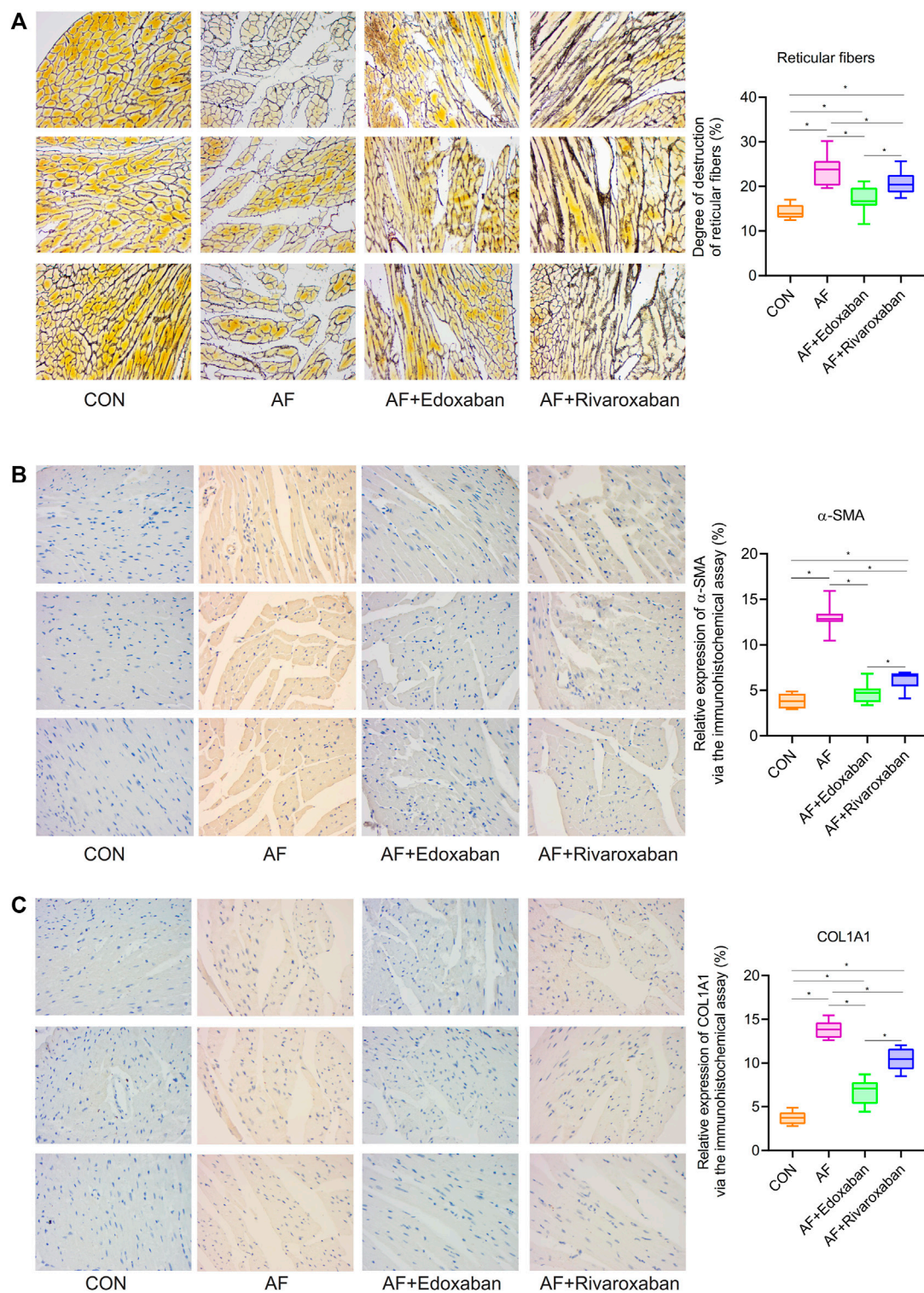


FIGURE 4 | Lower degree of destruction of reticular fibers in the AF + edoxaban group and expressions of α-SMA and COL1A1 in the AF mice. **(A)** Degree of destruction of reticular fibers in the AF + edoxaban group or the AF + rivaroxaban group was lower than the AF group. After using edoxaban or rivaroxaban, the expressions of **(B)** α-SMA and **(C)** COL1A1 were significantly decreased via the immunohistochemistry assay ($p < 0.05$).

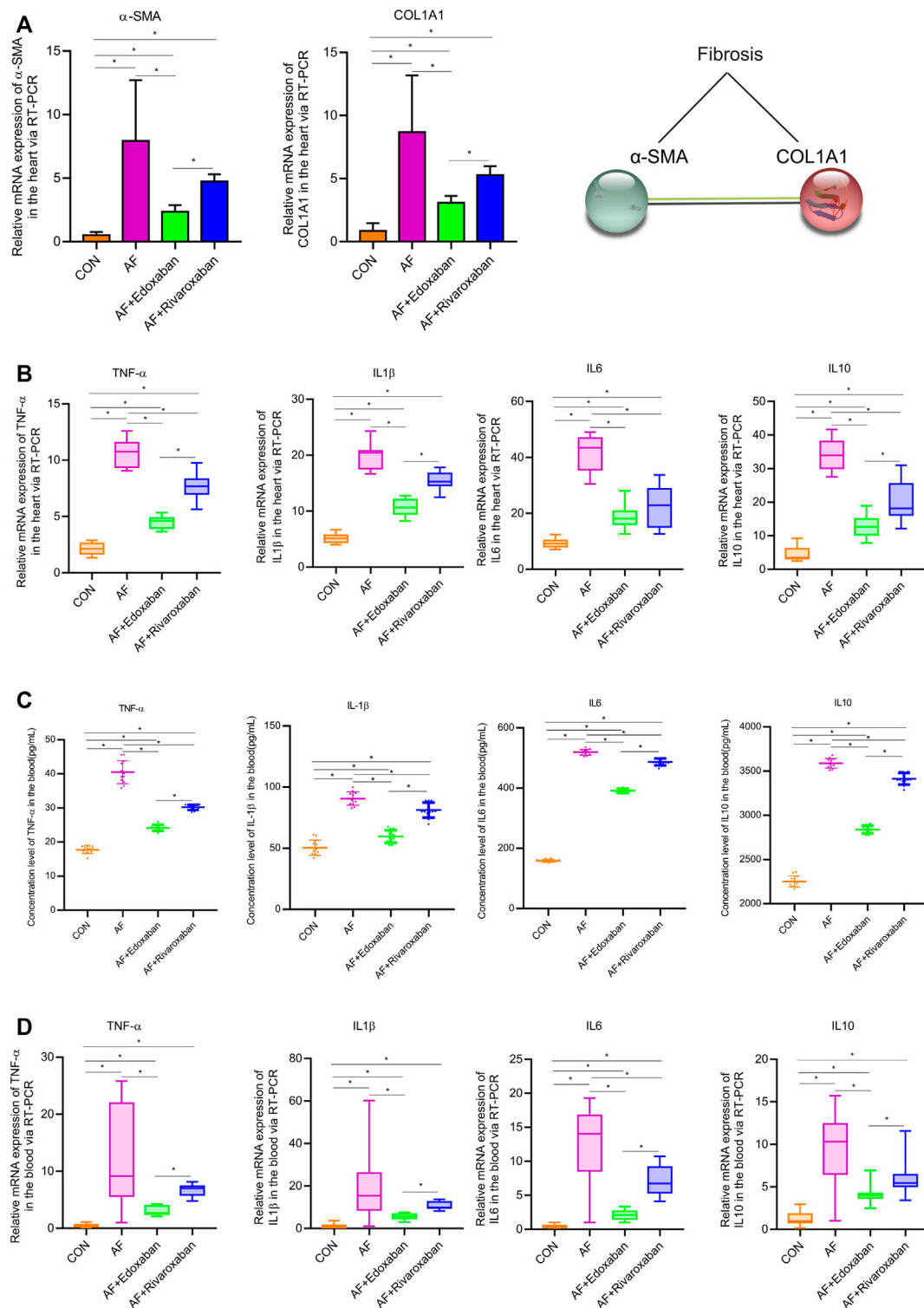


FIGURE 5 | mRNA levels of α-SMA and COL1A1 via the RT-PCR, and edoxaban reduced the level of inflammation in the heart of the AF mouse model. **(A)** Compared with the AF group, the mRNA expressions of α-SMA and COL1A1 in the cardiac muscle tissue were downregulated in the AF + edoxaban group and AF + rivaroxaban group ($p < 0.05$). **(B)** After using edoxaban or rivaroxaban, the mRNA expressions of inflammatory biomarkers (TNF-α, IL-1β, IL-6, and IL-10) in the heart were significantly decreased via the RT-PCR ($p < 0.05$). **(C)** Through the ELISA, the inflammatory biomarkers (TNF-α, IL-1β, IL-6, and IL-10) in the blood were upregulated in the AF group than in the AF + edoxaban group. **(D)** Inflammatory biomarkers (TNF-α, IL-1β, IL-6, and IL-10) in the blood were also detected via the RT-PCR assay. Compared with the AF group, the mRNA expressions of TNF-α, IL-1β, IL-6, and IL-10 were downregulated in the AF + edoxaban group and the AF + rivaroxaban group ($p < 0.05$).

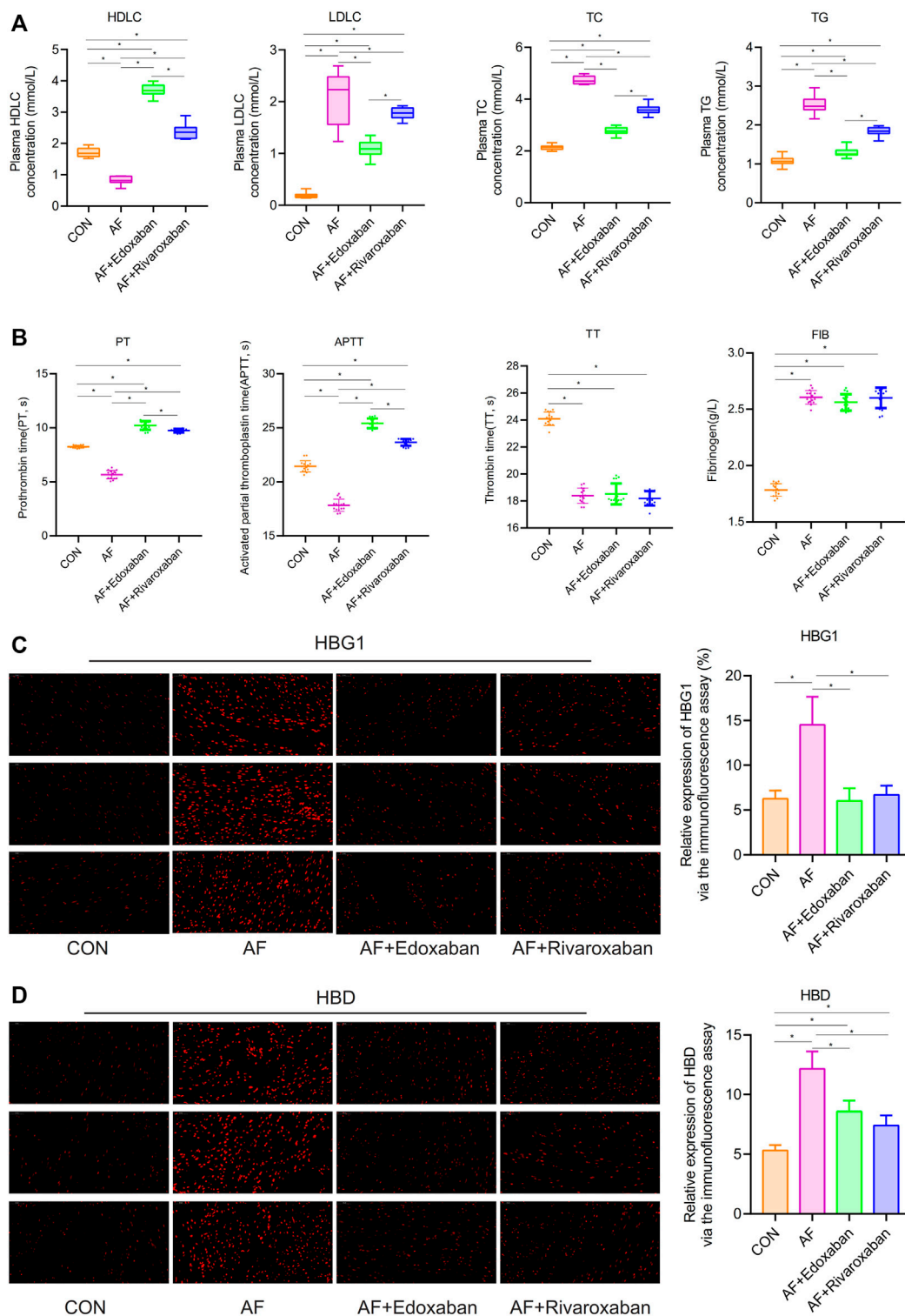


FIGURE 6 | Effect of edoxaban on decreasing blood lipids, coagulation, HBG1, and HBD in the AF mice. **(A)** Compared with the AF group, the blood lipids' parameters (LDL-C, TC, and TG) were downregulated in the AF + edoxaban group and the AF + rivaroxaban group. **(B)** PT and APTT in the AF + edoxaban group and the AF + rivaroxaban group were more increasing than in the AF mice. **(C,D)** Compared with the AF group, the expressions of **(C)** HBG1 and **(D)** HBD were downregulated in the AF + edoxaban group and the AF + rivaroxaban group ($p < 0.05$) through the immunofluorescence assay.

IL-6, and IL-10) in the AF group were higher. After using edoxaban or rivaroxaban, the expressions of inflammatory biomarkers (TNF- α , IL-1 β , IL-6, and IL-10) were significantly decreased ($p < 0.05$). Furthermore, compared with the AF + rivaroxaban group, the expressions of inflammatory biomarkers (TNF- α , IL-1 β , IL-6, and IL-10) in the AF + edoxaban group were downregulated ($p < 0.05$), which presented that edoxaban was superior to rivaroxaban in the aspect of reducing the inflammation in the AF mice (**Figure 5B**).

Lower Expression of the Inflammatory Biomarkers in the Blood of Atrial Fibrillation + Edoxaban Mice

Through the ELISA, the inflammatory biomarkers (TNF- α , IL-1 β , IL-6, and IL-10) in the blood were upregulated in the AF group than in the CON group ($p < 0.05$). However, compared with the AF group, the expressions of inflammatory biomarkers (TNF- α , IL-1 β , IL-6, and IL-10) were downregulated in the AF + edoxaban group and the AF + rivaroxaban group ($p < 0.05$). Furthermore, the expressions of inflammatory biomarkers in the AF + edoxaban group were lower than in the AF + rivaroxaban group (**Figure 5C**). The inflammatory biomarkers (TNF- α , IL-1 β , IL-6, and IL-10) in the blood were also detected via the RT-PCR assay, and the results were further demonstrated (**Figure 5D**).

Effect of Edoxaban on Decreasing Blood Lipids in the Atrial Fibrillation Mice

Compared with the CON group, plasma HDL-C concentration in the AF group was significantly lower ($p < 0.05$). However, the plasma HDL-C concentration in the AF + edoxaban group and AF + rivaroxaban group was higher than in the AF mice ($p < 0.05$). In addition, compared with the AF + rivaroxaban group, the plasma HDL-C concentration in the AF + edoxaban group was higher ($p < 0.05$). The blood lipids' parameters (LDL-C, TC, and TG) were upregulated in the AF group compared with the CON group ($p < 0.05$). However, compared with the AF group, the blood lipids' parameters (LDL-C, TC, and TG) were downregulated in the AF + edoxaban group and the AF + rivaroxaban group ($p < 0.05$). Furthermore, the blood lipids' parameters (LDL-C, TC, and TG) in the AF + edoxaban group were lower than in the AF + Rivaroxaban group (**Figure 6A**).

Reducing Coagulation by the Edoxaban in the Atrial Fibrillation Mice

Compared with the CON group, PT and APTT in the AF group were significantly decreasing ($p < 0.05$). However, the PT and APTT in the AF + edoxaban group and AF + rivaroxaban group were more increasing than in the AF mice ($p < 0.05$). In addition, compared with the AF + rivaroxaban group, the PT and APTT in the AF + edoxaban group were longer ($p < 0.05$). Compared with the CON group, the TT was significantly shorter in the AF, the AF + edoxaban, and the AF + rivaroxaban groups ($p < 0.05$). However, there were no differences among the three groups (AF, AF + edoxaban, and AF + rivaroxaban group) in the aspect of TT. Compared with the CON group, the FIB was significantly higher in the AF, the AF + edoxaban, and the AF +

rivaroxaban groups ($p < 0.05$). However, there were no differences among the three groups (AF, AF + edoxaban, and AF + rivaroxaban groups) in the aspect of FIB (**Figure 6B**).

Effect of Edoxaban in Reducing HBG1 and HBD in the Atrial Fibrillation Mouse Model

Through immunofluorescence, the expressions of HBG1 and HBD were upregulated in the AF group compared with those of the CON group ($p < 0.05$). However, compared with the AF group, the expressions of HBG1 and HBD were downregulated in the AF + edoxaban group and the AF + rivaroxaban group ($p < 0.05$) (**Figure 6C**). In addition, the results were also demonstrated by the RT-PCR assay. Furthermore, in the PCR assay, the results showed that the expressions of HBG1 and HBD in the AF + edoxaban group were lower than in the AF + rivaroxaban group (**Figure 7A**). Also, there exists a significant interaction between HBG1, HBD, and MASP1(Xa), which were the parameters reflecting the coagulation function (**Figure 7B**).

Molecular Docking Among HBG1, HBD, and MASP1(Xa)

The binding score of HBG1 to HBD protein was -240.26 kcal/mol. The binding site of HBG1 protein included THR-135, GLN-127, ASN-108, TYR-35, VAL-33, and ASN-102. The binding site of HBD protein included GLN-127, ARG-116, ASN-108, TYR-35, TRP-37, and ARG-104. HBG1 and HBD protein contact residues can form a variety of interactions, such as salt bridge, hydrogen bond, hydrophobic interaction, and other interactions. Also, these interactions can effectively improve the stability of the HBG1 and HBD protein complex. In addition, according to the binding surface diagram of the two proteins, it was found that HBD protein matched well with HBG1 protein surface, which was conducive to forming a stable binding effect (**Figure 7C**; **Table 2**).

The binding score of HBG1 to MASP1 protein was -256.39 kcal/mol. The binding site of HBG1 protein included ARG-144, TYR-35, GLN-127, THR-135, LYS-104, GLU-101, and GLY-1. The binding site of MASP1 protein included ASN-159, LEU-132, ASN-264, ASP-158, SER-93, ASP-35, TYR-225, and TYR-227. HBG1 and MASP1 protein contact residues can form a variety of interactions, such as salt bridge, hydrogen bond, hydrophobic interaction, and other interactions. Also, these interactions can effectively improve the stability of HBG1 and MASP1 protein complex. In addition, according to the binding surface diagram of the two proteins, it was found that MASP1 protein matched well with HBG1 protein surface, which was conducive to forming a stable binding effect (**Figure 7D**; **Table 2**).

Successful Construction of the BP Neural Network Among HBG1, HBD, and PT

After training of 3000 epochs, the best training performance is 0.019307, which is less than 0.05, showing that it is of significance (**Figure 8A**). The correlation (R), calculated from the network, is 0.97557. Also, there exists a significant interaction among HBG1,

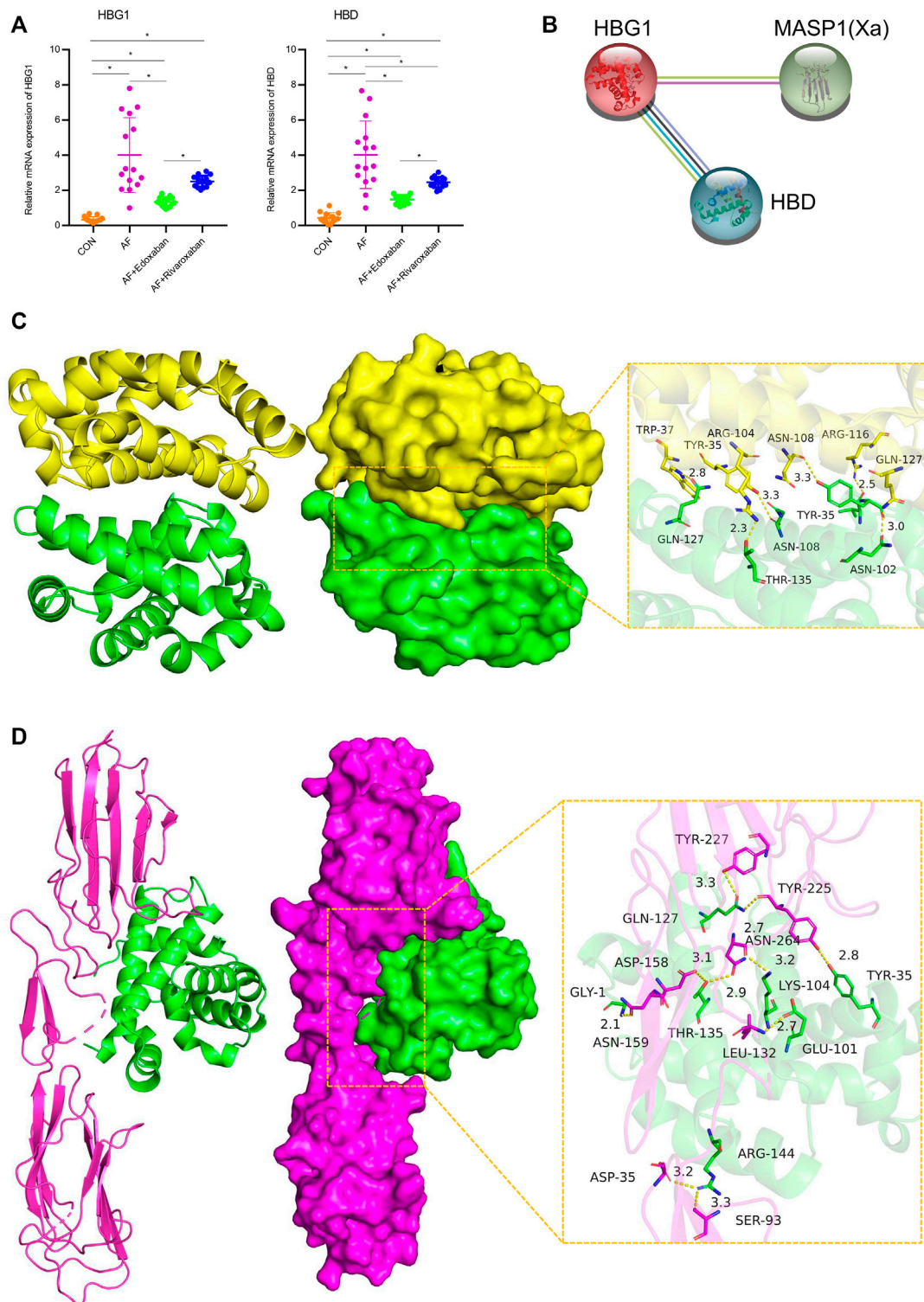


FIGURE 7 | mRNA expressions of HBG1 and HBD via the RT-PCR and the interaction between HBG1, HBD, and MASP1 (Xa). **(A)** In the PCR assay, the results showed that the expressions of HBG1 and HBD in the AF + edoxaban group were lower than in the AF + rivaroxaban group. **(B)** There exists a significant interaction between HBG1, HBD, and MASP1(Xa). **(C)** Binding mode of the complex HBG1 with HBD. The backbone of protein was rendered in tube and colored in green (HBG1) and yellow (HBD). HBG1 and HBD proteins are rendered by the surface. The detail binding mode of HBG1 with HBD. Yellow dash represents the hydrogen bond or salt bridge. **(D)** Binding mode of the complex HBG1 with MASP1. The backbone of protein was rendered in tube and colored in green (HBG1) and red (MASP1). HBG1 and MASP1 proteins are rendered by the surface. The detailed binding mode of HBG1 with MASP1. Yellow dash represents the hydrogen bond or salt bridge.

TABLE 2 | Docking results of three target proteins.

Protein 1	Protein 2	Binding energy (kcal/mol)	Contact sites (protein 1)	Contact sites (protein 2)	Combination type
HBG1	HBD	−240.26	THR-135, GLN-127, ASN-108, TYR-35, VAL-33, and ASN-102	GLN-127, ARG-116, ASN-108, TYR-35, TRP-37, and ARG-104	Salt bridge, hydrogen bond, and hydrophobic interaction
HBG1	MASP1	−256.39	ARG-144, TYR-35, GLN-127, THR-135, LYS-104, GLU-101, and GLY-1	ASN-159, LEU-132, ASN-264, ASP-158, SER-93, ASP-35, TYR-225, and TYR-227	Salt bridge, hydrogen bond, and hydrophobic interaction

HBD, and PT (**Figure 8B**). Furthermore, the model was verified by the ten individuals, and the variation tendency between the raw data and forecast data was close (**Figure 8C**). The curve of percentage error was also drawn, and the percentage errors were all less than 5% (**Figure 8D**). Quantitative predictions of HBG1 and HBD for the PT in the cubic spline interpolation were performed, and when $2.0 < \text{HBD} < 5.0$, $0 < \text{HBG1} < 3.5$, the value of PT is larger (**Figure 8E,F**).

Significant Effect of HBG1 and HBD on the Blood Coagulation Function Based on the Support Vector Machine

Through the comparison between the actual value and the predicted value, the variation tendency was similar. The model that used HBG1 and HBD expressions to predict PT was valuable (**Figure 9A**). Then, the most absolute errors were less than 0.5 (**Figure 9B**). The error histogram with 20 bins is shown in **Figure 9C**. The curve of percentage error was also drawn, and the most percentage errors were all less than 5% (**Figure 9D**). In the scatter fitting diagram, the relationship between the predicted value and the actual value is given by $y = 0.7363 \times X + 2.4433$ (**Figure 9E**).

A Strong Interaction Between HBG1 and HBD

HBG1 and HBD were co-expressed in the blood via the COIP assay, which showed that when HBG1 occurred in the samples, the HBD was also expressed (**Figure 10A**). The protein–protein interaction (PPI) network presented a strong interaction between the genes related to HBG1 and HBD. Furthermore, HBG1 and HBD were at the core of the PPI network. Furthermore, through calculation by the MCODE and cytoHubba, HBG1 and HBD were hub genes in the network, and there was a strong interaction between HBG1 and HBD (**Figure 10B**).

Enrichment Analysis for the Relative Genes of HBG1 and HBD

Through the DAVID analysis, in the aspect of the biological process (BP), the relative genes of HBG1 and HBD were mainly enriched in the blood coagulation, regulation of immune response, positive regulation of JNK cascade, and stimulatory C-type lectin receptor. In the BP analysis, the p -values of terms in the top 18 were less than 0.05 (**Figure 11A**). In the aspect of the cellular component

(CC), the relative genes of HBG1 and HBD were mainly enriched in the blood microparticle, extracellular region, haptoglobin–hemoglobin complex, and hemoglobin complex (**Figure 11B**). In the aspect of cellular molecular function (MF), the relative genes of HBG1 and HBD were mainly enriched in hemoglobin alpha binding, oxygen binding, oxygen transporter activity, and haptoglobin binding. The top 12 in CC and MF were less than 0.05, but others were more than 0.05. (**Figure 11C**). In the aspect of KEGG, the relative genes of HBG1 and HBD were mainly enriched in apoptosis, cell adhesion molecules, and regulation of actin cytoskeleton (**Figure 11D**).

Furthermore, through the Metascape analysis, the relative genes of HBG1 and HBD were mainly enriched in oxygen transport, regulation of cell activation, apoptosis, and regulation of ATP-dependent activity (**Figure 12A**). **Figure 12B** shows the network of enriched terms colored by cluster ID, where nodes that share the same cluster ID are typically close to each other, and **Figure 12C** presents the network of enriched terms colored by p -value ($p < 0.05$). The enrichment PPI network by the Metascape and MCODE components identified in the gene lists showed that HBG1 and HBD were at the core of the network (**Figure 12D,E**).

Small Molecule Compounds Related to HBG1 and HBD

HBD might be involved in the metabolic process of small molecule compounds including enzyme inhibitors, estradiol, ethinylestradiol, and vincristine, which might be related to edoxaban (**Figure 13A**). HBG1 might be involved in the metabolic process of small molecule compounds including tebuconazole, sodium selenite, sodium arsenite, propylthiouracil, and propionaldehyde, which might be related to edoxaban (**Figure 13B**). Through CTD analysis, we found that the small molecule compounds involved in HBG1/HBD contain an important component of edoxaban (methyl methanesulfonate), and then concluded that edoxaban can effectively reduce lipids and fibrosis through HBG1/HBD biomarkers to prevent AF and coagulation.

General Idea Diagram of the Effect of Edoxaban on the Atrial Fibrillation

Edoxaban might inhibit the expression of HBG1 and HBD and then inhibit the inflammation, blood lipids, and fibrosis further.

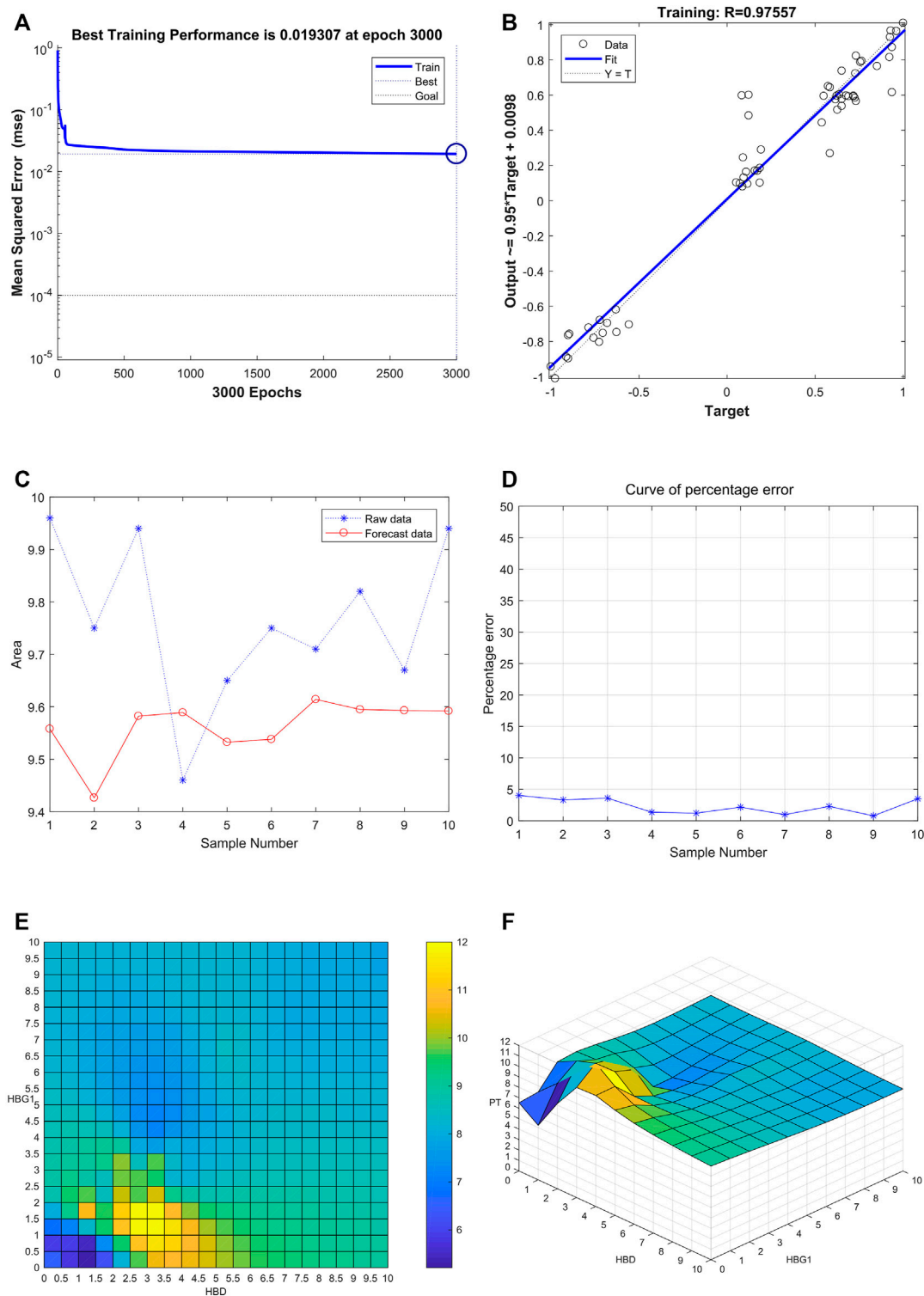


FIGURE 8 | Successful construction of the BP neural network among HBG1, HBD and PT. **(A)** After training of 3000 epochs, the best training performance is 0.019307. **(B)** There exists a significant interaction between HBG1, HBD, and PT. Also, the correlation coefficient is 0.97557. **(C)** Variation tendency between the raw data and forecast data was close. **(D)** Curve of the percentage error was also drawn, and the percentage errors were all less than the 5%. **(E,F)** Quantitative predictions of HBG1 and HBD for the PT in the cubic spline interpolation were performed, and when $2.0 < \text{HBD} < 5.0$, $0 < \text{HBG1} < 3.5$, the value of PT is larger.

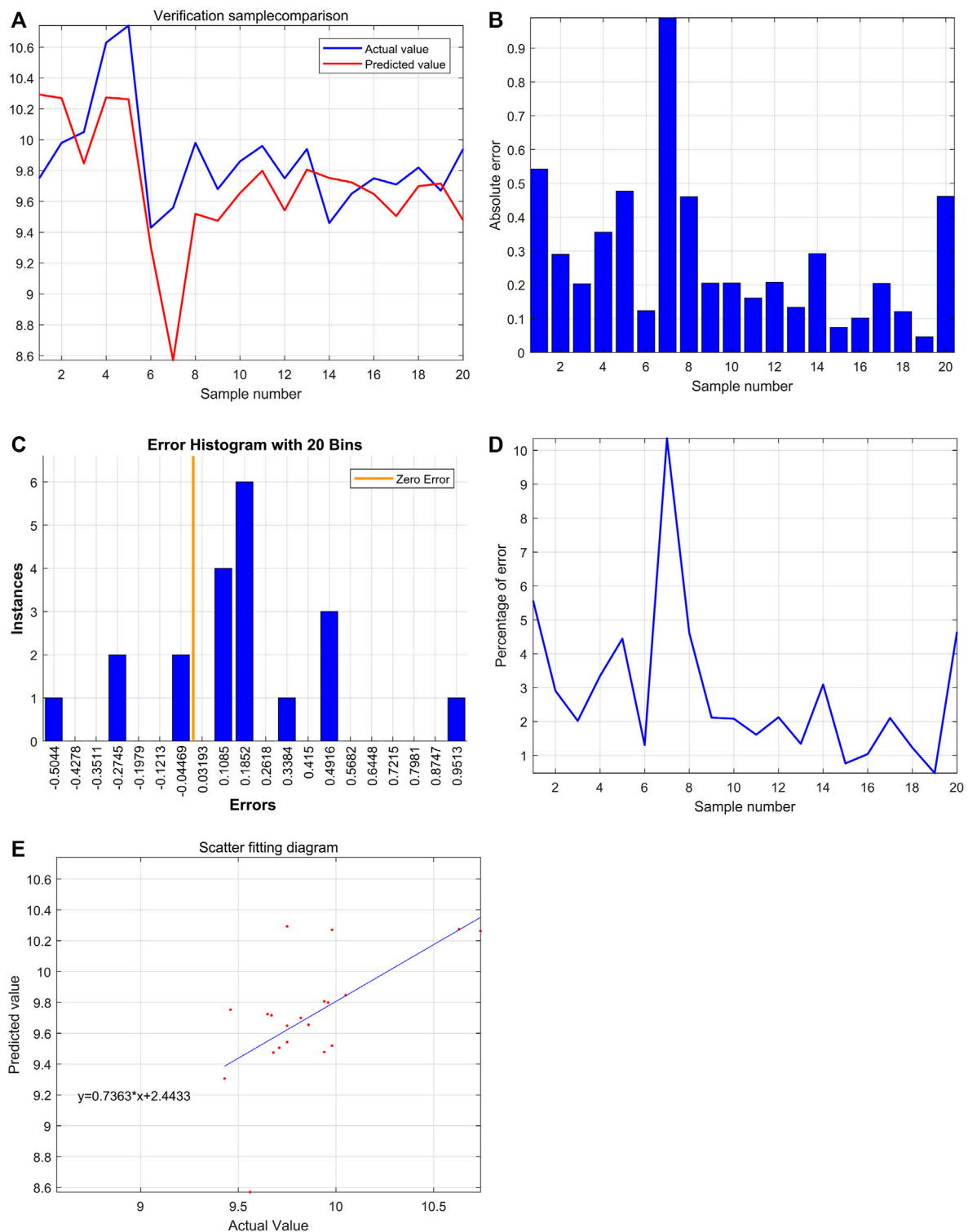


FIGURE 9 | Significant effect of HBG1 and HBD on the blood coagulation function based on the support vector machine. **(A)** Through the comparison between actual value and predicted value, the variation tendency was similar. **(B)** Most absolute errors were less than 0.5. **(C)** Error histogram with 20 bins. **(D)** Curve of the percentage error was also drawn, and the most percentage errors were all less than 5%. **(E)** In the scatter fitting diagram, the relationship between the predicted value and the actual value is given by $y = 0.7363X + 2.4433$.

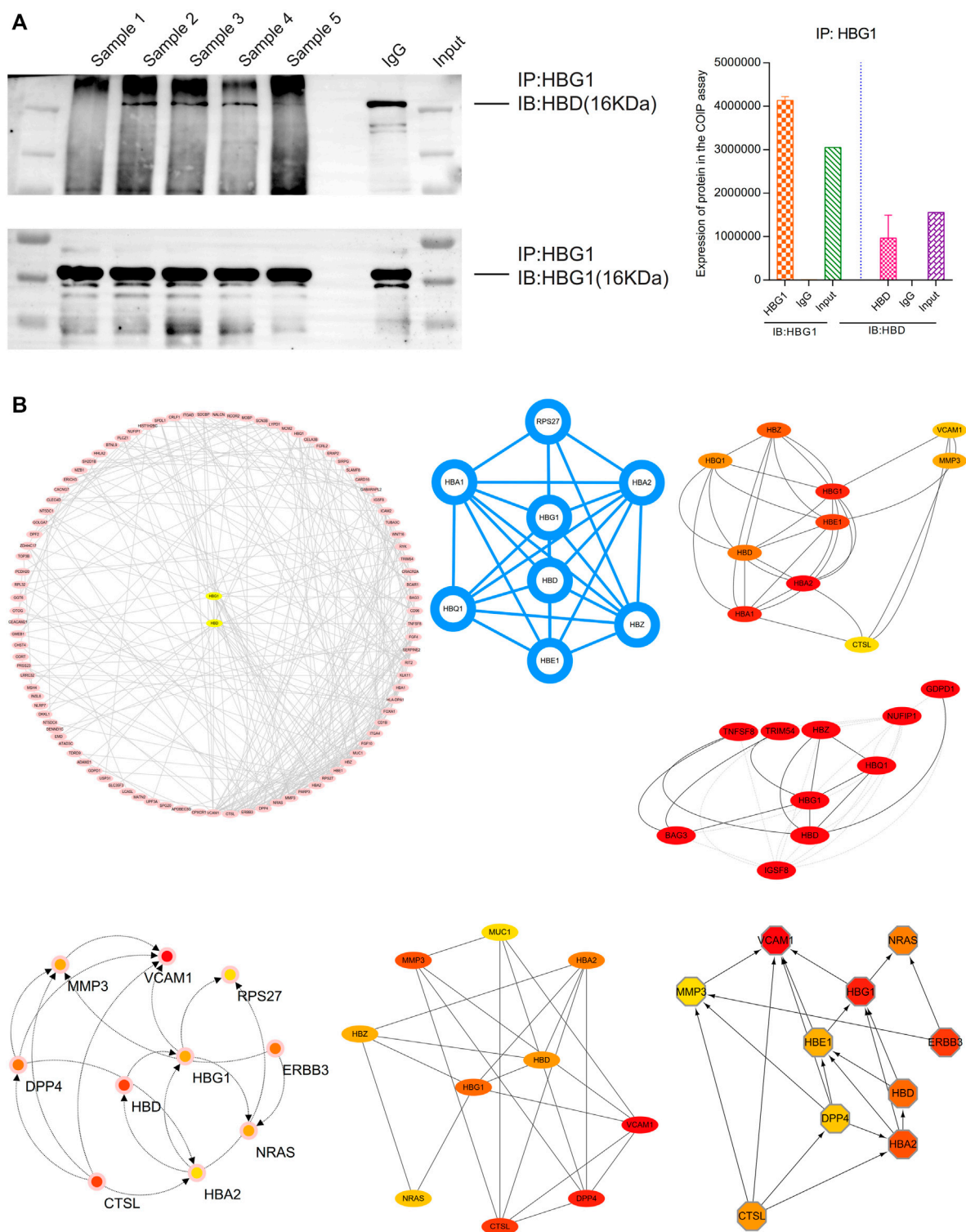
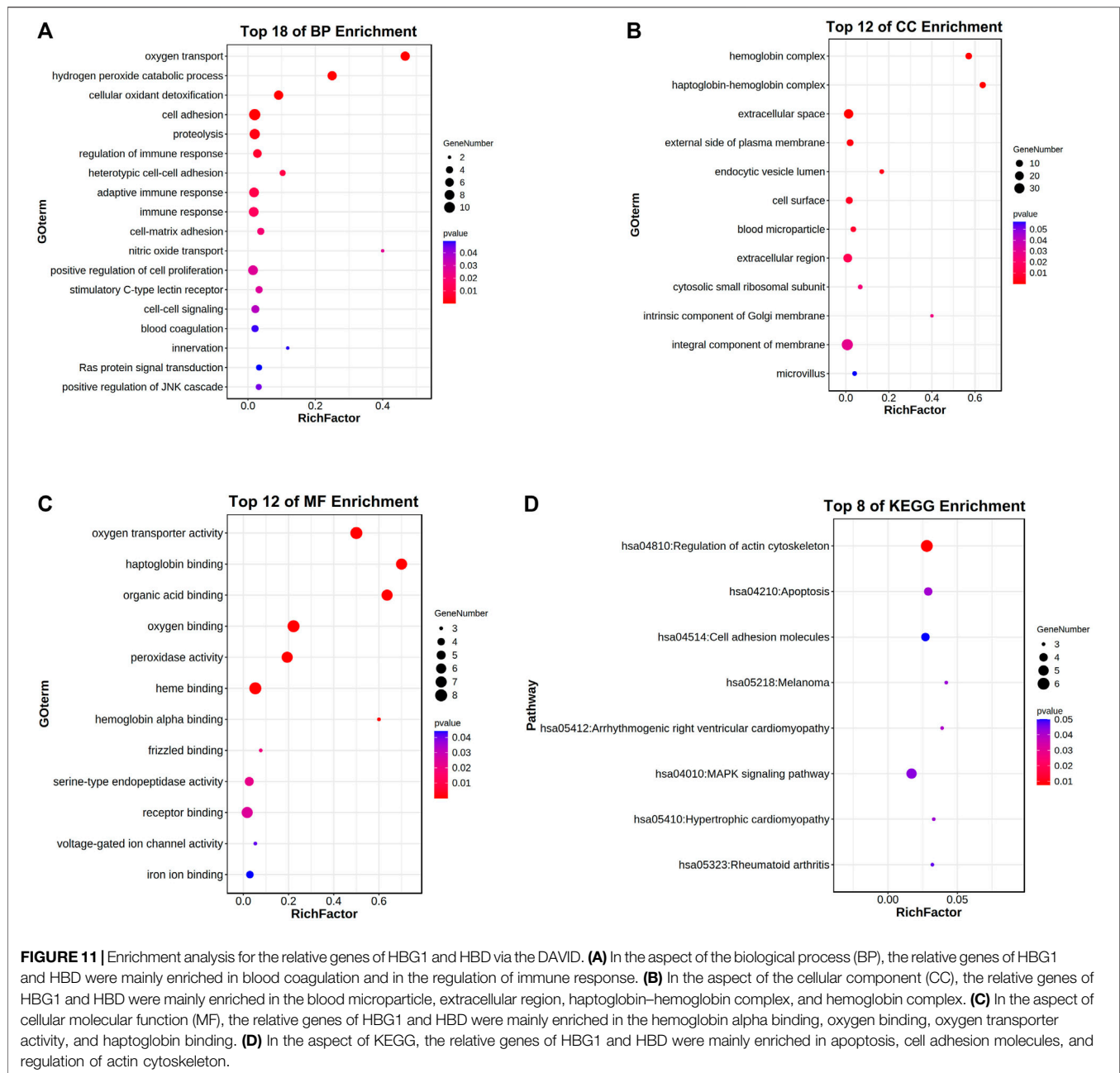


FIGURE 10 | Strong interaction between HBG1 and HBD. **(A)** HBG1 and HBD were co-expressed in the blood via the COIP assay. **(B)** HBG1 and HBD were at the core of the PPI network. Furthermore, through calculation by MCODE and cytoHubba, HBG1 and HBD were hub genes in the network, and there was a strong interaction between HBG1 and HBD.

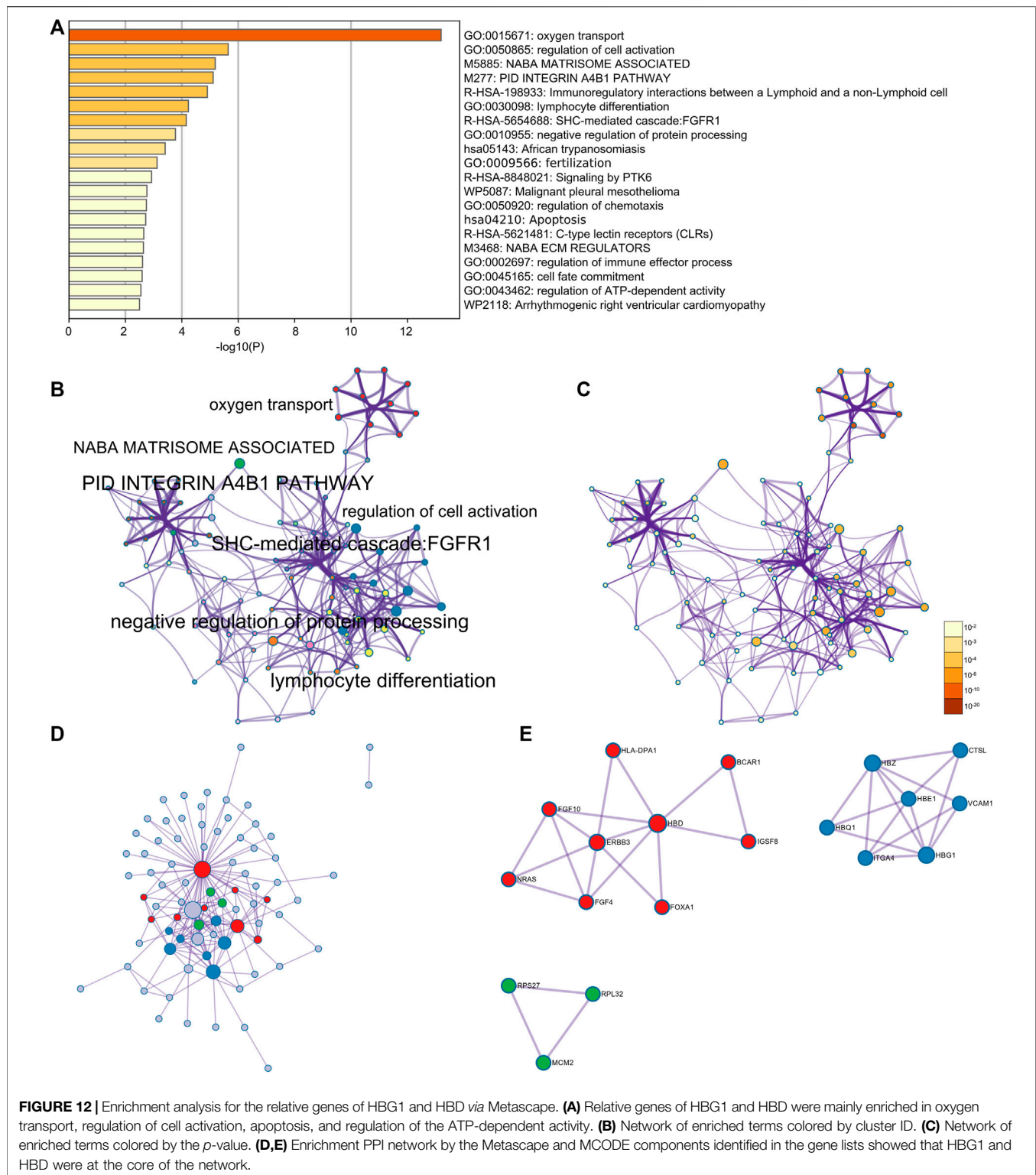


Furthermore, the coagulation was inhibited and the fibrinolysis was activated at the effect of edoxaban. Finally, the development of AF to the stroke was prevented (Figure 13C).

DISCUSSION

Atrial fibrillation (AF) is the most common persistent arrhythmia in adults (Hindricks et al., 2021). Uncoordinated atrial excitation can lead to the deterioration of cardiac function (Subahi et al., 2018), and the occurrence of atrial fibrillation can also lead to the formation of atrial mural thrombus, which in turn leads to

thromboembolic events such as ischemic stroke, myocardial infarction, and peripheral arterial embolism (Tsuchiya et al., 1992; Hossmann 2006; Pandya et al., 2011). Atrial fibrillation can double the risk of ischemic stroke, and stroke caused by atrial fibrillation often has a poor prognosis. Also, stroke has also become one of the important causes of death in patients with atrial fibrillation. Therefore, the prevention of thromboembolic events caused by atrial fibrillation is the cornerstone of the treatment of atrial fibrillation. Our results showed that edoxaban might inhibit the expression of HBG1 and HBD and then inhibit inflammation, blood lipids, and fibrosis further. The expressions of HBG1 and HBD in the red blood cells of the



patients with atrial fibrillation were decreased. Compared with the AF group, the expressions of HBG1 and HBD were downregulated in the AF + edoxaban group ($p < 0.05$).

The results showed that after using edoxaban or rivaroxaban, the expressions of inflammatory biomarkers (TNF- α , IL-1 β , IL-6,

and IL-10) were significantly decreased ($p < 0.05$). Atrial fibrillation (AF) is the most common clinical arrhythmia. There is strong evidence for a systemic prothrombotic and proinflammatory state in AF. Inflammation is an important link in the pathophysiology of cerebrovascular diseases,

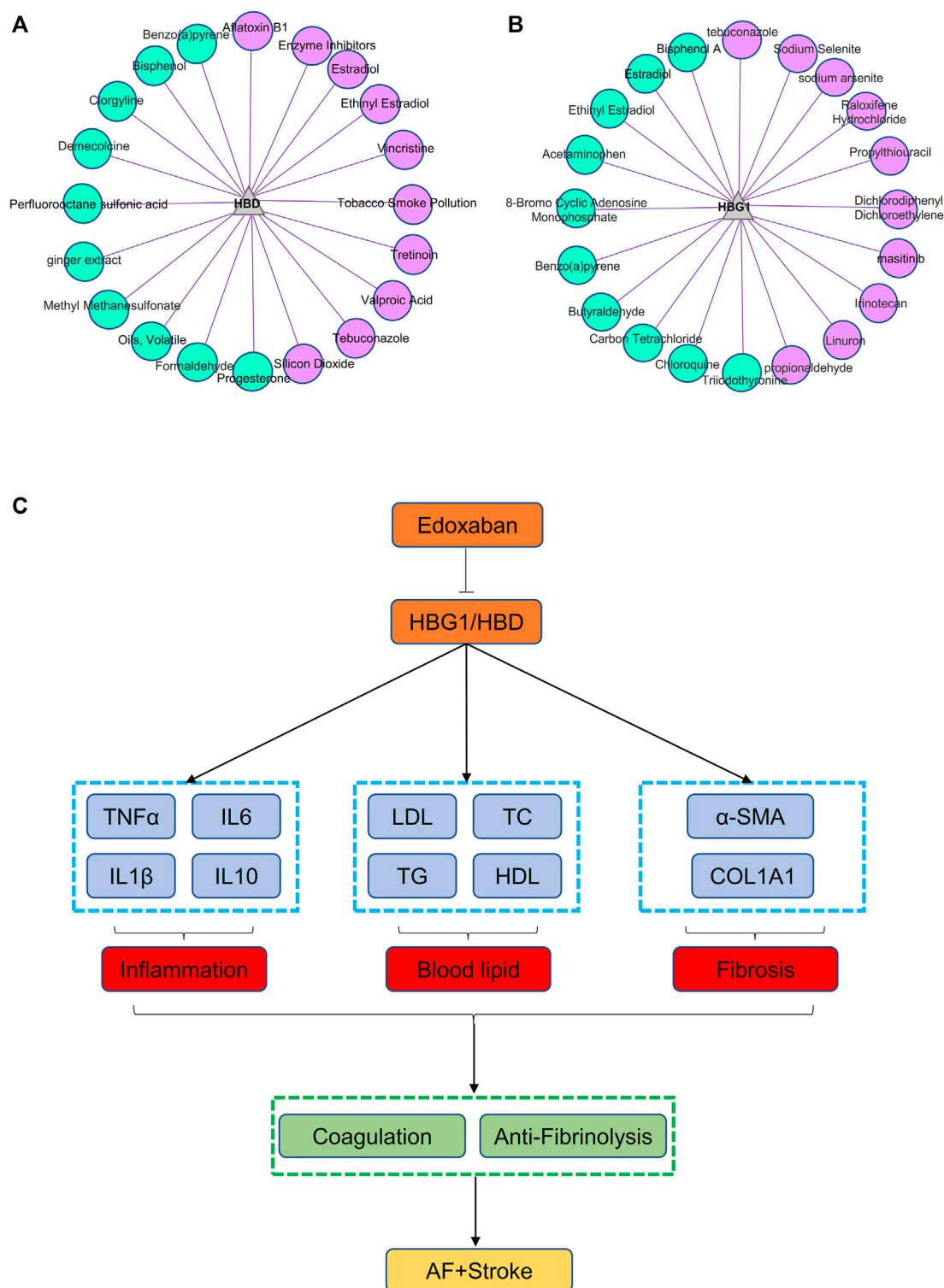


FIGURE 13 | Small molecule compounds related to HBG1 and HBD and the general idea diagram of the effect of edoxaban on the AF. **(A)** Small molecule compounds related to HBD. **(B)** Small molecule compounds related to HBG1. **(C)** General idea diagram of the effect of edoxaban on the AF. Edoxaban might inhibit the expressions of HBG1 and HBD and then inhibit inflammation, blood lipids, and fibrosis further. Furthermore, coagulation was inhibited, and fibrinolysis was activated at the effect of edoxaban. Finally, the development of AF to the stroke was prevented.

especially ischemic stroke. A study showed that post-stroke neuroinflammation is an important factor affecting the long-term prognosis of ischemia. Various factors, such as ROS formation, necrotic cells, and damaged tissue, can cause the activation of inflammatory cells, which can cause an inflammatory response. Furthermore, these activated inflammatory cytokines are involved in tissue remodeling. The inflammatory process is associated with several different cell types, inflammatory cytokines, and cellular receptors such as Toll-like receptors (TLRs) (Fernandes et al., 2014).

There is increasing evidence that FXa exerts non-hemostatic cellular effects, is mediated primarily through protease-activated receptor 1, and is associated with pathophysiological conditions such as atherosclerosis, inflammation, and fibrosis. FXa induces the expression of proinflammatory cytokines, including interleukin-6 (IL-6) and IL-8 and monocyte chemoattractant protein-1 (MCP-1) in ECs, promoting inflammatory processes (Busch et al., 2005; Daubie et al., 2006). FXa can exert a protective physiological role in endothelial cells but under specific conditions can lead to an inflammatory response by activating PAR-1, PAR-2, and possibly PAR-3 if FXa is activated uncontrollably, leading to an increased expression in inflammatory cytokines and adhesion molecules in ECs. Factor Xa is an important target for antithrombotic therapy due to its critical role in coagulation and thrombosis (Esmon 2014). In recent years, three DOACs (rivaroxaban, apixaban, and edoxaban) have been developed that inhibit the effects of FXa. Direct oral anticoagulants are small molecules that bind rapidly and reversibly to the active site of FXa, exhibiting higher selectivity compared with other serine proteases. FXa and atrial tachyarrhythmias act synergistically, resulting in an increased expression of myocardial PARs and subsequent activation of ERK/MAPK and NF- κ B pathways. As a result, the expression of inflammatory molecules increases. Rivaroxaban inhibits the activation of ERK/MAPK and NF- κ B and the expression of inflammatory molecules in human atrial tissue (32). Another study showed that rivaroxaban elicits anti-inflammatory end products (AGEs) by inhibiting the production of reactive oxygen species and the formation of advanced glycation, as well as the genes for MCP-1 and ICAM-1 in AGE-exposed HUVEC Express. Previous studies have shown that FXa inhibitors such as rivaroxaban have anti-inflammatory properties in addition to their anticoagulant effects (Bukowska et al., 2013; Katoh et al., 2017).

Edoxaban, the latest DOAC, is an oral factor Xa inhibitor. One study evaluated the effects of edoxaban on coagulation parameters, microvascular thrombosis, organ injury parameters, and inflammatory cytokines in endotoxin-injected rats. In this LPS-induced thrombosis model, the direct FXa inhibitor edoxaban significantly inhibited hypercoagulability, fibrin deposition in the liver, and elevation of liver injury parameters in a dose-dependent manner. Edoxaban significantly inhibited coagulation activation, intrahepatic microvascular thrombosis, and liver injury in endotoxin-injected rats, and reduced mortality. However, edoxaban did not cause kidney damage and inflammatory cytokine production. These results suggest that FXa inhibition by

edoxaban may be a beneficial therapy for reducing inflammation-related thrombosis (Morishima et al., 2021).

The anti-inflammatory effects of FXa inhibitors were further demonstrated in a study in which rivaroxaban or apixaban treatment for 6 months reduced the pentaxin-related protein (PTX-3), a protein mainly produced by macrophages and vascular endothelial cells, in response to early proinflammatory signals. The authors then propose that PTX3 rapidly responds to left atrial and vascular endothelial changes as a useful marker for determining the anti-inflammatory effects of FXa inhibitors (Katoh et al., 2017). The anti-inflammatory activity of rivaroxaban was found to be associated with the inhibition of FXa-activated inflammatory responses. The expressions of ICAM-1 and IL-8 were increased when human atrial tissue sections were exposed to FXa. The combination of rapid pacing and FXa, which mimics AF, promoted significant upregulation of protease-activated receptor (PAR-1), PAR-2, ICAM-1, and IL-8. Rivaroxaban blocked the upregulation of PAR, ICAM-1, and IL-8. Taken together, these results suggest that FXa may mediate inflammatory signaling in atrial tissue by activating protease-activated receptors (Bukowska et al., 2013). Considering the evidence that FXa can bind to PARs and activate them (Steinberg 2005), the potential anti-inflammatory effect of rivaroxaban may be due to direct FXa inhibition.

It is widely accepted that inflammation and oxidative stress play important roles in the development of atrial fibrillation (Dudley et al., 2005; Neuman et al., 2007). Since the first report by Bruins et al., there has been increasing evidence that inflammatory conditions are closely related to the development of atrial fibrillation (Zhang et al., 2017; Zhou and Dudley 2020). Whether atrial fibrillation is a cause or a consequence of the inflammatory process, it is closely related to oxidative stress fixed by infiltration of the myocardium by inflammatory cells such as macrophages, accompanied by the release of reactive oxygen species (ROS) (Li et al., 2010). The inflammatory state leads to the activation of RAAS, which in turn activates NADPH oxidase. Thus, these processes trigger TGF- β pathway signaling and structural and electrical remodeling of the left atrium (Jalife 2014). An increased expression of various inflammatory cytokines and chemokines such as interleukin-1 and interleukin-6, tumor necrosis factor- α (TNF- α), or monocyte chemoattractant protein-1 (MCP-1) can be observed to have progression to chronic atrial fibrillation and recurrence of atrial fibrillation after cardioversion (Hu et al., 2015).

Our research found that HBG1 protein matched well with HBD and MASP1(Xa) protein surfaces, which was conducive to forming a stable binding effect. There exists a significant interaction between HBG1, HBD, and PT via the BP neural network and support vector machine. Enrichment analysis showed that HBG1 and HBD were mainly enriched in the blood coagulation and in the regulation of immune response. James et al. found that HBD is closely related to inflammation, and observed upregulation of HBD expression during infection and inflammation (Özdemir et al., 2020). Chen et al. found that HBD included oxygen transport, iron binding, coagulation, and binding to oxygen in GO annotations (Chen et al., 2020). HBG1 induces fetal hemoglobin (HbF) expression and reduces

morbidity and mortality in hemoglobin disorders (Platt et al., 1994). The two β -hemoglobins produced by HBG1 and HBD β -like globin genes may be involved in the occurrence and development of atrial fibrillation through inflammation and stress. Katayama et al. found that in patients with normal LV systolic function, increased LV mass index and low Hb concentrations were independently associated with LV enlargement (Katayama et al., 2010). This result suggests that hemodynamic changes in low or high hemoglobin levels can affect the development of LA remodeling and AF before overt changes such as LV hypertrophy or systolic dysfunction occur. It is further suggested that the two β -like globin genes, HBG1 and HBD, may directly affect the development of left atrial remodeling and atrial fibrillation and the state of blood coagulation by changing the level of hemoglobin or the inflammatory state. The blood lipids' parameters (LDL-C, TC, and TG) were downregulated in the AF + edoxaban group. There were significant differences in blood lipid parameters (HDL-C, LDL-C, TC, and TG) between the AF group and the CON group. We consider the reason may be that changes in blood lipids cause increased blood viscosity, leading to poor coronary blood flow, which in turn induces the occurrence of AF; AF itself is an inflammatory reaction process, and inflammation affects the process of blood lipid metabolism. Since hyperlipidemia is a risk factor for other heart diseases, it appears that hyperlipidemia may also be a risk factor for AF. However, there is a "cholesterol paradox" in AF, and the association between lipid levels and the risk of new-onset AF is less clear. A number of recent epidemiological studies have explored the relationship between lipid levels and the risk of new-onset AF, with some studies showing no significant association, and some studies have shown that low blood lipid levels are associated with a lower risk of new-onset AF (Li et al., 2018; Yao et al., 2020).

The PT and APTT in the AF + edoxaban group and AF + rivaroxaban group were more increasing than in the AF mice ($p < 0.05$). AF is a hypercoagulable state. Through bioinformatics analysis in the previous stage, compared with the CON group, HBG1 and HBD were significantly increased in the AF group, while HBG1 and HBD were the main molecules involved in oxygen transport, and HBG1 and HBD had a significant protein interaction with factor Xa, resulting in a significant difference in coagulation function between the AF group and the CON group; Mariya Negreva et al. found that paroxysmal AF tends to have an early hypercoagulable state, involving intrinsic and extrinsic coagulation pathways in their study (Negreva et al., 2020). Rivaroxaban is a commonly used clinical anticoagulant. It specifically inhibits the activity of plasma factor Xa, thereby inhibiting the activity of prothrombin, preventing the activation of internal and extrinsic coagulation, reducing blood viscosity, and inhibiting the formation and expansion of thrombosis. It has high bioavailability, fast onset, and significant curative effect. It is widely used in acute coronary syndrome, stable coronary artery disease, thrombosis after atrial fibrillation, etc., which can greatly reduce the risk of adverse cardiac events (Carter et al., 2018).

The structure of cardiac muscle tissue in the AF + edoxaban group was better than that in the AF group and the AF + rivaroxaban group ($p < 0.05$). Compared with the AF group, the collagen fiber percentage in the AF + edoxaban group was decreased significantly

($p < 0.05$). Rivaroxaban has been shown to have endothelial protective and repairing properties, as the drug significantly enhanced HUVEC viability, growth, and wound healing. These effects may be mediated by the upregulation of u-PA and its enhanced functional activity. Rivaroxaban also counteracted the proinflammatory effects of FXa at the endothelial cell level, possibly through its direct inhibitory effect, and showed functional significance in inhibiting FXa-induced platelet adhesion to endothelial cells. More importantly, rivaroxaban appears to increase endothelial fibrinolytic pathway activity via u-PA activation, which together with its known anticoagulant activity will help create a global antithrombotic environment within the blood vessel (Álvarez et al., 2018).

There exist significant differences in blood lipids and coagulation between the AF + edoxaban group and the AF + rivaroxaban group. In the previous bioinformatics analysis, compared with the CON group, HBG1 and HBD were significantly increased in the AF group. HBG1 and HBD are the main molecules involved in oxygen transport. At the same time, HBG1 and HBD have significant protein interactions with factor Xa. Therefore, HBG1 and HBD affect the state of blood lipids and coagulation function. Our results show that edoxaban reduces HBG1/HBD more significantly, resulting in differences in blood lipids and coagulation indexes between the two groups.

However, this study also has certain shortcomings. First, we did not include edoxaban in clinical studies of patients with atrial fibrillation. Therefore, in future research, we will apply for the inclusion of edoxaban in clinical application, then detect the expression of HBG1 and HBD in the blood of patients with atrial fibrillation before and after taking edoxaban, and obtain more sufficient clinical evidence.

CONCLUSIONS

Edoxaban might inhibit the expressions of HBG1 and HBD and then inhibit the inflammation, blood lipids, and fibrosis further. Furthermore, coagulation was inhibited, and fibrinolysis was activated at the effect of edoxaban. Finally, the development of AF to stroke was prevented. In addition, the effect of edoxaban was superior to rivaroxaban.

DATA AVAILABILITY STATEMENT

The original contributions presented in the study are included in the article/Supplementary Material, further inquiries can be directed to the corresponding authors.

ETHICS STATEMENT

The studies involving human participants were reviewed and approved by the Ethics Committee of Beijing Hospital. The patients/participants provided their written informed consent to participate in this study. The animal study and the

experimental protocol were approved by the Animal Care and Use Committee of the Institute of Laboratory Animal Sciences, Chinese Academy of Medical Sciences (CAMS) & Peking Union Medical College.

AUTHOR CONTRIBUTIONS

CGY and XW performed the experiment, and was a major contributor in writing the manuscript and submitting the manuscript. MD and FW made substantial contributions to research conception. She also designed the draft of the research process as corresponding author. YG, and YL had been involved in the development of the intervention and the study protocol. They also supported the study design to avoid the

confounding factor. XYM, CXX had been involved in revising manuscript critically for important intellectual content. XW and LBM modified the manuscript format, discussed reviewer opinions, and clarified the professional name. All authors read and approved the final manuscript.

ACKNOWLEDGMENTS

We are thankful to the funding, National Key R and D Program of China (2020YFC2008106), and Beijing Hospital Research Project (No. BJ-2021-188, from Min Dong), and we are thankful to all respondents of this study and workers from the long-term care facilities for their cooperation.

REFERENCES

- Álvarez, E., Paradelo-Dobarró, B., Raposeiras-Roubín, S., and González-Juanatey, J. R. (2018). Protective, Repairing and Fibrinolytic Effects of Rivaroxaban on Vascular Endothelium. *Br. J. Clin. Pharmacol.* 84 (2), 280–291. doi:10.1111/bcp.13440
- Bruins, P., te Velthuis, H., Yazdanbakhsh, A. P., Jansen, P. G., van Hardevelt, F. W., de Beaumont, E. M., et al. (1997). Activation of the Complement System during and after Cardiopulmonary Bypass Surgery: Postsurgery Activation Involves C-Reactive Protein and Is Associated with Postoperative Arrhythmia. *Circul.* 96 (10), 3542–3548. doi:10.1161/01.cir.96.10.3542
- Bukowska, A., Zacharias, I., Weinert, S., Skopp, K., Hartmann, C., Huth, C., et al. (2013). Coagulation Factor Xa Induces an Inflammatory Signalling by Activation of Protease-Activated Receptors in Human Atrial Tissue. *Eur. J. Pharmacol.* 718 (1–3), 114–123. doi:10.1016/j.ejphar.2013.09.006
- Busch, G., Seitz, I., Steppich, B., Hess, S., Eckl, R., Schömig, A., et al. (2005). Coagulation Factor Xa Stimulates Interleukin-8 Release in Endothelial Cells and Mononuclear Leukocytes: Implications in Acute Myocardial Infarction. *Arterioscler Thromb. Vasc. Biol.* 25 (2), 461–466. doi:10.1161/01.ATV.0000151279.35780.2d
- Carter, R. L. R., Talbot, K., Hur, W. S., Meixner, S. C., Van Der Gugten, J. G., Holmes, D. T., et al. (2018). Rivaroxaban and Apixaban Induce Clotting Factor Xa Fibrinolytic Activity. *J. Thromb. Haemost.* 16 (11), 2276–2288. doi:10.1111/jth.14281
- Chen, L., Bai, J., and Li, Y. (2020). The Change of Interleukin-6 Level-Related Genes and Pathways Induced by Exercise in Sedentary Individuals. *J. Interferon Cytokine Res.* 40 (5), 236–244. doi:10.1089/jir.2019.0169
- Chugh, S. S., Havmoeller, R., Narayanan, K., Singh, D., Rienstra, M., Benjamin, E. J., et al. (2013). Worldwide Epidemiology of Atrial Fibrillation: a Global Burden of Disease 2010 Study. *Circul.* 129 (8), 837–847. doi:10.1161/CIRCULATIONAHA.113.005119
- Daubie, V., Cauwenberghs, S., Senden, N. H., Pochet, R., Lindhout, T., Buurman, W. A., et al. (2006). Factor Xa and Thrombin Evoke Additive Calcium and Proinflammatory Responses in Endothelial Cells Subjected to Coagulation. *Biochim. Biophys. Acta* 1763 (8), 860–869. doi:10.1016/j.bbamcr.2006.04.010
- Dudley, S. C., Hoch, N. E., Mccann, L. A., Honeycutt, C., Diamandopoulos, L., Fukai, T., et al. (2005). Atrial Fibrillation Increases Production of Superoxide by the Left Atrium and Left Atrial Appendage: Role of the NADPH and Xanthine Oxidases. *Circul.* 112 (9), 1266–1273. doi:10.1161/CIRCULATIONAHA.105.538108
- Esmon, C. T. (2014). Targeting Factor Xa and Thrombin: Impact on Coagulation and beyond. *Thromb. Haemost.* 111 (4), 625–633. doi:10.1160/TH13-09-0730
- Fernandes, A., Miller-Fleming, L., and Pais, T. F. (2014). Microglia and Inflammation: Conspiracy, Controversy or Control? *Cell Mol Life Sci* 71 (20), 3969–3985. doi:10.1007/s00018-014-1670-8
- Giugliano, R. P., Ruff, C. T., Braunwald, E., Murphy, S. A., Wiviott, S. D., Halperin, J. L., et al. (2013). Edoxaban versus Warfarin in Patients with Atrial Fibrillation. *N. Engl. J. Med.* 369 (22), 2093–2104. doi:10.1056/NEJMoa1310907
- Gyöngyösi, M., Winkler, J., Ramos, I., Do, Q. T., Firat, H., McDonald, K., et al. (2017). Myocardial Fibrosis: Biomedical Research from Bench to Bedside. *Eur. J. Heart Fail.* 19 (2), 177–191. doi:10.1002/ehf.696
- Hindricks, G., Potpara, T., Dagres, N., Arbelo, E., Bax, J. J., Blomström-Lundqvist, C., et al. (2021). 2020 ESC Guidelines for the Diagnosis and Management of Atrial Fibrillation Developed in Collaboration with the European Association of Cardio-Thoracic Surgery (EACTS). *Eur. Heart J.* 42 (5), 373–498. doi:10.1093/eurheartj/ehaa612
- Hossmann, K. A. (2006). Pathophysiology and Therapy of Experimental Stroke. *Cell Mol Neurobiol* 26 (7–8), 1057–1083. doi:10.1007/s10571-006-9008-1
- Hu, Y. F., Chen, Y. J., Lin, Y. J., and Chen, S. A. (2015). Inflammation and the Pathogenesis of Atrial Fibrillation. *Nat. Rev. Cardiol.* 12 (4), 230–243. doi:10.1038/nrcardio.2015.2
- Issac, T. T., Dokainish, H., and Lakkis, N. M. (2007). Role of Inflammation in Initiation and Perpetuation of Atrial Fibrillation: a Systematic Review of the Published Data. *J. Am. Coll. Cardiol.* 50 (21), 2021–2028. doi:10.1016/j.jacc.2007.06.054
- Jalife, J. (2014). Mechanisms of Persistent Atrial Fibrillation. *Curr. Opin. Cardiol.* 29 (1), 20–27. doi:10.1097/HCO.000000000000027
- James, C. P., Bajaj-Elliott, M., Abujaber, R., Forya, F., Klein, N., David, A. L., et al. (2018). Human Beta Defensin (HBD) Gene Copy Number Affects HBD2 Protein Levels: Impact on Cervical Bactericidal Immunity in Pregnancy. *Eur. J. Hum. Genet.* 26 (3), 434–439. doi:10.1038/s41431-017-0061-7
- Katayama, T., Fujiwara, N., and Tsuruya, Y. (2010). Factors Contributing to Left Atrial Enlargement in Adults with normal Left Ventricular Systolic Function. *J. Cardiol.* 55 (2), 196–204. doi:10.1016/j.jcc.2009.10.008
- Katoh, H., Nozue, T., and Michishita, I. (2017). Anti-inflammatory Effect of Factor-Xa Inhibitors in Japanese Patients with Atrial Fibrillation. *Heart Vessels* 32 (9), 1130–1136. doi:10.1007/s00380-017-0962-y
- Katritsis, D. G. (2006). Is Atrial Fibrillation an Inflammatory Disorder. *EUROPEAN HEART JOURNAL* 27 (7), 136–149. doi:10.1093/eurheartj/ehi780
- Kirchhof, P., Benussi, S., Kotecha, D., Ahlsson, A., Atar, D., Casadei, B., et al. (20162016). ESC Guidelines for the Management of Atrial Fibrillation Developed in Collaboration with EACTS. *Eur. J. Cardiothorac. Surg.* 50, e1–e88. doi:10.1093/ejcts/ezw313
- Li, J., Solus, J., Chen, Q., Rho, Y. H., Milne, G., Stein, C. M., et al. (2010). Role of Inflammation and Oxidative Stress in Atrial Fibrillation. *Heart Rhythm* 7 (4), 438–444. doi:10.1016/j.hrthm.2009.12.009
- Li, Z. Z., Du, X., Guo, X. Y., Tang, R. B., Jiang, C., Liu, N., et al. (2018). Association between Blood Lipid Profiles and Atrial Fibrillation: A Case-Control Study. *Med. Sci. Monit.* 24, 3903–3908. doi:10.12659/MSM.907580
- Lim, W. H., Choi, E. K., Han, K. D., Lee, S. R., Cha, M. J., and Oh, S. (2020). Impact of Hemoglobin Levels and Their Dynamic Changes on the Risk of Atrial Fibrillation: A Nationwide Population-Based Study. *Sci. Rep.* 10 (1), 6762. doi:10.1038/s41598-020-63878-9
- Lip, G. Y., Patel, J. V., Hughes, E., and Hart, R. G. (2007). High-sensitivity C-Reactive Protein and Soluble CD40 Ligand as Indices of Inflammation and Platelet Activation in 880 Patients with Nonvalvular Atrial Fibrillation:

- Relationship to Stroke Risk Factors, Stroke Risk Stratification Schema, and Prognosis. *Stroke* 38 (4), 1229–1237. doi:10.1161/01.STR.0000260090.90508.3e
- Miyasaka, Y., Barnes, M. E., Gersh, B. J., Cha, S. S., Bailey, K. R., Abhayaratna, W. P., et al. (2006). Secular Trends in Incidence of Atrial Fibrillation in Olmsted County, Minnesota, 1980 to 2000, and Implications on the Projections for Future Prevalence. *CIRCULATION* 114 (2), 119–125. doi:10.1161/CIRCULATIONAHA.105.595140
- Morishima, Y., Shibutani, T., Noguchi, K., Ito, Y., and Honda, Y. (2021). Edoxaban, a Direct Oral Factor Xa Inhibitor, Ameliorates Coagulation, Microvascular Thrombus Formation, and Acute Liver Injury in a Lipopolysaccharide-Induced Coagulopathy Model in Rats. *J. Thromb. Thrombolysis* 52 (1), 9–17. doi:10.1007/s11239-021-02381-y
- Negreva, M., Zarkova, A., Prodanova, K., and Petrov, P. (2020). Paroxysmal Atrial Fibrillation: Insight into the Intimate Mechanisms of Coagulation. *Cardiol. Res.* 11, 22–32. doi:10.14740/cr972
- Neuman, R. B., Bloom, H. L., Shukrullah, I., Darrow, L. A., Kleinbaum, D., Jones, D. P., et al. (2007). Oxidative Stress Markers Are Associated with Persistent Atrial Fibrillation. *Clin. Chem.* 53 (9), 1652–1657. doi:10.1373/clinchem.2006.083923
- Özdemir, M., Caglayan, F., Bikker, F. J., Pussinen, P., Könönen, E., Yamalik, N., et al. (2020). Gingival Tissue Human Beta-Defensin Levels in Relation to Infection and Inflammation. *J. Clin. Periodontol.* 47 (3), 309–318. doi:10.1111/jcpe.13227
- Pandya, R. S., Mao, L., Zhou, H., Zhou, S., Zeng, J., Popp, A. J., et al. (2011). Central Nervous System Agents for Ischemic Stroke: Neuroprotection Mechanisms. *Cent. Nerv. Syst. Agents Med. Chem.* 11 (2), 81–97. doi:10.2174/187152411796011321
- Patrinos, G. P., Kollia, P., and Papadakis, M. N. (2005). Molecular Diagnosis of Inherited Disorders: Lessons from Hemoglobinopathies. *Hum. Mutat.* 26 (5), 399–412. doi:10.1002/humu.20225
- Platt, O. S., Brambilla, D. J., Rosse, W. F., Milner, P. F., Castro, O., Steinberg, M. H., et al. (1994). Mortality in Sickle Cell Disease. Life Expectancy and Risk Factors for Early Death. *N. Engl. J. Med.* 330 (23), 1639–1644. doi:10.1056/NEJM199406093302303
- Popović, M., Smiljanić, K., Dobutović, B., Syrovets, T., Simmet, T., and Isenović, E. R. (2012). Thrombin and Vascular Inflammation. *Mol. Cell Biochem* 359 (1–2), 301–313. doi:10.1007/s11010-011-1024-x
- Roldán, V., Marín, F., Díaz, J., Gallego, P., Jover, E., Romera, M., et al. (2012). High Sensitivity Cardiac Troponin T and Interleukin-6 Predict Adverse Cardiovascular Events and Mortality in Anticoagulated Patients with Atrial Fibrillation. *J. Thromb. Haemost.* 10 (8), 1500–1507. doi:10.1111/j.1538-7836.2012.04812.x
- Smorodinova, N., Bláha, M., Melenovský, V., Rozsivalová, K., Přidal, J., Ďurišová, M., et al. (2017). Analysis of Immune Cell Populations in Atrial Myocardium of Patients with Atrial Fibrillation or Sinus Rhythm. *PLoS One* 12 (2), e0172691. doi:10.1371/journal.pone.0172691
- Steinberg, S. F. (2005). The Cardiovascular Actions of Protease-Activated Receptors. *Mol. Pharmacol.* 67 (1), 2–11. doi:10.1124/mol.104.003103
- Subahi, A., Munir, A., Abubakar, H., Akintoye, E., Yassin, A. S., Adegba, O., et al. (2018). The Impact of Atrial Fibrillation on Transcatheter Mitral Valve Repair Outcomes: A Propensity-Matched Analysis. *J. Interv. Cardiol.* 31 (6), 925–931. doi:10.1111/joic.12568
- Tsuchiya, M., Sako, K., Yura, S., and Yonemasu, Y. (1992). Cerebral Blood Flow and Histopathological Changes Following Permanent Bilateral Carotid Artery Ligation in Wistar Rats. *Exp. Brain Res.* 89 (1), 87–92. doi:10.1007/BF00229004
- Wang, X., Meng, X., Meng, L., Guo, Y., Li, Y., Yang, C., et al. (2022). Joint Efficacy of the Three Biomarkers SNCA, GYPB and HBG1 for Atrial Fibrillation and Stroke: Analysis via the Support Vector Machine Neural Network. *J. Cel Mol Med* 26 (7), 2010–2022. doi:10.1111/jcmm.17224
- Wolf, P. A., Mitchell, J. B., Baker, C. S., Kannel, W. B., and D'Agostino, R. B. (1998). Impact of Atrial Fibrillation on Mortality, Stroke, and Medical Costs. *Arch. Intern. Med.* 158 (3), 229–234. doi:10.1001/archinte.158.3.229
- Yao, Y., Liu, F., Wang, Y., and Liu, Z. (2020). Lipid Levels and Risk of New-Onset Atrial Fibrillation: A Systematic Review and Dose-Response Meta-Analysis. *Clin. Cardiol.* 43, 935–943. doi:10.1002/clc.23430
- Zhang, H., Li, J., Chen, X., Wu, N., Xie, W., Tang, H., et al. (2017). Association of Systemic Inflammation Score with Atrial Fibrillation: A Case-Control Study with Propensity Score Matching. *Heart Lung Circ.* 27, 489–496. doi:10.1016/j.hlc.2017.04.007
- Zhou, X., and Dudley, S. C. (2020). Evidence for Inflammation as a Driver of Atrial Fibrillation. *Front. Cardiovasc. Med.* 7, 62. doi:10.3389/fcvm.2020.00062

Conflict of Interest: The authors declare that the research was conducted in the absence of any commercial or financial relationships that could be construed as a potential conflict of interest.

Publisher's Note: All claims expressed in this article are solely those of the authors and do not necessarily represent those of their affiliated organizations, or those of the publisher, the editors, and the reviewers. Any product that may be evaluated in this article, or claim that may be made by its manufacturer, is not guaranteed or endorsed by the publisher.

Copyright © 2022 Yang, Wang, Guo, Meng, Li, Xia, Meng, Dong and Wang. This is an open-access article distributed under the terms of the Creative Commons Attribution License (CC BY). The use, distribution or reproduction in other forums is permitted, provided the original author(s) and the copyright owner(s) are credited and that the original publication in this journal is cited, in accordance with accepted academic practice. No use, distribution or reproduction is permitted which does not comply with these terms.



Screening of Biomarkers and Toxicity Mechanisms of Rifampicin-Induced Liver Injury Based on Targeted Bile Acid Metabolomics

Yang Deng^{1,2†}, Xilin Luo^{1†}, Xin Li^{1,2*}, Yisha Xiao¹, Bing Xu^{1,2} and Huan Tong^{1,2}

¹Department of Pharmacy, The Third Hospital of Changsha, Changsha, China, ²The Clinical Application Research Institute of Antibiotics in Changsha, Changsha, China

OPEN ACCESS

Edited by:

Ren-ai Xu,

First Affiliated Hospital of Wenzhou Medical University, China

Reviewed by:

Vik Meadows,

Rutgers, The State University of New Jersey—Busch Campus, United States

Dezhi Kong,

Hebei Medical University, China

*Correspondence:

Xin Li

xin-li@cssdsyy.com

[†]These authors have contributed equally to this work

Specialty section:

This article was submitted to Drug Metabolism and Transport, a section of the journal Frontiers in Pharmacology

Received: 21 April 2022

Accepted: 24 May 2022

Published: 10 June 2022

Citation:

Deng Y, Luo X, Li X, Xiao Y, Xu B and Tong H (2022) Screening of Biomarkers and Toxicity Mechanisms of Rifampicin-Induced Liver Injury Based on Targeted Bile Acid Metabolomics. *Front. Pharmacol.* 13:925509. doi: 10.3389/fphar.2022.925509

Rifampicin (RIF) is a critical first-line drug for tuberculosis. However, long-term or high-dose treatment with RIF can induce severe liver injury; the underlying mechanism of this effect has not yet been clarified. This study was performed to screen reliable and sensitive biomarkers in serum bile acids (BAs) using targeted BA metabolomics and evaluate the toxicity mechanisms underlying RIF-induced liver injury through the farnesoid x receptor (Fxr)-multidrug resistance-associated proteins (Mrps) signaling pathway. Thirty-two Institute of Cancer Research mice were randomly divided into four groups, and normal saline, isoniazid 75 mg/kg + RIF 177 mg/kg (RIF-L), RIF-L, or RIF 442.5 mg/kg (RIF-H) was orally administered by gavage for 21 days. After treatment, changes in serum biochemical parameters, hepatic pathological conditions, BA levels, Fxr expression, and BA transporter levels were measured. RIF caused notable liver injury and increased serum cholic acid (CA) levels. Decline in the serum secondary BAs (deoxycholic acid, lithocholic acid, taurodeoxycholic acid, and tauroursodeoxycholic acid) levels led to liver injury in mice. Serum BAs were subjected to metabolomic assessment using partial least squares discriminant and receiver operating characteristic curve analyses. CA, DCA, LCA, TDCA, and TUDCA are potential biomarkers for early detection of RIF-induced liver injury. Furthermore, RIF-H reduced hepatic BA levels and elevated serum BA levels by suppressing the expression of Fxr and Mrp2 messenger ribonucleic acid (mRNA) while inducing that of Mrp3 and Mrp4 mRNAs. These findings provide evidence for screening additional biomarkers based on targeted BA metabolomics and provide further insights into the pathogenesis of RIF-induced liver injury.

Keywords: rifampicin, liver injury, targeted bile acid metabolomics, farnesoid x receptor, multidrug resistance-associated proteins

1 INTRODUCTION

Tuberculosis (TB) is an infectious disease caused by *Mycobacterium tuberculosis*, the second leading cause of death from a single infectious agent after severe acute respiratory syndrome coronavirus 2 (World Health Organization, 2021). Treatment for drug-susceptible TB requires a combination of rifampicin (RIF), isoniazid (INH), ethambutol, and pyrazinamide for 2-months followed by RIF and INH for 4 months, while 6–20 months for multidrug-resistant TB (Lange et al., 2019; World Health Organization, 2021). Prolonged RIF administration or the combination of RIF and INH would

significantly increase the risk of drug-induced liver injury with an undefined mechanism (Devarbhavi et al., 2021). The current standard RIF dose of 10 mg/kg daily is suboptimal and has remained unchanged since the early 1970s (Grobbelaar et al., 2019; Te Brake et al., 2021). In RIF clinical trials, doses of 20, 25, 30, 35, and 50 mg/kg have been administered. The safety of RIF 50 mg/kg should be verified in further investigation, given its poor tolerance in humans (Boeree et al., 2015; Abulfathi et al., 2019; Te Brake et al., 2021). Long-term RIF treatment can cause hepatocyte dysfunction and cholestatic liver injury (Grobbelaar et al., 2019; Yang et al., 2020c). The mechanism of RIF-induced drug-induced liver injury (DILI) remains undefined and may occur by cholestasis, oxidative stress, inflammatory response, mitochondrial damage, and apoptosis (Moussavian et al., 2016; Yang et al., 2020c; Luo et al., 2021).

Bile acids (BAs), a major component of bile, regulate glucose and lipid metabolism, as well as energy homeostasis (Chiang and Ferrell, 2020). A previous study indicated that the disorder of BAs was associated with primary sclerosing cholangitis, primary biliary cholangitis, previously known as primary biliary cirrhosis, nonalcoholic fatty liver, and nonalcoholic steatohepatitis (Choudhuri and Klaassen, 2022). It is essential to evaluate therapeutic agents to treat liver injury and elucidate the relationship between BA metabolism and the mechanisms of liver injury. Farnesoid x receptor (Fxr), which is abundantly expressed in the liver, gastrointestinal tract, kidney, and adrenal glands, plays an essential role in regulating BA and lipid metabolism and glucose homeostasis. Fxr is activated by chenodeoxycholic acid (CDCA), cholic acid (CA), deoxycholic acid (DCA), lithocholic acid (LCA), and their taurine and glycine conjugates, and promotes BAs flow (Yang et al., 2017; Gottlieb and Canbay, 2019; Keitel et al., 2019; Chiang and Ferrell, 2020). Fxr represses the *de novo* synthesis and uptake of BAs in the liver and protects hepatocytes from the accumulation of toxic BAs under cholestatic conditions. Multidrug resistance-associated proteins (Mrps) are BAs efflux transporters, the regulation of BAs by Fxr is related to the regulation of subtypes of Mrps, such as Mrp2, Mrp3, and Mrp4 (Xu et al., 2005; Yuan et al., 2018; Fiorucci et al., 2021). Uridine diphosphate-glucuronosyltransferases (UGTs), which can co-express Mrp2, are associated with the phase II metabolic pathway. UGTs substrates are metabolized by glucuronidation, increasing hydrophilicity and facilitating the excretion of conjugated metabolites into bile and urine, thus further reducing toxicity (Xu et al., 2005). Furthermore, the prognosis of DILI can be improved by considering and detecting changes in BA efflux transporter levels (Ali et al., 2017).

Serum alanine aminotransferase (ALT) and aspartate aminotransferase (AST) levels are less sensitive and liver-specific for DILI relative to the new biomarkers, such as BAs and glutamate dehydrogenase (McGill and Jaeschke, 2019; Tian et al., 2022). The reason for the increase in ALT activity is also correlated with skeletal muscle, cardiac injury or metabolic state, except for histopathology change (Zhao et al., 2017). Moreover, a previous study found that the levels of hepatic and serum BAs and BA-related genes increase notably, with no elevation in serum ALT, AST, and alkaline phosphatase levels after administering a

dose of RIF (Sanoh et al., 2019). Another study showed that the levels of serum conjugated BAs [glycocholic acid (GCA) and taurocholic acid (TCA)] increase in the rats with bile duct hyperplasia without significant changes in ALT and AST levels (Slopianka et al., 2017). It was shown that ALT and AST indicated lower sensitivity and specificity for the detection of liver injury than BAs. BA metabolism was closely related to the pathologic changes in the hepatic and biliopancreatic diseases. Since the 1950s, enzymatic methods of quantifying the “total” bile acid pool in blood have been established (Hurlock and Talalay, 1957). In recent years, many metabolomics studies have demonstrated that BAs are potential biomarkers for the diagnosis, follow-up and prognosis of liver injury and dysfunction (Ambros-Rudolph et al., 2007; Crosignani et al., 2007; Dong et al., 2015; Tian et al., 2022). Tian and others found that serum glycochenodeoxycholic acid (GUDCA), taurodeoxycholic acid (TDCA), and taurolithocholic acid (TLCA) were helpful for evaluating Cd-induced liver injury and Cd exposure in humans based on targeted BA metabolomics (Tian et al., 2022). In another study, glycodeoxycholic acid (GDCA) in the bile and hyodeoxycholic acid (HDCA) in the serum could be potential biomarkers for *Polygonum multiflorum*-induced liver injury (Dong et al., 2015). Therefore, analysis of individual BAs has the potential to unravel valuable biomarkers for the differentiation and diagnosis of various forms of liver injury (Luo et al., 2018). It is necessary to adopt targeted BA metabolomic approaches using liquid chromatography-tandem mass spectrometry (LC-MS/MS) to identify potential biomarkers from serum BAs.

In a study of liver injury in mice, RIF treatment suppressed Na⁺/taurocholate cotransporter, one of the targets of Fxr signaling (Yang et al., 2020b). Besides, it is clear that the expression levels of organic solute transporter β were increased following treatment with RIF (Zhang et al., 2017). Mrps play an essential role in disorders of BAs metabolism and DILI (Cuperus et al., 2014). The relationship between the change of Fxr and Mrp2, Mrp3, Mrp4 mRNA, and RIF-induced DILI is still insufficient. Therefore, Our study aims to establish an experimental mouse model of RIF-induced liver injury to analyze the changes in the metabolic profile of BAs in the liver and serum using LC-MS/MS and unravel the potential serum biomarkers for liver injury. Comprehensive analysis of the role of the Fxr-Mrps signaling pathway in BA metabolism, we could better understand the hepatotoxicity mechanism of RIF action and further provide a theoretical basis for DILI prevention and rational clinical application in anti-TB therapy.

2 MATERIALS AND METHODS

2.1 Chemicals and Reagents

RIF and INH were purchased from Meilun Biotechnology Co. Ltd (Dalian, China). Ursodeoxycholic acid (UDCA), HDCA, CA, CDCA, DCA, taurochenodeoxycholic acid (TUDCA), and taurochenodeoxycholic acid (TCDCA) were purchased from On-Road Biotechnology Co., Ltd (Changsha, China). TCA, LCA, GCA, glycochenodeoxycholic acid (GCDCA), GDCA, TLCA, and TDCA were purchased from Sigma Reagents, Inc

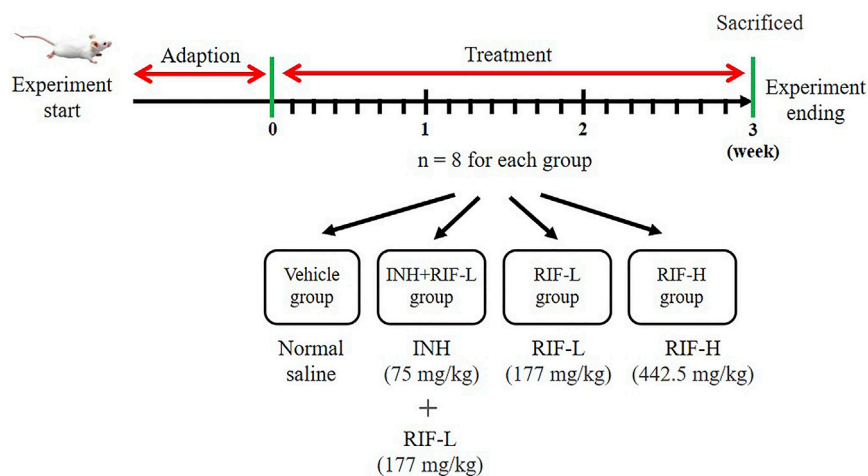


FIGURE 1 | The scheme of animal experiment. The mice were divided into four groups: vehicle, INH (75 mg/kg)+RIF-L (144 mg/kg), RIF-L, and RIF-H (442.5 mg/kg) group, with eight mice in each group.

(St. Louis, MO, United States). Taurohyodeoxycholic acid (THDCA) and GUDCA were purchased from Aikeda Chemical Reagent Co., Ltd (Chengdu, China). Cyproterone acetate was purchased from China National Institutes for Food and Drug Control (Beijing, China). Acetonitrile and methanol (chromatographic grade purity) were purchased from Merck (Darmstadt, Germany). Formic acid and ammonium acetate (chromatographic grade purity) were purchased from ROE Scientific Inc (United States). The EVOM-MLV reverse transcription kit, SYBR Green Premix Pro Taq HS premixed quantitative real-time polymerase chain reaction (PCR) kit, nuclease-free water, and AG RNAex Pro ribonucleic acid (RNA) extraction reagent were purchased from Aicerui Biological Engineering Co., Ltd. (Hunan, China).

2.2 Animals and Experimental Design

All animal experiments were conducted in compliance with the Guide for the Care and Use of Laboratory Animals. Healthy Institute of Cancer Research mice, weighing 18–22 g, were provided by Hunan Slack Jingda Experimental Animal Co., Ltd (Hunan, China). The mice were provided *ad libitum* access to water and chow and kept at $20 \pm 2^\circ\text{C}$ at $50 \pm 10\%$ relative humidity with a 12-h/12-h light/dark cycle. Thirty-two mice were randomly divided into four groups (eight mice in each group) and treated as follows: normal saline (vehicle), INH 75 mg/kg + RIF 177 mg/kg (RIF-L), RIF-L, and RIF 442.5 mg/kg (RIF-H). RIF and INH were administered daily by gavage for 21 days (Figure 1). After day 21, the mice fasted for 12 h before anatomical examination. Blood samples and liver tissues from the mice were collected for further experiments. The animal experiment was approved by Animal Ethics Review Regulations of Hunan Academy of Traditional Chinese Medicine and was reviewed and approved by the Animal Ethics Review Committee. (Number:2019-0024).

2.3 Biochemical and Histological Analyses

ALT, AST, total bilirubin (TBil), and indirect bilirubin (IBil) levels and liver index (liver weight/body weight $\times 100$) were measured as described earlier (Luo et al., 2020). The fixed liver tissue was embedded in paraffin blocks. Next, 4- μm -thick slices were cut and stained with hematoxylin and eosin to investigate histopathological changes.

2.4 LC-MS/MS for Liver and Serum BAs

2.4.1 Instruments and Conditions

LC-MS/MS for BAs (Supplementary Figure S1) was performed using the LCMS-8050 triple quadrupole mass spectrometer (Shimadzu, Japan). The separation was performed on an Ultimate AQ-C18 (3.0 mm \times 100 mm, 3.0 μm ; Welch, United States) analytical column connected with a top C18 column (Guard cartridge System, United States). The column temperature was maintained at 40°C . The gradient system consisted of solvent A (0.005% formic acid containing 7 mmol/L ammonium acetate) and solvent B (methanol) at a flow rate of 0.60 ml/min, and the gradient program was as follows: 40%:60% (v/v, 0–2 min), 5%:95% (v/v, 13.0–17.3 min), and 40%:60% (v/v, 17.4–29.3 min). Cyproterone acetate was used as the internal standard (IS). The multiple reaction monitoring functions used MS in the electrospray ionization negative mode. Other MS parameters were as follows: Interface: ESI(-); Drying gas flow: 10.0 L/min; Heat block temperature: 400°C . The multiple reactions monitoring the ion pairs of the BAs were listed in Table 1.

2.4.2 Sample Preparation

To analyze 16 BAs in the mouse liver, liver tissue was weighed and added to the saline solution according to the ratio of 1:10, and the mixtures were homogenized using a tissue homogenizer (Servicebio, China). After the homogenation, 50 μL hepatic homogenate was added to 150 μL of IS solution. The mixture was vortexed for 2 min before centrifugation at 4°C and 10,000 g for 10 min. The supernatant (150 μL) was volatilized to dryness in a centrifugal

TABLE 1 | The optimum LC-MS/MS working parameters for BAs.

BAs	MRM m/z	CE/V-	Dwell time (msec)	Retention time (min)
CA	407.30/407.30	10.0	50.0	11.83
CDCA	391.30/391.30	10.0	50.0	14.27
DCA	391.30/391.30	10.0	50.0	14.70
LCA	375.50/375.50	10.0	50.0	16.45
UDCA	391.30/391.30	10.0	50.0	9.80
HDCA	391.30/391.30	10.0	50.0	10.80
TCA	514.20/80.00	55.0	50.0	10.40
TCDCA	498.20/80.05	55.0	50.0	12.80
TDCA	498.20/80.05	55.0	50.0	13.39
TLCA	482.20/80.00	55.0	50.0	14.98
TUDCA	498.20/80.05	55.0	50.0	8.06
THDCA	498.20/80.05	55.0	50.0	9.04
GCA	464.20/74.00	38.0	50.0	10.62
GCDCA	448.20/73.90	37.0	50.0	13.03
GDCA	448.20/73.90	37.0	50.0	13.60
GUDCA	448.20/73.90	37.0	50.0	8.20

TABLE 2 | Primer sequences used for quantitative real-time PCR.

Gene	Primer
glyceraldehyde-3-phosphate dehydrogenase	Forward: 5'-AGGTCGGTGTGAACGGATTTG-3' Reverse: 5'-GGGGTCGTTGATGGCAACA-3'
Fxr	Forward: 5'-AGCTAATGAGGACGACAGCG-3' Reverse: 5'-TGCCGTGAGTTCGGTTTTCT-3'
Mrp2	Forward: 5'-TGAGGAAGAGGATGGTGA CTGTGG-3' Reverse: 5'-GTTCCGGCGAAGGCTGTTC TCC-3'
Mrp3	Forward: 5'-ATCACCATACACAACGGC ACCTTC-3' Reverse: 5'-TCCGAGTAAGGCAGACAC CAGAG-3'
Mrp4	Forward: 5'-TCTACCAGGACGCCGACA TCTAC-3' Reverse: 5'-ACAGTTGGAACAGGTGCT TGCC-3'
UGT1a1	Forward: 5'-TTCCTGTGCCTCTCCTTT AACT-3' Reverse: 5'-TCATCCAGTCAAACCAGC C-3'

vacuum concentration system, carefully collected, and resuspended in 50 μ L 50% methanol. Finally, the supernatant was injected into the LC-MS/MS system. The IS method was used for quantitation. For each serum sample, the experiment was processed separately as described above. That is, 50 μ L serum was added to 150 μ L of the IS solution, and the other processes remained unchanged.

2.5 Quantitative Real-Time PCR

Quantitative real-time PCR was performed on the ABI 7500 Fast Real-Time PCR system (Thermo Fisher Scientific, United States). Total RNA was extracted using the reverse transcription kit with the TRIzol reagent and reverse-transcribed into complementary

deoxyribonucleic acid (cDNA). cDNA was amplified and analyzed using the SYBR Green Premix Pro Taq HS qPCR kit (Ackeri Bioengineering Co., Ltd.). Glyceraldehyde-3-phosphate dehydrogenase (*Gapdh*) was used as a control. The primer sequences used in our study are listed in **Table 2**.

2.6 Statistical Analyses

Partial least squares-discriminant analysis (PLS-DA) is accomplished by linking two data matrices X and Y to maximize the covariance between the independent variables X and the corresponding dependent variable Y of highly multidimensional data by finding a linear subspace of the explanatory variables. VIP (variable importance) is mainly used for screening the important variables. The technology of VIP can be used in the case of small sample size and a strong correlation between several independent variables. It means an important variable in the model with a value of $VIP \geq 1$ (Gromski et al., 2015; Lee et al., 2018). Differential markers could be screened by VIP value and SPSS statistical analysis of PLS-DA variables ($p < 0.05$). PLS-DA is widely used for the data analysis of metabolomics. Simca-p 14.1 software was used for PLS-DA to assess the data. VIP was calculated for the liver and serum BA levels using this software. Statistical and receiver operating characteristic (ROC) curve analyses were performed using GraphPad Prism eight and SPSS 25.0, respectively, following recommendations in the pharmacology field. All experimental data obtained in this study are presented as the mean \pm standard deviation. Data from multiple groups were compared using a one-way analysis of variance, followed by the least significant difference test. Correlation analysis was performed using Pearson's test. Differences were considered statistically significant at $p < 0.05$.

3 RESULTS

3.1 Effects of RIF on Biochemical and Histological Changes

To evaluate RIF-induced liver injury, some biochemical indicators were analyzed. As exhibited in **Figure 2**,

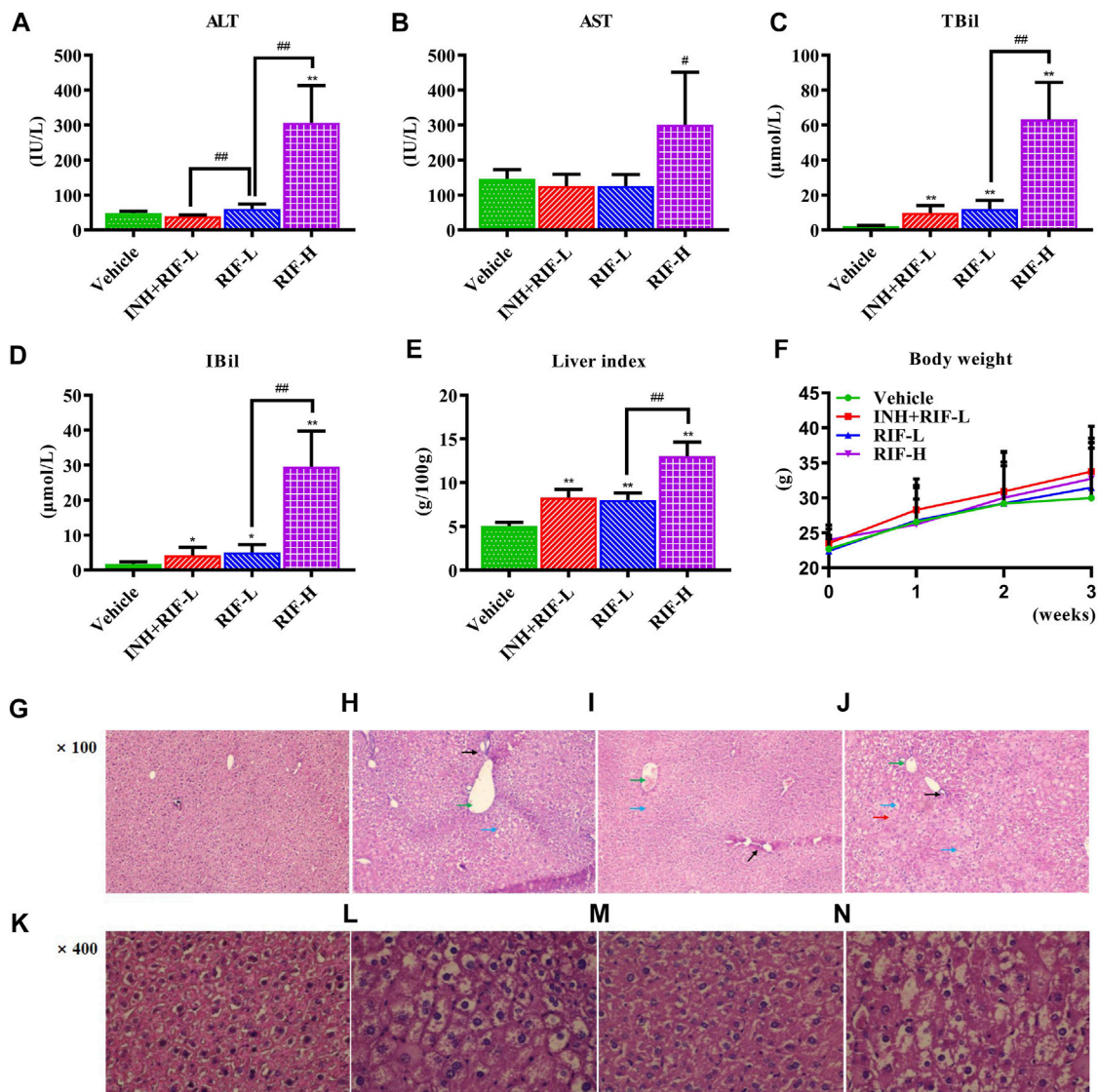


FIGURE 2 | Effects of RIF on serum biomarkers, liver indexes, and histological parameters (HE staining) **(A)** ALT **(B)** AST **(C)** TBil **(D)** IBil **(E)** Liver index **(F)** Body weight **(G)** The vehicle group in HE, $\times 100$ **(H)** The INH + RIF-L group in HE, $\times 100$ **(I)** The RIF-L group in HE, $\times 100$ **(J)** The RIF-H group in HE, $\times 100$ **(K)** The vehicle group in HE, $\times 400$ **(L)** The INH + RIF-L group in HE, $\times 400$ **(M)** The RIF-L group in HE, $\times 100$ **(N)** The RIF-H group in HE, $\times 400$. Data are expressed as mean \pm SD ($n = 6$). $^*p < 0.05$, $^{**}p < 0.01$ versus the vehicle group; $^{\#}p < 0.05$, $^{##}p < 0.01$ versus the RIF-L group.

compared with the vehicle group, the serum levels of ALT, AST, TBil, IBil, and liver index in the RIF-H group were increased by 6.4-, 2.1-, 29.1-, 17.0-, and 2.6- fold, respectively; but only TBil, IBil, and the liver index increased significantly in the INH + RIF-L and RIF-L groups. Histopathological analysis showed that a typical structure with well-arranged hepatocyte cords and obvious hepatic sinusoids was observed in the vehicle group. The liver sections of mice treated with INH + RIF-L and RIF-L showed a typical arrangement of the hepatic cords and central veins, except for some nuclear disappearance and partial vacuoles. Meanwhile, biliary duct dilatation features can be observed in the INH + RIF-L and RIF-L groups, marked in **Figures 2H,I**, respectively. The RIF-

H group showed steatosis, hepatocyte swelling, dissolution, the disappearance of the nucleus, and increased intracellular damage (Luo et al., 2020). These results indicated that RIF induced hepatotoxicity in a dose-dependent manner (**Figure 2**).

3.2 Changes in Liver and Serum BA Profiles

LC-MS/MS was performed to detect the liver and serum BA profiles (**Figure 3**). The results showed that the levels of serum-free and total BAs were significantly elevated in the RIF-H group. Serum CA was upregulated in the RIF-H group, whereas secondary BAs (DCA, LCA, TDCA, and TUDCA) were downregulated in all the RIF-administered mice.

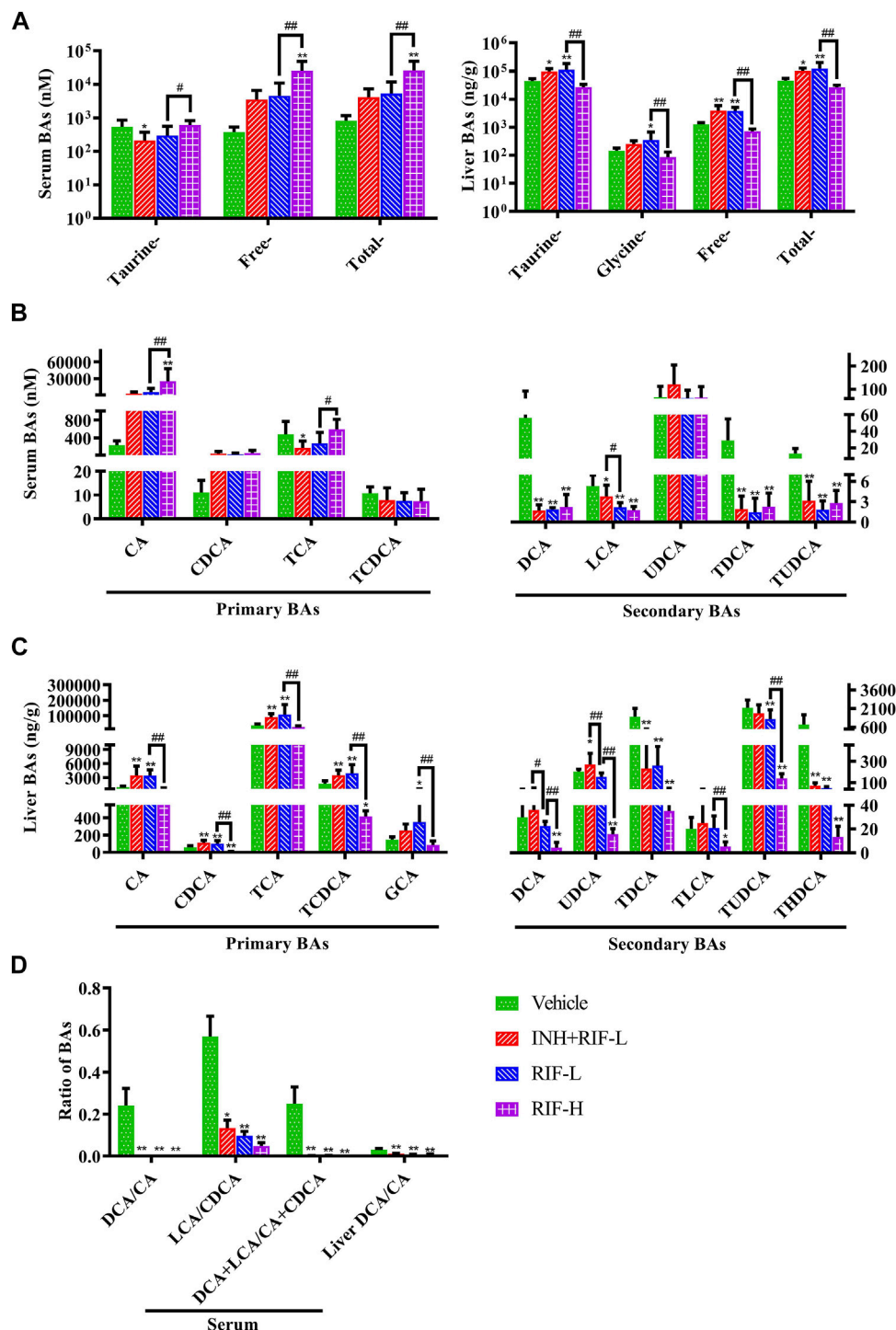


FIGURE 3 | Effects of RIF on the serum and liver BA levels in mice **(A)** Taurine, free, total BAs in the serum and liver **(B)** Primary and secondary BAs in the serum **(C)** Primary and secondary BAs in the liver **(D)** The ratio of secondary BAs to primary BAs. Data are expressed as mean \pm SD ($n = 5-8$). * $p < 0.05$, ** $p < 0.01$ versus the vehicle group; # $p < 0.05$, ## $p < 0.01$ versus the RIF-L group. Green arrows indicate dilatation of central veins, blue arrows indicate hepatocellular hydropic degeneration, red arrow indicate necrosis, black arrows indicate cholangiectasis.

The levels of hepatic taurine-conjugated, free, and total BAs significantly increased in the RIF-L and INH + RIF-L groups. In addition, RIF significantly increased the levels of hepatic primary

BAs such as CA, CDCA, TCA, and TCDCA in the RIF-L and INH + RIF-L groups. However, the levels of all hepatic BAs reduced considerably in the RIF-H group.

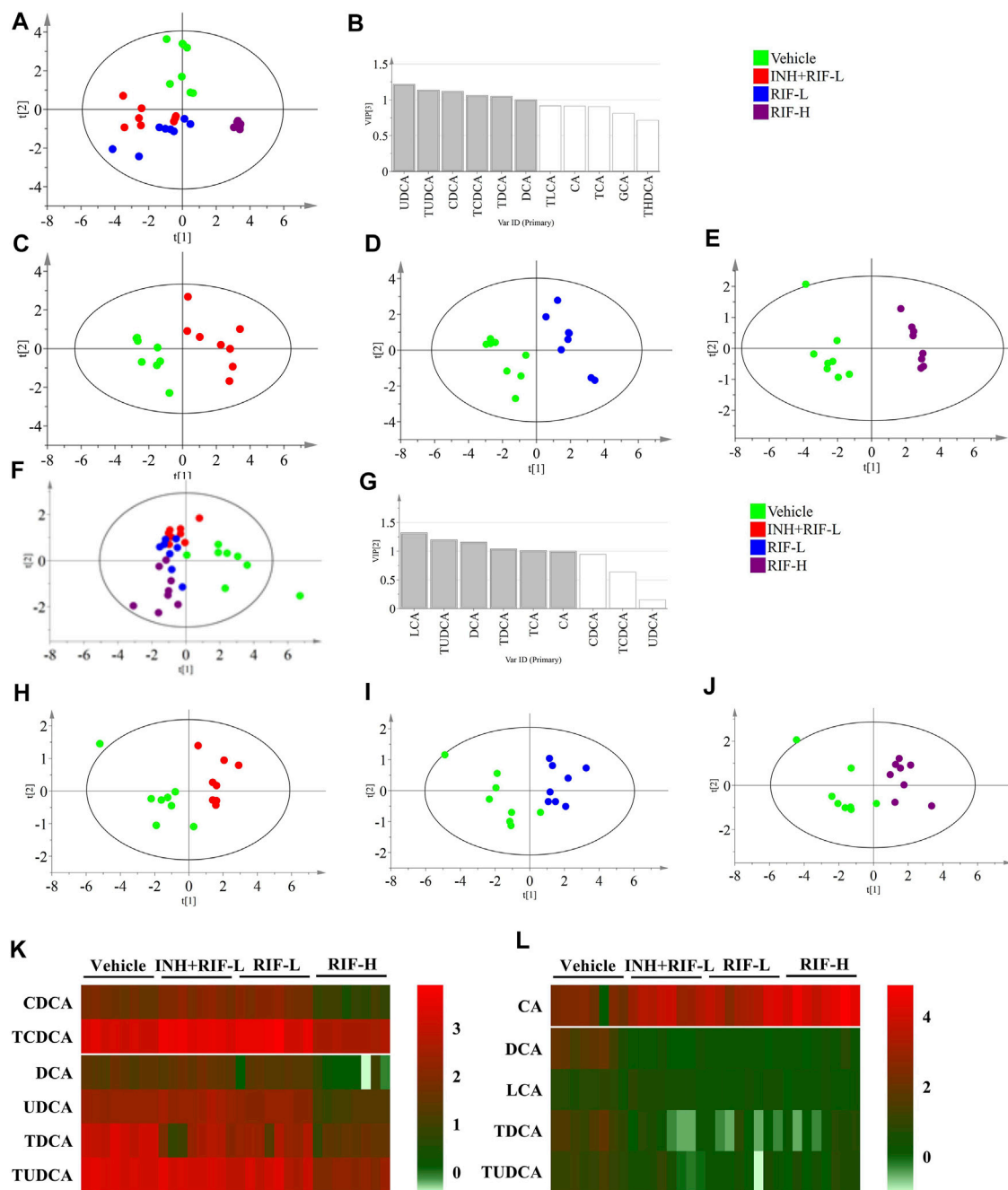


FIGURE 4 | Targeted metabolomics of BA profiles **(A)** Score plots of PLS-DA for the liver in the vehicle, INH + RIF-L, RIF-L, and RIF-H groups **(B)** VIP value in the liver between the vehicle and RIF-H groups **(C)** Score plots of PLS-DA of the liver between the vehicle and INH + RIF-L groups **(D)** Score plots of PLS-DA of the liver between the vehicle and RIF-L groups **(E)** Score plots of PLS-DA of the liver between the vehicle and RIF-H groups **(F)** Score plots of PLS-DA of the serum among the vehicle, INH + RIF-L, RIF-L, and RIF-H groups **(G)** VIP value for the serum between the vehicle and RIF-H groups **(H)** Score plots of PLS-DA of the serum between the vehicle and INH + RIF-L groups **(I)** Score plots of PLS-DA of the serum between the vehicle and RIF-L groups **(J)** Score plots of PLS-DA of the serum between the vehicle and RIF-H groups **(K)** Heatmap of BAs (VIP ≥ 1) in the liver **(L)** Heatmap of serum potential BAs biomarkers. Data are expressed as mean ± SD ($n = 5-8$).

RIF, administered alone or in combination with INH, significantly reduced the ratio of secondary to primary BAs in the liver and serum ($p < 0.01$ or 0.05), including DCA/CA, LCA/CDCA, and LCA + DCA/CDCA + CA (Figure 3).

3.3 Screening Targeted BAs for RIF-Induced Liver Injury in Mice

Targeted metabolomic analysis was performed to examine the changes in BA homeostasis using PLS-DA (Figure 4). The

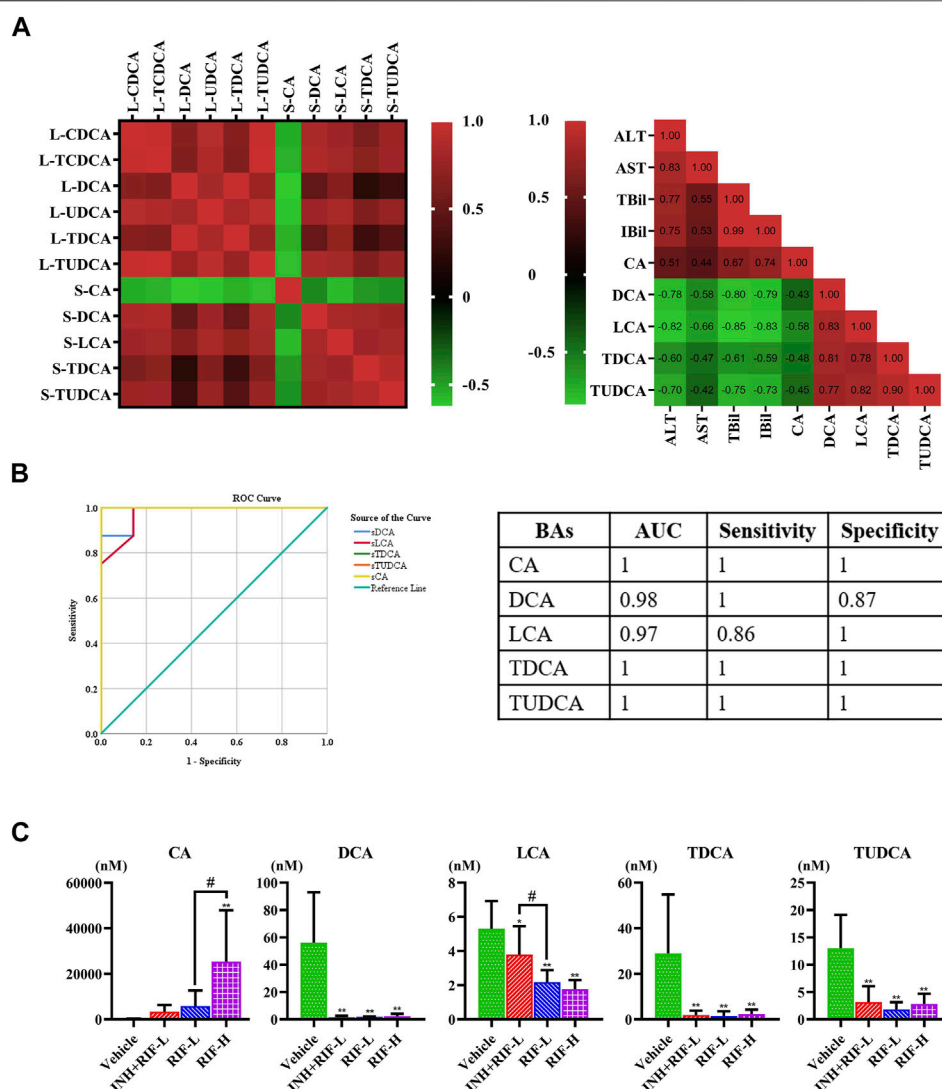
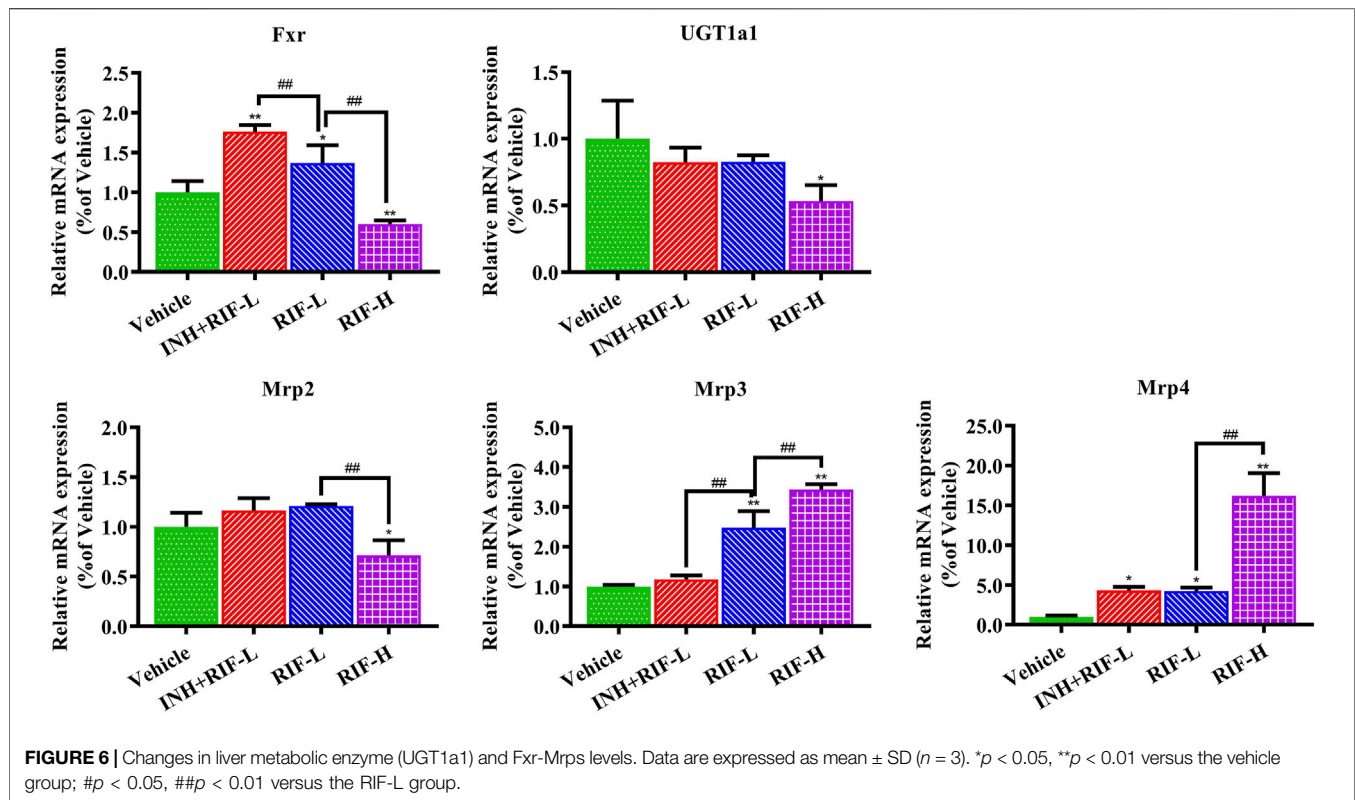


FIGURE 5 | Screening targeted serum BAs **(A)** Correlations between serum and liver BAs ($VIP \geq 1$) and between serum BAs and serum biochemical parameters, were analyzed using Spearman's correlation analysis ($n = 5-8$) **(B)** ROC curve for serum CA, DCA, LCA, TDCA, and TUDCA **(C)** Comparative analysis of alterations in the serum BA levels in mice. Data are expressed as mean \pm SD ($n = 5-8$). * $p < 0.05$, ** $p < 0.01$ versus the vehicle group; # $p < 0.05$, ## $p < 0.01$ versus the RIF-L group.

analysis revealed a distribution pattern in the four groups of mice. Scatter plots were clearly separated for the four groups in the liver (cumulative $R^2X = 80.2\%$, cumulative $R^2Y = 63.7\%$, cumulative $Q^2Y = 55.7\%$) and the serum BAs (cumulative $R^2X = 57.1\%$, cumulative $R^2Y = 45.2\%$, cumulative $Q^2Y = 37.3\%$). Targeted metabolomic analysis of BAs was performed between the vehicle and other groups. The explanatory ability (R^2X) of liver modeling consisting of the vehicle and INH + RIF-L groups, the vehicle and RIF-L groups, and the vehicle and RIF-H groups were 74.3, 66.5, and 89.1%, respectively; the stability of modeling (R^2Y) was 94.2, 94.5, and 99.4%, respectively; the predictability of modeling (Q^2Y) was 80.8, 90.8, and 97.5%, respectively. In parallel, in the serum, R^2X of modeling was 59.3, 62.2, and 61.1%; R^2Y was 82.3, 80.2, and 86.9%; and Q^2Y was 40, 54.1, and 73.2%, respectively.

BAs with $VIP \geq 1$ were UDCA, TUDCA, CDCA, TCDCA, TDCA, and DCA in the liver in the PLS-DA modeling consisting of the vehicle and RIF-H groups, and LCA, TUDCA, DCA, TDCA, and CA in the parallel serum modeling. The variable BAs with $VIP \geq 1$ were modeled for re-analysis, and the R^2X of the liver BA model between the vehicle and RIF-H groups improved to 92.4%. The serum R^2X level of the corresponding model was 82.3%. After re-analysis, the screening variables in models with $VIP \geq 1$ showed notable improvement in the explanatory ability, maintenance of high stability, and predictability.

Furthermore, the secondary BAs (DCA, LCA, TDCA, and TUDCA) were positively correlated with hepatic BAs ($VIP \geq 1$), such as CDCA, TCDCA, DCA, UDCA, TDCA, and TUDCA. The primary BA (CA) was inversely associated with hepatic BAs ($VIP \geq 1$). Pearson correlation analyses of BAs (CA, DCA, LCA, TDCA,



and TUDCA) and the levels of ALT, AST, TBil, and IBil were conducted. CA showed a significant positive correlation with the levels of ALT, AST, TBil, and IBil (the correlation coefficients were 0.51, 0.44, 0.67, and 0.74, respectively). Levels of DCA, LCA, TDCA, and TUDCA were inversely associated with those of ALT, AST, TBil, and IBil, especially DCA and LCA. Moreover, the ROC curve analysis was performed for serum DCA, LCA, TDCA, TUDCA, and CA levels to distinguish abnormal liver injury from normal healthy cases without any injury (Figure 5). The cut-off value for sensitivity and specificity were determined among the different BAs in the ROC curve analysis. Our findings suggest that all of the above BAs are good indicators of RIF-induced liver injury with high sensitivity and specificity.

3.4 Effects of RIF on Fxr, Mrps, and UGT1a1 Expression

Relative to the vehicle group, Fxr and Mrp4 messenger ribonucleic acid (mRNA) expressions increased in the INH + RIF-L and RIF-L groups, whereas that of Mrp3 was elevated in the RIF-L group. Fxr, Mrp2, and UGT1a1 mRNA expression levels notably decreased, whereas those of Mrp3 and Mrp4 increased in the RIF-H group in a dose-dependent manner (Figure 6).

4 DISCUSSION

DILI is the primary reason for poor drug approval rates and drug withdrawal; it is also the most common severe adverse reaction to

anti-TB therapy (Yang et al., 2020a). In a 14-days study on RIF dosing in mice, accumulation of lipids due to upregulation of peroxisome proliferator-activated receptor- γ was found to be the primary cause of RIF-induced toxicity at 177 mg/kg (LD₁₀, equivalent to approximately 20 mg/kg in humans), while 442.5 mg/kg RIF caused another type of unspecified liver damage (LD₂₅, equivalent to approximately 50 mg/kg in humans) (Kim et al., 2017). Thus, it is necessary to further investigate the pathogenesis at the early stages of liver injury caused by RIF at 442.5 mg/kg. On the other hand, previous studies indicated that the long-term administration of low-dose RIF in combination with INH was more likely to aggravate the occurrence of drug-induced liver injury than RIF alone (Devarbhavi et al., 2021). The underlying mechanisms of DILI caused by RIF or INH + RIF *via* LC-MS/MS-based targeted metabolomics approach had not been previously reported. As shown in Figure 2, our findings suggested that RIF aggravated BA metabolism disorders, thereby causing liver injury. The leading cause was intrahepatic cholestasis for RIF-L and INH + RIF-L, but extrahepatic cholestasis for RIF-H. Moreover, targeted metabolomic analysis of BAs and screening of biomarkers for liver injury showed that transportation of BAs, mediated by Fxr-Mrps, was closely related to RIF-induced liver injury.

Hepatic cholesterol is converted into CA and CDCA in classical and alternative metabolic pathways and then amidated with taurine or glycine. The conjugation with taurine and glycine lowers pKa and increases solubility to facilitate easier efflux into bile (Fiorucci et al., 2021).

Monoanionic bile salts are secreted into the bile duct by the bile salt export pump, and dianionic bile salts; phase II-conjugated BAs are secreted into bile by Mrp2 (Meier and Stieger, 2002; Morgan et al., 2013). Under normal conditions, Mrp3 and Mrp4 are expressed in the basolateral membranes (Köck et al., 2014; Song et al., 2016). Mrp3 mediates the efflux of BAs, except for glutathione-conjugated BAs, from the basolateral membrane into the blood, while Mrp4 transports different types of BAs into the blood and plays a more critical role than Mrp3 (Jetter and Kullak-Ublick, 2020). Additionally, when primary BAs enter the terminal ileum through the bile duct, 95% of intestinal BAs are reabsorbed and transported back to the liver *via* the hepatic portal vein. Conjugated BAs are deamidated into free BAs in the intestine by bile salt hydrolase, expressed by *Bacteroides*, *Lactobacillus*, *Bifidobacterium*, and *Clostridium*. This is followed by transformation into secondary BAs (DCA, LCA, or UDCA) with 7 α dehydrogenase, from *Clostridium* and *Eubacteria*, acting as the catalyst (Fiorucci et al., 2021).

Intrahepatic cholestasis might be observed in the RIF-L and INH + RIF-L groups, with significant elevation in the levels of primary BAs, including CA, CDCA, TCA, and TCDCA (Figure 3). Consistent with these results, Kim et al. (Kim et al., 2017) reported that RIF-induced hepatotoxicity did not significantly increase ALP level, indicating a type of mixed liver injury *via* cholestasis and hepatocellular injury. In our study, RIF-induced liver injury was evaluated by measuring ALT, AST, bilirubin changes and H&E staining according to relevant studies (Lin et al., 2019; Fan et al., 2019; Yang et al., 2020c; Yan et al., 2021). We did not measure or quantify CK19 + bile duct mass or ALP levels to analyze hepatotoxicity caused by biliary duct dilatation, which is a limitation in the present study. As shown in Figure 2, the hepatic cord and central vein arrangements were similar in the vehicle, RIF-L, and INH + RIF-L groups, except for slight nuclear disappearance and partial vacuoles. The degree of liver tissue injury in the INH + RIF-L group was slightly higher than that in the RIF-L group; however, the ALT and AST levels showed no significant changes. We speculated that these changes in BAs could reflect the early responses to liver injury better than the changes in liver enzymes, consistent with the results of a previous study (Slopianka et al., 2017). In addition, mild liver injury in the INH + RIF-L and RIF-L groups could be attributed to activation of the Fxr signaling pathway, which causes elevation of CA, CDCA, TCA, and TCDCA levels. The upregulation of Mrp4 expression in the INH + RIF-L group facilitated the BA efflux into the blood, whereas increased expression of Mrp3 and Mrp4 in the RIF-L group synergistically promoted the transport of BAs, resulting in lesser damage to the liver relative to the INH + RIF-L group.

Previous studies report that RIF inhibits the expression of UGT1a1 and the UGT1a1-related phase II metabolic pathway, which reduces the excretion of toxic components of RIF through Mrp2, and increases the risk of DILI (Cao et al., 2017). Additionally, our results showed that Fxr and Mrps mRNA expressions were significantly changed, a possible reason why the reduction in BA levels inhibited Fxr mRNA expression, in turn reducing those of Mrp2 and UGT1a1 and inducing a significant compensatory increase in Mrp3 and Mrp4 mRNA expression (Xu et al., 2005; Vanwijngaerden et al., 2011; Carino

et al., 2020; Jetter and Kullak-Ublick, 2020). CA is a hydrophobic BA that induces hepatocyte death and cholestatic liver injury in mice (Wei et al., 2020). Previous studies demonstrate that the CA levels in patients with end-stage chronic cholestatic liver injury are substantially elevated (Fischer et al., 1996; Fu et al., 2022). Slopianka M et al. suggest that serum CA, CDCA, DCA, beta muricholic acid, and UDCA levels may serve as new DILI biomarkers (Slopianka et al., 2017). It is also believed that serum CA, TCA, and GCA can be DILI biomarkers with higher specificity relative to standard biomarkers, such as ALT (Luo et al., 2014). On establishing the PLS-DA model of BAs, in the vehicle and RIF-H groups, we found significant decreases in the levels of serum biomarkers (DCA, LCA, TDCA, TUDCA) which were positively correlated with liver BAs (CDCA, TCDCA, DCA, UDCA, TDCA, and TUDCA). We speculated that the significant decreases in the levels of secondary BAs and the ratio of secondary to primary BA levels could be attributed to the considerable induction of *Bacteroides* and reduction in *Clostridium* and *Eubacter* abundance (Namasivayam et al., 2017; Khan et al., 2019). RIF administration suppressed the biotransformation of 7 α dehydrogenase-mediated dehydroxylation and intestinal bile salt hydrolase production, thereby reducing the biotransformation of CA and CDCA into DCA and LCA, respectively (Fiorucci et al., 2021). Interestingly, significantly elevated serum primary BA (CA) levels negatively correlated with those of liver BAs. Consistent with previous research, the elevation of serum CA levels may be related to increased intrahepatic CA efflux into the blood *via* Mrp3 and Mrp4 (Matye et al., 2021). In addition, the reduced secondary BA generation led to lower levels of CA and other BAs in the RIF-H group relative to those in the vehicle group. Disruption of liver BA and blood BA homeostasis results in liver injury. ROC curves for serum CA, DCA, LCA, TDCA, and TUDCA were highly sensitive, specific, and strongly correlated with ALT and AST, suggesting a particular value indicating RIF-induced DILI. Our study provided further insights into the pathogenesis of RIF-induced liver injury and a theoretical basis for DILI prevention and rational clinical application in anti-TB therapy.

In addition, it has been reported that the activation of Fxr can inhibit the nuclear receptor nuclear factor- κ B (NF- κ B) signaling pathway, inhibiting the expression of inflammatory factors tumor necrosis factor- α , interleukin-1 β , and interleukin-6, which play an anti-inflammatory role (Wang et al., 2008; Ming et al., 2021). Wang and others (Wang et al., 2008) also described negative crosstalk between the FXR and NF- κ B signaling pathways in the hepatic inflammatory response. However, Yu et al. found that GW4064 can activate the Fxr signaling pathway and the NF- κ B signaling pathway in normal human gastric epithelial cells (Yu et al., 2019). Consistent with these results, Lee et al. (Lee et al., 2011) reported that downregulation of FXR in pancreatic carcinoma cells decreases NF- κ B activity and consequently inhibits its target genes, indicating that NF- κ B may participate in the regulation of FXR activity (Gadaleta et al., 2011), involving a positive crosstalk mechanism. In summary, the mechanisms between Fxr regulation of BA metabolism, anti-inflammatory and NF- κ B causing inflammatory damage are complex and remain unclear. Further researches are required to explore and verify in the future.

5 CONCLUSION

Exposure to different doses of RIF induces various types of liver injury. RIF-H treatment might lead to extrahepatic cholestasis, with significantly elevated serum CA levels. In this study, CA, DCA, LCA, TDCA, and TUDCA were identified as potential biomarkers for the early detection of RIF-induced liver injury, reflecting initial responses to and the severity of the liver injury. The hepatic toxicity mechanisms of RIF may be related to the liver metabolic enzymes (UGT1a1) and BA transporters, including Mrp2, Mrp3, and Mrp4.

DATA AVAILABILITY STATEMENT

The original contributions presented in the study are included in the article/**Supplementary Materials**, further inquiries can be directed to the corresponding author.

ETHICS STATEMENT

The animal study was reviewed and approved by the Animal Ethics Review Committee of Hunan Academy of Traditional Chinese Medicine.

REFERENCES

- Abulfathi, A. A., Decloedt, E. H., Svensson, E. M., Diacon, A. H., Donald, P., and Reuter, H. (2019). Clinical Pharmacokinetics and Pharmacodynamics of Rifampicin in Human Tuberculosis. *Clin. Pharmacokinet.* 58, 1103–1129. doi:10.1007/s40262-019-00764-2
- Ali, I., Welch, M. A., Lu, Y., Swaan, P. W., and Brouwer, K. L. R. (2017). Identification of Novel MRP3 Inhibitors Based on Computational Models and Validation Using an *In Vitro* Membrane Vesicle Assay. *Eur. J. Pharm. Sci.* 103, 52–59. doi:10.1016/j.ejps.2017.02.011
- Ambros-Rudolph, C. M., Glatz, M., Trauner, M., Kerl, H., and Müllegger, R. R. (2007). The Importance of Serum Bile Acid Level Analysis and Treatment with Ursodeoxycholic Acid in Intrahepatic Cholestasis of Pregnancy: a Case Series from Central Europe. *Arch. Dermatol.* 143 (6), 757–762. doi:10.1001/archderm.143.6.757
- Boeree, M. J., Diacon, A. H., Dawson, R., Narunsky, K., du Bois, J., Venter, A., et al. (2015). A Dose-Ranging Trial to Optimize the Dose of Rifampin in the Treatment of Tuberculosis. *Am. J. Respir. Crit. Care Med.* 191, 1058–1065. doi:10.1164/rccm.201407-1264OC
- Cao, L., Greenblatt, D. J., and Kwara, A. (2017). Inhibitory Effects of Selected Antituberculosis Drugs on Common Human Hepatic Cytochrome P450 and UDP-Glucuronosyltransferase Enzymes. *Drug Metab. Dispos.* 45, 1035–1043. doi:10.1124/dmd.117.076034
- Carino, A., Biagioli, M., Marchianò, S., Fiorucci, C., Bordoni, M., Roselli, R., et al. (2020). Opposite Effects of the FXR Agonist Obeticholic Acid on Mafg and Nrf2 Mediate the Development of Acute Liver Injury in Rodent Models of Cholestasis. *Biochim. Biophys. Acta Mol. Cell Biol. Lipids.* 1865, 158733. doi:10.1016/j.bbalip.2020.158733
- Chiang, J. Y. L., and Ferrell, J. M. (2020). Bile Acid Receptors FXR and TGR5 Signaling in Fatty Liver Diseases and Therapy. *Am. J. Physiol. Gastrointest. Liver Physiol.* 318, G554–G573. doi:10.1152/ajpgi.00223.2019
- Choudhuri, S., and Klaassen, C. D. (2022). Molecular Regulation of Bile Acid Homeostasis. *Drug Metab. Dispos.* 50 (4), 425–455. doi:10.1124/dmd.121.000643
- Crosignani, A., Del Puppo, M., Longo, M., De Fabiani, E., Caruso, D., Zuin, M., et al. (2007). Changes in Classic and Alternative Pathways of Bile Acid Synthesis

AUTHOR CONTRIBUTIONS

YD, XLuo, and XL conceived and designed the animal experiments. YD and XLuo conducted the statistical analysis and wrote the manuscript. XL, YX, BX, and HT were responsible for reviewing the manuscript draft. YD, XLuo, and XL are responsible for the second check. All authors assume accountability for the content in the manuscript.

FUNDING

This work was supported by the grants from the Natural Science Foundation of Hunan, China (2019JJ50680); the Clinical Pharmacy Project of Medical Research Fund of Hunan Medical Association, China (HMA202001009).

SUPPLEMENTARY MATERIAL

The Supplementary Material for this article can be found online at: <https://www.frontiersin.org/articles/10.3389/fphar.2022.925509/full#supplementary-material>

- in Chronic Liver Disease. *Clin. Chim. Acta* 382 (1–2), 82–88. doi:10.1016/j.cca.2007.03.025
- Cuperus, F. J., Claudel, T., Gautherot, J., Halilbasic, E., and Trauner, M. (2014). The Role of Canalicular ABC Transporters in Cholestasis. *Drug Metab. Dispos.* 42 (4), 546–560. doi:10.1124/dmd.113.056358
- Devarbhavi, H., Aithal, G., Treeprasertsuk, S., Takikawa, H., Mao, Y., Shasthry, S. M., et al. (2021). Drug-induced Liver Injury: Asia Pacific Association of Study of Liver Consensus Guidelines. *Hepatol. Int.* 15 (2), 258–282. doi:10.1007/s12072-021-10144-3
- Dong, Q., Li, N., Li, Q., Zhang, C. E., Feng, W. W., Li, G. Q., et al. (2015). Screening for Biomarkers of Liver Injury Induced by Polygonum Multiflorum: a Targeted Metabolomic Study. *Front. Pharmacol.* 6, 217. doi:10.3389/fphar.2015.00217
- Fan, S., Liu, C., Jiang, Y., Gao, Y., Chen, Y., Fu, K., et al. (2019). Lignans from Schisandra Sphenanthera Protect against Lithocholic Acid-Induced Cholestasis by Pregnane X Receptor Activation in Mice. *J. Ethnopharmacol.* 245, 112103. doi:10.1016/j.jep.2019.112103
- Fiorucci, S., Distrutti, E., Carino, A., Zampella, A., and Biagioli, M. (2021). Bile Acids and Their Receptors in Metabolic Disorders. *Prog. Lipid Res.* 82, 101094. doi:10.1016/j.plipres.2021.101094
- Fischer, S., Beuers, U., Spengler, U., Zwiebel, F. M., and Koebe, H. G. (1996). Hepatic Levels of Bile Acids in End-Stage Chronic Cholestatic Liver Disease. *Clin. Chim. Acta.* 251, 173–186. doi:10.1016/0009-8981(96)06305-x
- Fu, K. L., Chen, P., Zhou, Y. Y., Jiang, Y. M., Gao, Y., Zhang, H. Z., et al. (2022). Hepatic Vps33b Deficiency Aggravates Cholic Acid-Induced Cholestatic Liver Injury in Male Mice. *Acta Pharmacol. Sin.* 43, 933–940. doi:10.1038/s41401-021-00723-3
- Gadaleta, R. M., Oldenburg, B., Willemsen, E. C., Spit, M., Murzilli, S., Salvatore, L., et al. (2011). Activation of Bile Salt Nuclear Receptor FXR Is Repressed by Pro-inflammatory Cytokines Activating NF-Kb Signaling in the Intestine. *Biochim. Biophys. Acta* 1812 (8), 851–858. doi:10.1016/j.bbdis.2011.04.005
- Gottlieb, A., and Canbay, A. (2019). Why Bile Acids Are So Important in Non-alcoholic Fatty Liver Disease (NAFLD) Progression. *Cells* 8, 1358. doi:10.3390/cells8111358
- Grobbelaar, M., Louw, G. E., Sampson, S. L., van Helden, P. D., Donald, P. R., and Warren, R. M. (2019). Evolution of Rifampicin Treatment for Tuberculosis. *Infect. Genet. Evol.* 74, 103937. doi:10.1016/j.meegid.2019.103937

- Gromski, P. S., Muhamadali, H., Ellis, D. I., Xu, Y., Correa, E., Turner, M. L., et al. (2015). A Tutorial Review: Metabolomics and Partial Least Squares-Discriminant Analysis-Aa Marriage of Convenience or a Shotgun Wedding. *Anal. Chim. Acta* 879, 10–23. doi:10.1016/j.aca.2015.02.012
- Hurlock, B., and Talalay, P. (1957). Principles of the Enzymatic Measurement of Steroids. *J. Biol. Chem.* 227 (1), 37–52. doi:10.1016/s0021-9258(18)70793-x
- Jetter, A., and Kullak-Ublick, G. A. (2020). Drugs and Hepatic Transporters: A Review. *Pharmacol. Res.* 154, 104234. doi:10.1016/j.phrs.2019.04.018
- Keitel, V., Dröge, C., and Häussinger, D. (2019). Targeting FXR in Cholestasis. *Handb. Exp. Pharmacol.* 256, 299–324. doi:10.1007/164_2019_231
- Khan, N., Mendonca, L., Dhariwal, A., Fontes, G., Menzies, D., Xia, J., et al. (2019). Intestinal Dysbiosis Compromises Alveolar Macrophage Immunity to *Mycobacterium tuberculosis*. *Mucosal Immunol.* 12, 772–783. doi:10.1038/s41385-019-0147-3
- Kim, J. H., Nam, W. S., Kim, S. J., Kwon, O. K., Seung, E. J., Jo, J. J., et al. (2017). Mechanism Investigation of Rifampicin-Induced Liver Injury Using Comparative Toxicoproteomics in Mice. *Int. J. Mol. Sci.* 18, 1417. doi:10.3390/ijms18071417
- Köck, K., Ferslew, B. C., Netterberg, L., Yang, K., Urban, T. J., Swaan, P. W., et al. (2014). Risk Factors for Development of Cholestatic Drug-Induced Liver Injury: Inhibition of Hepatic Basolateral Bile Acid Transporters Multidrug Resistance-Associated Proteins 3 and 4. *Drug Metab. Dispos.* 42, 665–674. doi:10.1124/dmd.113.054304
- Lange, C., Kalsdorf, B., Maurer, F. P., and Heyckendorf, J. (2019). Tuberkulose. *Internist (Berl.)* 60, 1155–1175. doi:10.1007/s00108-019-00685-z
- Lee, J. Y., Lee, K. T., Lee, J. K., Lee, K. H., Jang, K. T., Heo, J. S., et al. (2011). Farnesoid X Receptor, Overexpressed in Pancreatic Cancer with Lymph Node Metastasis Promotes Cell Migration and Invasion. *Br. J. Cancer* 104 (6), 1027–1037. doi:10.1038/bjc.2011.37
- Lee, L. C., Liong, C. Y., and Jemain, A. A. (2018). Partial Least Squares-Discriminant Analysis (PLS-DA) for Classification of High-Dimensional (HD) Data: a Review of Contemporary Practice Strategies and Knowledge Gaps. *Analyst* 143 (15), 3526–3539. doi:10.1039/c8an00599k
- Lin, H., Zhou, C., Hou, Y., Li, Q., Qiao, G., Wang, Y., et al. (2019). Paracrine Fibroblast Growth Factor 1 Functions as Potent Therapeutic Agent for Intrahepatic Cholestasis by Downregulating Synthesis of Bile Acid. *Front. Pharmacol.* 10, 1515. doi:10.3389/fphar.2019.01515
- Luo, L., Aubrecht, J., Li, D., Warner, R. L., Johnson, K. J., Kenny, J., et al. (2018). Assessment of Serum Bile Acid Profiles as Biomarkers of Liver Injury and Liver Disease in Humans. *PLOS ONE* 13, e0193824. doi:10.1371/journal.pone.0193824
- Luo, L., Schomaker, S., Houle, C., Aubrecht, J., and Colangelo, J. L. (2014). Evaluation of Serum Bile Acid Profiles as Biomarkers of Liver Injury in Rodents. *Toxicol. Sci.* 137, 12–25. doi:10.1093/toxsci/kft221
- Luo, X. L., Qin, L., Li, X., Xu, B., Deng, Y., and Tong, H. (2021). Research Progress in Toxicological Mechanisms of Rifampicin-Induced Liver Injury and Detoxification Mechanisms of Chinese Herbal Medicine. *Chin. J. Mod. Appl. Pharm.* 38, 1125–1132. doi:10.13748/j.cnki.issn1007-7693.2021.09.020
- Luo, X. L., Qing, D., Deng, Y., Xu, B., Li, X., and Wang, Y. Y. (2020). Establishment of Rifampicin-Induced Liver Injury Model in Mice and Evaluation of Nephrotoxicity. *Chin. J. Clin. Pharmacol.* 36, 1488–1491. doi:10.13699/j.cnki.1001-6821.2020.11.023
- Matye, D. J., Li, Y., Chen, C., Chao, X., Wang, H., Ni, H., et al. (2021). Gut-restricted Apical Sodium-dependent Bile Acid Transporter Inhibitor Attenuates Alcohol-Induced Liver Steatosis and Injury in Mice. *Alcohol. Clin. Exp. Res.* 45, 1188–1199. doi:10.1111/acer.14619
- McGill, M. R., and Jaeschke, H. (2019). Biomarkers of Drug-Induced Liver Injury. *Adv. Pharmacol.* 85, 221–239. doi:10.1016/b.s.apha.2019.02.001
- Meier, P. J., and Steiger, B. (2002). Bile Salt Transporters. *Annu. Rev. Physiol.* 64, 635–661. doi:10.1146/annurev.physiol.64.082201.100300
- Ming, J., Xu, Q., Gao, L., Deng, Y., Yin, J., Zhou, Q., et al. (2021). Kinsenoside Alleviates 17 α -Ethinylestradiol-Induced Cholestatic Liver Injury in Rats by Inhibiting Inflammatory Responses and Regulating FXR-Mediated Bile Acid Homeostasis. *Pharm. (Basel)* 14 (5), 452. doi:10.3390/ph14050452
- Morgan, R. E., van Staden, C. J., Chen, Y., Kalyanaraman, N., Kalanzi, J., Dunn, R. T., 2nd, et al. (2013). A Multifactorial Approach to Hepatobiliary Transporter Assessment Enables Improved Therapeutic Compound Development. *Toxicol. Sci.* 136, 216–241. doi:10.1093/toxsci/kft176
- Moussavian, M. R., Laschke, M. W., Schlachtenberger, G., von Heesen, M., Wagner, M., Glanemann, M., et al. (2016). Perigraft Vascularization and Incorporation of Implanted Dacron Prostheses Are Affected by Rifampicin Coating. *J. Vasc. Surg.* 64, 1815–1824. doi:10.1016/j.jvs.2015.07.104
- Namasivayam, S., Maiga, M., Yuan, W., Thovara, V., Costa, D. L., Mittereder, L. R., et al. (2017). Longitudinal Profiling Reveals a Persistent Intestinal Dysbiosis Triggered by Conventional Anti-tuberculosis Therapy. *Microbiome* 5, 71. doi:10.1186/s40168-017-0286-2
- Sanoh, S., Tamura, Y., Fujino, C., Sugahara, G., Yoshizane, Y., Yanagi, A., et al. (2019). Changes in Bile Acid Concentrations after Administration of Ketoconazole or Rifampicin to Chimeric Mice with Humanized Liver. *Biol. Pharm. Bull.* 42, 1366–1375. doi:10.1248/bpb.b19-00249
- Slopianka, M., Herrmann, A., Pavkovic, M., Ellinger-Ziegelbauer, H., Ernst, R., Mally, A., et al. (2017). Quantitative Targeted Bile Acid Profiling as New Markers for DILI in a Model of Methapyriline-Induced Liver Injury in Rats. *Toxicology* 386, 1–10. doi:10.1016/j.tox.2017.05.009
- Song, Y. N., Zhang, G. B., Lu, Y. Y., Chen, Q. L., Yang, L., Wang, Z. T., et al. (2016). Huangqi Decoction Alleviates Dimethylnitrosamine-Induced Liver Fibrosis: An Analysis of Bile Acids Metabolic Mechanism. *J. Ethnopharmacol.* 189, 148–156. doi:10.1016/j.jep.2016.05.040
- Te Brake, L. H. M., de Jager, V., Narunsky, K., Vanker, N., Svensson, E. M., Phillips, P. P. J., et al. (2021). Increased Bactericidal Activity but Dose-Limiting Intolerability at 50 Mg·kg⁻¹ Rifampicin. *Eur. Respir. J.* 58, 2000955. doi:10.1183/13993003.00955-2020
- Tian, M., Yan, J., Zhang, H., Wei, Y., Zhang, M., Rao, Z., et al. (2022). Screening and Validation of Biomarkers for Cadmium-Induced Liver Injury Based on Targeted Bile Acid Metabolomics. *Environ. Pollut.* 300, 118837. doi:10.1016/j.envpol.2022.118837
- Vanwijngaerden, Y. M., Wauters, J., Langouche, L., Vander Perre, S., Liddle, C., Coulter, S., et al. (2011). Critical Illness Evokes Elevated Circulating Bile Acids Related to Altered Hepatic Transporter and Nuclear Receptor Expression. *Hepatology* 54, 1741–1752. doi:10.1002/hep.24582
- Wang, Y. D., Chen, W. D., Wang, M., Yu, D., Forman, B. M., and Huang, W. (2008). Farnesoid X Receptor Antagonizes Nuclear Factor kappaB in Hepatic Inflammatory Response. *Hepatology* 48 (5), 1632–1643. doi:10.1002/hep.22519
- Wei, S., Ma, X., and Zhao, Y. (2020). Mechanism of Hydrophobic Bile Acid-Induced Hepatocyte Injury and Drug Discovery. *Front. Pharmacol.* 11, 1084. doi:10.3389/fphar.2020.01084
- World Health Organization (2021). Global Tuberculosis Report 2021. Available at: <https://www.who.int/publications/i/item/9789240037021> (Accessed April 20, 2022).
- Xu, C., Li, C. Y., and Kong, A. N. (2005). Induction of Phase I, II and III Drug Metabolism/transport by Xenobiotics. *Arch. Pharm. Res.* 28, 249–268. doi:10.1007/BF02977789
- Yan, M., Guo, L., Yang, Y., Zhang, B., Hou, Z., Gao, Y., et al. (2021). Glycyrrhetic Acid Protects α -Naphthylisothiocyanate-Induced Cholestasis through Regulating Transporters, Inflammation and Apoptosis. *Front. Pharmacol.* 12, 701240. doi:10.3389/fphar.2021.701240
- Yang, J., Peng, T., Huang, J., Zhang, G., Xia, J., Ma, M., et al. (2020a). Effects of Medium- and Long-Chain Fatty Acids on Acetaminophen- or Rifampicin-Induced Hepatocellular Injury. *Food Sci. Nutr.* 8, 3590–3601. doi:10.1002/fsn3.1641
- Yang, J., Xiang, D., Xiang, D., He, W., Liu, Y., Lan, L., et al. (2020b). Baicalin Protects against 17 α -Ethinylestradiol-Induced Cholestasis via the Sirtuin 1/ Hepatic Nuclear Receptor-1 α /Farnesoid X Receptor Pathway. *Front. Pharmacol.* 10, 1685. doi:10.3389/fphar.2019.01685
- Yang, T., Shu, T., Liu, G., Mei, H., Zhu, X., Huang, X., et al. (2017). Quantitative Profiling of 19 Bile Acids in Rat Plasma, Liver, Bile and Different Intestinal Section Contents to Investigate Bile Acid Homeostasis and the Application of Temporal Variation of Endogenous Bile Acids. *J. Steroid Biochem. Mol. Biol.* 172, 69–78. doi:10.1016/j.jsmb.2017.05.015
- Yang, Y., Liu, L., Zhang, X., Jiang, X., and Wang, L. (2020c). Tanshinone IIA Prevents Rifampicin-Induced Liver Injury by Regulating BSEP/NTCP Expression via Epigenetic Activation of NRF2. *Liver Int.* 40 (1), 141–154. doi:10.1111/liv.14262
- Yu, J. H., Zheng, J. B., Qi, J., Yang, K., Wu, Y. H., Wang, K., et al. (2019). Bile Acids Promote Gastric Intestinal Metaplasia by Upregulating CDX2 and MUC2

- Expression via the FXR/NF- κ B Signalling Pathway. *Int. J. Oncol.* 54 (3), 879–892. doi:10.3892/ijo.2019.4692
- Yuan, Z., Wang, G., Qu, J., Wang, X., and Li, K. (2018). 9-cis-retinoic Acid Elevates MRP3 Expression by Inhibiting Sumoylation of RXR α to Alleviate Cholestatic Liver Injury. *Biochem. Biophys. Res. Commun.* 503, 188–194. doi:10.1016/j.bbrc.2018.06.001
- Zhang, W., Chen, L., Feng, H., Wang, W., Cai, Y., Qi, F., et al. (2017). Rifampicin-induced Injury in HepG2 Cells Is Alleviated by TUDCA via Increasing Bile Acid Transporters Expression and Enhancing the Nrf2-Mediated Adaptive Response. *Free Radic. Biol. Med.* 112, 24–35. doi:10.1016/j.freeradbiomed.2017.07.003
- Zhao, D. S., Jiang, L. L., Fan, Y. X., Dong, L. C., Ma, J., Dong, X., et al. (2017). Identification of Urine Tauro- β -Muricholic Acid as a Promising Biomarker in Polygoni Multiflori Radix-Induced Hepatotoxicity by Targeted Metabolomics of Bile Acids. *Food Chem. Toxicol.* 108 (Pt B), 532–542. doi:10.1016/j.fct.2017.02.030

Conflict of Interest: The authors declare that the research was conducted in the absence of any commercial or financial relationships that could be construed as a potential conflict of interest.

Publisher's Note: All claims expressed in this article are solely those of the authors and do not necessarily represent those of their affiliated organizations, or those of the publisher, the editors and the reviewers. Any product that may be evaluated in this article, or claim that may be made by its manufacturer, is not guaranteed or endorsed by the publisher.

Copyright © 2022 Deng, Luo, Li, Xiao, Xu and Tong. This is an open-access article distributed under the terms of the Creative Commons Attribution License (CC BY). The use, distribution or reproduction in other forums is permitted, provided the original author(s) and the copyright owner(s) are credited and that the original publication in this journal is cited, in accordance with accepted academic practice. No use, distribution or reproduction is permitted which does not comply with these terms.

GLOSSARY

ALT alanine aminotransferase

AST aspartate aminotransferase

ALP alkaline phosphatase

ALT alanine aminotransferase

mRNA messenger ribonucleic acid

RNA ribonucleic acid

RIF rifampicin

BA bile acid

Fxr farnesoid x receptor

Mrp multidrug resistance-associated protein

UGT uridine diphosphate-glucuronosyltransferase

TB Tuberculosis

DILI drug-induced liver injury

CA cholic acid

CDCA chenodeoxycholic acid

DCA deoxycholic acid

LCA lithocholic acid

UDCA ursodeoxycholic acid

HDCA hyodeoxycholic acid

TCA taurocholic acid

TCDCA taurochenodeoxycholic acid

TDCA taurodeoxycholic acid

TLCA tauroolithocholic acid

TUDCA tauroursodeoxycholic acid

THDCA taurohyodeoxycholic acid

GCA glycocholic acid

GCDCA glycochenodeoxycholic acid

GDCA glycodeoxycholic acid

GUDCA Glycoursodeoxycholic acid

TBil total bilirubin

IBil indirect bilirubin

LC-MS/MS liquid chromatography-tandem mass spectrometry

IS internal standard; PCR, polymerase chain reaction

PLS-DA partial least squares discriminant analysis

VIP variable importance value

ROC receiver operating characteristic

NF-κB nuclear factor-κB



UPLC-MS/MS Technology for the Quantitative Methodology and Pharmacokinetic Analysis of Voxtalisib in Rat Plasma

Qingqing Li^{1,2}, Ya-nan Liu^{1,2}, Jing Wang^{1,2}, Yingying Hu¹, Jinyu Hu¹, Ren-ai Xu¹, Liu Shao^{3*} and Lianguo Chen^{1*}

¹The First Affiliated Hospital of Wenzhou Medical University, Wenzhou, China, ²Institute of Molecular Toxicology and Pharmacology, School of Pharmaceutical Sciences, Wenzhou Medical University, Wenzhou, China, ³Chongqing University Cancer Hospital, Chongqing, China

OPEN ACCESS

Edited by:

Grover Paul Miller,
University of Arkansas for Medical
Sciences, United States

Reviewed by:

Dustyn Barnette,
National Center for Toxicological
Research (FDA), United States
Zhixia Qiu,
China Pharmaceutical University,
China

*Correspondence:

Liu Shao
1041863198@qq.com
Lianguo Chen
lianguochen@126.com

Specialty section:

This article was submitted to
Drug Metabolism and Transport,
a section of the journal
Frontiers in Pharmacology

Received: 07 April 2022

Accepted: 30 May 2022

Published: 14 June 2022

Citation:

Li Q, Liu Y-n, Wang J, Hu Y, Hu J,
Xu R-a, Shao L and Chen L (2022)
UPLC-MS/MS Technology for the
Quantitative Methodology and
Pharmacokinetic Analysis of Voxtalisib
in Rat Plasma.
Front. Pharmacol. 13:914733.
doi: 10.3389/fphar.2022.914733

Voxtalisib, is a specific, effective, and reversible dual inhibitor, which inhibits both pan-class I phosphoinositide 3-kinase (PI3K) and mechanistic target of rapamycin (mTOR). To date, vixtalisib has been studied in trials for melanoma, lymphoma, glioblastoma, breast cancer, and other cancers. In this study, a highly sensitive and rapid ultra-performance liquid chromatography tandem mass spectrometry (UPLC-MS/MS) technology was applied to the quantitative methodology and pharmacokinetic analysis of vixtalisib in rat plasma. After protein precipitation of the analyte by acetonitrile, the chromatographic separation was performed by gradient elution on an Acquity BEH C18 column (2.1 mm × 50 mm, 1.7 μm) with acetonitrile (solvent A) and 0.1% formic acid (solvent B) as the mobile phase. In the positive ion mode, the mass transfer detection of the analyte and IS was m/z 270.91 > 242.98 and m/z 572.30 > 246.10, respectively. In the concentration range of 1–2000 ng/ml, a good linear relationship of vixtalisib was successfully established by the UPLC-MS/MS technology, and the lower limit of quantification (LLOQ) of the analyte was identified as 1 ng/ml. Intra-day and inter-day precisions for vixtalisib were 7.5–18.7% and 13.0–16.6%, respectively, and the accuracies were in the ranges of –14.0–2.0% and –7.2–3.1%, respectively. The matrix effect, extraction recovery, carryover and stability of the analyte were all in compliance with the acceptance criteria of bioassays recommended by FDA. Finally, the pharmacokinetic profile of the analyte had been available studied by the UPLC-MS/MS bio-analytical method after rats were treated by intragastric administration with vixtalisib (5 mg/kg). The results indicated that the UPLC-MS/MS technology can effectively and quickly quantify the analyte, and this method can also be used for the pharmacokinetic study of vixtalisib, which can provide reference for the optimization of clinical drug management in the later period.

Keywords: vixtalisib, quantitative methodology, pharmacokinetic analysis, UPLC-MS/MS technology, rat plasma

INTRODUCTION

Voxtalisisib (**Figure 1A**), also called as SAR245409 or XL765, is a dual inhibitor that inhibits both pan-class I phosphoinositide 3-kinase (PI3K) and mechanistic target of rapamycin (mTOR) by competitively binding specific adenosine triphosphate (ATP) to the catalytic domain of PI3K and mTOR (Janne et al., 2014; He et al., 2018). Voxtalisisib plays an anti-tumor role mainly by inhibiting the formation of tumor blood vessels and inducing apoptosis of cancer cells, and its anti-tumor activity has been proved (Markman et al., 2010; Prasad et al., 2011; Zhao et al., 2019). Voxtalisisib achieved its therapeutic effect by apoptotic caspase-dependent primary chronic lymphocytic leukemia cells with a half-maximum inhibitory concentration (IC_{50}) of 0.86 μ M and a maximum duration of action of 48 h. In addition, voxtalisisib blocked the adhesion, proliferation, and *in vitro* survival of chronic lymphocytic leukemia cells and effectively inhibits T-cell-mediated cytokines that support the production of chronic lymphocytic leukemia (Thijssen et al., 2016; Brown et al., 2018; Zhang et al., 2018). As pharmacokinetic information is essential for the optimization of clinical administration, it is necessary to quantify and monitor the plasma concentration of voxtalisisib.

Therefore, in this experiment, we intended to measure the concentration of voxtalisisib in rat plasma by using a high-efficiency UPLC-MS/MS technology. Then, we demonstrated the robustness of our method by measuring the linearity, carryover, precision and accuracy, matrix effect and extraction recovery, and stability of the analyte. Subsequently, the pharmacokinetic studies of voxtalisisib in rat plasma confirmed the specificity and repeatability of this method.

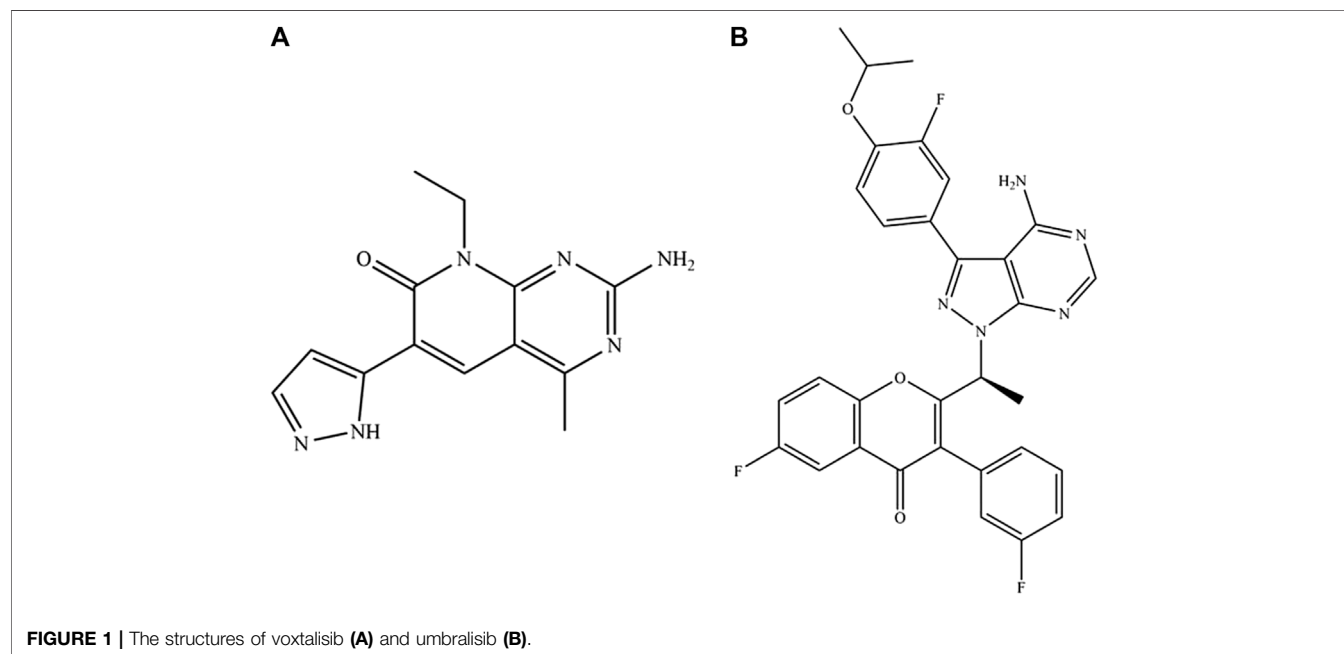
EXPERIMENT

Chemical Materials

Voxtalisisib, and umbralisib (**Figure 1B**) as the internal standard (IS) were purchased from Beijing sunflower Technology Development Co., Ltd. (Beijing, China). The LC grade methanol and acetonitrile were supplied by Merck (Darmstadt, Germany) and LC grade pure formic acid was produced by Anaqua Chemicals Supply (ACS, American). At the same time, the ultra-pure water from the laboratory was pretreated by the Milli-Q Water Purification System (Millipore, Bedford, Unnited States).

Animal Experiments

Six male SD rats (300 ± 20 g) were collected from the Experimental Animal Research Center of The First Affiliated Hospital of Wenzhou Medical University (Wenzhou, China), and were given fresh water and plenty of food every day. In the formal pharmacokinetic study, each rat was given 5 mg/kg voxtalisisib in the 0.5% carboxymethylcellulose sodium (CMC-Na) by single intragastric administration after fasting for 12 h. Then, blood samples (approximately 0.3 ml) were acquired at 0.333, 0.667, 1, 1.5, 2, 3, 4, 6, 8, 12, 24 and 48 h, respectively, and placed into polyethylene tubes containing heparin. The samples were immediately centrifuged at $13,000 \times g$ for 10 min at 4°C for separation. The centrifuged supernatants were then transferred into new 0.5 ml polythene tubes and then stored at -80°C for further analysis. In this experiment, the plasma concentration of voxtalisisib in rats was measured by UPLC-MS/MS technology, and the main pharmacokinetic parameters of voxtalisisib in non-compartmental model were calculated using Drugs and Statistics (DAS) 3.0 software (Mathematical Pharmacology Professional Committee of China, Shanghai, China).



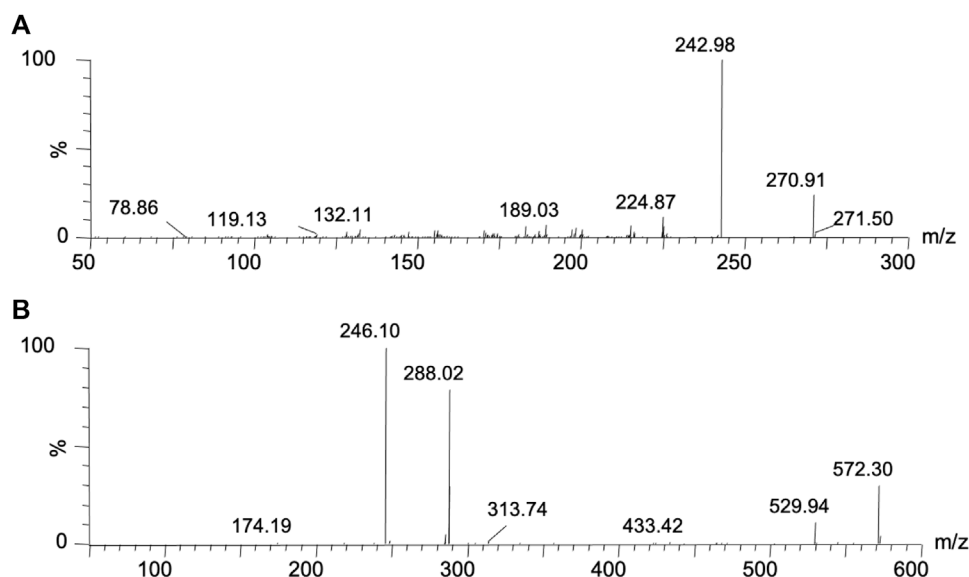


FIGURE 2 | Mass spectrum of voxelisib (A) and umbralisib (B) in this study.

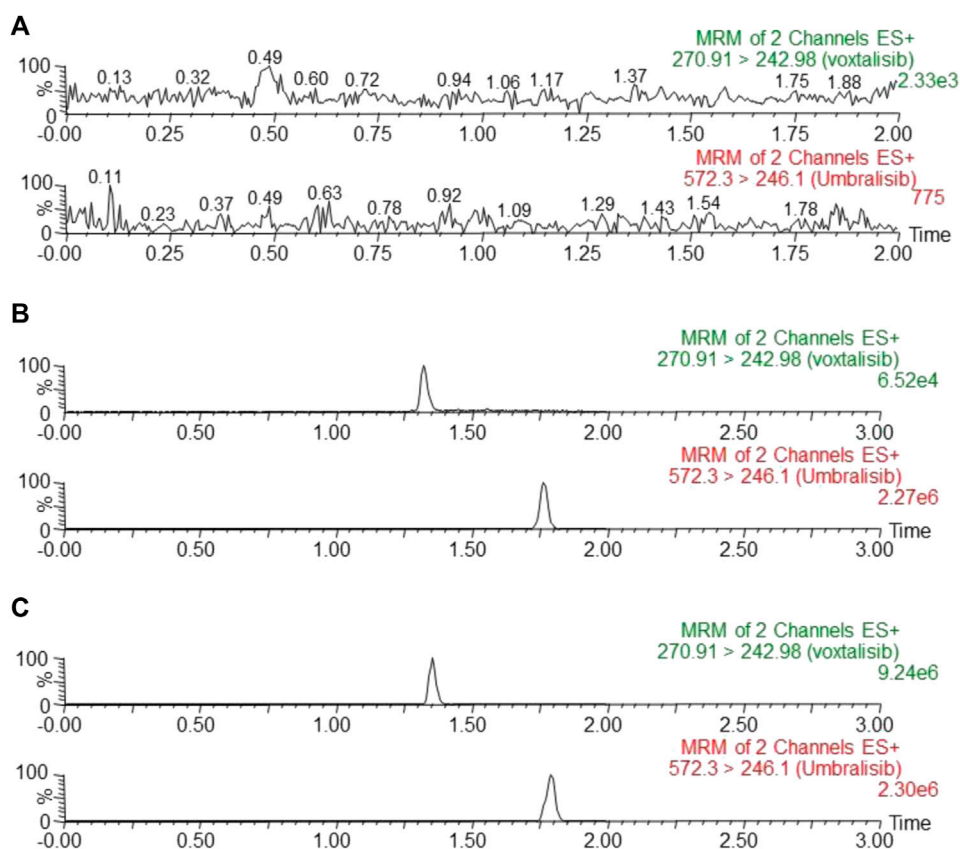


FIGURE 3 | Representative chromatograms of voxelisib and IS in rat plasma: (A) blank plasma; (B) blank plasma spiked with analyte at LLOQ and IS; (C) plasma sample collected from a rat at 20 min after intragastric administration of 5 mg/kg voxelisib.

TABLE 1 | The precision and accuracy of voxelisib in rat plasma ($n = 6$).

Analyte	Concentration (ng/ml)	Intra-day		Inter-day	
		RSD (%)	RE (%)	RSD (%)	RE (%)
Voxelisib	1	18.7	2.0	16.6	3.1
	2	10.6	-14.0	14.0	-4.5
	800	8.7	-4.0	14.3	-4.4
	1600	7.5	-8.5	13.0	-7.2

TABLE 2 | Recovery and matrix effect of voxelisib in rat plasma ($n = 6$).

Analyte	Concentration (ng/ml)	Recovery (%)		Matrix effect (%)	
		Mean \pm SD	RSD (%)	Mean \pm SD	RSD (%)
Voxelisib	2	100.5 \pm 8.6	8.5	94.1 \pm 12.4	13.2
	800	106.8 \pm 4.2	3.9	94.2 \pm 3.7	3.9
	1600	105.1 \pm 10.2	9.7	96.7 \pm 5.7	5.9

Analytical Conditions of the Instrumentation

Chromatographic separation of voxelisib and IS were performed using a Waters Acquity ultra-performance liquid chromatography (UPLC) system (Milford, MA, Unnited States) equipped with an Acquity BEH C18 column (2.1 mm \times 50 mm, 1.7 μ m; Milford, MA, Unnited States), and it was operated under the condition of 40°C column temperature. The mobile phases of gradient elution were acetonitrile (solvent A) and 0.1% formic acid (solvent B), respectively. At the flow rate of 0.30 ml/min, the elution process was 90% B from 0 to 0.5 min; 90–10% B from 0.5 to 1.0 min; 10% B from 1.0 to 1.4 min; 10–90% B from 1.4 to 1.5 min, and finally at 1.5–2.0 min, 90% B was maintained for equilibration. The whole process of analysis was 2.0 min, the temperature of the auto-sampler was set at 10°C, and the injection volume was 1.0 μ L for each running process.

Mass spectrometry information of voxelisib and IS were obtained by a Waters Xevo TQS triple-quadrupole tandem mass spectrometer (Milford, MA, Unnited States) with an electrospray ionization (ESI) source and a positive ion mode detection by MS/MS. Using selective response monitoring (SRM), the ion transitions of voxelisib and IS were m/z 270.91 $>$ 242.98 and m/z 572.30 $>$ 246.10, respectively (**Figure 2**). Optimized cone voltages and collision energies were 20 V and 20 eV for voxelisib, 30 V and 35 eV for IS, respectively. The flow rate of collision gas, cone gas and desolvation gas filled with high purity of nitrogen was 0.15 ml/min, 200 L/h and 1000 L/h, respectively. The optimized desolvation temperature reached 600°C.

Stock Solutions, Calibration and Quality Control Samples

Voxelisib and IS were dissolved in methanol as the stock solutions, and the concentration of each stock solution was 1 mg/ml. Then, the stock solution was gradient diluted with methanol to obtain the calibration and quality control (QC) samples. The concentrations of the working solutions for calibration curve were 10, 20, 50, 100, 500, 1000, 2000, 5000, 10000, 20000 ng/ml, and the IS concentration was 100 ng/ml. Fresh calibration standards with final concentrations of 1, 2, 5, 10, 50, 100, 200, 500, 1000, 2000 ng/ml were prepared by adding the corresponding concentration of voxelisib working solutions (10 μ L) to the blank rat plasma (90 μ L). Then, the same method was used to prepare QC samples with different concentrations (2, 800, 1600 ng/ml) and the lower limit of quantification (LLOQ, 1 ng/ml). Finally, all the stock and working solutions were stored at -80°C until further analysis.

Sample Preparation

The plasma samples were treated with a simple and rapid protein precipitation method. Firstly, adding 10 μ L IS working solution to 100 μ L plasma sample; Secondly, precipitate the plasma protein by adding 300 μ L acetonitrile; Thirdly, the plasma samples in each tube were fully swirled for 2.0 min and centrifuged for 10 min at 13000 \times g under 4°C. Finally, we took 100 μ L centrifuged supernatant into the special detection bottle of UPLC-MS/MS system, and then used UPLC-MS/MS

TABLE 3 | Stability results of voxelisib in rat plasma under different conditions ($n = 5$).

Analyte	Concentration (ng/ml)	Room temperature, 3 h		Auto-sampler 10°C, 4 h		Three freeze-thaw		-80°C, 3 weeks	
		RSD (%)	RE (%)	RSD (%)	RE (%)	RSD (%)	RE (%)	RSD (%)	RE (%)
Voxelisib	2	8.5	2.0	4.4	-1.8	8.2	2.2	8.2	7.4
	800	5.5	14.6	4.5	7.0	2.4	10.6	3.8	0.9
	1600	5.1	7.1	5.1	4.6	3.8	9.5	6.5	-10.8

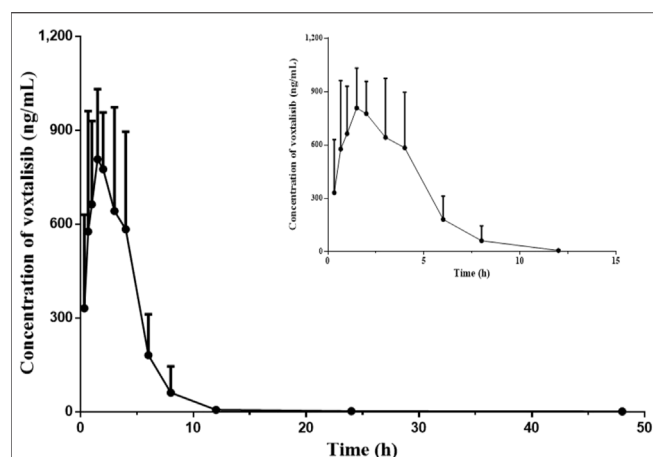


FIGURE 4 | Mean plasma concentration-time curves of voxelisib in rats after intragastric administration of voxelisib (5 mg/kg). ($n = 6$).

TABLE 4 | The main pharmacokinetic parameters of voxelisib in rat plasma after intragastric administration of voxelisib at a single dose of 5 mg/kg. ($n = 6$, Mean \pm SD).

Parameters	Voxelisib
AUC_{0-t} (ng/mL \cdot h)	3762.79 ± 1165.22
$AUC_{0-\infty}$ (ng/mL \cdot h)	3785.27 ± 1175.14
MRT_{0-t} (h)	3.77 ± 0.30
$MRT_{0-\infty}$ (h)	4.23 ± 0.20
$t_{1/2}$ (h)	10.47 ± 5.00
T_{max} (h)	2.45 ± 1.42
$CL_{z/F}$ (L/h/kg)	1.47 ± 0.58
C_{max} (ng/ml)	977.74 ± 250.40

AUC_{0-t} , area under the curve from 0 to t ; $AUC_{0-\infty}$, area under the curve from 0 to infinity; MRT_{0-t} , mean residence time from 0 to t ; $MRT_{0-\infty}$, mean residence time from 0 to infinity; $t_{1/2}$, elimination half-life; C_{max} , peak plasma concentration; T_{max} , time to C_{max} ; $CL_{z/F}$, clearance.

technology for analysis. In order to ensure the stability of the sample, it is recommended to test immediately. If immediate detection is not available, it can be stored at 4°C in the short-term, and should be stored at -80°C in the long-term.

Method Validation

According to the principle of bio-assay validation of FDA, a novel bio-assay method based on UPLC-MS/MS technology was established, including the specificity, carryover, calibration curve, LLOQ, precision, accuracy, matrix effect, recovery, and stability, as similar with those validated in our previous papers (Qiu et al., 2019; Xu et al., 2019; Tang et al., 2020).

Specificity and Carryover Effect

The specificity of UPLC-MS/MS analytical method was determined by analyzing plasma samples from three different batches: blank plasma without analyte and IS, blank plasma spiked with the analyte at LLOQ and IS, as well as rat plasma

samples. Then, the retention times of the analyte and IS in the SRM chromatogram were observed to determine whether there were endogenous interference. Carryover was assessed by injecting plasma samples at upper limit of quantification (ULOQ) followed by blank injections.

Calibration Curve Linearity and LLOQ

The linear regression analysis of voxelisib/IS peak area ratio (Y) and voxelisib concentration (X) was performed by the least square regression analysis with a weighted factor ($1/x^2$) to obtain the calibration curve. The sensitivity of the UPLC-MS/MS bio-analytical method was evaluated by analyzing six replicates of spiked LLOQ samples.

Precision and Accuracy

Six replicate QC samples (2, 800 and 1600 ng/ml) were determined on the same day and on three different days. The intra and inter-day precisions of the method were calculated, which is usually shown as relative standard deviation (RSD%), and the accuracy is commonly represented by relative error (RE%).

Matrix Effect and Recovery

At low, medium and high concentrations (2, 800 and 1600 ng/ml, $n = 6$), the peak areas of voxelisib added to the post-extracted blank plasma were compared with those of QC sample with corresponding concentration obtained by diluting standard solution with methanol to calculate matrix effect.

Voxelisib was added into the blank plasma before and after extraction, respectively, and the extraction recovery was evaluated by comparing the peak area of the two, also at three different levels (2, 800 and 1600 ng/ml, $n = 6$).

Stability

We evaluated the stability of this bioassay by measuring rat plasma concentrations of QC samples of voxelisib at three different concentrations (2, 800 and 1600 ng/ml, $n = 5$) under four different placement conditions, including short-term stability (3 h at room temperature), long-term stability (3 weeks at -80°C), post-preparation stability (4 h at 10°C in an auto-sampler), and stability through complete three freeze-thaw cycles.

RESULTS

The Optimal Condition of UPLC-MS/MS

In the pre-experiment, different organic buffers (such as methanol and acetonitrile) and water buffers (such as formic acid and ammonium acetate) on different types of analytical columns (Waters Acquity UPLC BEH C18 column, HSS C18 column, and CSH C18 column) were evaluated. After comparing different types of analytical columns in the experiment, the Acquity BEH C18 column (2.1 mm \times 50 mm, 1.7 μ m) provided good peak shapes, short chromatographic retention times and high chromatographic responses for both the analyte and IS, and the separation effect was better. In

addition, acetonitrile and 0.1% formic acid aqueous solution was the best mobile phase, and the analyte and IS obtained better signals and responses.

In pharmacokinetic study, we chose simple, time-saving and economical organic protein precipitation method to prepare plasma samples. We precipitated plasma proteins with acetonitrile. The results showed that acetonitrile had higher efficiency of protein precipitation.

Validation of the Method

Specificity and Carryover

According to SRM chromatograms under three different conditions in **Figure 3**, voxtalisisib and IS can be significantly distinguished by this chromatographic condition. The three different conditions were as follows: blank rat plasma sample (**Figure 3A**: no analyte, no IS), LLOQ concentration (1 ng/ml) of the analyte and IS added to blank rat plasma sample (**Figure 3B**), and a rat sample collected 20 min later in pharmacokinetic study after given intragastric administration of voxtalisisib (5 mg/kg) (**Figure 3C**). **Figure 3** showed that the retention times of voxtalisisib and IS were 1.32 and 1.77 min, respectively. In addition, no carryover was observed for either analyte or IS in rat plasma, because the peak area of the interference peak was less than 20% for the analyte in the LLOQ samples and less than 5% for the IS following injection of ULOQ samples.

Linearity and LLOQ

In this experiment, the linear regression equation of calibration standard curve in the concentration range of 1–2000 ng/ml was $y = 0.0231301x + 0.00967189$ ($r^2 = 0.999$). As shown in **Table 1**, the LLOQ of voxtalisisib was 1 ng/ml, where precision and accuracy were acceptable within 20%.

Precision and Accuracy

Table 1 indicated that the intra and inter-day precision values (RSD%) of voxtalisisib at three QC concentrations were 7.5–10.6% and 13.0–14.3%, respectively, and the intra and inter-day accuracy values (RE%) were –14.0% to –4.0% and –7.2% to –4.4%, respectively. According to the FDA guidance, this bioassay was used to quantify voxtalisisib in rat plasma with high accuracy and reproducibility.

Matrix Effect and Extraction Recovery

Table 2 displayed the results of matrix effect and extraction recovery of QC samples of voxtalisisib at three different concentration levels (2, 800, 1600 ng/ml). The matrix effect of voxtalisisib in blank rat plasma was 94.1–96.7%. In addition, its extraction recovery ranged from 100.5 to 106.8%. And these results were within the reasonable limits.

Stability

Table 3 showed the stability results of QC samples of voxtalisisib in rat plasma under four different placement conditions. These indicated that voxtalisisib had no significant difference under a variety of placement conditions (3 h at room temperature, 3 weeks at –80°C, 4 h at 10°C in an auto-sampler, and freeze–thaw stability for 3 times).

Pharmacokinetic Study in Rats

The pharmacokinetic study of voxtalisisib in rat plasma was performed by UPLC-MS/MS technology. **Figure 4** depicted the relationship between mean plasma concentration (ng/ml) and time (0–48 h) of voxtalisisib in rats. Since voxtalisisib was fully eliminated from the body at around 12 h, the relationship between the mean plasma concentration (ng/ml) of voxtalisisib in rats and the time of 0–12 h was added to illustrate the relationship more clearly. **Table 4** showed the main pharmacokinetic parameters of voxtalisisib, which were calculated by non-compartment analysis using DAS software.

According to **Figure 4** and **Table 4**, after the rats were given 5 mg/kg voxtalisisib in a single dose, voxtalisisib was rapidly absorbed into the blood and spread throughout the whole body, reaching a maximum plasma concentration (C_{\max}) of 977.74 ± 250.40 ng/ml at 2.45 ± 1.42 h (time to C_{\max} , T_{\max}). Moreover, the half-life ($t_{1/2}$) of its elimination in rats was 10.47 ± 5.00 h.

DISCUSSION

In a phase I dose-escalation study on the safety and pharmacokinetics of voxtalisisib tablets in patients with solid tumors, $C_{\max} = 301 \pm 101$ ng/ml, $T_{\max} = 1.53$ h, $t_{1/2} = 3.94 \pm 0.79$ h on the first day after giving patients 50 mg/kg once daily (Mehnert et al., 2018). The existence of these differences in patient and rat data may be related to ethnic and individual differences, and in addition, our experimental results have only been verified in a few rats ($n = 6$), compared to 49 patients in the clinical trial. Consequently, the pharmacokinetics of voxtalisisib need to be further studied. Furthermore, this pharmacokinetics of voxtalisisib in patients with solid tumors did not provide enough data for repeating the approach in other laboratories (specificity, accuracy, precision, etc.), so our method effectively achieved the need of high sample throughput for biological analysis (Mehnert et al., 2018).

CONCLUSION

In summary, in this experiment, we determined the specificity, carryover, precision, accuracy, extraction recovery, matrix effect, and stability of voxtalisisib in rat plasma. This UPLC-MS/MS assay can effectively and quickly quantify the analyte, and this method can also be used for the pharmacokinetic study of voxtalisisib in rats, which can provide reference for the optimization of clinical drug management in the later period.

DATA AVAILABILITY STATEMENT

The original contributions presented in the study are included in the article/Supplementary Material, further inquiries can be directed to the corresponding authors.

ETHICS STATEMENT

The animal study was reviewed and approved by The First Affiliated Hospital of Wenzhou Medical University.

AUTHOR CONTRIBUTIONS

QL: Investigation; Writing—original draft; Conceptualization; Data curation; Formal analysis; Y-nL: Investigation; Methodology; Visualization, Writing—original draft; JW: Data curation; editing; YH: Investigation; Methodology; JH: Data curation; Formal analysis; R-aX: Supervision;

Writing—review and editing; Validation; LS: Project administration; Resources; Software; Supervision; Writing—review and editing; Validation; LC: Project administration; Resources; Software; Supervision; Writing—review and editing; Validation.

FUNDING

This work was supported by National Key Research and Development Program of China (2020YFC2008301) and PhD Start-up Funds from The First Affiliated Hospital of Wenzhou Medical University (2022QD23).

REFERENCES

- Brown, J. R., Hamadani, M., Hayslip, J., Janssens, A., Wagner-Johnston, N., Ottmann, O., et al. (2018). Voxelisib (XL765) in Patients with Relapsed or Refractory Non-hodgkin Lymphoma or Chronic Lymphocytic Leukemia: an Open-Label, Phase 2 Trial. *Lancet Haematol.* 5, e170–e180. doi:10.1016/S2352-3026(18)30030-9
- He, J., Fang, P., Zheng, X., Wang, C., Liu, T., Zhang, B., et al. (2018). Inhibitory Effect of Celecoxib on Agomelatine Metabolism *In Vitro* and *In Vivo*. *Drug Des. Devel Ther.* 12, 513–519. doi:10.2147/DDDT.S160316
- Jänne, P. A., Cohen, R. B., Laird, A. D., Macé, S., Engelman, J. A., Ruiz-Soto, R., et al. (2014). Phase I Safety and Pharmacokinetic Study of the PI3K/mTOR Inhibitor SAR245409 (XL765) in Combination with Erlotinib in Patients with Advanced Solid Tumors. *J. Thorac. Oncol.* 9, 316–323. doi:10.1097/JTO.000000000000088
- Markman, B., Atzori, F., Pérez-García, J., Tabernero, J., and Baselga, J. (2010). Status of PI3K Inhibition and Biomarker Development in Cancer Therapeutics. *Ann. Oncol.* 21, 683–691. doi:10.1093/annonc/mdp347
- Mehnert, J. M., Edelman, G., Stein, M., Camisa, H., Lager, J., Dedieu, J. F., et al. (2018). A Phase I Dose-Escalation Study of the Safety and Pharmacokinetics of a Tablet Formulation of Voxelisib, a Phosphoinositide 3-kinase Inhibitor, in Patients with Solid Tumors. *Invest. New Drugs* 36, 36–44. doi:10.1007/s10637-017-0467-7
- Prasad, G., Sottero, T., Yang, X., Mueller, S., James, C. D., Weiss, W. A., et al. (2011). Inhibition of PI3K/mTOR Pathways in Glioblastoma and Implications for Combination Therapy with Temozolomide. *Neuro Oncol.* 13, 384–392. doi:10.1093/neuonc/noq193
- Qiu, X., Xie, S., Ye, L., and Xu, R. A. (2019). UPLC-MS/MS Method for the Quantification of Ertugliflozin and Sitagliptin in Rat Plasma. *Anal. Biochem.* 567, 112–116. doi:10.1016/j.ab.2018.12.016
- Tang, C., Niu, X., Shi, L., Zhu, H., Lin, G., and Xu, R. A. (2020). *In Vivo* Pharmacokinetic Drug-Drug Interaction Studies between Fedratinib and Antifungal Agents Based on a Newly Developed and Validated UPLC/MS-MS Method. *Front. Pharmacol.* 11, 626897. doi:10.3389/fphar.2020.626897
- Thijssen, R., Ter Burg, J., Van Bochove, G. G., De Rooij, M. F., Kuil, A., Jansen, M. H., et al. (2016). The pan Phosphoinositide 3-kinase/mammalian Target of Rapamycin Inhibitor SAR245409 (voxalisib/XL765) Blocks Survival, Adhesion and Proliferation of Primary Chronic Lymphocytic Leukemia Cells. *Leukemia* 30, 337–345. doi:10.1038/leu.2015.241
- Xu, R. A., Lin, Q., Qiu, X., Chen, J., Shao, Y., Hu, G., et al. (2019). UPLC-MS/MS Method for the Simultaneous Determination of Imatinib, Voriconazole and Their Metabolites Concentrations in Rat Plasma. *J. Pharm. Biomed. Anal.* 166, 6–12. doi:10.1016/j.jpba.2018.12.036
- Zhang, L., Wang, Z., Khishignyam, T., Chen, T., Zhou, C., Zhang, Z., et al. (2018). *In Vitro* anti-leukemia Activity of Dual PI3K/mTOR Inhibitor Voxelisib on HL60 and K562 Cells, as Well as Their Multidrug Resistance Counterparts HL60/ADR and K562/A02 Cells. *Biomed. Pharmacother.* 103, 1069–1078. doi:10.1016/j.biopha.2018.04.089
- Zhao, H., Chen, G., and Liang, H. (2019). Dual PI3K/mTOR Inhibitor, XL765, Suppresses Glioblastoma Growth by Inducing ER Stress-dependent Apoptosis. *Onco Targets Ther.* 12, 5415–5424. doi:10.2147/OTT.S210128

Conflict of Interest: The authors declare that the research was conducted in the absence of any commercial or financial relationships that could be construed as a potential conflict of interest.

Publisher's Note: All claims expressed in this article are solely those of the authors and do not necessarily represent those of their affiliated organizations, or those of the publisher, the editors and the reviewers. Any product that may be evaluated in this article, or claim that may be made by its manufacturer, is not guaranteed or endorsed by the publisher.

Copyright © 2022 Li, Liu, Wang, Hu, Hu, Xu, Shao and Chen. This is an open-access article distributed under the terms of the Creative Commons Attribution License (CC BY). The use, distribution or reproduction in other forums is permitted, provided the original author(s) and the copyright owner(s) are credited and that the original publication in this journal is cited, in accordance with accepted academic practice. No use, distribution or reproduction is permitted which does not comply with these terms.



An Efficient UPLC-MS/MS Method Established to Detect Relugolix Concentration in Rat Plasma

Liying Xing^{1†}, Ya-nan Liu^{2†}, Hongye Yao¹, Tingting Wang¹, Fuchen Xie³, Shunbin Luo³, Pingping Luo^{3*} and Shengling Tang^{3*}

¹The First People's Hospital of Jiashan, Jiashan, China, ²The First Affiliated Hospital of Wenzhou Medical University, Wenzhou, China, ³The People's Hospital of Lishui, Lishui, China

OPEN ACCESS

Edited by:

Jiao Zheng,
Shanghai Jiao Tong University, China

Reviewed by:

Guru Raghavendra Valicherla,
University of Pittsburgh, United States
Yi Tao,
Zhejiang University of Technology,
China

*Correspondence:

Pingping Luo
lpingping19@163.com
Shengling Tang
tangshengling3068@163.com

[†]These authors contributed equally to
this work

Specialty section:

This article was submitted to
Drug Metabolism and Transport,
a section of the journal
Frontiers in Pharmacology

Received: 13 February 2022

Accepted: 17 May 2022

Published: 16 June 2022

Citation:

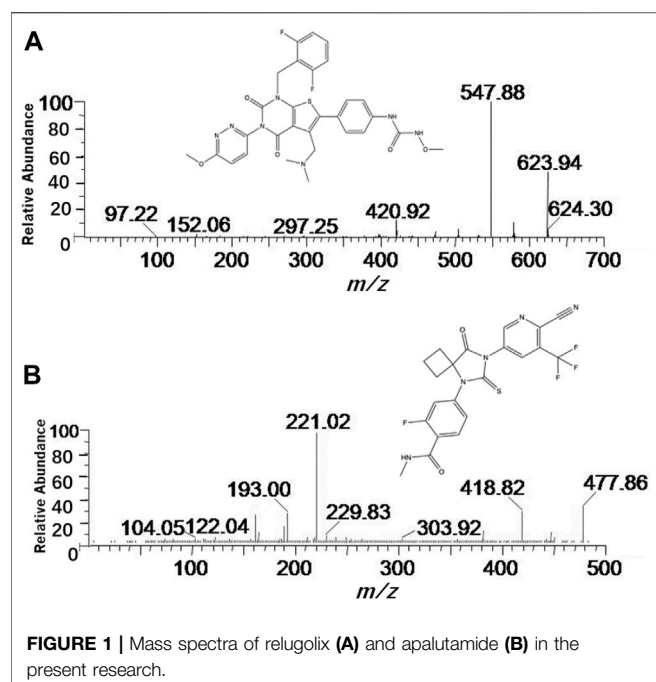
Xing L, Liu Y-n, Yao H, Wang T, Xie F,
Luo S, Luo P and Tang S (2022) An
Efficient UPLC-MS/MS Method
Established to Detect Relugolix
Concentration in Rat Plasma.
Front. Pharmacol. 13:874973.
doi: 10.3389/fphar.2022.874973

Relugolix, a gonadotropin-releasing hormone (GnRH) receptor antagonist, has been well studied in the treatment of endometriosis symptomatic. It is mainly metabolized by the CYP3A subfamily of P450 enzymes, while minorly metabolized by CYP2C8. Daidzein in different dose groups exhibited a certain induction on the mRNA expression level of CYP3A4 and resulted in the potent induction of CYP3A4. However, it is still unknown whether daidzein and relugolix interact. We developed an effective ultra-performance liquid chromatography tandem mass spectrometry (UPLC-MS/MS) method to study the effect of daidzein on the pharmacokinetics of relugolix in rats after oral administration of 12 mg/kg relugolix in a single or mixed of 50 mg/kg daidzein. The results showed that the method had respectable linearity ($r^2 > 0.999$) on the scale of 0.7–1000 ng/mL. The intra-day precision was between 3.0% and 8.4% in this assay, and the inter-day was between 4.0% and 11.7%. The intra-day accuracy was from -4.3% to 6.1%, and the inter-day was 2.9% to 12.1%. Another three key indicators, including the stability, the recovery rate of extraction and the new technique's matrix effect, were perfectly in accord with the test verification rule in the biological medium by the United States Food and Drug Administration. Meanwhile, treatment with daidzein led to a decrease in C_{max} and AUC_{0-t} of relugolix by about 15.56% and 21.36%, respectively. Although there was no statistical difference in pharmacokinetic parameters, it reflected the induction trend of daidzein on relugolix metabolism for food-drug interaction. It would provide reference and improvement value for subsequent experiments.

Keywords: GnRH antagonist, relugolix, daidzein, uterine fibroids, endometriosis

INTRODUCTION

Female reproductive health is a growing area of interest. Uterine fibroids (UF) and endometriosis are estrogen-related chronic gynecological disorders and affect millions of women worldwide. UF is a common benign uterine neoplasm in females, and the prevalence increases throughout the premenopausal years, estimated at 33–77% during their reproductive years and 70–80% by menopause (Parker, 2007; Stewart et al., 2016; Baird and Harmon, 2021). Primary symptoms are pelvic pressure or pain, menorrhagia and urinary symptoms, which are related to its size, number and location in the uterus (Leppert et al., 2021). Endometriosis that characterized by endometrial and stromal tissue abnormally located outside the uterine cavity has an estimated prevalence of 14% to 35% per year in women (Sarria-Santamera et al., 2020). It is predominantly associated with chronic



pelvic pain, severe dysmenorrhea, menorrhagia, dyspareunia, and infertility during reproductive age (As-Sanie et al., 2019; Zannoni et al., 2020). In previous reports, women with UF were more likely to have endometriosis than those without fibroids, which suggested that the two disorders may be associated and their etiology has many similarities (Uimari et al., 2011; Teresinski et al., 2019; Yadav et al., 2021). There are very few discoverable ideal treatment methods for the above two diseases. For UF, the common treatment options are hysterectomy and myomectomy by surgery (Schlaff et al., 2020). As drug interventions, the medication for UF is similar to endometriosis, including oral contraceptives hormones (estrogen and progestin-based) (Berlanda et al., 2016), levonorgestrel, nonsteroidal anti-inflammatory drugs (Gezer and Oral, 2015; Lewis et al., 2018), and Gonadotropin-releasing hormone (GnRH) agonists, particularly, alleviating the symptom of heavy menstrual bleeding (Dunselman et al., 2014). Nevertheless, combined oral contraceptive medications were not effective in every patient and associated with an increasing risk of thromboembolic events (Rafique and Decherney, 2017). Progestin-only products, similar to GnRH agonists and danazol, can relieve pelvic pain effectively but may increase the risk of uterine bleeding (Gezer and Oral, 2015). In addition, injectable GnRH agonist peptides, such as leuporelin, are likely to cause a transient increase in gonadotropins secretion and finally lead to a temporary worsening of symptoms (Stewart et al., 2016; Yao et al., 2017).

With the potential to overcome the limits of GnRH-agonists, GnRH antagonists are characterized by causing a sustained drop of serum estrogen with dose-dependent, permitting to avoid hormonal add-back therapy and the absence of the flare effect (Chaichian et al., 2017; Pohl et al., 2020). Relugolix (Figure 1A), a newly-found non-peptide GnRH antagonist to treat the two diseases above, takes effect more rapidly than GnRH agonists

developed by Takeda and ASKA Pharmaceutical (Markham, 2019). The drug suppresses the release of gonadotropin from the pituitary resulting in reduced levels of estradiol, progesterone and testosterone, without an initial rise in hormone levels (Ali et al., 2021; Relugolix, 2021). Relugolix recently has got the permission for marketing in Japan to treat symptoms associated with UF. The results of relevant studies, attempting to assess the efficacy of the drug in the treatment of endometriosis-associated pain and prostate cancer, are shown an ideal way (Dearnaley et al., 2020; Jena, 2020; Osuga et al., 2021). Relugolix may become a new oral therapy option for its significant improvements in symptoms and good tolerability, especially, in women who refused other hormonal therapies simply or contraindication.

Isoflavonoids, the subfamily of Leguminosae, a group of polyphenolic plant compounds, are particularly prevalent in the plant kingdom. Daidzein and genistein are the most ingredients in the isoflavonoids (Havsteen, 1983). Daidzein isolated from natural products, such as soybean, pasture grasses and cereals, showed biologically actives, like unique estrogenic activity and strong antioxidant activity (Cherdsheewasart and Sutjit, 2008). As a dietary antioxidant, it may protect against oxidative stress, an important mechanism, linked to inflammation and macromolecule damage by free radicals and oxygen-related and N-oxidizing agents. The property of antioxidant may protect the body from hormone-related cancers, like breast, prostatic and endometrial cancerization (Miadokova, 2009; Toktay et al., 2020).

According to the literature, daidzein in different dose groups exhibited certain induction on the mRNA expression level of CYP3A4 and resulted in the potent induction of CYP3A4 (Kopceva-Zapletalova et al., 2017). Relugolix is mainly metabolized by the CYP3A subfamily of P450 enzymes, while with a minor metabolism by CYP2C8. In addition, co-administration with rifampin (P-gp and strong CYP3A inducer) decreased the AUC and C_{max} of relugolix by 55% and 23%, respectively (https://www.accessdata.fda.gov/drugsatfda_docs/label/2020/214621s000lbl.pdf).

Thus, it is important to set up a rapid and effective method for detecting relugolix concentration *in vivo*, for there is few effective monitoring method currently. In this research, we developed and validated an efficient UPLC-MS/MS method for the detection of relugolix in rat plasma. For implementation, we got the plasma samples of rats that have taken relugolix at a single dose of 12 mg/kg orally (control group) and a recombination dose of 50 mg/kg daidzein orally (experiment group) for the pharmacokinetics study. Moreover, the pharmacokinetic profiles of relugolix determined by UPLC-MS/MS would be a preponderance for further drug concentration monitoring studies including food-drug or drug-drug interactions.

MATERIALS AND METHODS

Chemicals

The analyte relugolix required high quality (purity >98%) was provided by Beijing Sunflower and Technology Development CO,

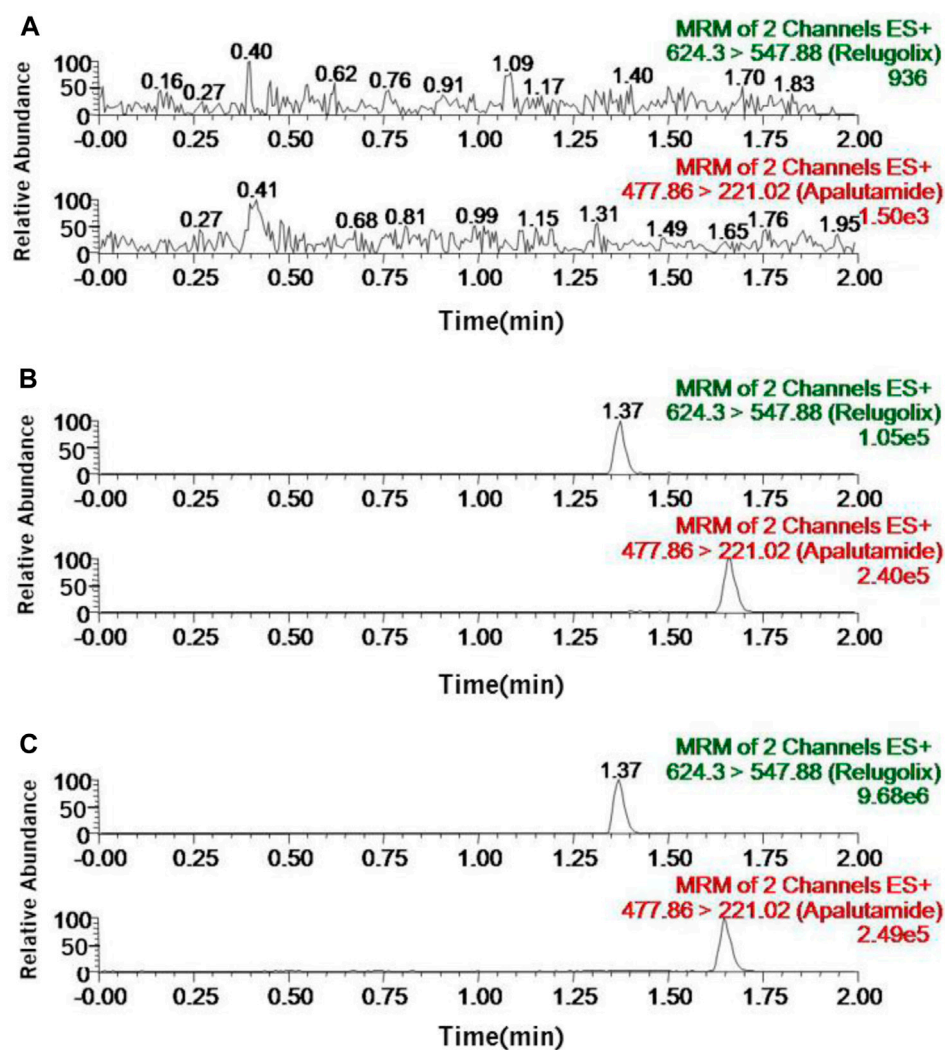


FIGURE 2 | Representative chromatograms of relugolix and IS in rat plasma samples: **(A)** the blank plasma sample; **(B)** the blank plasma sample with relugolix at the LLOQ concentration (0.7 ng/mL) and IS; **(C)** the rat plasma sample after oral administration of 12 mg/kg relugolix.

Ltd (Beijing, China), as well apalutamide selected to be the internal standard (IS). Daidzein was from Shanghai Chuangsai Technology Co., Ltd (Shanghai, China). The chemical reagent methanol and acetonitrile, as HPLC grade, purchased from Merck Company (Darmstadt, Germany). Deionized water produced by Milli-Q water purification system (Millipore, Bedford, United States) met academic reagent criterion.

UPLC-MS/MS Conditions

The analytical work was performed on the liquid chromatograph with a 1.7 μm Acquity BEH C18 column of 2.1 mm \times 50 mm, set at 40°C, as a core component of UPLC Acquity system (Waters Corp, Milford, MA, United States). The gradient elution was composed with organic phase solution of acetonitrile (A), and water phase contained 0.1% formic acid (B). The program for gradient elution (B): 90% at 0–0.5 min, 90%–10% at 0.5–1.0 min,

maintain at 10% for 0.4 min, fast conversion from 10% to 90% at 1.4–1.5 min, then balance with 90% for 0.5 min. A speed of 0.30 mL per min was set for the flow while 2.0 min was carried out for a specimen circulation.

The Acquity UPLC system, equipped with an electrospray ionization (ESI) source and a Xevo TQ-S triple quadrupole mass spectrometer, was used to detect the analyte in positive ionization mode. Other than that, multiple reaction monitoring (MRM) was applied to determine the analyte with the precursor-to-product ion transitions: m/z 624.30 \rightarrow 547.88 and m/z 477.86 \rightarrow 221.02 for the quantification of relugolix and IS, respectively. The collision energy and cone voltage were 25 eV and 30 V for IS, 20 eV and 30 V for relugolix. The results were verified when the best conditions were set as below: the optimum desolvation temperature was 600°C, the optimum capillary voltage was 1.0 kV, the optimum collision gas was 0.15 mL/min, the optimum

TABLE 1 | Accuracy, precision, matrix effect and recovery of QC samples of relugolix from plasma in rats ($n = 6$).

Concentration (ng/mL)	RSD (%)		RE (%)		Matrix Effect (%)	Recovery (%)
	Intra-day	Inter-day	Intra-day	Inter-day		
0.7	8.4	11.7	-4.3	8.7	—	—
1.4	7.1	8.9	0.0	10.0	112.6 ± 10.2	80.5 ± 8.5
80	5.0	6.6	6.1	12.1	110.7 ± 8.3	86.2 ± 6.0
800	3.0	4.0	-0.3	2.9	108.8 ± 12.8	88.3 ± 3.5

RSD, relative standard deviation; RE, relative error.

conic gas was 150 L/h and the optimum desolation gas was 1000 L/h. Finally, the data was collected by using the Masslynx 4.1 software which was furnished on the new UPLC-MS/MS analysis system.

Preparation of Stock Solution, Calibration Standard, and Quality Control (QC)

The exact concentration of standard substance was dissolved in methanol to obtain 1.0 mg/mL relugolix for preparing quality control (QC) and calibration curve specimens. Calibration standard for specimens was diluted from the corresponding stock solutions with methanol to gradient concentrations, as well as the dilution of IS solution to 100 ng/mL. The levels of calibration curve were 0.7–1000 ng/mL and QC samples were 1.4, 80, 800 ng/mL by adding 10 μ L of the corresponding solution to 90 μ L blank plasma of rat. The stock solution and working fluids were stored in a refrigerator at 4°C, and put at room temperature for at least 10 min to reduce temperature interference before the test.

Specimen Preparatory Procedure

In this study, protein isolation method was used to prepare specimens. In short, adding 20 μ L apalutamide (IS) solution into 100 μ L plasma in a 2.0 mL Eppendorf tube before vortexing for 30 s, then 300 μ L acetonitrile was added to precipitate the plasma protein and vortexed for 2.0 min. Samples were centrifugated 10 min at 13,000 \times g to get the supernatant for the new employed UPLC-MS/MS system for the purpose of making a specific measurement.

METHOD VERIFICATION

The bioanalytical validation method in this test was based on the principles and the guidelines of the China Food and Drug Administration (FDA), as well as the United States FDA, and a guiding force of the European Drug Administration also played an important role in this study (Feng et al., 2021; Zhao et al., 2021).

For the purpose of assessing the specificity of this newly developed method, plasma samples from six rats in the different batches were collected. To verify the influence from different source samples, tests of the representative

chromatograms were performed during which relugolix (as analyte) and apalutamine (as IS) were set to make the certain curve with coverage area. On the calibration curved line, y represents the ratio of the peak area of relugolix to the IS, x describes the theoretical concentrations, and $1/x^2$ was employed to be an important indicator as the weight factor. Moreover, the concentration of relugolix at 0.7 ng/mL was the lower limit of quantitation (LLOQ) and defined as the minimum solution concentration in the calibration curved line. It requires that relative standard deviation (RSD, %), the visual indicator for precision, need to be less than 20% and relative error (RE, %), the indicator for accuracy, is supposed to be the same requirement.

A comparison was made between the area of blank samples after extraction and methanol added at respective concentration levels to investigate the influence of matrix effect. To get the data of the recovery rate, it is an important step to calculate the ratio of the concentration of those samples before and after separation. Six comparative and repeated trials were carried out to assess the indicators above, during which the samples were set at three different QC levels (1.4, 80 and 800 ng/mL) for the purpose of ascertaining both the data of recovery rate and matrix effect. Besides, intra-day and inter-day data of both the relative standard deviation (RSD%) and relative error (RE%) were calculated with six repetitions per day for three consecutive days.

In this study, we evaluated the stability of six duplicate specimen of rat plasma with relugolix levels of 1.4, 80 and 800 ng/mL, under four probable circumstances: first test was to freeze/thaw the experimental samples completely three times; store the samples at 10°C for 3 h, room temperature for 2 h and -40°C for 28 days as the storage tests. With the work of experiments above, the assessment of stability of relugolix in rat plasma and quality of specimens was rigorous.

Pharmacokinetic Application

In this study, the female Sprague-Dawley (SD) rats were 2 months of age (weight 200 \pm 20 g) and provided from Wenzhou Medical University (Zhejiang, China). The animal experiments were adhered to its corresponding Care and Use of Laboratory Animal Regulation and Rule regards, and approved by the Animal Protection and Use Committee of Wenzhou Medical University. Water was not restricted before the experiments during fasting 12 h. As oral administration drugs of rats, daidzein and relugolix were dissolved in a 0.5% CMC-Na aqueous solution to 10 mg/mL and 2.4 mg/mL, respectively. A

TABLE 2 | Stability findings of relugolix from plasma in rats under different conditions ($n = 6$).

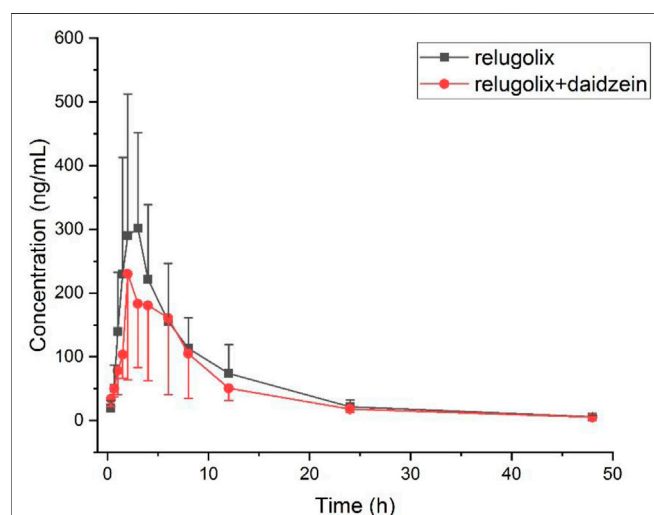
Concentration (ng/mL)	Room Temperature, 2 h		10°C, 3 h		Three Freeze-Thaw		-40°C, 28 days	
	RSD (%)	RE (%)	RSD (%)	RE (%)	RSD (%)	RE (%)	RSD (%)	RE (%)
1.4	7.8	0.7	11.7	-9.4	11.3	6.1	7.2	14.2
80	4.1	-1.0	9.9	-4.0	5.8	6.8	5.0	10.0
800	2.6	-14.2	5.8	-10.6	3.2	-3.7	3.4	-1.9

RSD, relative standard deviation; RE, relative error.

TABLE 3 | Main pharmacokinetic parameters after taking a single oral dose of relugolix with or without daidzein to rats ($n = 6$).

Parameters	Relugolix	Relugolix + daidzein
$T_{1/2}$ (h)	8.95 ± 0.75	8.45 ± 1.30
T_{max} (h)	2.33 ± 0.82	2.42 ± 0.92
C_{max} (ng/mL)	350.17 ± 190.35	295.70 ± 135.01
CL (L/h•kg)	5.50 ± 3.29	6.62 ± 3.44
AUC _{0→t} (ng/mL•h)	2743.18 ± 1353.80	2157.35 ± 964.50
AUC _{0→∞} (ng/mL•h)	2813.49 ± 1390.68	2196.56 ± 975.10

$T_{1/2}$, half-life time; C_{max} , maximum plasma concentration; T_{max} , time to C_{max} ; CL, clearance; AUC, Area under the concentration-time curve; MRT, mean residence time.

**FIGURE 3** | Plasma concentration versus time after oral administration of 12 mg/kg relugolix with or without daidzein in six rats for each group (Mean ± SD).

dose of 50 mg/kg daidzein was orally administrated for the experimental group, meanwhile the same volume of solvent was given to the control group. After 30 min, relugolix, a single dose of 12 mg/kg, was orally administrated to the experimental group and control group simultaneously. Then blood samples were collected at 0, 0.33, 0.67, 1, 1.5, 2, 3, 4, 6, 8, 12, 24, and 48 h independently, and about 300 μ L were put into EP tubes with heparin anticoagulant. All the samples were separated under centrifugation at $4000 \times g$ for 8 min immediately and kept at -40°C for later study. The pharmacokinetic parameters of relugolix *in vivo* were

evaluated by Drug and Statistics (DAS) version 3.0 bought from Shanghai University of Traditional Chinese Medicine, in a non-compartmental model. Pharmacokinetic parameters between two groups were compared through independent-samples *t* test by Statistical Package for the Social Sciences (version 23.0; SPSS Inc, Chicago, IL, United States). $p < 0.05$ is statistically significant.

RESULTS AND DISCUSSION

Approach Validation and Improvement

The present study corroborated a new efficient method to determinate the concentration of relugolix, which was separated from the biological plasma in rats by an effective UPLC-MS/MS study. Three improvements should be considered, including the majorization of chromatography conditions, the decrease in performing period, and the enhancement of the detectability. In order to reach a high level of precision and the minimum amount of experimental error, we used apalutamide as IS (the perfect match). The reason that acetonitrile was chosen as the organic media was due to its lower background noise level than methanol. Eventually, good separation and peak shape were obtained with 0.1% formic acid water channel and acetonitrile solution organic channel as mobile phase. In order to remove protein and potential interferences, an efficient extract preparation played a key role in preference to UPLC-MS/MS assay. Compared with the current extraction technology, researchers used an easy but resultful way rather than complicated solid-phase extraction and liquid-liquid extraction technology, which was demonstrated by predecessors (Chen et al., 2015; Liu et al., 2016; Tomai et al., 2021). A series of solvents were tested to find the most proper one for protein precipitation. Finally, because of acetonitrile's better recovery, it was chosen.

Selectivity and Matrix Effect

Figure 2 demonstrated the selectivity of this approach. It showed the typical chromatograms of three different conditions: the sample of blank plasma (A); the blank plasma sample with relugolix at the LLOQ concentration and IS (B); the rat plasma sample of oral administration of 12 mg/kg relugolix (C). The chromatograms showed the fact that the retention time of IS was 1.65 min while the retention time of relugolix was 1.37 min, and interfering peaks induced by endogenic compounds were insignificant, which even could be neglected. At three concentration gradients of 1.4, 80 and 800 ng/mL, the

matrix effect value was $(112.6 \pm 10.2)\%$, $(110.7 \pm 8.3)\%$ and $(108.8 \pm 12.8)\%$, respectively, being well accepted, and interference factor of the matrix could be ignored.

Linearity and Sensitivity

The calibration standard, which y represented as the ratio of relugolix to the IS and x as the plasma level of relugolix, was shown as follows: $y = 20.3899x + 3.05209$, with correlation coefficient $r^2 = 0.999,935$ in the scope of 0.7–1000 ng/mL. This standard of relugolix for quantification was satisfying. The LLOQ (0.7 ng/mL) was kept high exactitude and the signal to noise ratio of LLOQ was >10 .

Accuracy, Precision, and Extraction Recovery

Under 1.4, 80, 800 ng/mL concentrations that included low-to-high levels, several tests were performed for six times. All the results were presented in **Table 1**. The relugolix recovery rate in plasma sample was $(80.5 \pm 8.5)\%$, $(86.2 \pm 6.0)\%$ and $(88.3 \pm 3.5)\%$, as the chart displayed, under the three QC levels, respectively. Moreover, the measurement of precision and accuracy was satisfied with the demands in three independent days.

Stability

The stability test was usually studied under four variable environments in the experimental process, including short period setting at ambient temperature for more than 2 h, 10°C for 3 h after sample extracted in a self-sampler, long period setting at -40°C for 28 days, and three complete freeze-thaw cycles as well. It was shown perfect stability under these conditions. All the outcomes of the study about stability of relugolix from rat plasma were exhibited in **Table 2**.

Application of This Approach in the Pharmacokinetics

The applicability of this method was verified in a preliminary study of plasma relugolix concentration levels in rats after oral administration alone or in combination with 50 mg/kg daidzein. Conclusions of the most important pharmacokinetic parameters discovered through the test were shown in **Table 3**. After oral administration with a single dose of 12 mg/kg relugolix in both groups, the data of plasma concentrations that changed with time was portrayed in **Figure 3**.

It turned out that after orally taking a certain capacity of relugolix, there was no significant statistical difference in the critical pharmacokinetic parameters. Nevertheless, it showed a tendency of induction for the experimental group in terms of $AUC_{0 \rightarrow t}$ compared $(2743.18 \pm 1353.80) \text{ g/mL} \cdot \text{h}$ to $(2157.35 \pm 964.50) \text{ ng/mL} \cdot \text{h}$; the terminal half-value elimination period ($t_{1/2}$) compared $(8.95 \pm 0.75) \text{ h}$ to $(8.45 \pm 1.30) \text{ h}$ and the total clearance rate data compared $(5.50 \pm 3.29) \text{ L/h} \cdot \text{kg}$ to $(6.62 \pm 3.44) \text{ L/h} \cdot \text{kg}$. The reason for the result without significant difference may be that: mainly, the sample sizes were too small, with only six

rats in each of the experimental group and the control group, and it caused the objective deviation. From this point, we will expand the sample sizes in subsequent studies. In addition, daidzein should be stratified into different concentration gradients, and each gradient is in line with a reasonable sample size for further study. Moreover, there are certain differences between rat metabolic enzymes and human liver drug enzymes. Finally, we should design experiments to prepare human hepatocytes *in vitro* to further explore the food-drug interaction for better verification. The *in vivo* experiment in rats is of a certain reference value, which provides important pharmacokinetic parameters for reference to subsequent experiments and it also hints at the significance of subsequent experiments.

CONCLUSION

Relugolix, as an effective GnRH receptor antagonistic drug, has demonstrated the optimized drug therapy effect and security when it was made use of in the process of treating bleeding in menstruation and estrogen-associated pain in UF and endometriosis. To conclude, this study is the first attempt to validate and verify a quantitative method of relugolix in rat plasma with ideal linearity in the range of 0.7–1000 ng/mL. A single dose of 12 mg/kg relugolix was administered orally to the experimental group (a combination dose of 50 mg/kg daidzein) and the control group for pharmacokinetics study, in which the new method was verified successfully as presumed. Moreover, after protein precipitation with acetonitrile, the relugolix in rat plasma could be recovered efficiently by UPLC-MS/MS method without matrix effect. This method had the characteristics of high precision, high sensitivity and high efficiency, and the detection error meets the standard range. Although there was no statistical difference in pharmacokinetic parameters, it still reflected the induction trend of daidzein on relugolix for food-drug interaction and it provided reference and improvement value for subsequent experiments.

DATA AVAILABILITY STATEMENT

The original contributions presented in the study are included in the article/Supplementary Material, further inquiries can be directed to the corresponding authors.

ETHICS STATEMENT

The animal study was reviewed and approved by the Wenzhou Medical University.

AUTHOR CONTRIBUTIONS

LX: Writing original draft; Conceptualization; Data curation; Formal analysis; revise; YL: Writing original draft;

Conceptualization; Data curation; Formal analysis; revise; HY: Investigation; Methodology; Resources; Supervision; revise; TW: Visualization; Writing original draft; FX: Investigation; Methodology; Resources; Supervision; revise; SL: Investigation; Methodology; Resources; Supervision; revise, Writing original draft; PL: Project administration; Resources; Supervision; Writing review and editing; Validation; revise; ST: Project administration;

Resources; Software; Supervision; Writing review and editing; Validation; revise.

ACKNOWLEDGMENTS

We would like to acknowledge Xuemei Ye for her help.

REFERENCES

- Ali, M., Raslan, M., Ciebiera, M., Zaręba, K., and Al-Hendy, A. (2021). Current Approaches to Overcome the Side Effects of GnRH Analogs in the Treatment of Patients with Uterine Fibroids. *Expert Opin. Drug Saf.* 21, 477–486. doi:10.1080/14740338.2022.1989409
- As-Sanie, S., Black, R., Giudice, L. C., Gray Valbrun, T., Gupta, J., Jones, B., et al. (2019). Assessing Research Gaps and Unmet Needs in Endometriosis. *Am. J. Obstet. Gynecol.* 221, 86–94. doi:10.1016/j.ajog.2019.02.033
- Baird, D. D., and Harmon, Q. E. (2021). Relugolix - New Treatment for Uterine Fibroid-Related Heavy Bleeding. *Nat. Rev. Endocrinol.* 17, 321–322. doi:10.1038/s41574-021-00493-2
- Berlanda, N., Somigliana, E., Viganò, P., and Vercellini, P. (2016). Safety of Medical Treatments for Endometriosis. *Expert Opin. Drug Saf.* 15, 21–30. doi:10.1517/14740338.2016.1121991
- Chaichian, S., Kabir, A., Mehdizadehkashi, A., Rahmani, K., Moghimi, M., and Moazzami, B. (2017). Comparing the Efficacy of Surgery and Medical Therapy for Pain Management in Endometriosis: A Systematic Review and Meta-Analysis. *Pain Physician* 20, 185–195.
- Chen, H. C., Wu, C., and Wu, K. Y. (2015). Determination of the Maleic Acid in Rat Urine and Serum Samples by Isotope Dilution-Liquid Chromatography-Tandem Mass Spectrometry with On-Line Solid Phase Extraction. *Talanta* 136, 9–14. doi:10.1016/j.talanta.2014.11.021
- Cherdsawasart, W., and Sutjit, W. (2008). Correlation of Antioxidant Activity and Major Isoflavonoid Contents of the Phytoestrogen-Rich Pueraria Mirifica and Pueraria Lobata Tubers. *Phytomedicine* 15, 38–43. doi:10.1016/j.phymed.2007.07.058
- Dai, Y., Zhou, Y., Zhang, X., Xue, M., Sun, P., Leng, J., et al. (2018). Factors Associated with Deep Infiltrating Endometriosis versus Ovarian Endometrioma in China: A Subgroup Analysis from the FEELING Study. *BMC Womens Health* 18, 205. doi:10.1186/s12905-018-0697-7
- Dearnaley, D. P., Saltzstein, D. R., Sylvester, J. E., Karsh, L., Mehlhaff, B. A., Pieczonka, C., et al. (2020). The Oral Gonadotropin-Releasing Hormone Receptor Antagonist Relugolix as Neoadjuvant/Adjuvant Androgen Deprivation Therapy to External Beam Radiotherapy in Patients with Localised Intermediate-Risk Prostate Cancer: A Randomised, Open-Label, Parallel-Group Phase 2 Trial. *Eur. Urol.* 78, 184–192. doi:10.1016/j.eururo.2020.03.001
- Dunselman, G. A., Vermeulen, N., Becker, C., Calhaz-Jorge, C., D'hooghe, T., De Bie, B., et al. (2014). ESHRE Guideline: Management of Women with Endometriosis. *Hum. Reprod.* 29, 400–412. doi:10.1093/humrep/det457
- Feng, X., Ding, Y., Zhang, P., Fu, Q., Zhang, L., and Zheng, H. (2021). Simultaneous Determination of Dacomitinib and its Major Metabolite, O-Desmethyl Dacomitinib in Human Plasma by LC-MS/MS and its Application to Clinical Testing in Patients with Non-small Cell Lung Cancer. *J. Chromatogr. B Anal. Technol. Biomed. Life Sci.* 1182, 122940. doi:10.1016/j.jchromb.2021.122940
- Gezer, A., and Oral, E. (2015). Progestin Therapy in Endometriosis. *Womens Health (Lond)* 11, 643–652. doi:10.2217/whe.15.42
- Havsteen, B. (1983). Flavonoids, a Class of Natural Products of High Pharmacological Potency. *Biochem. Pharmacol.* 32, 1141–1148. doi:10.1016/0006-2952(83)90262-9
- Jena, R. (2020 Oct-Dec). Relugolix - The Novel Oral Androgen Deprivation Therapy for Prostate Cancer. *Indian J. Urol.* 36, 327–328. doi:10.4103/iju.IJU_362_20
- Kopečná-Zapletalová, M., Krasulová, K., Hodek, P., Anzenbacherová, P., and Anzenbacherová, E. (2017). Interaction of Isoflavonoids with Human Liver Microsomal Cytochromes P450: Inhibition of CYP Enzyme Activities. *Xenobiotica* 47, 324–331. doi:10.1080/00498254.2016.1195028
- Leppert, P. C., Al-Hendy, A., Baird, D. D., Bulun, S., Catherino, W., Dixon, D., et al. (2021). Summary of the Proceedings of the Basic Science of Uterine Fibroids Meeting: New Developments February 28, 2020. *F. S. Sci.* 2, 88–100. doi:10.1016/j.xfss.2020.11.001
- Lewis, T. D., Malik, M., Britten, J., San Pablo, A. M., and Catherino, W. H. (2018). A Comprehensive Review of the Pharmacologic Management of Uterine Leiomyoma. *BioMed. Res. Int.* 2018, 1–11. doi:10.1155/2018/2414609
- Liu, Z., Yu, W., Zhang, H., Gu, F., and Jin, X. (2016). Salting-Out Homogenous Extraction Followed by Ionic Liquid/Ionic Liquid Liquid-Liquid Micro-Extraction for Determination of Sulfonamides in Blood by High Performance Liquid Chromatography. *Talanta* 161, 748–754. doi:10.1016/j.talanta.2016.09.006
- Markham, A., and Keam, S. J. (2019). Camrelizumab: First Global Approval. *Drugs* 79, 1355–1361. doi:10.1007/s40265-019-01105-010.1007/s40265-019-01167-0
- Miadoková, E. (2009). Isoflavonoids - An Overview of Their Biological Activities and Potential Health Benefits. *Interdiscip. Toxicol.* 2, 211–218. doi:10.2478/v10102-009-0021-3
- Osuga, Y., Seki, Y., Tanimoto, M., Kusumoto, T., Kudou, K., and Terakawa, N. (2021). Relugolix, an Oral Gonadotropin-Releasing Hormone Receptor Antagonist, Reduces Endometriosis-Associated Pain in a Dose-Response Manner: A Randomized, Double-Blind, Placebo-Controlled Study. *Fertil. Steril.* 115, 397–405. doi:10.1016/j.fertnstert.2020.07.055
- Parker, W. H. (2007). Etiology, Symptomatology, and Diagnosis of Uterine Myomas. *Fertil. Steril.* 87, 725–736. doi:10.1016/j.fertnstert.2007.01.093
- Pohl, O., Marchand, L., Bell, D., and Gotteland, J. P. (2020). Effects of Combined GnRH Receptor Antagonist Linzagolix and Hormonal Add-Back Therapy on Vaginal Bleeding-Delayed Add-Back Onset Does Not Improve Bleeding Pattern. *Reprod. Sci.* 27, 988–995. doi:10.1007/s43032-020-00172-z
- Rafique, S., and Decherney, A. H. (2017). Medical Management of Endometriosis. *Clin. Obstet. Gynecol.* 60, 485–496. doi:10.1097/GRF.0000000000000292
- Relugolix (2021). Relugolix, Estradiol, and Norethindrone Acetate. *Am. J. Health Syst. Pharm.* 78, 1755–1760. doi:10.1093/ajhp/zxab268
- Sarria-Santamera, A., Orazumbekova, B., Terzic, M., Issanov, A., Chaowen, C., and Asúnsolo-del-Barco, A. (2020). Systematic Review and Meta-Analysis of Incidence and Prevalence of Endometriosis. *Healthcare* 9, 29. doi:10.3390/healthcare9010029
- Schlaff, W. D., Ackerman, R. T., Al-Hendy, A., Archer, D. F., Barnhart, K. T., Bradley, L. D., et al. (2020). Elagolix for Heavy Menstrual Bleeding in Women with Uterine Fibroids. *N. Engl. J. Med.* 382, 328–340. doi:10.1056/NEJMoa1904351
- Stewart, E. A., Laughlin-Tommaso, S. K., Catherino, W. H., Lalitkumar, S., Gupta, D., and Vollenhoven, B. (2016). Uterine Fibroids. *Nat. Rev. Dis. Prim.* 2, 16043. doi:10.1038/nrdp.2016.43
- Teresinski, L., Sipak, O., Ryl, A., Masiuk, M., Rotter, I., Ratajczak, W., et al. (2019). Assessment of Morphological Changes and Steroid Receptors in the Uteri of Postmenopausal Women. *Histol. Histopathol.* 34, 631–644. doi:10.14670/HH-18-063
- Toktay, E., Selli, J., Gurbuz, M. A., Tastan, T. B., Ugan, R. A., Un, H., et al. (2020). Effects of Soy Isoflavonoids (Genistein and Daidzein) on Endometrial Receptivity. *Iran. J. Basic Med. Sci.* 23, 1603–1609. doi:10.22038/ijbms.2020.48294.11089

- Tomai, P., Gentili, A., Curini, R., Gottardo, R., Franco Tagliaro, T., and Fanali, S. (2021). Dispersive Liquid-Liquid Microextraction, an Effective Tool for the Determination of Synthetic Cannabinoids in Oral Fluid by Liquid Chromatography-Tandem Mass Spectrometry. *J. Pharm. Anal.* 11, 292–298. doi:10.1016/j.jppha.2020.11.004
- Uimari, O., Järvelä, I., and Ryyänen, M. (2011). Do Symptomatic Endometriosis and Uterine Fibroids Appear Together? *J. Hum. Reprod. Sci.* 4, 34–38. doi:10.4103/0974-1208.82358
- Yadav, G., Rao, M., Gothwal, M., Singh, P., Kathuria, P., and Sharma, P. P. (2021). Detection of Nerve Fibers in the Eutopic Endometrium of Women with Endometriosis, Uterine Fibroids and Adenomyosis. *Obstet. Gynecol. Sci.* 64, 454–461. doi:10.5468/ogs.21114
- Yao, X., Stewart, E. A., Laughlin-Tommaso, S. K., Heien, H. C., and Borah, B. J. (2017). Medical Therapies for Heavy Menstrual Bleeding in Women with Uterine Fibroids: A Retrospective Analysis of a Large Commercially Insured Population in the USA. *BJOG* 124, 322–330. doi:10.1111/1471-0528.14383
- Zannoni, L., Del Forno, S., Raimondo, D., Arena, A., Giaquinto, I., Paradisi, R., et al. (2020). Adenomyosis and Endometriosis in Adolescents and Young Women with Pelvic Pain: Prevalence and Risk Factors. *Minerva Pediatr.* 2020. doi:10.23736/S0026-4946.20.05842-9
- Zhao, M., Chen, Y., Yang, D., Lyu, C., Bian, X., Li, X., et al. (2021). Regulatory Utility of Pharmacometrics in the Development and Evaluation of Antimicrobial Agents and its Recent Progress in China. *CPT. Pharmacom. Syst. Pharma.* 10, 1466–1478. doi:10.1002/psp4.12716
- Conflict of Interest:** The authors declare that the research was conducted in the absence of any commercial or financial relationships that could be construed as a potential conflict of interest.
- Publisher's Note:** All claims expressed in this article are solely those of the authors and do not necessarily represent those of their affiliated organizations, or those of the publisher, the editors and the reviewers. Any product that may be evaluated in this article, or claim that may be made by its manufacturer, is not guaranteed or endorsed by the publisher.
- Copyright © 2022 Xing, Liu, Yao, Wang, Xie, Luo, Luo and Tang. This is an open-access article distributed under the terms of the Creative Commons Attribution License (CC BY). The use, distribution or reproduction in other forums is permitted, provided the original author(s) and the copyright owner(s) are credited and that the original publication in this journal is cited, in accordance with accepted academic practice. No use, distribution or reproduction is permitted which does not comply with these terms.



Population Pharmacokinetics and Dosing Regimen of Lithium in Chinese Patients With Bipolar Disorder

Zi-bin Jin^{1†}, Zhuo Wu^{2†}, Yi-fan Cui^{3,4}, Xue-peng Liu¹, Hong-bo Liang¹, Jia-yong You⁵ and Chen-yu Wang^{3*}

¹Department of Medical Psychology, The Affiliated Xuzhou Eastern Hospital of Xuzhou Medical University, Xuzhou, China, ²Department of Pharmacy, Huashan Hospital, Fudan University, Shanghai, China, ³Department of Pharmacy, Shanghai Chest Hospital, Shanghai Jiao Tong University, Shanghai, China, ⁴School of Basic Medicine and Clinical Pharmacy, China Pharmaceutical University, Nanjing, China, ⁵Department of Medical Service, Xuzhou Civil Affairs Psychiatric Hospital, Xuzhou, China

OPEN ACCESS

Edited by:

Ren-ai Xu,

First Affiliated Hospital of Wenzhou Medical University, China

Reviewed by:

Weng Qing Hua,

Wenzhou People's Hospital, China

Martin Šima,

Charles University, Czechia

*Correspondence:

Chen-yu Wang

378990110@qq.com

orcid.org/0000-0003-1808-361X

[†]These authors have contributed equally to this work and share first authorship

Specialty section:

This article was submitted to Drug Metabolism and Transport, a section of the journal Frontiers in Pharmacology

Received: 06 April 2022

Accepted: 23 May 2022

Published: 04 July 2022

Citation:

Jin Z-b, Wu Z, Cui Y-f, Liu X-p, Liang H-b, You J-y and Wang C-y (2022) Population Pharmacokinetics and Dosing Regimen of Lithium in Chinese Patients With Bipolar Disorder. *Front. Pharmacol.* 13:913935. doi: 10.3389/fphar.2022.913935

Background: Lithium is an effective medication approved for the treatment of bipolar disorder (BD). It has a narrow therapeutic index (TI) and requires therapeutic drug monitoring. This study aimed to conduct a population pharmacokinetics (PPK) analysis of lithium and investigate the appropriateness of the dosing regimen according to different patient characteristics.

Methods: A total of 476 lithium concentrations from 268 patients with bipolar disorder were analyzed using nonlinear mixed-effects modeling. Monte Carlo simulations were employed to investigate the influence of covariates, such as weight, creatinine clearance, and daily doses of lithium concentrations, and to determine the individualized dosing regimens for patients.

Results: Lithium PK was described by a one-compartment model with first-order absorption and elimination processes. The typical estimated apparent clearance was 0.909 L/h^{-1} with 16.4% between-subject variability in the 62 kg patients with 116 ml/min creatinine clearance and 600 mg daily doses. To achieve a target trough concentration (0.4–0.8 mmol/L) in the maintenance phase, the regimen of 500 mg than 750 mg daily dose was recommended for patients with renal insufficiency and weighing 100 kg.

Conclusion: A PPK model for lithium was developed to determine the influence of patient characteristics on lithium pharmacokinetics. Weight, creatinine clearance, and total daily dose of lithium can affect the drug's clearance. These results demonstrate the nonlinear renal excretion of lithium; hence, dosage adjustments are recommended for patients with renal insufficiency.

Keywords: lithium, bipolar disorder, population pharmacokinetics, Monte Carlo simulation, dosage regimen

1 INTRODUCTION

Lithium is a first-line choice for the treatment of bipolar disorder (BD) for over 60 years (Malhi et al., 2017). Owing to the narrow therapeutic index of lithium and the therapeutic dose reaching drug toxicity, serum levels of lithium should be closely monitored during treatment (Yatham et al., 2018). Usually, 0.4 mmol/L is the minimum effective lithium concentration for bipolar disorder (Severus et al., 2008). Some patients experiencing acute manic phase episodes may need concentrations as high as 0.6–1.2 mmol/L. However, the range can be changed according to patients' outcomes (Grandjean and Aubry, 2009).

After oral administration, lithium is completely absorbed in the upper gastrointestinal tract. *In vivo*, lithium ions do not bind to plasma proteins and are unevenly distributed throughout the body. In addition, lithium is not metabolized and is primarily excreted in the urine in its original form (Ward et al., 1994). Eighty percent of lithium is reabsorbed by passive diffusion at the renal tubules after it is filtered by the glomerulus, which may cause nonlinearity in the fractional excretion of lithium when the transporter is supersaturated (Price and Heninger, 1994).

With the rapid development of pharmacokinetics and computational modelling, population pharmacokinetics (PPK) has been widely used in the monitoring of clinical drug treatments and the optimization of personalized drug administration. Methaneethorn et al. investigated the influence of body weight and age on lithium clearance in a PPK analysis including 222 Thai patients with acute mania (Methaneethorn and Sringam, 2019). They reported that lithium clearance decreased as age increased in patients with equal body weight. In 52 children with intellectual disability aged 4–10 years old, Yuan et al. found that the lithium concentration over time was adequately described by a two-compartment model, with a transient absorption and first-order elimination process (Yuan et al., 2021). The inclusion of body weight as an allometric factor significantly improved the model fit, while age and sex were not associated with PKs of lithium. Yu et al. studied lithium carbonate PPK in 20 healthy young male Chinese volunteers; no covariate was retained in the final model because of the narrow distribution of demographic and biological variables (Yu et al., 2016). This limits the usefulness of this model in predicting the PK of lithium carbonate in the elderly. The effectiveness and accuracy of this model in predicting the PK of lithium carbonate in patients also needs to be further validated. To date, the PPK model is insufficient in the Chinese adult population with bipolar disorder, and the influence of disease physiological factors on the pharmacokinetics and pharmacodynamics of this population requires further investigation.

In this study, by using NONMEM and Monte Carlo, we attempted to establish a PPK model of lithium carbonate in patients with bipolar disorder, investigate the influence of covariates on drug concentration in the blood, and establish dosage recommendations for the personalized use of lithium carbonate in this population.

2 MATERIALS AND METHODS

2.1 Population Pharmacokinetic Data

Chinese patients with bipolar disorder who received lithium carbonate between September 2016 and August 2021 at the Affiliated Xuzhou Eastern Hospital of Xuzhou Medical University were pooled to conduct this PPK analysis. The inclusion criteria were: 1) patients diagnosed with bipolar disorder; 2) patients on maintenance treatment of lithium; and 3) at least one corresponding lithium concentration sample. The exclusion criteria were as follows: 1) the use of any medication that might have clinically important interactions with lithium, such as diuretics, renin-angiotensin system antagonists, or serotonergic drugs (LITHIUM, 2020); and 2) a history of allergies or adverse reactions to lithium. This study was approved by the ethics committee of the Affiliated Xuzhou Eastern Hospital of Xuzhou Medical University (No. 20210928004). All the patients were exempt from informed consent for the research project as it does not involve personal privacy and commercial interests.

Serum lithium levels were measured before the morning dose and assessed using a phosphatase assay with the ADVIA 1800 clinical chemistry analyzer (Siemens Healthcare GmbH, Germany). The experimental procedures were performed in accordance with the manufacturer's instructions. The calibration range of this method was 0.19–3.0 mmol/L. If the proportion of samples which are below the limit of quantification in the entire dataset is less than 10%, these samples were ignored. (Byon et al., 2013).

The following information was collected from each patient: age, weight (WT), sex, white blood cells (WBC), red blood cells (RBC), hematocrit (HCT), platelet count (PLT), albumin, alanine aminotransferase (ALT), aspartate aminotransferase (AST), blood urea nitrogen (BUN), total bilirubin (TBIL), serum creatinine (SCR), creatinine clearance (CRCL), and total daily dose (TDD). Referring to guidance in population modeling, if the missing covariates were less than 10%, the missing values were imputed using the median for continuous covariates (Byon et al., 2013).

2.2 Population Pharmacokinetic Analyses

Nonlinear mixed-effects modeling software (NONMEM, version 7.4.2, ICON Development Solutions, MD, United States) was used to develop a population PK model using first-order conditional estimation with interaction. NONMEM output was analyzed using Perl-speaks-NONMEM (PSN, version 4.7.0, Department of Pharmaceutical Biosciences, Uppsala University, Sweden) and R (version 3.4.1, R Foundation for Statistical Computing, Vienna, Austria).

2.2.1 Base Model

As only trough concentrations were collected in this population PK analysis, a one-compartment model with first-order absorption and elimination was used to describe the PK of lithium. The PK model was parameterized in terms of apparent clearance (CL/F) and apparent volume of distribution (V/F). The absorption rate constant (Ka) was

TABLE 1 | Demographic and characteristics of patients.

Covariate	Median (min-max)	Mean \pm SD
Number of patients	268 (100%)	
Number of PK Samples	476 (100%)	
Sex		
Male (%)	89 (33.2%)	
Female (%)	179 (66.8%)	
Age group		
Adult (%)	241 (89.9%)	
Child (%)	27 (10.1%)	
Dosage form		
Ordinary tablet	64 (23.9%)	
Sustained release tablet	204 (76.1%)	
Age (years)	31.0 (13.0–77.0)	35.0 \pm 14.5
Weight (kg)	62.0 (35.0–110)	63.7 \pm 11.1
Total daily dose (mg)	600 (150–1,500)	720 \pm 236
WBC ($10^9/L$)	7.03 (2.86–16.5)	7.32 \pm 2.25
RBC ($10^{12}/L$)	4.43 (2.88–10.2)	4.52 \pm 0.734
Hematocrit (%)	40.7 (29.5–52.8)	40.7 \pm 4.7
PLT ($10^9/L$)	232 (60.0–734)	236 \pm 70.8
Albumin (g/L)	41.9 (33.3–68.0)	42.2 \pm 3.66
TBIL ($\mu\text{mol/L}$)	9.40 (2.62–34.5)	10.3 \pm 4.9
AST (U/L)	19.0 (6.00–303)	23.4 \pm 20.5
ALT (U/L)	20.0 (5.00–298)	27.1 \pm 27.5
BUN (mmol/L)	3.88 (1.29–13.5)	4.09 \pm 1.35
SCR ($\mu\text{mol/L}$)	62.0 (40.0–115)	63.7 \pm 12.6
CRCL (ml/min)*	116 (61.7–226)	118 \pm 30.3

*CRCL = [(140-Age) \times weight (kg)]/[0.818 \times Scr($\mu\text{mol/L}$)] \times k, where k is 1 for male and 0.85 for female.

ALT, alanine aminotransferase; AST, aspartate aminotransferase; BUN, blood urea nitrogen; CRCL, creatinine clearance rate; PLT, platelet count; RBC, red blood cell; SCR, serum creatinine; TBIL, total bilirubin; WBC, white blood cells.

fixed at 0.293 h⁻¹ based on published data because no sampling was collected during the absorption phase.

An exponential model was chosen to describe between-subject variability (BSV) (Ahamadi et al., 2019):

$$P_i = P_{TV} \times e^{(\eta_i)} \quad (1)$$

where P_i represents the parameter of the i th individual, P_{TV} is the typical value of the population parameter, and η_i is the BSV for the i th individual with a mean of zero and variance of ω^2 .

A proportional, additive or a combination model was used to describe the residual variability:

$$C_i = C_{pred} \times (1 + \varepsilon_1) \quad (2)$$

$$C_i = C_{pred} + \varepsilon_2 \quad (3)$$

$$C_i = C_{pred} \times (1 + \varepsilon_1) + \varepsilon_2 \quad (4)$$

where C_i is the observed concentration of the i th individual, C_{pred} is the individual predicted concentration, ε_1 and ε_2 are proportional and additive portions of residual variability. Both ε_1 and ε_2 are normally distributed with a mean of zero and variance σ^2 , respectively.

Based on the changes of object function value (OFV), parameter rationality, condition number, and plots of goodness-of-fit, base model selection was conducted (Donohue et al., 2011).

2.2.2 Covariate Model

The covariate analysis was conducted using a three-step approach (Byon et al., 2013). In the first step, a graphical display of the correlation between the random effects of PK parameters and covariates was evaluated to explore the sources of variability. Only covariates of interest were used in the next step. Secondly, stepwise forward inclusion selection was evaluated. Statistically significant covariates were determined with a decrease of OFV by > 3.84 ($p < 0.05$). Finally, a stepwise backward elimination process was initiated. The covariate was temporarily removed with an increase of OFV by < 6.63 ($p > 0.01$).

Relationships between potential covariates and parameters were explored using linear additive and power functions for the continuous covariates (Eqs 5, 6), and categorical covariates (Eq. 7) (Mandema et al., 1992):

$$P_i = P_{TV} \times \left(1 + \theta \times \frac{Cov_i}{Cov_{median}} \right) \quad (5)$$

$$P_i = P_{TV} \times \left(\frac{Cov_i}{Cov_{median}} \right)^\theta \quad (6)$$

$$P_i = P_{TV} \times (1 + \theta^{Cov_i}) \quad (7)$$

where P_i represents the parameter for the i th individual, P_{TV} is the typical value of the parameter, Cov_i is the covariate value of

TABLE 2 | Population-pharmacokinetic parameter estimates and bootstrap evaluation.

Parameters	Base model		Final model		
	Parameter estimates (RSE%)	Shrinkage (%)	Parameter estimates (RSE%)	Shrinkage (%)	Bootstrap median (2.5%–97.5%)
CL (L/h)	0.969 (4)		0.909 (3)		0.906 (0.855–0.954)
V(L)	9.27 (16)		10.9 (12)		10.8 (8.0–13.4)
Ka (h ⁻¹)	0.293 [fixed]		0.293 [fixed]		0.293 [fixed]
WT on CL	—		0.33 (29)		0.330 (0.134–0.520)
CRCL on CL	—		0.186 (29)		0.184 (0.075–0.291)
TDD on CL	—		0.354 (12)		0.351 (0.267–0.435)
Between subject variability					
CL (%)	20.8 (9)	24	16.4 (10)	30	16.1 (12.8–19.5)
V(%)	40.4 (21)	63	40.2 (20)	62	39.4 (16.0–52.6)
Residual variability					
Additive error (mmol/L)	0.0236 (14)	22	0.0218 (13)	20	0.0216 (0.0166–0.0274)

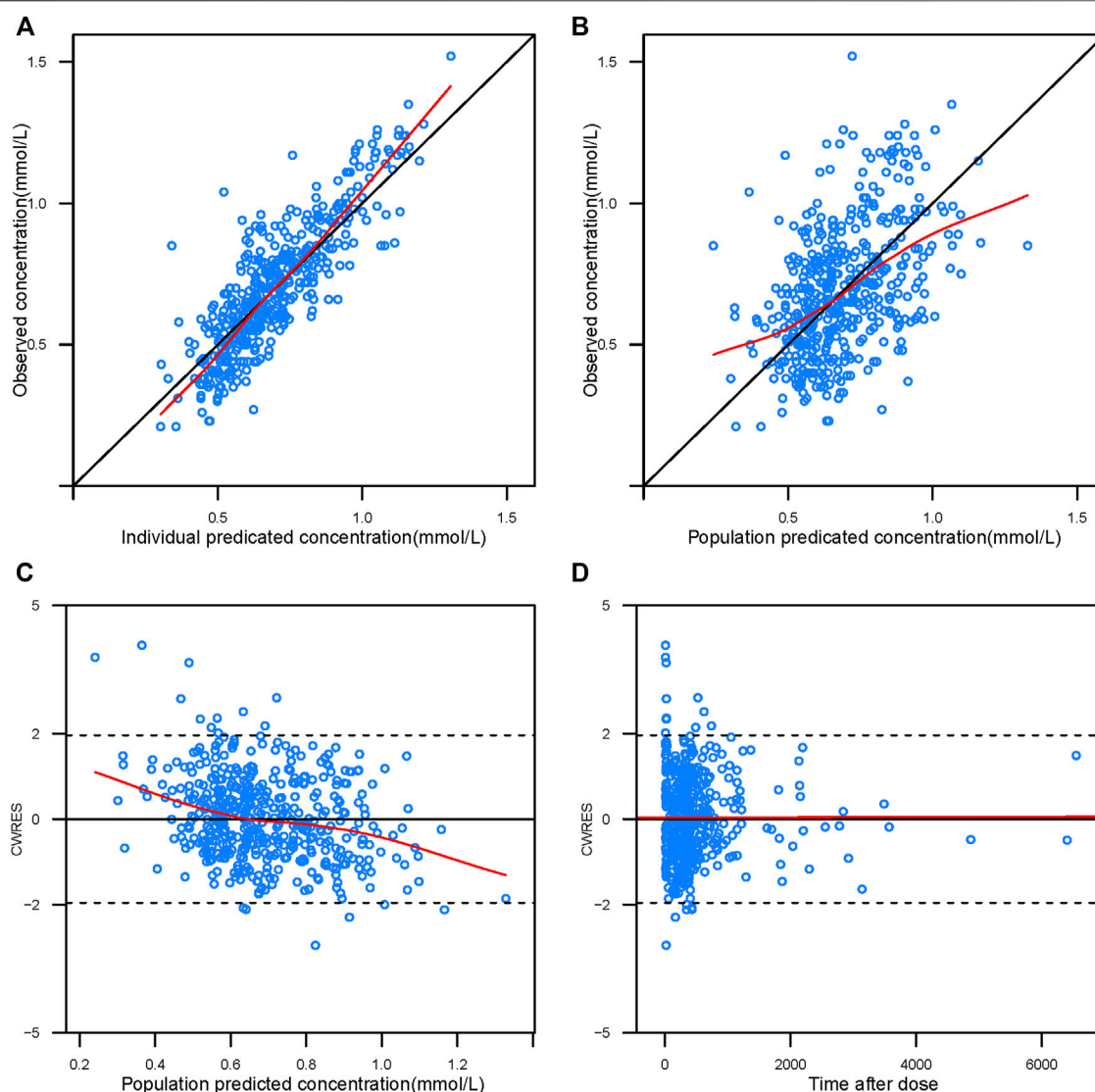


FIGURE 1 | Goodness-of-fit plots of the final population-pharmacokinetic model. The upper left plot represents the observations versus the population predictions (A). The upper right plot represents the observations versus the individual predictions (B). The lower left plot represents the conditional weighted residuals versus the population predictions (C). The lower right plot represents the conditional weighted residuals versus the time after dose (D). The red line represents the locally weighted scatterplot smoothing line.

the i th individual, Cov_{median} is the median value of the continuous covariate and θ is the coefficient term of the covariate effect to be estimated.

2.3 Model Evaluation

Goodness-of-fit plots were used to evaluate the fitness of the final model to the data. Scatterplots were used to evaluate observed concentration (DV) versus population predicted concentration (PRED), DV versus individual predicted concentrations (IPRED), conditional weighted residuals (CWRES) versus PRED and CWRES versus time.

The model was also evaluated internally using a bootstrap analysis (Ette et al., 2003). During the bootstrap process, each parameter was evaluated repeatedly by applying the final model to

1,000 bootstrapped datasets. The 2.5th, 50th, and 97.5th percentiles of the population PK parameter values from bootstrap datasets were compared with those from the final model.

To evaluate the predictive performance of the final model, a visual predictive check (VPC) was stratified to compare the observed concentrations and model predictions. The VPC approach was conducted by simulating 1,000 datasets from the final model and comparing the observed data with the simulated data.

2.4 Model-Based Simulation

Monte Carlo simulations were performed to predict the trough concentration after 7-day multiple oral doses of different dosing regimens based on the final population PK model. The daily dose

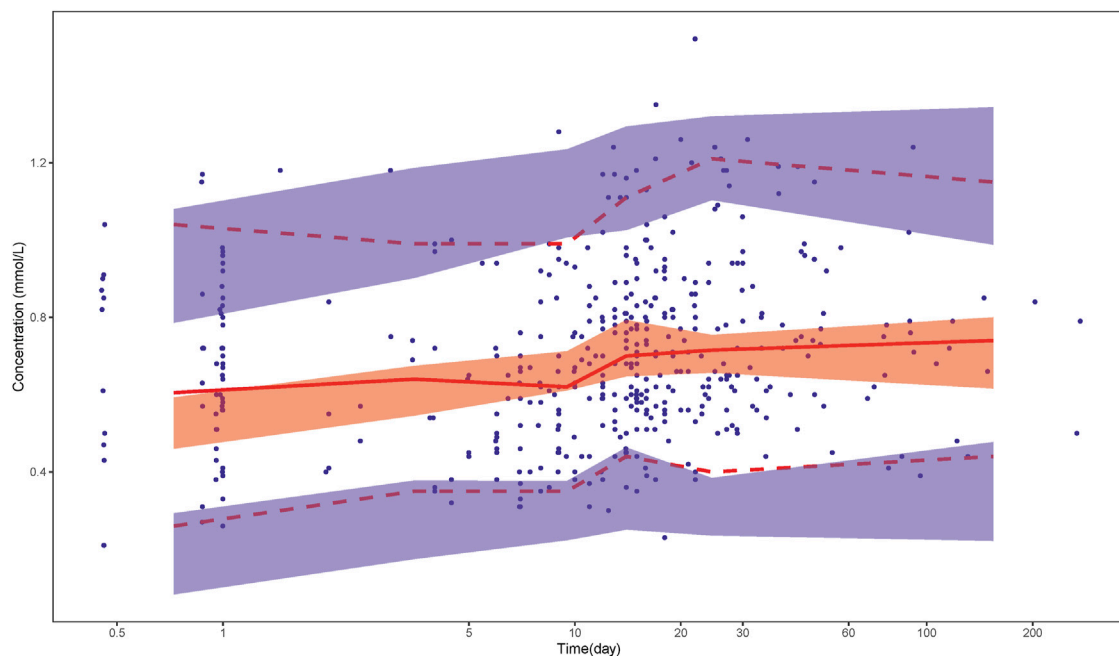


FIGURE 2 | Visual predictive check. Solid dots represent observed data. Lines represent the 5% (dashed), 50% (solid), and 95% (dashed) percentiles of the observed data. Shaded areas represent nonparametric 95% confidence intervals about the 5% (light blue), 50% (light red), and 95% (light blue) percentiles of the predicted concentrations.

of lithium carbonate was simulated from 250 to 1,000 mg. One thousand simulations were performed using the initial dataset, and the steady-state trough concentrations of each simulated subject were calculated.

3 RESULTS

3.1 Demographics

A total of 476 plasma lithium measurements obtained from 268 patients were used for pharmacokinetic analysis. The baseline demographic and general clinical information of the patients used for model building is summarized in **Table 1**. The proportion of women and men in this study was 66.8 and 33.2%, respectively. The median age was 31.0 (13.0–77.0) years, and 89.9% of them were adults (age > 16 years). The median weight and daily lithium dose used in the population were 62.0 (35.0–110) kg and 600 (150–1,500) mg, respectively. The mean creatinine clearance rate was 118 ml/min, ranging from 61.7 to 226 ml/min.

3.2 Population Pharmacokinetic Model

The random effects of CL/F were significantly correlated with weight, creatinine clearance, daily lithium dose, and sex by analyzing the correlation diagram. Therefore, the influence of these covariates on the CL/F ratio was tested using a stepwise approach. We observed a statistically significant drop in OFV (70.12) during the covariate screening of daily dose. The decrease in OFV was also greater than 3.84 after we included weight and creatinine clearance in the final model. However, the addition of sex did not meet the criteria for

statistical significance ($p < 0.05$). No covariates were removed during backward elimination ($p < 0.01$). The final pharmacokinetic parameters of lithium are listed in **Table 2** and **Eqs 8–10**:

$$CL/F (L/h) = 0.909 \times (TDD/600)^{0.354} \times (WT/62)^{0.33}$$

$$\times (CRCL/116)^{0.186} \times e^{0.027} \quad (8)$$

$$V/F (L) = 10.9 \times e^{0.162} \quad (9)$$

$$K_a (h^{-1}) = 0.293 (FIX) \quad (10)$$

3.3 Model Evaluation

The goodness-of-fit plots of the final model are shown in **Figure 1**. The population and individual prediction values of the final model were evenly distributed on both sides of the reference line (**Figures 1A, B**). CWRES plots illustrating individual predicted concentrations and time after dose are randomly scattered with most CWRES ranging from -2 to $+2$, and the trend line is close to zero (**Figures 1C, D**). In other words, all figures illustrate the good predictive performance of the proposed model.

Additionally, one thousand bootstrap datasets generated by resampling from the original dataset were repeatedly fitted with the final model to estimate the model parameters, yielding 96.5% successful convergence. The estimates from the original models were within the 95% CIs of the bootstrap estimates (**Table 2**), confirming the robustness of the model.

The VPC results (**Figure 2**) show that the observed plasma concentration data mostly fits within the 95% confidence intervals of the 5th, 50th, and 95th percentiles of the simulated data, which

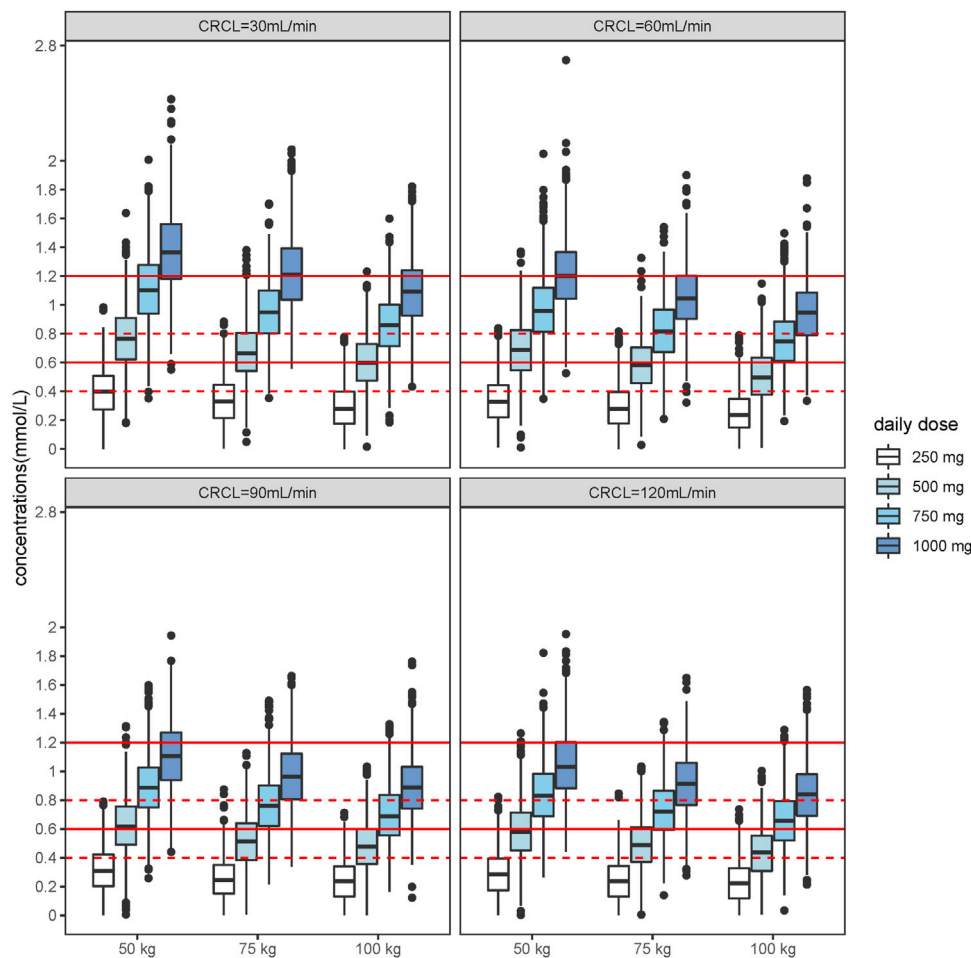


FIGURE 3 | Boxplot of the distributions of simulated steady state trough lithium concentrations for patients with different weight and CRCL levels. Patients with different weight levels from 50, 75, 100 kg, and CRCL levels from 30 ml/min, 60 ml/min, 90 ml/min, 120 ml/min were set for the simulation. Dashed horizontal lines represent the therapeutic target range (0.6–1.2 mmol/L) for the acute phase and point horizontal lines represent the therapeutic target range (0.4–0.8 mmol/L) for maintenance phase.

indicates that the final pharmacokinetic model can adequately describe the observed concentrations.

We performed a sensitivity analysis to determine the effect of fixed K_a on the final model by varying the K_a values within the range of $0.146\text{--}0.586\text{ h}^{-1}$, and the estimated value of CL/F was slightly changed between 0.825 and 0.959 L/h .

3.4 Model-Based Simulation

The lithium steady-state trough concentrations of 1,000 individuals were simulated under different scenarios, including significant covariates based on the final model. The ranges we set were 50–100 kg for weight, 250–1,000 mg for lithium daily dose, and creatinine clearance rate between 30 and 120 ml/min. The simulation results are shown in **Figure 3**.

Appropriate dosage regimens meeting the target lithium concentrations were selected for individualized administration according to the simulation results. During the maintenance

period, a daily dose of 750 mg is recommended for patients weighing 100 kg with normal renal function ($CrCL = 120\text{ ml/min}$). The CL/F of patients would decrease by 23% when their renal function is poor ($CrCL = 30\text{ ml/min}$), presenting a 500 mg daily dose as a better choice for maintenance. Patients need higher doses in the acute phase, and the concentration of lithium is in the effective treatment window of 1,000 mg daily for 100 kg patients with normal renal function. However, a daily dose of 750 mg is recommended for patients with poor renal function during the acute period.

4 DISCUSSION

To the best of our knowledge, this is the first study to report a population PK model of lithium in Chinese patients with bipolar disorder. The PK of lithium was characterized using a one-compartment model with first-order absorption and elimination. WT, CRCL, and TDD were identified as the CL/F

covariates. Our study showed that for a typical 62 kg patient with a CRCL of 116 ml/min receiving a daily lithium dose of 600 mg, the typical CL/F value was estimated to be 0.909 L/h, which is consistent with previous reported clearance between 0.51 to 1.47 L/h (Wing et al., 1997; ElDesoky et al., 2008; Findling et al., 2010; Landersdorfer et al., 2017).

In this population PK study, we found that TDD could be incorporated into the final model as a covariate, indicating nonlinear clearance of the drug in patients with bipolar disorder. In the PPK model conducted by Yuan et al., TDD was also evaluated as a covariate. However, it was not found that TDD could significantly influence the PK parameter of lithium, which may be because only 170 lithium plasma concentrations were included in the analysis (Yuan et al., 2021). In our study, a total number of 476 concentrations were included, which is the largest of all previously reported population PK studies. The CL/F ratio of lithium increased nonlinearly with TDD, which is consistent with the results of Uwai et al. They reported that the infusion of an inhibitor of sodium-phosphate cotransporter decreased the fractional reabsorption of lithium in rats administered 2.5 mg/kg of lithium chloride but did not affect it in rats administered 25 mg/kg (Uwai et al., 2018). These results demonstrate the nonlinearity of renal excretion of lithium. Further research with a larger sample size and intensive sampling will provide a more specific picture of the nonlinear behavior of lithium kinetics.

And the impact of CRCL and WT on the PK of lithium has been previously reported (Jermain et al., 1991; ElDesoky et al., 2008; Perez-Castello et al., 2016; Alqahtani et al., 2020). This is an expected result, as lithium is mainly cleared via the kidney. Lithium is freely filtered through the glomeruli, and protein binding of lithium in the plasma is negligible. In our study, when patients had severe renal insufficiency (CRCL = 30 ml/min), the typical CL/F of lithium decreased by 23%, which was consistent with the results of the Alqahtani group (Alqahtani et al., 2020). Their study in patients with bipolar disorder in Saudi Arabia suggested that the 15% lowering of CL, was attributed to the reduced renal clearance from 120 to 30 ml/min. Similarly, as body weight increases, renal blood flow and lithium clearance decrease. As the weight levels increased from 50 to 100 kg, the CL increased by 28% from 0.83 L/h to 1.06 L/h.

To guide therapeutic dosing of lithium, we added a simulation based on the PK parameters. The acute treatment concentration range is 0.6–1.2 mmol/L for Chinese patients, and the maintenance treatment concentration range is 0.4–0.8 mmol/L. Several conclusions can be drawn from this study. First, lithium concentration can be maintained in the range of 0.4–0.8 mmol/L for 500–750 mg daily and the range of 0.6–1.2 mmol/L for 750–1,000 mg daily in patients with normal renal function. Second, the lithium concentration can be maintained in the range of 0.4–0.8 mmol/L for 500 mg daily and in the range of 0.6–1.2 mmol/L for 500–750 mg daily in patients with poor renal function.

This study had some limitations. First, owing to the retrospective nature of this study, all information may not have been properly controlled. For example, all available concentrations were collected as trough, the K_a parameter was fixed, and V_d/F couldn't be a reliable estimate. Secondly, all samples were from the same hospital. More validations of this model required samples from other hospitals.

CONCLUSION

In summary, we developed a population PK model of lithium in patients with bipolar disorder. Based on the model simulation results, the optimal strategy depends on renal function and weight. We also demonstrated the nonlinearity of the renal excretion of lithium, but further research is required.

DATA AVAILABILITY STATEMENT

The raw data supporting the conclusion of this article will be made available by the authors, without undue reservation.

ETHICS STATEMENT

The studies involving human participants were reviewed and approved by the ethics committee of the Affiliated Xuzhou Eastern Hospital of Xuzhou Medical University. Written informed consent from the participants' legal guardian/next of kin was not required to participate in this study in accordance with the national legislation and the institutional requirements.

AUTHOR CONTRIBUTIONS

Z-BJ: conceptualization, data curation, writing-review and editing; ZW: conceptualization, writing—original draft, writing—review and editing; Y-FC: software, formal analysis, visualization; X-PL and H-BL: data curation, writing—review and editing; J-YY: writing—review and editing; C-YW: methodology, software, formal analysis, writing—original draft, writing—review and editing.

FUNDING

The study was supported by the Shanghai Municipal Health Commission Special Project for Clinical Research in Health Care Industry (No. 202040424) and Shanghai “Rising Stars of Medical Talent” Youth Development Program Clinical Pharmacist Program (SHWRS(2021)_099).

ACKNOWLEDGMENTS

We would like to thank Editage (www.editage.cn) for English language editing.

SUPPLEMENTARY MATERIAL

The Supplementary Material for this article can be found online at: <https://www.frontiersin.org/articles/10.3389/fphar.2022.913935/full#supplementary-material>

REFERENCES

- Ahamadi, M., Largajolli, A., Diderichsen, P. M., de Greef, R., Kerbusch, T., Witjes, H., et al. (2019). Operating Characteristics of Stepwise Covariate Selection in Pharmacometric Modeling. *J. Pharmacokinet. Pharmacodyn.* 46, 273–285. doi:10.1007/s10928-019-09635-6
- Alqahtani, S., Aljuma'ah, N., Aydan, N. B., Alsultan, A., Alsarhani, E., and Asiri, Y. (2020). Estimation of Lithium Clearance in Patients with Bipolar Disorder. *Int. Clin. Psychopharmacol.* 35, 157–162. doi:10.1097/YIC.0000000000000301
- Byon, W., Smith, M. K., Chan, P., Tortorici, M. A., Riley, S., Dai, H., et al. (2013). Establishing Best Practices and Guidance in Population Modeling: an Experience with an Internal Population Pharmacokinetic Analysis Guidance. *CPT Pharmacometrics Syst. Pharmacol.* 2, e51. doi:10.1038/psp.2013.26
- Donohue, M. C., Overholser, R., Xu, R., and Vaida, F. (2011). Conditional Akaike Information under Generalized Linear and Proportional Hazards Mixed Models. *Biometrika* 98, 685–700. doi:10.1093/biomet/asr023
- ElDesoky, E. S., Kumar, V., Alorainy, M. S., Hamdi, M. M., and Derendorf, H. (2008). Estimation of Lithium Clearance from Routine Clinical Data in Egyptian Bipolar Patients. A Population Pharmacokinetic Approach. *Int. J. Clin. Pharmacol. Ther.* 46, 617–626. doi:10.5414/cpp46617
- Ette, E. I., Williams, P. J., Kim, Y. H., Lane, J. R., Liu, M. J., and Capparelli, E. V. (2003). Model Appropriateness and Population Pharmacokinetic Modeling. *J. Clin. Pharmacol.* 43, 610–623. doi:10.1177/0091270003253624
- Findling, R. L., Landersdorfer, C. B., Kafantaris, V., Pavuluri, M., McNamara, N. K., McClellan, J., et al. (2010). First-dose Pharmacokinetics of Lithium Carbonate in Children and Adolescents. *J. Clin. Psychopharmacol.* 30 (4), 404–410. doi:10.1097/JCP.0b013e3181e66a62
- Grandjean, E. M., and Aubry, J. M. (2009). Lithium: Updated Human Knowledge Using an Evidence-Based Approach. Part II: Clinical Pharmacology and Therapeutic Monitoring. *CNS drugs* 23, 331–349. doi:10.2165/00023210-200923040-00005
- Jermain, D. M., Crismon, M. L., and Martin, E. S., 3rd (1991). Population Pharmacokinetics of Lithium. *Clin. Pharm.* 10, 376–381. doi:10.3389/fphar.2021.650298
- Landersdorfer, C. B., Findling, R. L., Frazier, J. A., Kafantaris, V., and Kirkpatrick, C. M. (2017). Lithium in Paediatric Patients with Bipolar Disorder: Implications for Selection of Dosage Regimens via Population Pharmacokinetics/pharmacodynamics. *Clin. Pharmacokinet.* 56 (1), 77–90. doi:10.1007/s40262-016-0430-3
- LITHIUM CARBONATE [package insert] (2020). Columbus, OH: Hikma Pharmaceuticals USA Inc.
- Malhi, G. S., Gessler, D., and Outhred, T. (2017). The Use of Lithium for the Treatment of Bipolar Disorder: Recommendations from Clinical Practice Guidelines. *J. Affect Disord.* 217, 266–280. doi:10.1016/j.jad.2017.03.052
- Mandema, J. W., Verotta, D., and Sheiner, L. B. (1992). Building Population Pharmacokinetic-Pharmacodynamic Models. I. Models for Covariate Effects. *J. Pharmacokinet. Biopharm.* 20, 511–528. doi:10.1007/BF01061469
- Methaneethorn, J., and Sringam, S. (2019). Factors Influencing Lithium Pharmacokinetics in Patients with Acute Mania: A Population Pharmacokinetic Analysis. *Hum. Psychopharmacol.* 34, e2697. doi:10.1002/hup.2697
- Pérez-Castelló, I., Mangas-Sanjuan, V., González-García, I., Gonzalez-Alvarez, I., Bermejo, M., Marco-Garbayo, J. L., et al. (2016). Population Pharmacokinetic Model of Lithium and Drug Compliance Assessment. *Eur. Neuropsychopharmacol.* 26, 1868–1876. doi:10.1016/j.euroneuro.2016.11.005
- Price, L. H., and Heninger, G. R. (1994). Lithium in the Treatment of Mood Disorders. *N. Engl. J. Med.* 331, 591–598. doi:10.1056/NEJM199409013310907
- Severus, W. E., Kleindienst, N., Seemüller, F., Frangou, S., Möller, H. J., and Greil, W. (2008). What Is the Optimal Serum Lithium Level in the Long-Term Treatment of Bipolar Disorder-Aa Review? *Bipolar Disord.* 10, 231–237. doi:10.1111/j.1399-5618.2007.00475.x
- Uwai, Y., Kawasaki, T., and Nabekura, T. (2018). Nonlinear Disposition of Lithium in Rats and Saturation of its Tubular Reabsorption by the Sodium-Phosphate Cotransporter as a Cause. *Biopharm. Drug Dispos.* 39, 83–87. doi:10.1002/bdd.2116
- Ward, M. E., Musa, M. N., and Bailey, L. (1994). Clinical Pharmacokinetics of Lithium. *J. Clin. Pharmacol.* 34, 280–285. doi:10.1002/j.1552-4604.1994.tb01994.x
- Wing, Y. K., Chan, E., Chan, K., Lee, S., and Shek, C. C. (1997). Lithium Pharmacokinetics in Chinese Manic-Depressive Patients. *J. Clin. Psychopharmacol.* 17, 179–184. doi:10.1097/00004714-199706000-00007
- Yatham, L. N., Kennedy, S. H., Parikh, S. V., Schaffer, A., Bond, D. J., Frey, B. N., et al. (2018). Canadian Network for Mood and Anxiety Treatments (CANMAT) and International Society for Bipolar Disorders (ISBD) 2018 Guidelines for the Management of Patients with Bipolar Disorder. *Bipolar Disord.* 20, 97–170. doi:10.1111/bdi.12609
- Yu, W., Sun, X., Li, Y., Li, M., Wang, K., and Li, H. (2016). Population Pharmacokinetics of Lithium Carbonate in Young Male Healthy Chinese Volunteers. *Pharmacopsychiatry* 49, 177–181. doi:10.1055/s-0042-103329
- Yuan, J., Zhang, B., Xu, Y., Zhang, X., Song, J., Zhou, W., et al. (2021). Population Pharmacokinetics of Lithium in Young Pediatric Patients with Intellectual Disability. *Front. Pharmacol.* 12, 650298. doi:10.3389/fphar.2021.650298

Conflict of Interest: The authors declare that the research was conducted in the absence of any commercial or financial relationships that could be construed as a potential conflict of interest.

Publisher's Note: All claims expressed in this article are solely those of the authors and do not necessarily represent those of their affiliated organizations, or those of the publisher, the editors, and the reviewers. Any product that may be evaluated in this article, or claim that may be made by its manufacturer, is not guaranteed or endorsed by the publisher.

Copyright © 2022 Jin, Wu, Cui, Liu, Liang, You and Wang. This is an open-access article distributed under the terms of the Creative Commons Attribution License (CC BY). The use, distribution or reproduction in other forums is permitted, provided the original author(s) and the copyright owner(s) are credited and that the original publication in this journal is cited, in accordance with accepted academic practice. No use, distribution or reproduction is permitted which does not comply with these terms.



Instability Mechanism of Osimertinib in Plasma and a Solving Strategy in the Pharmacokinetics Study

Zheng Yuan^{1†}, Xin Yu^{1†}, Siyang Wu¹, Xiaonan Wu², Qiutao Wang³, Wenhao Cheng⁴, Weiyu Hu⁵, Chen Kang¹, Wei Yang¹, Yingfei Li^{1*} and Xiao-Yang Zhou^{6*}

¹Center for DMPK Research of Herbal Medicines, Institute of Chinese Materia Medica, China Academy of Chinese Medical Sciences, Beijing, China, ²Department of Oncology, Beijing Hospital, National Center of Gerontology, Institute of Geriatric Medicine, Chinese Academy of Medical Sciences, Beijing, China, ³School of Traditional Chinese Medicine, Shandong University of Traditional Chinese Medicine, Jinan, China, ⁴School of Chinese Pharmacy, Beijing University of Chinese Medicine, Beijing, China, ⁵Department of Hepatobiliary Pancreatic Surgery, The Affiliated Hospital of Qingdao University, Qingdao, China, ⁶The Key Laboratory of Geriatrics, Beijing Institute of Geriatrics, Institute of Geriatric Medicine, Chinese Academy of Medical Sciences, Beijing Hospital/National Center of Gerontology of National Health Commission, Beijing, China

OPEN ACCESS

Edited by:

Sabina Passamonti,
University of Trieste, Italy

Reviewed by:

Hemant Jadhav,
Birla Institute of Technology and
Science, India
Umberto Malapelle,
University of Naples Federico II, Italy

*Correspondence:

Xiao-Yang Zhou
keenall@sina.com
Yingfei Li
yfli@icmm.ac.cn

[†]These authors have contributed
equally to this work

Specialty section:

This article was submitted to
Drug Metabolism and Transport,
a section of the journal
Frontiers in Pharmacology

Received: 26 April 2022

Accepted: 20 June 2022

Published: 22 July 2022

Citation:

Yuan Z, Yu X, Wu S, Wu X, Wang Q,
Cheng W, Hu W, Kang C, Yang W, Li Y
and Zhou X-Y (2022) Instability
Mechanism of Osimertinib in Plasma
and a Solving Strategy in the
Pharmacokinetics Study.
Front. Pharmacol. 13:928983.
doi: 10.3389/fphar.2022.928983

Osimertinib is a third-generation epidermal growth factor receptor tyrosine kinase inhibitor (EGFR-TKI) and a star medication used to treat non-small-cell lung carcinomas (NSCLCs). It has caused broad public concern that osimertinib has relatively low stability in plasma. We explored why osimertinib and its primary metabolites AZ-5104 and AZ-7550 are unstable in rat plasma. Our results suggested that it is the main reason inducing their unstable phenomenon that the Michael addition reaction was putatively produced between the Michael acceptor of osimertinib and the cysteine in the plasma matrix. Consequently, we identified a method to stabilize osimertinib and its metabolite contents in plasma. The assay was observed to enhance the stability of osimertinib, AZ-5104, and AZ-7550 significantly. The validated method was subsequently applied to perform the pharmacokinetic study for osimertinib in rats with the newly established, elegant, and optimized ultra-performance liquid chromatography–tandem mass spectrometer (UPLC-MS/MS) strategy. The assay was assessed for accuracy, precision, matrix effects, recovery, and stability. This study can help understand the pharmacological effects of osimertinib and promote a solution for the similar problem of other Michael acceptor-contained third-generation EGFR-TKI.

Keywords: osimertinib, plasma stability, UPLC-MS/MS, acetonitrile, cysteine, non-small-cell lung cancer

Abbreviations: ACN, Acetonitrile; AR, analytical reagent; DMSO, dimethyl sulfoxide; EGFR-TKI, epidermal growth factor receptor tyrosine kinase inhibitor; EDTA-2Na, ethylenediaminetetraacetic acid disodium salt; FA, formic acid; HQC, high quality control; HS, human serum albumin; IS, inner standard; IPA, isopropanol; Cys, L-cysteine; LLE, liquid–liquid extraction; LLOQ, lower limit of quantitation; LQC, low quality control; MeOH, methanol; MQC, middle quality control; MWCO, molecular weight cut-off; NSCLCs, non-small-cell lung carcinomas; PFS, progression-free survival; RE, relative error; RSD, relative standard deviation; CMC-Na, sodium carboxymethyl cellulose; SD rats, Sprague–Dawley rats; UPLC-MS/MS, ultra-performance liquid chromatography–tandem mass spectrometer.

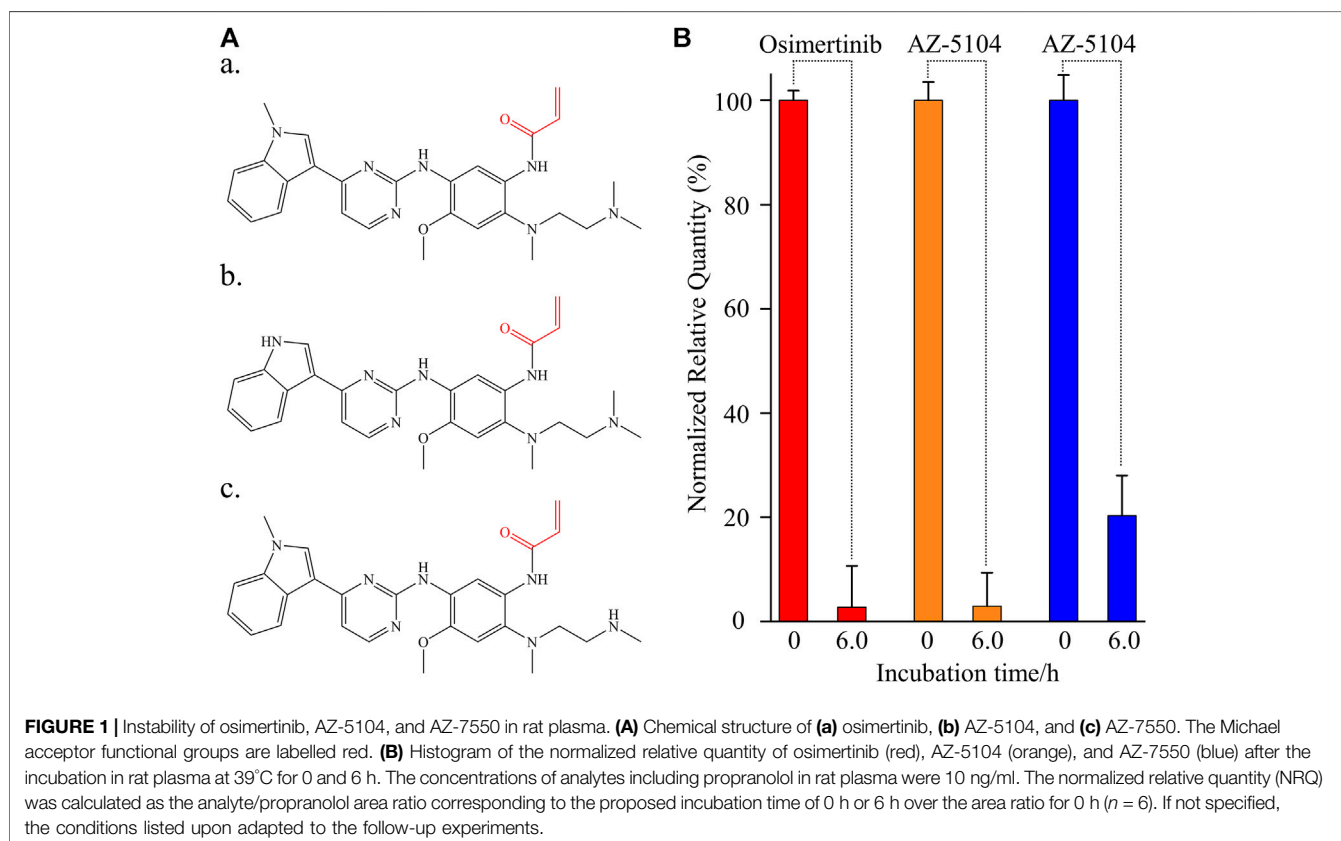
1 INTRODUCTION

Non-small-cell lung cancer (NSCLC) is the largest pulmonary carcinoma subgroup of lung cancer and belongs to the most frequent malignant diseases (Xue et al., 2011; Gridelli et al., 2015). Also, the popular tyrosine kinase inhibitor (TKI) application has been well testified to benefit NSCLC patients with epidermal growth factor receptor (EGFR) mutations (Ke and Wu, 2016; Zhou et al., 2020). Osimertinib is a third-generation EGFR-TKI, selectively inhibits mutated EGFR (e.g., EGFR with exon 19 deletion, L858R, T790M, G719X, L861Q, and S768I), and has recently become the prominent star medicine for treating EGFR-mutated patients reaching a median progression-free survival (PFS) of 18.9 months (Remon et al., 2018; Soria et al., 2018; Cho et al., 2020; Floc'h et al., 2020). In addition, apart from the role of osimertinib as an anticancer drug, it has been found as a promising adjuvant agent to sensitize drug-resistant cancer cells to chemotherapy (Barbuti et al., 2019). Therefore, the analysis of osimertinib and its metabolites may promise better profiling of the distribution of components and enhance the understanding of the pharmacodynamics effects and toxicity of drugs in pre-clinic and clinic trials, and as a result in promoting osimertinib-related new drug research and development.

The osimertinib analysis in the matrix such as human serum, human plasma, human urine, rat plasma, and mouse brain has been constructed through liquid chromatography–tandem mass spectrometric (LC-MS) assay (Ballard et al., 2016; Rood et al., 2016; Irie et al., 2019; Mitchell et al., 2019; Fresnais et al., 2020;

Xiong et al., 2022). However, the instability of osimertinib in plasma and whole blood at an ambient temperature drew attention recently. Rood et al. (2016) measured osimertinib in human plasma (either lithium heparin- or sodium EDTA-treated) stored at -30°C by salting-out assisted liquid–liquid extraction (LLE) using acetonitrile and magnesium sulfate (Rood et al., 2016). However, Veerman et al. (2019) found that the mass response of osimertinib decreased after incubation of plasma with osimertinib, whether at an ambient or higher temperature, thus pointing that both blood and plasma samples should be kept and processed solely on ice. This harsh environment may be uncomfortable for laboratory operators. In addition, Veelen et al. (2020) validated the sample preparation of human plasma containing osimertinib. Even if they pointed out that acidification of serum samples enhanced the stability of osimertinib, a lower temperature under 2°C was needed whether for storing or preparing the samples. A method is severely needed for storing and operating plasma containing osimertinib. Hence, a practical, convenient, and universal approach is urgently required for plasma preparation to keep the stability of osimertinib.

In the perspective of organic chemistry, whether osimertinib or its circulating metabolites, AZ-5104 and AZ-7550, contain the same Michael acceptor responsible for the covalent reaction with the cysteine-797 residue in the ATP-binding site of the EGFR kinase *in vivo* (Figure 1A) (Wu and Shih, 2018; Lategahn et al., 2019; Gao et al., 2022). Coincidentally, Dickinson et al. (2016) found that the



remaining osimertinib decreased in the plasma of mice, rats, dogs or humans at 37°C for 6 h. Significantly, they found that human serum albumin (HSA) contributes to decreasing osimertinib during incubation. To the best of our understanding, serum albumin is the major protein component in mammal plasma (Minchiotti et al., 2008). In addition, we also noticed that the total cysteine concentration in human plasma is as high as 38,650 ng/ml (Wang et al., 2018). The evidence reviewed here suggests that a pertinent role of free or non-free cysteine in plasma may induce the reduction of osimertinib during the related investigation.

This study seeks to understand and explain that cysteine's potential role in plasma may affect the stability of osimertinib, AZ-5104, and AZ-7550 during the storage of plasma samples at room or higher temperatures. A strategy was applied to keep osimertinib stability by directly adding acetonitrile during preparation in plasma. In addition, we studied the oral pharmacokinetic study in five Sprague–Dawley (SD) rats using our newly validated UPLC-MS/MS coupling stability strategy. In general, we successfully set up an available and reliable method to increase osimertinib stability and apply it to the osimertinib pharmacokinetics study in rats.

2 MATERIALS AND METHODS

2.1 Chemicals, Drugs, and Equipment

Osimertinib (purity 99.9%), AZ-5104 (purity 99.7%), and AZ-7550 hydrochloride (purity 99%) standards were purchased from MedChemExpress (Monmouth Junction, NJ, United States). Propranolol was used as inner standard (IS) during UPLC-MS/MS analysis and was bought from Sigma-Aldrich (Dorset, United Kingdom). Acetonitrile (ACN), formic acid (FA), methanol (MeOH), isopropanol (IPA), and dimethyl sulfoxide (DMSO) were all analytical reagents (ARs) provided by Merck (Darmstadt, Germany). L-Cysteine (Cys, 99%) was purchased from Bailingke (Haidian, Beijing, China). A TAGRISSO® (osimertinib) tablet (80 mg) produced by AstraZeneca (United States) was obtained from Beijing Hospital. Sodium carboxymethyl cellulose (CMC-Na) was supplied by Tianjin Chemical Reagent Company (Tianjin, China). 1 × PBS (0.01 M, pH 7.2–7.4, cell culture) was obtained from Solarbio (Beijing, China). Ethylenediaminetetraacetic acid disodium salt (EDTA-2Na) was purchased from National Pharmaceutical Group Chemical Reagent Company (Beijing, China). Male Sprague–Dawley (SD) rats (weighed 180–200 g) were provided by Beijing Vital River Laboratory Animal Technology Co., Ltd. (Beijing, China). All solutions were prepared using a Milli-Q system (Millipore, Massachusetts, United States) with an electrical resistivity of 18.2 MΩ except for L-cysteine using 1 × PBS instead. All solutions were filtered through a 0.45-μm filter. Two kinds of centrifugal filter units with a molecular weight cut-off (MWCO) of 3.0 kDa and 30 kDa were also bought from Millipore. An electronic thermostatic mixing water bath pot (DFD-700) was provided by Zhongxing (Beijing, China).

2.2 UPLC-MS/MS Instrumentation Setting and Operating Conditions

An AB Sciex API 5500 QTrap mass spectrometer (Toronto, Canada) interfaced with a Waters Acquity UPLC separation module was used to detect and quantify osimertinib, AZ-5104, AZ-7550, and propranolol. Empower 3.0 was used in UPLC and Analyst 1.6.2 software in the mass spectrometer. Other settings for mass spectrometry parameters of the four compounds are shown in Table 1.

Chromatographic separation was achieved on a Waters Acquity UPLC HSS T3 1.8 μm column (2.1 mm × 50 mm) at 40°C using a mobile phase containing 0.1% FA that consisted of solvent A (water) and solvent B (ACN). The mobile phase was delivered at 0.3 ml/min, and an elegant gradient program was used as follows: 0–0.5 min, at 10% solvent B; 0.5–2.0 min, from 10 to 90% solvent B; 2.0–2.5 min, at 100% solvent B; and 2.5–3.0 min, at 10% solvent B. To eliminate carryover as much as possible, the injection needle was washed with 2.5 ml strong needle wash solution [ACN–MeOH–IPA–water (25:25:25:25, v/v) and 2.5 ml weak needle wash solution (FA–ACN–water (0.5:50:50, v/v))] before each injection.

2.3 Sample Preparation

For researching drug–plasma interaction and validating the UPLC-MS/MS method, enough blank SD rat plasma must be prepared before relative experiments. First, about 200 ml of rat blood was extracted with 5.0 mM EDTA-2Na from the abdominal aorta. Second, the blood was centrifuged at 4.0°C at 12,000 rpm for 5.0 min. The plasma (upper layer) was then aliquoted in a 1.0-ml/tube and stored at –70°C until use.

About 10 ml of rat plasma was added into one centrifugal filter unit as molecular weight cut-off in need and filtered by centrifuging for 40 min at 5,000 rpm at 4°C. The filtered-out liquid turned transparent and was stored at –70°C until use.

Osimertinib, AZ-5104, AZ-7550, and propranolol powders were dissolved to 1.0 mg/ml by an appropriate amount of DMSO as a stock solution, aliquoted in a 100-μl/tube and stored at –70°C until use. Working solutions were prepared extemporaneously by diluting stock solutions with 50% acetonitrile.

The L-cysteine powder was fast dissolved to 1.0 mg/ml by 1 × PBS as storage solution and quickly stored at –70°C as soon as possible. To inhibit the spontaneous dimerization of cysteine to cystine in PBS, the cysteine solution was freshly prepared before each experiment.

An osimertinib tablet was ground into a powder using a mortar and pestle. Then, a certain mass of powder samples converted into 8.0 mg osimertinib was weighed and added into 10 ml 12.5 mM CMC-Na. The sample was subjected to vortex mixing (3.0 min), sonicated (3.0 min), and vortex mixing again. The vortex–sonication cycle was repeated three times.

2.4 Plasma/Cysteine–Drug Incubation

Generally, each 45 μl L-cysteine solution with a certain concentration (diluted by 1 × PBS) or rat plasma was added with 5.0 μl working solution and mixed using vortex apparatus. Then, 5.0 μl propranolol with a 100 ng/ml concentration was

TABLE 1 | Optimized MRM parameters of the analytes and IS in this study.

Analyte	Retention time (min)	Precursor ion species	MRM transition Precursor ion→product ion (m/z)	Dp (V)	Ce (eV)
Propranolol	2.23	[M + H] ⁺	260.1→116.0	140	23
Osimertinib	2.02	[M + H] ⁺	500.2→72.1	80	60
AZ-5104	1.84	[M + H] ⁺	486.4→72.1	80	55
AZ-7550	1.97	[M + H] ⁺	486.3→429.3	80	32

added and mixed as described previously. The mixture was incubated at 37°C in a thermostatic mixing water bath pot for a certain period of time. Afterward, the tube was added with 350 µl ACN, vortexed (room temperature, 2000 rpm, 5.0 min), sonicated (4°C, 5.0 min), and centrifuged (4°C, 12,000 rpm, 5.0 min). Then, 200 µl upper liquid was taken into sample tubes for UPLC-MS/MS analysis.

2.5 UPLC-MS/MS Validation

The linearity, accuracy, precision, selectivity, specificity, matrix effect, recovery, and stability were all experimentally validated. The detailed validation process descriptions are as follows:

2.5.1 Linearity

Seven calibration standards samples with sequential concentrations of 1.0 (lower limit of quantitation, LLOQ), 3.0, 9.0, 27, 81, 243, and 729 ng/ml for osimertinib, AZ-5104, and AZ-7550 in rat plasma with additional 10 ng/ml propranolol (inner standard, IS) were made up in three successive batches. Calibration curves were obtained by plotting each analyte's peak area ratio to IS versus the nominal concentration of calibration standards. The weighting factor was set at $1/x^2$. The deviations from the mean for each calibration standard should be within ± 15%. The LLOQ should not exceed ± 20%.

2.5.2 Specificity and Selection

The specificity of the method was assessed by analyzing six batches of blank SD rat plasma to validate the interference induced by chromatographic conditions at each analyte's retention time. The criteria of acceptance for the method specificity and selectivity are that the peak areas in the double blank samples should be less than 20% of the peak areas of LLOQ samples in each batch.

2.5.3 Accuracy and Precision

Three standards samples with sequential concentrations of 2.0, 27, and 583 ng/ml for osimertinib, AZ-5104, and AZ-7550 in rat plasma with additional 10 ng/ml propranolol (inner standard, IS) were set as the low-quality control (LQC), middle-quality control (MQC), and high-quality control (HQC), respectively. The intra- and inter-batch precision was indicated as the percent relative standard deviation (RSD%). The intra- and inter-batch accuracy was indicated as the nominal concentration's relative error (RE). Both precision and accuracy were determined by analyzing six replicates of QC in three consecutive batches. The acceptance criteria of precision for the intra- and inter-batch of QC should be

within ± 15%, except ± 20% for LLOQ. The acceptance criteria for the intra- and inter-batch accuracy are that the RE of QC should be within 85–115% of their nominal concentration at each QC concentration except 80–120% for LLOQ.

2.5.4 Matrix Effect and Recovery

The degree of the matrix influencing each analyte's tandem mass spectrum signal was assessed by comparing the peak area of the analyte spiked after extraction and the peak area of standard in neat solution at each QC concentration using six batches of the blank matrix from different sources. The matrix effect's acceptance criteria are that the coefficient of variation of the IS-normalized matrix effect calculated from the six batches of the matrix should be within 85–115%. The relative recovery was determined by comparing each extracted sample's obtained value with the extracts of the spiked blank matrix with the analyte post-extraction at three QC concentration levels.

2.5.5 Stability

Each QC analyte's long-term and freeze-thaw stability in the SD rat plasma matrix with the addition of ACN (350 µl) for osimertinib was evaluated. To assess the analyte's long-term stability, all QC samples were preserved at –70°C for 2 months before sample processing and analyzing whether ACN was pre-added or not. For assessing the analyte's freeze-thaw stability, all QC samples were processed three cycles of freezing (–70°C) and thawing at room temperature for 1.0 h before sample processing and analyzing, ignoring the addition of ACN. The acceptance criteria were less than 15% of the nominal values for accuracy and within 15% for precision.

2.6 Pharmacokinetics Study

Five male SD rats (180–200 g) were fed autoclaved standard laboratory food and free to access sterile water and kept in an environmentally controlled breeding room (temperature, 20 ± 2°C; humidity, 60 ± 5%; 12-h dark/light cycle) for at least 6 days before experimentation. All rats were fasted for 12 h before the experiment but were allowed free access to water. The rats were given osimertinib dissolved by CMC-Na orally at 8.0 mg/kg. The rats were anesthetized by isoflurane at 0.08, 0.25, 0.5, 1.0, 2.0, 4.0, 6.0, 8.0, 10, and 24 h after oral administration. Blood samples (about 200 µl) were immediately collected from an eye socket vein and preserved in EDTA tubes. Then, the blood sample was centrifuged in an Eppendorf laptop centrifuge 5417C (Hamburg, Germany) for 5.0 min at 12,000 rpm to obtain plasma. Plasma with a volume of 50 µl was transferred into a tube added with 350 µl ACN beforehand. The mixture was quickly

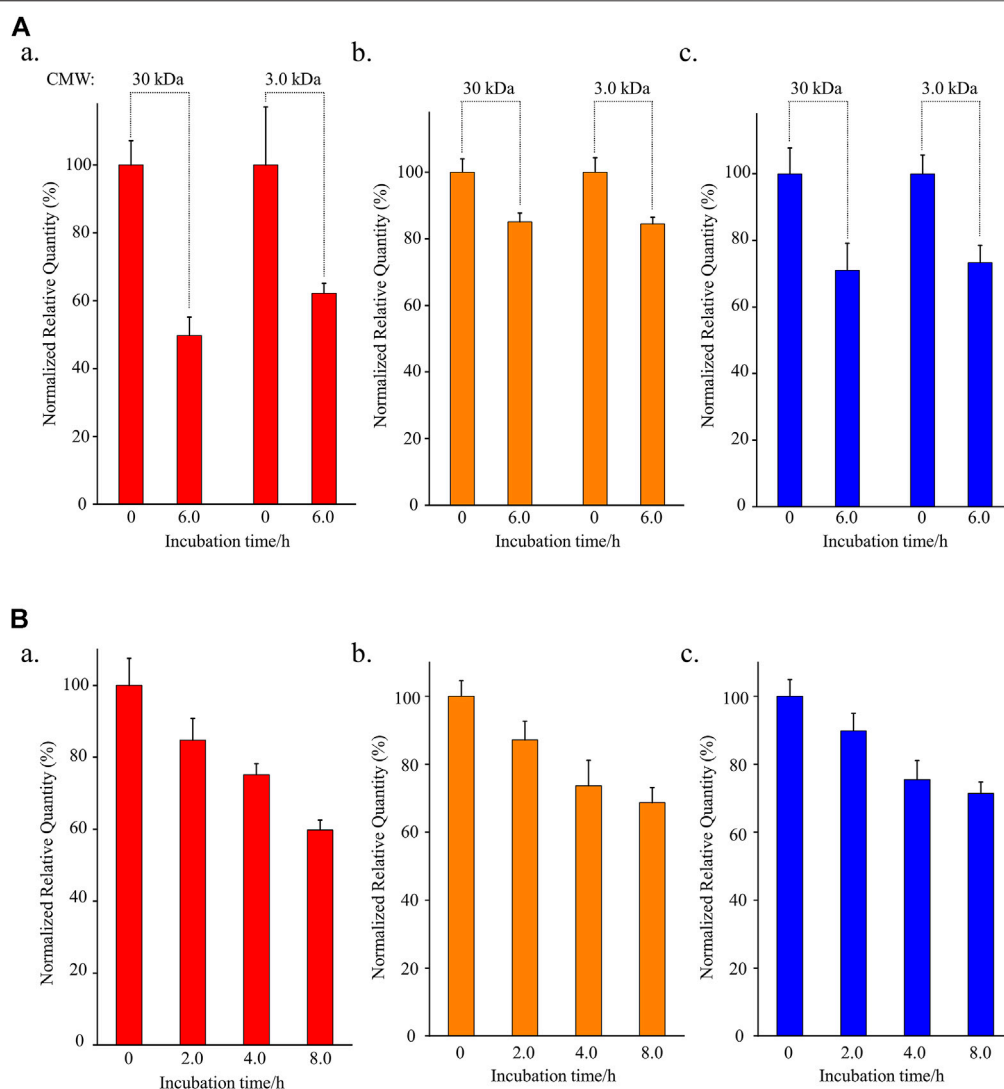


FIGURE 2 | Investigation of the stabilities of (a) osimertinib (red), (b) AZ-5104 (orange), and (c) AZ-7550 (blue) in (A) filtered rat plasma and (B) L-cysteine. In (A), the cut-off molecular weight (CMW) was 30 kDa or 3.0 kDa. In (B), L-cysteine concentration was 10.0 µg/ml. Note: the working solutions except for L-cysteine were kept at 39°C for the longest incubation time to eliminate all four chemicals' temperature instability.

vortexed by an MS3 basic vortex mixer (IKA GmbH, Germany) at 2000 rpm for 2.0 min and stored at -70°C until further processed.

Animal welfare and experimental procedures strictly followed the Guide for the Care and Use of Laboratory Animals (The Ministry of Science and Technology of China, 2006) and the related ethical regulations of the China Academy of Chinese Medical Sciences (CACMS).

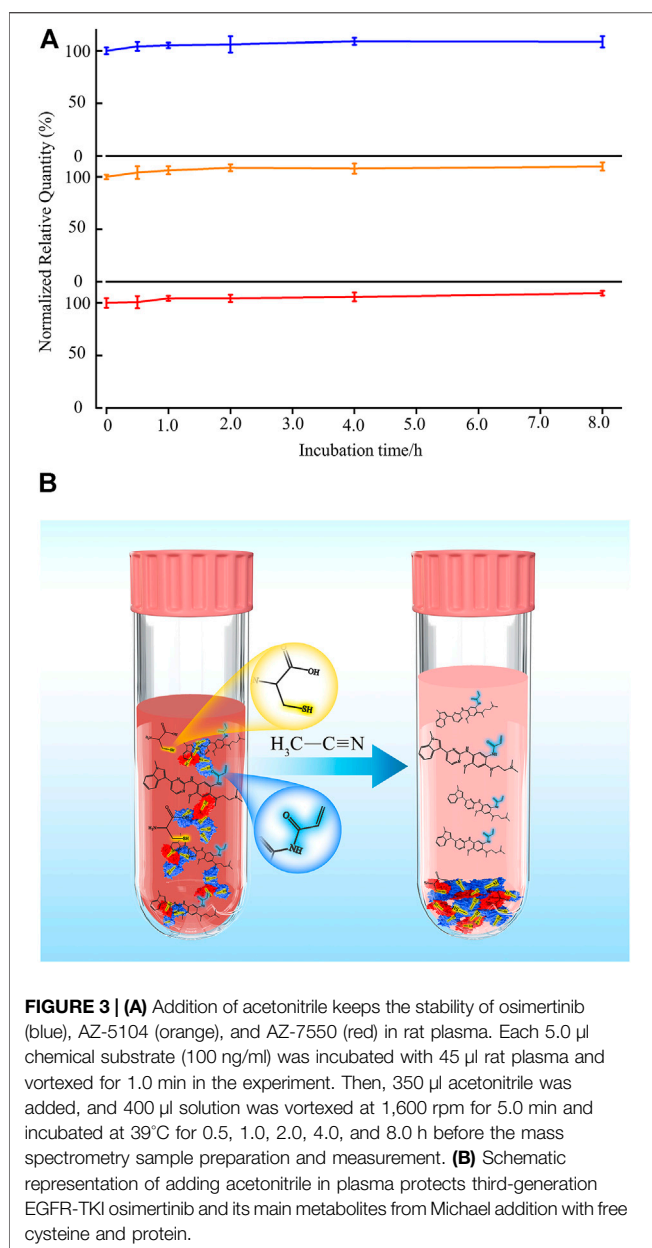
3 RESULTS AND DISCUSSION

3.1 The Instability of Osimertinib/AZ-5104/AZ-7550 in Rat Plasma

The stability of osimertinib, AZ-5104, and AZ-7550 was investigated by observing the relative quantitative change after incubating each 10 ng/ml chemical with 50 µl rat plasma ($n = 6$)

for 0 and 6.0 h. For a better description, the three negative control experiments (incubation time = 0) were used for normalization (Figure 1B). After 6.0 h of incubation, the detected relative quantity of osimertinib, AZ-5104, and AZ-7550 fell sharply to 2.76%, 2.96%, and 20.3%, respectively, strongly showing severe instability of the three chemicals in rat plasma. These phenomena are consistent with a previous study using human plasma as a warm bath matrix (Dickinson et al., 2016), thus excluding the possibility induced by species differences. Then, the instability of all three chemicals should be attributed to the typical chemical structure of all three drugs and the material basis of animal plasma.

Similar to other third-generation anti-tumor-targeted drugs, osimertinib contains two primary functional groups. One is the skeleton which can recognize the ATP-binding site of the EGFR kinase (To et al., 2019), and the other is the



Michael acceptor (red part of **Figures 1A, a**), which can react with the cysteine-797 residue of the EGFR kinase to form irreversible covalent bond formation. AZ-5104 and AZ-7550 are the primary demethylated metabolites of osimertinib (Jiang et al., 2018), sharing the same active Michael acceptor with osimertinib (red part of **Figures 1A–C**). The instability of all three chemicals is likely due to the Michael addition reaction deriving from the Michael acceptor and the cysteine in the plasma matrix. Considering that the high concentration of total cysteine in plasma is elevated to 10 μ M and the pharmacology of osimertinib, we propose that the protein-containing cysteine residue and free cysteine in plasma are significant factors causing the decline of osimertinib, AZ-5104, and AZ-7550 in plasma.

3.2 Protein and Free Cysteine Reduce the Stability of Osimertinib/AZ-5104/AZ-7550

To test the contribution of plasma protein in the instability of osimertinib, AZ-5104, and AZ-7550, rat plasma filtered by a centrifugal filter unit with a specific molecular weight cut-off (MWCO) was used to incubate with the three chemicals, respectively, instead of untreated plasma. The centrifugal filter unit was used to cut off macromolecule proteins above 30 kDa or 3.0 kDa from plasma. The normalized relative quantity of osimertinib was 49.8% and 62.2% (**Figure 2A, a**) after incubating with plasma treated by the centrifugal filter with MWCO 30 kDa or 3.0 kDa for 6.0 h, respectively. Furthermore, the values were 85.1% and 84.5% for AZ-5104 (**Figures 2A,B**) and 71.0% and 73.3% for AZ-7550 (**Figures 2A,C**). Through comparing with the detected osimertinib, AZ-5104, and AZ7550 using untreated plasma as substrates (**Figure 1B**), protein-filtered plasma enhanced the stability of osimertinib, AZ5104, and AZ7550. Therefore, macromolecular protein in plasma is one of the main factors inducing the instability of osimertinib, AZ-5104, and AZ-7550 in plasma.

To further identify the influence of free cysteine on the stability of osimertinib, AZ-5104, and AZ-7550, another experiment that incubates 10 μ g/ml cysteine aqueous solution with 10 ng/ml chemical substrate for 2.0, 4, 0, and 8.0 h was designed. In addition, PBS with a pH of 7.2–7.4 was used as a solvent to mimic the rat plasma's pH environment. The detected osimertinib, AZ-5104, and AZ-7550 present a highly negative relationship with the incubation duration (**Figures 2A,B,C**), and the normalized relative quantity was 59.8%, 68.7% and 71.4%, respectively, after 8.0 hours of incubation.

It is well known that only 20 amino acids are involved in protein synthesis in mammals, in which there is only one amino acid containing biological thiol, cysteine. However, osimertinib, carrying α , β -unsaturated carbonyls, was designed to be able to react with biological thiols, resulting in irreversible small-molecule-thiol adducts. No amino acid can react with osimertinib, AZ-5104, and AZ-7550 except for cysteine. However, homocysteine, an intermediate product of methionine metabolism in mammals (Kumar et al., 2017), contains one sulfhydryl group, can react with the Michael acceptor of osimertinib, AZ-5104, and AZ-7550. The average homocysteine concentration in mammals such as human is 10 μ M (Brouwer et al., 1998), much lower than that of cysteine (319 μ M) (Wang et al., 2018). Overall, these results indicate that the protein and free cysteine in plasma are the main factors inducing the instability of osimertinib in plasma.

3.3 Acetonitrile Maintains the Stability of Osimertinib in Plasma

In general, adding an appropriate additive is an efficient strategy to promise the stability of chemicals in a matrix. For example, adding enough complexing agent such as EDTA can enhance the stability of drugs and foods in plasma (Keowmaneechai and McClements, 2002; Song et al., 2014). This strategy is based on the fact that a complexing agent can decrease the quantity of free metal ions, which is the

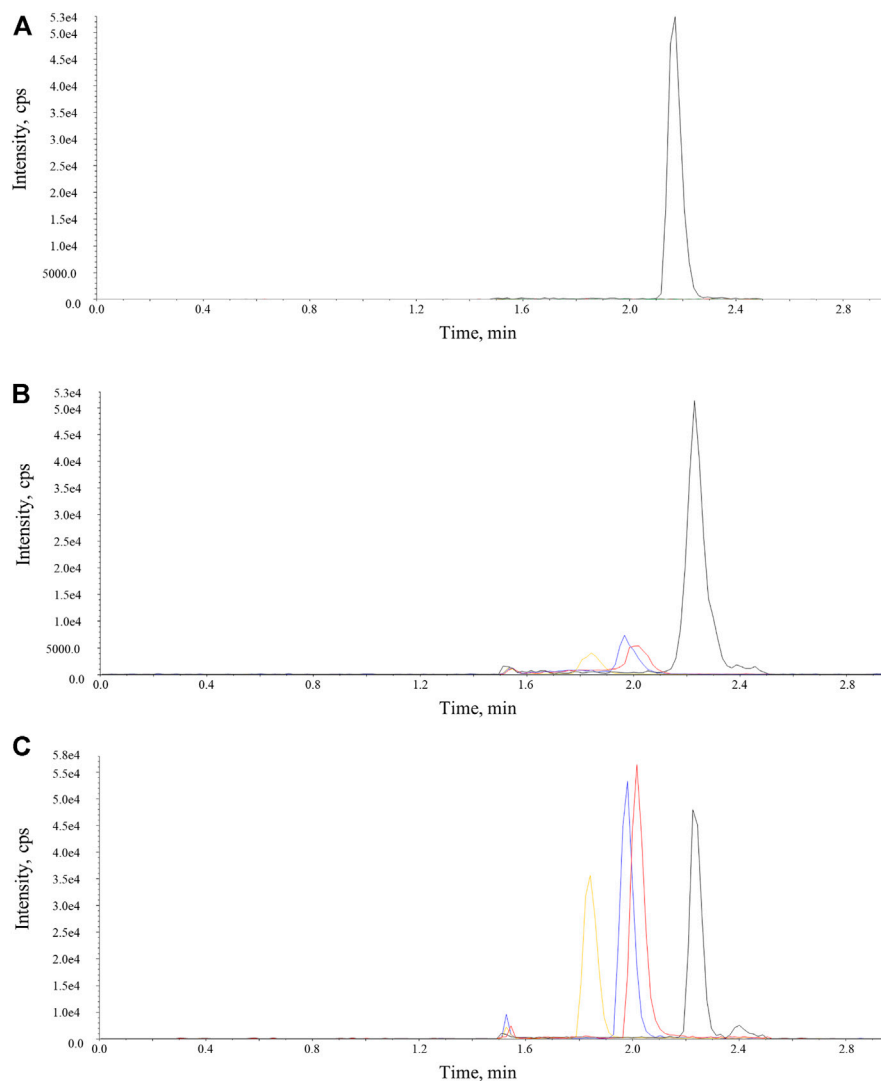


FIGURE 4 | Representative chromatograms of osimertinib, AZ-5104, AZ-7550, and IS in SD rat plasma samples. The red, orange, and blue lines represent osimertinib, AZ-5104, and AZ-7550. The black line represents IS. **(A)** Blank, **(B)** LLOQ, and **(C)** real SD rat plasma sample.

cofactor to the protein that can degrade the chemical. In addition, the incubation of proteinase K can also enhance the stability of several chemicals in plasma. Such a method is based on proteinase K that can disrupt the three-dimensional structure of proteins in plasma which degrades the target drug (Kim et al., 2019). However, based on our findings, the instability of osimertinib in plasma is due to protein and the free small organic molecule cysteine. As a result, both strategies targeting reducing protein activity were limited in overcoming the effect of free cysteine or cysteine residue in the plasma matrix. In addition, phenylmethylsulfonyl fluoride (PMSF), sodium fluoride (NaF), and diisopropyl fluorophosphate (DFP) were also applied to improve the stability of osimertinib, AZ-5104, and AZ-7550 in rat plasma based on the previous experiment. However, we did not achieve the desired results (data not shown). Therefore, a new additive is urgently needed to breach such barrier based on the chemical or physical theory.

Organic solvents such as acetonitrile, methanol, isopropanol, and acetone are primary solvents used to precipitate protein in the plasma sample (Bruce et al., 2009). Interestingly, the solubility of cysteine in acetonitrile is the lowest among other solvents (Han et al., 2020), indicating that acetonitrile is an appropriate additive for precipitating both protein and cysteine in plasma. To test this hypothesis, the stability of osimertinib in plasma while adding acetonitrile at 39°C (rat temperature *in vivo*) was tested (Figure 3A). Excitingly, no substantial changes were noticed in osimertinib levels even under incubation for 8.0 h (Figure 3, line in blue). Moreover, the same phenomenon was also observed using AZ-5104 and AZ-7550 as chemical substrates (Figure 3, lines in orange and red, respectively). Apparently, acetonitrile is an effective stabilizer for osimertinib in plasma (Figure 3B).

TABLE 2 | Accuracy and intra- and inter-day precision of (A) osimertinib, (B) AZ-5104, and (C) AZ-7550 in SD rat plasma ($n = 6$). (A)

Nominal concentration (ng/ml)		Measured concentration (ng/ml) (mean \pm SD)	Accuracy (%)	Intra-day precision (CV)	Inter-day precision (%) (CV)
2.0	Day 1	1.83 \pm 0.09	91.5	4.9	6.0
	Day 2	2.07 \pm 0.05	103.5	2.4	
	Day 3	1.92 \pm 0.08	96.0	4.2	
27	Day 1	26.30 \pm 1.00	97.4	3.8	4.2
	Day 2	27.65 \pm 0.81	102.4	2.9	
	Day 3	28.53 \pm 0.58	105.7	2.0	
583	Day 1	570.53 \pm 13.40	97.9	2.3	2.2
	Day 2	572.33 \pm 13.60	98.2	2.4	
	Day 3	565.17 \pm 10.03	96.9	1.8	
Nominal concentration (ng/ml)		Measured concentration (ng/ml) (mean \pm SD)	Accuracy (%)	Intra-day precision (CV)	Inter-day precision % (CV)
2.0	Day 1	2.11 \pm 0.15	105.5	7.1	6.6
	Day 2	1.96 \pm 0.06	98.0	3.1	
	Day 3	1.89 \pm 0.03	94.5	1.6	
27	Day 1	26.3 \pm 0.83	97.4	3.2	3.6
	Day 2	27.50 \pm 0.89	101.9	3.2	
	Day 3	26.63 \pm 0.93	98.6	3.5	
583	Day 1	564.50 \pm 13.31	96.8	2.4	3.1
	Day 2	575.00 \pm 21.81	98.6	3.8	
	Day 3	566.50 \pm 22.43	97.2	4.0	
Nominal concentration (ng/ml)		Measured concentration (ng/ml) (Mean \pm SD)	Accuracy (%)	Intra-day precision (CV)	Inter-day precision % (CV)
2.0	Day 1	1.92 \pm 0.15	96.0	7.8	7.8
	Day 2	2.13 \pm 0.16	106.5	7.5	
	Day 3	1.93 \pm 0.07	96.5	3.6	
27	Day 1	26.32 \pm 0.75	97.5	2.8	3.6
	Day 2	26.11 \pm 0.93	96.7	3.6	
	Day 3	27.55 \pm 0.51	102.0	1.9	
583	Day 1	566.17 \pm 14.57	97.1	2.6	3.3
	Day 2	560.17 \pm 11.48	96.1	2.0	
	Day 3	597.50 \pm 12.00	102.5	2.0	

TABLE 3 | Matrix effect and recovery of osimertinib, AZ-5104, and AZ-7550 in SD rat plasma ($n = 6$).

	Nominal concentration (ng/ml)	Matrix effect (%)	Recovery (%)
Osimertinib	2.0	93.5	90.2
	27	98.4	93.2
	583	96.3	92.5
AZ-5104	2.0	90.1	96.7
	27	103.2	93.3
	583	96.3	95.0
AZ-7550	2.0	95.6	91.2
	27	105.3	94.7
	583	103.9	90.2

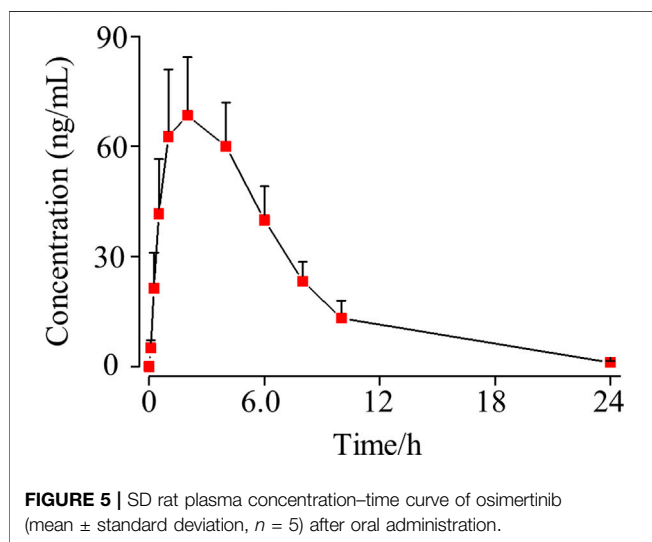
3.4 Method Validation

On the basis of aforementioned results, a systemic method validation for measuring osimertinib, AZ-5104, and AZ-7550 assisted by adding acetonitrile was performed according to

guidelines set by Pharmacopoeia of the People's Republic of China (2020) and the US Food and Drug Administration (2013). The UPLC-MS/MS condition was first optimized and four samples including blank, LLOQ, and plasma, were

TABLE 4 | Stability of osimertinib in SD rat samples ($n = 6$).

	Nominal concentration (ng/ml)	Measured concentration (ng/ml) (mean \pm SD)	Accuracy (%)	RSD (%)
Long-term stability	2.0	1.92 \pm 0.10	96.00	5.2
	27	28.12 \pm 0.83	104.15	3.0
	583	565.50 \pm 17.82	97.00	3.2
Freeze–thaw stability	2.0	1.93 \pm 0.14	96.50	7.3
	27	25.72 \pm 1.69	95.26	6.6
	583	570.33 \pm 18.96	97.83	3.3



separated and detected successfully (**Figure 4**), showing no significant interference from SD rat plasma observed at the retention time of analytes and IS. In addition, the representative calibration curve equation was $y = 0.00941x + 0.00158$ ($r = 0.9987$) to osimertinib, $y = 0.00758x + 0.000415$ ($r = 0.9983$) to AZ-5104, and $y = 0.0102x + 0.00235$ ($r = 0.9978$) to AZ-7550. The accuracy and intra- and inter-day precision of osimertinib, AZ-5104, and AZ-7550 in SD rat plasma were calculated and summarized as given in **Tables 2A–C**, respectively. The data of extraction recovery and matrix effect obtained are presented in **Table 3**. In particular, the long-term stability and freeze–thaw stability in the SD rat plasma matrix with the addition of ACN were studied, and the results are summarized in **Table 4**, indicating that acetonitrile keeps the stability of osimertinib in plasma efficiently.

3.5 Pharmacokinetics Study of Osimertinib in Rat Plasma

To further apply such an assay in a pre-clinical pharmacokinetics study, we performed pharmacokinetics study of osimertinib in rat plasma using five male SD rats. Unlike the conventional pre-clinical pharmacokinetics experimental scheme, the preparation of rat plasma was

online. The rat blood was taken from the eye socket vein at the appropriate time point and immediately followed by high-speed centrifugation for plasma preparation. Then, 50 μ l of freshly made rat plasma was mixed with a seven-order volume of acetonitrile for maintaining the stability of osimertinib. Each concentration of osimertinib in rat plasma was obtained by the validated UPLC-MS/MS assay, and all data are described statistically as a concentration–time curve (**Figure 5**), displaying the concentration of osimertinib in rat plasma peaks (65.5 ng/ml) after 2.5 h of oral administration which slowly reduced in the following 20 h. Also after 24 h of oral administration, osimertinib was not detectable in rat plasma. Such a pre-clinical experiment indicates the applicability of the strategy that stabilizes osimertinib in plasma by adding ACN and the methodology in processing rat plasma online.

One should note that acetonitrile treatment should be concomitant with the whole animal experiment before sample storage, thus adding tension and complexity to a certain extent. Therefore, an optimal and feasible protocol is needed to make the proposed strategy convenient for operation in future research applications.

4 CONCLUSION

In summary, we confirmed that both the protein and cysteine in plasma are the main factors that induce the instability of osimertinib and its primary metabolites AZ-5104 and AZ-7550 through a series of experiments. A new strategy stabilizing osimertinib by adding enough acetonitrile was proposed and validated based on the physicochemical properties of plasma and cysteine. In addition, coupled with the online biological sample processing method, the strategy was successfully applied in a pre-clinical pharmacokinetics study. The proposed strategy adapts to human subjects, and a relative work is underway. It is notable that most third-generation EGFR-TKIs (such as naquotinib and olmutinib) contain at least one Michael acceptor targeting cysteine whether free in plasma or imported into the protein (Attwa et al., 2018; Alrabiah et al., 2019). Therefore, the organic additive-assisted method coupled with the online biological sample processing methodology may promote the research and development of other third-generation EGFR-TKI in the future study.

DATA AVAILABILITY STATEMENT

The original contributions presented in the study are included in the article/Supplementary Material. Further inquiries can be directed to the corresponding authors.

ETHICS STATEMENT

The animal study was reviewed and approved by the Experimental Animal Welfare Ethics Committee, Institute of Chinese Materia Medica, China Academy of Chinese Medical Sciences.

AUTHOR CONTRIBUTIONS

ZY: methodology, investigation, writing—original draft, and funding acquisition. XY, SW, and WC: supervision and validation. XW: resources and supervision. XY, QW, WH, CK, and WY: participating in experiments. YL: writing—review and editing, conceptualization, supervision, funding acquisition, and

validation. X-YZ: resources, supervision, subject design, editing and revisions, and funding acquisition.

FUNDING

This work was supported by the National Key R&D Program of China (2020YFC2008106, 2017ZX09304026), the Scientific and Technological Innovation Project of China Academy of Chinese Medical Sciences (CI2021B015 and CI2021A04909), the National Science and Technology Major Project (2017ZX09304026), the Fundamental Research Funds for Central Scientific Research Institutes of the Institute of China Academy of Chinese Medical Sciences, Chinese Materia Medica (L2020031), the Fundamental Research Funds for the Central Public Welfare Research Institutes (ZXKT20031), and the grant from the Special Fund for Outstanding Young Scientific and Technological Talents (ZZ14-YQ-030).

REFERENCES

- Ke, E. E., and Wu, Y. L. (2016). EGFR as a Pharmacological Target in EGFR-Mutant Non-small-cell Lung Cancer: Where Do We Stand Now? *Trends Pharmacol. Sci.* 37 (11), 887–903. doi:10.1016/j.tips.2016.09.003
- Alrabiah, H., Kadi, A. A., Attwa, M. W., and Abdelhameed, A. S. (2019). A Simple Liquid Chromatography-Tandem Mass Spectrometry Method to Accurately Determine the Novel Third-Generation EGFR-TKI Naquotinib with its Applicability to Metabolic Stability Assessment. *RSC Adv.* 9, 4862–4869. doi:10.1039/C8RA09812C
- Attwa, M. W., Kadi, A. A., Darwish, H. W., and Abdelhameed, A. S. (2018). Investigation of the Metabolic Stability of Osimertinib by Validated LC-MS/MS: Quantification in Human Plasma. *RSC Adv.* 8, 40387–40394. doi:10.1039/C8RA08161A
- Ballard, P., Yates, J. W., Yang, Z., Kim, D. W., Yang, J. C., Cantarini, M., et al. (2016). Preclinical Comparison of Osimertinib with Other EGFR-TKIs in EGFR-Mutant NSCLC Brain Metastases Models, and Early Evidence of Clinical Brain Metastases Activity. *Clin. Cancer Res.* 22 (20), 5130–5140. doi:10.1158/1078-0432.CCR-16-0399
- Barbuti, A. M., Zhang, G.-N., Gupta, P., Narayanan, S., and Chen, Z.-S. (2019). “EGFR and HER2 Inhibitors as Sensitizing Agents for Cancer Chemotherapy,” in *Protein Kinase Inhibitors as Sensitizing Agents for Chemotherapy*. Editors Z.-S. Chen, and D.-H. Yang (United States: Academic Press), 1–11. doi:10.1016/B978-0-12-816435-8.00001-8
- Brouwer, D. A., Welten, H. T., Reijngoud, D. J., van Doormaal, J. J., and Muskiet, F. A. (1998). Plasma folic acid cutoff value, derived from its relationship with homocyst(e)ine. *Clin. Chem.* 44, 1545–1550. doi:10.1093/clinchem/44.7.1545
- Bruce, S. J., Tavazzi, I., Parisod, V., Rezzi, S., Kochhar, S., and Guy, P. A. (2009). Investigation of Human Blood Plasma Sample Preparation for Performing Metabolomics Using Ultrahigh Performance Liquid Chromatography/Mass Spectrometry. *Anal. Chem.* 81 (9), 3285–3296. doi:10.1021/ac8024569
- Cho, J. H., Lim, S. H., An, H. J., Kim, K. H., Park, K. U., Kang, E. J., et al. (2020). Osimertinib for Patients with Non-small-cell Lung Cancer Harboring Uncommon EGFR Mutations: A Multicenter, Open-Label, Phase II Trial (KCSG-LU15-09). *J. Clin. Oncol.* 38 (5), 488–495. doi:10.1200/JCO.19.00931
- Dickinson, P. A., Cantarini, M. V., Collier, J., Frewer, P., Martin, S., Pickup, K., et al. (2016). Metabolic Disposition of Osimertinib in Rats, Dogs, and Humans: Insights into a Drug Designed to Bind Covalently to a Cysteine Residue of Epidermal Growth Factor Receptor. *Drug Metab. Dispos.* 44 (8), 1201–1212. doi:10.1124/dmd.115.069203
- Floc'h, N., Lim, S., Bickerton, S., Ahmed, A., Orme, J., Urošević, J., et al. (2020). Osimertinib, an Irreversible Next-Generation EGFR Tyrosine Kinase Inhibitor, validation. X-YZ: resources, supervision, subject design, editing and revisions, and funding acquisition.
- Exerts Antitumor Activity in Various Preclinical NSCLC Models Harboring the Uncommon EGFR Mutations G719X or L861Q or S768I. *Mol. Cancer Ther.* 19 (11), 2298–2307. doi:10.1158/1535-7163.MCT-20-0103
- Fresnais, M., Roth, A., Foerster, K. I., Jäger, D., Pfister, S. M., Haefeli, W. E., et al. (2020). Rapid and Sensitive Quantification of Osimertinib in Human Plasma Using a Fully Validated MALDI-IM-MS/MS Assay. *Cancers (Basel)* 12 (7). doi:10.3390/cancers12071897
- Gao, N., Zhang, X., Hu, X., Kong, Q., Cai, J., Hu, G., et al. (2022). The Influence of CYP3A4 Genetic Polymorphism and Proton Pump Inhibitors on Osimertinib Metabolism. *Front. Pharmacol.* 13, 794931. Available at: <https://www.frontiersin.org/article/10.3389/fphar.2022.794931>. doi:10.3389/fphar.2022.794931
- Gridelli, C., Rossi, A., Carbone, D. P., Guarize, J., Karachaliou, N., Mok, T., et al. (2015). Non-small-cell Lung Cancer. *Nat. Rev. Dis. Prim.* 1, 15009. doi:10.1038/nrdp.2015.9
- Han, J., Liu, H., Hu, S., Qiu, J., Yi, D., An, M., et al. (2020). Determination and Correlation of the Solubility of L-Cysteine in Several Pure and Binary Solvent Systems. *J. Chem. Eng. Data* 65 (5), 2649–2658. doi:10.1021/acs.jced.0c00031
- Irie, K., Nanjo, S., Hata, A., Yamasaki, Y., Okada, Y., Katakami, N., et al. (2019). Development of an LC-MS/MS-based Method for Quantitation of Osimertinib in Human Plasma and Cerebrospinal Fluid. *Bioanalysis* 11 (9), 847–854. doi:10.4155/bio-2018-0292
- Jiang, T., Su, C., Ren, S., Cappuzzo, F., Rocco, G., Palmer, J. D., et al. (2018). A Consensus on the Role of Osimertinib in Non-small Cell Lung Cancer from the AME Lung Cancer Collaborative Group. *J. Thorac. Dis.* 10 (7), 3909–3921. doi:10.21037/jtd.2018.07.61
- Keowmaneechai, E., and McClements, D. J. (2002). Influence of EDTA and Citrate on Physicochemical Properties of Whey Protein-Stabilized Oil-In-Water Emulsions Containing CaCl₂. *J. Agric. Food Chem.* 50 (24), 7145–7153. doi:10.1021/jf020489a
- Kim, J., Basiri, B., Hassan, C., Punt, C., van der Hage, E., den Besten, C., et al. (2019). Metabolite Profiling of the Antisense Oligonucleotide Eluforsen Using Liquid Chromatography-Mass Spectrometry. *Mol. Ther. Nucleic Acids* 17, 714–725. doi:10.1016/j.omtn.2019.07.006
- Kumar, A., Palfrey, H. A., Pathak, R., Kadowitz, P. J., Gettys, T. W., and Murthy, S. N. (2017). The Metabolism and Significance of Homocysteine in Nutrition and Health. *Nutr. Metab. (Lond)* 14, 78. doi:10.1186/s12986-017-0233-z
- Lategahn, J., Keul, M., Klöveborn, P., Tumbrink, H. L., Niggenaber, J., Müller, M. P., et al. (2019). Inhibition of Osimertinib-Resistant Epidermal Growth Factor Receptor EGFR-T790M/C797S. *Chem. Sci.* 10 (46), 10789–10801. doi:10.1039/C9SC03445E
- Minchiotti, L., Galliano, M., Kragh-Hansen, U., and Peters, T., Jr. (2008). Mutations and Polymorphisms of the Gene of the Major Human Blood

- Protein, Serum Albumin. *Hum. Mutat.* 29 (8), 1007–1016. doi:10.1002/humu.20754
- Mitchell, R., Bailey, C., Ewles, M., Swan, G., and Turpin, P. (2019). Determination of Osimertinib in Human Plasma, Urine and Cerebrospinal Fluid. *Bioanalysis* 11 (10), 987–1001. doi:10.4155/bio-2018-0262
- Remon, J., Steuer, C. E., Ramalingam, S. S., and Felip, E. (2018). Osimertinib and Other Third-Generation EGFR TKI in EGFR-Mutant NSCLC Patients. *Ann. Oncol.* 29, i20–i27. doi:10.1093/annonc/mdx704
- Rood, J. J. M., van Bussel, M. T. J., Schellens, J. H. M., Beijnen, J. H., and Sparidans, R. W. (2016). Liquid Chromatography-Tandem Mass Spectrometric Assay for the T790M Mutant EGFR Inhibitor Osimertinib (AZD9291) in Human Plasma. *J. Chromatogr. B Anal. Technol. Biomed. Life Sci.* 1031, 80–85. doi:10.1016/j.jchromb.2016.07.037
- Song, Y., Huang, Z., Song, Y., Tian, Q., Liu, X., She, Z., et al. (2014). The Application of EDTA in Drug Delivery Systems: Doxorubicin Liposomes Loaded via NH4EDTA Gradient. *Int. J. Nanomedicine* 9, 3611–3621. doi:10.2147/IJN.S64602
- Soria, J. C., Ohe, Y., Vansteenkiste, J., Reungwetwattana, T., Chewaskulyong, B., Lee, K. H., et al. (2018). Osimertinib in Untreated EGFR-Mutated Advanced Non-small-cell Lung Cancer. *N. Engl. J. Med.* 378 (2), 113–125. doi:10.1056/NEJMoa1713137
- To, C., Jang, J., Chen, T., Park, E., Mushajiang, M., De Clercq, D. J. H., et al. (2019). Single and Dual Targeting of Mutant EGFR with an Allosteric Inhibitor. *Cancer Discov.* 9 (7), 926–943. doi:10.1158/2159-8290.CD-18-0903
- van Veelen, A., van Geel, R., de Beer, Y., Dingemans, A. M., Stolk, L., Ter Heine, R., et al. (2020). Validation of an Analytical Method Using HPLC-MS/MS to Quantify Osimertinib in Human Plasma and Supplementary Stability Results. *Biomed. Chromatogr.* 34 (4), e4771. doi:10.1002/bmc.4771
- Veerman, G. D. M., Lam, M. H., Mathijssen, R. H. J., Koolen, S. L. W., and de Bruijn, P. (2019). Quantification of Afatinib, Alectinib, Crizotinib and Osimertinib in Human Plasma by Liquid Chromatography/triple-Quadrupole Mass Spectrometry; Focusing on the Stability of Osimertinib. *J. Chromatogr. B Anal. Technol. Biomed. Life Sci.* 1113, 37–44. doi:10.1016/j.jchromb.2019.03.011
- Wang, N., Wang, Y., Gao, J., Ji, X., He, J., Zhang, J., et al. (2018). A Ratiometric Fluorescent BODIPY-Based Probe for Rapid and Highly Sensitive Detection of Cysteine in Human Plasma. *Analyst* 143 (23), 5728–5735. doi:10.1039/C8AN01438H
- Wu, S. G., and Shih, J. Y. (2018). Management of Acquired Resistance to EGFR TKI-Targeted Therapy in Advanced Non-small Cell Lung Cancer. *Mol. Cancer* 17 (1), 38. doi:10.1186/s12943-018-0777-1
- Xiong, X., Zhang, Y., Wang, Z., Zhou, C., Yang, P., Du, X., et al. (2022). Simultaneous Quantitative Detection of Afatinib, Erlotinib, Gefitinib, Icotinib, Osimertinib and Their Metabolites in Plasma Samples of Patients with Non-small Cell Lung Cancer Using Liquid Chromatography-Tandem Mass Spectrometry. *Clin. Chim. Acta* 527, 1–10. doi:10.1016/j.cca.2021.12.028
- Xue, W., Meylan, E., Oliver, T. G., Feldser, D. M., Winslow, M. M., Bronson, R., et al. (2011). Response and Resistance to NF- κ B Inhibitors in Mouse Models of Lung Adenocarcinoma. *Cancer Discov.* 1 (3), 236–247. doi:10.1158/2159-8290.CD-11-0073
- Zhou, X., He, X., Shi, K., Yuan, L., Yang, Y., Liu, Q., et al. (2020). Injectable Thermosensitive Hydrogel Containing Erlotinib-Loaded Hollow Mesoporous Silica Nanoparticles as a Localized Drug Delivery System for NSCLC Therapy. *Adv. Sci. (Weinh)* 7 (23), 2001442. doi:10.1002/advs.202001442

Conflict of Interest: The authors declare that the research was conducted in the absence of any commercial or financial relationships that could be construed as a potential conflict of interest.

Publisher's Note: All claims expressed in this article are solely those of the authors and do not necessarily represent those of their affiliated organizations, or those of the publisher, the editors, and the reviewers. Any product that may be evaluated in this article, or claim that may be made by its manufacturer, is not guaranteed or endorsed by the publisher.

Copyright © 2022 Yuan, Yu, Wu, Wu, Wang, Cheng, Hu, Kang, Yang, Li and Zhou. This is an open-access article distributed under the terms of the Creative Commons Attribution License (CC BY). The use, distribution or reproduction in other forums is permitted, provided the original author(s) and the copyright owner(s) are credited and that the original publication in this journal is cited, in accordance with accepted academic practice. No use, distribution or reproduction is permitted which does not comply with these terms.



OPEN ACCESS

EDITED BY

Sabina Passamonti,
University of Trieste, Italy

REVIEWED BY

Nico P.E. Vermeulen,
Faculty of Science, VU Amsterdam,
Netherlands
Stefan Oswald,
Rostock University Medical Center,
Germany
Pavel Anzenbacher,
Palacký University, Czechia
Dapeng Dai,
Peking University, China
Pius S Fasinu,
University of Alabama at Birmingham,
United States

*CORRESPONDENCE

Min Huang,
huangmin@mail.sysu.edu.cn
Guoping Zhong,
zhonggp@mail.sysu.edu.cn

[†]These authors have contributed equally
to this work and share first authorship

SPECIALTY SECTION

This article was submitted to Drug
Metabolism and Transport,
a section of the journal
Frontiers in Pharmacology

RECEIVED 28 March 2022

ACCEPTED 05 July 2022

PUBLISHED 17 August 2022

CITATION

Jiang F, Zhang C, Lu Z, Liu J, Liu P,
Huang M and Zhong G (2022),
Simultaneous absolute protein
quantification of seven cytochrome
P450 isoforms in rat liver microsomes
by LC-MS/MS-based isotope internal
standard method.
Front. Pharmacol. 13:906027.
doi: 10.3389/fphar.2022.906027

COPYRIGHT

© 2022 Jiang, Zhang, Lu, Liu, Liu, Huang
and Zhong. This is an open-access
article distributed under the terms of the
[Creative Commons Attribution License](https://creativecommons.org/licenses/by/4.0/)
(CC BY). The use, distribution or
reproduction in other forums is
permitted, provided the original
author(s) and the copyright owner(s) are
credited and that the original
publication in this journal is cited, in
accordance with accepted academic
practice. No use, distribution or
reproduction is permitted which does
not comply with these terms.

Simultaneous absolute protein quantification of seven cytochrome P450 isoforms in rat liver microsomes by LC-MS/MS-based isotope internal standard method

Fulin Jiang^{1†}, Chang Zhang^{1†}, Zihan Lu¹, Jingyu Liu¹,
Peiqing Liu², Min Huang^{1*} and Guoping Zhong^{1*}

¹Institute of Clinical Pharmacology, Guangdong Provincial Key Laboratory of New Drug Design and Evaluation, School of Pharmaceutical Sciences, Sun Yat-sen University, Guangzhou, China, ²School of Pharmaceutical Sciences, National and Local United Engineering Lab of Druggability and New Drugs Evaluation, Sun Yat-sen University, Guangzhou, China

The cytochrome P450 (CYP) enzymes play a pivotal role in drug metabolism. LC-MS/MS-based targeting technology has been applied to the analysis of CYP enzymes, promoting drug development and drug-drug interaction studies. Rat is one of the most commonly used models for drug metabolism assessment, but LC-MS/MS assay quantifying the abundance of CYP enzymes in rats is rarely reported. Herein, an accurate and stable LC-MS/MS based method was developed and validated for the simultaneous quantification of seven major rat CYP isoforms (CYP1A2, 2B1, 2C6, 2C11, 2D1, 2E1, and 3A1) in liver microsomes. The careful optimization of trypsin digestion and chromatography combined with isotope-labeled peptide as internal standard improved the efficiency and accuracy of the analysis. Highly specific surrogate peptides were obtained by a procedure including trypsin digestion for six hours and separated on a Hypersil Gold C18 column (100 × 2.1 mm, 3 μm) using gradient elution for 15 min with a mobile phase of water containing 0.1% formic acid and acetonitrile. In the method validation, linearity, matrix effect, recovery, stability, accuracy, and precision all meet the requirements. Subsequently, this method was applied to detect seven enzymes in rat liver microsomes from four different sources, and the correlation between the abundance and activity of CYP enzymes was further analyzed. The high-throughput detection method provided in this study will provide support for pertinent pharmaceutical research based on rat models.

Abbreviations: ACE, acetic acid; CYP, cytochrome P450; DMSO, dimethyl sulfoxide; DTT, dithiothreitol; ELISA, enzyme linked immunosorbent assay; FA, formic acid; IAA, iodoacetamide; LC-MS/MS, liquid chromatography-tandem mass spectrometry; RT-PCR, real-time polymerase chain reaction; TFA, trifluoroacetic acid; WB, Western blotting.

KEYWORDS

cytochrome P450, absolute quantification, LC-MS/MS, rat liver microsomes, isotope internal standard

1 Introduction

The cytochrome P450 (CYP) superfamily is an important enzyme system that mediates a major proportion of phase I metabolism of most drugs, xenobiotics, and endogenous compounds. CYPs are expressed in various tissues and organs, and the liver tissue has the most abundant (Zanger and Schwab, 2013). The expression and activity of drug-metabolizing enzymes in rat liver microsomes have long been the focus of *in vitro* and *in vivo* evaluation of drug disposition and drug-drug interactions (Singh et al., 2011; Manikandan and Nagini, 2018). The CYPs proteins expressed in rat liver mainly include CYP 1–3 families, which not only biotransform a wide variety of drugs, but can also be induced or inhibited by them (Martignoni et al., 2006). Consequently, reliable methods must be considered to quantify these proteins for drug development and evaluation (Xie et al., 2016).

Several biochemical approaches for the determination of CYP isoforms have been developed, mainly including: Western blotting (WB), enzyme linked immunosorbent assay (ELISA), quantification of mRNA levels using real-time polymerase chain reaction (RT-PCR) and determination of metabolic activities by the probe substrate method. Data comparisons between these different techniques show a great deal of variability, which is the most likely cause of the contradictory results (Dostalek et al., 2011; Grangeon et al., 2019; Ren et al., 2020). WB has the characteristics of a semi-quantitative method, and immunological methods such as WB and ELISA also have limitations including weak antibody specificity, poor reproducibility and lack of high-throughput capability (Li and Zhu, 2020). The RT-PCR method is simple, rapid and highly selective. However, the regulation of mRNA at the translational level and the post-translational modification of proteins are affected by many factors, so measured mRNA levels cannot accurately reflect the expression of CYP enzymes (Pearce et al., 2016; Zhang et al., 2016; Couto et al., 2020). The probe substrate method takes into account the effects of genes and environmental factors on enzyme activity, but due to the questionable specificity of the probe-substrate, this method lacks a unified standard when it is widely used.

Targeted proteomics techniques based on liquid chromatography-tandem mass spectrometry (LC-MS/MS) have been a powerful tool for quantifying CYP enzymes. LC-MS/MS combines the high separation ability of liquid chromatography with the high selectivity and sensitivity of mass spectrometry, and also has a high-throughput capability. Several studies have applied this method to

detect CYP enzymes in human liver microsomes (Bhatt and Prasad, 2018). However, there are few reports on the detection of CYPs in rat liver, which is one of the most widely used research models. Shao Y et al. established total protein concentration to establish the “Standard Curve Slope” method to assess the gender difference of CYPs in rat liver microsomes (Shao et al., 2017). Hammer H et al. used a targeted mass spectrometry-based immunoassay to directly quantify CYPs and drug transporters (Hammer et al., 2021). The above methods were not fully validated and may have potential variations in quantification (Wegler et al., 2017). Thus, this study aims to develop and validate a highly accurate and stable LC-MS/MS assay for absolute protein quantification of CYP isoforms in rat liver microsomes. We identified seven major CYPs (CYP1A2, 2B1, 2C6, 2C11, 2D1, 2E1, and 3A1) based on the main metabolic enzymes in the human liver and the species differences between human and rat metabolic enzymes (Martignoni et al., 2006; Zhang et al., 2016). All these CYPs were widely used in the study of drug metabolism (Shao et al., 2017; Hammer et al., 2021). Many challenges can affect protein quantification in a bottom-up proteomic workflow, and the pretreatment process including efficient enzymatic digestion is critical to the robustness and sensitivity of the method. Denaturation, reduction, alkylation and digestion of proteins can all affect the acquisition of surrogate peptides. In addition, the complex composition of biological samples may lead to the matrix effect that also affect peptide quantification (An et al., 2019), so chromatography needs to be optimized for efficient separation, which has led many studies to take more than an hour for an analysis (Grangeon et al., 2019; Wenzel et al., 2021). To correct for the matrix effect, an isotope internal standard is usually chosen because it has similar physicochemical properties to the target peptide. Isotope internal standards can also correct for biases introduced by pretreatment and errors in the injection system (De Nicolo et al., 2017). All of these advantages make the isotope internal standard method the first choice for LC-MS/MS based quantification.

To sum up, we developed and validated herein a quantification assay by LC-MS/MS for simultaneously detecting the abundance of seven CYP enzymes in rat liver microsomes. The isotope-labeled peptide corresponding to the surrogate peptide was used as the internal standard to improve the quantitative accuracy. Finally, this method was successfully applied to detect the expression of CYP enzymes in rat liver microsomes, and a correlation analysis was carried out between the measured abundance of CYPs and their activity detected by the probe substrate method.

TABLE 1 Overview of surrogate peptides and their respective ions and mass transitions used for CYP enzyme quantification (*isotope-labeled amino acid).

Protein	Peptide	Molecular weight	Precursor	z	Product	Ion/z	CE (V)	Tube lens (V)
CYP1A2	YTSFVPFTIPHSSTR	1754.0	877.7	2+	698.4	b12/2+	30	110
	YTSFVPFTI*PHSSTR	1761.0	587.9	3+	581.9	y10/2+	20	100
	NFNDNFVLFQK	1498.7	500.5	3+	647.8	y5/1+	13	78
CYP2B1	FSDLVPIGVPHR	1336.6	446.4	3+	409.1	y3/1+	15	75
	FSDL*VPIGVPHR	1343.5	448.6	3+	409.2	y3/1+	13	86
	EALVGQAEDFSGR	1378.5	690.1	2+	966.0	y9/1+	25	98
CYP2C6	EALIDHGEEFAER	1515.6	506.1	3+	602.2	y10/2+	12	80
	EAL*IDHGEEFAER	1522.7	508.4	3+	601.8	y10/2+	20	80
	EHQESLDVTNPR	1424.5	713.2	2+	703.9	y6/1+	18	100
CYP2C11	YIDLVPNTLPHLVTR	1751.2	584.9	3+	574.7	y10/2+	15	80
	YIDL*VPTNLPHLVTR	1758.2	587.0	3+	574.7	y10/2+	17	93
	EALVDLGEFSGR	1421.5	711.8	2+	1010.0	y9/1+	22	101
CYP2D1	GTTLIINLSSVLK	1358.7	680.1	2+	446.2	y4/1+	14	90
	GTTL*IINLSSVLK	1365.7	683.6	2+	446.2	y4/1+	14	90
	NLTDAFLAEVEK	1349.6	675.6	2+	906.2	y8/1+	15	97
CYP2E1	FINLVPSNLPHEATR	1708.0	570.2	3+	1121.4	y10/1+	18	86
	FINL*VPSNLPHEATR	1715.0	572.6	3+	1121.9	y10/1+	15	90
	FKPEHFLNENGK	1459.6	487.5	3+	592.8	y9/2+	14	84
CYP3A1	QGLLQPTKPIILK	1448.9	483.9	3+	477.9	— ^a	12	84
	QGL*LQPTKPIILK	1455.9	486.2	3+	479.9	— ^a	12	80

^aThe daughter ion is the ion after amino-terminal cyclization.

2 Material and methods

2.1 Chemicals and reagents

The male Sprague Dawley rat liver microsomes (Protein content, 20 mg/ml) were obtained from IPHase Pharma Services (Beijing, China), Corning Gentest (Corning, American), PrimeTox (Wuhan, China) and Meilunbio (Dalian, China). Recombinant Trypsin (Porcine pancreas) was provided by Yuanye (Shanghai, China). Bupropion and glibenclamide were purchased from National Institutes for Food and Drug Control (Beijing, China). Phenacetin, acetaminophen, tolbutamide, 4-Hydroxy-tolbutamide, dextromethorphan, dextrorphan chlorzoxazone and 6-Hydroxy-chlorzoxazone were purchased from Sigma-Aldrich Inc (United States). Hydroxy-bupropion, phenytoin, 4-Hydroxymephenytoin, testosterone and 6 β -Hydroxy-testosterone were purchased from Zzstandard (Shanghai, China). Ammonium bicarbonate (NH₄HCO₃), trifluoroacetic acid (TFA), and formic acid (FA) were purchased from Macklin (Shanghai, China). HPLC-MS grade acetonitrile (ACN) and iodoacetamide (IAA) were purchased from Merck (Darmstadt, Germany). Dithiothreitol (DTT) was provided by Thermo Fisher Scientific (Waltham, United States). Dimethyl sulfoxide (DMSO) was provided by MP Biomedicals (France).

Acetic Acid (ACE) was from Guangzhou chemical reagent (Guangzhou, China). Deionized water was generated using the Milli-Q Direct 8 water system (Germany). Surrogate peptides and their stable isotope-labeled internal standards (Table 1) were synthesized by Bankpeptid (Hefei, China). All peptide purity was superior to 95.0% and the concentration/net peptide was determined by amino acid analysis. Standards were weighed using a balance of one ten thousandths from METTLER TOLEDO (Switzerland).

2.2 Selection of surrogate peptides

Suitable surrogate peptides for absolute quantification of the aforementioned metabolic enzymes were selected by combining *in silico* and *in vitro* methods (Bhatt and Prasad, 2018). At first, the respective protein sequences were retrieved from the UniProtKB/Swiss-Prot database and underwent an *in-silico* trypsin digestion ([http://web.expasy.org/peptide mass/](http://web.expasy.org/peptide_mass/)). According to the mass range of the MS and to ensure protein specificity, peptides with a sequence length of 7–20 amino acids were considered as suitable candidates (Supplementary Table S1). Several criteria were chosen to establish the principles for selecting peptides: 1) surrogate peptides do not contain cysteine, methionine and/or tryptophan amino acids that can cause

TABLE 2 The intra- and inter-batch precision and accuracy of QC samples for surrogate peptides. The results of three analysis batches were used for inter-batch calculation. RSD, relative standard deviation; RE, relative error.

Protein	Peptide	Conc	Intra-batch (<i>n</i> = 6)			Inter-batch		
		(nM)	Mean ± SD (nM)	RSD (%)	RE (%)	Mean ± SD (nM)	RSD (%)	RE (%)
CYP1A2	YTSFVPFTIPHSTTR	5	4.33 ± 0.37	8.5	−13.3	4.94 ± 0.63	12.8	−1.3
		15	12.99 ± 0.03	0.2	−13.4	13.64 ± 1.04	7.6	−9.1
		150	132.93 ± 3.01	2.3	−11.4	140.43 ± 9.90	7.1	−6.4
		750	805.70 ± 43.89	5.4	7.4	810.98 ± 34.89	4.3	8.1
CYP2B1	FSDLVPIGVPHR	0.5	0.50 ± 0.08	15.6	−0.7	0.50 ± 0.07	13.8	−0.3
		1.5	1.34 ± 0.06	4.2	−10.7	1.46 ± 0.15	10.5	−2.8
		15	14.65 ± 0.57	3.9	−2.4	14.08 ± 0.84	6.0	−6.1
		75	77.99 ± 5.02	6.4	4.0	76.22 ± 5.00	6.6	1.6
CYP2C6	EALIDHGEEFAER	2	2.10 ± 0.29	13.9	5.0	2.21 ± 0.20	9.0	10.6
		6	5.63 ± 0.56	10.0	−6.1	5.67 ± 0.58	10.2	1.3
		60	57.10 ± 5.36	9.4	−4.8	56.22 ± 4.02	7.2	−4.1
		300	318.63 ± 11.45	3.6	6.2	307.89 ± 19.85	6.4	1.0
CYP2C11	YIDLVPNTLPHLVTR	5	4.44 ± 0.41	9.3	−11.2	4.53 ± 0.48	10.5	−8.4
		15	13.31 ± 0.68	5.1	−11.2	14.10 ± 1.21	8.6	−3.4
		150	143.94 ± 7.16	5.0	−4.0	143.73 ± 5.74	4.0	−4.2
		750	744.86 ± 59.31	8.0	−0.7	741.59 ± 54.62	7.4	−1.3
CYP2D1	GTTLIINLSSVLK	5	4.84 ± 0.45	9.3	−3.3	4.75 ± 0.58	12.3	−6.1
		15	13.80 ± 0.68	5.0	−8.0	13.72 ± 0.66	4.8	−8.8
		150	139.44 ± 10.51	7.5	−7.0	135.92 ± 7.45	5.5	−10.6
		750	664.79 ± 21.48	3.2	−11.4	674.67 ± 25.84	3.8	−9.3
CYP2E1	FINLVPSNLPHEATR	2	2.17 ± 0.23	10.8	8.5	1.98 ± 0.28	14.4	−4.3
		6	5.53 ± 0.42	7.7	−7.9	5.72 ± 0.43	7.5	−3.3
		60	56.53 ± 3.09	5.5	−5.8	54.89 ± 4.51	8.2	−9.9
		300	326.91 ± 19.61	6.0	9.0	311.22 ± 23.83	7.7	0.9
CYP3A1	QGLLQPTKPIILK	0.5	0.46 ± 0.06	13.0	−7.6	0.51 ± 0.08	15.0	2.2
		1.5	1.41 ± 0.19	13.4	−6.0	1.45 ± 0.12	8.3	−3.1
		15	14.04 ± 0.58	4.2	−6.4	14.22 ± 0.59	4.1	−5.2
		75	80.03 ± 2.60	3.3	6.7	76.46 ± 5.11	6.7	2.0

oxidative instability; 2) non-synonymous genetic polymorphisms with a frequency <1.0% in the population are required; 3) surrogate peptides with high specificity are preferentially selected by NCBI protein raw search; 4) repeated sequences of arginine and lysine should be avoided due to the risk of missed cleavages by trypsin.

2.3 Calibration standard and quality control samples

Stock solutions were prepared by dissolving about 1 mg of surrogate peptides or isotope-labeled peptides to obtain 1 mg/ml in ACN: Water: ACE: DMSO (15:80:5:0.5, v/v). All stock solutions were stored at −80°C. DMSO in the mixed solvent

was used to reduce the adsorption of peptides to plastic centrifuge tubes (van Midwoud et al., 2007; Li et al., 2022). The calibration standards were prepared by diluting stock solutions in the mixed solvent to generate analytical ranges of 5–1000 nM for CYP1A2, 2C11 and CYP2D1, 0.5–100 nM for CYP2B1 and 3A1, 2–400 nM for CYP2C6 and 2E1, and the quality control (QC) samples were set according to their respective standard curve ranges (Table 2). An internal standard solution containing all stable isotope-labeled internal standards was prepared and their final concentration was 50 nM except for GTTL*IINLSSVLK (CYP2D1) which was 500 nM. The high concentration of the internal standard was used for CYP2D1 to avoid the response reduction of isotope internal standard due to ion suppression caused by the analyte (Tan et al., 2011; Liu et al., 2019).

2.4 LC-MS/MS analysis

LC-MS/MS analyses were conducted on TSQ Quantum Access Max API mass spectrometer (ThermoFisher Scientific, Massachusetts, United States) with an electrospray ionization (H-ESI) interface coupled to an UHPLC system (ThermoFisher Scientific, Massachusetts, U.S.). Tune Plus® software 2.4 was used to control this instrument.

Chromatographic separation was performed using a C18 (100 × 2.1 mm, 3 μm) analytical column (Thermo Scientific, Massachusetts, United States). The column oven temperature was set to 35°C while the autosampler temperature was adjusted to 4°C. The flow rate of the mobile phase was set at 0.25 ml/min and the injection volume was 20 μL. For all peptides, elution was achieved under a gradient program. The initial mobile phase condition consisted of water with 0.1% FA (solvent A) and ACN (solvent B) (95:5, v/v). Gradient elution steps were 5–50% B (0–12 min), 50–95% B (12–12.5 min), 95% B (12.5–13 min), 95–5% B (13–13.5 min) and 5% B (13.5–15 min).

The mass spectrometer was equipped with the electrospray ionization and operated in the positive ion mode to monitor the m/z transitions for all peptides and their internal standards. Mass spectrometry parameters such as declustering potential and collision energy were manually optimized for every single peptide and were summarized in Table 1. The following ion source parameters were applied: the ESI spray voltage was set at 4000 V; vaporizer temperature was set at 350°C; capillary temperature was set at 300°C; sheath gas pressure and aux gas pressure were set at 20 and 10, respectively.

2.5 Digestion procedure

The rat liver microsome was diluted in NH₄HCO₃ (50 mM, pH7.8) to a total protein concentration of 1 mg/ml. 150 μL of diluted proteins were denatured at 95°C for 5 min and then added by 7.5 μL of DTT (500 mM) for the reduction of disulfide bonds in proteins. Samples were left at room temperature for 5 min and then incubated for 20 min at 60°C. Proteins were then alkylated with 15 μL of IAA (500 mM) and incubated at 37°C for 15 min in the dark. Samples were digested with trypsin at a trypsin/protein ratio of 1:40 at 37°C for 6 h. Digestion was terminated by adding 20 μL of ACN: Water: TFA (40:60:1, v/v/v). The mixture was vortexed for approximately 5 s and then centrifuged at 15,000 g for 10 min at 4°C. Internal standards solution was added to 160 μL of the clear supernatant and the mixed solution was evaporated to dryness under vacuum. The dried extract was re-suspended with 160 μL of ACN: Water: ACE: DMSO (15:80:5: 0.5, v/v) and transferred to an injection vial for analysis. Liver microsome samples (IPhase Pharma Services) were used to optimize the digestion time in the above process, and six samples were measured in parallel at each time point. The standard curve and quality control samples were prepared by

the above pretreatment steps after the standard solution was used to replace the rat liver microsomes.

2.6 Method validation

As shown in the current absolute quantitative analysis of proteomics, there is still no clear methodological guideline (Prasad et al., 2019). Therefore, we carried out the validation of the main content according to the bioanalytical guidelines combined with the needs of this research (FDA, 2018). We verified the accuracy, precision, linearity, stock solution stability, working solution stability, recovery, matrix effect and other parameters of the method.

2.7 Evaluation of matrix effect and recovery

The matrix effect was assessed by comparing the internal standard normalized response values of the standard solution group ($R_{Standard}$) and the rat liver microsome-spiked group (R_{Spiked}), and the latter needed to subtract the basal response ($R_{Non-spiked}$) for comparison. The internal standard used for normalization was added during the final reconstitution in pretreatment. The specific calculation is shown in formula 1.

$$Matrix\ effect\ (\%) = \frac{R_{Spiked} / R_{Spiked(IS)} - R_{Non-spiked} / R_{Non-spiked(IS)}}{R_{Standard} / R_{Standard(IS)}} \quad (1)$$

The relative recovery was calculated by comparing the spiked group with the internal standard added before vacuum evaporation (R'_{Spiked}) and the spiked group with the internal standard added during reconstitution (R_{Spiked}). Calculation was also performed using the base-subtracted response Eq. (2).

$$Recovery\ (\%) = \frac{R'_{Spiked} / R'_{Spiked(IS)} - R'_{Non-spiked} / R'_{Non-spiked(IS)}}{R_{Spiked} / R_{Spiked(IS)} - R_{Non-spiked} / R_{Non-spiked(IS)}} \quad (2)$$

2.8 Enzyme activity detection by probe substrate method

The enzyme activity of CYPs was calculated according to the formation rate of the substrate metabolite. The substrate drugs and metabolism of seven CYP enzymes are phenacetin and acetaminophen (CYP1A2), bupropion and hydroxy-bupropion (CYP2B1), tolbutamide and 4-Hydroxy-tolbutamide (CYP2C6), phenytoin and 4-Hydroxymephenytoin (CYP2C11), dextromethorphan and dextrorphan (CYP2D1), chlorzoxazone

and 6-Hydroxy-chlorzoxazone (CYP2E1), testosterone and 6 β -Hydroxytestosterone (CYP3A1). LC-MS/MS detection method refers to previous research reports (He et al., 2007; Zhang et al., 2021). The probe drug and NADPH (1 mM) were mixed in 195 μ L PBS (pH 7.4) for 1 min at 37°C. The enzymatic reaction was initiated by adding 5 μ L of rat liver microsomes (protein 20 mg/ml), incubated for 30 min at 37°C, and then terminated by adding ice-cold methanol containing IS glibenclamide. The sample was centrifuged at 15,000 g for 10 min at 4°C and 5 μ L supernatant was analyzed by LC-MS/MS to quantify the metabolites formed during these incubations. Each microsomal sample was assayed in triplicate.

2.9 Statistical analysis

The raw data was sorted using Microsoft Excel. Plotting used GraphPad Prism 8 (GraphPad Software Inc., San Diego, CA, United States). The Xcalibur software was used to establish the calibration curves fitted with weighted (1/X²) and to calculate the accuracy and precision of the QC samples for method validation ($n = 6$).

3 Results and discussion

3.1 Selection of surrogate peptide

Ideal surrogate peptides for metabolic enzymes require good chemical stability and specificity. Peptides of suitable length were first screened according to the trypsin cleavage site, and they do not contain labile amino acids such as cysteine, methionine, and tryptophan. Once selected, each peptide was evaluated with BLAST to confirm their specificity toward an isoform. According to parameters such as the E value, two surrogate peptides were finally selected for each metabolic enzyme, one for quantification and the other for qualitative research (Supplementary Table S1). For CYP3A1, although only one peptide was eligible for this study, it was fortunate that this peptide went well in the development and validation of the LC-MS/MS method. Furthermore, the surrogate peptide we used for CYP2E1 was consistent with those reported in a previous study (Ren et al., 2020), indicating the reproducibility of trypsin digestion across different laboratories. We also compared the surrogate peptides of the corresponding metabolic enzymes in rat and human liver microsomes, and found that the surrogate peptides of the reported enzyme isoforms were significantly different between species, except that the peptide of CYP2E1 was highly similar (Groer et al., 2014; Li and Zhu, 2020; Wenzel et al., 2021).

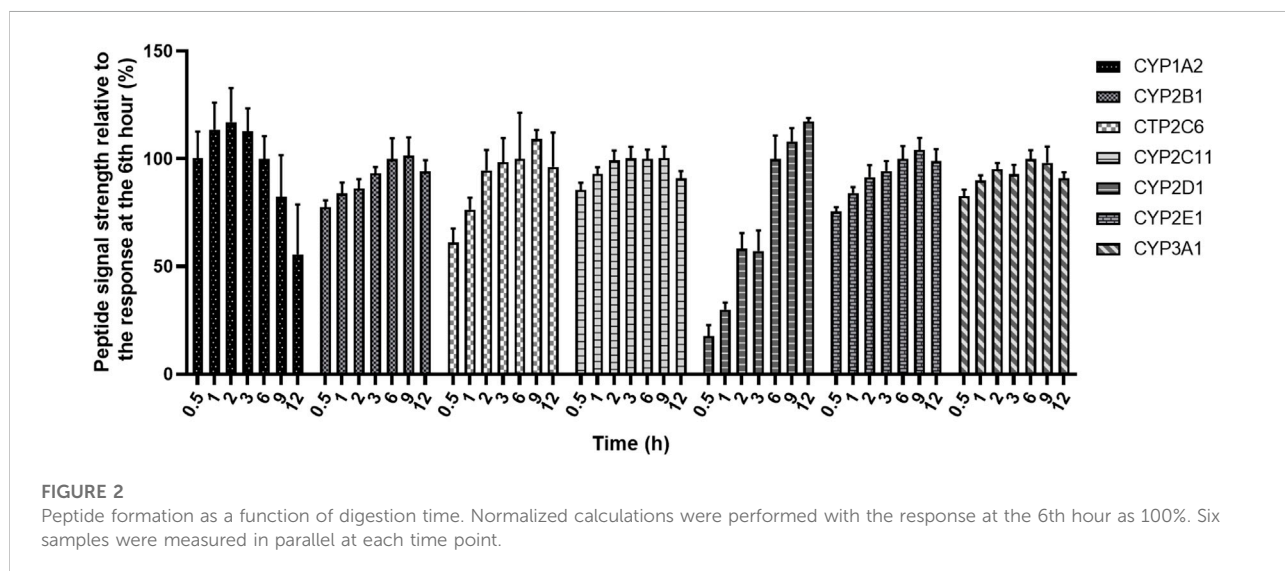
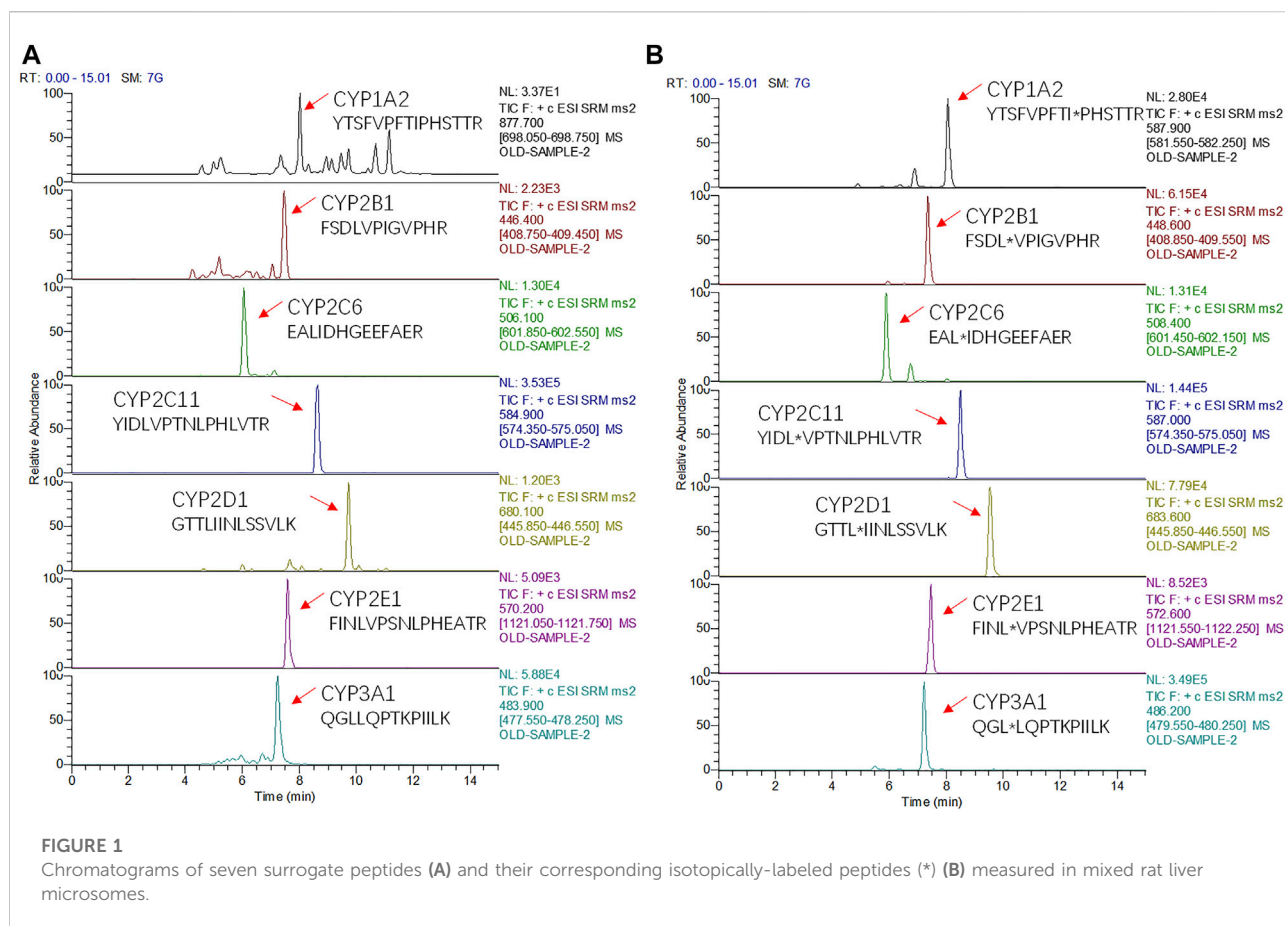
Stable isotope-labeled internal standards were synthesized for all surrogate peptides. With the ¹³C and ¹⁵N labeling, the

molecular weight of the stable isotope-labeled peptide was increased by 7 Da for leucine (L), as well as isoleucine (I). The sequences of surrogate peptides containing deuterated amino acids were shown in Table 1.

3.2 LC-MS/MS optimization

The mass spectrometer was operated in positive mode using electrospray ionization. The standard solution was continuously injected into the liquid phase and mixed before entering the mass spectrometer, and then the mass spectrometry conditions were optimized. For maximum sensitivity, we used the m/z ratio of the precursor ion with the highest signal intensity as the Q1 filter setting. Among most of the surrogate peptides screened this time, the signal intensity of the triple-charged or double-charged precursor ions was dominant. The precursor ions were then scanned for product ions to identify fragments showing the highest signal intensities, and the following parameters were optimized to determine optimal fragmentation conditions: collision energy, declustering potential, entry potential and collision cell exit potential. Final acceptance of ions used for quantification also required blank testing to exclude possible matrix-induced interferences. The optimal parameters used in the analysis method are shown in Table 1. It is worth mentioning that for the surrogate peptide of CYP3A1, the amino-terminal glutamine undergoes the cyclization to pyroglutamate and loses 17 Da, thereby changing the triple-charged precursor ion from m/z 484.0 to 478.0 (actual value: 477.9) (Purwaha et al., 2014).

The principle of chromatographic optimization is to avoid the matrix effect on the premise of ensuring the chromatographic peak shape. To capture all seven peptides of interest in one analytical run and to consider the expected complexity of the digested samples, a 15 min gradient elution method was used and all surrogate peptides could be separated by chromatography (Figure 1, Supplementary Figure S1). The use of 0.1% formic acid as the aqueous phase avoided the poor peak shape associated with pure water and the reduced signal caused by volatile salts. Compared with methanol, using acetonitrile for the organic phase increased the elution power and reduced the column pressure. The method established in this study combined the advantages of analysis time and quantity, which was superior to other methods of the same type reported in other studies. For example, Yi Ren et al. reported that a 16.5-min gradient method was used to detect only CYP2E1 in rat liver microsomes (Ren et al., 2020). In studies of metabolic enzymes and/or transporters in human liver microsomes, these simultaneous assays took about an hour longer (Kawakami et al., 2011; Groer et al., 2014; Grangeon et al., 2019). Therefore, this study greatly improved the analysis efficiency.



3.3 Optimization of digestion

The use of surrogate peptides as substitutes for quantifying target proteins requires robust and efficient digestion, which includes reduction, alkylation and

digestion duration. The time required for trypsin digestion is crucial. Therefore, this parameter needed to be optimized, and the digestion time was set to 0.5, 1, 2, 3, 6, 9, and 12 h in this study. As shown in Figure 2, there were differences in the digestion profiles of seven CYP proteins. All the substituted

TABLE 3 Stability of seven surrogate peptides. Results are expressed as percent nominal \pm SD ($n = 6$).

Protein	Peptide	Conc	Stock solution (4 months, -80°C)	Standard working solution (1 week, -80°C)	Stability during digestion (6 h, 37°C)	In autosampler (12 h, 10°C)
		(nM)	%Nominal (mean \pm SD)	%Nominal (mean \pm SD)	%Nominal (mean \pm SD)	%Nominal (mean \pm SD)
CYP1A2	YTSFVPFTIPHSSTR	15	96.88 \pm 9.41	99.21 \pm 8.86	103.68 \pm 5.04	104.85 \pm 10.52
		150	98.85 \pm 6.53	96.52 \pm 8.61	102.47 \pm 6.15	103.94 \pm 6.22
		750	95.66 \pm 4.03	102.23 \pm 2.99	96.36 \pm 7.96	99.73 \pm 5.05
CYP2B1	FSDLVPIGVPHR	1.5	101.83 \pm 8.97	98.70 \pm 8.00	90.37 \pm 7.02	105.46 \pm 7.06
		15	101.53 \pm 4.37	99.62 \pm 5.81	92.09 \pm 6.96	103.46 \pm 4.74
		75	99.67 \pm 5.93	99.97 \pm 5.08	104.14 \pm 4.20	103.75 \pm 2.65
CYP2C6	EALIDHGEEFAER	6	108.03 \pm 4.08	97.95 \pm 7.49	102.72 \pm 7.10	104.84 \pm 12.60
		60	99.27 \pm 8.92	99.45 \pm 8.15	103.23 \pm 7.32	112.76 \pm 2.46
		300	103.38 \pm 3.67	99.67 \pm 6.83	102.80 \pm 4.41	103.78 \pm 8.46
CYP2C11	YIDLVPNTLPHLVTR	15	95.67 \pm 2.18	107.26 \pm 3.12	95.55 \pm 5.26	111.18 \pm 3.53
		150	102.42 \pm 1.48	100.86 \pm 5.45	90.85 \pm 1.46	106.67 \pm 4.02
		750	97.24 \pm 2.69	97.27 \pm 2.49	91.36 \pm 4.42	102.22 \pm 3.75
CYP2D1	GTTLIINLSSVLK	15	95.53 \pm 4.37	100.29 \pm 9.50	100.72 \pm 8.13	100.32 \pm 7.31
		150	96.77 \pm 8.78	94.47 \pm 4.87	102.16 \pm 9.29	96.04 \pm 5.43
		750	108.56 \pm 5.33	111.13 \pm 8.98	106.07 \pm 1.62	112.42 \pm 2.77
CYP2E1	FINLVPSNLPHEATR	6	105.74 \pm 5.24	101.60 \pm 9.15	96.63 \pm 3.16	100.66 \pm 9.82
		60	101.31 \pm 8.05	107.21 \pm 7.09	101.14 \pm 7.30	99.02 \pm 8.73
		300	94.76 \pm 8.14	97.32 \pm 5.14	89.64 \pm 0.67	95.49 \pm 5.93
CYP3A1	QGLLQPTKPIILK	1.5	95.47 \pm 5.18	95.20 \pm 5.21	99.91 \pm 12.61	111.87 \pm 3.36
		15	100.91 \pm 3.68	103.24 \pm 2.83	98.61 \pm 3.60	107.38 \pm 7.30
		75	100.37 \pm 6.11	103.16 \pm 6.18	95.81 \pm 6.93	101.50 \pm 2.84

peptides except CYP1A2 reached the content plateau at the 6th hour, and CYP2D1 content increased significantly with time until the 6th hour. However, the content of CYP1A2 has been relatively stable at 0.5 h, and has a downward trend from 6 h later. This phenomenon has also been reported by other studies (Grangeon et al., 2019; Ren et al., 2020). The stability experiment has proved that the peptide itself was stable during digestion (Table 3), so the possible reason for the decline may be the influence of its own digestive enzymes in rat liver microsomes. In conclusion, it was decided to terminate the digestion at the 6th hour.

3.4 Selection of blank matrix

The current LC-MS/MS-based CYP enzyme quantification methods mainly use the following three types of blank matrices to establish standard curves and QC samples: 1) Other tissues or serum of the same species or different species, such as 5% rat serum (Ren et al., 2020), human serum albumin (Groer et al., 2014), bovine serum albumin (Wenzel et al., 2021); 2) the same matrix, standard curve correction by subtracting the substrate (Sakamoto

et al., 2011; Ohtsuki et al., 2012); 3) Standard solution without biological matrix (Grangeon et al., 2019). Serum protein is significantly different from that in liver microsomes, which may lead to different matrix effects affecting the quantitative analysis. If the standard curve is prepared using the same matrix or the same matrix diluted, the calculation process is complicated, and the subtraction of the blank matrix response may introduce bias, especially for low-concentration samples. Therefore, in this study, the influence of the matrix effect on quantification was significantly reduced by optimizing the chromatographic conditions, so that the standard curve prepared with the standard solution became simple and practical. Although the method still has a slight matrix effect and different degrees of absolute recovery (Supplementary Table S2), the isotope internal standard normalized matrix effect and relative recovery were all around 100% and the relative standard deviation was also less than 20% (Table 4). Therefore, in this method, it is reasonable and reliable to use a standard solution instead of liver microsomes to prepare standard curve and QC samples, and the internal standard for the above samples was added after the termination of digestion and before vacuum drying.

TABLE 4 Summary of internal standard normalized matrix effect and relative recovery in rat liver microsomes for all surrogate peptides. Results are expressed as percent nominal; RSD, relative standard deviation ($n = 6$).

Protein	Peptide	Conc	Matrix effect		Absolute recovery	
		(nM)	%Nominal	RSD (%)	%Nominal	RSD (%)
CYP1A2	YTSFVPFTIPHSTTR	15	111.14	12.5	98.55	14.1
		150	119.69	7.7	96.32	9.9
		750	117.96	5.8	98.89	11.6
CYP2B1	FSDLVPIGVPHR	1.5	111.48	16.9	95.59	16.8
		15	98.40	5.0	91.94	5.1
		75	99.41	5.0	95.14	7.1
CYP2C6	EALIDHGEEFAER	6	119.36	15.2	103.19	3.9
		60	98.33	7.8	90.64	8.0
		300	100.92	12.2	91.77	6.4
CYP2C11	YIDLVPNTNPLHLVTR	15	93.59	17.2	107.23	6.1
		150	81.05	9.1	104.87	11.6
		750	95.31	9.4	94.24	11.2
CYP2D1	GTTLIINLSSVLK	15	107.25	8.5	111.40	14.4
		150	118.57	11.7	109.98	10.9
		750	118.40	8.6	109.30	12.3
CYP2E1	FINLVPSNLPHEATR	6	108.97	14.0	101.79	18.6
		60	98.61	14.6	91.68	13.7
		300	96.21	12.0	98.79	6.2
CYP3A1	QGLLQPTKPIILK	1.5	98.42	8.6	107.05	15.8
		15	94.22	3.4	97.53	10.4
		75	95.51	4.3	98.02	5.9

TABLE 5 Protein amounts of CYP enzymes as observed in pooled rat liver microsomes from four sources (IPhase Pharma Services, Corning Gentest, PrimeTox and Meilunbio). Results are expressed as concentration (Mean \pm SD) ($n = 4$).

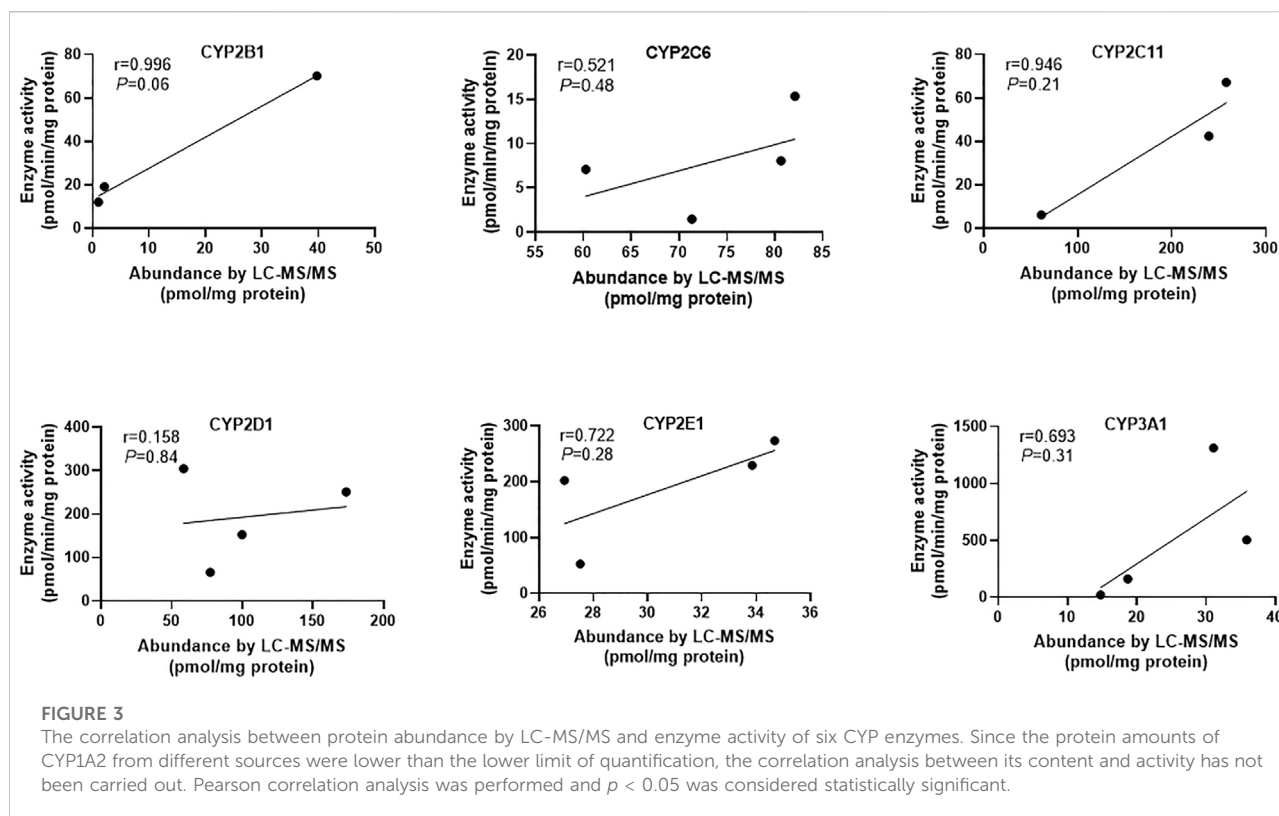
Protein	Peptide	Protein amount (pmol/mg of protein, mean \pm SD)			
		Source 1	Source 2	Source 3	Source 4
CYP1A2	YTSFVPFTIPHSTTR	-	-	-	-
CYP2B1	FSDLVPIGVPHR	1.02 \pm 0.05	2.06 \pm 0.05	39.77 \pm 1.52	-
CYP2C6	EALIDHGEEFAER	60.25 \pm 4.46	82.11 \pm 2.72	80.65 \pm 3.95	71.34 \pm 7.31
CYP2C11	YIDLVPNTNPLHLVTR	239.46 \pm 10.89	258.00 \pm 8.73	61.34 \pm 2.55	-
CYP2D1	GTTLIINLSSVLK	173.52 \pm 10.35	58.36 \pm 5.79	99.76 \pm 9.63	77.29 \pm 10.01
CYP2E1	FINLVPSNLPHEATR	26.94 \pm 0.51	34.68 \pm 1.23	33.85 \pm 1.78	27.52 \pm 1.20
CYP3A1	QGLLQPTKPIILK	18.69 \pm 0.99	14.77 \pm 0.76	35.86 \pm 0.75	31.06 \pm 2.24

3.5 Method validation

3.5.1 LLOQ and linearity

The method was found to be linear over the appropriate calibration range for all surrogate peptides. Linear regression (weighted $1/X^2$) yielded the best fit of the

concentration-response relationship. During assay validation, the correlation coefficient (r^2) for all calibration curves ranged between 0.985 and 1.0 (Supplementary Table S3). Therefore, the LLOQ was set 5 nM (CYP1A2, 2C11 and 2D1), 0.5 nM (CYP2B1 and 3A1), or 2 nM (CYP2C6 and 2E1) (Table 2). For LLOQ, the



precision was better than 15%, and the accuracy was between 80.0–120%.

3.5.2 Precision and accuracy

The precision and accuracy were assessed by observing the analysis of QC samples at three concentrations (low, medium and high) in three analytical runs ($n = 6$). Precision was reflected by the relative standard deviation (RSD) and should be better than 15%. Accuracy was assessed using relative error (RE) and should be within the recommended range of acceptance (85.0–115.0%). Intra- and inter-batch precision and accuracy for all surrogate peptides met the above requirements. The results were shown in Table 2.

3.5.3 Stability

To assess the stability of the surrogate peptides, we performed several stability experiments. For stability data, the precision ($n = 6$) should not exceed 15% and the mean accuracy value should be within $\pm 15\%$ of the nominal value. Stock stability was assessed by comparing stocks stored at -80°C for four months with fresh stocks. QC samples were stored at -80°C for 1 week to assess the short-term stability of the peptides. After trypsin digestion for six hours, the QC concentration peptides were compared with

the QC samples without this process to investigate the stability of these peptides in the digestion process. The QC samples were placed in the autosampler for 12 h and compared with the freshly prepared samples for the stability test in the autosampler. All stability results met the above criteria and indicated that all peptides were stable during the method validation (Table 3).

3.6 Determination of CYPs in rat liver microsomes

This absolute quantification method was successfully applied to the quantification of seven CYP isoforms in commercial mixed rat liver microsomes from four different sources (Table 5). The abundance of the metabolic enzymes including CYP2B1, 2C11, 2D1 and 3A1 in rat liver microsomes from these four sources was significantly different. The results of CYPs determined from sources 1 and 2 were similar, and CYP2C11 was the highest. The content of CYP2C11 in source 3 was low, while the result in source 4 was lower than the lower limit of quantification (6.25 pmol/mg). Since CYP2C11 is not expressed in immature rats and is induced dramatically at puberty (beginning 4–5 weeks of age) in male rats (Martignoni et al., 2006), we

speculated that the age of rats was the main factor leading to the low content of CYP2C11 in 3 and 4 sources. For the content of CYPs in liver microsomes of SD rats, CYP2E1 has been reported to be about 5–25 pmol/mg, which is higher than the enzyme content in liver S9 fractions (2–8 pmol/mg) (Ren et al., 2020). The CYP2E1 content determined in this study was close to the upper limit of the content reported above. In the study of Hammer H et al., the contents of CYP1A2, 2B1/2, 2C11 and 2E1 in liver tissue samples of male Wistar rats were 1.3, 0.2, 58 and 5.9 fmol/ μ g (pmol/mg) respectively (Hammer et al., 2021). These results were lower than those of this study. In addition to species, sample types should be a key factor in the difference between the two studies.

In addition, the relationship between the abundance and activity of CYPs was also studied. The results showed that the content and activity of each CYP enzyme had a positive correlation trend, but there was no statistical significance (Figure 3). The reasons for the above phenomena include: 1) the absolute protein quantitative method based on LC-MS/MS has very high specificity for CYP isoforms, while the drug indicating enzyme activity in the probe substrate method usually lacks sufficient specificity, so there is a potential deviation in the results of enzyme activity (Giri et al., 2019); 2) The number of samples measured in this study was small, so it is necessary to expand the samples to further explore the law. It has been reported that immunological methods including WB are not specific enough for the determination of CYPs content, which may lead to contradictory conclusions (Ren et al., 2020). LC-MS/MS method has the advantages of high specificity and high throughput. Therefore, the method established in this study will greatly improve the reliability of related research in the field of drug metabolism based on the rat liver microsomal model.

4 Conclusion

In the present work, we developed and validated an LC-MS/MS-based targeted proteomics for simultaneous absolute quantification of seven major CYP enzymes in rat liver microsomes. The optimized pretreatment and chromatographic conditions ensured the robustness of the method, and the assays were validated for selectivity, linearity, matrix effect, recovery, stability, precision and accuracy. Finally, this method was successfully applied to the detection of rat liver microsome samples from four sources. This study provides a high-throughput and stable technical basis for the study of drug metabolism in the rat.

Data availability statement

The original contributions presented in the study are included in the article/Supplementary Material, further inquiries can be directed to the corresponding authors.

Author contributions

FJ designed and performed the experiments, analyzed the data, and wrote the manuscript. CZ performed the experiments and statistical analysis. ZL and JL assisted in performing the experiments. PL and MH gave technical guidance. MH and GZ revised the manuscript. All authors read and approved the final manuscript.

Funding

The authors appreciate the financial support provided by the National Natural Science Foundation of China (No. 82173776); Natural Science Foundation of Guangdong Province (No. 2021A1515010574); China Postdoctoral Science Foundation (No. 2020M683140); Guangdong Basic and Applied Basic Research Foundation (No. 2021A1515110346).

Conflict of interest

The authors declare that the research was conducted in the absence of any commercial or financial relationships that could be construed as a potential conflict of interest.

Publisher's note

All claims expressed in this article are solely those of the authors and do not necessarily represent those of their affiliated organizations, or those of the publisher, the editors and the reviewers. Any product that may be evaluated in this article, or claim that may be made by its manufacturer, is not guaranteed or endorsed by the publisher.

Supplementary material

The Supplementary Material for this article can be found online at: <https://www.frontiersin.org/articles/10.3389/fphar.2022.906027/full#supplementary-material>

References

- An, B., Zhang, M., Pu, J., Shen, S., Qu, Y., Chen, Y. J., et al. (2019). High-throughput, sensitive LC-MS quantification of biotherapeutics and biomarkers using antibody-free, peptide-level, multiple-mechanism enrichment via strategic regulation of pH and ionic and solvent strengths. *Anal. Chem.* 91 (5), 3475–3483. doi:10.1021/acs.analchem.8b05046
- Bhatt, D. K., and Prasad, B. (2018). Critical issues and optimized practices in quantification of protein abundance level to determine interindividual variability in DMET proteins by LC-MS/MS proteomics. *Clin. Pharmacol. Ther.* 103 (4), 619–630. doi:10.1002/cpt.819
- Couto, N., Al-Majdoub, Z. M., Gibson, S., Davies, P. J., Achour, B., Harwood, M. D., et al. (2020). Quantitative proteomics of clinically relevant drug-metabolizing enzymes and drug transporters and their intercorrelations in the human small intestine. *Drug Metab. Dispos.* 48 (4), 245–254. doi:10.1124/dmd.119.089656
- De Nicolo, A., Cantu, M., and D'Avolio, A. (2017). Matrix effect management in liquid chromatography mass spectrometry: the internal standard normalized matrix effect. *Bioanalysis* 9 (14), 1093–1105. doi:10.4155/bio-2017-0059
- Dostalek, M., Court, M. H., Yan, B. F., and Akhlaghi, F. (2011). Significantly reduced cytochrome P450 3A4 expression and activity in liver from humans with diabetes mellitus. *Br. J. Pharmacol.* 163 (5), 937–947. doi:10.1111/j.1476-5381.2011.01270.x
- Fda (2018). Bioanalytical method validation guidance for industry. Available at: <https://www.fda.gov/regulatory-information/search-fda-guidance-documents/bioanalytical-method-validation-guidance-industry>.
- Giri, P., Patel, H., and Srinivas, N. R. (2019). Use of cocktail probe drugs for indexing cytochrome P450 enzymes in clinical Pharmacology studies - review of case studies. *Drug Metab. Lett.* 13 (1), 3–18. doi:10.2174/1872312812666181119154734
- Grangeon, A., Clermont, V., Barama, A., Gaudette, F., Turgeon, J., Michaud, V., et al. (2019). Development and validation of an absolute protein assay for the simultaneous quantification of fourteen CYP450s in human microsomes by HPLC-MS/MS-based targeted proteomics. *J. Pharm. Biomed. Anal.* 173, 96–107. doi:10.1016/j.jpba.2019.05.006
- Groer, C., Busch, D., Patrzyk, M., Beyer, K., Busemann, A., Heidecke, C. D., et al. (2014). Absolute protein quantification of clinically relevant cytochrome P450 enzymes and UDP-glucuronosyltransferases by mass spectrometry-based targeted proteomics. *J. Pharm. Biomed. Anal.* 100, 393–401. doi:10.1016/j.jpba.2014.08.016
- Hammer, H., Schmidt, F., Marx-Stoelting, P., Potz, O., and Braeuning, A. (2021). Cross-species analysis of hepatic cytochrome P450 and transport protein expression. *Arch. Toxicol.* 95 (1), 117–133. doi:10.1007/s00204-020-02939-4
- He, F., Bi, H. C., Xie, Z. Y., Zuo, Z., Li, J. K., Li, X., et al. (2007). Rapid determination of six metabolites from multiple cytochrome P450 probe substrates in human liver microsome by liquid chromatography/mass spectrometry: application to high-throughput inhibition screening of terpenoids. *Rapid Commun. Mass Spectrom.* 21 (5), 635–643. doi:10.1002/rcm.2881
- Kawakami, H., Ohtsuki, S., Kamiie, J., Suzuki, T., Abe, T., Terasaki, T., et al. (2011). Simultaneous absolute quantification of 11 cytochrome P450 isoforms in human liver microsomes by liquid chromatography tandem mass spectrometry with *in silico* target peptide selection. *J. Pharm. Sci.* 100 (1), 341–352. doi:10.1002/jps.22255
- Li, J., and Zhu, H. J. (2020). Liquid chromatography-tandem mass spectrometry (LC-MS/MS)-Based proteomics of drug-metabolizing enzymes and transporters. *Molecules* 25 (11), E2718. doi:10.3390/molecules25112718
- Li, Q., Jiang, F., Guan, Y., Jiang, X., Wu, J., Huang, M., et al. (2022). Development, validation and application of a UHPLC-MS/MS method for quantification of the adiponectin-derived active peptide ADP355 in rat plasma. *Biomed. Chromatogr.* 36, e5358. doi:10.1002/bmc.5358
- Liu, Q., Jiang, F., Zhu, J., Zhong, G., and Huang, M. (2019). Development, validation, and application of a New method to correct the nonlinearity problem in LC-MS/MS quantification using stable isotope-labeled internal standards. *Anal. Chem.* 91 (15), 9616–9622. doi:10.1021/acs.analchem.9b00947
- Manikandan, P., and Nagini, S. (2018). Cytochrome P450 structure, function and clinical significance: a review. *Curr. Drug Targets* 19 (1), 38–54. doi:10.2174/1389450118666170125144557
- Martignoni, M., Groothuis, G. M. M., and de Kanter, R. (2006). Species differences between mouse, rat, dog, monkey and human CYP-mediated drug metabolism, inhibition and induction. *Expert Opin. Drug Metab. Toxicol.* 2 (6), 875–894. doi:10.1517/17425255.2.6.875
- Ohtsuki, S., Schaefer, O., Kawakami, H., Inoue, T., Liehner, S., Saito, A., et al. (2012). Simultaneous absolute protein quantification of transporters, cytochromes P450, and UDP-glucuronosyltransferases as a novel approach for the characterization of individual human liver: comparison with mRNA levels and activities. *Drug Metab. Dispos.* 40 (1), 83–92. doi:10.1124/dmd.111.042259
- Pearce, R. E., Gaedigk, R., Twist, G. P., Dai, H., Riffel, A. K., Leeder, J. S., et al. (2016). Developmental expression of CYP2B6: A comprehensive analysis of mRNA expression, protein content and bupropion hydroxylase activity and the impact of genetic variation. *Drug Metab. Dispos.* 44 (7), 948–958. doi:10.1124/dmd.115.067546
- Prasad, B., Achour, B., Artursson, P., Hop, C., Lai, Y., Smith, P. C., et al. (2019). Toward a consensus on applying quantitative liquid chromatography-tandem mass spectrometry proteomics in translational Pharmacology research: a white paper. *Clin. Pharmacol. Ther.* 106 (3), 525–543. doi:10.1002/cpt.1537
- Purwaha, P., Silva, L. P., Hawke, D. H., Weinstein, J. N., and Lorenzi, P. L. (2014). An artifact in LC-MS/MS measurement of glutamine and glutamic acid: in-source cyclization to pyroglutamic acid. *Anal. Chem.* 86 (12), 5633–5637. doi:10.1021/ac501451v
- Ren, Y., Ding, Y., Meng, F., Jiang, L., Li, H., Huang, J., et al. (2020). Quantification of CYP2E1 in rat liver by UPLC-MS/MS-based targeted proteomics assay: a novel approach for enzyme activity assessment. *Anal. Bioanal. Chem.* 412 (22), 5409–5418. doi:10.1007/s00216-020-02757-8
- Sakamoto, A., Matsumaru, T., Ishiguro, N., Schaefer, O., Ohtsuki, S., Inoue, T., et al. (2011). Reliability and robustness of simultaneous absolute quantification of drug transporters, cytochrome P450 enzymes, and Udp-glucuronosyltransferases in human liver tissue by multiplexed MRM/selected reaction monitoring mode tandem mass spectrometry with nano-liquid chromatography. *J. Pharm. Sci.* 100 (9), 4037–4043. doi:10.1002/jps.22591
- Shao, Y., Yin, X., Kang, D., Shen, B., Zhu, Z., Li, X., et al. (2017). An integrated strategy for the quantitative analysis of endogenous proteins: a case of gender-dependent expression of P450 enzymes in rat liver microsome. *Talanta* 170, 514–522. doi:10.1016/j.talanta.2017.04.050
- Singh, D., Kashyap, A., Pandey, R. V., and Saini, K. S. (2011). Novel advances in cytochrome P450 research. *Drug Discov. Today* 16 (17–18), 793–799. doi:10.1016/j.drudis.2011.08.003
- Tan, A., Levesque, I. A., Levesque, I. M., Viel, F., Boudreau, N., Levesque, A., et al. (2011). Analyte and internal standard cross signal contributions and their impact on quantitation in LC-MS based bioanalysis. *J. Chromatogr. B Anal. Technol. Biomed. Life Sci.* 879 (21), 1954–1960. doi:10.1016/j.jchromb.2011.05.027
- van Midwoud, P. M., Rieux, L., Bischoff, R., Verpoorte, E., and Niederlander, H. A. (2007). Improvement of recovery and repeatability in liquid chromatography-mass spectrometry analysis of peptides. *J. Proteome Res.* 6 (2), 781–791. doi:10.1021/pr0604099
- Wegler, C., Gaugaz, F. Z., Andersson, T. B., Wisniewski, J. R., Busch, D., Groer, C., et al. (2017). Variability in mass spectrometry-based quantification of clinically relevant drug transporters and drug metabolizing enzymes. *Mol. Pharm.* 14 (9), 3142–3151. doi:10.1021/acs.molpharmaceut.7b00364
- Wenzel, C., Drozdzik, M., and Oswald, S. (2021). Mass spectrometry-based targeted proteomics method for the quantification of clinically relevant drug metabolizing enzymes in human specimens. *J. Chromatogr. B Anal. Technol. Biomed. Life Sci.* 1180, 122891. doi:10.1016/j.jchromb.2021.122891
- Xie, F., Ding, X., and Zhang, Q. Y. (2016). An update on the role of intestinal cytochrome P450 enzymes in drug disposition. *Acta Pharm. Sin. B* 6 (5), 374–383. doi:10.1016/j.apsb.2016.07.012
- Zanger, U. M., and Schwab, M. (2013). Cytochrome P450 enzymes in drug metabolism: regulation of gene expression, enzyme activities, and impact of genetic variation. *Pharmacol. Ther.* 138 (1), 103–141. doi:10.1016/j.pharmthera.2012.12.007
- Zhang, H. F., Wang, H. H., Gao, N., Wei, J. Y., Tian, X., Zhao, Y., et al. (2016). Physiological content and intrinsic activities of 10 cytochrome P450 isoforms in human normal liver microsomes. *J. Pharmacol. Exp. Ther.* 358 (1), 83–93. doi:10.1124/jpet.116.233635
- Zhang, Y. J., Zhou, W. L., Yu, F., Wang, Q., Peng, C., Kan, J. Y., et al. (2021). Evaluation of the effect of bovis calculus artifactus on eight rat liver cytochrome P450 isozymes using LC-MS/MS and cocktail approach. *Xenobiotica* 51 (9), 1010–1018. doi:10.1080/00498254.2021.1959673

Advantages of publishing in Frontiers



OPEN ACCESS

Articles are free to read
for greatest visibility
and readership



FAST PUBLICATION

Around 90 days
from submission
to decision



HIGH QUALITY PEER-REVIEW

Rigorous, collaborative,
and constructive
peer-review



TRANSPARENT PEER-REVIEW

Editors and reviewers
acknowledged by name
on published articles

Frontiers

Avenue du Tribunal-Fédéral 34
1005 Lausanne | Switzerland

Visit us: www.frontiersin.org

Contact us: frontiersin.org/about/contact



REPRODUCIBILITY OF RESEARCH

Support open data
and methods to enhance
research reproducibility



DIGITAL PUBLISHING

Articles designed
for optimal readership
across devices



FOLLOW US

@frontiersin



IMPACT METRICS

Advanced article metrics
track visibility across
digital media



EXTENSIVE PROMOTION

Marketing
and promotion
of impactful research



LOOP RESEARCH NETWORK

Our network
increases your
article's readership